COBALT COMPLEXES WITH BIS-IMIDAZOLE & BIS-BENZAZOLE LIGANDS AS CATALYSTS FOR THE HYDROGEN EVOLUTION REACTION

SANDER DINAND DE VOS

Cobalt Complexes with Bis-Imidazole and Bis-Benzazole Ligands as Catalysts for the Hydrogen Evolution Reaction

Kobaltcomplexen met Bis-imidazool en Bis-benzazol liganden als katalysatoren voor de waterstofevolutiereactie

(met een samenvatting in het Nederlands)

Proefschrift

ter verkrijging van de graad van doctor aan de Universiteit Utrecht op gezag van de rector magnificus, prof. dr. H.R.B.M. Kummeling, ingevolge het besluit van het college voor promoties in het openbaar te verdedigen op vrijdag 27 oktober 2023 des middags te 2.15 uur

door

Sander Dinand de Vos

geboren op 6 november 1992 te Deventer

Promotor:

Prof. dr. R. J. M. Klein Gebbink

Copromotor:

Dr. Daniël L. J. Broere

Beoordelingscommissie:

Prof. dr. P.C.A. Bruijnincx

Dr. D.G.H. Hetterscheid

Prof. dr. A. Meijerink

Prof. dr. P. Schollhammer

Prof. dr. E.T.C. Vogt

The work described in this thesis was financially supported by the Netherlands Organization for Scientific Research within its joint NWO-NSFC program on *Supramolecular Chemistry and Catalysis* (grant number 729.001.034)

Cobalt Complexes with Bis-Imidazole and Bis-Benzazole Ligands as Catalysts for the Hydrogen Evolution Reaction

Voor mijn moeder Jantien de Vos - Holtland en
vader Henk de Vos† (24-02-1952 – 21-10-2017)

De Vos, Sander Dinand

Cobalt Complexes with Bis-Imidazole and Bis-Benzazole Ligands as Catalysts for the Hydrogen Evolution Reaction

The work described in this doctoral thesis was carried out in the Organic Chemistry and Catalysis (OCC) group, Institute for Sustainable and Circular Chemistry, Faculty of Science, Utrecht University, The Netherlands.

Cover: In the top right corner of the cover is the sun depicted, from which almost all our energy (99%) originates. The sun can only shine on one-half of the Earth, if clouds do not prevent this, and therefore we need energy carriers, such as hydrogen gas, to store the energy for all moments that this energy is not accessible. On the back are a collection of planets depicted that contain the most hydrogen gas (Mercury, Jupiter, Saturn, Uranus Neptune).

Cover design: Nathan Roos

Print: Ridderprint | www.ridderprint.nl

Contents

Chapter 1

Introduction

Abstract

The development of hydrogen evolution catalysts based on non-noble metals has gained severe interest over the last 20 years, mainly because of the strong desire to store renewable energy into chemical bonds with a low carbon footprint. In nature, hydrogenase enzymes, holding catalytic centers based on non-noble metals, can form hydrogen with good efficiency, meaning that its production occurs at a significant rate while a minimum amount of energy is lost in the process. Synthetically, the same efficiency can only be achieved using scarce and expensive Pt-group catalysts. As a result, chemists try to design new non-noble metal catalysts that catalyze the hydrogen evolution reaction in an efficient manner. This introduction chapter aims to explain the necessity for the development of new catalytic hydrogen evolution materials and the use of molecular complexes in perusing this goal, with a special focus on cobalt complexes. Throughout the chapter, design principles, mechanistic insights, activity, stability, and operational conditions of molecular cobalt catalysts for hydrogen evolution are highlighted. At the end of the chapter, the aim and scope of this thesis is outlined.

1.1 General Introduction

1.1.1 A global energy challenge

Since the industrial revolution in the 18th century an ever-increasing amount of fossil fuel has been burned to supply the energy for our society.[1] In recent decades, a major downside of these energy sources has come to light. By burning accumulated carbon reservoirs, large amounts of CO_2 and other greenhouse gases are released into the atmosphere. As a result, the CO_2 concentration in the atmosphere in the Antarctic is currently above 300 ppm and still rising, where it has not been above 300 ppm for thousands of years (**Figure 1**).[2,3] Greenhouse gases

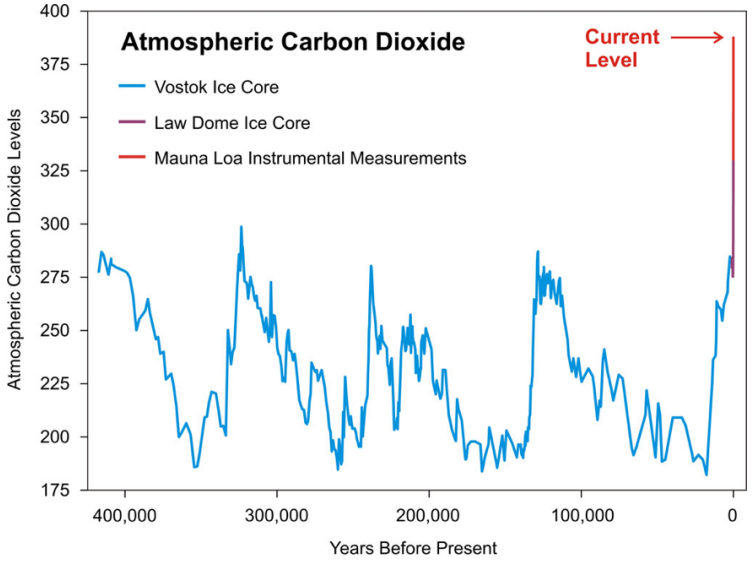

Figure 1. The CO_2 concentration (ppm) over the course of 400,000 years, measured by samples from the air trapped in Antarctic ice (blue), and more recent atmospheric CO_2 measurements in the Antarctic (purple) and Hawaii (red).[2,3,11] CO_2 levels measured at Vostok, Antarctica (blue); Law Dome, East Antarctica (purple); and Mauna Loa, Hawaii (red).[12] Reproduced from Skeptical Science with permission (creative commons).

in the atmosphere repeatedly absorb and re-radiate infrared radiation (heat), impeding the loss of heat from our atmosphere to space and therefore causing global warming.[4] As a result, the arctic ice melts,[5] sea levels rise,[5] weather conditions intensify,[6,7] and oceans acidify and deoxygenate.[8] These consequences already induced severe problems in some highly populated areas all over the world, such as Japan, the Philippines, Madagascar, India, and Puerto Rico, but also in our neighboring country Germany, which in 2018 experienced the hottest year since records began due to a severe heatwave resulting in 70% of the soil being affected by drought.[9] In The Netherlands we are more often affected by extreme weather, there will be more torrential rain, heavier storms, and longer periods of drought and heat. The Netherlands is also particularly vulnerable to flooding because 26% of our country lies below sea level.[10] Today

our energy consumption is still growing, while 85% of the energy is produced by fossil fuels.[13,14] Therefore, the quest for renewable energy is urgent.[15] Renewable energy sources include reserves that are functionally inexhaustible or can be supplemented at the same rate as consumption, such as solar, wind, geothermal energy, biomass, ocean thermal energy conversion (OTEC), hydroelectric power, and tidal/waves power.[16] Luckily, these resources are sufficiently rich in energy to easily meet the estimated near future (30 years) energy demands (**Figure 2**).[16] Especially solar energy is of interest, as one hour of sunlight hitting the earth is enough to provide energy for the world for a whole year and a single year of sunshine exceeds all known energy reserves of coal, petroleum, natural gas, and uranium put together.[16,17] With the current technology efficiencies we can capture enough energy with 20 m^2 of solar panels per household, although it should be mentioned that the energy consumption around the world is far from balanced. In addition, the energy flux of sunlight that arrives at the earth's surface is not constant and varies significantly along the day, the season of the year, weather conditions, and location. And unlike natural non-renewable recourses, we can't store sunshine to use its energy when we need it to make more electricity.[18] So, if the sun hides

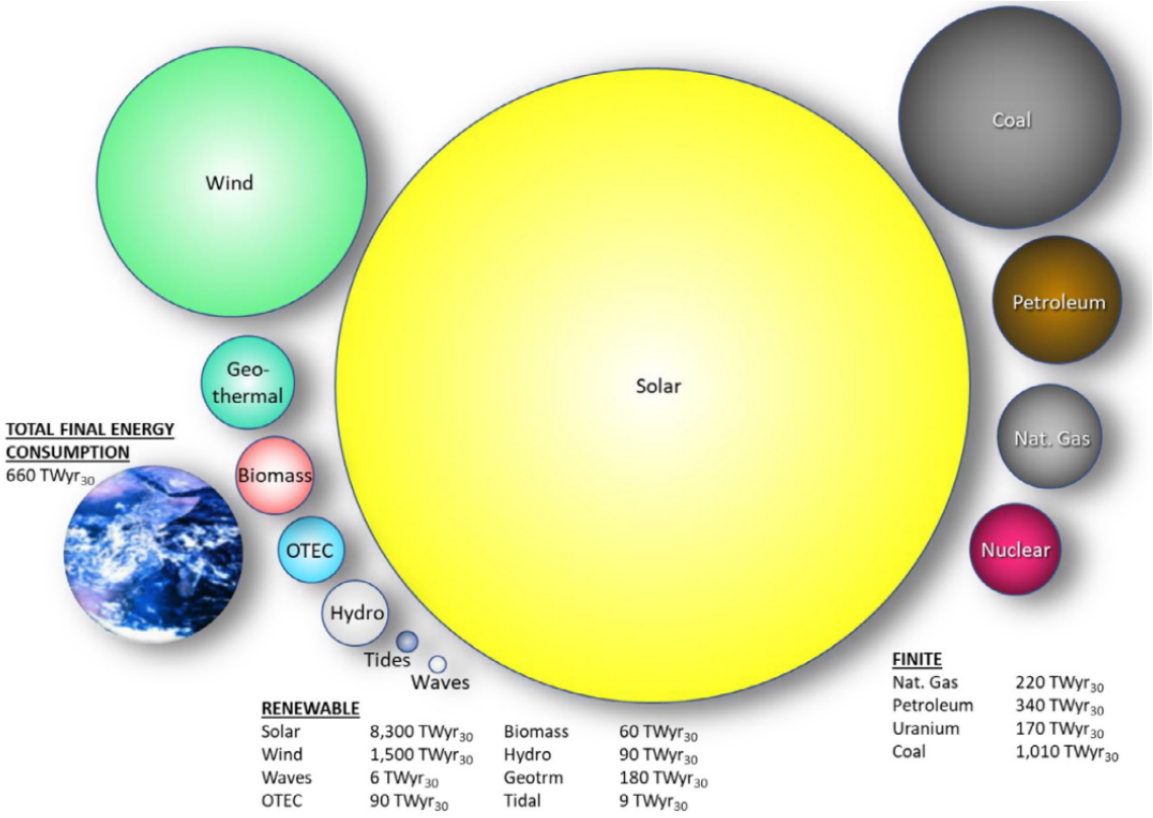

Figure 2. Reasonably assured recoverable reserves (RARs) of renewable and finite energy resources. The area of the circles represents RARs from both finite and renewable resources over the next 30 years. These areas can be compared with total demand (earth image) over that same period. Reproduced from Perez and Perez.[16]

behind clouds, there sometimes isn't enough energy for everyone. Therefore, we need to capture the sunlight and directly use the energy or convert it into a different, storable form. Capturing sunlight happens through photovoltaics or photoelectrochemical solar cells that can convert sunlight to electricity, making the efficient storage of large amounts of electric energy one of the biggest challenges today. Electricity itself cannot be stored on a large scale, but it can be converted to other forms of energy which can be stored on larger scales and later reconverted to electricity on demand. Storage systems for electricity include flywheel, compressed air, pumped hydro and battery storage. The process for battery energy storage works in reverse, transforming electrical energy into chemical energy. When excess electricity is produced in the grid, it can be channeled into a battery system and stored in the chemical system. One of the most efficient batteries up to date is the lithium-ion battery, for which the inventors were honored with the Nobel Prize in chemistry in 2019. The recent development of the lithium battery made a huge impact on society and with its use the electrification of our energy system took a jump forward.[19] Nevertheless, the current chemical systems for batteries still require a low energy-to-material ratio for storage (around 0.9 MJ kg^{-1}) and suffer from long-term discharge losses.[20] Therefore, one of the challenges scientists face today is to find a high energy density chemical system with a low carbon footprint that allows for reversible electricity storage.[21] In this perspective, hydrogen is a prominent candidate as it produces a relatively high energy density chemical (around 120 MJ kg^{-1}),[22] and only water as a product upon combustion (no greenhouse gas emission).[23] Furthermore, hydrogen gas is already an important chemical in our society.

1.1.2 The hydrogen challenge

The demand for hydrogen gas is growing in our society.[17] Hydrogen is used as a chemical building block while it also can store and deliver usable energy. It is used in many processes essential to society, such as in refineries to lower the sulfur content in our fuels, in the Haber Bosch process for producing ammonia for our fertilizers, in the production of sponge iron for our high-quality steel, the production of food grade iron powder, the production of medicines, and directly as a fuel.[24] Unfortunately, hydrogen gas does not typically exist by itself in nature but is vastly found combined with other elements in hydrocarbons and water and must be produced from these compounds.[23] Currently, 96% of the hydrogen gas is produced from fossil fuels (hydrocarbons), mainly from natural gas in the steam reforming process, rendering the perceived status of hydrogen as a clean fuel questionable.[22] Therefore, there is a strong desire

to increase the production of hydrogen obtained from renewable water electrolysis processes that now account for only 4% of the global industrial hydrogen being produced.[22,25,26] Developing new systems or optimizing current systems that efficiently produce hydrogen during water electrolysis will therefore contribute to both our energy and hydrogen challenges.

1.1.3 Water electrolysis

In 1800, English chemists Anthony Carlisle and William Nicholson discovered that water could be separated into its elements by electricity, while in the same year Johann Wilhelm Ritter discovered the process independently (**Figure 3**).[27] Based on these scientific contributions, water electrolysis became an effective and well-known method to produce H_2. The splitting of

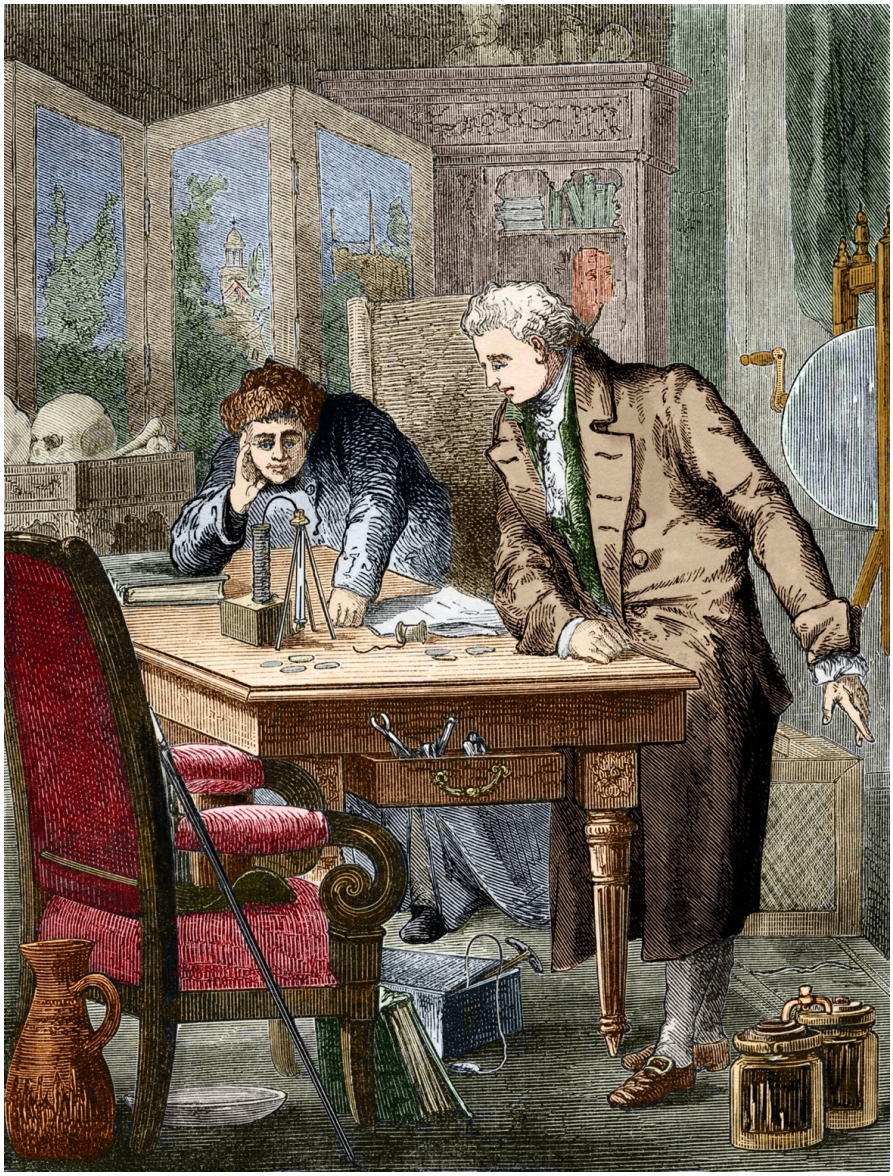

Figure 3. Anthony Carlisle (left) and William Nicholson, London, May 1800 succeeded in separating water into hydrogen and oxygen by electrolysis.[29]

water is thermodynamically disfavored and therefore the overall reaction is driven by supplying electrical energy in the form of a potential. The thermodynamic decomposition voltage of water, by means of the oxygen evolution reaction (OER), requires a minimum voltage difference (thermodynamic potential) of 1.23 V (eq. 1), and the subsequent hydrogen evolution reaction (HER) requires 0 V (eq. 2), both with a current efficiency of 100%. In practice voltages of 1.8-2.6 V are used to accelerate the reaction to a practical rate.[27] However, the potential

Oxygen Evolution reaction (OER)

$$2\ H_2O \rightarrow O_2 + 4\ H^+ + 4\ e^- \qquad E = 1.23\ V - 0.059\ pH\ V\ vs.\ NHE \qquad (1)$$

Hydrogen Evolution reaction (HER):

$$4\ H^+ + 4\ e^- \rightarrow 2\ H_2 \qquad E = 0\ V - 0.059\ pH\ V\ vs.\ NHE \qquad (2)$$

applied above the thermodynamic potential (overpotential) will not be stored, and thus will the energy be lost and released as heat. As a result, energy efficiencies for water electrolysis are generally between 50-70%.[27,28] To lower the overpotential requirement, an electrocatalyst can be used. At the cathode, where the HER takes place, metal electrocatalysts based on Fe, Co, Ni, Cu, Au, Ag, W tend to have medium overpotentials, and Pt and Pd have low overpotentials.[28]

In industry, alkaline electrolyzers have been used for more than 100 years to produce hydrogen gas from water with electric energy.[30] These use nickel derivatives as an electrocatalyst for both half-reactions. These electrolyzers are bulky, produce medium-purity hydrogen, operate at moderate current densities and are vulnerable towards inconsistent power supplies, similarly to most renewable energy sources. Alternatively, proton exchange membrane (PEM) electrolyzers in acidic solutions are used.[26] These are more suited to match the variability of renewable energies, are compact, produce high-purity hydrogen, and are compatible with higher current densities. Currently, the state-of-the-art electrocatalysts for water splitting in PEM electrolyzers use IrO_2 or RuO_2 and Pt for H_2 production.[31] However, the necessity of these precious metals as catalysts makes PEM electrolyzers expensive and inconvenient for large-scale usage. As a result, current efforts in academia and industry are focused on the development of methodologies that can produce hydrogen from water using renewable energy sources with the use of affordable and abundant metals as catalysts.

1.1.4 Nature's approach to hydrogen production

To replace the precious metal Pt for the HER, one strategy is to promote the activity of earth-abundant metals with medium overpotentials. Nature provides examples, as hydrogenase metalloenzymes, present in green algae and bacteria, are competent to reversibly convert electrons and protons to hydrogen at low overpotentials and ambient conditions using iron and nickel.[32] Research in the late 90s[33-37] and 00s[38-45] provided insight into the design and functions of hydrogenases.[46] The hydrogenase enzymes are classified into three types: [FeFe], [NiFe], and [Fe] hydrogenases, based on the metal ion present in the active sites (**Figure 4**).[46] [FeFe]- and [NiFe]-hydrogenases are found to catalyze reversible hydrogen formation at high rates, functioning to either oxidize H_2 in energy-producing processes or reduce protons to hydrogen during fermentation.[47,48] The direction of this reaction (H_2 oxidation or production) relies on the cellular location of the hydrogenase, which is accordingly tuned for hydrogen uptake or evolution. The [Fe]-hydrogenase enzyme can heterolytically cleave H_2 and transfer the resulting hydride, using a methenyl tetrahydro-methanopterin cofactor, to an unsaturated substrate, making it a hydrogenation catalyst.[49,50]

The reversible hydrogen formation reactions by hydrogenases take place at dedicated iron and nickel metal centers that drastically increase the heterolytic bond-breaking and making rates for hydrogen. Crucial to the activity are the presence of appropriate ligands for the metals, a pocket for the catalytic reactions, and a nearby base that facilitates proton transfers. These combined features lower the kinetic barriers of difficult reaction steps by avoiding charged or high oxidation state intermediates through metal-ligand cooperativity. Furthermore, the active site is part of an optimized functional protein matrix that holds iron-sulfur centers for electron transfer and pathways/gas channels through the protein surface for reactant and product transfer from and towards the active site (**Figure 5**).[46] Generally speaking, [FeFe]-hydrogenase exhibits better activity for hydrogen production, while [NiFe]-hydrogenase has a higher rate of hydrogen oxidation.[52] Isolated [FeFe] hydrogenase enzymes have been demonstrated to

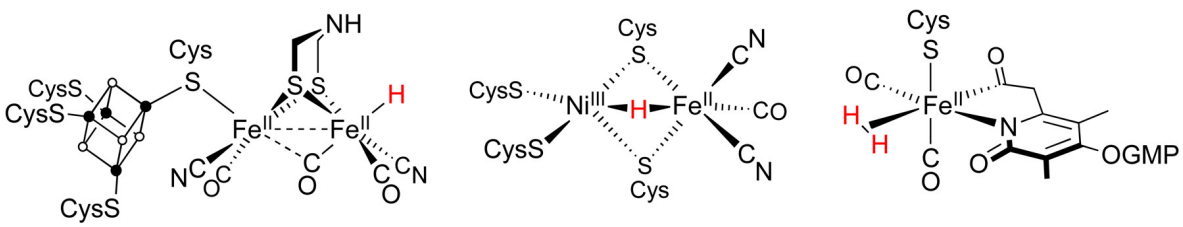

Figure 4. Structural representation of the active sites of [FeFe]- (left), [NiFe]- (center), and [Fe]- (right) hydrogenase, the hydrogen atoms in red are the proposed expected coordination site, but not yet confirmed (Cys = Cysteine; GMP = Glycomacropeptide).[51]

catalyze the production of H_2 up to 10^4 molecules of H_2 per enzyme per second at ambient temperature.[53,54] The structural investigation of the hydrogenases and understanding of their enzymatic reactions provided a structural and functional basis for the development of methodologies and techniques for artificial proton reduction catalysis.

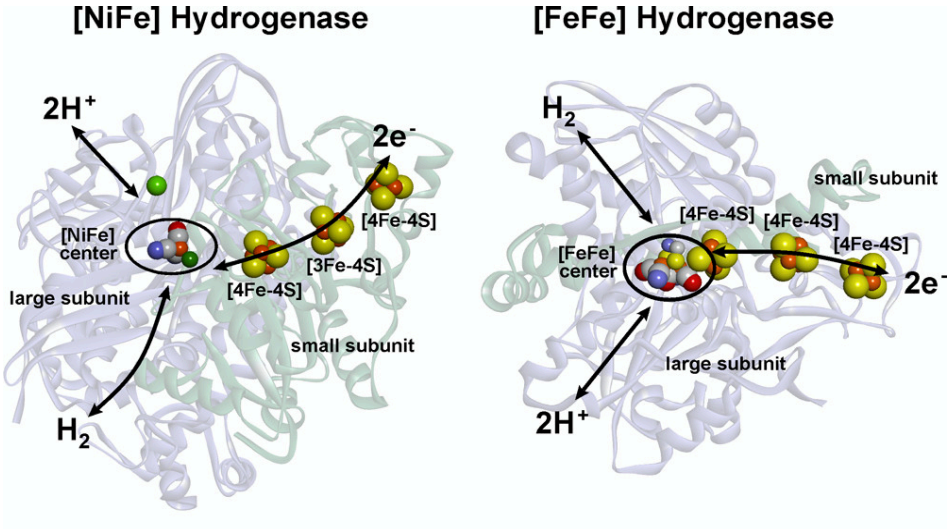

Figure 5. Structures of the [NiFe] hydrogenase[55] and of the [FeFe] hydrogenase[56]. Schematically indicated are the ET chain (via iron-sulfur centers) and pathways for hydrogen and H^+ transfer. Reproduced from Lubitz, Ogata, Rüdiger, and Reijerse with permission,[46] Copyright 2014 American Chemical Society.

1.1.5 Applied artificial photosynthesis

Inspired by efficient biological photosynthesis that stores solar energy in chemical bonds, the research field of artificial photosynthesis deals with, among other reactions, the storage of renewable energy in clean carriers such as molecular hydrogen. Over the last decades, three major systems for storing solar energy in molecular hydrogen have emerged, including photovoltaic–electrolysis (PV-EC) (see **Chapters 2-4**), particulate photocatalysis (PC) (see **Chapter 5**), and photoelectrochemical (PEC) cells (**Figure 6**).[57]

In a PV-EC system, a PV device (*i.e.,* a solar panel) is connected in series to an electrolyzer, in which the energy is independently collected and transformed into electricity, and subsequently directly used to power an EC cell. The EC cell comprises two electrodes, separated by a proton exchange membrane (PEM), the anode and cathode being the site for OER and HER, respectively. Interestingly, the EC cell is also compatible with other renewable energy sources. In a PV-EC, the PV is separated from the aqueous solution, thus preventing its degradation. Both PV and EC systems have been well-developed independently over recent years and,

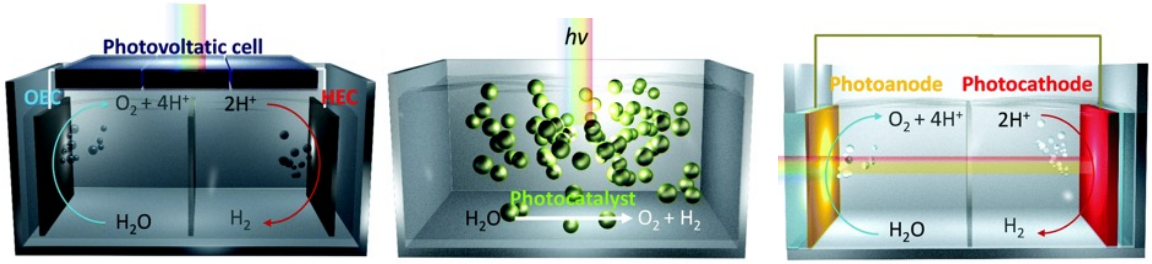

photovoltaic–electrolysis particulate photocatalysis photoelectrochemical

Figure 6. Photo-driven water splitting systems and their charge flows upon light absorption; photovoltaic–electrolysis PV-EC (left), particulate photocatalysis PC (middle), and photoelectrochemical PEC (right). Adapted from Kim, Hansora, Sharma, Jang and Lee with permission.[57] Copyright 2019 Royal Society of Chemistry.

combined, they efficiently perform solar-to-hydrogen conversion (above 10%).[58-60] To note, efficiencies for solar-driven hydrogen production are fundamentally determined based on the PV performance, making <30% acceptable under 1 sun illumination intensity (an average day of sunlight).[61] Overall efficiencies also depend on the EC-cell, hence efficient electrocatalysts with low overpotentials are crucial for the OER and HER.[62] Today, PV-ECs are already used to produce valuable high-purity hydrogen gas with purely renewable solar energy for the refueling of hydrogen gas stations.[57] Nevertheless, hydrogen produced in a PV-EC is still considerably expensive due to the cost of coupling costly PV and EC equipment, thereby diminishing the industrial viability.[63] Furthermore, the total PV-EC system is considered to be somewhat complex, due to the combined use of multiple independent systems. In contrast, only one system is used during water splitting based on PC, as photo-electrocatalysts directly absorb sunlight and use it for the OER and HER in the same aqueous solution.[58,59,64] Upon light absorbance by a chromophore, a photogenerated charge is formed that diffuses to the active sites of the catalyst, where the OER and HER take place. In such a system, gaseous O_2 and H_2 products are not separated and are obtained as a 1:2 mixture. Challenges in PC systems include the necessity to combine a chromophore with an appropriate band gap and stability with efficient and stable OER and HER catalysts, which together enable fast electron transfer kinetics. The photo-electrocatalyst's design, assembly, and testing is therefore extremely complex, hampering the overall ease of development.[64] Furthermore, achieving high photocatalyst selectivity in a single-compartment cell is also quite challenging due to competing reactions such as oxygen reduction and hydrogen oxidation (*i.e.*, the reverse reactions), that are energetically favorable.[65] Currently, the reported efficiencies are low (<1%)

and often accompanied by poor stability of the photo-electrocatalysts, which makes this technique far from practical commercial application.[66]

Various types of PEC cells exist, with quite different design principles.[67] Therefore, PEC cells are only briefly discussed in this section, using more general concepts. PECs consist of one or two photoelectrode(s), often separated by a proton exchange membrane, and are equipped with a photo-absorber semiconductor and an OER and HER catalyst.[68,69] The different compartments mimic the photosystem II and photosystem I components of the natural photosynthesis system.[67] Under illumination, the semiconductors absorb photons and induce photo-charges. Different semiconductor materials with different light absorption ranges can be used to construct tandem cells in order to broaden the spectral range of the cell. Alternatively, the semiconductor is functionalized with an external photosensitizer (*i.e.*, a molecular dye like $[Ru(bpy)_3]^{2+}$ or $[Ir(ppy)_2(bpy)]^{+}$).[67,70] The induced charges lead to the generation of a photo potential required for electrochemical reactions. The semiconductor materials used are generally available metal oxides (TiO_2, $BiVO_4$ and $CdTe/TiO_2$)[71,72] that are relatively stable under aqueous conditions, but also less conductive compared to the PV-grade materials. In a PEC, the water-splitting reaction can be summarized into four steps: light absorption by a photo-absorber, charge separation in the photo-absorber, charge transfer to an electrocatalyst (for OER or HER), and catalyst-mediated water oxidation or hydrogen evolution at the surface of the electrode. Thus, photo-absorbers and electrocatalysts are key components for manufacturing an effective PEC cell. At the current level of development, PEC water splitting efficiencies are between those of PV-EC and PC systems (≈ 2.5%),[59], and thus cannot compete with PV–EC devices in terms of efficiency and stability.[57]

From the above, it is clear that novel catalytic materials with increased stability are needed to lower the overpotential requirement for the OER/HER in artificial photosynthesis processes to make the produced hydrogen economically attractive and the technique scalable. In academia, both half-reactions are often separately investigated by using a sacrificial proton and/or electron donor.[73] The advantages of focusing on a specific half-reaction are the ease of the analysis of key reaction components and parameters for catalysis, as well as an increased ability to study the catalyst stability, reproducibility, and activity, but foremost the rapid benchmarking under nearly identical conditions of novel catalytic materials developed all over the world. Over the last 50 years, a lot of (inorganic) heterogeneous materials have been developed to catalyze water electrolysis.[62,74-77] In addition, molecular complexes that mimic natural photosynthetic catalytic reaction centers are also extensively investigated, such as various Ru, Ir, Ni, Fe, and Co complexes.[78-90] Compared with heterogeneous catalysts,

molecular catalysts exhibit different strategic benefits as the environment and redox property of the catalyst can be tuned with precision through ligand design. This enables an understanding of structure-reactivity relationships, which can be difficult to achieve with heterogeneous catalysts. To add, these well-defined molecular structures have an outstanding metal-atom economy and proved to be particularly useful for experimental reproducibility as well as during mechanistic analysis. One downside is the decreased electron transfer kinetic between solid-state electrode materials and homogeneous molecular complexes. However, over the last decade, an increased interest emerged in the immobilization of molecular catalysts onto the surface of electrode materials, photosensitizers, semiconductors, and dye-sensitized semiconductors.[91-104] In this PhD project the focus is on the design, use, and optimization of molecular catalysts for the HER half-reaction and the following subsections will concentrate on the development of such catalysts.

1.2 Evaluation and Benchmarking of Molecular Hydrogen Evolution Electro- and Photocatalysts

To evaluate the performance of molecular catalysts for the HER, the following essential parameters are generally considered: 1) Turnover number (TON), which is defined as the number of moles of hydrogen generated per mole of molecular catalyst (eq. 3). For

Turn over number

$$\mathrm{TON} = n_{H_2} / n_{\mathrm{cat}} \qquad (3)$$

electrocatalytic reactions, catalysis often takes place only near the electrode surface and therefore the TON is not merely a feature determined by the catalyst but also defined by the metrics of the electrochemical cell and electrode.[105] When catalysis is finished within the reaction time, the TON can directly be related to the lifetime of the catalyst and is a parameter used to determine the stability of the catalyst. 2) Turnover Frequency (TOF), which is the rate of hydrogen production per catalyst per unit of time. For molecular electrocatalysts, the TOF is determined by CV and defined as the rate of charge consumption under catalytic conditions and expressed by eq. 4, where k_{obs} is the observed rate constant and equal to the TOF, i_p is the peak current of the uncatalyzed redox couple (in the absence of the sacrificial proton donor), i_{cat} the catalytic current in the presence of the sacrificial proton donor, n is the electron stoichiometry, R is the ideal gas constant (8.314 JK^{-1} mol^{-1}), T is the temperature in Kelvin, F is the Faraday constant (96485.33 A/mol), and v is the scan rate in V/s.[106] For a two-electron

Turnover frequency electrocatalyst

$$\frac{i_{cat}}{i_p} = \frac{n}{0.4463}\sqrt{\frac{RTk_{obs}}{Fv}} \qquad (4)$$

Turnover frequency (simplified for a 2 e^- process)

$$k_{obs}(TOF) = 1.94 \cdot v \cdot \left(\frac{i_{cat}}{i_p}\right)^2 \qquad (5)$$

chemical process (such as the HER), taking place at 298 K (25 °C), the expression can be simplified to eq. 5. 3) Overpotential (η), which is the extra voltage used to enable or speed up an electrocatalytic HER and is defined as the difference between the standard reduction potential (thermodynamic potential) $E°_{HA/H2}$ and the observed catalytic potential E_{cat} (eq. 6). For the HER half reaction evaluation, the $E°_{HA/H2}$ of various sacrificial proton donors in organic media are well-documented[107,108] and the expression in aqueous media is shown in eq. 7.[109] Where $E°_{HA/H2}$ is the standard potential for the reduction of protons, C_0 is the acid concentration, C_{H2} is the concentration of dissolved H_2, ϵ_D is the diffusion rate of products vs. reactants,[109] R is the ideal gas constant (8.314 JK^{-1} mol^{-1}), T = 298 K, and F is the Faraday constant. The E_{cat} can be reported as the onset potential of the catalytic wave (E_{on}) or the peak potential at the maximum current (E_p), but is over the last decade most commonly reported as the half-wave potential ($E_{cat/2}$), which is the potential at 50% of the peak current (i_p).[110] 4) Faradaic efficiency (FE) for an electrocatalytic HER is defined as the percentage of consumed electrons that end up in H_2 (eq. 8). n_{H2} is the total amount of hydrogen produced (mol), Q is the

Overpotential

$$\eta = |\, E_{cat} - E°_{HA/H2} \,| \qquad (6)$$

Standard potential

$$E°_{HA/H2} = E°_{H+/H2} - \frac{2.303\,RT}{F} pK_a + \epsilon_D - \frac{RT}{2F}\ln\frac{C_0}{C_{H2}} \qquad (7)$$

total amount of charge passed through the cell, 2 is the number of electrons in H_2 and F is the Faraday constant. The FE is calculated during bulk electrolysis, by comparing the measured amount of hydrogen, measured by a GC-apparatus, to the total amount of charge passed during electrolysis. 5) For photocatalytic reactions the quantum yield (ϕ) is sometimes reported, which is determined by comparing the moles of hydrogen obtained with the moles of monochromatic photons incident on the sample during photocatalysis. The absorption band, longevity, and

redox properties of the photosensitizer greatly affect the system's quantum yield and consequently its overall performance. Therefore, the quantum yield is mostly used as a measure of the system efficiency and often not reported for studies that focus on the development of hydrogen evolution catalysts.

Faradaic Efficiency

$$FE = n_{H2} / (Q/2F) \cdot 100\% \quad (8)$$

1.3 Molecular Hydrogen Evolution Catalysis

The HER process requires two protons and two electrons to form molecular hydrogen (eq. 2), which is on paper one of the easiest reactions known, but in practice, slow reaction rates are observed due to severe kinetic barriers and a catalyst is necessary to speed up the reaction. The most efficient materials known for the electrochemical production of H_2 by the HER are Pt group metals which operate at low overpotential through well-established mechanistic steps.[111] However, platinum is scarce and relatively expensive ($36 per gram in April 2023),[112] providing a strong desire for the development of cheaper alternatives. In nature, proton reduction occurs at iron and nickel sites in hydrogenase enzymes (see section 1.1.4). These enzymes can catalyze the HER at high rates (>10^4 s^{-1} $enzyme^{-1}$) and at overpotentials as low as 100 mV using earth-abundant metals. Thus, considerable efforts have focused on the development of functional hydrogenase models in the form of robust molecular catalysts, based on non-noble metals.[81,113-116] The many recent reviews on first-row transition metal molecular complexes for electro- and photocatalytic HER highlight this strong interest by the chemistry community.[87,89,92,114,116-128] While having no biological relevance in proton reduction, cobalt has been positioned as one of the most promising metals in the field over the last 15 years, because of its catalytic activity and low overpotentials.[86,87,89] Next to its activity, cobalt is also less scarce and relatively inexpensive ($0.037 per gram in April 2023) compared to platinum.[129] In the next sections, some of the most important contributions to the development of cobalt-based molecular complexes for electro- and photocatalytic HER are discussed.

1.3.1 Cobalt-based molecular electrocatalyst

In 1986 the first cobalt-based molecular HER catalyst was reported by Connolly and Espenson.[130] They described a cobaloxime system $[Co(dmgBF_2)_2(H_2O)_2]$ (**1**, $dmgBF_2$ = difluoroboryl-dimethylglyoxime, **Figure 7**) that catalyzes the $Cr^{2+} + Cl^- + H^+ = CrCl^{2+} + ½\ H_2$ reaction, producing H_2. An important feature of the cobaloximes is the π-acceptor character of

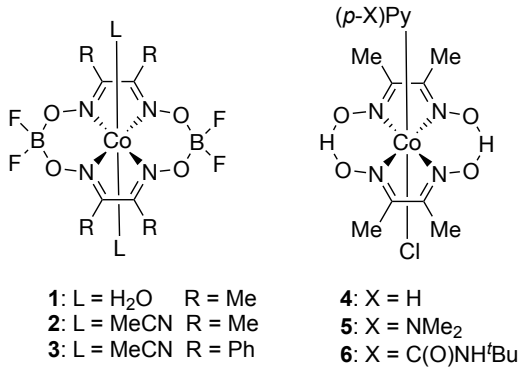

1: L = H_2O R = Me
2: L = MeCN R = Me
3: L = MeCN R = Ph

4: X = H
5: X = NMe_2
6: X = C(O)NH^{t}Bu

Figure 7. Cobalt complexes with cyclic amine donor ligands ((*p*-X)Py = para-substituted pyridine).

the oxime ligands, which leads to the stabilization of reduced cobalt species that are key intermediates for the HER.[131] Then the field had to wait almost 20 years until gaining a renewed interest in cobaloxime complexes in the 00s. Guided by research efforts in the groups of Peters and Fontecave, several electrocatalytic studies on known cobaloximes (complexes **1**-**4**, **Figure 7**) demonstrated the potential of molecular cobalt catalysts as efficient HER mediators.[131-135] In a nonaqueous DCM solution, **4** reached a TON of 100 in 2.5 h with 85-100% FE during electrolysis at –0.90 V/(Ag/AgCl), using a graphite electrode and Et_3NH^+ as a sacrificial proton donor, while **1** was less active, but more stable,[136,137] reaching 80 TON in 17 h with 75–100% FE during electrolysis at –0.90 V/(Ag/AgCl).[131] The introduction of an electron-donating/withdrawing *para*-substituent on the axial pyridine ligand in complexes **5** and **6** increased/decreased the rate constant of catalysis, respectively. The effect is linearly correlated with the Hammett coefficients of the introduced substituents.[131] In a different study, effective modulation of the Co(I/II) redox potential was achieved by replacing the methyl substituent on the oxime ligands in **2** for phenyl substituents in **3**. The diphenylglyoxime complex **3** showed a more positive Co(I/II) redox couple at −0.28 V vs. SCE compared to −0.55 V vs. SCE for dimethylglyoxime complex **2**.[134] However, the positive shift came with a price of lower electrocatalytic HER activity. A few years later **1** and **4** were also successfully applied to photo-catalytically reduce protons in combination with Pt, Ir, Re, and organic PSs (see next section).[138-140] The activity of the more stable hydrogen evolution catalyst (HEC) **1** was further increased by grafting the molecular complex onto electrode surfaces. Adsorbed onto a glassy carbon electrode **1** is active in an aqueous solution at pH < 4.5 and an overpotential of only 100 mV.[100] At 400 mV overpotential, **1** was active for 16 h reaching a TON of 5 x 10^6 with 75 (±10)% FE. These early examples made it clear that creating a single catalyst that generates hydrogen from protons at minimal overpotentials and has high stability is an exceptional

challenge. As such, no system possessed all the desired properties and the field started to develop different ligand frameworks. In 2010, Chang *et al.* reported cobalt complex **7** as a novel HER catalyst, which holds a novel polypyridyl-based PY4 ligand (PY4 = 2-bis(2-pyridyl)(methoxy)-methyl-6-pyridylpyridine) (**Figure 8**).[141] **7** is active in MeCN and 50:50 (v/v) water:MeCN mixtures and reduces protons from trifluoroacetic acid (TFA) to hydrogen with an overpotential of 400 mV in MeCN. Isostructural Zn analog $\mathbf{7^{Zn}}$ and free ligand PY4 are electrochemically silent within the same potential range, which highlights the necessity of a redox-active metal center. Modifications on the ligand scaffold, by introducing CF_3 substituents, and changing the counterions from PF_6 to OTf, yielded complexes **8** and **9** that demonstrated electrocatalytic proton reduction under full aqueous conditions, although these types of complexes were more extensively tested under photocatalytic conditions (see next section).[142] Remarkably, **9** demonstrates a decreased electrocatalytic activity compared to **7**, which, like the cobalt glyoxime complexes, demonstrated that the introduction of electron-withdrawing groups decreases the reactivity in cobalt HER catalysts. In a follow-up study, Chang *et al*. reported cobalt complexes **10**-**12**, bearing a $PY5Me_2$ ligand ($PY5Me_2$ = 2,6-bis(1,1-bis(2-pyridyl)ethyl)pyridine), whose ligand was previously used in a molybdenum-oxo complex that generates H_2 from water.[143,144] The CV of **10** and control experiments with isostructural $\mathbf{10^{Zn}}$, cobalt salt $CoCl_2$, and free ligand $PY5Me_2$ in a pH 7 phosphate buffered solution demonstrated the necessity of the cobalt center. The Co(I/II) reductive response for **10** was found at –1.00 V vs. SHE and its catalytic wave 0.2 V more cathodic, while the control experiments featured significantly more cathodic redox responses (**Figure** 9, left). Upon substituting the central pyridine ring of the $PY5Me_2$ ligand with an electron-withdrawing CF_3 group (**11**) or an electron-donating NMe_2 group (**12**), the redox properties of the cobalt center were successfully modulated as the catalytic processes showed up at a more anodic potential

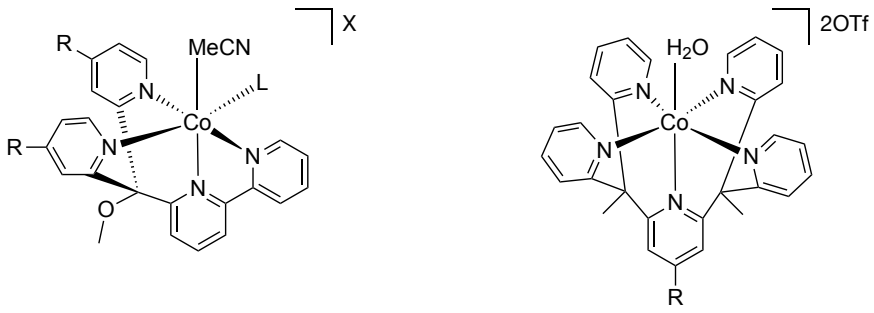

7: R = H, L = MeCN, X = $2PF_6$
8: R = H, L = OTf, X = OTf
9: R = CF_3, L = MeCN, X = 2OTf

10: R = H
11: R = CF_3
12: R = NMe_2

Figure 8. Cobalt polypyridyl complexes reported by the group of Chang.

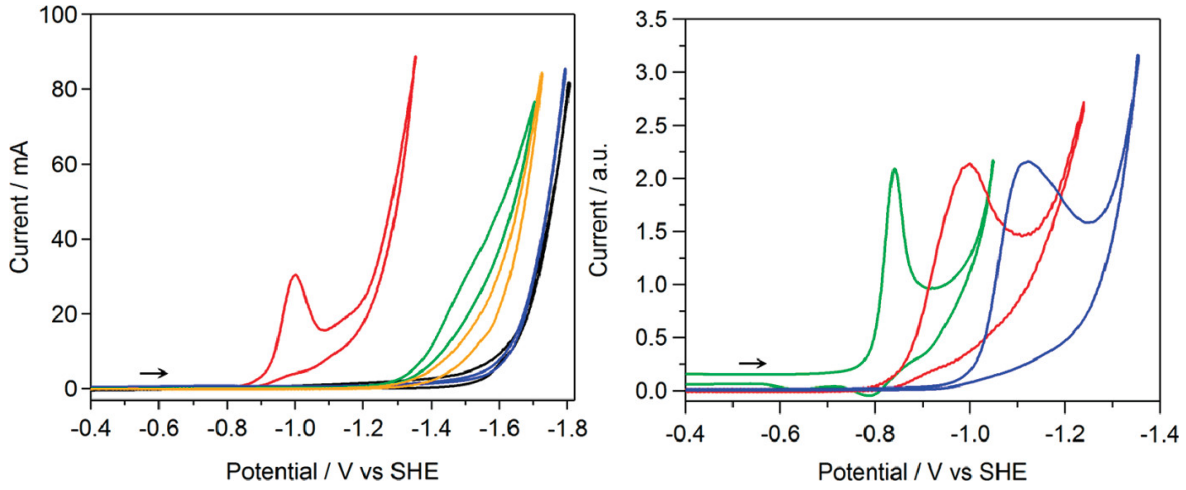

Figure 9. Left: Cyclic voltammograms of **10** (red), **10^{Zn}** (yellow), free ligand PY5Me2 (green), $CoCl_2$ (blue), and blank control (black) measured in aqueous solution buffered to neutral pH (1.0 M phosphate, pH 7). Right: Normalized cyclic voltammograms of **10** (red), **11** (green), and **12** (blue), at pH 7 in a 1.0 M aqueous phosphate buffer solution showing the effect of introducing electron-withdrawing CF_3 and electron-donating NMe_2-substituents on the PY5Me2 ligand framework. Reproduced from Chang *et al.* with permission.[143] Copyright 2011 American Chemical Society.

for **11** and at a more cathodic potential for **12** (**Figure 9**, right). Thus, the redox potential of the Co(I/II) wave and the overpotential requirement for electrocatalytic HER can be modulated through ligand design.[143,145] Furthermore, **10** demonstrated to be a stable and active electrocatalyst, with near quantitative FE and 5.5 x 10^4 TONs during a 60 h controlled potential electrolysis (CPE) experiment. Today, the many contributions of cobalt(II) polypyridyl complexes have demonstrated that these ligands offer high robustness thanks to their resistance to hydrogenation and ability to stabilize low oxidation states of the metal centers involved in the catalytic cycle, making this class of complexes promising catalysts for hydrogen evolution.[115]

A mechanistic study on a polypyridyl cobalt(II) complex was reported by Artero *et al,* who investigated complex **13** based on a bapbpy (6,6′-bis(2-aminopyridyl)-2,2′-bipyridine) ligand (**Figure 10**). Complex **13** is also photo-catalytically active for HER (see next section).[146] In **13,** the ligand is redox-active and holds pendant amine proton relays that participate in the electrocatalytic HER. In DMF, using proton sources with increasing pK_a values (from 3.4 to 13.5) and different operating potentials, distinct mechanistic pathways were determined based on a combination of voltammetry and electrolysis. **13** has its Co(I/II) redox couple at –1.44 V vs. Fc^+/Fc and a ligand centered reduction at –1.99 V vs Fc^+/Fc. When acetic acid (pK_a 13.5 in DMF) was used as a proton source no significant changes in the redox responses were observed

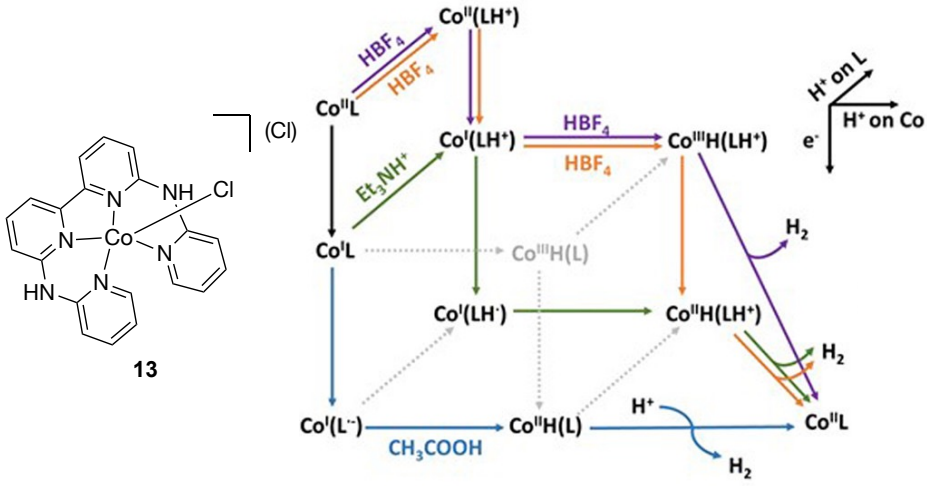

Figure 10. Left: Cobalt polypyridyl complex **13** reported by the group of Artero. Right: The proposed mechanistic pathways of complex **13** ($Co^{II}L$) during electrocatalytic HER in the presence of blue: CH_3COOH at −2.0 V vs Fc+/Fc; green: $HNEt_3^+$ at −1.9 V vs Fc^+/Fc; orange: HBF_4 at −1.65 V vs $Fc^{+/}$Fc; and purple: HBF_4 at −1.35 V vs Fc^+/Fc) in DMF. Arrows downwards are electron reduction steps and arrows to the right/diagonal up are protonation steps on cobalt/ligand. Reproduced from Artero *et al.* with permission.[146] Copyright 2020 American Chemical Society.

by CV, but electrolysis at –2.00 vs Fc^+/Fc demonstrated H_2 evolution. Therefore, an EECC mechanism was proposed (where E corresponds to an electron transfer step and C to a chemical reaction, here protonation), in which **13** is first electrochemically reduced twice (EE) followed by chemical protonation steps (CC) and the formation of hydrogen. Using a stronger acid like Et_3NHBF_4 (pK_a 9.3 in DMF), the Co(I/II) redox couple progressively shifted towards a more anodic potential suggesting an electrochemical reduction (E), followed by a chemical ligand pronation step (C). Under these conditions, a catalytic wave appeared at a more negative potential of –1.9 V vs. Fc^+/Fc, and at this potential hydrogen formation was detected. These observations pointed towards an ECEC mechanism. When the strong acid HBF_4 (pK_a 3.4) was used, the complex already gets protonated on the ligand before any electrochemical reduction takes place. The catalytic wave was observed slightly more cathodic of the Co(I/II) redox couple at which H_2 was detected during electrolysis, suggestive of a CECE mechanism. These findings highlight different electrocatalytic mechanistic pathways, in which proton relays can be used to facilitate the HER. Recently, our group has reported on the synthesis of dicationic cobalt complex $[Co(HBMIM^{Ph2})_2](BF_4)_2$ (**14**), comprising two neutral $HBMIM^{Ph2}$ diimine ligands, and its use as an HER electrocatalyst.[147] Cyclic voltammetry experiments showed an irreversible, peak-shaped reductive response for **14** in MeCN at –1.96 V vs Fc^+/Fc, which was assigned to the fast reduction to Co^I (**A**), (**Figure 11**). In the presence of a weak proton source

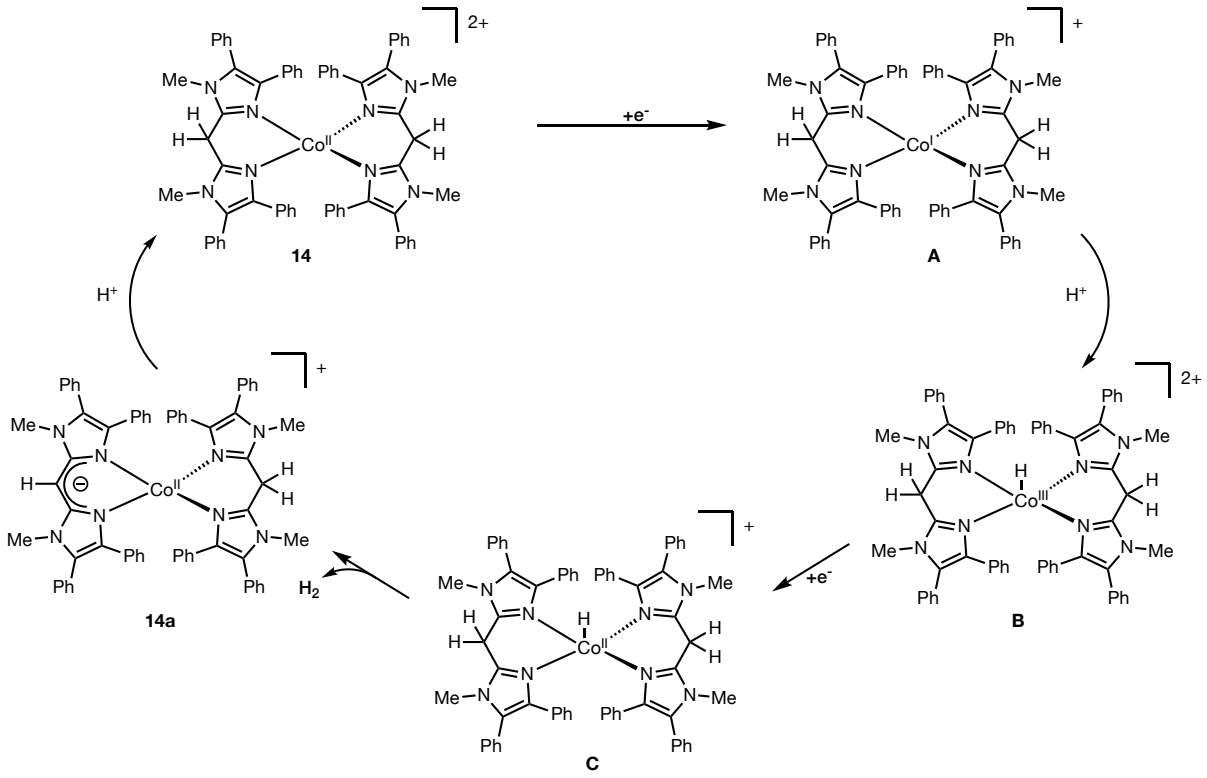

Figure 11. Proposed ligand-mediated HER reactivity for **14**.[147]

(acetic acid) this current develops into an electrocatalytic current with a TOF of 200 s^{-1} for HER. Combined experimental and DFT studies supported that **14** undergoes H-atom loss upon reduction (either electrochemically or chemically using KC_8) and consecutive H_2 formation, resulting in formal deprotonation and generation of cobalt complex $[Co(HBMIM^{Ph2})(BMIM^{Ph2-})](BF_4)$ (**14a**), containing one deprotonated $BMIM^{Ph2-}$ ligand. Under catalytic conditions, protonation restores complex **14** and closes the catalytic cycle. Isolation and characterization of **14a** in combination with mechanistic investigations using DFT suggested that dihydrogen formation proceeds via the protonation of **A** forming a Co^{III}–H (**B**), which is again reduced to form a Co^{II}–H (**C**). Then, the intramolecular combination of the cobalt hydride moiety with a ligand C–H proton forms H_2, providing a unique HER mechanism. Robustness tests were carried out by means of bulk electrolysis with acetic acid (as sacrificial proton source) in MeCN using a mercury electrode and demonstrated a 590 mV catalytic overpotential for HER, in which **14** suffered from fast deactivation with a total turnover number of 0.25. Nevertheless, the involvement of the ligand C–H moiety was further demonstrated as a dimethylated analogue of **14**, which is devoid of a proton relay functionality in the ligand backbone shows no activity.

Phosphine ligands are good σ-donors and have π-accepting properties and are therefore interesting to use as ligands for molecular HER catalysts as they can form stable complexes

and reduced oxidation states can be stabilized by the ligand. Some of the most prominent molecular HER complexes known are the nickel bis(diphosphine) complexes with pendant amines as proton relays developed by DuBois and coworkers.[148-150] Due to the high activity and appealing redox and proton transfer features of the nickel complexes, the same bis(diphosphine) ligands have been applied to prepare molecular cobalt electrocatalyst **15** (**Figure 12**). In MeCN solution, loss of a diphosphine ligand was observed in the presence of triflic acid forming **16**, which was independently synthesized and demonstrated to be active as an electrocatalyst. **16** has its Co(I/II) redox couple at –0.99 vs. Fc^+/Fc in MeCN, which turns into a catalytic wave in the presence of *p*-bromoanilinium tetrafluoroborate, corresponding to an overpotential of 285 mV with a TOF up to 90 s^{-1}. Compared to the nickel analog, **16** demonstrates a lower TOF (Ni = 350 s^{-1}), but also a lower overpotential (Ni = 350 mV). Upon replacing the Ph groups on the phosphorous atoms in **16** by ^{t}Bu groups, as in **17**, an increase in TOF was observed (160 s^{-1}) at the price of an increase in overpotential (445 mV).[151] Later, Dubois and Bullock *et al.* reported on tetraphosphine complex **18** (**Figure 12**), which has a relatively high HER overpotential requirement of 1210 mV in a $[(DMF)H]^+$/DMF buffer, with TOFs up to 980 s^{-1}.[152] Interestingly, catalysis could be drastically increased upon the addition of water, resulting in a TOF of 18,000 s^{-1} at an overpotential of 1270 mV. Furthermore, mechanistic investigations using Co^I and Co^{III}–H analogues of **18** suggested a mononuclear HER process in which a Co^I–H or Co^{II}–H intermediate reacts with a proton (residing on the amine proton relay) on the time scale of the voltammetry experiment.[153] In contrast, related electrolysis experiments were consistent with a dinuclear route.[153] Another relevant contribution to the development of efficient molecular HER catalysts based on cobalt was reported in 2014 by Sun *et al.* (**Figure 13**). Complex **19** holds a multihydroxy-functionalized tetraphosphine ligand around the Co^{II} metal ion and is catalytically active in an aqueous pH 7 phosphate buffer with an onset potential of −0.50 V vs. NHE, which corresponds to an extremely low overpotential of 80 mV.[154] Iron analog $\mathbf{19^{Fe}}$ exhibits much less favorable

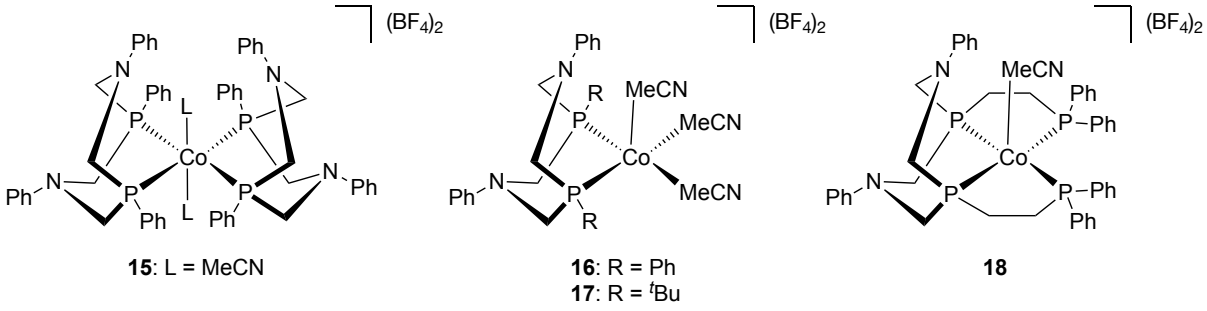

Figure 12. Cobalt diphosphine complexes reported by the Dubois group.

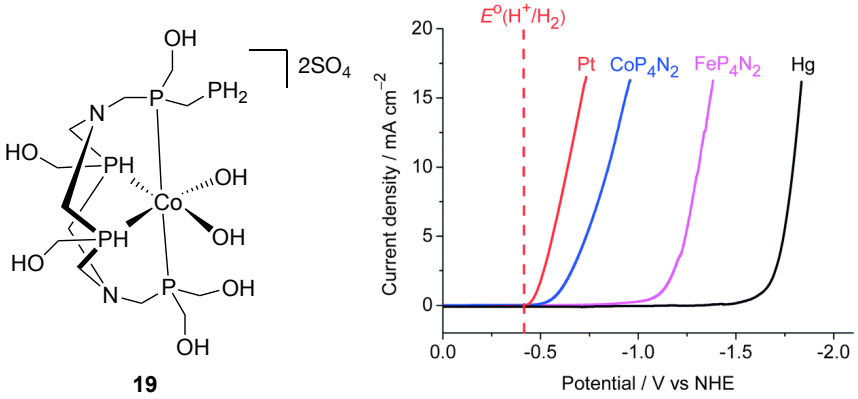

Figure 13. Left: Cobalt phosphine complex **19** reported by the group of Sun. Right: Cathodic scans of **19** (CoP_4N_2 blue line) and isostructural analog **19^{Fe}** (FeP_4N_2 pink line) in 1.0 M phosphate buffer at pH 7. The black and red lines indicate the cathodic scans of buffer solution in the absence of a catalyst using a Hg pool and Pt disc as working electrodes, respectively, under otherwise identical conditions. Reproduced from Sun *et al.* with permission[154] Copyright 2014 Royal Society of Chemistry.

electrocatalytic properties, featuring an onset potential at −1.03 V vs. NHE. During CPE at 1.0 V vs. NHE, **19** turned out to be a stable electrocatalyst for 20 h reaching a TON of 9.24×10^4. Next to amines and phosphines, molecular cobalt catalysts based on porphyrin ligand systems[125] and on non-innocent sulfur-based ligands[126] also pose interesting redox features for HER, which have been independently reviewed by Hung *et al.* and Mitsopoulou *et al.*, respectively.

Overall, these examples show that great lessons have been learned on the interplay between ligands and cobalt metal centers during HER catalysis. Especially the use and effects of proton relays have been demonstrated. In terms of molecular design, it has become clear that functionalization of the ligand framework, sometimes far away from the first coordination sphere around cobalt, can induce profound modulations in the cobalt-based redox potentials and catalytic HER activity. These modulations have been demonstrated for different families of molecular complexes. The introduction of electron-withdrawing drawing groups usually leads to an anodic shift in the cobalt-based redox potentials, accompanied by a lowering of the overpotential requirement and catalytic activity for HER. However, some recent studies by Dubois and co-workers on molecular HER catalysts based on Ni bypassed the tradeoff between overpotential and catalytic rate.[155] The observed reactivity trend was attributed to a bifunctional HER mechanism, in which a basic functionality in the ligand framework facilitates the (rate determining) product release step. In the introduction of **Chapter 2** of this Doctoral Thesis, this system is further explained.

1.3.2 Cobalt-based molecular photocatalysts

Molecular complexes capable of homogeneous light-driven hydrogen evolution based on Co, Ni, Fe, and Cu complexes have been frequently reported over the last decades. The mechanism depicted in **Figure 14** represents a typical catalytic cycle for photochemical hydrogen evolution. Upon irradiation of the reaction mixture, excitation of the photosensitizer (PS) yields the excited (triplet state) photosensitizer (PS^*), which can subsequently be reduced by the sacrificial electron donor, forming a strong photoreductor (PS^-).[156] Then, electron transfer to the hydrogen evolution catalyst (Cat) regenerates PS. This sequence is known as the reductive quenching pathway as the excited PS^* gets reduced by the sacrificial electron donor. Alternatively, the excited PS^* can directly reduce the Cat under the formation of oxidized PS^+, which can be reduced by a sacrificial electron donor to regenerate PS; which is known as the oxidative quenching pathway. However, in practice often only the reductive quenching pathway is considered due to the large excess of sacrificial electron donors compared to Cat, making the effective quenching of the PS^* by any Cat unlikely.

A recent review by Pellegrino *et al.* provides an extensive overview on the light-driven HER achieved with first-row molecular hydrogen evolution photocatalysts, in which cobalt-based systems vastly outnumber systems based on the other metals.[124] In most of these systems $[Ru(bpy)_3](X_2)$ (X = PF_6 or Cl) is the PS of choice, because of its favorable electron transfer kinetics under acidic conditions, but there is also an increased interest in the use of noble metal-free PSs.[124] For comparison studies on PSs used for HER, the reader is referred to recent review articles by Zou *et al.* and Abbotto *et al.*.[157,158] In this section, a number of typical contributions to the development of cobalt-based HER photocatalysts using noble-metal free conditions are described, including some highly active systems. $Co(dmgH)_2(Py)Cl$ (**4**), is one of the most studied hydrogen evolution catalysts (HECs) and is frequently applied as a benchmarking catalyst for new molecular HECs (**Figure 15**). In 2008, **4** was first used as a hydrogen evolution

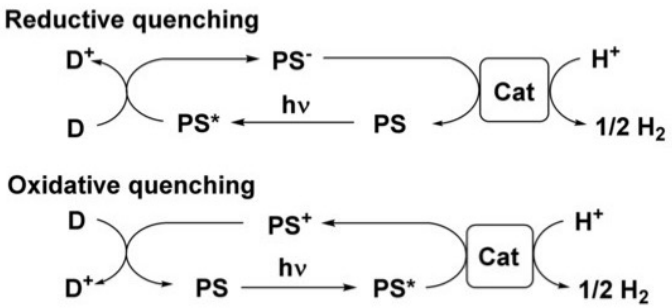

Figure 14. Reductive and oxidative quenching pathways for H_2 evolution driven by molecular photosystems, where * denotes its triplet state.[156]

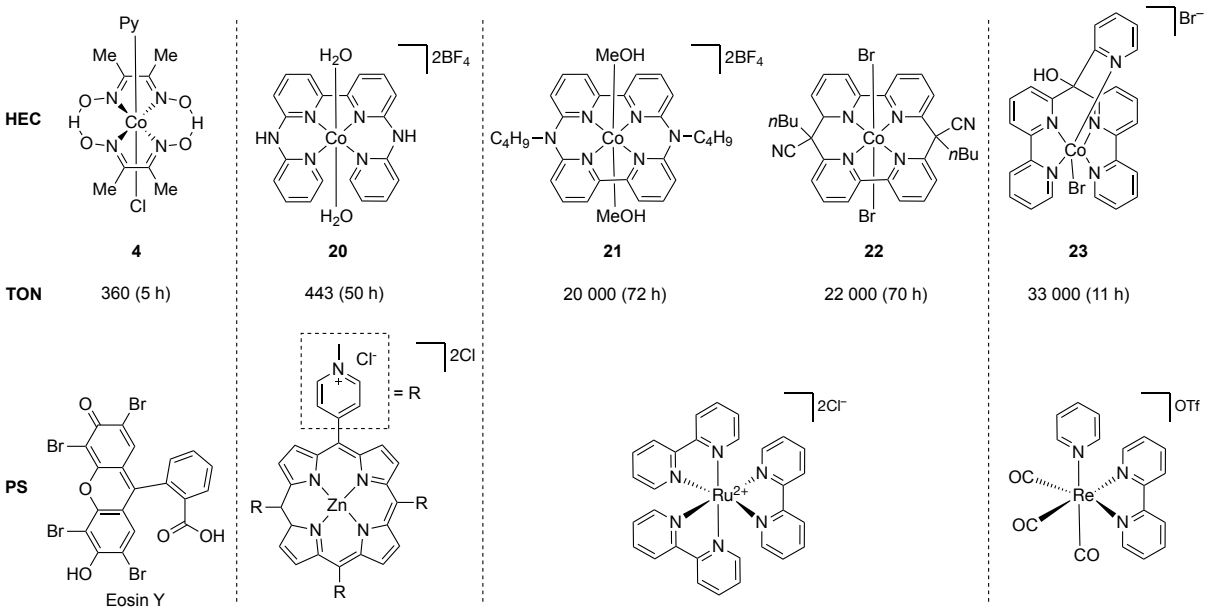

Figure 15. Selected contributions to cobalt-based HEC and the corresponding PSs.

photocatalyst by Eisenberg *et al.,* using a Pt(II) complex as a PS.[139] One year later, the same group reported that **4** could reach a TON of 360 after 5 h in a noble-metal free system using triethanolamine (TEOA) as the sacrificial proton/electron donor and the organic dye Eosin Y as a photosensitizer in MeCN/H_2O at pH 7 (**Figure 15**).[140] Not much later, cobalt pyridine complexes emerged as more stable and efficient HECs with increased water solubility, compared to the cobaloxime systems.[118,159] In these systems the ligands play an important part in the HER, providing π-accepting properties that stabilize reduced cobalt intermediates, and sometimes the ligands show non-innocent behavior, temporarily storing electrons. Cobalt(II) bapbpy complex **20**, an analog of electrocatalyst **13**, catalyzes photochemical hydrogen generation from a fully aqueous solution using a Zn porphyrin photosensitizer with a TON of 443 after 50 h in the presence of ascorbic acid (AscH), as proton/electron donor, and tris-(2-carboxyethyl)phosphine (TCEP), as an ultimate electron donor (**Figure 15**).[160] The role of TCEP needs some clarification. For reductive catalysis, typical sacrificial electron donors such as AscH (generally used under acidic conditions) and tertiary amines (generally used under neutral to basic conditions) are thermodynamically compatible with the photoexcited states of suitable photosensitizers but suffer to some extent from unproductive back electron transfer steps to their oxidized products.[161] Upon using two electrons and two protons from AscH, hydrogen gas and dehydroascorbic acid (DHA) are formed. The accumulation of DHA limits photocatalytic HER activity since DHA can also be reduced by the reduced PS. In 2014, Alberto *et al.* reported that TCEP could enhance HER catalysis by regenerating AscH from

DHA (**Figure 16**).[162] TCEP is a strong, pH-dependent reductant, which can reduce DHA to AscOH.[163] In water, at pH 4, TCEP has two of its carboxylic acid moieties deprotonated (**Figure 16**, top left).[164] During the regeneration process, DHA is reduced to $AscO^-$ (as AscH is present in dissociated from at pH 4), while TCEP is oxidized to TCEPO, which has a higher barrier for reduction than DHA. As a result, the recycling of DHA with the 2nd electron donor TCEP diminishes the back electron transfer step during HER photocatalysis and makes AscH an electron relay or redox mediator, while TCEP is the ultimate sacrificial electron donor (**Figure 16**, left reaction). TCEP does not always enhance catalysis, as this phosphine can also coordinate to dicationic cobalt centers, causing the precipitation of the molecular complex and termination of HER catalysis, which was also demonstrated by Alberto *et al*.[165] After regeneration of AscH, an electron can be transferred to the excited PS^* and hydrogen evolution can proceed through the oxidative or reductive mechanism explained above (**Figure 14**). Mulfort *et al.* reported on macrocyclic polypyridyl cobalt complex **21,** which is able to reach nearly 20,000 TON over 72 h under full aqueous conditions with AscH, TCEP, and $[Ru(bpy)_3](Cl)_2$ as a PS (**Figure 15**). In these studies, they further investigated the participation of TCEP, and a dual role for TCEP was demonstrated, as it was found that it also stabilizes the reduced Co(I) intermediate upon phosphine coordination to the cobalt metal center.[166] Stabilizing Co(I) intermediates with phosphines, and therewith enhancing catalysis, was also successfully applied for cobaloxime-based photocatalysts.[167] The highest TONs for molecular cobalt systems were reported by Alberto *et al.,* using an optimized tetradentate, bipyridine-based macrocyclic cobalt complex **22**, in combination with a $[Ru(bpy)_3]$ PS, AscH, and TCEP to reach 22,000 TONs in 70 h (**Figure 15**).[168] In **22**, the bromide ligands are weakly bound and dissociate in water. The same group also reported on complex **23** based on a pentadentate poly-

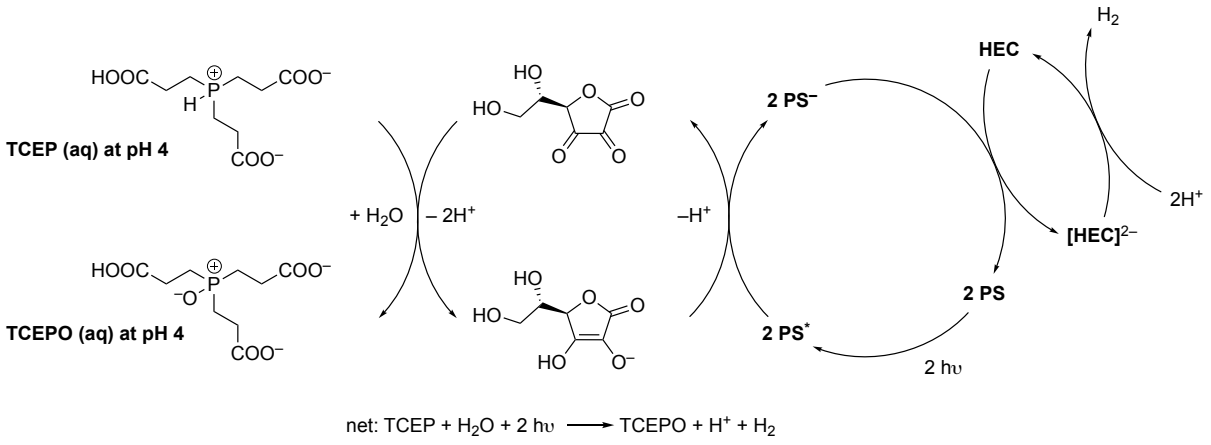

Figure 16. HER by ascorbate coupled photocatalysis with TCEP as the sacrificial electron donor.[162]

pyridyl ligand, which reaches 33,000 TON in 11 h in combination with $[Re(CO)_3(bpy)Py]OTf$ PS, AscH, and TCEP (**Figure 15**).[162]

1.3.2.1 Thermodynamic redox potential analysis

For photocatalytic hydrogen evolution reactions using $[Ru(bpy)_3]^{2+}$ as the photosensitizer and AscH as the proton/electron donor under aqueous conditions, the mechanisms including the thermodynamic energy levels are well documented and are depicted in **Figure 17**.[169] $[Ru(bpy)_3]^{2+}$ features a Ru(II/III) redox couple at +1.12 V and a Ru(I/II) redox couple at –1.52 V, both vs. Ag/AgCl.[170-172] The oxidation of AscH occurs at +0.33 V vs. Ag/AgCl, indicating that no spontaneous electron transfer reaction occurs between AscH and $[Ru(bpy)_3]^{2+}$.[173] Upon excitation (*nhv*) of $[Ru(bpy)_3]^{2+}$ to $[Ru(bpy)_3]^{2+*}$, the energy levels of both its redox couples $[Ru(bpy)_3]^{2+*}$ to $[Ru(bpy)_3]^{3+}$ and $[Ru(bpy)_3]^{2+*}$ to $[Ru(bpy)_3]^{+}$ change significantly.[174] The calculated reduction potential for the $[Ru(bpy)_3]^{2+*}$ excited state is estimated to be +0.32 V vs. Ag/AgCl (original data presented as +0.77 V vs. SCE in acetonitrile).[174-176] Hence, $[Ru(bpy)_3]^{2+*}$ is thermodynamically susceptible to reductive quenching by AscH. In other words, excited state $[Ru(bpy)_3]^{2+*}$ is a much stronger oxidant than ground state $[Ru(bpy)_3]^{2+}$.[177] Reductive quenching of $[Ru(bpy)_3]^{2+*}$ forms reduced $[Ru(bpy)_3]^{+}$ (in the above section this species would equal PS^{-}) as a reactive intermediate. Electron transfer from $[Ru(bpy)_3]^{+}$ to the HEC (e.g. through facilitating a Co(I/II) reduction) regenerates the ground state photosensitizer, $[Ru(bpy)_3]^{2+}$ and a reduced HEC^{-}. Finally, HEC^{-} forms hydrogen through a

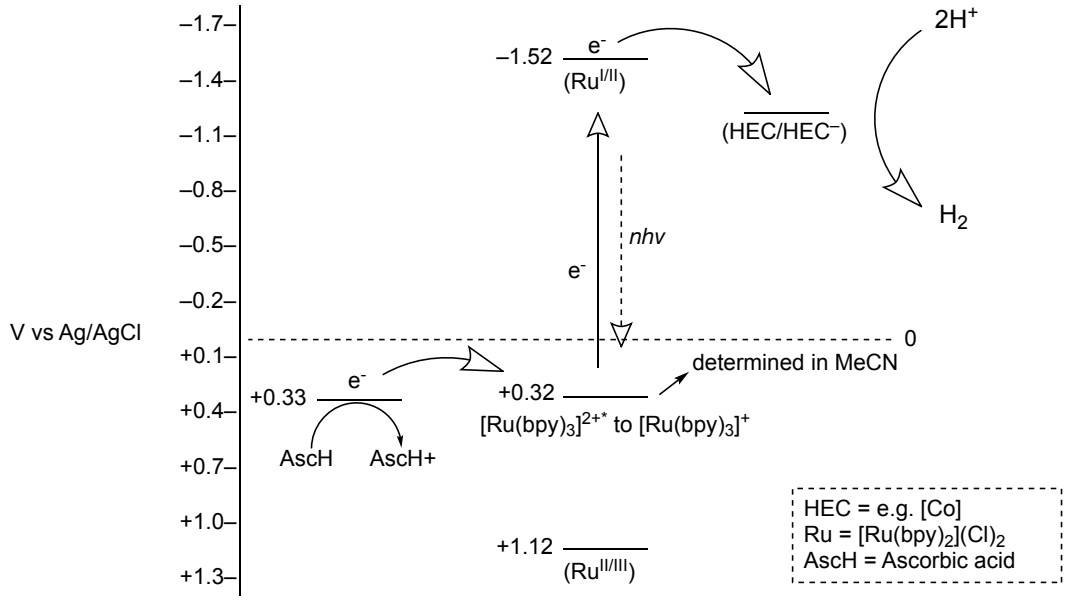

Figure 17. A thermodynamic redox potential analysis for the reductive quenching pathway of $[Ru(bpy)_3]^{2+}$ by AscH under aqueous conditions.

series of consecutive protonation and reduction steps, in which the sequences of the mechanistic steps can greatly change depending on the HEC and reaction conditions (see, e.g., **Figure 10**). The overall rate of H_2 formation is determined by the yield of reductive quenching,[142,178] the rate of electron transfer to the catalyst, the rate for decomposition of PS^-,[179-181] the rate of re-reduction of the ascorbic acid oxidation products,[162] and the total rate for H_2 formation on the HEC.

1.4 Aim and Scope of This Thesis

To move away from fossil fuels and therewith retard the current climate change, the demand for accessible renewable energy is increasing, leading to significant developments in the artificial photosynthesis research area. In this field, storing energy in hydrogen gas, by means of splitting water into oxygen and hydrogen, is regarded as one of the most important strategies. Historically, catalysts have been used and further developed to solve the accompanying scientific challenges, such as mediating slow reaction steps like the hydrogen evolution reaction (HER). Efficient candidates were found in platinum-based materials, but their low abundance and high cost prevent their use in large-scale applications. Accordingly, different materials need to be developed that mediate the HER and are readily accessible and affordable. As an outcome of these research endeavors, cobalt-based molecular complexes have appeared as interesting HER catalyst candidates.

In this thesis, new synthetic molecular cobalt complexes are developed and tested as catalysts for the HER. More specifically, the aim of the thesis is to take on a recent lead from our research group, in which the HER was enabled through the use of a novel cobalt complex comprising diphenylbisimidazolemethane ligands (**Figure 18**). Complex **14**, holds a bis heterocyclic chelate (green) with a C–H proton relay (red) and bears significant steric bulk (purple) favoring

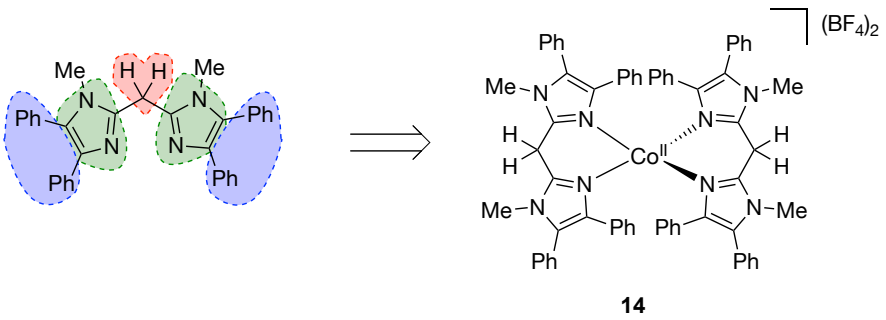

Figure 18. Bis(diphenylimidazole)methane ligand design and corresponding cobalt complex **14**, including heterocyclic coordinating moieties (green), a C–H proton relay (red) and significant steric bulk (purple).

a tetrahedral geometry. The HER with **14** operates via a unique mechanism (see section 1.4.2, complex **14**), and its structure-reactivity relationships are further studied in this thesis. Furthermore, the thesis aims to investigate the operational conditions and catalyst transformations during HER catalysis using molecular cobalt catalysts. In **Chapter 2**, electronic ligand effects on the (redox)properties of complex **14** and its catalytic HER activity are investigated. To this end, the bisimidazolemethane ligands in **14** are equipped with *para*-substituted aryl rings, holding different electron-donating and -withdrawing groups. Installation of the aryl ring is achieved by replacing one of the C–H methylene bonds in the ligand, retaining the coordinating environment around cobalt and one C–H proton relay functionality. Electrochemical and electrocatalytic analysis reveals that the (redox)properties and catalytic HER reactivity of the complex can be modulated upon altering the *para*-aryl substituents. **Chapter 3** focuses on the exploration of ligands containing benzazole groups, with different heteroatoms in the heterocycle, as substitutes for the bisimidazole ligands found in complex **14**. The smaller steric encumbrance and the different electronic nature of the resulting bisbenzazolemethane ligands over the bisdiphenylimidazolemethane ligand allow for a greater coordination flexibility as well as significant changes in the redox properties of the corresponding cobalt complexes. Accordingly, the HER performance of these cobalt complexes is explored. In **Chapter 4**, the catalytic performance of **14** is studied in greater detail by specifically investigating its bulk electrolysis performance. A new analysis setup with in-line product detection is developed to continuously monitor catalytic rates and efficiencies. The bulk HER performances are benchmarked to typical molecular HER catalysts in the field and **14** is identified as an overall competitive catalyst. This chapter also investigates catalyst stability and transformations during bulk catalysis. **Chapter 5** studies water-soluble molecular cobalt complexes in electrocatalytic HER. Particular attention is paid to the possibility to apply these complexes to the photocatalytic HER under aqueous conditions. Finally, **Chapter 6** closes this thesis with a perspective on the design and structure-reactivity studies of bioinspired molecular cobalt complexes in HER catalysis. Important design principles are discussed, leading to some crucial considerations for future HER research.

1.5 Authors Contributions

S.D. de Vos devised the aim, scope, and structure of this introduction and wrote the manuscript. D.L.J Broere and R.J.M. Klein Gebbink provided input on the manuscript during its creation.

1.6 References

(1) Smil, V. Energy transitions: global and national perspectives; 2nd ed.; *ABC-CLIO*, **2016**.

(2) Lüthi, D.; Le Floch, M.; Bereiter, B.; Blunier, T.; Barnola, J.-M.; Siegenthaler, U.; Raynaud, D.; Jouzel, J.; Fischer, H.; Kawamura, K.et al. High-resolution carbon dioxide concentration record 650,000–800,000 years before present. *Nature* **2008,** *453* (7193), 379.

(3) Barnola, J.; Raynaud, D.; Lorius, C.; Barkov, N. "Historical Carbon Dioxide Record from the Vostok Ice Core (417,160-2,342 years BP)," Environmental System Science Data Infrastructure for a Virtual Ecosystem, 2003.

(4) Trenberth, K. E. Has there been a hiatus? *Science* **2015,** *349* (6249), 691.

(5) Noyes, P. D.; McElwee, M. K.; Miller, H. D.; Clark, B. W.; Van Tiem, L. A.; Walcott, K. C.; Erwin, K. N.; Levin, E. D. The toxicology of climate change: Environmental contaminants in a warming world. *Environ. Int.* **2009,** *35* (6), 971.

(6) Choat, B.; Jansen, S.; Brodribb, T. J.; Cochard, H.; Delzon, S.; Bhaskar, R.; Bucci, S. J.; Feild, T. S.; Gleason, S. M.; Hacke, U. G. Global convergence in the vulnerability of forests to drought. *Nature* **2012,** *491* (7426), 752.

(7) Wheeler, T.; Von Braun, J. Climate change impacts on global food security. *Science* **2013,** *341* (6145), 508.

(8) Hoegh-Guldberg, O.; Mumby, P. J.; Hooten, A. J.; Steneck, R. S.; Greenfield, P.; Gomez, E.; Harvell, C. D.; Sale, P. F.; Edwards, A. J.; Caldeira, K. Coral reefs under rapid climate change and ocean acidification. *Science* **2007,** *318* (5857), 1737.

(9) Eckstein, D.; Künzel, V.; Schäfer, L.; Winges, M. Global climate risk index 2020. *Bonn: Germanwatch* **2019**.

(10) Schiermeier, Q. Few fishy facts found in climate report. *Nature* **2010,** *466* (7303), 170.

(11) https://climate.nasa.gov/news/2535/satellite-data-confirm-annual-carbon-dioxide-minimum-above-400-ppm/. Access data 01/10/2022.

(12) https://www.co2.earth/co2-ice-core-data Access date 13/01/2023

(13) Panwar, N. L.; Kaushik, S. C.; Kothari, S. Role of renewable energy sources in environmental protection: A review. *Renew. Sust. Energ. Rev.* **2011,** *15* (3), 1513.

(14) Mathews, A. P. Renewable Energy Technologies: Panacea for World Energy Security and Climate Change? *Procedia Comput. Sci.* **2014,** *32*, 731.

(15) McCollum, D. L.; Zhou, W.; Bertram, C.; de Boer, H.-S.; Bosetti, V.; Busch, S.; Després, J.; Drouet, L.; Emmerling, J.; Fay, M.et al. Energy investment needs for fulfilling the Paris Agreement and achieving the Sustainable Development Goals. *Nat. Energy* **2018,** *3* (7), 589.

(16) Perez, M.; Perez, R. Update 2022 – A fundamental look at supply side energy reserves for the planet. *Solar Energy Advances* **2022,** *2*, 100014.

(17) Lewis, N. S.; Nocera, D. G. Powering the planet: Chemical challenges in solar energy utilization. *Proc. Natl. Acad. Sci. U.S.A* **2006,** *103* (43), 15729.

(18) Sen, S.; Ganguly, S. Opportunities, barriers and issues with renewable energy development–A discussion. *Renew. Sust. Energ. Rev.* **2017,** *69*, 1170.

(19) Zubi, G.; Dufo-López, R.; Carvalho, M.; Pasaoglu, G. The lithium-ion battery: State of the art and future perspectives. *Renew. Sust. Energ. Rev.* **2018,** *89*, 292.

(20) Goodenough, J. B.; Kim, Y. Challenges for Rechargeable Li Batteries. *Chem. Mater.* **2010,** *22* (3), 587.

(21) Detz, R. J.; Reek, J. N. H.; van der Zwaan, B. C. C. The future of solar fuels: when could they become competitive? *Energy Environ. Sci.* **2018,** *11* (7), 1653.

(22) Nikolaidis, P.; Poullikkas, A. A comparative overview of hydrogen production processes. *Renew. Sust. Energ. Rev.* **2017,** *67*, 597.
(23) Møller, K. T.; Jensen, T. R.; Akiba, E.; Li, H.-w. Hydrogen - A sustainable energy carrier. *Prog. Nat. Sci* **2017,** *27* (1), 34.
(24) Kovač, A.; Paranos, M.; Marciuš, D. Hydrogen in energy transition: A review. *Int. J. Hydrogen Energy* **2021,** *46* (16), 10016.
(25) Dincer, I. Green methods for hydrogen production. *Int. J. Hydrogen Energy* **2012,** *37* (2), 1954.
(26) Shiva Kumar, S.; Himabindu, V. Hydrogen production by PEM water electrolysis – A review. *Materials Science for Energy Technologies* **2019,** *2* (3), 442.
(27) Rashid, M.; Al Mesfer, M. K.; Naseem, H.; Danish, M. Hydrogen production by water electrolysis: a review of alkaline water electrolysis, PEM water electrolysis and high temperature water electrolysis. *Int. j. adv. eng. technol.* **2015**, 4 , (3), 80-93.
(28) Wang, M.; Wang, Z.; Gong, X.; Guo, Z. The intensification technologies to water electrolysis for hydrogen production – A review. *Renew. Sust. Energ. Rev.* **2014,** *29*, 573.
(29) Terry, S.; Science Photo Library.
(30) Grigoriev, S. A.; Fateev, V. N.; Millet, P. In *Comprehensive Renewable Energy* 2nd ed.; Letcher, T. M., Ed.; Elsevier: Oxford, 2022.
(31) You, B.; Sun, Y. Innovative Strategies for Electrocatalytic Water Splitting. *Acc. Chem. Res.* **2018,** *51* (7), 1571.
(32) Nurttila, S. S.; Zaffaroni, R.; Mathew, S.; Reek, J. N. H. Control of the overpotential of a [FeFe] hydrogenase mimic by a synthetic second coordination sphere. *Chem. Commun.* **2019,** *55* (21), 3081.
(33) Volbeda, A.; Charon, M.-H.; Piras, C.; Hatchikian, E. C.; Frey, M.; Fontecilla-Camps, J. C. Crystal structure of the nickel–iron hydrogenase from Desulfovibrio gigas. *Nature* **1995,** *373* (6515), 580.
(34) Adams, M. W. The structure and mechanism of iron-hydrogenases. *Biochi. et Biophys. Acta* **1990,** *1020* (2), 115.
(35) Albracht, S. P. Nickel hydrogenases: in search of the active site. *Biochi. et Biophys. Acta* **1994,** *1188* (3), 167.
(36) Thauer, R. K.; Klein, A. R.; Hartmann, G. C. Reactions with molecular hydrogen in microorganisms: evidence for a purely organic hydrogenation catalyst. *Chem. Rev.* **1996,** *96* (7), 3031.
(37) Cammack, R.; Frey, M.; Robson, R. *Hydrogen as a fuel: learning from nature*; CRC Press, 2001.
(38) Vignais, P. M.; Billoud, B. Occurrence, classification, and biological function of hydrogenases: an overview. *Chem. Rev.* **2007,** *107* (10), 4206.
(39) Thauer, R. K.; Kaster, A.-K.; Goenrich, M.; Schick, M.; Hiromoto, T.; Shima, S. Hydrogenases from Methanogenic Archaea, Nickel, a Novel Cofactor, and H2 Storage. *Annu. Rev. Biochem.* **2010,** *79* (1), 507.
(40) Fontecilla-Camps, J. C.; Volbeda, A.; Cavazza, C.; Nicolet, Y. Structure/function relationships of [NiFe]-and [FeFe]-hydrogenases. *Chem. Rev.* **2007,** *107* (10), 4273.
(41) De Lacey, A. L.; Fernandez, V. M.; Rousset, M.; Cammack, R. Activation and inactivation of hydrogenase function and the catalytic cycle: spectroelectrochemical studies. *Chem. Rev.* **2007,** *107* (10), 4304.
(42) Lubitz, W.; Reijerse, E.; van Gastel, M. [NiFe] and [FeFe] hydrogenases studied by advanced magnetic resonance techniques. *Chem. Rev.* **2007,** *107* (10), 4331.
(43) Vincent, K. A.; Parkin, A.; Armstrong, F. A. Investigating and exploiting the electrocatalytic properties of hydrogenases. *Chem. Rev.* **2007,** *107* (10), 4366.

(44) Siegbahn, P. E.; Tye, J. W.; Hall, M. B. Computational studies of [NiFe] and [FeFe] hydrogenases. *Chem. Rev.* **2007,** *107* (10), 4414.
(45) Lubitz, W.; Tumas, W. Hydrogen: an overview. *Chem. Rev.* **2007,** *107* (10), 3900.
(46) Lubitz, W.; Ogata, H.; Rüdiger, O.; Reijerse, E. Hydrogenases. *Chem. Rev.* **2014,** *114* (8), 4081.
(47) Frey, M. Hydrogenases: Hydrogen-Activating Enzymes. *ChemBioChem* **2002,** *3* (2-3), 153.
(48) Jugder, B.-E.; Welch, J.; Aguey-Zinsou, K.-F.; Marquis, C. P. Fundamentals and electrochemical applications of [Ni–Fe]-uptake hydrogenases. *RSC Advances* **2013,** *3* (22), 8142.
(49) Shima, S.; Ermler, U. Structure and Function of [Fe]-Hydrogenase and its Iron–Guanylylpyridinol (FeGP) Cofactor. *Eur. J. Inorg. Chem.* **2011,** *2011* (7), 963.
(50) Yang, X.; Hall, M. B. Monoiron hydrogenase catalysis: hydrogen activation with the formation of a dihydrogen, Fe− $H^{\delta-}\cdots H^{\delta+}$− O, bond and methenyl-H4MPT$^+$ triggered hydride transfer. *J. Am. Chem. Soc.* **2009,** *131* (31), 10901.
(51) Schilter, D.; Camara, J. M.; Huynh, M. T.; Hammes-Schiffer, S.; Rauchfuss, T. B. Hydrogenase Enzymes and Their Synthetic Models: The Role of Metal Hydrides. *Chem. Rev.* **2016,** *116* (15), 8693.
(52) Vignais, P. M.; Billoud, B.; Meyer, J. Classification and phylogeny of hydrogenases. *FEMS Microbiol. Rev.* **2001,** *25* (4), 455.
(53) Cammack, R. Hydrogenase sophistication. *Nature* **1999,** *397* (6716), 214.
(54) Hatchikian, E. C.; Forget, N.; Fernandez, V. M.; Williams, R.; Cammack, R. Further characterization of the [Fe]-hydrogenase from Desulfovibrio desulfuricans ATCC 7757. *Eur. J. Biochem.* **1992,** *209* (1), 357.
(55) Ogata, H.; Hirota, S.; Nakahara, A.; Komori, H.; Shibata, N.; Kato, T.; Kano, K.; Higuchi, Y. Activation process of [NiFe] hydrogenase elucidated by high-resolution X-ray analyses: conversion of the ready to the unready state. *Structure* **2005,** *13* (11), 1635.
(56) Nicolet, Y.; Piras, C.; Legrand, P.; Hatchikian, C. E.; Fontecilla-Camps, J. C. Desulfovibrio desulfuricans iron hydrogenase: the structure shows unusual coordination to an active site Fe binuclear center. *Structure* **1999,** *7* (1), 13.
(57) Kim, J. H.; Hansora, D.; Sharma, P.; Jang, J.-W.; Lee, J. S. Toward practical solar hydrogen production – an artificial photosynthetic leaf-to-farm challenge. *Chem. Soc. Rev.* **2019,** *48* (7), 1908.
(58) Sapountzi, F. M.; Gracia, J. M.; Fredriksson, H. O.; Niemantsverdriet, J. H. Electrocatalysts for the generation of hydrogen, oxygen and synthesis gas. *Prog. Energy Combust. Sci.* **2017,** *58*, 1.
(59) Li, R.; Li, C. In *Advances in Catalysis*; Song, C., Ed.; Academic Press, 2017; Vol. 60.
(60) Sapountzi, F. M.; Gracia, J. M.; Weststrate, C. J.; Fredriksson, H. O. A.; Niemantsverdriet, J. W. Electrocatalysts for the generation of hydrogen, oxygen and synthesis gas. *Prog. Energy Combust. Sci.* **2017,** *58*, 1.
(61) Polman, A.; Knight, M.; Garnett, E. C.; Ehrler, B.; Sinke, W. C. Photovoltaic materials: Present efficiencies and future challenges. *Science* **2016,** *352* (6283), aad4424.
(62) McCrory, C. C. L.; Jung, S.; Ferrer, I. M.; Chatman, S. M.; Peters, J. C.; Jaramillo, T. F. Benchmarking Hydrogen Evolving Reaction and Oxygen Evolving Reaction Electrocatalysts for Solar Water Splitting Devices. *J. Am. Chem. Soc.* **2015,** *137* (13), 4347.
(63) Sivula, K.; *J. Phys. Chem. Lett.* **2015**, 6, 6, 975–976
(64) Lakhera, S. K.; Rajan, A.; T.P, R.; Bernaurdshaw, N. A review on particulate photocatalytic hydrogen production system: Progress made in achieving high energy

conversion efficiency and key challenges ahead. *Renew. Sust. Energ. Rev.* **2021,** *152*, 111694.
(65) Osterloh, F. E. Photocatalysis versus Photosynthesis: A Sensitivity Analysis of Devices for Solar Energy Conversion and Chemical Transformations. *ACS Energy Letters* **2017,** *2* (2), 445.
(66) Chen, S.; Takata, T.; Domen, K. Particulate photocatalysts for overall water splitting. *Nat. Rev. Mater.* **2017,** *2* (10), 17050.
(67) Yao, T.; An, X.; Han, H.; Chen, J. Q.; Li, C. Photoelectrocatalytic Materials for Solar Water Splitting. *Adv. Energy Mater.* **2018,** *8* (21), 1800210.
(68) Walter, M. G.; Warren, E. L.; McKone, J. R.; Boettcher, S. W.; Mi, Q.; Santori, E. A.; Lewis, N. S. Solar Water Splitting Cells. *Chem. Rev.* **2010,** *110* (11), 6446.
(69) Nielander, A. C.; Shaner, M. R.; Papadantonakis, K. M.; Francis, S. A.; Lewis, N. S. A taxonomy for solar fuels generators. *Energy Environ. Sci.* **2015,** *8* (1), 16.
(70) Shon, J.-H.; Teets, T. S. Molecular photosensitizers in energy research and catalysis: design principles and recent developments. *ACS Energy Letters* **2019,** *4* (2), 558.
(71) Sivula, K.; van de Krol, R. Erratum: Semiconducting materials for photoelectrochemical energy conversion. *Nat. Rev. Mater.* **2016**.
(72) Hu, S.; Shaner, M. R.; Beardslee, J. A.; Lichterman, M.; Brunschwig, B. S.; Lewis, N. S. Amorphous TiO2 coatings stabilize Si, GaAs, and GaP photoanodes for efficient water oxidation. *Science* **2014,** *344* (6187), 1005.
(73) Berardi, S.; Drouet, S.; Francàs, L.; Gimbert-Suriñach, C.; Guttentag, M.; Richmond, C.; Stoll, T.; Llobet, A. Molecular artificial photosynthesis. *Chem. Soc. Rev.* **2014,** *43* (22), 7501.
(74) Fujishima, A.; Honda, K. Electrochemical Photolysis of Water at a Semiconductor Electrode. *Nature* **1972,** *238* (5358), 37.
(75) Zhong, H.; Campos-Roldán, C. A.; Zhao, Y.; Zhang, S.; Feng, Y.; Alonso-Vante, N. Recent Advances of Cobalt-Based Electrocatalysts for Oxygen Electrode Reactions and Hydrogen Evolution Reaction. *Catalysts* **2018,** *8* (11), 559.
(76) Zhang, W.; Cui, L.; Liu, J. Recent advances in cobalt-based electrocatalysts for hydrogen and oxygen evolution reactions. *J. Alloys Compd.* **2020,** *821*, 153542.
(77) Wang, J.; Cui, W.; Liu, Q.; Xing, Z.; Asiri, A. M.; Sun, X. Recent Progress in Cobalt-Based Heterogeneous Catalysts for Electrochemical Water Splitting. *Adv. Mater.* **2016,** *28* (2), 215.
(78) Fukuzumi, S.; Yamada, Y.; Suenobu, T.; Ohkubo, K.; Kotani, H. Catalytic mechanisms of hydrogen evolution with homogeneous and heterogeneous catalysts. *Energy Environ. Sci.* **2011,** *4* (8), 2754.
(79) Blakemore, J. D.; Crabtree, R. H.; Brudvig, G. W. Molecular Catalysts for Water Oxidation. *Chem. Rev.* **2015,** *115* (23), 12974.
(80) Wang, M.; Yang, Y.; Shen, J.; Jiang, J.; Sun, L. Visible-light-absorbing semiconductor/molecular catalyst hybrid photoelectrodes for H_2 or O_2 evolution: recent advances and challenges. *Sustainable Energy & Fuels* **2017,** *1* (8), 1641.
(81) Tard, C.; Pickett, C. J. Structural and functional analogues of the active sites of the [Fe]-,[NiFe]-, and [FeFe]-hydrogenases. *Chem. Rev.* **2009,** *109* (6), 2245.
(82) Canaguier, S.; Artero, V.; Fontecave, M. Modelling NiFe hydrogenases: nickel-based electrocatalysts for hydrogen production. *Dalton Trans.* **2008,** (3), 315.
(83) Dismukes, G. C.; Brimblecombe, R.; Felton, G. A. N.; Pryadun, R. S.; Sheats, J. E.; Spiccia, L.; Swiegers, G. F. Development of Bioinspired Mn_4O_4−Cubane Water Oxidation Catalysts: Lessons from Photosynthesis. *Acc. Chem. Res.* **2009,** *42* (12), 1935.

(84) Brimblecombe, R.; Dismukes, G. C.; Swiegers, G. F.; Spiccia, L. Molecular water-oxidation catalysts for photoelectrochemical cells. *Dalton Trans.* **2009,** (43), 9374.
(85) Wang, M.; Sun , L. Hydrogen Production by Noble-Metal-Free Molecular Catalysts and Related Nanomaterials. *ChemSusChem* **2010,** *3* (5), 551.
(86) Artero, V.; Chavarot-Kerlidou, M.; Fontecave, M. Splitting Water with Cobalt. *Angew. Chem. Int. Ed.* **2011,** *50* (32), 7238.
(87) Losse, S.; Vos, J. G.; Rau, S. Catalytic hydrogen production at cobalt centres. *Coord. Chem. Rev.* **2010,** *254* (21), 2492.
(88) Li, J.; Triana, C. A.; Wan, W.; Adiyeri Saseendran, D. P.; Zhao, Y.; Balaghi, S. E.; Heidari, S.; Patzke, G. R. Molecular and heterogeneous water oxidation catalysts: recent progress and joint perspectives. *Chem. Soc. Rev.* **2021,** *50* (4), 2444.
(89) Zaccaria, F.; Menendez Rodriguez, G.; Rocchigiani, L.; Macchioni, A. Molecular Catalysis in "Green" Hydrogen Production. *Frontiers in Catalysis* **2022,** *2*.
(90) Tong, L.; Duan, L.; Zhou, A.; Thummel, R. P. First-row transition metal polypyridine complexes that catalyze proton to hydrogen reduction. *Coord. Chem. Rev.* **2020,** *402*, 213079.
(91) Zhang, B.; Fan, L.; Ambre, R. B.; Liu, T.; Meng, Q.; Timmer, B. J. J.; Sun, L. Advancing Proton Exchange Membrane Electrolyzers with Molecular Catalysts. *Joule* **2020,** *4* (7), 1408.
(92) Zhang, B.; Sun, L. Artificial photosynthesis: opportunities and challenges of molecular catalysts. *Chem. Soc. Rev.* **2019,** *48* (7), 2216.
(93) Margonis, C. M.; Ho, M.; Travis, B. D.; Brennessel, W. W.; McNamara, W. R. Iron polypyridyl complex adsorbed on carbon surfaces for hydrogen generation. *Chem. Commun.* **2021**, 57, 7697-7700
(94) Lee, K. J.; McCarthy, B. D.; Dempsey, J. L. On decomposition, degradation, and voltammetric deviation: the electrochemist's field guide to identifying precatalyst transformation. *Chem. Soc. Rev.* **2019,** *48* (11), 2927.
(95) Bullock, R. M.; Das, A. K.; Appel, A. M. Surface Immobilization of Molecular Electrocatalysts for Energy Conversion. *Chem. Eur. J.* **2017,** *23* (32), 7626.
(96) Kaeffer, N.; Morozan, A.; Fize, J.; Martinez, E.; Guetaz, L.; Artero, V. The Dark Side of Molecular Catalysis: Diimine–Dioxime Cobalt Complexes Are Not the Actual Hydrogen Evolution Electrocatalyst in Acidic Aqueous Solutions. *ACS Catalysis* **2016,** *6* (6), 3727.
(97) Martin, D. J.; McCarthy, B. D.; Donley, C. L.; Dempsey, J. L. Electrochemical hydrogenation of a homogeneous nickel complex to form a surface adsorbed hydrogen-evolving species. *Chem. Commun.* **2015,** *51* (25), 5290.
(98) Anxolabéhère-Mallart, E.; Costentin, C.; Fournier, M.; Robert, M. Cobalt-Bisglyoximato Diphenyl Complex as a Precatalyst for Electrocatalytic H_2 Evolution. *J. Phys. Chem. C* **2014,** *118* (25), 13377.
(99) Ghachtouli, S. E.; Guillot, R.; Brisset, F.; Aukauloo, A. Cobalt-Based Particles Formed upon Electrocatalytic Hydrogen Production by a Cobalt Pyridine Oxime Complex. *ChemSusChem* **2013,** *6* (12), 2226.
(100) Berben, L. A.; Peters, J. C. Hydrogen evolution by cobalt tetraimine catalysts adsorbed on electrode surfaces. *Chem. Commun.* **2010,** *46* (3), 398.
(101) Kaeffer, N.; Chavarot-Kerlidou, M.; Artero, V. Hydrogen Evolution Catalyzed by Cobalt Diimine–Dioxime Complexes. *Acc. Chem. Res.* **2015,** *48* (5), 1286.
(102) Andreiadis, E. S.; Jacques, P.-A.; Tran, P. D.; Leyris, A.; Chavarot-Kerlidou, M.; Jousselme, B.; Matheron, M.; Pécaut, J.; Palacin, S.; Fontecave, M; Artero. V. Molecular engineering of a cobalt-based electrocatalytic nanomaterial for H_2 evolution under fully aqueous conditions. *Nat. Chem.* **2013,** *5* (1), 48.

(103) Kaeffer, N.; Massin, J.; Lebrun, C.; Renault, O.; Chavarot-Kerlidou, M.; Artero, V. Covalent Design for Dye-Sensitized H_2-Evolving Photocathodes Based on a Cobalt Diimine–Dioxime Catalyst. *J. Am. Chem. Soc.* **2016,** *138* (38), 12308.
(104) Windle, C. D.; Kumagai, H.; Higashi, M.; Brisse, R.; Bold, S.; Jousselme, B.; Chavarot-Kerlidou, M.; Maeda, K.; Abe, R.; Ishitani, O; Artero. V. Earth-Abundant Molecular Z-Scheme Photoelectrochemical Cell for Overall Water-Splitting. *J. Am. Chem. Soc.* **2019,** *141* (24), 9593.
(105) Bard, A. J. High Speed Controlled Potential Coulometry. *Anal. Chem.* **1963,** *35* (9), 1125.
(106) Bullock, R. M.; Appel, A. M.; Helm, M. L. Production of hydrogen by electrocatalysis: making the H–H bond by combining protons and hydrides. *Chem. Commun.* **2014,** *50* (24), 3125.
(107) Felton, G. A. N.; Glass, R. S.; Lichtenberger, D. L.; Evans, D. H. Iron-Only Hydrogenase Mimics. Thermodynamic Aspects of the Use of Electrochemistry to Evaluate Catalytic Efficiency for Hydrogen Generation. *Inorg. Chem.* **2006,** *45* (23), 9181.
(108) McCarthy, B. D.; Martin, D. J.; Rountree, E. S.; Ullman, A. C.; Dempsey, J. L. Electrochemical Reduction of Brønsted Acids by Glassy Carbon in Acetonitrile—Implications for Electrocatalytic Hydrogen Evolution. *Inorg. Chem.* **2014,** *53* (16), 8350.
(109) Fourmond, V.; Jacques, P.-A.; Fontecave, M.; Artero, V. H_2 Evolution and Molecular Electrocatalysts: Determination of Overpotentials and Effect of Homoconjugation. *Inorg. Chem.* **2010,** *49* (22), 10338.
(110) Stratakes, B. M.; Dempsey, J. L.; Miller, A. J. M. Determining the Overpotential of Electrochemical Fuel Synthesis Mediated by Molecular Catalysts: Recommended Practices, Standard Reduction Potentials, and Challenges. *ChemElectroChem* **2021***, 8,* 4161–4180.
(111) Zou, X.; Zhang, Y. Noble metal-free hydrogen evolution catalysts for water splitting. *Chem. Soc. Rev.* **2015,** *44* (15), 5148.
(112) https://www.macrotrends.net/2540/platinum-prices-historical-chart-data. *Platinum Prices - Interactive Historical Chart*, Access date 13 April 2023.
(113) Coutard, N.; Kaeffer, N.; Artero, V. Molecular engineered nanomaterials for catalytic hydrogen evolution and oxidation. *Chem. Commun.* **2016,** *52* (95), 13728.
(114) Wang, J.-W.; Liu, W.-J.; Zhong, D.-C.; Lu, T.-B. Nickel complexes as molecular catalysts for water splitting and CO2 reduction. *Coord. Chem. Rev.* **2019,** *378*, 237.
(115) Queyriaux, N.; Jane, R. T.; Massin, J.; Artero, V.; Chavarot-Kerlidou, M. Recent developments in hydrogen evolving molecular cobalt (II)–polypyridyl catalysts. *Coord. Chem. Rev.* **2015,** *304*, 3.
(116) Wang, M.; Chen, L.; Sun, L. Recent progress in electrochemical hydrogen production with earth-abundant metal complexes as catalysts. *Energy Environ. Sci.* **2012,** *5* (5), 6763.
(117) Gao, S.; Fan, W.; Liu, Y.; Jiang, D.; Duan, Q. Artificial water-soluble systems inspired by [FeFe]-hydrogenases for electro- and photocatalytic hydrogen production. *Int. J. Hydrogen Energy* **2020,** *45* (7), 4305.
(118) Eckenhoff, W. T. Molecular catalysts of Co, Ni, Fe, and Mo for hydrogen generation in artificial photosynthetic systems. *Coord. Chem. Rev.* **2018,** *373*, 295.
(119) Luo, G.-G.; Pan, Z.-H.; Lin, J.-Q.; Sun, D. Tethered sensitizer–catalyst noble-metal-free molecular devices for solar-driven hydrogen generation. *Dalton Trans.* **2018,** *47* (44), 15633.

(120) Fukuzumi, S.; Lee, Y.-M.; Nam, W. Thermal and photocatalytic production of hydrogen with earth-abundant metal complexes. *Coord. Chem. Rev.* **2018,** *355*, 54.
(121) Dalle, K. E.; Warnan, J.; Leung, J. J.; Reuillard, B.; Karmel, I. S.; Reisner, E. Electro- and Solar-Driven Fuel Synthesis with First Row Transition Metal Complexes. *Chem. Rev.* **2019,** *119* (4), 2752.
(122) Corredor, J.; Rivero, M. J.; Rangel, C. M.; Gloaguen, F.; Ortiz, I. Comprehensive review and future perspectives on the photocatalytic hydrogen production. *J. Chem. Technol. Biotechnol.* **2019,** *94* (10), 3049.
(123) Wang, M.; Han, K.; Zhang, S.; Sun, L. Integration of organometallic complexes with semiconductors and other nanomaterials for photocatalytic H_2 production. *Coord. Chem. Rev.* **2015,** *287*, 1.
(124) Mazzeo, A.; Santalla, S.; Gaviglio, C.; Doctorovich, F.; Pellegrino, J. Recent progress in homogeneous light-driven hydrogen evolution using first-row transition metal catalysts. *Inorg. Chim. Acta* **2021,** *517*, 119950.
(125) Beyene, B. B.; Hung, C.-H. Recent progress on metalloporphyrin-based hydrogen evolution catalysis. *Coord. Chem. Rev.* **2020,** *410*, 213234.
(126) Drosou, M.; Kamatsos, F.; Mitsopoulou, C. A. Recent advances in the mechanisms of the hydrogen evolution reaction by non-innocent sulfur-coordinating metal complexes. *Inorg. Chem. Front.* **2020,** *7* (1), 37.
(127) Zhao, X.; Wang, P.; Long, M. Electro- and Photocatalytic Hydrogen Production by Molecular Cobalt Complexes With Pentadentate Ligands. *Comments Inorg. Chem.* **2017,** *37* (5), 238.
(128) Queyriaux, N.; Jane, R. T.; Massin, J.; Artero, V.; Chavarot-Kerlidou, M. Recent developments in hydrogen evolving molecular cobalt(II)–polypyridyl catalysts. *Coord. Chem. Rev.* **2015,** *304-305*, 3.
(129) https://www.lme.com/en-GB/Metals/Minor-metals/Cobalt#tabIndex=0. *London Metal Exchange: LME Cobalt* Access date 13 April 2023.
(130) Connolly, P.; Espenson, J. H. Cobalt-catalyzed evolution of molecular hydrogen. *Inorg. Chem.* **1986,** *25* (16), 2684.
(131) Razavet, M.; Artero, V.; Fontecave, M. Proton Electroreduction Catalyzed by Cobaloximes: Functional Models for Hydrogenases. *Inorg. Chem.* **2005,** *44* (13), 4786.
(132) Hu, X.; Cossairt, B. M.; Brunschwig, B. S.; Lewis, N. S.; Peters, J. C. Electrocatalytic hydrogen evolution by cobalt difluoroboryl-diglyoximate complexes. *Chem. Commun.* **2005,** (37), 4723.
(133) Baffert, C.; Artero, V.; Fontecave, M. Cobaloximes as Functional Models for Hydrogenases. 2. Proton Electroreduction Catalyzed by Difluoroborylbis(dimethylglyoximato)cobalt(II) Complexes in Organic Media. *Inorg. Chem.* **2007,** *46* (5), 1817.
(134) Hu, X.; Brunschwig, B. S.; Peters, J. C. Electrocatalytic Hydrogen Evolution at Low Overpotentials by Cobalt Macrocyclic Glyoxime and Tetraimine Complexes. *J. Am. Chem. Soc.* **2007,** *129* (29), 8988.
(135) Jacques, P.-A.; Artero, V.; Pécaut, J.; Fontecave, M. Cobalt and nickel diimine-dioxime complexes as molecular electrocatalysts for hydrogen evolution with low overvoltages. *Proc. Natl. Acad. Sci. U.S.A* **2009,** *106* (49), 20627.
(136) Lance, K. A.; Goldsby, K. A.; Busch, D. H. Effective new cobalt (II) dioxygen carriers derived from dimethylglyoxime by the replacement of the linking protons with difluoroboron (1+). *Inorg. Chem.* **1990,** *29* (22), 4537.
(137) Bakac, A.; Espenson, J. H. Unimolecular and bimolecular homolytic reactions of organochromium and organocobalt complexes. Kinetics and equilibria. *J. Am. Chem. Soc.* **1984,** *106* (18), 5197.

(138) Fihri, A.; Artero, V.; Pereira, A.; Fontecave, M. Efficient H_2-producing photocatalytic systems based on cyclometalated iridium- and tricarbonylrhenium-diimine photosensitizers and cobaloxime catalysts. *Dalton Trans.* **2008,** (41), 5567.
(139) Du, P.; Knowles, K.; Eisenberg, R. A homogeneous system for the photogeneration of hydrogen from water based on a platinum (II) terpyridyl acetylide chromophore and a molecular cobalt catalyst. *J. Am. Chem. Soc.* **2008,** *130* (38), 12576.
(140) Lazarides, T.; McCormick, T.; Du, P.; Luo, G.; Lindley, B.; Eisenberg, R. Making hydrogen from water using a homogeneous system without noble metals. *J. Am. Chem. Soc.* **2009,** *131* (26), 9192.
(141) Bigi, J. P.; Hanna, T. E.; Harman, W. H.; Chang, A.; Chang, C. J. Electrocatalytic reduction of protons to hydrogen by a water-compatible cobalt polypyridyl platform. *Chem. Commun.* **2010,** *46* (6), 958.
(142) Khnayzer, R. S.; Thoi, V. S.; Nippe, M.; King, A. E.; Jurss, J. W.; El Roz, K. A.; Long, J. R.; Chang, C. J.; Castellano, F. N. Towards a comprehensive understanding of visible-light photogeneration of hydrogen from water using cobalt(II) polypyridyl catalysts. *Energy Environ. Sci.* **2014,** *7* (4), 1477.
(143) Sun, Y.; Bigi, J. P.; Piro, N. A.; Tang, M. L.; Long, J. R.; Chang, C. J. Molecular Cobalt Pentapyridine Catalysts for Generating Hydrogen from Water. *J. Am. Chem. Soc.* **2011,** *133* (24), 9212.
(144) Karunadasa, H. I.; Chang, C. J.; Long, J. R. A molecular molybdenum-oxo catalyst for generating hydrogen from water. *Nature* **2010,** *464*, 1329.
(145) Nippe, M.; Khnayzer, R. S.; Panetier, J. A.; Zee, D. Z.; Olaiya, B. S.; Head-Gordon, M.; Chang, C. J.; Castellano, F. N.; Long, J. R. Catalytic proton reduction with transition metal complexes of the redox-active ligand bpy2PYMe. *Chemical Science* **2013,** *4* (10), 3934.
(146) Queyriaux, N.; Sun, D.; Fize, J.; Pécaut, J.; Field, M. J.; Chavarot-Kerlidou, M.; Artero, V. Electrocatalytic Hydrogen Evolution with a Cobalt Complex Bearing Pendant Proton Relays: Acid Strength and Applied Potential Govern Mechanism and Stability. *J. Am. Chem. Soc* **2020,** *142* (1), 274.
(147) Ghosh, P.; de Vos, S.; Lutz, M.; Gloaguen, F.; Schollhammer, P.; Moret, M.-E.; Klein Gebbink, R. J. M. Electrocatalytic Proton Reduction by a Cobalt Complex Containing a Proton-Responsive Bis(alkylimdazole)methane Ligand: Involvement of a C−H Bond in H_2 Formation. *Chem. Eur. J.* **2020,** *26* (55), 12560.
(148) Wilson, A. D.; Newell, R. H.; McNevin, M. J.; Muckerman, J. T.; Rakowski DuBois, M.; DuBois, D. L. Hydrogen Oxidation and Production Using Nickel-Based Molecular Catalysts with Positioned Proton Relays. *J. Am. Chem. Soc.* **2006,** *128* (1), 358.
(149) Wilson, A. D.; Shoemaker, R. K.; Miedaner, A.; Muckerman, J. T.; DuBois, D. L.; Rakowski DuBois, M. Nature of hydrogen interactions with Ni(II) complexes containing cyclic phosphine ligands with pendant nitrogen bases. *Proc. Natl. Acad. Sci. U.S.A.* **2007,** *104*, 6951.
(150) Rakowski DuBois, M.; DuBois, D. L. The roles of the first and second coordination spheres in the design of molecular catalysts for H_2 production and oxidation. *Chem. Soc. Rev.* **2009,** *38* (1), 62.
(151) Wiedner, E. S.; Yang, J. Y.; Dougherty, W. G.; Kassel, W. S.; Bullock, R. M.; Rakowski DuBois, M.; DuBois, D. L. Comparison of Cobalt and Nickel Complexes with Sterically Demanding Cyclic Diphosphine Ligands: Electrocatalytic H_2 Production by $[Co(P^{tBu}_2N^{Ph}_2)(CH_3CN)_3](BF_4)_2$ *Organometallics* **2010,** *29*, 5390.
(152) Wiedner, E. S.; Appel, A. M.; DuBois, D. L.; Bullock, R. M. Thermochemical and Mechanistic Studies of Electrocatalytic Hydrogen Production by Cobalt Complexes Containing Pendant Amines. *Inorg. Chem.* **2013,** *52* (24), 14391.

(153) Wiedner, E. S.; Roberts, J. A. S.; Dougherty, W. G.; Kassel, W. S.; DuBois, D. L.; Bullock, R. M. Synthesis and Electrochemical Studies of Cobalt(III) Monohydride Complexes Containing Pendant Amines. *Inorg. Chem.* **2013,** *52* (17), 9975.
(154) Chen, L.; Wang, M.; Han, K.; Zhang, P.; Gloaguen, F.; Sun, L. A super-efficient cobalt catalyst for electrochemical hydrogen production from neutral water with 80 mV overpotential. *Energy Environ. Sci.* **2014,** *7* (1), 329.
(155) Kilgore, U. J.; Roberts, J. A. S.; Pool, D. H.; Appel, A. M.; Stewart, M. P.; DuBois, M. R.; Dougherty, W. G.; Kassel, W. S.; Bullock, R. M.; DuBois, D. L. $[Ni(P^{Ph}_2N^{C6H4X}_2)_2]^{2+}$ Complexes as Electrocatalysts for H_2 Production: Effect of Substituents, Acids, and Water on Catalytic Rates. *J. Am. Chem. Soc.* **2011,** *133* (15), 5861.
(156) Tsuji, Y.; Yamamoto, K.; Yamauchi, K.; Sakai, K. Near-Infrared Light-Driven Hydrogen Evolution from Water Using a Polypyridyl Triruthenium Photosensitizer. *Angew. Chem. Int. Ed.* **2018,** *57* (1), 208.
(157) Yuan, Y.-J.; Yu, Z.-T.; Chen, D.-Q.; Zou, Z.-G. Metal-complex chromophores for solar hydrogen generation. *Chem. Soc. Rev.* **2017,** *46* (3), 603.
(158) Decavoli, C.; Boldrini, C. L.; Manfredi, N.; Abbotto, A. Molecular Organic Sensitizers for Photoelectrochemical Water Splitting. *Eur. J. Inorg. Chem.* **2020,** *2020* (11-12), 978.
(159) Zee, D. Z.; Chantarojsiri, T.; Long, J. R.; Chang, C. J. Metal–polypyridyl catalysts for electro-and photochemical reduction of water to hydrogen. *Acc. Chem. Res.* **2015,** *48* (7), 2027.
(160) Queyriaux, N.; Giannoudis, E.; Windle, C. D.; Roy, S.; Pécaut, J.; Coutsolelos, A. G.; Artero, V.; Chavarot-Kerlidou, M. A noble metal-free photocatalytic system based on a novel cobalt tetrapyridyl catalyst for hydrogen production in fully aqueous medium. *Sustainable Energy & Fuels* **2018,** *2* (3), 553.
(161) Shan, B.; Baine, T.; Ma, X. A. N.; Zhao, X.; Schmehl, R. H. Mechanistic Details for Cobalt Catalyzed Photochemical Hydrogen Production in Aqueous Solution: Efficiencies of the Photochemical and Non-Photochemical Steps. *Inorg. Chem.* **2013,** *52* (9), 4853.
(162) Bachmann, C.; Probst, B.; Guttentag, M.; Alberto, R. Ascorbate as an electron relay between an irreversible electron donor and Ru (II) or Re (I) photosensitizers. *Chem. Commun.* **2014,** *50* (51), 6737.
(163) Wechtersbach, L.; Cigić, B. Reduction of dehydroascorbic acid at low pH. *J. Biochem. and Biophys. Methods* **2007,** *70* (5), 767.
(164) Krężel, A.; Latajka, R.; Bujacz, G. D.; Bal, W. Coordination Properties of Tris(2-carboxyethyl)phosphine, a Newly Introduced Thiol Reductant, and Its Oxide. *Inorg. Chem.* **2003,** *42* (6), 1994.
(165) Joliat-Wick, E.; Weder, N.; Klose, D.; Bachmann, C.; Spingler, B.; Probst, B.; Alberto, R. Light-Induced H_2 Evolution with a Macrocyclic Cobalt Diketo-Pyrphyrin as a Proton-Reducing Catalyst. *Inorg. Chem.* **2018,** *57* (3), 1651.
(166) Kohler, L.; Niklas, J.; Johnson, R. C.; Zeller, M.; Poluektov, O. G.; Mulfort, K. L. Molecular Cobalt Catalysts for H_2 Generation with Redox Activity and Proton Relays in the Second Coordination Sphere *Inorg. Chem.* **2019,** *58* (2), 1697.
(167) Zhang, P.; Jacques, P.-A.; Chavarot-Kerlidou, M.; Wang, M.; Sun, L.; Fontecave, M.; Artero, V. Phosphine Coordination to a Cobalt Diimine–Dioxime Catalyst Increases Stability during Light-Driven H_2 Production. *Inorg. Chem.* **2012,** *51* (4), 2115.
(168) Joliat, E.; Schnidrig, S.; Probst, B.; Bachmann, C.; Spingler, B.; Baldridge, K. K.; von Rohr, F.; Schilling, A.; Alberto, R. Cobalt complexes of tetradentate, bipyridine-based

macrocycles: their structures, properties and photocatalytic proton reduction. *Dalton Trans.* **2016,** *45* (4), 1737.
(169) Beyene, B. B.; Hung, C.-H. Photocatalytic hydrogen evolution from neutral aqueous solution by a water-soluble cobalt(II) porphyrin. *Sustainable Energy & Fuels* **2018,** *2* (9), 2036.
(170) Deponti, E.; Natali, M. Photocatalytic hydrogen evolution with ruthenium polypyridine sensitizers: unveiling the key factors to improve efficiencies. *Dalton Trans.* **2016,** *45* (22), 9136.
(171) Martindale, B. C.; Hutton, G. A.; Caputo, C. A.; Reisner, E. Solar hydrogen production using carbon quantum dots and a molecular nickel catalyst. *J. Am. Chem. Soc.* **2015,** *137* (18), 6018.
(172) Natali, M. Elucidating the key role of PH on light-driven hydrogen evolution by a molecular cobalt catalyst. *ACS Catalysis* **2017,** *7* (2), 1330.
(173) Ellgen, P. C.; Gerlach, J. N. Kinetics and mechanism of the substitution reactions of bis(mercaptotricarbonyliron) complexes. *Inorg. Chem.* **1973,** *12* (11), 2526.
(174) Creutz, C.; Sutin, N. Electron-transfer reactions of excited states. Reductive quenching of the tris (2, 2'-bipyridine) ruthenium (II) luminescence. *Inorg. Chem.* **1976,** *15* (2), 496.
(175) Jones Jr, W. E.; Fox, M. A. Determination of excited-state redox potentials by phase-modulated voltammetry. *J. Phys. Chem. A* **1994,** *98* (19), 5095.
(176) Pavlishchuk, V. V.; Addison, A. W. Conversion constants for redox potentials measured versus different reference electrodes in acetonitrile solutions at 25°C. *Inorg. Chim. Acta* **2000,** *298* (1), 97.
(177) Kalyanasundaram, K. Photophysics, photochemistry and solar energy conversion with tris(bipyridyl)ruthenium(II) and its analogues. *Coord. Chem. Rev.* **1982,** *46*, 159.
(178) Krishnan, C.; Sutin, N. Homogeneous catalysis of the photoreduction of water by visible light. 2. Mediation by a tris (2, 2'-bipyridine) ruthenium (II)-cobalt (II) bipyridine system. *J. Am. Chem. Soc.* **1981,** *103* (8), 2141.
(179) Krishnan, C. V.; Creutz, C.; Mahajan, D.; Schwarz, H. A.; Sutin, N. Homogeneous Catalysis of the Photoreduction of Water by Visible Light. 3. Mediation by Polypyridine Complexes of Ruthenium(II) and Cobalt(II). *Isr. J. Chem.* **1982,** *22* (2), 98.
(180) Mulazzani, Q. G.; Emmi, S.; Fuochi, P. G.; Hoffman, M. Z.; Venturi, M. On the nature of tris(2,2'-bipyridine)ruthenium(1+) ion in aqueous solution. *J. Am. Chem. Soc.* **1978,** *100* (3), 981.
(181) Mulazzani, Q. G.; D'Angelantonio, M.; Camaioni, N.; Venturi, M. Reactivity of Ru $(bpy)_3^+$ towards the radicals originating from the scavenging of hydrogen atoms and hydroxyl radicals by methanol, ethanol, propan-2-ol, *tert*-butyl alcohol and formate ions in aqueous solution: a pulse radiolytic study. *J. Chem. Soc., Faraday Trans.* **1991,** *87* (14), 2179.

Chapter 2

Modulation of the Co(I/II) Redox Couple and Electrocatalytic HER Activity of a Molecular Cobalt Complex by the Introduction of *para*-Aryl Substituents on the Outer Sphere

Abstract

The synthesis, characterization, and electrochemical studies of $[Co((H,pArX)BMIM^{Ph_2})_2](BF_4)_2$ **9-12** (X = H, Cl, CF_3, and OMe) are described. All complexes adopt tetrahedral geometries and each features an irreversible Co(I/II) reduction in MeCN that shifts anodically up to 130 mV as the electron-donating character of the substituent decreases. In THF, the Co(I/II) redox couple is more reversible, while demonstrating the same electrochemical trend. **9-12** are all active as hydrogen evolution reaction (HER) catalysts in MeCN, using 100 mM phenol as a sacrificial proton donor, and complexes with lower catalytic overpotential (η) demonstrate higher rates, ranging from TOF = 53 s^{-1} at η = 620 mV for **12** (OMe) to TOF = 153 s^{-1} at η = 580 mV for **10** (Cl). This trend opposes the typical situation in which additional potential (overpotential) speeds up the HER and was ascribed to bifunctional catalysis, in which a ligand C–H proton form hydrogen upon combining with a cobalt hydride. Bulk electrolysis experiments confirmed the formation of H_2 with complexes **9-12**, albeit at a poor Faradaic efficiency (11-24%). These results demonstrate that modulation of the outer coordination sphere of molecular bis(imidazole)methane cobalt complexes causes distinct and effective changes in the electrochemical and electrocatalytic HER properties of the complexes, and lend further credit to the bifunctional behavior of the complexes in HER catalysis.

S.D. de Vos, M. Otten, L. Killian, M.R. de Vries, K. C. Pons, M. Lutz, D.L.J. Broere, R.J.M. Klein Gebbink, *manuscript in preparation*

2.1 Introduction

The search for transition metal complexes that are capable of catalyzing the reduction of protons to dihydrogen at low overpotentials and high catalytic rates presents an exciting challenge for coordination chemists.[1-4] Nature uses hydrogenase enzymes to produce hydrogen with nearly no overpotential and high efficiency.[5] In the beginning of this century, much attention has been drawn to spectroscopically analyzing the enzymes and developing structural models of their active sites.[6,7] These studies demonstrated that nature has optimized the electronic environment of the first, second, and outer coordination spheres of the active sites.[8] To facilitate the formation of hydrogen, the enzymes use iron-sulfur clusters for efficient electron transfer, as well as proton channels of multiple proton relays for substrate supply.[7,9-11] Today, the lessons learned are used to develop novel functional models that produce hydrogen gas based on earth-abundant metals that can directly be reduced at an electrode surface at a low overpotential and are equipped with a proton relay in the second coordination sphere to facilitate hydrogen production at high catalytic rates.[12-26] For example, Nocera exploited cobalt and nickel porphyrin complexes with a carboxylic acid group as a proton relay,[20,22,23,26] while Dubois reported on nickel complexes with diphosphine ligands, featuring pendant amine functionalities as proton relays.[19,21,24,25] Our group recently reported on cobalt complex $[Co(HBMIM^{Ph2})_2](BF_4)_2$ that uses a C–H bond in a bisimidazole ligand as a proton relay (Figure 1).[27] A combined UV-vis and voltammetry experiment demonstrated the formation of deprotonated complex $[Co(HBMIM^{Ph2})_2(BMIM^{Ph2-})_2](BF_4)$ upon electrochemical reduction of $[Co(HBMIM^{Ph2})_2](BF_4)_2$. Controlled potential electrolysis studies demonstrated a significantly increased charge consumption when using $[Co(HBMIM^{Ph2})_2](BF_4)_2$ compared to using cobalt complex $[Co(Me_2BMIM^{Ph2})_2](BF_4)_2$, that lacks methylene C–H bonds (**Figure 1**). In addition, computational studies point at an energetically favorable H–H bond formation process through the coupling of a cobalt metal hydride and a methylene proton. Using $[Co(HBMIM^{Ph2})_2](BF_4)_2$

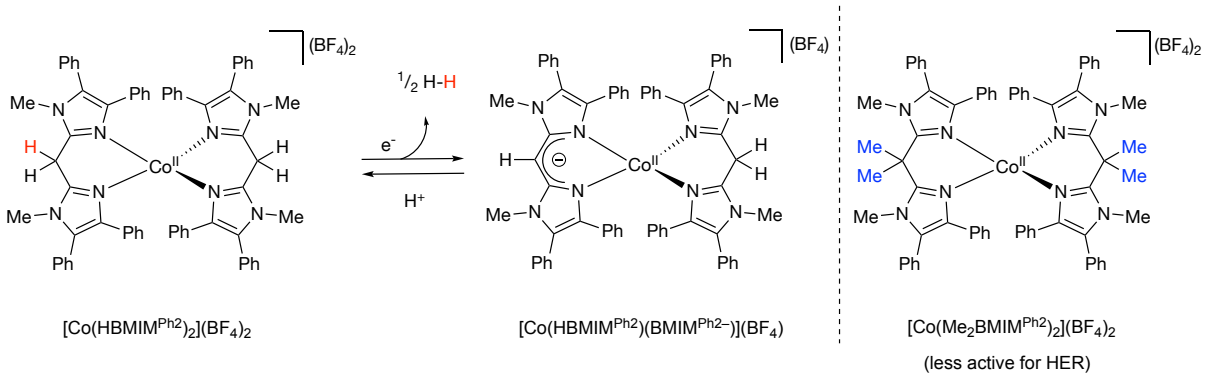

Figure 1. HER-reactivity by cobalt complex $[Co(HBMIM^{Ph2})_2](BF_4)_2$ through the involvement

as an electrocatalyst, hydrogen evolution occurs at an overpotential of 590 mV in MeCN. The overpotential represents an undesirable loss of energy (as heat)[28] and lowering the overpotential requirement for an electrocatalytic process increases the overall energy efficiency of the process.[29] When studying the HER, the overpotential is expressed as the difference between the thermodynamic and electrocatalytic HER potentials for a particular combination of a sacrificial proton source and a molecular complex.[28-32] For molecular cobalt and nickel complexes, the electrocatalytic HER potential is correlated with the metal-based reduction potential,[33-37] but is often hard to predict from the molecular structure of the complex and needs to be experimentally determined.[3] Strategies to lower the overpotential requirement are therefore focused on modifying ligand frameworks with electron-donating (EDG) and -withdrawing (EWG) groups to modulate the metal-based reduction potentials. A number of studies have reported on the relationship between the cobalt- and nickel-based reduction potentials (and HER activity in some cases) and the electronics of *para*-functionalized aryl groups on the ligand scaffold (**Figure 2**).[25,38-42] In these studies, the variation of the *para*-functionality alters the electron-donating character of the ligand with minimal changes in the steric encumbrance, providing an elegant method to study the redox and catalytic HER properties of the complex. Batiste *et al*. reported on bis(imino)pyridine cobalt complexes in which the Co(I/II) redox couple was effectively modulated by +400 mV, when the para-substituent on the aryl group is a NMe_2 ($\sigma_p = -0.83$), OMe, NH_2, Me, H, CF_3, or a CN ($\sigma_p = 0.66$) substituent (no HER studies were reported).[41] Using a series with the same extreme para-substituents, Si *et al.* reported on a +60 mV modulation of the Co(II/III) and Co(I/II) redox couples in cobalt triaryl corrole complexes.[38] Interestingly, the CN ($\sigma_p = 0.66$) substituted complex, which has the most anodic redox potentials in this series of complexes, was demonstrated to be most active for HER under identical conditions (838 mV overpotential). Using different substituents on cobalt *meso*-tetra-(*p*-phenyl) porphyrin complexes, Hung *et al.* reported on a +320 mV and + 240 mV modulation of the Co(I/II) and Co(0/I) redox couples, respectively, varying from an OH ($\sigma_p = -0.37$) to a COOMe ($\sigma_p = 0.45$) substituent.[40] The difference in catalytic onset potential is only +150 mV for porphyrin complexes bearing these specific substituents. Hence, the electrocatalytic onset potentials for the HER were modulated as well but turned out to be non-linearly related to the observed metal-based redox potentials. Furthermore, the authors demonstrated that the Brønsted acidic substituents play a key role during the HER, as porphyrin complexes bearing NH_2, SO_3H, and COOH substituents are

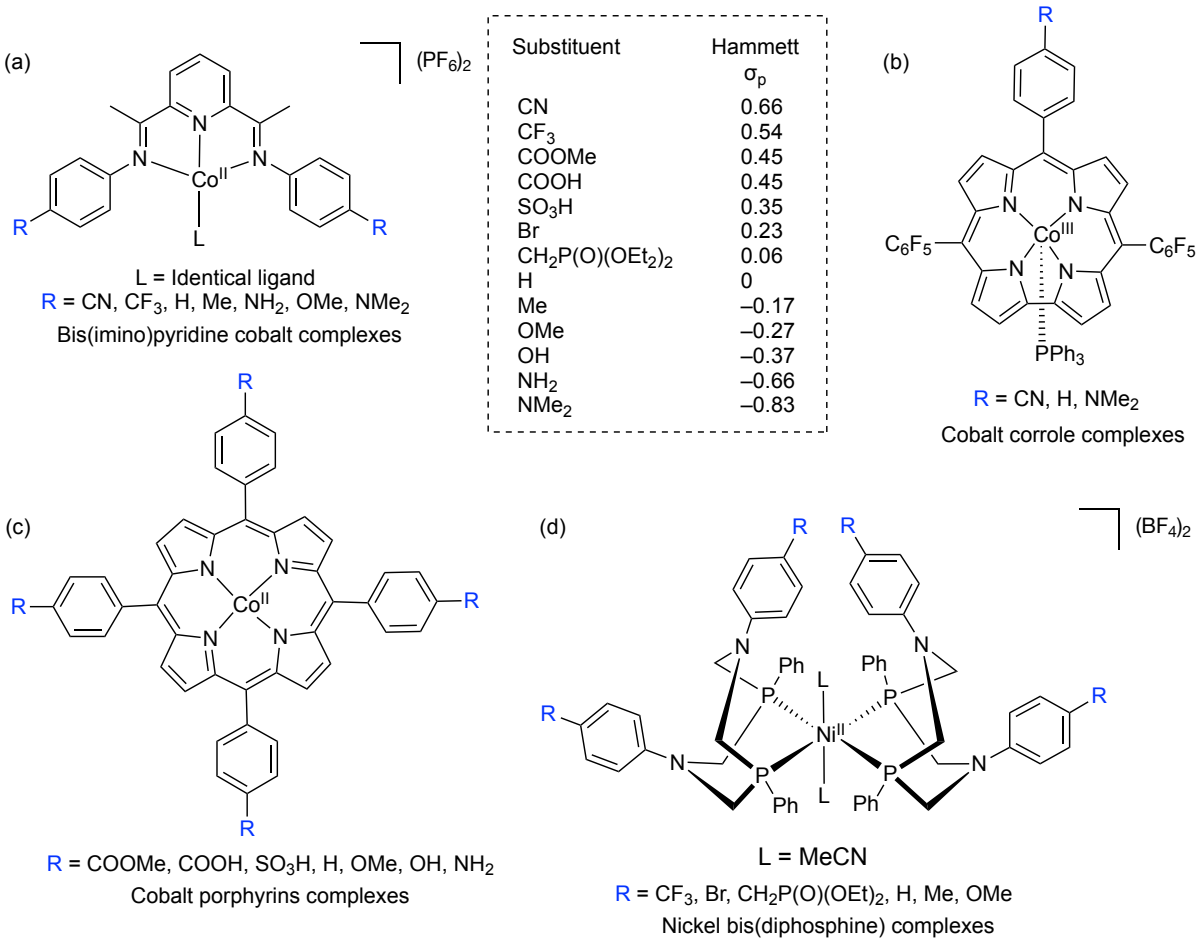

Figure 2. Selected cobalt and nickel complexes with *para*-substituted aryl groups, demonstrated to have modulated metal-based redox (and HER) potentials: (a) Co-bis(imino)pyridine; (b) Co-triaryl corrole; (c) Co-pophyrin; and (d) Ni-bis(diphosphine) complexes. The ED/EW character of the substituents can be ranked based on their Hammet σ_{para} (σ_p) parameter.[43-45]

significantly more active than those bearing COOMe, H, OMe, and, remarkably, OH substituents. Thus, where overpotentials are usually undesirable, but necessary to speed up the HER reaction, this study demonstrated that lowering the catalytic overpotential is not always accompanied by a lower catalytic rate. Lastly, Dubois *et al.* reported on bifunctional nickel bis(diphosphine) complexes, comprising amine proton relays with a functionalized *p*-aryl group, in which electron-withdrawing substituents on the aryl modulate the Ni(I/II) and Ni(0/I) redox couples by +140 mV and +180 mV, from OMe (σ_p = –0.27) to CF_3 (σ_p = 0.54), respectively.[25] During HER catalysis, EWGs decrease the basicity of the pendant amines (making the N–H more acidic), favoring product (H_2) release from the complex and increasing the catalytic HER rate. Thus, higher rates for HER were observed at lower overpotentials. These studies show that the introduction of EDG/EWG substituents on molecular complexes

is a promising strategy to modulate the metal-based redox potentials and catalytic HER activity. In general, a large overpotential is undesirable but necessary to obtain practical rates for HER, and molecular catalysts working with small overpotentials usually display low catalytic activities.[46-49] Yet, catalytic HER rates can sometimes be enhanced by functionalities in the ligand that influence the substrate or product transfer steps by means of metal-ligand cooperativity. A few examples of specially designed systems, with proton relays in their ligands, demonstrate that the tradeoff between rate and overpotential can be bypassed.[25,40,50,51] The breaking of this relationship is possible due to a potential-independent catalytic rate (turnover frequency (TOF)), meaning that the rate-limiting step of the catalysis is not the metal-centered reduction event.[52-54]

Here, we aim to study the overpotential-HER-reactivity relationship by changing the cobalt-based redox potentials through ligand modifications for our reported bifunctional HER catalyst, $[Co(HBMIM^{Ph2})_2](BF_4)_2$. We approach this aim by introducing a functionalized aryl group on the methylene bridge of the $HBMIM^{Ph2}$ ligand and thereby retain a C–H bond that can participate as a proton relay in the HER. To this end, a series of complexes of the formula $[Co((H,pArX)BMIM^{Ph_2})_2](BF_4)_2$, where the *para*-phenyl substituent X = H, Cl, CF_3, and OMe, were synthesized and characterized (**Figure 3**). The electrochemical and electrocatalytic HER properties of this series of complexes demonstrate an untraditional but beneficial overpotential-HER-reactivity relation, in which higher catalytic rates are obtained at lower overpotentials.

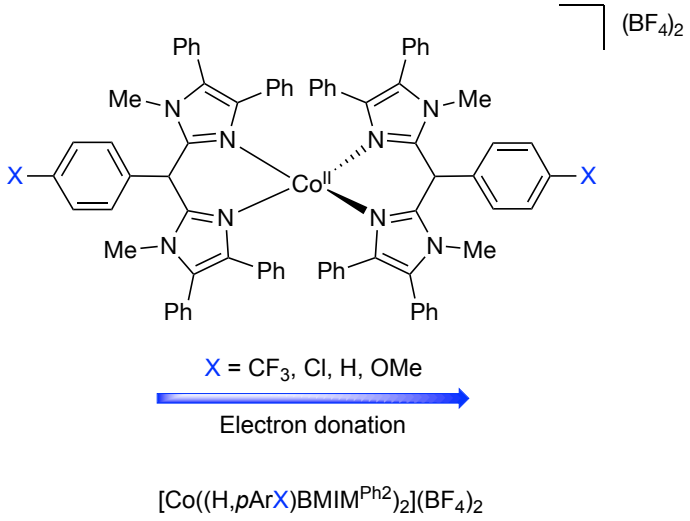

Figure 3. *para*-Aryl-substituted bisimidazolemethane cobalt complexes $[Co((H,pArX)BMIM^{Ph_2})_2](BF_4)_2$ reported in this work.

2.2 Results and Discussion

2.2.1 Synthesis and characterization of ligands 5-8 and complexes 9-12

The ligands used in this study were prepared using a two-step reaction sequence (**Scheme 1**). 1-Methyl-4,5-diphenyl-1*H*-imidazole was lithiated with *n*-butyl-lithium, followed by the addition of half an equivalent of a *para*-substituted methyl benzoate to form alcohol derivatives **1**-**4**. Reduction of the alcohol group was accomplished by applying an adapted procedure by Zhou *et al.*, in which a large excess of trifluoroacetic anhydride (TFAA) and a hydride donor were added.[55] In all cases, the treatment of the alcohol derivative with TFAA in DCM produced an intense ocean blue solution, presumed to be the corresponding cation. Subsequent reductive quenching with $NaBH_4$ only yielded desired ligand **8**. Replacing $NaBH_4$ for Et_3SiH gave **5**-**7**. All ligands were obtained as pale-yellow solids in overall yields varying from 25-96%. The

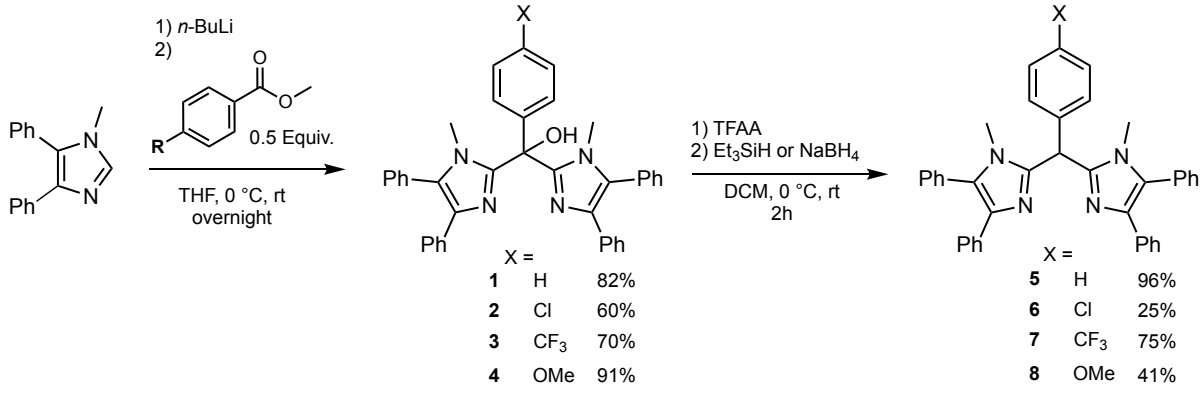

Scheme 1. Synthesis of (H,*p*ArX)BMIM^{Ph_2} ligands **5**-**8**. In the second step Et_3SiH was used for **5**-**7** and $NaBH_4$ for **8**.

addition of 0.5 equiv. of $[Co(H_2O)_6](BF_4)_2$ to THF solutions of **5**-**8** resulted in the formation of complexes $[Co((H,pArX)BMIM^{Ph_2})_2](BF_4)_2$ (**9**-**12**), which were isolated in 64-75% yield as pink-purple solids by evaporating the solvent and subsequent washing with diethyl ether (**Scheme 2**). The formation of complexes **9**-**12** was confirmed by positive mode high-resolution ESI-MS spectrometry, showing the doubly charged $[Co((H,pArX)BMIM^{Ph_2})_2]^{2+}$ ion peak in all cases (Appendix A, Figures A35, 37, 39, 42). Furthermore, **9**-**12** demonstrate singly charged ligand $[(H,pPArX)BMIM^{Ph_2}) + H]^+$ ion peaks and for **10**-**12** singly charged $[Co((H,pPArX)BMIM^{Ph_2})_2] + F]^+$ ion peaks were also observed. The ^{1}H-NMR spectra of the paramagnetic cobalt complexes **9**-**12** show broad and strongly shifted signals between –46 and 124 ppm in MeCN-d_3 (**Figure 4**). The signals could tentatively be assigned by comparing the spectra with those of $[Co(BMIM^{Ph2})](BF_4)_2$ and $[Co(Me_2BMIM^{Ph2})](BF_4)_2$ (**Figure 4** and Appendix A, Figures A44-45).[27] For complexes **9**-**12**, a doubling of the resonances was

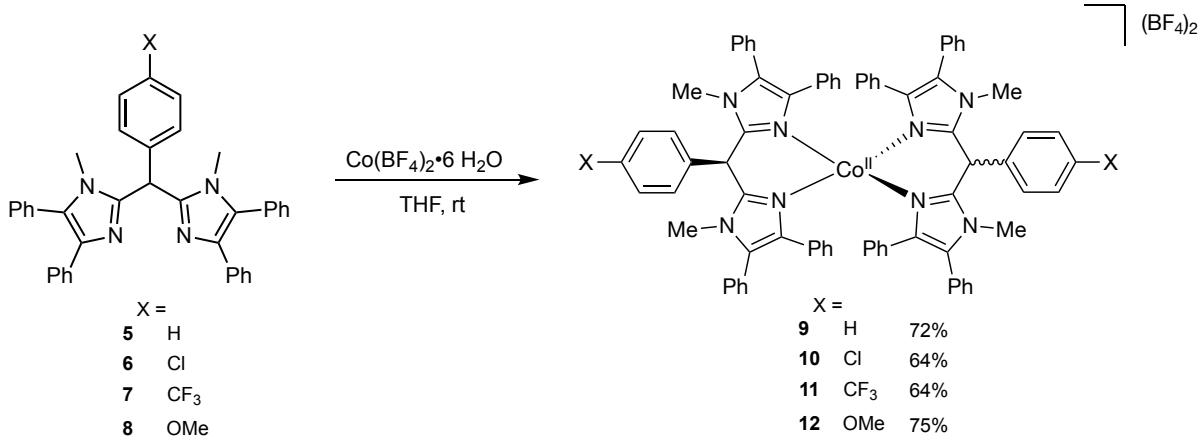

Scheme 2. Synthesis of $[Co((H,pArX)BMIM^{Ph_2})_2](BF_4)_2$ complexes **9-12** from the corresponding $(H,pArX)BMIM^{Ph_2}$ ligands **5-8** and $Co(BF_4)_2 \cdot 6\ H_2O$.

observed compared to the earlier reported analogs $[Co(BMIM^{Ph2})](BF_4)_2$ and $[Co(Me_2BMIM^{Ph2})](BF_4)_2$.[27] This is attributed to the introduction of the aryl substituent at the methylene position, which becomes diastereotopic upon complexation to cobalt, causing the formation of two enantiomers and making the two diphenylimidazole moieties spectroscopically inequivalent.[56,57] In our previous study, X-ray crystal structure of $[Co(BMIM^{Ph2})](BF_4)_2$ revealed that the methylene and some diphenyl imidazole *o*-Ph-CH hydrogen atoms are in close proximity to the metal center, and are therefore expected to be strongly shifted and broadened in ^{1}H-NMR.[27] Complexes **9-12** all show a broad single resonance between 120-123 ppm with similar integration, while $[Co(BMIM^{Ph2})](BF_4)_2$ shows a similar signal at 182 ppm and $[Co(Me_2BMIM^{Ph2})](BF_4)_2$ shows no signal in this region (> 50 ppm). Therefore, we ascribe this broad signal to the methylene hydrogen atom(s). For **9-12**, the broad signal around 50 ppm is assigned to two *o*-PhIm CH hydrogen atoms. Two signals that relatively integrate for 3 hydrogen atoms, compared to the other paramagnetic signals, are found between 40 and 30 ppm and are assigned to the N-methyl hydrogen atoms. In $[Co(BMIM^{Ph2})](BF_4)_2$ and $[Co(Me_2BMIM^{Ph2})](BF_4)_2$, a single resonance assigned to the N-methyl hydrogen atoms was found at 28 and 34 ppm, respectively. Between 25 and 0 ppm the observed resonances in the spectra of complexes **9-12** deviate slightly from each other, while for each complex a tentative assignment could be made based on the relative integration (see the experimental section). Around –3 to –4 ppm two overlapping signals are found for **9-12**, which were assigned to the *o*-Ar and *m*-Ar hydrogen atoms of the functionalized phenyl groups at the methylene position, as such signals are absent for $[Co(BMIM^{Ph2})](BF_4)_2$ and $[Co(Me_2BMIM^{Ph2})](BF_4)_2$. Finally, two broad signals of similar shape are found for all

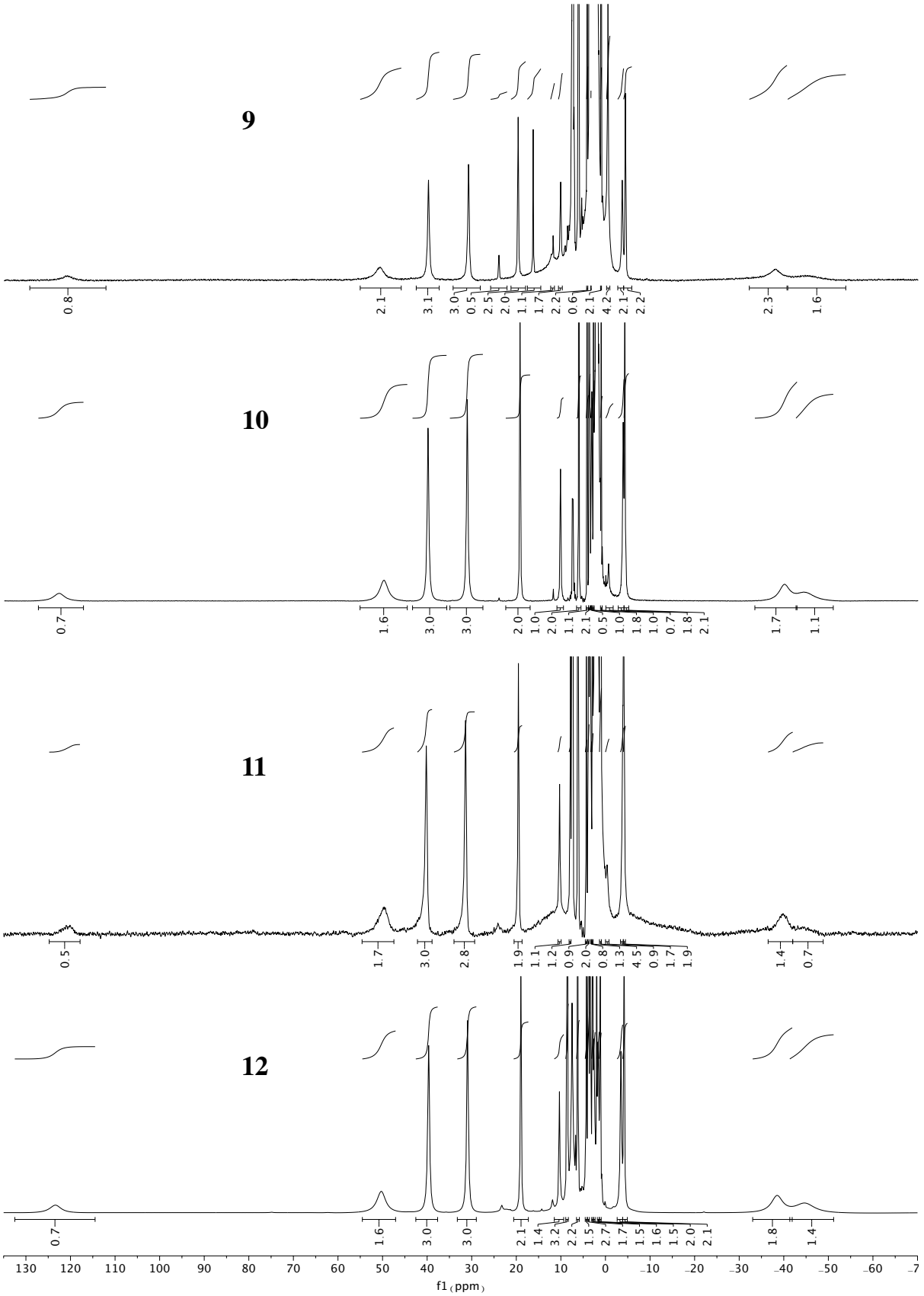

Figure 4. ^{1}H-NMR spectra of [Co((H,*p*ArX)BMIM^{Ph_2})$_2$](BF$_4$)$_2$ complexes **9** (X=H), **10** (X=Cl), **11** (X=CF$_3$), and **12** (X=OMe) in MeCN-d_3. Peak picking is omitted for clarity and reported in the experimental section.

the metal center. The assignment of all paramagnetic resonances and the apparent overall symmetry of the complexes in solution suggests no coordination of MeCN solvent molecules for **9-12**. Overall, these NMR spectra are consistent with one molecular cobalt species in which two equivalent ligands chelate the metal center, and in which the symmetry within the ligand is lifted due to the orientation of the *para*-phenyl group of the other ligand. The high similarity between the spectra of complexes **9-12** points out that the complexes are structurally strongly related. The ^{19}F NMR spectrum of **11** shows a single, sharp signal at –75.28 ppm corresponding to the CF_3 groups, while the typically broad resonance for BF_4^- ions between –140 and –160 ppm was not detected in MeCN-d_3 (Appendix A, Figure A41; recording the spectrum in THF-d_8 did show the BF_4^- signal). For **11**, the solution state magnetic susceptibility, measured by the Evans method, demonstrated a value of μ_{eff} = 3.72 μ_B consistent with three unpaired electrons (S = 3/2), which we expect to be consistent in **9-12**.[58,59] UV-Vis spectroscopy was used to probe the d-d transitions of **9-12** (Appendix A, Figure A46 and Table A1). For all complexes, two absorption bands were observed around 523 nm and 561 nm. The relatively small λ_{max} differences indicate that the *para*-functionalization of the phenyl groups on the ligands does not significantly affect the difference in energy levels of the molecular frontier orbitals of the complexes. [Co(BMIM^{Ph2})](BF$_4$)$_2$ shows d-d transitions at 510 nm and 555 nm, indicating that in the absence of a phenyl substituent the energy difference between the frontier orbitals is somewhat larger.[27] Purple crystals, suitable for single X-ray diffraction, were obtained from slow vapor diffusion of Et_2O into a concentrated solution of **11** in MeCN at –18 °C over several days. The structure reveals a [Co((H,*p*ArCF$_3$)BMIM^{Ph_2})$_2$](BF$_4$)$_2$ composition with no solvent molecules coordinated to the tetrahedral cobalt center (**Figure 5**). A list of selected bond lengths and angles for **11** and [Co(HBMIM^{Ph2})](BF$_4$)$_2$ are given in **Table 1**.

Table 1. Selected bond lengths and bond angles of the crystal structures of [Co((H,*p*ArCF$_3$)BMIM^{Ph_2})$_2$](BF$_4$)$_2$ **11** and [Co(HBMIM^{Ph2})](BF$_4$)$_2$.[27]

[Co((H,*p* ArCF$_3$)BMIM^{Ph2})$_2$](BF$_4$)$_2$ (**11**)				[Co(BMIM^{Ph2})$_2$](BF$_4$)$_2$			
Bond	Lenghts (Å)	Bond Angle	Degrees	Bond	Lenghts (Å)[a]	Bond Angle	Degrees[a]
Co1–N11	1.9876(16)	N11–Co1–N12	104.78(7)	Co1-N11	1.986(4)	N11-Co1-N12	128.95(17)
Co1–N12	1.9951(16)	N31–Co1–N32	128.94(7)	Co1-N12	1.985(4)	N31-Co1-N32	124.03(16)
Co1–N31	2.0012(16)	N11–Co1–N31	93.80(6)	Co1-N31	2.008(4)	N11-Co1-N31	97.00(16)
Co1–N32	1.9940(16)	N12–Co1–N32	94.42(6)	Co1-N32	1.996(4)	N12-Co1-N32	95.60(16)
Chelate motif				Chelate motif			
N11–C21	1.333(2)			N11-C21	1.320(6)		
C11–C21	1.508(3)			C11-C21	1.495(7)		
C11–C181	1.503(3)			C11-C181	1.485(7)		
N31–C181	1.333(2)			N31-C181	1.334(6)		

[a]Values for one two independent molecules.

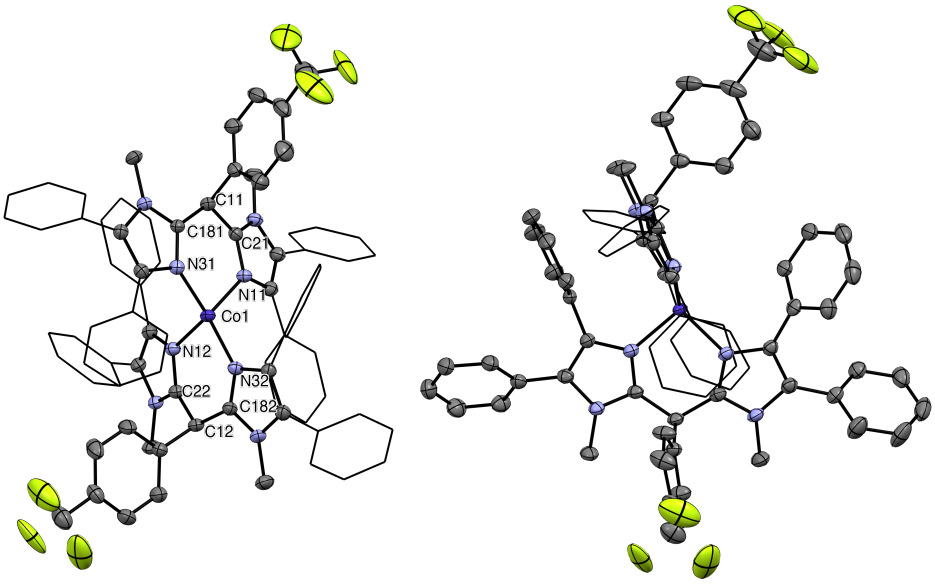

Figure 5. Molecular structure of $[Co((H,pArCF_3)BMIM^{Ph_2})_2](BF_4)_2$ **11** in the crystal. Left: 'side view' along the N_{12}–Co–N_{32} chelate perspective, showing the imidazole binding modes; Right: 'top view' perpendicular to the plane of the N_{12}–Co–N_{32} chelate, showing the tilting of the ligand and the orientation of the *p*-CF_3-aryl groups. Ellipsoids are plotted at the 50% probability level. H-atoms, BF_4 counter anions, and disordered solvent molecules have been omitted for clarity. Only the major conformation of the disordered CF_3 groups is shown.

Complex **11** shows a slightly distorted tetrahedral geometry around the cobalt(II) ion, with a dihedral angle between the N11–Co1–N31 and N12–Co1–N32 planes of 87.39(9)°, compared to the smaller dihedral angles of 74.1(2) and 77.4(2) ° between the N-Co-N planes in $[Co(HBMIM^{Ph2})](BF_4)_2$.[27] However, the *p*-CF_3-phenyl substituent on the ligand backbone causes the ligand framework to be tilted aside from the perpendicular plane (**Figure 5**, right). The Co–N bond lengths of 1.9876(16)-2.0012(16) Å are almost identical to the 1.985(4)-2.008(4) Å bond lengths in $[Co(HBMIM^{Ph2})](BF_4)_2$, indicating a similar interaction between the ligands and cobalt.[27] The chelator angles N_{11}–Co–N_{31} and N_{12}–Co–N_{32} of 93.80(6) and 94.42(6) ° in **11** are slightly smaller than in $[Co(HBMIM^{Ph2})](BF_4)_2$ (94.75(17)-97.00(16) °).[27] The BF_4 anions are too far away from the Co center for any bonding interaction (Appendix A, Figure A47). The overall structure of the tetrahedral complex is chiral. Upon complex formation, the *p*-CF_3-aryl substituents become diastereotopic and, accordingly, the complex is chiral at cobalt. The two enantiomers of **11** are present in equal amounts within the crystal.[56,57] Due to the centrosymmetry of the space group, the overall crystal structure is racemic. Obviously, similar symmetry considerations apply to the other complexes reported here, as discussed for their NMR spectra (*vide supra*). The crystal packing is characterized by

alternating *S* and *R* enantiomers that form large channels which are filled with ordered and disordered solvent molecules (**Figure 6**, and Appendix A, Figure A48). Attempts to grow single crystals of sufficient quality for **9**, **10,** and **12** were unsuccessful.

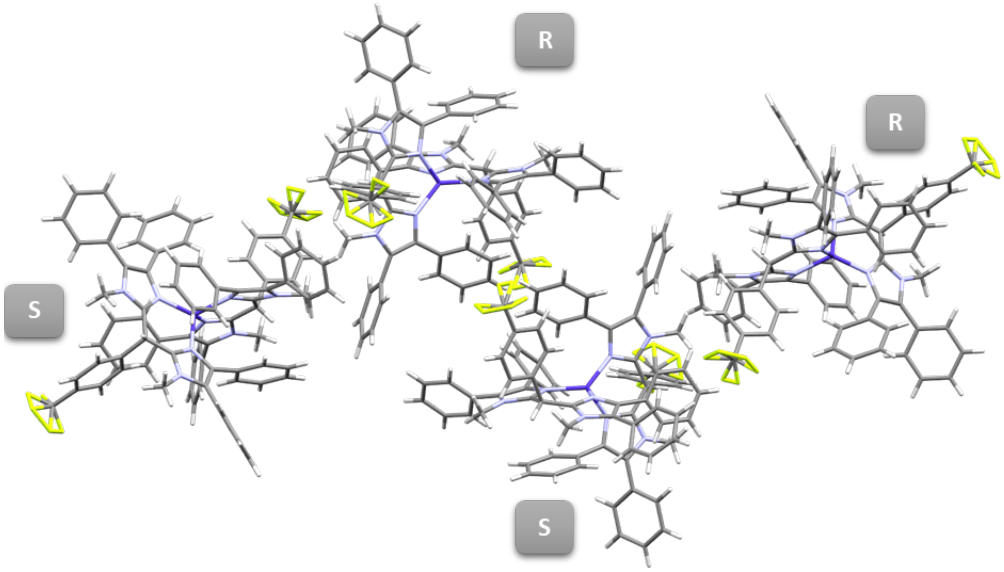

Figure 6. Packing of the *S* and *R* enantiomers of complex [Co((H,*p*PhCF$_3$)BMIM^{Ph_2})$_2$](BF$_4$)$_2$ **11** within the crystal.

2.2.2 Cyclic voltammetry studies of 9-12

To investigate the redox properties of cobalt complexes **9-12**, CV measurements were performed in 0.1 M *n*Bu$_4$NPF$_6$ in MeCN at 100 mV/s, scanning in the cathodic direction, and absolutely referenced to the Fc$^+$/Fc couple (**Figure 7**, **Table 2**, and Appendix A, Figure A49, for the explanation of the electrochemical parameters).[60] The redox properties of [Co(HBMIM^{Ph2})$_2$](BF$_4$)$_2$ are included in **Table 2** for clarity.[27] Upon scanning in the cathodic direction, a broad irreversible reduction for **9** was found at E_{onset} = –1.63 V and $E_{p,c}$ = –1.79 V, with a broad pre-wave. Based on the similar shape and position as the reductive event observed for [Co(HBMIM^{Ph2})$_2$](BF$_4$)$_2$, we ascribe this redox event to a Co(I/II) reduction followed by H$_2$ formation with formal deprotonation of the ligand (EC mechanism).[27] The broadening of the signal is indicative of a slow electron transfer. The Co(I/II) redox feature is reproducible over two consecutive scans. Upon scanning in the reserved anodic direction also a single oxidation at $E_{p,a}$ = –0.51 V was observed, which is of similar shape to the oxidation observed for [Co(HBMIM^{Ph2})$_2$](BF$_4$)$_2$ (at $E_{p,a}$ = –0.64 V) (Appendix A, Figure A50).[27] The phenyl functionalization of the methylene bridge results in a 170-200 mV anodic shift in the Co(I/II) reduction potential compared to [Co(HBMIM^{Ph2})$_2$](BF$_4$)$_2$ (E_{onset} = –1.83 V and $E_{p,c}$ = –1.96 V

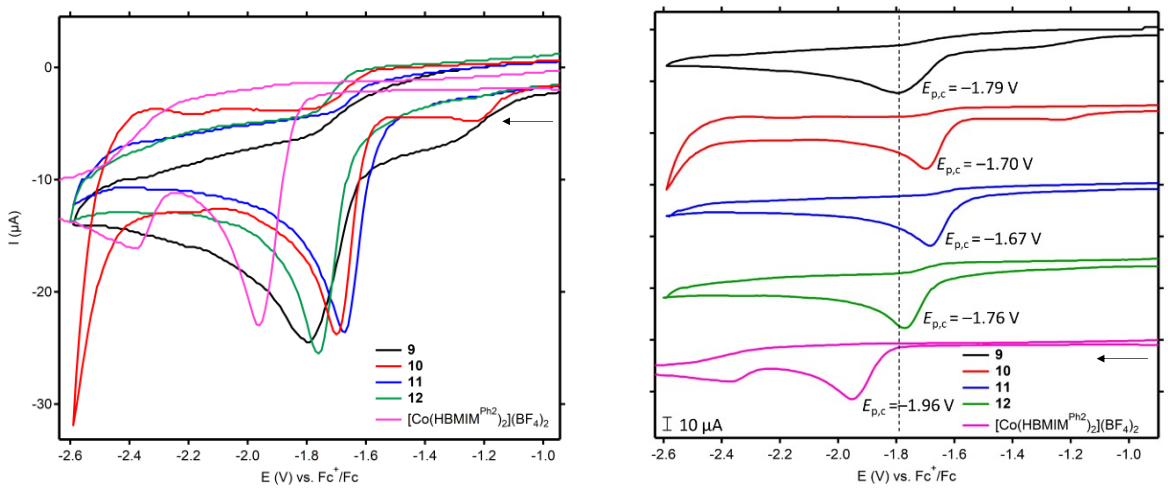

Figure 7. Segmented voltammograms of 1 mM **9** (H), **10** (Cl), **11** (CF_3), **12** (OMe), and $[Co(HBMIM^{Ph2})_2](BF_4)_2$ in 0.1 M nBu$_4$NPF$_6$ in MeCN, referenced *vs.* the ferrocenium/ferrocene redox couple at a scan rate of 100 mV/s. The arrow indicates the initial scan direction. Left: stacked voltammograms. Right: overlaying voltammograms.

Table 2. Electrochemical data for $[Co((H,pArX)BMIM^{Ph_2})_2](BF_4)_2$ complexes **9-12** (1 mM) in MeCN (0.1 M nBu$_4$NBF$_4$).[a]

Complex	MeCN		Hammett
	$E_{p,c}$ (V)	E_{onset} (V)	σ_{para} X
9 (X = H)	–1.79	–1.63	0
10 (X = Cl)	–1.70	–1.59	0.24
11 (X = CF_3)	–1.67	–1.54	0.53
12 (X = OMe)	–1.76	–1.65	–0.27
$[Co(HBMIM^{Ph2})_2](BF_4$	–1.96	–1.83	-

[a]Referenced to the Fc^+/Fc couple

in MeCN, 0.1 M nBu$_4$NPF$_6$).[27] This observation confirms the possibility to modify the redox chemistry of bisimidazolemethane-derived complexes by installing a phenyl substituent at the methylene position of the ligand and confirms the electron-withdrawing character of the phenyl substituent. For **10**, **11,** and **12** an irreversible Co(I/II) reduction was found at E_{onset} = –1.59, –1.54, –1.65 V and $E_{p,c}$ = –1.70, –1.67, and –1.76 V, respectively. Complex **10** also features a pre-wave. In the reversed anodic scan, different oxidative features were observed for **11** and **12**, which are not systematic and were not further investigated (Appendix A, Figure A51). The reduction events are all peak shaped, indicative of a fast electron transfer process. Finally, a scan rate analysis was performed for **11** and **12**, which feature the utmost reduction potentials amongst complexes **9-12**. Plots of the peak currents ($i_{p,c}$) versus the square root of the scan rate are linear, indicating that these redox reactions are diffusion-controlled and therefore originate

from solvated species (Appendix A, Figure A51).[60] The numerical redox data of complexes **9-12** show that upon decreasing the electron-donating ability of the para substituent of the aryl moieties, as determined by the Hammett σ_{para},[43-45] the potentials of the Co(I/II) couple become more positive (**Table 2**, **Figure 8** black traces). Both the $E_{p,c}$ and E_{onset} values show a cathodic trend in reduction potential from **12** to **9**, to **10** to **11**. Due to the broadening of the redox event as a result of slower electron transfer kinetics, the $E_{p,c}$ value of **9** is the only data point off-trend in this data set. Overall, this linear trend features a positive ρ value of ~0.16 (average of the MeCN (~0.14) and THF (~0.18) trends, *vide infra*), which points out that the redox properties of the cobalt center in this series of complexes can be modulated in a predictable manner, in-line with the electronic effect of substituents as described by the Hammett sigma values.[43,44] This observation also shows that there is effective electronic communication between the cobalt metal center and the aryl substituents at the methylene position of the ligand. To further investigate the Co(I/II) redox behavior of **9-12**, voltammetry experiments were run in THF, as the electrochemical interference on reduced species is less in THF (compared to MeCN), due to its lower electron acceptance properties as described by the acceptor number by Gutmann and Gerger.[61-63] **Figure 9** depicts the cyclic and differential pulse voltammograms of **9-12** in 0.1 M nBu$_4$NPF$_6$ in THF and in **Table 3** the numerical data is reported. All voltammograms demonstrate a single redox event when scanning up to –2.00 V, ascribed to the (reversible) Co(I/II) redox couple. While a broadening of the irreversible Co(I/II) response was observed for **9** in MeCN, the same response of **9** appears peak shaped in THF, likewise to **10-12**. Interestingly, the series demonstrates intensifying oxidative Co(I/II) responses ($i_{p,a}$) from **9** and **12** to **10** and **11**, showing that the electrochemical behavior in THF is distinct from that in MeCN. The differences in the $i_{p,c}$ and $i_{p,a}$ values of the Co(I/II) redox couples in **9-12** are constant with chemical quasi-reversibility for in **9** and **12** and chemically reversibility for **10** and **11**. This demonstrates a difference in the energy barrier for electron transfer for EDG/neutral substituents (OMe, H) and EWG substituents (Cl, CF_3), which further underlines that the metal-centered redox events are affected by the *para*-substituents on the aryl groups. The CVs of **9-12** in THF show redox couples at $E_{1/2}$ = –1.74, –1.68, –1.65, and –1.78 V, respectively, which follow the same trend as the peak potentials ($E_{p,c}$) in THF and as the trend observed for the onset potentials in MeCN (**Figure 8**), indicating that electronic communication between the substituents and the metal center is not influenced by the solvent. The peak-to-peak separation ΔE_p amounts to 130-180 mV, indicating electrochemical quasi-reversibility. Between the utmost substituents, **11** (CF_3) and **12** (OMe), an $E_{1/2}$ difference of 130 mV was observed, which is similar to the 140 mV difference observed by Dubois and co-

workers for their nickel complexes bearing the same substituents (**Figure 2**).[25] DPV experiments of **9-12** in THF demonstrate symmetric Co(I/II) peaks in both scan directions, which is consistent with chemically reversible reactions, and none of the sweeps show additional cathodic or anodic events.[60] The E_p values for **9-12** were observed at –1.80, –1.77, –1.70, –1.81 V, respectively. For complexes with fast electron transfer kinetics (high reversibility), the DPV peak potentials correlate with the $E_{1/2}$ value found in CV. For **9-12**, these values differentiate with 30-90 mV indicative of the quasi-reversibility. For **9** and **10**, the base of the peak and the peak width at half height ($W_{1/2}$) widens, while the peak height decreases, compared to **11** and **12**, which is ascribed to slower electron transfer kinetics (irreversibility). Between MeCN and THF we observe increased chemical reversibility in all cases in THF, but especially for **10** and **11**. Overall, we conclude that functionalizing the *para*-aryl group, located on the outer sphere of the complexes and no less than eight chemical bonds away from the cobalt metal center, has a significant effect on the metal-based redox properties of the complexes, which correlates with the Hammett sigma parameter.[43,44] An electronic communication of this magnitude is likely to be established by conjugation, but in **9-12** the conjugated pathway is lifted by the sp^3 hybridized methylene group. Alternatively, inductive effects can cause electronic changes, but the functionalities are relatively remote (8 bonds) such that inductive forces are likely faded at the cobalt center and not responsible for the magnitude of the observed redox modulations. A more convoluted explanation is that the reduction event

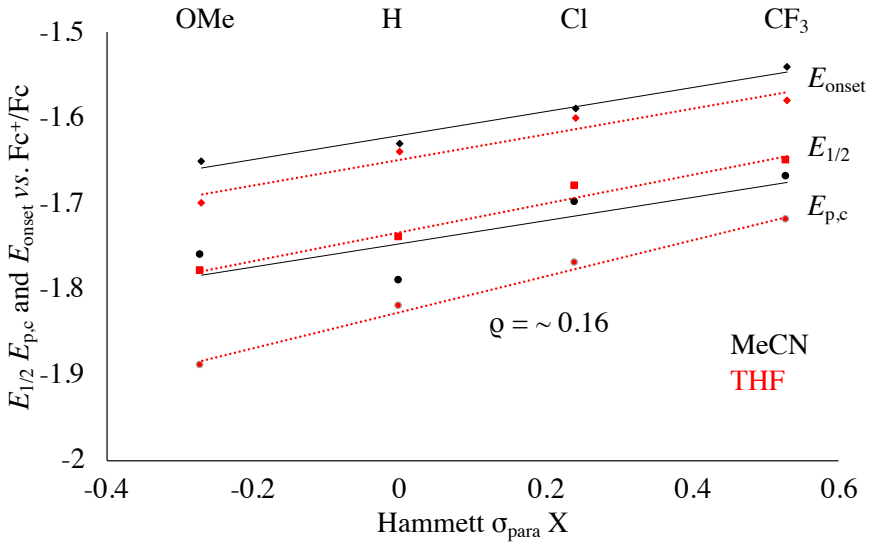

Figure 8. Variation of the CV E_{onset} (diamond), and $E_{p,c}$ (circle) values for the Co(I/II) reductions of $[Co((H,pArX)BMIM^{Ph_2})_2](BF_4)_2$ complexes **9** (H), **10** (Cl), **11** (CF_3) and, **12** (OMe) in MeCN (black) and (additional $E_{1/2}$ (square)) in THF (red) as a function of the Hammett σ_{para} parameter.

is coupled to H_2 formation with formal deprotonation of the ligand (an EC mechanism), as was previously described for $[Co(HBMIM^{Ph2})_2](BF_4)$.[27] As a result, the *para*-aryl substituents influence the stabilization of the product (a conjugated anionic ligand) and therewith simultaneously change the activation energy required for this transformation, resulting in a change in the observed redox potentials. This explanation does not certify the trend observed in THF, where the Co(I/II) responses are more reversible and an E mechanism seems operable that is not followed by formal deprotonation. This would imply a significant inductive effect of the *para*-aryl-substituents on the Co(I/II) redox potential in THF solution. Based on these considerations, the electronic communication between the *para*-aryl-substituents and cobalt is not fully understood.

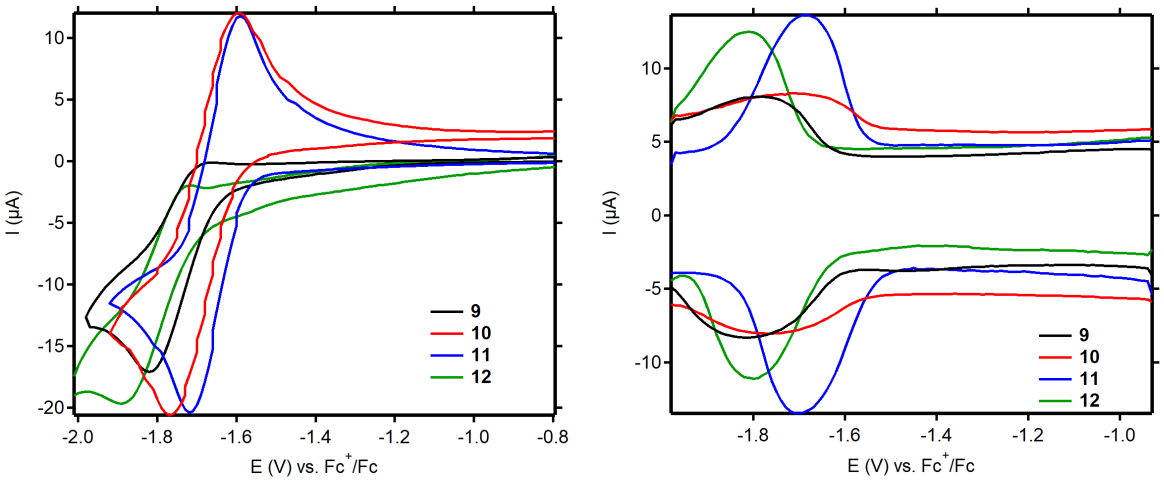

Figure 9. Electrochemical analysis of complexes **9** (H), **10** (Cl), **11** (CF_3) and, **12** (OMe) (5 mM) in 0.1 M nBu$_4$NPF$_6$ in THF referenced *vs.* the ferrocenium/ferrocene redox couple. Left: cyclic voltammograms at a scan rate of 100 mV/s; Right: differential pulse voltammograms at a modulation time of 0.003 s, interval time 0.05 s, modulation amplitude 0.05 V.

Table 3. Electrochemical data for $[Co((H,pArX)BMIM^{Ph_2})_2](BF_4)_2$ complexes **9-12** (5mM) in THF (0.1 M nBu$_4$NBF$_4$).[a]

Complex	THF								Hammett
	$i_{p,c}$ (μA)	$i_{p,a}$ (μA)	$E_{1/2}$ (V)	ΔE_p (mV)	$E_{p,c}$ (V)	$E_{p,a}$(V)	DPV E_p (V)	DPV $W_{1/2}$(mV)	σ_{para} X
9 (X = H)	13	6	–1.74	160	–1.82	–1.66	–1.80	260	0
10 (X = Cl)	20	19	–1.68	180	–1.77	–1.59	–1.77	300	0.24
11 (X = CF_3)	18	18	–1.65	130	–1.72	–1.59	–1.70	200	0.53
12 (X = OMe)	13	6	–1.78	170	–1.89	–1.72	–1.81	210	–0.27

[a]Referenced to the Fc^+/Fc couple

2.2.4 Electrocatalytic proton reduction

To probe the catalytic activity of **9-12** towards electrocatalytic hydrogen production, the complexes were analyzed with CV in the presence of a weak acid as a sacrificial proton donor. Our initial electrocatalytic HER investigation started with a study on 0.5 mM solutions of **11** in 0.1 M nBu$_4$NPF$_6$ in THF at a glassy carbon electrode (**Figure 10**). **11** was selected as starting point for the electrocatalytic studies because this complex shows the most anodic reduction potential in THF, and therefore seemed most suited to identify electrocatalytic HER activity.[32] In the absence of acid, **11** shows a reversible reduction at $E_{1/2}$ = –1.65 V vs. Fc$^+$/Fc (blue traces),

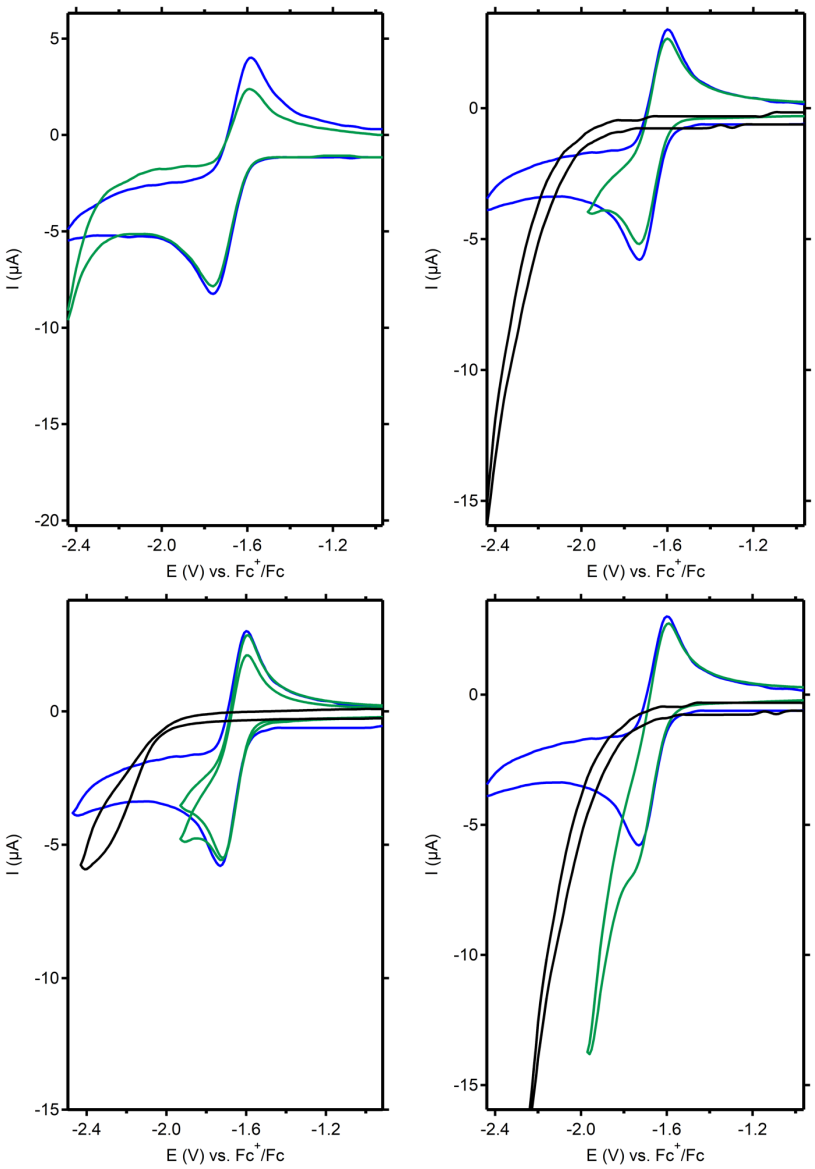

Figure 10. Cyclic voltammograms of complex **11** in THF (0.5 mM; 0.1 M nBu$_4$NPF$_6$). Top left: **11** (blue), **11** + 100 mM phenol (green); top right **11** (blue), **11** + 50 mM AcOH (green), 50 mM AcOH (black); bottom left: **11** (blue), **11** + 3 or 20 mM benzoic acid (green), 20 mM benzoic acid (black); bottom right: **11** (blue), **11** + 1 mM Et$_3$NHPF$_6$ (green), 1 mM Et$_3$NHPF$_6$ (black). Scan rate 100 mV/s. Working electrode: glassy carbon electrode.

corresponding to the Co(I/II) redox couple and identical to the response at 5 mM (**Figure 9**). Upon the addition of an excess of a weak proton donor, such as phenol (200 equiv.), acetic acid (100 equiv.), or benzoic acid (40 equiv.) no electrocatalytic wave was observed (green traces). The acid-only experiments demonstrate direct reduction at the glassy carbon electrode at more negative (cathodic) potentials for acetic acid and benzoic acid (black traces), while direct phenol reduction at the glassy carbon electrode happens outside the solvent window. Upon the addition of a relatively stronger acid Et_3NHPF_6 (2 equiv.) a slight increase in current was observed at the reduction potential ($E_{p,c}$) of the complex, followed by the start of an even stronger current.[31] The E_{onset} of the direct reduction of the Et_3NHPF_6 protons at the glassy carbon electrode starts at an only slightly more cathodic potential (black trace). To avoid overlap with this competitive background feature, we moved to a Hg-electrode, which is less active to direct proton reduction.[31] **Figure 11** depicts the cyclic voltammograms of a 0.5 mM solution of **11** at a hanging drop mercury electrode (HDME) in 0.1 M nBu$_4$NPF$_6$ in THF. In the absence of acid (blue trace), **11** shows a reversible reduction at $E_{1/2}$ = –1.1 V vs. Ag/AgCl, corresponding to the Co(I/II) redox couple (–1.65 vs. Fc^+/Fc). Upon the addition of an excess of Et_3NHPF_6 (20 equiv.; yellow trace), a minimal lowering of the $i_{p,c}$ of **11** was observed, followed by a strong current, which is close to the direct reduction of the acid at the Hg electrode (dotted line). From these observations, we conclude that **11** is not an electro-catalyst for the HER under mildly acidic conditions in THF. Next, we tested the electrocatalytic properties of complex **12**, since this complex has the most cathodic $E_{p,c}$ for the Co(I/II) reduction, and also shows a less reversible redox behavior compared to **11**. **Figure 12** depicts the cyclic voltammogram of a 1.0 mM solution of **12** at a hanging drop mercury electrode

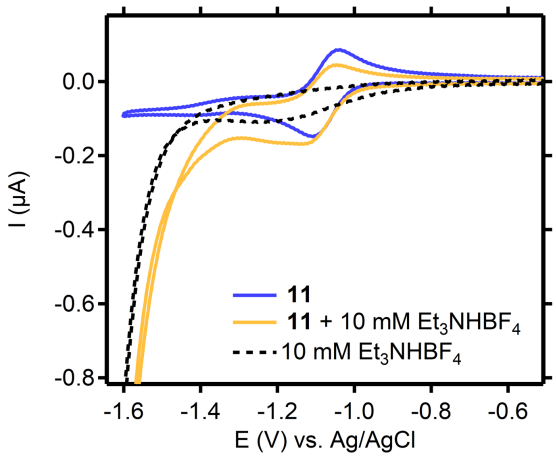

Figure 11. Cyclic voltammograms of complex **11** (0.5 mM) in THF 0.1 M nBu$_4$NPF$_6$. **11** (blue trace), **11** + 10 mM Et_3NHPF_6 (yellow) and 10 mM Et_3NHPF_6 only (dotted). Scan rate 100 mV/s. Working electrode: hanging drop mercury electrode (HDME).

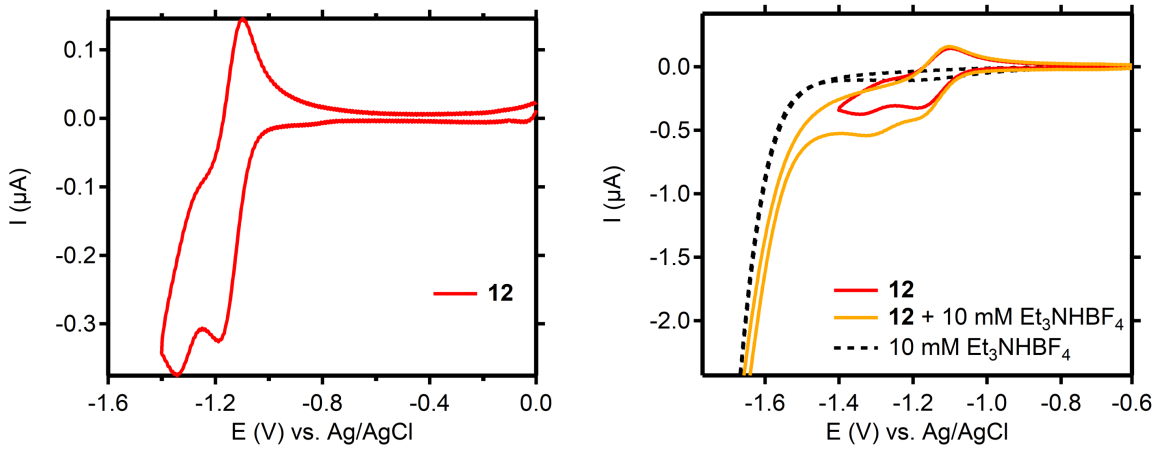

Figure 12. Left: Cyclic voltammograms of complex **12** (1.0 mM) Right: CV of **12** + 10 mM Et_3NHPF_6 (yellow) and 10 mM Et_3NHPF_6 only (dotted) in THF 0.1 M nBu$_4$NPF$_6$. Scan rate 100 mV/s; working electrode: hanging drop mercury electrode (HDME).

(HDME) in 0.1 M nBu$_4$NPF$_6$ in THF. In the absence of acid, **12** shows a reversible reduction at $E_{1/2}$ = –1.18 V vs Ag/AgCl (–1.74 vs. Fc^+/Fc), corresponding to the Co(I/II) redox couple, followed by an irreversible reduction at $E_{p,c}$ = –1.35 V, which was tentatively assigned to a species formed in the reduction of **12** (red traces). Upon the addition of an excess of Et_3NHPF_6 (10 equiv.), a slight current increase was observed at both redox events, followed by a strong current (yellow trace), which is close to the direct reduction of the acid at the Hg electrode (dotted line). We conclude that **12** and its reduced forms do not participate as fast electrocatalysts in HER. Since these experiments shown that **11** as well as **12** show no appreciable electrocatalytic HER activity in THF, we decided to continue our HER studies using MeCN as the solvent.

The same proton sources (triethylammonium tetrafluoroborate, benzoic acid, acetic acid, and phenol) were used for the electrocatalytic studies in MeCN, as these are described as recommended Brønsted acids for electrocatalytic HER studies in MeCN because of their increasing thermodynamic reduction potentials E^0_{HA} = –1.25, –1.36, –1.46, –1.75, respectively (Appendix A, Table A4), and their stability.[64] **Figure 13** depicts the voltammograms of **11** in the presence (blue), and absence (red) of 1 equiv. of the four different proton sources. Current enhancements of the same order of magnitude were observed at the Co(I/II) reduction potential of **11** in combination with all four proton sources. We attribute this behavior to an increased electron transfer rate between the electrode and complex under acidic conditions, in which the mutual differences in pK_a of the selected Brønsted acids do not significantly alter this rate. In the presence of phenol and benzoic acid, a small anodic shift in the peak potential was also observed. The enhanced redox events are followed by a second reduction event that adopts the

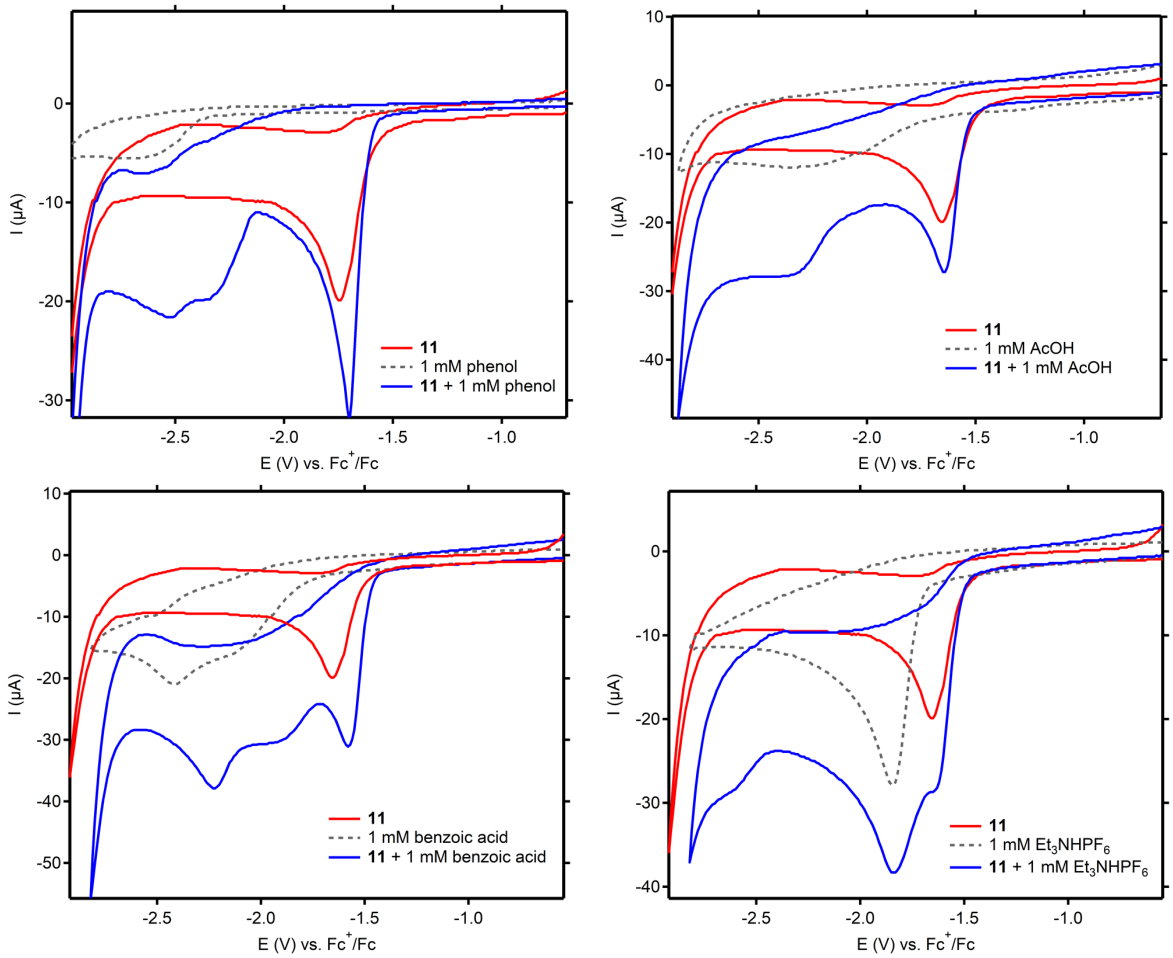

Figure 13. Cyclic voltammograms of 1 mM **11** in the presence/absence of 1 mM of the Brønsted acids phenol (top left), acetic acid (top right), benzoic acid (bottom left), and Et_3NHBF_4 (bottom right) (blue/red traces) in combination with voltammograms of the acids (dotted). Recorded in 0.1 M nBu$_4$NPF$_6$ in MeCN at a scan rate of 100 mV/s at a glassy carbon electrode and referenced *vs.* the ferrocenium/ferrocene redox couple.

same shape as the one observed for the individual Brønsted acids (dotted lines). For AcOH and Et_3NHBF_4, this event is found at a similar potential as the acid-only event, while for benzoic acid and phenol, this feature has shifted anodically by 200-300 mV. Based on previous research and the electrochemical responses, we propose that **11** forms hydrogen using a C–H methylene proton, in which the resulting deprotonated ligand is readily protonated by a weak proton source. Attempts to isolate [Co((H,pArCF$_3$)BMIM^{Ph_2})(pArCF$_3$)BMIM$^{Ph_2-}$)$_2$](BF$_4$), by treating **11** with an alkali metal hydride or base/reductant KC_8 were unsuccessful. Phenol demonstrates the strongest current enhancement compared to its background, making it the acid of choice for further studies. Next, we increased the phenol concentration to 100 mM and ran voltammetry in the presence of complexes **9-12**. **Figure 14** shows the voltammograms of **9-12** in the presence of 100 equiv. phenol and the corresponding numerical data are presented in

Table 4. In all cases, a small current enhancement was observed at the Co(I/II) reduction potential. For **9** and **10** a slight anodic shift of the Co(I/II) potential was also observed, which

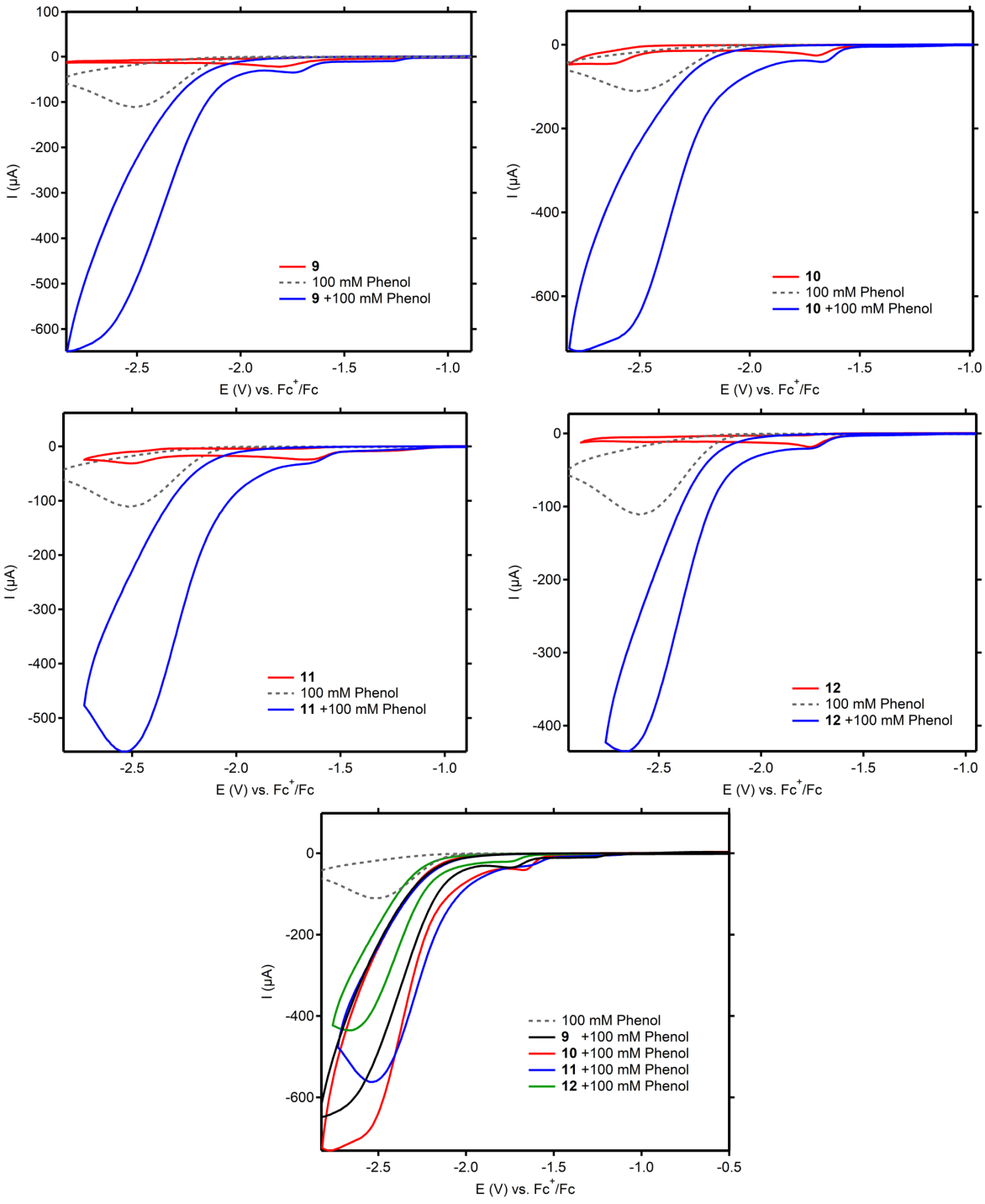

Figure 14. Cyclic voltammograms of complexes **9** (H), **10** (Cl), **11** (CF_3) and, **12** (OMe) (1.0 mM): complex only (red), complex + 100 mM phenol (blue), and 100 mM phenol only (dotted) in MeCN 0.1 M nBu$_4$NPF$_6$. Bottom: overlay of the CV's for **9-12** in the presence of 100 mM phenol (colored traces) and the acid-only trace (dotted). Scan rate 100 mV/s. Working electrode: Glassy carbon and referenced *vs.* the ferrocenium/ferrocene redox couple.

Table 4. Electrocatalytic data for [Co((H,*p*ArX)BMIM^{Ph_2})$_2$](BF$_4$)$_2$ complexes **9-12** (1 mM) in the presence of proton donor phenol (100 mM) in MeCN (0.1 M *n*Bu$_4$NBF$_4$)[a]

Complex	$E_{onset\ cat.}$ (V)	$E_{p,cat}$ (mV)	$E_{p,cat/2}$ (mV)	Overpotential (η) (mV)	$i_{cat.}$ (μA)	k_{obs} (TOF)	Hammett σ_{para} X
9 (X = H)	–2.08	–2.83	–2.36	610	649	144	0
10 (X = Cl)	–1.98	–2.78	–2.33	580	731	154	0.24
11 (X = CF$_3$)	–1.95	–2.54	–2.24	490	562	110	0.53
12 (X = OMe)	–2.13	–2.67	–2.37	620	435	53	-0.27

[a]Referenced to the Fc$^+$/Fc couple

is an indicative feature of a coupled chemical step, such as the protonation of the ligand or the formation of a metal hydride.[65] At more cathodic potentials, the onset of an electrocatalytic current was observed at $E_{onset\ cat.}$ = 1.95, –1.98, –2.08, and –2.13 V for **9-12**, respectively, (approx. –400 mV of the Co(I/II) E_{onset} potentials). The direct reduction potential of phenol at the GC electrode in the absence of **9-12** was found as a much weaker feature at a more cathodic potential $E_{p,c}$ = –2.65 V (dotted line).[64] The order in the catalytic onset potentials ($E_{onset,\ cat}$) is **11** > **10** > **9** > **12**, which equals the order in the Co(I/II) reduction potentials (E_{onset}) in the absence of substrate (acid) and correlates to the Hammett sigma values for the *para*-substituents on the installed aryl group. When considering the overpotential requirement for HER as determined by the potential difference between $E_{cat/2}$ and E^0_{HA}, which is –1.75 V for phenol in MeCN (see Figure A3 for definitions),[64] the overpotentials vary between 490 and 620 mV (from **11** to **12**). This indicates that the redox potential of the metal center is linearly correlated to the catalytic HER potential ($E_{cat/2}$) and that the *para*-substituents similarly influence both potentials. Furthermore, we observed differences in the enhancements of the electrocatalytic current and thus in the electrocatalytic rates. Using equation 1 by Bullock *et al.*, the turnover frequency (TOF) for a two-electron chemical process was determined using the observed current intensities (see the experimental section and Figure A49 for definitions).[66] For complexes **9-12** the corresponding TOF are: **9** = 144, **10** = 154, **11** = 110, **12** = 53 s^{-1} (**Figure 15**). This series might indicate that the electrocatalytic rate of the complexes increases as the electrocatalytic potential ($E_{cat/2}$) for HER becomes more positive. Yet, the TOF value of **11** is an outlier in this series and further data points would be necessary to confirm this trend. In essence, these observations are remarkable since positive (anodic) shifts in redox potentials

$$k_{obs}(TOF) = 1.94 \cdot v \cdot \left(\frac{i_{cat}}{i_p}\right)^2 \qquad \text{(eq.1)}$$

(*i.e.* lower overpotentials) typically lead to decreases in catalytic rates for reductive processes such as H_2 production (see also introduction).[46,67,68] A similar observation was made by Dubois *et al.* for their dicationic nickel complexes, $[Ni(P^{Ph}_2N^{C6H4X}_2)_2]$.[25] In that case, the increased rates were attributed to the bifunctional nature of the molecular catalyst, *i.e.* a redox-active metal center acting in concert with an intramolecular proton relay moiety. In these nickel complexes, an N–H proton relay mediates the HER and EWG substituents on the N–Ar moiety enhance the reaction rate by increasing the N–H acidity. For nickel complexes with EWG substituents more positive electrocatalytic potentials were found, which generally decrease the reactivity (basicity) at the metal center, but in this case, the catalytic rate was found to increase. This was attributed to an increase in the acidity of the proton relay, confirming the product release step as the rate-determining step. Interestingly, for the series of complexes studied by Dubois, the *para*-(CF_3)-aryl substituted complex also did not follow the observed trend. The similar trend observed for the nickel complexes of Dubois and complexes **9**-**12** would suggest that HER catalysis also in this case is oppositely influenced by the introduction of EWG/EDG substituents, lending credit to a bifunctional role of these molecular catalysts, in line with our previous proposal. Accordingly, the rate-determining step in HER catalysis by these complexes is not exclusively influenced by the overpotential but also by the electronic substituent effects. Based on our previous mechanistic work, we propose a bifunctional mode of action of the cobalt complexes in which a C–H methylene proton relay participates in the hydrogen bond-making process together with a cobalt-hydride moiety, and where EWG substituents on the phenyl groups not only lead to lower catalytic overpotentials but also make the C–H bond more acidic to result in an overall increased HER activity.[27] The HER characteristics of Dubois's

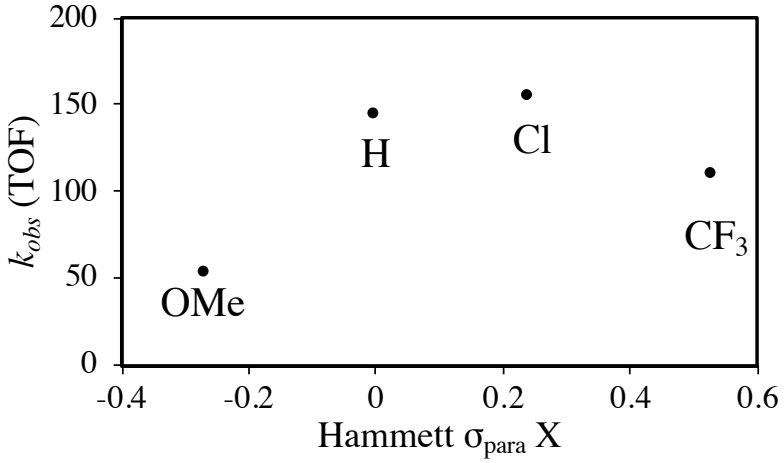

Figure 15. k_{obs}(TOF) of complexes **9** (H), **10** (Cl), **11** (CF_3) and, **12** (OMe) in the presence of 100 mM phenol in MeCN as a function of the Hammett σ_{para} parameter.

nickel catalyst and the cobalt catalysts presented here point out that in a bifunctional catalyst system, a more anodic electrocatalytic reduction potential does not necessarily decrease the catalytic HER rate.

For the non-substituted complex $[Co(HBMIM^{Ph2})_2](BF_4)_2$, the overpotential, a measurement of the catalytic HER efficiency, was measured under similar conditions (100 equiv. sacrificial proton donor in MeCN and a glassy carbon electrode) and is 590 mV with a TOF of 125 s^{-1}.[27] The introduction of a phenyl group, as in complex **9**, resulted in an overpotential of 610 with a TOF of 144 s^{-1} (**Table 4**) and therefore does not seem to significantly alter the HER performance. Further functionalization of the phenyl group with EWG substituents (complexes **10** and **11**) enhances overall catalysis, based on TOF numbers and the overpotential requirement. For $[Co(HBMIM^{Ph2})_2](BF_4)_2$, we proposed the Co(I/II) reduction to be the rate-determining step, as the $E_{onset,cat}$ was equal to the $E_{p,c}$ and theoretical studies revealed the highest energy barrier for this step.[27] For **9-12**, on the other hand, we observed a $E_{onset,cat}$ that does not coincide with the Co(I/II) reduction event, but occurs at more negative (cathodic) potentials. Unfortunately, attempts to further study the HER mechanism operating for complexes **9-12** through the isolation of reduced or deprotonated forms of the complexes, as possible intermediates, have thus far turned out to be unsuccessful.

2.2.5 Bulk electrolysis

To detect H_2 as the reaction product and to quantify H_2 formation, bulk electrolysis experiments were carried out using our in-house developed setup with inline product detection (see experimental section). Next to complexes **9-12**, $[Co(HBMIM^{Ph_2})_2](BF_4)_2$ and the well-known glyoxime complex $[Co(dmgBF_2)_2]$ were tested for benchmarking.[46,69,70] Controlled potential electrolysis was performed for 3 h in 10 mL MeCN using 100 mM phenol as the proton source at –2.00 V *vs.* Fc^+/Fc. The chosen potential is corresponding to an overpotential of only 250 mV, and is slightly anodic of the E_{onset} for **9** and **12** and slightly cathodic of the E_{onset} for **10** and **11** (**Table 4**), which would accordingly lead to sharp differences in activity.[64] However, in the presence of 1 mM **9-12**, $[Co(HBMIM^{Ph_2})_2](BF_4)_2$ and $[Co(dmgBF_2)_2]$ poor current densities (1.44–4.85 mA/cm^2) were recorded in all cases with poor Faradaic efficiencies (11-24%) (**Table 5**). No hydrogen formation was detected in the absence of any cobalt complex. After all experiments, a deposit was observed to have formed on the electrode surface. The influence of such a deposit on the observed catalytic HER performance was unclear and stimulated us to investigate bulk electrolysis using molecular cobalt complexes in more detail (see **Chapter 4**).

From this study, we conclude that the combination of phenol as a sacrificial proton donor in MeCN with a glassy carbon electrode is not optimal for our HER electrolysis studies. Nevertheless, from this benchmarking study, we conclude that the observed currents originate from H_2 formation in all cases with concomitant reductive degradation of the complexes at the electrode surface. We also conclude that **9**-**12** are competitive electrocatalyst to $[Co(HBMIM^{Ph_2})_2](BF_4)_2$, and $[Co(dmgBF_2)_2]$ with **10** being the best in this series.

Table 5. Summary of bulk electrolysis results using $[Co((H,pArX)BMIM^{Ph_2})_2](BF_4)_2$ complexes **9** (H), **10** (Cl), **11** (CF_3) and, **12** (OMe) (1 mM), $[Co(HBMIM^{Ph_2})_2](BF_4)_2$, and $[Co(dmgBF_2)_2]$, with phenol (0.1 M) in 10 mL MeCN (0.1 M nBu$_4$NPF$_6$) at –2.00 V vs Fc^+/Fc.[a]

Complex (1 mM)	Charge (C)	Current. Dens. (mA/cm^2)	FE (%)
-	0.025	0.01	0
9 (X = H)	3.03	1.44	21
10 (X = Cl)	10.27	4.85	24
11 (X = CF_3)	3.16	1.50	17
12 (X = OMe)	3.90	1.85	11
$[Co(HBMIM^{Ph2})_2](BF_4)_2$	5.20	2.46	20
$[Co(dmgBF_2)_2](BF_4)_2$	4.84	2.29	15

[a]glassy carbon electrode, 3 h. H_2 quantification by gas chromatography analysis.

2.3 Conclusion

Previous studies on the bisimidazolemethane-based cobalt complex $[Co(HBMIM^{Ph2})_2](BF_4)_2$ have demonstrated its activity as an HER electrocatalyst and have pointed at the participation of the methylene protons in the ligand backbone as a C–H proton relay during catalysis, a bifunctional mechanism. Here, we have sought to explore the effect on the cobalt-based redox potentials and catalytic activity when introducing para-substituted aryl groups next to the proton relay, but away from the first coordination sphere of the metal center. To this end, a series of $[Co((H,pPArX)BMIM^{Ph_2})_2](BF_4)_2$ complexes, where the *para*-aryl substituent X = H, Cl, CF_3, or OMe, were synthesized, holding a wide range of electronic-donor/acceptor abilities for X. It was observed that in MeCN the Co(I/II) reduction shift anodically by 170 mV upon the introduction of a non-substituted phenyl ring, as in **9**. The introduction of a *para*-aryl substituent varied the Co(I/II) reduction by 130 mV between the most donating substituent in **12** (OMe) and the least donating in **11 (**CF_3), while all Co(I/II) features remain irreversible. In THF, the Co(I/II) reductions are more reversible, indicating a different electrochemical

behavior and reactivity in THF and MeCN. Electrocatalytic studies in THF showed no HER catalysis for complexes **11** and **12**, while in MeCN each of the complexes **9**-**12** is active in HER catalysis. Interestingly, for **9**-**12** we observed an increasing HER-activity (TOF) for complexes with more electron withdrawing substituents and a lower overpotential (driving force). This observation is consistent with a bifunctional mechanism for HER in which the cobalt-based reduction potential is not directly correlated to the electrocatalytic performance. During electrolysis studies, the formation of hydrogen was confirmed and HER performance benchmarking to $[Co(HBMIM^{Ph_2})_2](BF_4)_2$ and $[Co(dmgBF_2)_2]$ demonstrated a competitive performance for **9**-**12**, although limited activity was observed in all cases.

Overall, we conclude that changes in the outer coordination sphere of bisimidazolemethane-based cobalt complexes can effectively modulate their redox properties and electrocatalytic HER performance. These observations illustrate the interesting coordination and catalytic chemistry of complexes derived from (functionalized) bisimidazolemethane ligands, which may find further application beyond cobalt and HER chemistry, such as the electrochemical activation of other small molecules like CO_2 and N_2. In terms of practical HER applications, the $[Co((H,pPhX)BMIM^{Ph_2})_2](BF_4)_2$ complexes have shown a low stability under bulk electrolysis conditions. Ongoing investigations in our laboratory aim at the development of more robust HER catalysts based on the bisimidazolemethane ligand design.

2.4 Experimental

2.4.1 General remarks

All reactions were carried out under an inert atmosphere of water- and oxygen-free N_2 gas using standard Schlenk techniques or were performed in an MBraun labmaster dp glovebox workstation. Dry acetonitrile (MeCN), dichloromethane (CH_2Cl_2), and methanol (MeOH) were used from an MBraun SPS-800 solvent purification system, dried over 3 or 4 Å molecular sieves, and degassed by bubbling N_2 for at least 30 min. Tetrahydrofuran (THF) was dried over sodium benzophenone after taking it from an MBraun SPS-800 solvent purification system, subsequently distilled and degassed by bubbling N_2 for at least 30 min. All other commercially obtained chemicals were used without further purification unless stated otherwise. Column chromatography was performed using Merck silica gel (60-200 mesh). ^{1}H-NMR, ^{13}C-NMR, and ^{19}F-NMR spectra were recorded at 400 MHz, 101 MHz, and 376 MHz respectively, at 298 K, on a Varian VNMRS400 or an Oxford NMR AS400 spectrometer. Chemical shifts (δ) are reported in ppm and referenced against the residual solvent signal. IR spectra were recorded

with a Perkin-Elmer Spectrum One FTIR spectrometer. UV-Vis-NIR spectra were recorded on a PerkinElmer 950 UV-Vis spectrometer, wavelengths are reported in nm, and extinction coefficients (ε) are given in L mol^{-1} cm^{-1}. Elemental analysis was performed by MEDAC Ltd. based in the United Kingdom. Electrospray Ionization (ESI) measurements were performed using an Advion Expression CMS mass spectrometer.

Electrochemical sweeping experiments were performed using a hanging mercury drop electrode setup in the fumehood (*vide infra*) or in a nitrogen-filled MBraun labmaster dp glovebox, on an IVIUM potentiostat/galvanostat using a 3-electrode setup including a Pt-wire counter electrode, a glassy carbon-working electrode (3 mm Ø) and an Ag/Ag(NO_3) reference electrode used directly in solution. The potentiostat was kept external to the glovebox, and the electrode leads were connected with a custom shielded electrode cable feedthrough. All scans were absolutely referenced to the ferrocenium/ferrocene redox couple taken at a scan rate of 100 mV/s, unless reported differently. The working electrodes were polished with 0.3 μm aluminium oxide powder deionized water slurries and rinsed with water for 30 seconds to remove the residual polishing powder. Before all experiments, background voltammograms were recorded at a scan rate of 100 mV/s. Solutions were mixed by shaking before each measurement and the working electrode surface was cleaned with a tissue after every scan. All measurements were recorded in a 0.1 M tetrabutylammonium tetrafluoroborate/hexafluorophosphate (*n*Bu_4NBF_4/*n*Bu_4NPF_6) solution in dry, degassed MeCN or THF.

Hanging mercury drop electrode setup: Electrochemical sweeping experiments were performed in a fume hood, on an Autolab PGSTAT204 potentiostat/galvanostat using a 663 VA stand of Metrohm. This 3-electrode setup includes a carbon counter electrode, a mercury-drop working electrode (≈ 0.01 mm Ø), and an Ag/AgCl reference electrode, used directly in the solution. Before all measurements, the cell was purged with solvent-saturated N_2. All scans were referenced to the Ag/AgCl redox couple (–0.4 V vs Fc^+/Fc) and taken at a scan rate of 100 mV/s, unless reported differently. For each experiment, a new mercury drop was used. Background voltammograms were recorded at a scan rate of 100 mV/s. Solutions were mixed by the rotator of the 663 VA stand before each measurement. All measurements were recorded in a 0.1 M tetrabutylammonium tetrafluoroborate/hexafluorophosphate (*n*Bu_4NBF_4/*n*Bu_4NPF_6) solution in dry, degassed THF.

Electrolysis solutions were prepared in the glovebox and electrolysis experiments were performed outside the glovebox using an Autolab PGSTAT204 potentiostat/galvanostat, using a 3-electrode setup including a Pt-plate counter electrode, an RDE glassy carbon-working

electrode (5 mm Ø) and a double junction Ag/Ag(NO_3) reference electrode used directly in solution. All electrodes for electrolysis experiments were purchased from Metrohm. For details on the electrochemical cell for electrolysis experiments, see below.

Appendix A contains the supplementary information for this Chapter.

The equations used for the calculation of the Turn Over Frequency from cyclic voltammograms are explained in **Chapter 1**, section 1.2, p18.

2.4.2 Electrochemical measurements coupled to gas chromatography for H_2-evolution quantification

Controlled potential and current measurements were carried out in a two-compartment three-electrode electrochemical cell (Appendix A, Figure A52). Prior to use, the catalytic cell was placed in a 1 M HCl solution for 12 h, followed by extensive washing with demineralized water, then it was put in an oven at 70 ºC for 2 h after which it was directly put under vacuum and entered in an O_2/H_2O-free glovebox. The working electrode and reference electrodes were placed in the same compartment filled with electrolyte solution, sacrificial proton donor, and a molecular cobalt complex. The counter electrode was placed in the second compartment of the cell filled with only electrolyte solution. Then the cell and electrodes are placed in-line with the GC apparatus. Subsequently, the system was flushed with N_2 for 5-10 min to remove residual oxygen, and electrolysis was started.

H_2 quantification was accomplished via an in-line gas chromatography (GC) configuration. The cell compartment of the working electrode was continuously flushed by N_2 carrier gas, whose rate was fixed through a Bronkhorst EL FLOW prestige mass flowmeter/controller at 5 mL/min. The output gas was analyzed with an InterScience CompactGC$^{4.0}$ gas chromatograph equipped with an Rt-QBond 3m * 0.32 mm capillary column and Molsieve 5 A 7 m * 0.32 mm capillary column thermostated at 65 °C and a TCD detector thermostated at 110 °C. The GC was mounted in the so-called continuous flow mode in which the carrier gas stream fills an injection loop of 50 µL in the GC. The content of the injection loop was fed every 76 sec into the GC setup, where gases (H_2 and O_2) are separated and the area under the peaks computed. Calibration of the GC-TCD was done by flushing mixed gases of N_2 and H_2 with different concentrations through the electrocatalytic cell (Appendix A, Figure A53). Under the applied flow (5 mL/min), no air leakages were determined, as confirmed by the absence of an oxygen

signal in the GC (Appendix A, Figure A54). The experimentally obtained values from the chromatogram were then used to determine the total production of H_2 in the electrochemical cell (η_{obs}).

The theoretical production rate for H_2 derived from the current i passed in the cell, assuming a unitary Faradaic yield, was calculated following the formula: $\eta_{curr} = i/(2 \times F)$ where F is the Faraday constant ($F = 96485\ C \cdot mol^{-1}$). The η_{obs}/η_{curr} ratio then gives the instantaneous Faradaic yield of the electrode for H_2-evolution.

2.4.3 Alcohol synthons and ligand synthesis

1-methyl-4,5-diphenylimidazole was synthesized using literature protocols.[71]

Bis(1-methyl-4,5-diphenyl-1H-imidazol-2-yl)(aryl)methanol (OH,*p*ArH)BMIM^{Ph_2}), (1): 1-Methyl-4,5-diphenylimidazole (1.00 g, 4.26 mmol) was dissolved in THF (30 mL) at ambient temperature. *n*-BuLi (2.67 mL, 4.26 mmol, 1.6 M in hexanes) was added dropwise, causing the solution to turn dark orange/brown. The mixture was allowed to stir for 40 min at ambient temperature before the dropwise addition of methyl benzoate (0.26 mL, 2.07 mmol). The mixture was stirred (orange) overnight and finally quenched by the addition of a saturated aqueous NH_4Cl solution (20 mL). DCM (3 x 30 mL) was used to extract the organics from the aqueous layer and the combined organic layers were washed once with distilled water (10 mL), before being dried over $MgSO_4$, and concentrated to afford a yellow oil/liquid. The product was added to petroleum ether (50 mL) and vigorously stirred, forming a yellow solid. The solids were filtered and air-dried before being washed with several portions of petroleum ether (3 x 10 mL) and methanol (2 x 10 mL). The title compound was isolated as an ochre-yellow fine powder (1.00 g, 82 %). **^{1}H NMR** (400 MHz, $CDCl_3$, 25 ˚C) δ = 7.46 (m, 11H, -CH_{arom}), 7.39 (m, 8H, -CH_{arom}), 7.17 (m, 4H, -CH_{arom}), 7.13 (m, 2H, -CH_{arom}), 3.37 (s, 6H, -NCH_3) ppm. **^{13}C NMR** (101 MHz, $CDCl_3$, 25 ˚C) δ = 148.21, 142.19, 134.87, 134.69, 131.47, 131.26, 131.14, 129.12, 128.82, 128.66, 128.50, 128.16, 127.73, 126.58, 126.25, 75.52, 33.20. **ESI-MS** (MeCN): m/z = 573.3 {$[M+H]^+$, calc. 573.27}. **ATR-IR** = 3187 (br. w), 3057 (w), 2922 (w), 1600 (w), 1502 (w), 1442 (w), 1382 (w), 1372 (w), 1062 (m), 969 (m), 917 (m), 767 (m), 695 (s), 520 (m) cm^{-1}.

Bis(1-methyl-4,5-diphenyl-1H-imidazol-2-yl)4-chloroarylmethanol (OH,*p*ArCl)BMIM^{Ph_2}), (2): 1-Methyl-4,5-diphenyl-1H-imidazole (3.00 g, 12.78 mmol) was

added to a flame dried 3-neck round-bottomed flask and dissolved in dry THF (80 mL). The solution was cooled to 0 °C and *n*-BuLi (8.0 mL 1.6 M in hexane, 12.78 mmol) was dropwise added, during which the solution turned dark quickly. The mixture was stirred overnight. Subsequently, methyl 4-chlorobenzoate (1.07 g, 6.23 mmol) was added in portions, whereafter the solution was again stirred overnight. The reaction mixture was quenched with saturated NH_4Cl solution (100 mL), which changed the color to light yellow. The organics were extracted from the aqueous layer with DCM (3 x 50 mL) and dried over $MgSO_4$. DCM was removed and a yellow-foamy substance formed. This was washed with petroleum ether (50 mL) and ethanol (30 mL) to yield the title compound as an off-white powder (2.31 g, 3.8 mmol, 60%). **^{1}H NMR** (400 MHz, $CDCl_3$, 25 °C) δ = 7.48-7.45 (m, 10H, -CH_{arom}), 7.40-7.35 (m, 6H, -CH_{arom}), 7.27-7.25 (m, 1H, -CH_{arom}), 7.20-7.16 (4H, -CH_{arom}), 7.13-7.09 (3H, -CH_{arom}), 3.34 (6H, -NCH_3). **^{13}C NMR** (100 MHz, $CDCl_3$, 25 °C) δ = 143.62, 136.89, 130.98, 130.51, 130.38, 127.53, 127.16, 126.94, 125.17, 125.09, 124.83, 124.74, 124.11, 122.49, 122.25, 71.02, 29.10. **ESI-MS** (MeCN) m/z = 607.0 {[M+H]+, calc. 607.22}. **ATR-IR** = 3345 (m), 1603 (m), 1504 (m), 1443 (m), 1349 (s), 1092 (m), 1045 (m), 1013 (m), 973 (m), 925 (m), 779 (s), 701 (s) cm^{-1}.

Bis(1-methyl-4,5-diphenyl-1H-imidazol-2-yl)(4-(trifluoromethyl)-aryl)methanol (OH,*p*ArCF$_3$)BMIM^{Ph_2}), (3): 1-Methyl-4,5-diphenylimidazole (2.00 g, 8.52 mmol) was dissolved in 60 mL THF at ambient temperature. *n*-BuLi (5.34 mL, 8.52 mmol, 1.6 M in hexanes) was added dropwise, causing the solution to turn dark red/brown. The mixture was allowed to stir for 40 min at ambient temperature before the dropwise addition of methyl 4-(trifluoromethyl)-benzoate (0.66 mL, 4.14 mmol). The mixture was stirred (orange/brown) overnight and finally quenched by the addition of a saturated aqueous NH_4Cl solution (40 ml), creating a yellow/orange solution. DCM (3 x 45 mL) was used to extract the organics from the aqueous layer and the combined organic layers were washed once with distilled water (1 x 30 mL), dried over $MgSO_4$, and concentrated to afford a yellow oil/liquid. The product was added to petroleum ether (70 mL) and vigorously stirred, during which beige solids formed, which were filtered and air-dried before being washed with several portions of petroleum ether (3 x 15 mL) and methanol (2 x 15 mL). The title compound was isolated as a beige fine powder (1.92 g, 70 %). **^{1}H NMR** (400 MHz, $CDCl_3$, 25 ˚C) δ = 7.66-7.64 (s, 2H, -CH_{arom}), 7.48-7.45 (m, 12H, -CH_{arom}), 7.39-7.37 (m, 4H, -CH_{arom}), 7.24-7.12 (m, 6H, -CH_{arom}), 3.33 (m, 6H, -NCH_3) ppm. **^{13}C NMR** (101 MHz, $CDCl_3$, 25 ˚C) δ = 141.91, 140.82, 129.64, 128.92, 126.11 126.31, 125.80, 125.35, 123.79, 123.60, 122.82, 122.80, 121.17, 121.07, 120.24, 120.20, 69.68, 27.76 ppm. **^{19}F NMR** (376 MHz, $CDCl_3$, 25 ˚C) δ = -63.35 (s, 3F, -CF_3). **ESI-MS** (MeCN):

m/z = 641.3 {[M+H]$^+$, calc. 641.25}. **ATR-IR** = 3294 (br. w), 3054 (w), 2922 (w), 1602 (w), 1502 (w), 1443 (w), 1329 (w), 1151 (m), 1121 (w), 1071 (w), 1037 (w), 967 (m), 917 (m), 828 (m), 775 (m), 706 (m), 695 (w) cm^{-1}.

Bis(1-methyl-4,5-diphenyl-1H-imidazol-2-yl)(4-(trifluoromethyl)-aryl)methanol (OH,*p*ArOMe)BMIM^{Ph_2}), (4): 1-Methyl-4,5-diphenylimidazole (2.00 g, 8.52 mmol) was dissolved in THF (60 mL) at ambient temperature. *n*-BuLi (5.34 mL, 8.52 mmol, 1.6 M in hexanes) was added dropwise, causing the solution to turn dark orange. The mixture was allowed to stir for 40 min at ambient temperature before the dropwise addition of methyl-4-methoxybenzoate (0.71 g, 4.26 mmol) turning the color of the solution slightly lighter. The mixture was stirred overnight, and the obtained yellow solution was finally quenched by the addition of saturated aqueous NH_4Cl solution (45 mL), creating a yellow/orange solution and a white precipitate. Ethyl acetate (3 x 30 mL) was used to extract the organics from the aqueous layer and the combined organic layers were washed once more with distilled water (1 x 30 mL), before being dried over $MgSO_4$, and concentrated to afford pale yellow solids. The product was added to petroleum ether (60 mL) and vigorously stirred, filtered, and air-dried before being washed with several portions of petroleum ether (3 x 15 mL) and methanol (2 x 15 mL). The title compound was isolated as a pale-yellow fine powder (2.34 g, 91 %). **^{1}H NMR** (400 MHz, MeCN-d_3, 25 ˚C): δ = 7.57-7.45 (m, 14H, -CH_{arom}), 7.28 (d, 2H, -CH_{arom}), 7.23 (t, 4H, -CH_{arom}), 7.17-7.12 (m, 2H, -CH_{arom}), 6.98 (d, 2H, CH_{arom}), 3.84 (s, 3H, OCH_3), 3.43 (s, 6H, -NCH_3) ppm. **^{13}C NMR** (101 MHz, $CDCl_3$, 25 ˚C) δ = 159.50, 148.35, 134.77, 134.68, 134.22, 131.31, 131.16, 131.12, 129.00, 128.99, 128.94, 128.69, 128.68, 128.05, 126.50, 126.47, 126.44, 126.10, 113.84, 75.10, 55.27, 33.11 ppm. **ESI-MS** (MeCN): m/z = 602.2 {[M+H]$^+$, calc. 602.3}. **ATR-IR** = 3294 (br. W), 3054 (w), 2922 (w), 1602 (w), 1502 (w), 1443 (w), 1329 (w), 1151 (m), 1121 (w), 1071 (w), 1037 (w), 967 (m), 917 (m), 828 (m), 775 (m), 706 (m), 695 (w) cm^{-1}.

2,2'-(Phenylmethylene)bis(1-methyl-4,5-diphenyl-1H-imidazole), (H,*p*ArH)BMIM^{Ph_2}), (5): To a yellow solution of **1** (0.50 g, 0.875 mmol) in DCM (40 mL), triethyl silane (1.35 mL, 8.45 mmol) was added. Subsequently, trifluoroacetic anhydride (1.2 mL, 8.7 mmol) was added dropwise at 0 °C, during which the solution progressively became dark green. After complete addition, the mixture was stirred at ambient temperature for 30 min before the second addition of triethyl silane (1.35 mL, 8.45 mmol). After stirring for 2 h the solution has turned yellow,

and water (25 mL) was added to quench the reaction. The organic layer was taken off and DCM (2 x 20 mL) was used to extract the organics from the aqueous layer. The combined organics were dried over $MgSO_4$ and the solvent was evaporated in vacuo, to afford a yellow oil/liquid. The product was co-evaporated in MeCN, added to petroleum ether (50 mL) and vigorously stirred, then filtered and air-dried. The title compound was isolated as a pale-yellow fine powder (0.46 g, 96 %). **^{1}H NMR** (400 MHz, MeCN-d_3, 25 ˚C) δ = 7.61-7.52 (m, 8H -CH_{arom}), 7.50-7.45 (m, 8H -CH_{arom}), 7.42-7.39 (m, 4H -CH_{arom}) 7.32-7.30 (m, 4H -CH_{arom}) 6.56 (s, 1H, -CH), 3.47 (s, 6H, -NCH_3) ppm. **^{13}C NMR** (101 MHz, MeCN-d_3, 25 ˚C) δ = 144.82, 134.84, 133.44, 132.06, 131.96, 131.61, 130.89, 130.61, 130.31, 129.80, 129.63, 129.14, 129.08, 127.98, 41.04, 33.10, 30.89 ppm. **ESI-MS** (MeCN) m/z = 557.3 {$[M+H]^+$, calc. 557.3}. **ATR-IR** = 3667 (w), 2988 (w), 2969 (w), 2901 (w), 1662 (w), 1599 (w), 1446 (w), 1411 (w), 1189 (s), 1131 (s), 1074 (m), 1025 (m) 916 (w), 798 (w), 772 (m), 696 (s), 593 (w), 518 (w), 489 (w) cm^{-1}. **E.A.** (Formula: $C_{39}H_{32}N_4$ Mw: 556.71 g mol^{-1}): calc. C 84.14, H 5.79, N 10.06; found C 83.88, H 5.59, N 10.45.

Bis(1-methyl-4,5-diphenyl-1H-imidazol-2-yl)4-chloroarylmethane, (H$_2$*p*ArCl)BMIM^{Ph_2}), (6): 2 (1.0 g, 1.65 mmol) was added to a flame dried 3-neck round-bottomed flask, dissolved in dry DCM (40 mL), cooled to 0 °C treated with triethylsilane (2.8 mL, 16.5 mmol). Subsequently, trifluoroacetic anhydride (1.2 mL, 8.6 mmol) was added dropwise, which caused the solution to turn dark blue-green. The reaction was stirred for 30 min before another addition of triethylsilane (2.8 mL, 16.5 mmol). The reaction was stirred overnight. The reaction mixture was quenched with water (50 mL) and the organics were extracted from the aqueous layer with DCM (3 x 30 mL). The product was purified over a silica gel column, eluted with EtOAc:petroleum ether (40–60 °C) 1:9. The title compound was obtained as a pale-yellow solid (245 mg, 0.41 mmol, 25%). **^{1}H NMR** (400 MHz, MeCN-d_3, 25 °C) δ = 7.49 (6H, -CH_{arom}), 7.43-7.38 (12H, -CH_{arom}), 7.17 (6H, -CH_{arom}), 5.97 (1H, -CH(bridging methane)), 3.31 (6H, -NCH_3). **^{13}C NMR** (100 MHz, MeCN-d_3, 25 °C) δ = 143.59, 133.87, 133.59, 133.26, 131.40, 131.05, 131.02, 130.92, 130.78, 130.44, 129.34, 129.25, 128.97, 128.77, 128.73, 128.66, 128.47, 127.68, 126.96, 40.21, 32.08. **ESI-MS** (MeCN) m/z = 591.5 {$[M+H]^+$, calc. 591.22}. **IR (ATR):** ν = 3104 (w), 1822 (w), 1699 (w), 1611 (m), 1504 (m), 1443 (m), 1349 (s), 1092 (m), 1045 (m), 1013 (m), 973 (m), 925 (m), 779 (s), 701 (s) cm^{-1}. **E.A.** (Formula: $C_{39}H_{31}N_4Cl$ Mw: 591.16 g mol^{-1}): calc. C 79.24, H 5.29, N 9.48; found C 79.47, H 5.49, N 9.50.

2,2'-((4-(Trifluoromethyl)aryl)methylene)bis(1-methyl-4,5-diphenyl-1H-imidazole), (H,*p*ArCF$_3$)BMIM^{Ph_2}), (7): To a pale yellow solution of **3** (0.5 g, 0.78 mmol) in DCM (40 mL), triethyl silane (1.20 mL, 7.50 mmol) was added. Trifluoroacetic anhydride (1.16 mL, 8.33 mmol) was added dropwise at 0 °C. During the addition, the solution instantly became dark green. After complete addition, the mixture was stirred at ambient temperature for 30 min before the second addition of triethyl silane (1.20 mL, 7.50 mmol). After stirring for 2-2.5 hours the solution had turned yellow and water (25 mL) was added to quench the reaction. The organic layer was taken off and DCM (3 x 20 mL) was used to extract the organics from the aqueous layer. The combined organic layers were dried over $MgSO_4$ and the solvent was evaporated in vacuo, to afford a yellow oil/liquid. Petroleum ether (40 mL) was added to the product and the mixture was vigorously stirred, while forming solids, which were filtered, washed with several portions of petroleum ether (5 x 5 mL), and air-dried. The title compound was isolated as a pale-yellow fine powder (0.37 g, 75 %). **^{1}H NMR** (400 MHz, MeCN-d_3, 25 ˚C) δ = 7.78 (d, 2H -CH$_{arom}$), 7.72 (d, 2H -CH$_{arom}$), 7.57-7.54 (m, 6H -CH$_{arom}$), 7.47-7.40 (m, 8H -CH$_{arom}$), 7.32-7.29 (m, 6H -CH$_{arom}$), 6.64 (s, 1H, -CH), 3.47 (s, 6H, -NCH$_3$) ppm. **^{13}C NMR** (101 MHz, MeCN-d_3, 25 ˚C) δ = 144.81, 142.25, 136.46, 134.95, 131.09, 131.01, 130.37, 129.42, 129.10, 128.97, 128.63, 128.00, 126.58, 126.55, 126.11, 125.65, 125.62, 125.59, 125.55, 125.51, 122.94, 41.46, 32.97 ppm. **^{19}F NMR** (376 MHz, $CDCl_3$, 25 ˚C) δ = -62.78 (s, 3F, -CF$_3$). **ESI-MS** (THF) m/z = 625.2 {[M+H]$^+$, calc. 625.26}. **ATR-IR** = 3064 (w), 2951 (w), 2912 (w), 2877 (w), 1668 (w), 1444 (w), 1416 (w), 1324 (w), 1260 (w), 1158 (s), 1057 (m), 1016 (m) 861 (w), 798 (w), 737 (m), 719 (s), 695 (w) cm^{-1}. **E.A.** (Formula: $C_{40}H_{31}F_3N_4$, Mw: 624.71 g mol^{-1}): calc. C 76.91, H 5.00, N 8.96; found C 76.65, H 5.00, N 8.93.

2,2'-((4-Methoxyaryl)methylene)bis(1-methyl-4,5-diphenyl-1H-imidazole), (H,*p*ArOMe)BMIM^{Ph_2}), (8): To a pale yellow solution of **4** (0.91 g, 1.5 mmol) in DCM (80 mL), sodium borohydride (561.4 mg, 15.1 mmol) was added. Trifluoroacetic anhydride (1.04 mL, 7.54 mmol) was added dropwise at 0 °C. During the addition, the solution instantly became dark blue. After complete addition, the mixture was stirred at ambient temperature for 30 min before the second addition of sodium borohydride (562.4 mg, 15.2 mmol). After stirring for 65 min the solution turned pale green/yellow and water (25 mL) was added to quench the reaction. The mixture was washed with DCM (3 x 30 mL) to extract the organics from the aqueous layer. The combined organic layers were dried over $MgSO_4$ and the solvent was evaporated in vacuo, to afford yellow crystals. The product was added to petroleum ether (60 mL) and vigorously

stirred, filtered, washed with several portions of petroleum ether (4 x 10 mL), and air-dried. Column chromatography, hexane-ethyl acetate (80:20 v/v) as mobile phase, was used to isolate the title compound. The title compound was isolated as a yellow powder (362 mg g, 41 %). **^{1}H NMR** (400 MHz, DCM-d_2, 25 ˚C) δ = 7.49-7.47 (m, 10H -CH_{arom}), 7.40-7.38 (m, 4H -CH_{arom}), 7.25 (d, 2H -CH_{arom}), 7.18 (t, 4H -CH_{arom}), 7.12 (m, 2H- CH_{arom}), 6.95-6.93 (m, 2H- CH_{arom}), 6.08 (s, 1H, -CH), 3.82 (s, 3H, -OCH_3), 3.42 (s, 6H, -NCH_3) ppm. **^{13}C NMR** (101 MHz, DCM-d_2, 25 ˚C) δ = 158.81, 145.91, 136.12, 135.12 131.31, 131.03, 130.14, 129.72, 129.38, 128.89, 128.48, 127.94, 126.52, 125.93, 114.00, 55.22, 43.98, 31.73 ppm. **ESI-MS** (acetonitrile) m/z = 587.3 {$[M+H]^+$, calc. 586.27}. **ATR-IR** = 3054 (w), 3025 (w), 2945 (w), 2922 (w), 2852 (w), 2828 (w), 1752 (w), 1601 (w), 1506 (w), 1443 (w), 1401 (w), 1252 (s), 1207 (m), 1175 (m) 1033 (w), 798 (w), 773 (m), 697 (w) cm^{-1}. **E.A.** (Formula: $C_{40}H_{34}N_4O$ Mw: 586.74 g mol^{-1}): calc (M + 1/2 H_2O). C 80.65, H 5.92, N 9.40; found C 80.86, H 5.95, N 9.28.

2.4.4 Complex synthesis

$[Co(HBMIM^{Ph_2})_2](BF_4)_2$, ($HBMIM^{Ph_2}$ = bis(1-methyl-4,5-diphenyl-1H-imidazol-2-yl)methane) was synthesized according to our previously reported method.[27] $[Co(dmgBF_2)_2]$, ($dmgBF_2$ = difluoroboryldimethylglyoximato), was synthesized according to a literature procedure.[69]

$[Co((H,pArH)BMIM^{Ph_2})_2](BF_4)_2$ (9): To a stirring light yellow solution of **5** (200 mg, 0.36 mmol) in THF (30 mL), cobalt(II) tetrafluoroborate hexahydrate (60 mg, 0.18 mmol) was added, causing the solution to immediately turn purple. The mixture was stirred overnight at ambient temperature. The solvent was evaporated *in vacuo*, to afford a dark red liquid. Diethyl ether (15 mL) was added to the obtained liquid and stirred for 30 min, immediately creating a purple/pink suspension. Diethyl ether was decanted, and the obtained purple solid was dissolved in MeCN (15 mL), creating a dark red solution. MeCN was evaporated *in vacuo*, to afford a red/purple liquid. To the obtained liquid, another 15 ml diethyl ether was added and stirred for 30 min, immediately creating a purple/pink suspension again. Diethyl ether was decanted, and the obtained purple solids were dried in vacuo. The title compound was isolated as a purple solid (151 mg, 72 %). **^{1}H NMR** (400 MHz, MeCN-d_3, 25 ˚C) δ = 121 (1H, -CH), 51 (2H, Ar *o*-CH), 40 (3H, CH_3), 31 (3H, CH_3), 24 (1H, Ar_{bridge} *p*-CH), 20 (2H, Ar *o*-CH), 12 (1H, Ar *p*-CH) 10 (2H, Ar *m*-CH), 4 (2H, Ar *m*-CH), 3 (1H, Ar *p*-CH), 4 (2H, Ar *p*-CH), 0 (4H, Ar *m*-CH), –4 (2H, *p*-Ar *m*-CH), –4 (2H, *p*-Ar *o*-CH), –38 (2H, Ar *o*-CH), –47 (2H, Ar *o*-

CH) ppm. Tentative peak assignments were based on relative integration, and broadness of the resonance, chemical shift, and similarity to structural analogs (see main text). **HRMS** (MeCN) m/z = 585.7289 {$[CoL_2]^{2+}$, calc. 585.7293}, m/z = 557.2690 {$[L+H]^+$, calc. 557.2705}. **ATR-IR** = 3535, 3060, 1634, 1599, 1505, 1486, 1446, 1310, 1283, 1222, 1183, 1161, 1058, 1002, 925, 879, 771, 699, 520, 498 cm^{-1}.

[Co((H,*p*ArCl)BMIM^{Ph_2})$_2$](BF$_4$)$_2$ (10): 6 (245 mg, 0.42 mmol) was dissolved in dry THF (35 mL). $Co(BF_4)_2 \cdot H_2O$ (70.4 mg, 0.21 mmol) was added, and the solution immediately turned from light yellow to dark purple. The reaction was stirred overnight before the solvent was evaporated. Et_2O (5 mL) was added, and the solution was stirred for 30 min. The Et_2O was decanted, and the product was dried under reduced pressure yielding the title compound as a red-purple crystalline powder (190.6 mg, 0.15 mmol, 64%) **^{1}H NMR** (400 MHz, MeCN-d_3, 25 ˚C) δ = 122 (1H, -CH), 50 (2H, Ar *o*-CH), 40 (3H, CH_3), 31 (3H, CH_3), 19 (2H, Ar *o*-CH), 10 (1H, Ar *p*-CH) 6 (2H, Ar *m*-CH), 4 (1H, Ar *p*-CH), 4 (2H, Ar *m*-CH), 3 (1H, Ar *p*-CH), 3 (1H, Ar *p*-CH), 3 (2H, Ar *m*-CH), 1 (1H, Ar *m*-CH), 1 (1H, Ar *m*-CH), –4 (2H, *p*-Ar *m*-CH), –4 (2H, *p*-Ar *o*-CH), –40 (2H, Ar *o*-CH), –46 (2H, Ar *o*-CH) ppm. Tentative peak assignments were based on relative integration, and broadness of the resonance (methylene and some *o*-Ar CH protons seemed to be in close proximity to the metal center (observed in a related solid-state single crystal X-ray structure), and therefore broaden), chemical shift, and similarity to structural analogs. **HRMS** (MeCN) m/z = 1258.3780 {$[CoL_2+F]^+$, calc. 1258.37905}, m/z = 619.6913 {$[CoL_2]^{2+}$, calc. 619.69032}, m/z = 591.2309 {$[L+H]^+$, calc. 591.2315}. **ATR-IR** = 3533 (br, w), 3059 (br, w), 2961 (br, w), 1623 (w), 1487 (s), 1444 (m), 1054 (br, s), 1024 (br, s), 787 (m), 698 (s), 520 (w) cm^{-1}.

[Co((H,*p*ArCF$_3$)BMIM^{Ph_2})$_2$](BF$_4$)$_2$ (11): To a stirring beige solution of **7** (166 mg, 0.27 mmol) in THF (30 mL) and cobalt(II) tetrafluoroborate hexahydrate (44.8 mg, 0.14 mmol) was added, causing the solution to immediately turn dark purple. The mixture was stirred overnight at ambient temperature. The solvent was evaporated in vacuo, to afford a purple liquid. Diethyl ether (15 mL) was added to the obtained liquid and stirred overnight, creating a purple suspension. Diethyl ether was decanted, and the pink/purple solid was dissolved in MeCN (15 mL), creating a pink/purple liquid. MeCN was evaporated in vacuo, to afford a red/purple liquid. Diethyl ether (15 mL) was added to the obtained liquid and stirred for 35 min, immediately creating a purple/pink suspension. Diethyl ether was decanted, and the obtained

purple solid was dried in vacuo. The title compound was isolated as a purple solid (123 mg, 64 %). **^{1}H-NMR** (400 MHz, MeCN-d_3, 25 ˚C) δ = 121(1H, -CH), 49 (2H, Ar *o*-CH), 40 (3H, CH_3), 31 (3H, CH_3), 12 (2H, Ar *o*-CH), 10 (1H, Ar *p*-CH) 8 (1H, Ar *m*-CH), 4 (1H, Ar *p*-CH), 4 (2H, Ar *m*-CH), 3 (1H, Ar *p*-CH), 3 (1H, Ar *p*-CH), 1 (4H, Ar *m*-CH), 0 (1H, Ar *m*-CH), –4 (2H, *p*- Ar *m*-CH), –4 (2H, *p*- Ar *o*-CH), –41(2H, Ar *o*-CH), –451 (2H, Ph *o*-CH) ppm. Tentative peak assignments were based on relative integration, and broadness of the resonance (methylene and some *o*-Ph CH protons seemed to be in close proximity to the metal center (observed in a solid-state single crystal X-ray structure), and therefore broaden), chemical shift, and similarity to structural analogs. $\boldsymbol{X_m}$ (Evans method, 1% TMS in MeCN-d_3) : μ_{eff} = 3.72 μ_B. **^{19}F NMR** (376 MHz, MeCN-d_3, 25 °C): δ = –75.28 ppm. **HRMS** (MeCN) m/z = 1326.4325 {$[CoL_2+F]^+$, calc. 1326.4317}, m/z = 653.7179 {$[CoL_2]^{2+}$, calc. 653.7167}, m/z = 625.2573 {$[L+H]^+$, calc. 625.2579}. **ATR-IR** = 3552, 3050, 1619, 1505, 1445, 1410, 1323, 1163, 1124, 1056, 1024, 1003, 993, 922, 881, 812, 788, 772, 699, 521 cm^{-1}. **X-ray crystal structure determination** $[C_{80}H_{62}CoF_6N_8](BF_4)_2 \cdot C_2H_3N$ + disordered solvent, Fw = 1522.98[*], purple plate, 0.67 × 0.25 × 0.06 mm^3, monoclinic, $P2_1/n$ (no. 14), a = 17.8506(5), b = 15.7774(5), c = 30.0749(13) Å, β = 100.863(1) °, V = 8318.4(5) $Å^3$, Z = 4, D_x = 1.216 g/cm^3[*], μ = 0.28 mm^{-1}[*]. The diffraction experiment was performed on a Bruker Kappa ApexII diffractometer with sealed tube and Triumph monochromator (λ = 0.71073 Å) at a temperature of 150(2) K up to a resolution of $(\sin\theta/\lambda)_{max}$ = 0.61 $Å^{-1}$. The Eval15 software[72] was used for the intensity integration. Anisotropic mosaicity[73] about *hkl*=(1,0,0) was taken into account for the prediction of reflection profiles. A multi-scan absorption correction and scaling was performed with SADABS[74] (correction range 0.61-0.75). A total of 148545 reflections was measured, 15485 reflections were unique (R_{int} = 0.070), 11332 reflections were observed [I>2σ(I)]. The structure was solved with Patterson superposition methods using SHELXT.[75] Structure refinement was performed with SHELXL-2018[76] on F^2 of all reflections. The crystal structure contains voids (1603 $Å^3$ / unit cell) filled with disordered acetonitrile and diethyl ether solvent molecules. Their contribution to the structure factors was secured by back-Fourier transformation using the SQUEEZE algorithm[77] resulting in 414 electrons / unit cell. Non-hydrogen atoms were refined freely with anisotropic displacement parameters. The CF_3 groups were refined with a disorder model. All hydrogen atoms were introduced in calculated positions and refined with a riding model. 1034 Parameters were refined with 363 restraints (distances, angles and displacement parameters in the disordered CF_3 groups and the acetonitrile solvent molecule). R1/wR2 [I > 2σ(I)]: 0.0417 / 0.1014. R1/wR2 [all refl.]: 0.0639 / 0.1101. S = 1.044. Residual

electron density between -0.32 and 0.44 e/Å^3. Geometry calculations and checking for higher symmetry was performed with the PLATON program.[78]
[*] Derived values do not contain the contribution of the disordered solvent molecules.

[Co((H,*p*ArOMe)BMIM^{Ph_2})$_2$](BF$_4$)$_2$ (12): To a stirring beige solution of **8** (80.8 mg, 0.14 mmol) in THF (15 mL), cobalt(II) tetrafluoroborate hexahydrate (24.0 mg, 0.07 mmol) was added, causing the solution to immediately turn dark purple. The mixture was stirred overnight at ambient temperature. The solvent was evaporated in vacuo, to afford purple solids. To the obtained solids, dry diethyl ether (10 mL) was added and stirred for 30 min, creating a purple suspension. Diethyl ether was decanted, and the obtained purple solid was dissolved in dry MeCN (10 mL), creating a purple solution. All volatiles were evaporated *in vacuo*, to afford a purple oil-like residue. To the residue, dry diethyl ether (10 mL) was added and stirred for 30 min, immediately creating a purple suspension. Diethyl ether was decanted, and the obtained purple solid was dried in vacuo. The title compound was isolated as a purple solid (65 mg, 75 %). **^{1}H-NMR** (400 MHz, MeCN-d_3, 25 ˚C) δ = 123 (1H, -CH), 50 (2H, Ar *o*-CH), 40 (3H, imidazole-CH$_3$), 31 (3H, imidazole-CH$_3$), 19 (2H, Ar *o*-CH), 10 (1H, Ar *p*-CH), 9 (3H, Ar-OCH$_3$), 6 (2H, Ar *m*-CH), 4 (1H, Ar *p*-CH), 4 (2H, Ar *m*-CH), 3 (1H, Ar *p*-CH), 3 (2H, Ar *m*-CH), 2 (1H, Ar *p*-CH), 1 (2H, Ar *m*-CH), –4 (2H, *p*- Ar *m*-CH), –4 (2H, *p*- Ar *o*-CH), –41 (2H, Ar *o*-CH), –45 (2H, Ar *o*-CH) ppm. Tentative peak assignments were based on relative integration, and broadness of the resonance (methylene and some *o*-Ph CH protons seemed to be in close proximity to the metal center (observed in a solid-state single crystal X-ray structure), and therefore broaden), chemical shift, and similarity to structural analogs. **HRMS** (MeCN) m/z = 1250.4773 {[CoL$_2$+F]$^+$, calc. 1250.4781}, m/z = 615.7416 {[CoL$_2$]$^{2+}$, calc. 615.7397}, m/z = 578.2798 {[L+H]$^+$, calc. 578.2811}. **ATR-IR** = 3054, 3028, 2961, 2899, 2836, 1603, 1511, 1487, 1442, 1406, 1303, 1257, 1177, 1052, 1025, 786, 689, 517 cm^{-1}.

2.5 Author Contributions

Synthesis, characterization, and electrochemical measurements were done by S.D. de Vos, M. Otten, L. Killian, M.R. de Vries, and K.C. Pons. X-ray crystal structure determinations were performed by M. Lutz. The project design was done by S.D. de Vos and R.J.M. Klein Gebbink. Funding acquisition, administration, and oversight were done by R.J.M. Klein Gebbink. The original draft was written by S.D. de Vos and reviewing, and editing was done by D.L.J Broere and R.J.M. Klein Gebbink with contributions by all authors.

2.6 References

(1) Lewis, N. S.; Nocera, D. G. Powering the planet: Chemical challenges in solar energy utilization. *Proc. Natl. Acad. Sci. U.S.A* **2006,** *103* (43), 15729.

(2) Zaccaria, F.; Menendez Rodriguez, G.; Rocchigiani, L.; Macchioni, A. Molecular Catalysis in "Green" Hydrogen Production. *Front. Cat.* **2022,** *2*.

(3) Wang, M.; Chen, L.; Sun, L. Recent progress in electrochemical hydrogen production with earth-abundant metal complexes as catalysts. *Energy Environ. Sci.* **2012,** *5* (5), 6763.

(4) Dalle, K. E.; Warnan, J.; Leung, J. J.; Reuillard, B.; Karmel, I. S.; Reisner, E. Electro- and Solar-Driven Fuel Synthesis with First Row Transition Metal Complexes. *Chem. Rev.* **2019**, 119, (4), 2752–2875

(5) Lubitz, W.; Ogata, H.; Rüdiger, O.; Reijerse, E. Hydrogenases. *Chem. Rev.* **2014,** *114* (8), 4081.

(6) Darensbourg, M. Y.; Lyon, E. J.; Zhao, X.; Georgakaki, I. P. The organometallic active site of [Fe] hydrogenase: Models and entatic states. *Proc. Natl. Acad. Sci. U.S.A* **2003,** *100* (7), 3683.

(7) Frey, M. Hydrogenases: Hydrogen-Activating Enzymes. *ChemBioChem* **2002,** *3* (2-3), 153.

(8) Darensbourg, M. Y.; Lyon, E. J.; Smee, J. J. The bio-organometallic chemistry of active site iron in hydrogenases. *Coord. Chem. Rev.* **2000,** *206-207*, 533.

(9) Fontecilla-Camps, J. C.; Volbeda, A.; Cavazza, C.; Nicolet, Y. *Chem. Rev.* **2007,** *107*, 4273.

(10) Peters, J. W.; Lanzilotta, W. N.; Lemon, B. J.; Seefeldt, L. C. X-ray Crystal Structure of the Fe-Only Hydrogenase (CpI) from *Clostridium pasteurianum* to 1.8 Angstrom Resolution. *Science* **1998,** *282* (5395), 1853.

(11) Nicolet, Y.; de Lacey, A. L.; Vernède, X.; Fernandez, V. M.; Hatchikian, E. C.; Fontecilla-Camps, J. C. *J. Am. Chem. Soc.* **2001,** *123*, 1596.

(12) Ott, S.; Kritikos, M.; Åkermark, B.; Sun, L.; Lomoth, R. *Angew. Chem., Int. Ed.* **2004,** *43*, 1006.

(13) Schwartz, L.; Eilers, G.; Eriksson, L.; Gogoll, A.; Lomoth, R.; Ott, S. *Chem. Commun.* **2006**, 520.

(14) Löscher, S.; Schwartz, L.; Stein, M.; Ott, S.; Haumann, M. Facilitated Hydride Binding in an Fe−Fe Hydrogenase Active− Site Biomimic Revealed by X-ray Absorption Spectroscopy and DFT Calculations. *Inorg. Chem.* **2007,** *46* (26), 11094.

(15) Jiang, S.; Liu, J.; Shi, Y.; Wang, Z.; Åkermark, B.; Sun, L. *Dalton Trans.* **2007**, 896.

(16) Barton, B. E.; Olsen, M. T.; Rauchfuss, T. B. *J. Am. Chem. Soc.* **2008,** *130*, 16834.

(17) Wang, N.; Wang, M.; Liu, J.; Jin, K.; Chen, L.; Sun, L. Preparation, facile deprotonation, and rapid H/D exchange of the μ-hydride diiron model complexes of the [FeFe]-Hydrogenase containing a pendant amine in a chelating diphosphine ligand. *Inorg. Chem.* **2009,** *48* (24), 11551.

(18) Lough, A. J.; Park, S.; Ramachandran, R.; Morris, R. H. Switching On and Off a New Intramolecular Hydrogen-Hydrogen Interaction and the Heterolytic Splitting of Dihydrogen. Crystal and Molecular Structure of $[Ir\{H(\eta^1\text{-}SC_5H_4NH)\}_2(PCy_3)_2]BF_4.2.7\ CH_2Cl_2$. *J. Am. Chem. Soc.* **1994,** *116* (18), 8356.

(19) Henry, R. M.; Shoemaker, R. K.; DuBois, D. L.; DuBois, M. R. Pendant Bases as Proton Relays in Iron Hydride and Dihydrogen Complexes. *J. Am. Chem. Soc.* **2006,** *128* (9), 3002.

(20) Yeh, C.-Y.; Chang, C. J.; Nocera, D. G. "Hangman" Porphyrins for the Assembly of a Model Heme Water Channel. *J. Am. Chem. Soc.* **2001,** *123* (7), 1513.

(21) Rakowski Dubois, M.; Dubois, D. L. Development of Molecular Electrocatalysts for CO_2 Reduction and H_2 Production/Oxidation. *Acc. Chem. Res.* **2009,** *42* (12), 1974.
(22) Graham, D. J.; Nocera, D. G. Electrocatalytic H_2 Evolution by Proton-Gated Hangman Iron Porphyrins. *Organometallics* **2014,** *33* (18), 4994.
(23) Roubelakis, M. M.; Bediako, D. K.; Dogutan, D. K.; Nocera, D. G. Proton-coupled electron transfer kinetics for the hydrogen evolution reaction of hangman porphyrins. *Energy Environ. Sci.* **2012,** *5* (7), 7737.
(24) Helm, M. L.; Stewart, M. P.; Bullock, R. M.; DuBois, M. R.; DuBois, D. L. A Synthetic Nickel Electrocatalyst with a Turnover Frequency Above 100,000 s^{-1} for H_2 Production. *Science* **2011,** *333* (6044), 863.
(25) Kilgore, U. J.; Roberts, J. A. S.; Pool, D. H.; Appel, A. M.; Stewart, M. P.; DuBois, M. R.; Dougherty, W. G.; Kassel, W. S.; Bullock, R. M.; DuBois, D. L. $[Ni(P^{Ph}{}_2N^{C6H4X}{}_2)_2]^{2+}$ Complexes as Electrocatalysts for H2 Production: Effect of Substituents, Acids, and Water on Catalytic Rates. *J. Am. Chem. Soc.* **2011,** *133* (15), 5861.
(26) Dogutan, D. K.; Bediako, D. K.; Teets, T. S.; Schwalbe, M.; Nocera, D. G. Efficient Synthesis of Hangman Porphyrins. *Org. Lett.* **2010,** *12* (5), 1036.
(27) Ghosh, P.; de Vos, S.; Lutz, M.; Gloaguen, F.; Schollhammer, P.; Moret, M.-E.; Klein Gebbink, R. J. M. Electrocatalytic Proton Reduction by a Cobalt Complex Containing a Proton-Responsive Bis(alkylimdazole)methane Ligand: Involvement of a C−H Bond in H2 Formation. *Chem. Eur. J.* **2020,** *26* (55), 12560.
(28) Appel, A. M.; Helm, M. L. Determining the Overpotential for a Molecular Electrocatalyst. *ACS Catalysis* **2014,** *4* (2), 630.
(29) Stratakes, B. M.; Dempsey, J. L.; Miller, A. J. M. Determining the Overpotential of Electrochemical Fuel Synthesis Mediated by Molecular Catalysts: Recommended Practices, Standard Reduction Potentials, and Challenges. *ChemElectroChem* **2021,** *8* (22), 4161.
(30) Fourmond, V.; Jacques, P.-A.; Fontecave, M.; Artero, V. H2 Evolution and Molecular Electrocatalysts: Determination of Overpotentials and Effect of Homoconjugation. *Inorg. Chem.* **2010,** *49* (22), 10338.
(31) Felton, G. A. N.; Glass, R. S.; Lichtenberger, D. L.; Evans, D. H. Iron-Only Hydrogenase Mimics. Thermodynamic Aspects of the Use of Electrochemistry to Evaluate Catalytic Efficiency for Hydrogen Generation. *Inorg. Chem.* **2006,** *45* (23), 9181.
(32) Rountree, E. S.; McCarthy, B. D.; Eisenhart, T. T.; Dempsey, J. L. Evaluation of Homogeneous Electrocatalysts by Cyclic Voltammetry. *Inorganic Chemistry* **2014,** *53* (19), 9983.
(33) Jacques, P.-A.; Artero, V.; Pécaut, J.; Fontecave, M. Cobalt and nickel diimine-dioxime complexes as molecular electrocatalysts for hydrogen evolution with low overvoltages. *Proc. Natl. Acad. Sci. U.S.A* **2009,** *106* (49), 20627.
(34) Berning, D. E.; Miedaner, A.; Curtis, C. J.; Noll, B. C.; Rakowski DuBois, M. C.; DuBois, D. L. *Organometallics* **2001,** *20*, 1832.
(35) Chen, S.; Raugei, S.; Rousseau, R.; Dupuis, M.; Bullock, R. M. Homogeneous Ni Catalysts for H_2 Oxidation and Production: An Assessment of Theoretical Methods, from Density Functional Theory to Post Hartree−Fock Correlated Wave-Function Theory. *J. Phys. Chem. A* **2010,** *114* (48), 12716.
(36) Chen, S.; Ho, M.-H.; Bullock, R. M.; DuBois, D. L.; Dupuis, M.; Rousseau, R.; Raugei, S. Computing Free Energy Landscapes: Application to Ni-based Electrocatalysts with Pendant Amines for H_2 Production and Oxidation. *ACS Catalysis* **2014,** *4* (1), 229.

(37) Solis, B. H.; Hammes-Schiffer, S. Substituent Effects on Cobalt Diglyoxime Catalysts for Hydrogen Evolution. *J. Am. Chem. Soc.* **2011,** *133* (47), 19036.
(38) Lin, H.; Hossain, M. S.; Zhan, S.-Z.; Liu, H.-Y.; Si, L.-P. Electrocatalytic hydrogen evolution using triaryl corrole cobalt complex. *Appl. Organomet. Chem.* **2020,** *34* (5), e5583.
(39) Beyene, B. B.; Hung, C.-H. Recent progress on metalloporphyrin-based hydrogen evolution catalysis. *Coord. Chem. Rev.* **2020,** *410*, 213234.
(40) Beyene, B. B.; Mane, S. B.; Hung, C.-H. Electrochemical Hydrogen Evolution by Cobalt (II) Porphyrins: Effects of Ligand Modification on Catalytic Activity, Efficiency and Overpotential. *J. Electrochem. Soc.* **2018,** *165* (9), H481.
(41) Moyses Araujo, C.; Doherty, M. D.; Konezny, S. J.; Luca, O. R.; Usyatinsky, A.; Grade, H.; Lobkovsky, E.; Soloveichik, G. L.; Crabtree, R. H.; Batista, V. S. Tuning redox potentials of bis(imino)pyridine cobalt complexes: an experimental and theoretical study involving solvent and ligand effects. *Dalton Trans.* **2012,** *41* (12), 3562.
(42) Letko, C. S.; Panetier, J. A.; Head-Gordon, M.; Tilley, T. D. Mechanism of the Electrocatalytic Reduction of Protons with Diaryldithiolene Cobalt Complexes. *J. Am. Chem. Soc.* **2014,** *136* (26), 9364.
(43) Hammett, L. P. Some relations between reaction rates and equilibrium constants. *Chem. Rev.* **1935,** *17* (1), 125.
(44) Hammett, L. P. *Physical Organic Chemistry, 2nd ed*; McGraw-Hill: New York, 1970.
(45) Hansch, C.; Leo, A.; Taft, R. W. A survey of Hammett substituent constants and resonance and field parameters. *Chem. Rev.* **1991,** *91* (2), 165.
(46) Hu, X.; Brunschwig, B. S.; Peters, J. C. Electrocatalytic Hydrogen Evolution at Low Overpotentials by Cobalt Macrocyclic Glyoxime and Tetraimine Complexes. *J. Am. Chem. Soc.* **2007,** *129* (29), 8988.
(47) Wakerley, D. W.; Reisner, E. Development and understanding of cobaloxime activity through electrochemical molecular catalyst screening. *Phys. Chem. Chem. Phys.* **2014,** *16* (12), 5739.
(48) Kilgore, U. J.; Stewart, M. P.; Helm, M. L.; Dougherty, W. G.; Kassel, W. S.; DuBois, M. R.; DuBois, D. L.; Bullock, R. M. Studies of a Series of $[Ni(P^{R}_2N^{Ph}_2)_2(CH_3CN)]^{2+}$ Complexes as Electrocatalysts for H_2 Production: Substituent Variation at the Phosphorus Atom of the P_2N_2 Ligand. *Inorg. Chem.* **2011,** *50* (21), 10908.
(49) Huo, P.; Uyeda, C.; Goodpaster, J. D.; Peters, J. C.; Miller, T. F., III. Breaking the Correlation between Energy Costs and Kinetic Barriers in Hydrogen Evolution via a Cobalt Pyridine-Diimine-Dioxime Catalyst. *ACS Catalysis* **2016,** *6* (9), 6114.
(50) Klug, C. M.; Cardenas, A. J. P.; Bullock, R. M.; O'Hagan, M.; Wiedner, E. S. Reversing the Tradeoff between Rate and Overpotential in Molecular Electrocatalysts for H_2 Production. *ACS Catalysis* **2018,** *8* (4), 3286.
(51) Shaw, W. J.; Helm, M. L.; DuBois, D. L. A modular, energy-based approach to the development of nickel containing molecular electrocatalysts for hydrogen production and oxidation. *Biochim. Biophys. Acta* **2013,** *1827* (8), 1123.
(52) Costentin, C.; Drouet, S.; Robert, M.; Savéant, J.-M. Turnover Numbers, Turnover Frequencies, and Overpotential in Molecular Catalysis of Electrochemical Reactions. Cyclic Voltammetry and Preparative-Scale Electrolysis. *J. Am. Chem. Soc.* **2012,** *134* (27), 11235.
(53) Lee, K. J.; Elgrishi, N.; Kandemir, B.; Dempsey, J. L. Electrochemical and spectroscopic methods for evaluating molecular electrocatalysts. *Nat. Rev. Chem.* **2017,** *1* (5), 0039.

(54) Pegis, M. L.; Wise, C. F.; Koronkiewicz, B.; Mayer, J. M. Identifying and Breaking Scaling Relations in Molecular Catalysis of Electrochemical Reactions. *J. Am. Chem. Soc.* **2017,** *139* (32), 11000.
(55) Zhou, L.; Powell, D.; Nicholas, K. M. Copper(I) Complexes of Tripodal Tris(imidazolyl) Ligands: Potential Mimics of the Cu(A) Site of Hydroxylase Enzymes. *Inorg. Chem.* **2007,** *46* (6), 2316.
(56) Von Zelewsky, A. *Stereochemistry of Coordination Compounds*; John Wiley & Sons: Chichester, U.K., 1996.
(57) Desvergnes-Breuil, V.; Hebbe, V.; Dietrich-Buchecker, C.; Sauvage, J.-P.; Lacour, J. NMR Evaluation of the Configurational Stability of Cu(I) Complexes. *Inorg. Chem.* **2003,** *42* (2), 255.
(58) Gispert, J. R. *Coordination chemistry*; Wiley-VCH Weinheim, 2008.
(59) Evans, D. 400. The determination of the paramagnetic susceptibility of substances in solution by nuclear magnetic resonance. *J. Chem. Soc. (Resumed)* **1959**, 2003.
(60) Bard, A. J.; Faulkner, L. R. Electrochemical Methods: Fundamentals and Applications, 2001.
(61) Kosuke Izutsu *Electrochemistry in Nonaqueous Solutions*, Wiley-VCH Weinheim, 2002.
(62) Mayer, U.; Gutmann, V.; Gerger, W. The acceptor number—A quantitative empirical parameter for the electrophilic properties of solvents. *Monatshefte für Chemie/Chemical Monthly* **1975,** *106* (6), 1235.
(63) Staemmler, V. The Donor-Acceptor Approach to Molecular Interactions. Von V. Gutmann. Plenum Press, New York 1978. XVI, 279 S. *Angew. Chem.* **1979,** *91*, 595.
(64) McCarthy, B. D.; Martin, D. J.; Rountree, E. S.; Ullman, A. C.; Dempsey, J. L. Electrochemical Reduction of Brønsted Acids by Glassy Carbon in Acetonitrile—Implications for Electrocatalytic Hydrogen Evolution. *Inorg. Chem.* **2014,** *53* (16), 8350.
(65) Elgrishi, N.; McCarthy, B. D.; Rountree, E. S.; Dempsey, J. L. Reaction Pathways of Hydrogen-Evolving Electrocatalysts: Electrochemical and Spectroscopic Studies of Proton-Coupled Electron Transfer Processes. *ACS Catalysis* **2016,** *6* (6), 3644.
(66) Bullock, R. M.; Appel, A. M.; Helm, M. L. Production of hydrogen by electrocatalysis: making the H–H bond by combining protons and hydrides. *Chem. Commun.* **2014,** *50* (24), 3125.
(67) Le Goff, A.; Artero, V.; Jousselme, B.; Tran, P. D.; Guillet, N.; Métayé, R.; Fihri, A.; Palacin, S.; Fontecave, M. From Hydrogenases to Noble Metal-Free Catalytic Nanomaterials for H_2 Production and Uptake. *Science* **2009,** *326* (5958), 1384.
(68) Koca, A.; Özçeşmeci, M.; Hamuryudan, E. Substituents Effects to the Electrochemical, and In Situ Spectroelectrochemical Behavior of Metallophthalocyanines: Electrocatalytic Application for Hydrogen Evolution Reaction. *Electroanalysis* **2010,** *22* (14), 1623.
(69) Hu, X.; Cossairt, B. M.; Brunschwig, B. S.; Lewis, N. S.; Peters, J. C. Electrocatalytic hydrogen evolution by cobalt difluoroboryl-diglyoximate complexes. *Chem. Commun.* **2005,** (37), 4723.
(70) Razavet, M.; Artero, V.; Fontecave, M. Proton Electroreduction Catalyzed by Cobaloximes: Functional Models for Hydrogenases. *Inorg. Chem.* **2005,** *44* (13), 4786.
(71) Braussaud, N.; Rüther, T.; Cavell, K. J.; Skelton, B. W.; White, A. H. Bridged 1-Methylbisimidazoles as Building Blocks for Mixed Donor Bi- and Tridentate Chelating Ligands. *Synthesis* **2001,** *2001* (04), 0626.
(72) Schreurs, A. M.; Xian, X.; Kroon-Batenburg, L. M. EVAL15: a diffraction data integration method based on ab initio predicted profiles. *J. Appl. Crystallogr.* **2010**, 43

(1), 70-82.
(73) A. J. M. Duisenberg. “Diffractometry and reflection profiles of anisotropic mosaic and split crystals”. *Acta Cryst.* **1983** A39, 211-216.
(74) G. M. Sheldrick. "*SHELXT* - Integrated space-group and crystal-structure determination". *Acta Cryst.* **2015**, A71, 3-8.
(75) Sheldrick, G. SHELXT - Integrated space-group and crystal-structure determination. *Acta Crystallogr. Sect. A* **2015**, 71 (1), 3.
(76) Sheldrick, G. M. Crystal structure refinement with SHELXL. *Acta Crystallogr. Sect. C: Structural Chemistry* **2015**, 71 (1), 3.
(77) Spek, A. PLATON SQUEEZE: a tool for the calculation of the disordered solvent contribution to the calculated structure factors. *Acta Crystallogr. Sect. C* **2015**, C71 (1), 9-18.
(78) A. L. Spek. "Structure validation in chemical crystallography". *Acta Cryst.* **2009**, D65, 148-155.

Chapter 3

Bis(benzazolyl)methane Cobalt Complexes as Electrocatalytic Hydrogen Evolution Catalyst

Abstract

Bis(benzazolyl)methane ligands bis(*N*-methylbenzimidazol-2-yl)methane (HBBIM), bis(benzoxazol-2-yl)methane (HBBZM), and bis(benzothiazol-2-yl)methane (HBBTM) were used to synthesize bis-ligated dicationic cobalt(II) complexes **1**-**3** of the type $[Co(L)_2](BF_4)_2$ (**1** L = HBBIM, **2** L = HBBZM, **3** L = HBBTM) and neutral bis-ligated cobalt(II) complexes **4**-**6** of the type $[Co(L)_2]$ (**4** L = $BBIM^-$, **5** L = $BBZM^-$, **6** L = $BBTM^-$). **1**-**6** were spectroscopically and electrochemically characterized using X-ray crystal structure analysis, ESI-MS, ^{1}H-NMR, and CV, respectively. Complexes **1**-**3** demonstrate an irreversible Co(I/II) reduction event at –1.90, –1.43, and –1.31 V, respectively, vs Fc/Fc^+ in MeCN, demonstrating an effective modulation of the metal-based electronic properties upon variation of the hetero-atom in the benzazole rings of the ligands. A similar modulation is found for the redox events in **4**-**6** and both corroborate the electronic trend reported by Abbotto *et al*. for the π-electron-withdrawing power of the ligands: $BBTM^-$ > $BBZM^-$ > $BBIM^-$. Electrocatalytic studies using **1**-**3** in MeCN in combination with 10 equiv. of proton donor Et_3NHBF_4 showed that the complexes are electrocatalysts for the hydrogen evolution reaction (HER) at overpotentials of 610, 580 and 490 mV, respectively. Complex **2** demonstrates the highest activity (TOF = 28 for **2** vs. 15 for **1** and 25 for **3**). Electrolysis studies on **2** showed electrocatalytic H_2 formation at a moderate Faradaic Efficiency (FE) of 72% and a current density of 2.00 mA/cm^2. This study demonstrates that the redox features of bis(benzazolyl)methane-derived cobalt complexes can effectively be modulated by changing the nature of their heterocycles and that the complexes are active as HER catalysts.

S.D. de Vos, S.I. Verboom, M. Basauri-Molina, M. Lutz, D.L.J. Broere, R.J.M. Klein Gebbink, *manuscript in preparation*

3.1 Introduction

Currently, the cleanest way to produce molecular hydrogen (H_2) is through water electrolysis, using sunlight and photovoltaic cells.[1] On the cathodic side of an electrolysis cell, hydrogen production is enabled by a conductive electrode material that catalyzes the reduction of protons to hydrogen, also known as the hydrogen evolution reaction (HER). Platinum-based catalysts are among the best-performing catalyst in the field due to their optimal binding strength for protons and hydrogen gas.[2] However, due to platinum's scarcity and high cost, there is a strong desire to move to more abundant and commercially attractive materials.[1] Metals like iron, nickel, and cobalt qualify for these requirements and have been investigated in metal alloys, on carbon-based supported electrode materials, or in molecular complexes.[3-5] Molecular complexes are an interesting class of materials because of their uniform and often well-defined modular scaffolds, allowing for thorough structural and activity studies.[6-11] In particular, molecular complexes based on cobalt have gained much attention thanks to their enhanced catalytic activity in HER electrocatalysis. In addition, complexes with a bifunctional character, in which a proton relay is built into the ligand to stimulate proton (substrate) transport to the metal center, have attracted a lot of attention. For example, amine and carboxylic acid groups are used as a proton relay in phosphine and porphyrin cobalt complexes that produce H_2 electrocatalytically, leading to enhanced catalytic rates.[12-19]

Our group reported on a dicationic cobalt(II) complex $[Co(HBMIM^{Ph2})_2](BF_4)_2$, ($HBMIM^{Ph2}$ = bis(1-methyl-4,5-diphenylimidazole)methane) with two β-diketimine ligands, that is active as an HER electrocatalyst.[20] Unique to this system is the involvement of a methylene C–H proton during the formation of hydrogen gas. The β-diketimine/β-diiminate motif in the $HBMIM^{Ph2}$ ligand can be reversibly (de)protonated, and thereby be partaking as a proton relay (**Figure 1**).

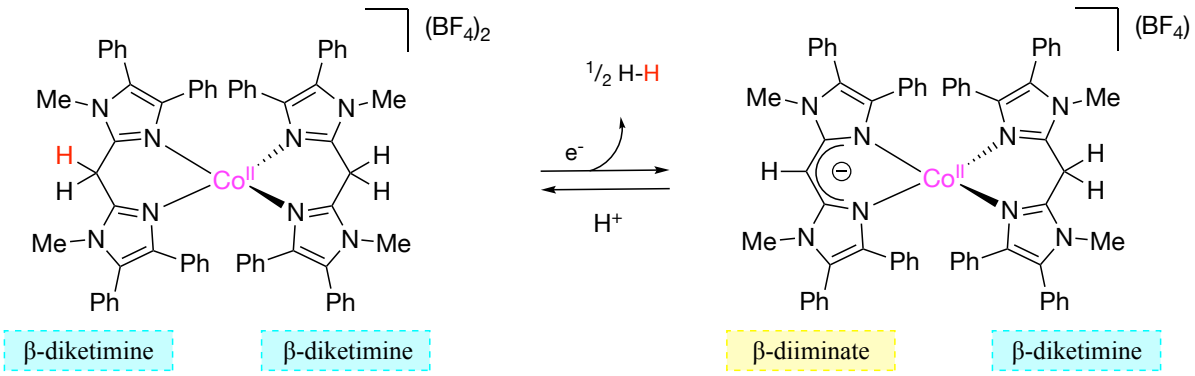

Figure 1. Ligand-mediated HER reactivity for electrocatalyst $[Co(HBMIM^{Ph2})_2](BF_4)_2$.[20] The proton-responsive property of the β-diketimine/β-diiminate motif is highlighted.

Both stoichiometric and electrocatalytic experiments demonstrated the formation of hydrogen gas upon reduction of $[Co(HBMIM^{Ph2})_2](BF_4)_2$ and combined spectroscopic and theoretic analysis suggested hydrogen gas formation upon the combination of a cobalt hydride and a ligand methylene proton. In **Chapter 2** we continued this lead and demonstrated that functionalization of the outer coordination sphere of analogous cobalt(II) complexes with phenyl-substituted bis-imidazole ligands of the type $[Co((H,pArX)BMIM^{Ph_2})_2](BF_4)_2$ (X = OMe, H, Cl, CF_3) has a significant effect on the cobalt-based redox properties and electrocatalytic HER performance. In the current study, we have taken a different approach with a similar aim to gain a further understanding of the electrocatalytic HER activity of cobalt complexes with a β-diketimine ligand motif. By altering the heteroatoms in the heterocyclic imidazole rings in $HBMIM^{Ph2}$, we intended to change the electronic environment of the β-diketimine and its coordination strength (and geometry) to cobalt. In doing so, the cobalt-centered reactivity may change as well, allowing for further insights into the effect of the heteroatoms on the metal-based redox chemistry and electrocatalytic HER. Accordingly, we set out to prepare and study a small series of cobalt complexes (**1**-**6**) based on the bis(benzazolyl)methane ligands bis(*N*-methylbenzimidazol-2-yl)methane (HBBIM), bis(benzoxazol-2-yl)methane (HBBZM), and bis(benzothiazol-2-yl)methane (HBBTM) (**Figure 2**). The different NMe, O, and S functionalities of these ligands enable the electronic

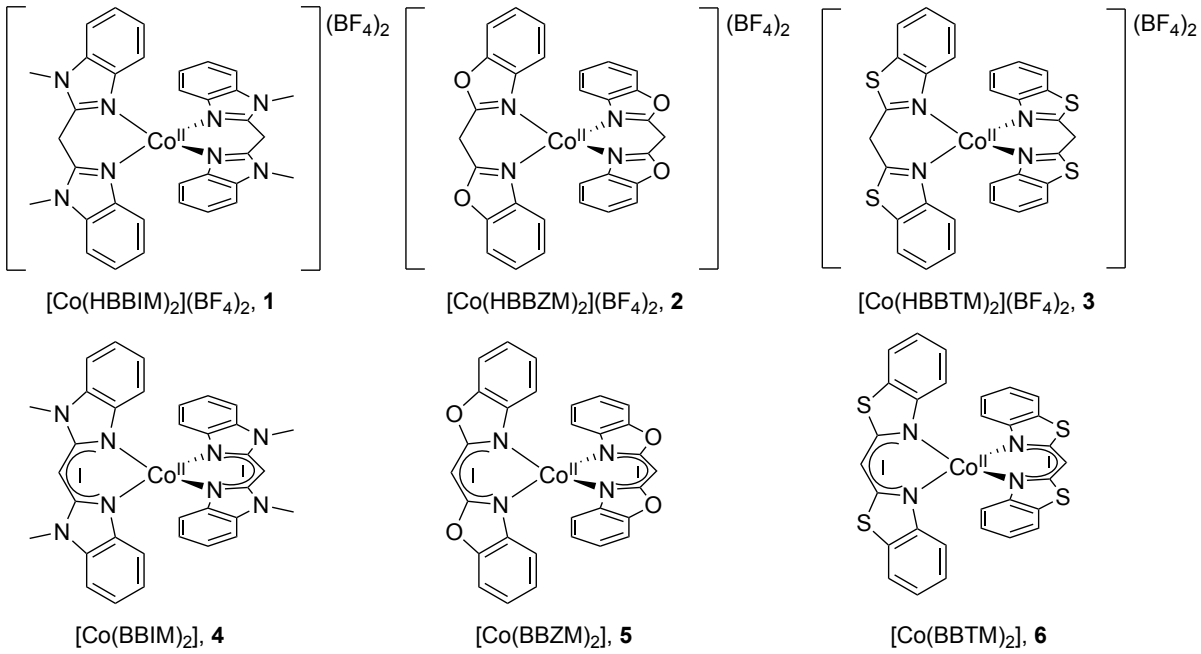

Figure 2. Overview of cobalt complexes **1**-**6** used in this study, bearing bis(2-benzazolyl)methanide and bis(2-benzazoyl)methane ligands. (Complex **2** was crystallized as its bis-acetonitrile adduct $\mathbf{2}^{\mathbf{2MeCN}}$; *vide infra*.)

properties of the β-diketimine chelators to be modulated in a controlled, systematic manner. The coordination chemistry of bis(benzazolyl)methane ligands with s-block and d-block metal is well studied over the last two decades, often leading to bis-ligated complexes with either tetrahedral or octahedral geometries, yet the application in (electrocatalytic) HER catalysis was not yet investigated.[21-40] Abbotto *et al.* previously reported on the electronic properties of β-diiminate moieties (deprotonated β-diketimines) in anionic bis(benzazolyl)methanide ligands coordinated to Zn and as free ligands. In their studies, the π-electron density residing on the trigonal carbanionic carbon was obtained from its ^{13}C chemical shift and used as an empirical parameter to rank the π-electron-withdrawing power of the heterocyclic rings, resulting in the order $BBTM^- >> BBZM^- > BBIM^-$ (**Figure 3**).[41-45] Interestingly, this order is different from the electronegativity order of the hetero atoms, S 2.5 < N 3.0 < O 3.5, demonstrating that the trend is not merely determined by inductive effects.

Using the bis(benzazolyl)methane/methanide ligands in either their neutral or deprotonated forms, we synthesized dicationic and neutral cobalt complexes **1**-**6** (**Figure 2**). Compared to the previously reported $[Co(HBMIM^{Ph2})_2](BF_4)_2$ complex, the replacement of the sterically demanding diphenylimidazole moieties with smaller benzazole moieties is expected to increase the coordinative flexibility of the ligands, possibly leading to other coordination geometries than the tetrahedral one in $[Co(HBMIM^{Ph2})_2](BF_4)_2$. In addition, bis(benzazole)methane ligands are expected to be less donating compared to their bis(azole)diphenylmethane counterparts, making the molecular cobalt complexes more prone to electrochemical reduction.[45] Complexes **1**-**6** have allowed us to study the influence of the different ligand heterocycles on the redox properties of the complexes, as well as the HER electrocatalytic behavior of dicationic complexes **1**-**3**. Complexes **4**-**6** in particular allowed for a further assessment of the electrochemical properties, in view of their similar structures to the complexes $[Co(BMIM^{Ph2-})_2]$ and $[Zn(BMIM^{Ph2-})_2]$ for which a series of reversible oxidation events have previously been observed in our group.[46]

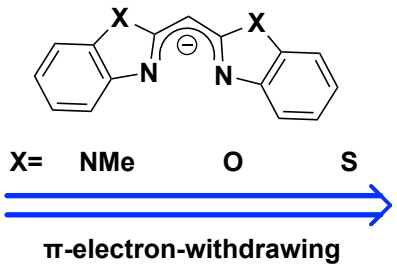

Figure 3. The π-electron-withdrawing power of the bis(benzazolyl)methanide periphery.[43]

3.2 Results and Discussion

3.2.1 Synthesis of cobalt complexes

Dicationic cobalt(II) complexes **1-3** were obtained by dissolving 2 equiv. of the neutral bisbenzazolyl ligand in dry THF followed by the addition of 1 equiv. of $[Co(BF_4)_2 \cdot 6H_2O]$ (**Scheme 1**). The corresponding cobalt complexes **1-3** precipitated as pink, off-white, and green powders, respectively, in moderate to high yields. Complexes **1-3** are all soluble in aprotic polar solvents such as acetone, acetonitrile, DMSO, and DMF. **2** and **3** are also soluble in the

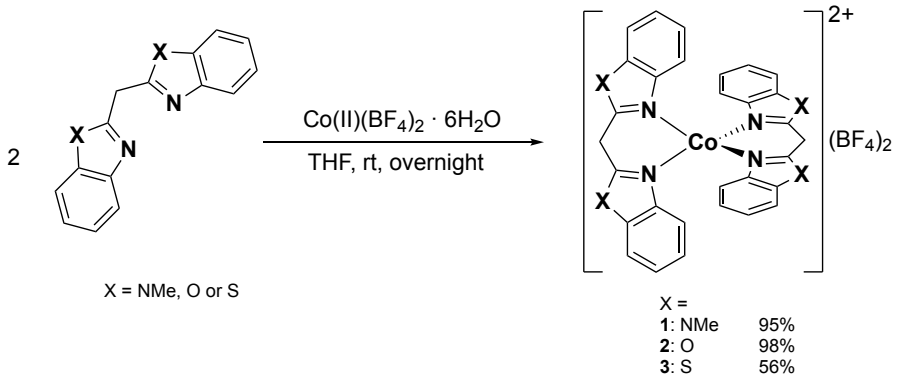

Scheme 1. Synthesis of complexes $[Co(BBIM)_2](BF_4)_2$ (**1**), $[Co(BBZM)_2](BF_4)_2$ (**2**), and $[Co(BBTM)_2](BF_4)_2$ (**3**).

non-polar solvents pentane and benzene. Elemental analysis revealed that **1-3** were obtained as bis-ligand dicationic complexes of the type $[Co(L)_2](BF_4)_2$ (L = HBBIM, HBBZM, HBBTM), in which **2** has a small solvent impurity and different batches of **3** contained the right element ratio but 3-7% lower absolute values, indicative of an inorganic impurity. Mass spectroscopy of **1-3** demonstrated a strong signal for $[CoL_2–H]^+$ (Appendix B, Figures B1, B3, and B5 for **1-3,** respectively). We also prepared $\mathbf{2^{Zn}}$, as a redox-innocent metal analog. $\mathbf{2^{Zn}}$ was obtained by dissolving 2 equiv. of the neutral HBBZM ligand in dry THF followed by the addition of 1 equiv. of $[Zn(BF_4)_2 \cdot 6H_2O]$ (**Scheme 2**). The elemental analysis of the isolated, white powder

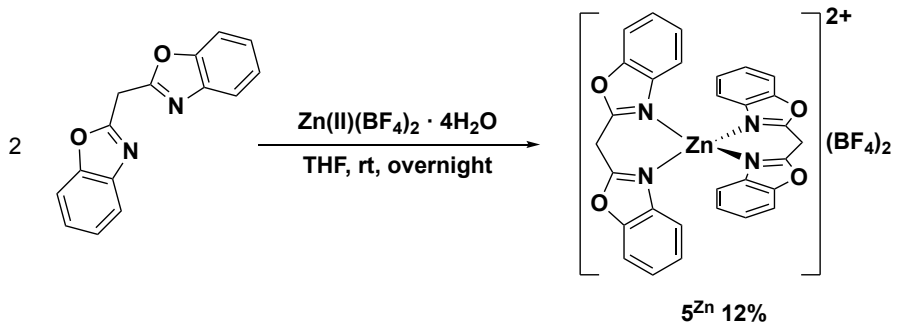

Scheme 2. Synthesis of complex $[Zn(HBBZM)_2](BF_4)_2$ $\mathbf{2^{Zn}}$.

was consistent with a $[Zn(HBBZM)_2](BF_4)_2$ composition and mass spectroscopy in acetonitrile showed an intense peak for $[Zn(HBBZM)_2–H]^+$ at 562.7 (cal. 563.07) (Appendix B, Figure B9). Neutral cobalt complexes **4**-**6** (**Figure 3**) were first reported by Abbotto *et al.* and synthesized using their reported procedure, in which the neutral ligand is mixed with cobalt(II) acetate in a 2:1 ratio in MeOH.[43,47] The acetate ions deprotonate the ligands *in situ* during this procedure. Abbotto *et al.* characterized the complexes by reporting on their physical appearance, color, mass (for **2** and **3**), and elemental analysis. Here, we provide additional characterization by means of single-crystal X-ray diffraction, ^{1}H-NMR, UV-vis, and cyclic voltammetry.[43,47] Complexes **4**-**6** were obtained as pinkish, orange, and blue/purple powders, respectively. In all cases, elemental analysis reveals that complexes **4**-**6** were obtained as pure, bis-ligand neutral complexes of the type $[Co^{II}(L^–)_2]$ ($L^–$ = $BBIM^–$, $BBZM^–$, $BBTM^–$). Abbotto *et al.* reported on the synthesis of $[Co(BBIM)(OAc)_2·2H_2O]$ using the same method,[43] which is in contrast to our isolation of $[Co(BBIM^–)_2]$ (**4**). Complexes **4**-**6** are air-sensitive and soluble in mid-polar and polar aprotic solvents like DMF, DMSO, and THF, but poorly soluble in MeCN, methanol, or water. These neutral complexes did not lend themselves for ESI-MS analysis, likely because of difficult ionization. We also reproduced the synthesis of Zn analog $\mathbf{5^{Zn}}$,[47] as a redox-innocent metal analog, and provide additional characterization by means of single crystal X-ray structure determination and cyclic voltammetry.

3.2.2 X-ray crystal structure analysis

3.2.2.1 Dicationic complexes $[Co(HBBIM)_2](BF_4)_2$ (1) and $[Co(HBBZM)_2](BF_4)_2$ (2)

Pink and yellow crystals suitable for single crystal X-ray diffraction were grown through slow vapor diffusion of diethyl ether into a concentrated solution of **1** or **2** in MeCN at –40 °C and 0 °C, respectively. The crystal structures of **1** and **2** are shown in **Figure 4** and reveal a tetrahedral geometry for **1**, while for $\mathbf{2^{2MeCN}}$ a centrosymmetric octahedral geometry was found in which the cobalt center is hexacoordinated, with two additional acetonitrile molecules on the axial positions and two bidentate HBBZM ligands in the equatorial plane. Acetonitrile coordination in $\mathbf{2^{2MeCN}}$ is remarkable, as crystals of analog complexes **1** and $[Co(HBMIM^{Ph2})_2](BF_4)_2$ that were also grown from MeCN solutions and adopt tetrahedral geometries.[20] The octahedral geometry in $\mathbf{2^{2MeCN}}$ brings the benzoxazole groups near to each other, causing the ligands to fold away from each other in order to prevent a steric clash in the equatorial plane. Key bond distances and angles for **1** and $\mathbf{2^{2MeCN}}$ are compiled in **Table 1**. The

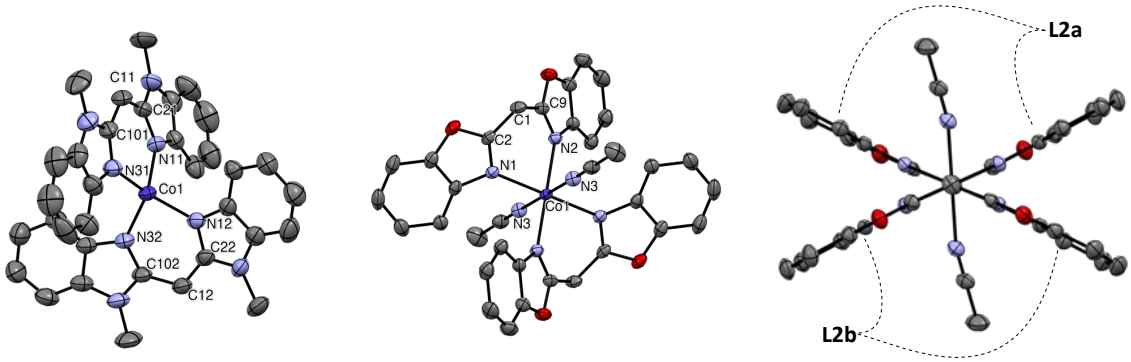

Figure 4. Displacement ellipsoid plots for tetrahedral $[Co(BBIM)_2](BF_4)_2$ **1** (left), and octahedral $[Co(BBZM)_2(MeCN)_2](BF_4)_2$ $\mathbf{2^{2MeCN}}$ (middle, right). The folding of the ligands away from each other and the equatorial plane in $\mathbf{2^{2MeCN}}$ is highlighted in the structure on the right (50 % probability). Only one of the two independent molecules is shown for **1**. H-atoms, counterions, and disordered solvent molecules have been omitted for clarity.

Table 1. Selected bond lengths (Å) and bond angles (º) for complex $[Co(BBIM)_2](BF_4)_2$ (**1**) and $[Co(BBZM)_2(MeCN)_2](BF_4)_2$ ($\mathbf{2^{2MeCN}}$). Only the ordered part of **1** is given.

$[Co(BBIM)_2](BF_4)_2$ (**1**)					
Mol A		Mol B		Bond Angle	
Bond	Length	Bond	Length	Bond Angle	Degrees
Co1–N11	1.981(4)	Co2–N13	1.992(4)	N12–Co1–N32	92.57(16)
Co1–N12	1.983(4)	Co2–N33	1.991(4)	N12–Co1–N11	113.31(16)
Co1–N31	1.984(4)			N11–Co1–N31	92.98(17)
Co1–N32	1.980(4)			N31–Co1–N32	113.27(17)
C12–C22	1.474(7)				
C12–C102	1.491(7)				

$[Co(BBZM)_2(MeCN)_2](BF_4)_2$ ($\mathbf{2^{2MeCN}}$)			
Bond	Length	Bond Angle	Degrees
Co1–N1	2.1460(15)	N1–Co1–N2	84.40(6)
Co1–N2	2.1156(15)	N1–Co1–N3	88.44(6)
Co1–N3	2.1266(17)	N2–Co1–N3	91.61(6)
N1–C2	1.295(2)		
C1–C2	1.487(3)		
C1–C9	1.495(3)		

asymmetric unit of **1** contains two independent molecules, of which one is well-defined and the other slightly disordered. In the ordered molecule, the angles between the methylene bridge and two azole units (C101-C11-C21 and C102-C12-C22) are 117.5(4) and 118.2(4)º in **1**, while

the corresponding angle (C2–C1–C9) in $\mathbf{2}^{\mathbf{2MeCN}}$ shows an almost perfectly sp^3-hybridized tetrahedral C-atom (110.03(16)º). In $[Co(HBMIM^{Ph2})_2](BF_4)_2$, angles of 116.3(4)-117.7(4)º were found, which is similar to **1**.[20] For complex **1**, a dihedral angle between the N11–Co1–N31 and N12–Co1–N32 planes of 81.2(2)° was found. Considering the Co–N metal-ligand coordination bond lengths in tetrahedral **1** and octahedral $\mathbf{2}^{\mathbf{2MeCN}}$ an elongation of ≈ +0.15 Å is observed in $\mathbf{2}^{\mathbf{2MeCN}}$. When comparing **1** to analog $Co[HBMIM^{Ph2}](BF_4)_2$,[20] it was observed that both metal centers are surrounded by two nearly planer NCCCN chelators, which are less twisted in **1,** and that the Co–N metal-ligand distances are similar. The latter is in contrast with our hypothesis that the benzimidazole moieties are less donating than diphenyl imidazole moieties (*vide supra*). Attempts to grow a single crystal of sufficient quality for **3** were unsuccessful.

3.2.2.1 Neutral complexes $[Co(BBIM^{-})_2]$ (4) and $[Co(BBZM^{-})_2]$ (5)

Crystals suitable for single X-ray diffraction were grown from a saturated solution of **4** (pink crystals) and **5** (orange crystals) in THF and pentane, respectively, at –40 °C over several weeks. Both crystal structures show a distorted tetrahedral geometry (**Figure 5**, **Table 2**). We were also able to obtain an X-ray crystal structure of $\mathbf{5}^{\mathbf{Zn}}$, which is of poorer quality, but sufficient enough to assign the structure as isostructural to **5** (see experimental section). Complex **4** has a dihedral angle between the N11–Co1–N31 and N12–Co1–N32 planes of 82.03(8)°, while the corresponding dihedral angles in the two independent molecules of **5** are

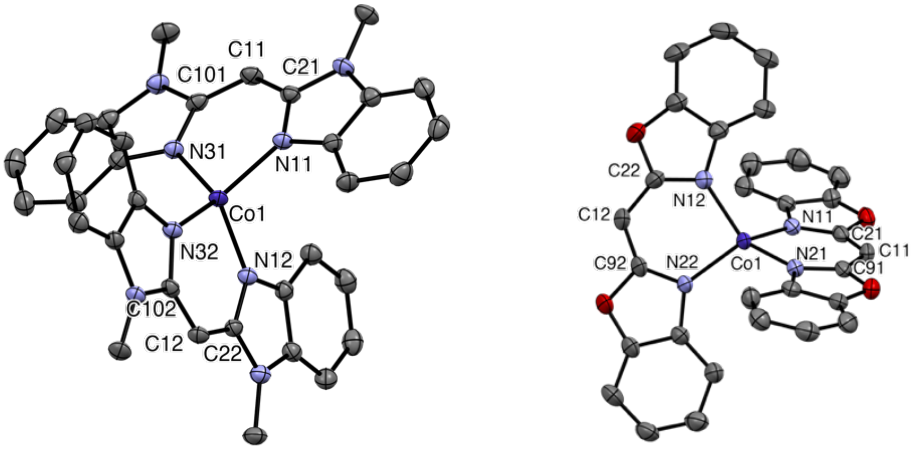

Figure 5. Displacement ellipsoid plot of $[Co(BBIM^{-})_2]$ (**4**) (left) and $[Co(BBZM^{-})_2]$ (**5**) (right) (50 % probability). Only one of two independent molecules is displayed for **5**. H-atoms and disordered solvent molecules have been omitted for clarity.

Table 2. Selected bond lengths (Å) and bond angles (º) for complexes [Co(BBIM^{-})$_2$] **4** and [Co(BBZM^{-})$_2$] **5**. Only one of two independent molecules is displayed for **5**.

[Co(BBIM^{-})$_2$ (**4**)			
Bond	Length (Å)	Bond Angle	Degrees
Co1–N11	1.9677(14)	N11–Co1–N12	111.61(6)
Co1–N12	1.9632(14)	N31–Co1–N32	115.35(6)
Co1–N31	1.9703(13)	N11–Co1–N31	92.93(6)
Co1–N32	1.9704(13)	N12–Co1–N32	93.34(6)
N31–C101	1.364(2)		
C11–C101	1.397(2)		
C11–C21	1.401(2)		
N11–C21	1.361(2)		

[Co(BBZM^{-})$_2$ (**5**)			
Bond	Length (Å)	Bond Angle	Degrees
Co1–N11	1.981(4)	N11–Co1–N12	101.97(16)
Co1–N12	1.986(4)	N12–Co1–N21	133.40(18)
Co1–N21	1.983(4)	N11–Co1–N21	92.70(16)
Co1–N22	1.994(4)	N12–Co1–N22	93.04(15)
N22-C92	1.339(6)		
C12–C22	1.402(9)		
C12–C92	1.373(7)		
N12–C22	1.326(6)		

64.7(2) and 64.0(2)°, making **5** more distorted. The Co–N metal-ligand distances in **5** are slightly longer (≈ +0.018 Å), indicating a lower donation from the ligand and a weaker bond between the BBZM^{-} ligands and cobalt compared to the BBIM^{-} ligands and cobalt. Considering the bond lengths of all bonds in the six-membered metallacycles of **4** and **5**, no significant difference was noticed. For **4**, the dihedral angle between the coordination planes (N(L1)–Co1–N(L1) and N(L2)–Co1–N(L2); *vide supra*) is almost equal to 81.2(2)° found in **1**, and the Co–N metal-ligand coordination bonds are slightly shorter in **4** (≈ –0.013 Å), together indicating that minimal structural rearrangement takes place upon deprotonation/protonation of both β-diketimine/β-diimine ligand motifs, which is further illustrated in the quaternion plot of **1** and **4** (**Figure 6**). When comparing the crystallographic parameters of **4** to those of [Co(BMIM^{Ph2-})$_2$] and [Co(NacNac)$_2$] (NacNac = dimethylpentane–2,4-diiminate),[46,48] all bearing a tetrahedral cobalt center with two coordinating bis-β-diiminate motifs, the bond lengths of the four Co–N metal-ligand coordination bonds in **4** are slightly shorter (≈ –0.02 Å) compared to [Co(BMIM^{Ph2})$_2$] and comparable to [Co(NacNac)$_2$], indicating slightly stronger coordination of the BBIM^{-} ligands over the BMIM^{Ph2-} ligands. The N–Co–N angles between

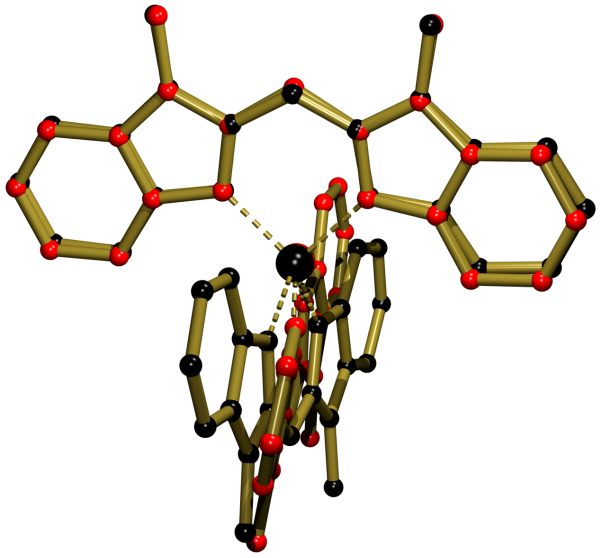

Figure 6. Quaternion plot of X-ray structures of $[Co(HBBIM)_2](BF_4)_2]$ **1** (red) and $[Co(BBZM)_2]$ **4** (black).

the cobalt center and the bidentate ligands in **4** (N11–Co1–N31 and N12–Co1–N32) are 92.93(6) and 93.34(6)°, which is smaller compared to that observed in $[Co(BMIM^{Ph2-})_2]$ (97.3(6)°) and $[Co(NacNac)_2]$ (95.8(5)°),[46,48] demonstrating a smaller distortion in **4**. The bond lengths in the NCCCN backbone are comparable for **4**, $[Co(BMIM^{Ph2-})_2]$, and $[Co(NacNac)_2]$; for example, the C–C bond distances are 1.393(2) – 1.399(3) Å in **4**, 1.400(3) – 1.404(3) Å in $[Co(BMIM^{Ph2-})_2]$, and 1.407(13) – 1.414(14) Å in $[Co(NacNac)_2]$. Direct comparison of the bis-β-diiminate coordination motifs in **4** to other reported $Co(NacNac)_2$ complexes reveals larger variances due to important geometric differences, *e.g.* in cases where octahedral or square planar coordination geometries were adopted,[49-57] such as square planar [Co(1-mesitylbutane-1,3-diimine)$_2$],[49] for which shorter (≈ 0.11 Å) Co–N metal-ligand coordination bonds are observed compared to **4**. Overall, the binding modes of the bis-β-diiminate ligands in the crystal structure of **4** and **5**, and reported analogs are considered similar. The comparison between dicationic **2** and neutral analog **5** was omitted due to their geometry differences in their solid-state structures (octahedral vs. tetrahedral). Attempts to grow a single crystal of sufficient quality for **6** were unsuccessful.

3.2.3 NMR analysis

Complexes **1**-**3** were analyzed by ^{1}H-NMR in MeCN-d_3 (**1**-**3**) and DMSO-d_6 (**1**) (**Figure 7**). In all cases, a paramagnetic spectrum was observed, including broad and strongly shifted signals ranging from 177 to –93 ppm, with some similarity in chemical shifts. All spectra of **1**-**3**

demonstrate multiple resonances between 80 and –70 ppm and one strongly shifted broad resonance between 140-180 ppm. The latter was assigned to an acidic proton (presumably the methylene proton in a coordinated benzazole ligand), as a similar extreme shift has been reported for $[Co(HBMIM^{Ph2})_2](BF_4)_2$.[20,58] The ^{1}H-NMR spectra of **1** in MeCN-d_3 (slightly purple solution) and DMSO-d_6 (brownish solution) show strongly shifted and broad resonances between 160 and –82 ppm and 140 and –61 ppm, respectively. The spectra of **1** in these solvents show only a small similarity in terms of the overall peak pattern and integration, which may be due to solvation and solvent coordination effects, leading to a decreased overall symmetry of the complex in solution. In comparison, the ^{1}H-NMR spectrum of $[Co(HBMIM^{Ph2})_2](BF_4)_2$ in MeCN-d_3 (pink solution) demonstrates a single paramagnetic species in which all signals could be tentatively assigned to the molecular structure based on their relative integration, broadness of resonances, and chemical shift, and does not indicate solvent coordination.[59] For **2** and **3**, ^{1}H-NMR analysis in MeCN-d_3 (yellow and greenish solution, respectively) revealed several strongly shifted and broad resonances between 177 and –61 ppm and 144 and –61 ppm, respectively, and, similar to **1**, integration does not match between all resonances, indicative of coordination equilibria that likely involve the solvent. These observations indicate that the decreased bulk of the ligands in complexes **1-3** with respect to $[Co(HBMIM^{Ph2})_2](BF_4)_2$ leads to an increase in coordination flexibility, allowing for solvent coordination. The effective magnetic moment (μ_{eff}) of **1-3** was determined by Evans NMR method (1% TMS in MeCN-d_3) and provided values of 3.9, 4.1, and 3.9 μ_B for **1-3**, respectively, which are consistent with

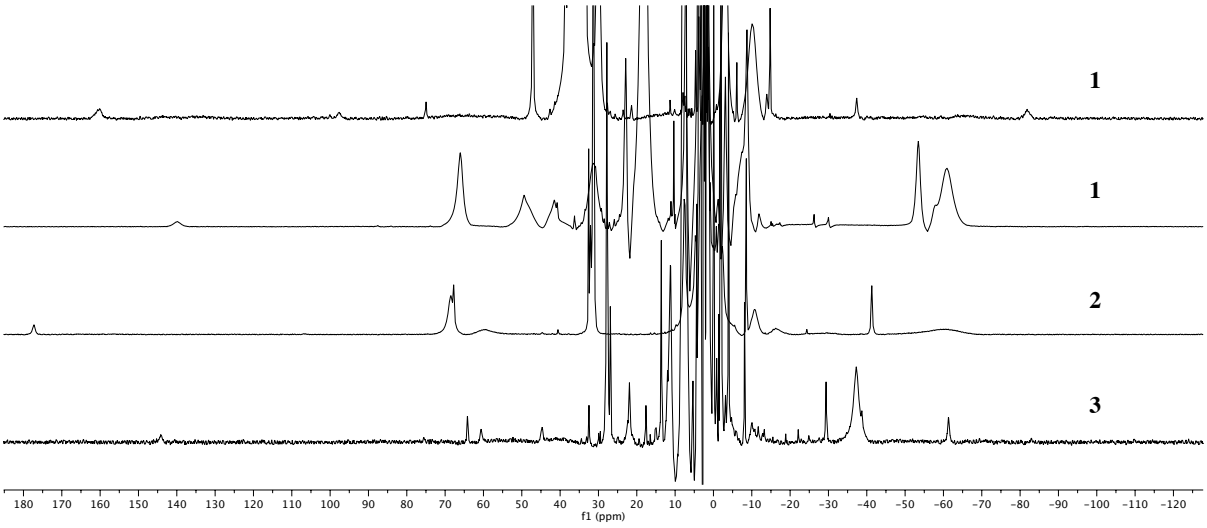

Figure 7. ^{1}H-NMR spectra of **1-3**: Top $[Co(HBBIM)_2](BF_4)_2$ **1** in MeCN-d_3; second $[Co(HBBIM)_2](BF_4)_2$ **1** in DMSO-d_6; third $[Co(HBBZM)_2](BF_4)_2$ **2** in MeCN-d_3; bottom $[Co(HBBTM)_2](BF_4)_2$ **3** in MeCN-d_3.

three unpaired spins in a ($S = 3/2$) cobalt(II) complex.[60] These values are similar to the magnetic susceptibility value of μ_{eff} = 3.82 μ_B reported for Co[HBMIM^{Ph2}]$_2$(BF$_4$)$_2$.[20] The ^{1}H-NMR spectrum of [Zn(HBBZM)$_2$](BF$_4$)$_2$ **2^{Zn}** in MeCN-*d$_3$* shows four sharp resonances in the aromatic region (Appendix B, Figure B8): two doublets that integrate for 1 and correspond to the aromatic protons next to the quaternary carbons of the fused benzene ring, one multiplet that integrates for 2H and corresponds to the protons in the benzene rings that are furthest away from the heterocycle, and one singlet outside the aromatic region with a lower integration than expected. The lower integration is suggested to originate from a slower longitudinal relaxation (T_1 relaxation). A similar integration pattern is observed for the reported complex **5^{Zn}** (see experimental section).[43] Based on the position and similar pattern to the free HBBZM ligand, we tentatively assign this signal to the methylene protons. Furthermore, the presence of two broad resonances at 5.5 and 6.2 ppm indicate some unidentified impurities. These impurities did not unbalance the elemental analysis nor did these demonstrate strong redox features in the subsequent electrochemical analysis. No remaining ligand precursor was observed. This spectrum indicates that the HBBZM ligands are spectroscopically equivalent and hold an internal mirror plan when coordinated to zinc.

Complexes **4**-**6** were analyzed by ^{1}H-NMR in DMSO-*d$_6$* (**4** (pinkish, not soluble in benzene) or benzene-*d$_6$* (**5** (orange) and **6** (green)) (**Figure 8**). The paramagnetic spectra demonstrate similar patterns, including broad and strongly shifted signals ranging from 40 to –93 ppm. In all cases, integration of the signals reveals four singlets with a relative integration of 1H (for **4** at 36, –1, –26, and –93 ppm, for **5** at 40, 2, –25, and –74 ppm, and for **6** at 32, 6, –23, and –63 ppm) and one singlet with a relative integration of 0.5H (for **4** at 5 ppm, for **5** at –16 ppm, and for **6** at –37 ppm). The former resonances are assigned to the aromatic protons of the fused benzene ring, in which the most strongly shifted and broad signals (for **4** at –93 ppm, for **5** at –74 ppm, and for **6** at –37 ppm) are assigned to the *ortho*-protons that are in close proximity of the metal center. The latter signals are assigned to the methylene proton on the ligand backbone. In the spectrum of **4**, an additional signal is found at 23 ppm, with a relative integration of 3H, and is assigned to the N-methyl protons. Furthermore, in the spectrum of **4,** an impurity in the diamagnetic region is observed, which was not further assigned. All spectra are consistent with a highly symmetric [Co^{II}(L$^-$)$_2$] (L = BBIM$^-$ for **4**, L = BBZM$^-$ for **5** and L = BBTM$^-$ for **6**) molecular structure, in which the cobalt center is surrounded by two spectroscopically identical ligands with an internal mirror plane. The structurally analogous complex [Co(BMIM^{Ph2})$_2$] was earlier reported in our group and demonstrated no distinct paramagnetic ^{1}H-NMR spectrum in benzene-d_6, indicative of the presence of different paramagnetic species in solution and

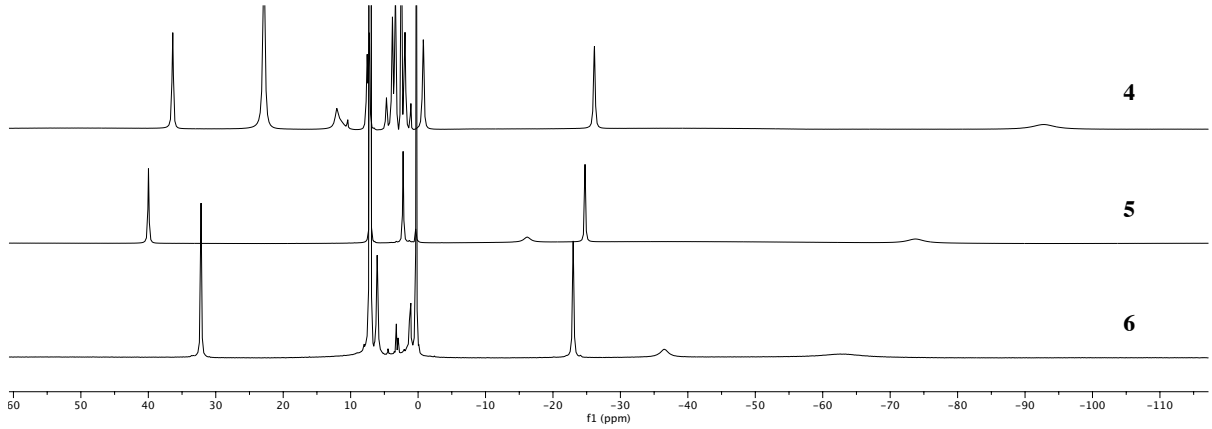

Figure 8. ^{1}H-NMR spectrum of [Co(BBIM^{-})$_2$] **4** (DMSO-d_6), [Co(BBZM^{-})$_2$] **5** (benzene-d_6) and [Co(BBTM^{-})$_2$] **6** (benzene-d_6).

therefore featuring a different solution state behavior compared to **4**.[46] These observations indicate that complexes **4**-**6** have a more well-defined coordination geometry in solution in comparison to complexes **1**-**3**, and do not seem susceptible to solvent coordination. This is most likely the result of the overall neutral charge of the complexes, leading to a less Lewis-acidic cobalt center. No effective magnetic moment was determined for **4**-**6.** Interestingly, upon the addition of 2 equiv. NaOAc to a brown solution of **1** in DMSO-d_6, an instant color change to pinkish was observed and ^{1}H-NMR analysis revealed the full conversion to **4**. This confirms the rather acidic nature of the methylene C–H moieties in **1** and shows that the complexes are rather easily interconvertible through acid-base chemistry.

3.2.4 Absorption spectroscopy

Dissolving the dicationic cobalt bis(benzazolyl)methanide complexes **1**-**3** in MeCN produces pink, yellow, and greenish solution, respectively. Therewith, **1** and **3** retain their solid-state color in solution, while **2** adopts a color that differs from its off-white, solid-state color. In line with the solid-state structure of **2^{2MeCN}** in crystals grown from MeCN solution, which includes two axially coordinated MeCN molecules (**Figure 4**), and the ^{1}H-NMR analysis of **2** in MeCN solution, the color change indicates solvent coordination upon dissolution of **2** in MeCN. Similar observations were made for complex [Co(HBMIM)$_2$](NO$_3$)$_2$ (HBMIM = bis(methylimidazole)methane) in **Chapter 5**. The UV-vis spectrum of complex **1** shows one weak absorption band below 350 nm, which we assign to π to π* transitions (**Figure 9**). The UV-vis spectra of complexes **2** and **3** show two absorption bands in the 300-500 nm region that were assigned as LMCT bands (**Figure 9**). The first band is sharp and intense (ε ~ 4000 and 20,000 M^{-1} cm^{-1}) with a λ_{max} at 358 nm and 414 nm for **2** and **3**, respectively. The second band

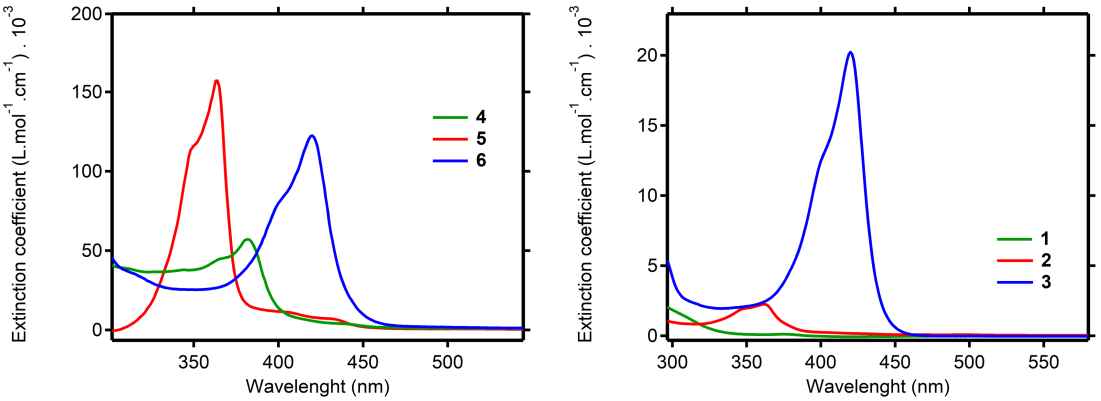

Figure 9. UV-vis absorption spectra of dicationic complexes in MeCN (1.0 x 10^{-5} M): $[Co(HBBIM)_2](BF_4)_2$ **1** (green line), $[Co(HBBZM)_2](BF_4)_2$ **2** (red line), $[Co(HBBTM)_2](BF_4)_2$ **3** (blue line) and neutral complexes in DMF (1.0x10^{-5} M): $[Co(BBIM^{-})_2]$ **4** (green line), $[Co(BBZM^{-})_2]$ **5** (red line) $[Co(BBTM^{-})_2]$ **6** (blue line).

is slightly less intense, and shoulders the first band, with a λ_{max} at 340 nm and 395 nm for **2** and **3**, respectively. Cobalt complexes **4**-**6** are not soluble in MeCN and UV-vis spectra were recorded in DMF. In all cases, the complexes form orange solutions in DMF, which contrasts with the pink and blue/purple solid-state colors for **4** (also pink crystals) and **6**, respectively (**5** remains its orange in solution). The color change is likely caused by the axial coordination of DMF to cobalt, as similar coordination and color changes were observed during parallel experiments with **2** in MeCN. On the other hand, **5** retains the orange color observed for its powders and its crystals grown from pentane, for which X-ray analysis shows no solvent coordination. UV-vis spectra of **4**-**6** are rather similar to each other, in particular for **5** and **6**, and show a number of (overlapping) absorption bands, including two bands that are intense and therefore assigned to LMCT (**Figure 9**).[61] The first LMCT band is sharp and intense (ε ~ 51,000 – 152,000 M^{-1} cm^{-1}) with a λ_{max} at 387, 365, and 421 nm for **4**, **5**, and **6**, respectively. The second band is slightly less intense, and shoulders the first band, with a λ_{max} at 370, 348, and 403 nm for **4**, **5**, and, **6**, respectively. The charge transfer bands are selection rule allowed and their high intensities indicate a high probability of these transitions taking place in all cases. These observations indicate very similar coordination geometries for the neutral complexes **4**-**6** in DMF solution. Interestingly, for all complexes, cationic as well as neutral, the color changes observed upon their dissolution in a coordinating solvent are reversible; *i.e.* evaporation of the solvents under reduced pressure and elevated temperatures brings back the original colors, and subsequent ^{1}H-NMR analysis confirmed the distinct and original resonances of the complexes. A further analysis of the LMCT bands observed in the UV-Vis spectra of complexes **1**-**6** shows a trend in the energy of the bands for the dicationic as well as

for neutral cobalt complexes. The LMCT bands for complexes **3** and **6** (derived from BBTZ) are the most red-shifted, while those for **2** and **5** (derived from BBMZ) are the most blue-shifted. The energy of the LMCT band of **4** is found in between those of **5** and **6**. Complex **1** does not show distinct LMTC bands in the 300-500 nm region. This observation is unexpected since NMR analysis did indicate solvent coordination, likely leading to similar coordination geometries as for **2** and **3**, for this complex as well. This observed trend in LMCT energies correlates directly with the electronegativity of the heteroatoms present in the ligand scaffolds (O = 3.5 > N = 3.0 > S = 2.5). In other words, the most electronegative ligand (BBZM) features the largest HOMO-LUMO gap (smaller wavelength), while the least electronegative ligand (BBTM) features a much smaller HOMO-LUMO gap.

3.2.5 Electrochemistry

To investigate the redox properties of cobalt complexes **1-3**, CV measurements were performed in 0.1 M nBu$_4$NPF$_6$ in MeCN at 100 mV/s, with potentials referenced to the Fc^+/Fc couple (**Figure 10**, **Table 3**, and Appendix A Figure A2, for the explanation of the electrochemical parameters).[62] The redox properties of [Co(HBMIM^{Ph2})$_2$](BF$_4$)$_2$ are included in **Table 3** for clarity.[20] Upon scanning in the cathodic direction, a broad unsymmetrical and irreversible reduction for **1** was found at $E_{p,c}$ = –1.90 V, with a small pre-wave. More cathodic, very weak and stronger quasi-reversible events were found at $E_{p,c}$ = –2.73 V and –2.90 V, respectively. In the reversed anodic scan a single irreversible oxidation feature with a small pre-wave was observed at $E_{p,a}$ = –0.12 V. Based on the similar irreversible nature and potential as the reductive event observed for [Co(HBMIM^{Ph2})$_2$](BF$_4$)$_2$, we ascribe the first redox event to a Co(I/II) reduction followed by H_2 formation with formal deprotonation of the ligand (EC mechanism).[20] The change from a bis(diphenylimidazole) ligand periphery in [Co(HBMIM^{Ph2})$_2$](BF$_4$)$_2$ to a bis(benzimidazole) ligand periphery in **1** results in a 60 mV anodic shift in the cobalt-centered reduction potential ([Co(HBMIM^{Ph2})$_2$](BF$_4$)$_2$ $E_{p,c}$ = –1.96 V in MeCN, 0.1 M nBu$_4$NPF$_6$).[20] Even though this potential difference is not very large, this observation does confirm the anticipated diminished electron-donating properties of the benzimidazole moieties in **1** with respect to the bis(imidazole)methane moieties in [Co(HBMIM^{Ph2})$_2$](BF$_4$)$_2$. The small magnitude of the redox shift could also be caused by solvent coordination, which moreover would change the redox chemistry. The redox events at more cathodic potentials were not further assigned. The oxidation in the reversed scan was tentatively assigned to the oxidation of a reaction product from the first irreversible reduction,

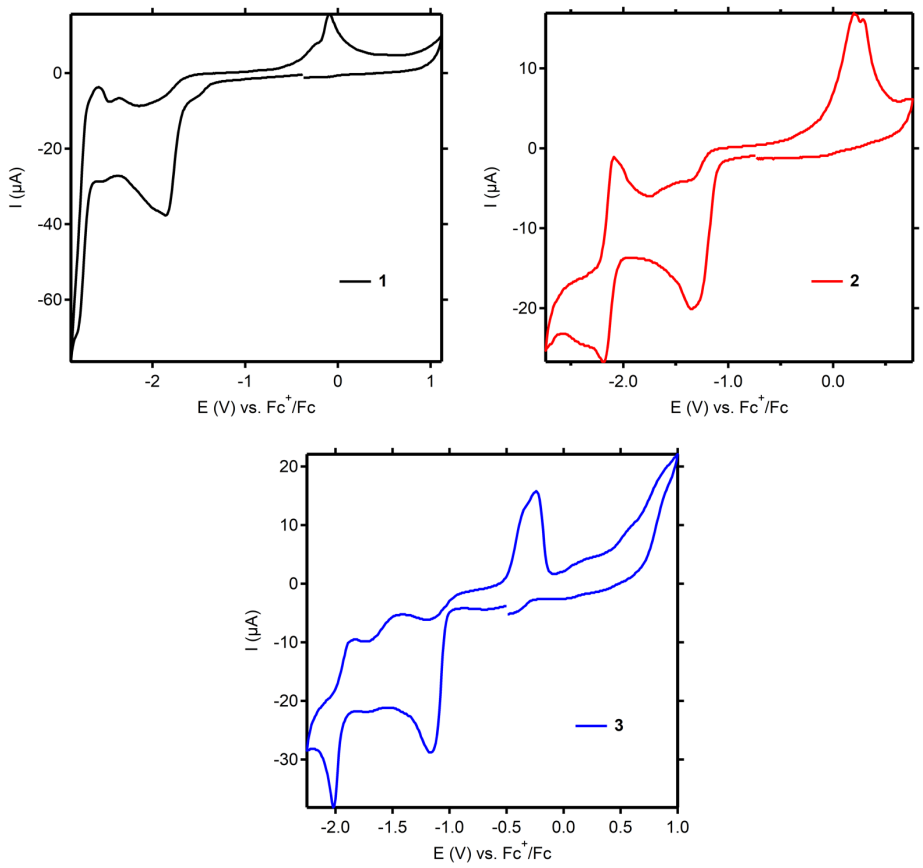

Figure 10. Cyclic voltammograms of 2 mM **1** (black trace), **2** (red trace), and **3** (blue trace) recorded in MeCN (0.1 mM nBu$_4$NBF$_4$) at a glassy carbon electrode at 100 mV/s. Referenced to the ferrocenium/ferrocene couple.

presumably [Co(HBBIM)(BBIM^{-})](BF$_4$), because of the similar shape and position compared to an oxidative feature observed for [Co(HBMIM^{Ph2})(BMIM^{Ph2-})](BF$_4$).[20] The observed pre-wave may be the result of solvent coordination to this singly reduced complex. For **2**, the irreversible Co(I/II) reduction was found at $E_{p,c}$ = –1.43 V, followed by a chemically reversible redox event at $E_{p,c}$ = –2.15 ($E_{1/2}$ = –2.08), and in the reversed scan an irreversible oxidation event with two maxima at $E_{p,a}$ = 0.17–0.19 V. Compared to **1**, the Co(I/II) reduction was found 470 mV more anodic, which is a large shift that is rather expected from a geometry change than from a change in the coordination strength of the ligand. Hence, this result further corroborates *trans*-MeCN coordination in **2**. For reference, octahedral cobaloximes with *trans*-MeCN coordination feature Co(I/II) reductions at –0.9 V vs. Fc^{+}/Fc.[63] The reversible redox event of **2** at more cathodic potentials could originate from a ligand-based event, a newly formed complex after the irreversible Co(I/II) reduction or another cobalt-based reduction (Co(0/I)), but this event was not further investigated. Similarly to **1**, an oxidation event was observed in the reversed scan, which is likewise shifted (300 mV), indicating that MeCN

Table 3. Selected electrochemical data of the major redox features for complexes **1**-**3**, $\mathbf{2^{Zn}}$, and $[Co(HBMIM^{Ph2})_2](BF_4)_2$ in MeCN (0.1 M nBu$_4$NBF$_4$)[a].

Complex	MeCN		
	Co(I/II)	2nd red	ox
	$E_{p,c}$ (V)	$E_{p,c}$ (V)	$E_{p,a}$ (V)
1 (HBBIM)	–1.90	–2.90	–0.12
2 (HBBZM)	–1.43	–2.15[b]	0.18
3 (HBBTM)	–1.31	–2.05	–0.25
$\mathbf{2^{Zn}}$ (HBBZM)	-	-	0.34[c]
$[Co(HBMIM^{Ph2})_2](BF_4)_2$	–1.96	–2.36	–0.64

[a]Referenced to the Fc^+/Fc couple, [b]$E_{1/2}$ = 2.08, [c]measured in DMF

coordination does not change the nature of the redox chemistry but mainly the energy barriers involved. This oxidation event is assigned to a ligand-based oxidation event, which will be further explained onwards where the redox chemistry of zinc analogs $\mathbf{2^{Zn}}$ and $\mathbf{5^{Zn}}$ is discussed. Complex **3** features an irreversible Co(I/II) reduction at $E_{p,c}$ = –1.31 V, weak and stronger quasi-reversible redox events at $E_{p,c}$ = –1.77 V and –2.05 V, respectively, and in the reversed scan the irreversible oxidation with prewave is observed at $E_{p,a}$ = –0.25 V followed by a broad additional wave at $E_{p,a}$ = 0.5 V. The position of the Co(I/II) reduction is even more anodic than in **2**, indicating also *trans*-MeCN coordination in **3**. The event cathodic of the Co(I/II) feature is similar in shape and position to that for **2** and is not further investigated. The oxidation event in the return wave is found more cathodic than those for **1** and **2**, which indicates similar reactivity of **3**, with a lower energy barrier for oxidation. These features demonstrate how the possibility to modify the redox chemistry of dicationic bis(benzazolyl)methane-derived cobalt complexes can be significantly modified by changing the periphery of the ligand backbone. The electrochemistry of cobalt complexes **4**-**6** was investigated by cyclic voltammetry (CV) in DMF solution, as these complexes are not soluble in MeCN (**Figure 11**, **Table 4**). Complex **4** features a weak irreversible reduction at $E_{p,c}$ = –1.82 V followed by a stronger irreversible reduction at $E_{p,c}$ = –2.78 V. We assign the former weak reductive event to an EC response of protonated **4** and assign the later event to the electrochemical Co(I/II) reduction of **4**. Furthermore, a single, strong irreversible oxidation event was observed at $E_{p,a}$ = –0.22 V and is assigned to a ligand-centered oxidation event, based on similar oxidation events in Zn and Co analogs (**Figure 11,** *vide infra*). The observation of a single and irreversible oxidation event is remarkable as our previous work on $[Co(BMIM^{Ph2-})_2]$ revealed four consecutive (quasi)reversible ligand-based oxidations between –1.0 and 0.5 V vs. Fc^+/Fc in MeCN.[46] This

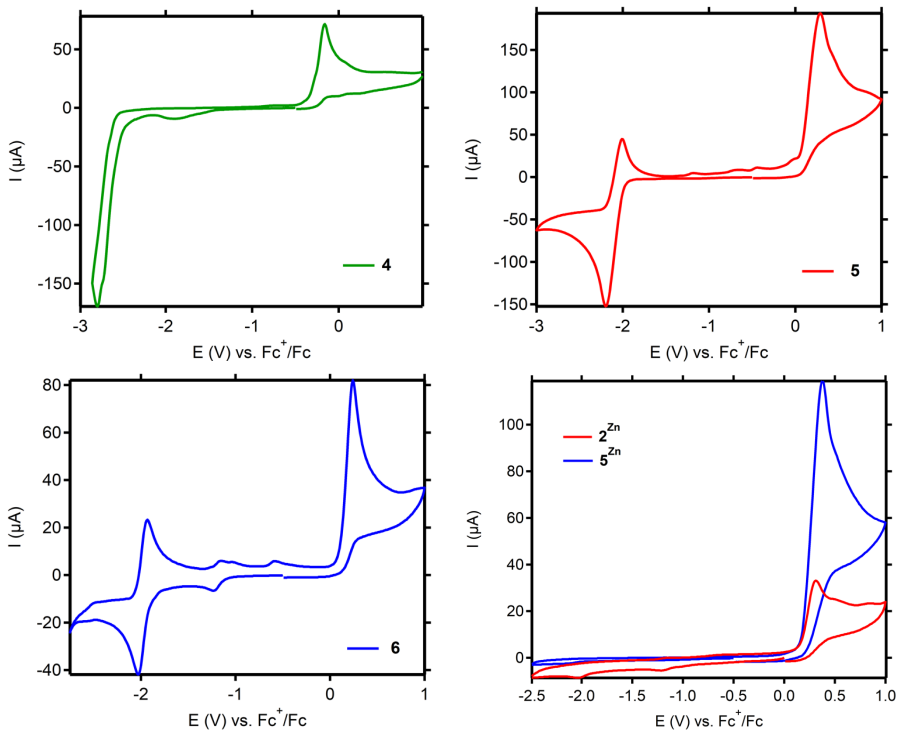

Figure 11. Cyclic voltammograms of: top left: **4** (green trace, 5 mM); top right: **5** (red trace, 5 mM); bottom left: **6** (blue trace, 5 mM); bottom right: $[Zn(HBBZM)_2](BF_4)_2$ ($\mathbf{2^{Zn}}$) (red trace, 5 mM) and $Zn[BBZM]_2$ ($\mathbf{5^{Zn}}$) (blue trace, 5 mM) recorded in DMF (0.1 mM nBu$_4$NBF$_4$) at a glassy carbon electrode at 100 mV/s. First scanned in the cathodic direction starting from the open circuit potential around 0 V.

significant difference prompted us to record the CV of $[Co(BMIM^{Ph2-})_2]$ in DMF, where we observed three oxidations between –1.0 and 0.5 V of which the first two have identical potentials and waveforms as in MeCN (Appendix B, Figure B12). The accessibility of higher oxidized forms for $[Co(BMIM^{Ph2-})_2]$ compared to **4** may be related to the larger steric bulk in $[Co(BMIM^{Ph2-})_2]$ and, consequently, its smaller structural flexibility. As such, the irreversible nature of the oxidation of **4** may be derived from the instability of the resulting oxidation product, in which the smaller steric bulk could render made structural rearrangements more energetically favorable. The strong anodic (positive) shift in the oxidation potential reveals that the $BBIM^-$ ligands in **4** are significantly less electron-donating compared to the $BMIM^{Ph2-}$ ligands in $[Co(BMIM^{Ph2-})_2]$. Complex **5** features a strong quasi-reversible reduction at $E_{p,c} = -2.08$ V ($E_{1/2} = -2.02$ V) assigned to the Co(I/II) redox couple. In the reversed anodic sweep several weak oxidations arise at $E_{p,a} = -1.17$ V, –0.88 V, –0.65 V, and +0.02 V, which were not further investigated, followed by a stronger oxidation event at $E_{p,a} = +0.19$ V. This oxidative response was assigned to a ligand-centered oxidation event, based on the electrochemical analysis of the zinc analogs $[Zn(BBZM)_2]$ ($\mathbf{5^{Zn}}$) and $[Zn(HBBZM)_2](BF_4)_2$ ($\mathbf{2^{Zn}}$), which features a single oxidation event at $E_{p,a} = +0.34$ V (**Figure 11**). Complex **6** features a weak

Table 4. Selected electrochemical data of the major redox features for complexes **4-6** and $\mathbf{5^{Zn}}$ in DMF (0.1 M nBu$_4$NBF$_4$)[a]

Complex	DMF	
	Co(I/II)	ox
	$E_{p,c}$ (V)	$E_{p,a}$ (V)
4 (BBIM$^-$)	–2.78	–0.22
5 (BBZM$^-$)	–2.08[b]	0.19
6 (BBTM$^-$)	–2.05[c]	0.35
$\mathbf{5^{Zn}}$ (BBZM$^-$)		0.34

[a]Referenced to the Fc^+/Fc couple. [b]$E_{1/2}$ = 2.02, [c]$E_{1/2}$ = 2.00

reversible event at $E_{p,c}$ = –1.10 V ($E_{1/2}$ = –1.05 V), which is suggested to originate from a small impurity or an analogous complex (for example formed through solvent coordination), followed by a stronger reversible redox event at $E_{p,c}$ = –2.05 V ($E_{1/2}$ = –2.00 V), assigned to the Co(I/II) redox couple. On the reverse anodic sweep, two weak oxidative features were observed at $E_{p,a}$ = –1.02 V, $E_{p,a}$ = –0.61 V, which were assigned to small impurities and were not further investigated, followed by a stronger oxidation event at $E_{p,a}$ = +0.35 V, which could be isolated as an independent event and was assigned to a ligand-centered oxidation event based on its similar shape, intensity, and position to Co and Zn analogues. The cobalt-centered reductions of **4** (–2.78 V), **5** (–2.08 V), and **6** (–2.05 V) occur at decreasing redox potentials and the ligand-centered oxidations occur at increasing redox potentials, **4** (–0.22 V), **5** (+0.19 V), and **6** (+0.35 V) indicating a decrease in the donating ability of the bis(benzazole)methane ligand, in which the differences between **4** and **5** are more pronounced than those between **5** and **6**. The observed trend is different from the order in LMCT bands observed by UV-vis spectroscopy (*vide supra*), indicating that the distinct chemical events are influenced differently by the heterocycles. The observed trend in the redox potentials correlates with the reported π-electron-withdrawing (EW) power of the periphery on the electron density of the trigonal carbanion, as determined by their ^{13}C shifts, in analogous Zn complexes as reported by Abbotto *et al.* (see introduction).[43] The mutual differences in ^{13}C shifts do not correlate with the observed reduction potentials, since Abbotto *et al*. reported more extreme ^{13}C shifts for **6** and similar values for **5** and **4**, while we observed a more extreme reduction potential for **4** and similar values for **5** and **6**. These differences might be influenced by the coordination number/geometry of the complexes as well as by the change in solvent (DMF vs. DMSO and $CDCl_3$).[43] In line with these electronic ligand effects, **4-6** have an accessible Co(I/II) reduction, which is not accessible for [Co(BMIM^{Ph2-})$_2$] (Appendix B, Figure B12). This lends further credit to the notion that complexes **4-6** are

relatively electron deficient. The observation that the reduction event becomes more reversible for **5** and again for **6** indicates a higher chemical and electrochemical stability of the Co(I) species for these complexes.

Overall, these voltametric investigations clearly show the redox differences between complexes **1**-**3** as well as complexes **4**-**6**, and their corresponding $HBMIM^{Ph2}$ and $BMIM^{Ph2–}$ analogues. The changes in the heteroatoms in the bis(benzazole)methane ligands lead to drastic changes in the reduction and oxidation potentials of complexes **1**-**3** and **4**-**6**, respectively, which follow the π-electron-withdrawing power trend of the ligands (HBBTM > HBBZM > HBBIM) as described by Abbotto *et al.*. For complexes **1**-**3**, this observation could be of relevance to their performance as HER electrocatalysts. Complex **1**, $[Co(BBIM)_2](BF_4)_2$ can be reduced at more anodic potentials (+60 mV) compared to $[Co(BMIM^{Ph2})_2](BF_4)_2$, which is in line with the suggested weaker donating abilities of bis-benzimidazole ligands, making the cobalt center less electron-rich and more prone for reduction. A similar but stronger effect was observed for their neutral analogues, as the cobalt center in **4** is significantly less electron-rich and is oxidized at more anodic potentials (+780 mV) compared to $[Co(BMIM^{Ph2–})_2]$. Between **1**-**3**, we observed that the Co(I/II) redox response shifts anodically from **1** to **2** and **3** with a total of 590 mV, which is slightly smaller than the shift of the Co(I/II) reductions in neutral analogues **4**-**6** of 720 mV, measured in DMF. The first oxidation event shifts from **2** to **1** to **3** with 420 mV in MeCN and from **4** to **5** to **6** with 570 mV in DMF. These potential spreads indicate that the reduction and oxidation events in **1**-**6** are influenced in a similar way but by a different magnitude. Furthermore, the difference between the first ligand-based oxidation of $[Co(BMIM^{Ph2–})_2]$ compared to that of **6** is no less than 1350 mV, indicating very distinct redox chemistry of the bis(diphenylimidazole)methane and bis(benzthiazole)methane ligands coordinated to cobalt. Next, we continued our studies by investigating complexes **1**-**3** as HER catalysts.

3.2.6 Electrocatalytic proton reduction

To probe the catalytic activity of **1**-**3** towards electrocatalytic hydrogen production, 2 mM solutions of the complexes were analyzed with CV in the presence of the weak acid Et_3NHBF_4 (5 equiv.) as a sacrificial proton donor (**Figure 12**, **Table 5**). Upon the addition of Et_3NHBF_4 to **1** a significant peak-shaped increase in current (i_{cat}) was observed at the (Co(I/II)) reduction potential ($E_{p,c}$) of the complex. Upon the addition of Et_3NHBF_4 to **2** and **3** a similar significant peak-shaped increase in current (i_{cat}) was observed cathodic of the (Co(I/II)) reduction potential

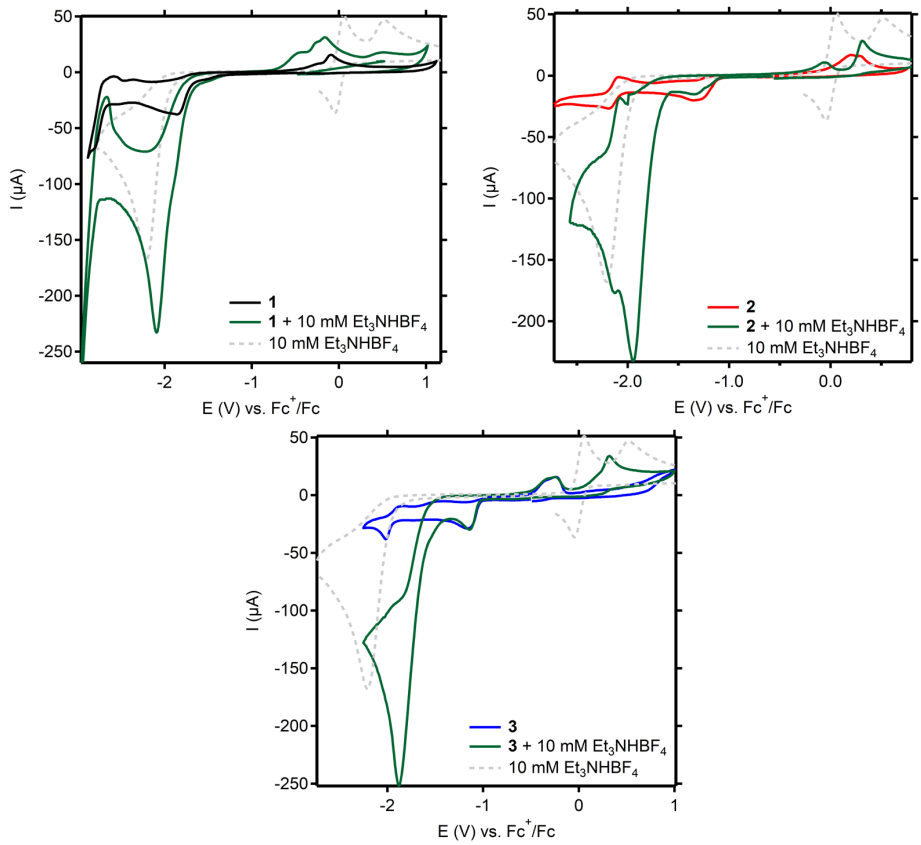

Figure 12. Cyclic voltammograms of **1** (black trace, 2 mM), **2** (red trace, 2 mM), and **3** (blue trace, 2 mM) recorded in the absence or presence of 10 mM Et_3NHBF_4 (green traces) and 10 mM Et_3NHBF_4 only (dotted) in MeCN (0.1 mM nBu$_4$NBF$_4$) vat a glassy carbon electrode at 100 mV/s. Referenced to the ferrocenium/ferrocene couple.

($E_{p,c}$) of the complexes. The E_{onset} of the direct reduction of the Et_3NHBF_4 protons at the glassy carbon electrode starts at more cathodic potentials for all complexes (dotted traces). In the reserved trace the Fc^+/Fc couple is visible, followed by an additional oxidation that is not further investigated. The absolute value of the catalytic currents (i_{cat}) is similar in all cases (218-249 µA), corresponding to a TOF of 15, 28, and 25 for **1**-**3**, respectively, obtained using the equation by Bullock *et al.*, for a 2 electron electrocatalytic reaction (see **Chapter 2**, section 2.4.2 for further information).[64] The electrocatalytic overpotential requirement is 490 mV for **3**, followed by 580 mV for **2** And 610 mV for **1** (see Appendix A, Figure A3 for definitions). This initial HER catalytic performance study demonstrates that **2** is the best HER catalyst in terms of rate and **3** operates at the lowest overpotential. The overpotential requirement allows for the comparison of molecular complexes under different operating conditions. For example, $[Co(HBMIM^{Ph2})_2](BF_4)_2$ features an overpotential requirement of 590 mV in MeCN using AcOH as a proton source and is therewith competitive towards **1** and **2**, while **3** features a significantly lower (100 mV) overpotential. The catalytic rate is harder to compare as this

Table 5. Electrocatalytic data for HER using complexes **1-3** (2 mM) in combination with Et_3NHBF_4 (10 mM) in MeCN (0.1 M nBu_4NBF_4)[a]

Electrocatalytic HER parameters in MeCN					
Complex	$E_{p,cat}$ (mV)	i_p (μA)	Overpotential (η) (mV)	$i_{cat.}$ (μA)	K_{obs} (TOF)
1 (X = NCH_3)	–2.02	26	610	227	15
2 (X = O)	–1.98	18	580	218	28
3 (X = S)	–1.93	22	490	249	25

[a]Referenced to the Fc^+/Fc couple.

performance indicator is also highly dependent on the acid concentration, size of the electrode, and substrate flux towards the electrode. Therefore, further electrocatalytic testing with different proton sources, catalyst loadings, and reference catalysts will be necessary to get more insight into the catalytic performances of **1-3**.

Overall, we conclude that upon altering the heteroatoms in the benzazolyl rings, the redox properties of **1-3** strongly shift over the potential axis, while the electrocatalytic HER potentials demonstrate smaller, but significant shifts. For **1-3** we do not observe the general trade-off between overpotential and catalytic rate, in which HER catalysts with a higher overpotential demonstrate also higher catalytic rate.[65] This could point to a bifunctional mechanism in which the cobalt-based reduction is not the rate-determining step and resembles the mechanism proposed for $[Co(HBMIM^{Ph2})_2](BF_4)_2$ in which a Co(III)-hydride and a ligand-based methylene C–H bond act in concert in the formation of the H–H bond.

3.2.7 Bulk electrolysis

To detect H_2 as the reaction product and to quantify H_2 formation, bulk electrolysis experiments were carried out using our in-house developed setup with inline product detection (see **Chapter 2**, section 2.4.3, p74). Using complex **2**, because of its highest TOF in the above electrocatalytic HER experiment, controlled potential electrolysis (CPE) was performed for 3 h at –2.00 V *vs.* Fc^+/Fc in 10 mL MeCN using 10 mM Et_3NHBF_4 as the proton source, corresponding to an overpotential of 690 mV, and a glassy carbon electrode rotated at 2000 rpm (**Figure 13**, **Table 6**).[66] In the presence of 1 mM **2**, 4.2 C was consumed corresponding to a current density of 2.00 mA/cm^2 with a Faradaic Efficiency (FE) of 72%. In the absence of any cobalt complex, 2.5 C was consumed corresponding to a current density of 1.19 mA/cm^2 with an FE of 86%. For reference, complex $[Co(HBMIM^{Ph2})_2](BF_4)_2$ is more efficient under slightly different conditions (100 mM proton source Et_3NHBF_4 instead of 10 mM in this work) with 16.8 C

charge consumption after 1 h vs 3.3 C for the acid-only experiment, both with high FE >98% (**Chapter 4**).[58] These results demonstrated that **2** is a catalyst for H_2 formation with moderate activity and selectivity. After the electrolysis experiment, an electrode deposit was found on the glassy carbon surface. The net influence of such an electrode deposit on the HER performance was unknown and led to an investigation of the HER performance of several reported dicationic cobalt complexes, in which the deposits turned out to be catalytically active. The results of this investigation are reported in **Chapter 4**.

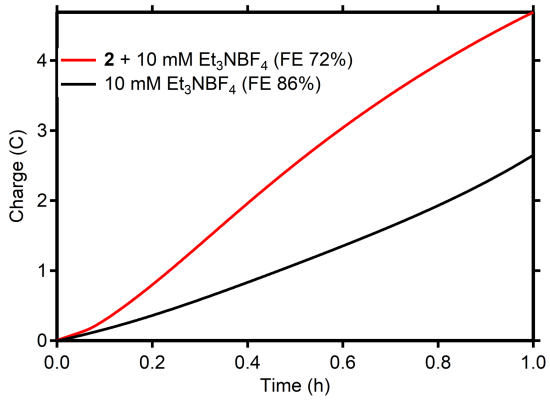

Figure 13. Charge passed over the course of 1 h controlled potential electrolysis performed in 0.01 M Et_3NHBF_4 in MeCN (containing 0.1 M nBu$_4$NBF$_4$ as the supporting electrolyte) at –2.00 V vs Fc^+/Fc at 2000 rpm. Red trace 1.0 mM **2**. Black trace acid only experiment.

Table 6. Bulk electrolysis results using $[Co(HBBZM)_2](BF_4)_2$ **2** using Et_3NHBF_4 (0.01 M) in MeCN (0.1 M nBu$_4$NBF$_4$) at –2.00 V vs Fc^+/Fc at 2000 rpm, 1 h.[a]

Complex (1 mM)	Charge (C)	Current. Dens. (mA/cm^2)	FE (%)
-	2.5	1.19	86
2 (X = O)	4.20	2.00	72

[a]Glassy working carbon electrode, H_2 quantification by gas chromatography analysis.

3.3 Conclusion

Previous electrocatalytic studies on the bis(methylimidazole)methane-based cobalt complex $[Co(HBMIM^{Ph2})_2](BF_4)_2$ demonstrated its activity in the HER. Effective modulation of this activity and the redox properties of the complex was achieved in **Chapter 2**, where the outer coordination sphere of the complex was alternated upon the installation of *para*-functionalized phenyl groups, affording complexes of the type $[Co((H,pArX)BMIM^{Ph_2})_2](BF_4)_2$. In this chapter, we successfully modulated the redox and HER properties by altering the nature of the heterocylic rings in the ligands. Our synthetic efforts yielded novel dicationic bis-ligated

complexes **1**-**3** that hold bis(benzazolyl)methane ligands with benzimidazole, benzoxazole and benzthiazole heterocycles. In addition, we included their neutral analogues, complexes **4**-**6** in this study, in order to further investigate the electronic trends. The smaller steric encumbrance of the bis(benzazolyl) ligands, as compared to the $HBMIM^{Ph2}$ ligand, resulted in a larger coordination flexibility, that allows for the formation of octahedral complexes by means of the *trans*-axial coordination of solvent molecules as in complex $\mathbf{2^{2MeCN}}$. Electrochemical analysis of complexes **1**-**3** and **4**-**6** in MeCN and DMF, respectively, revealed accessible redox events with distinct trends in which complexes with less electron-donating ligands **3** < **2** < **1** and **4** < **5** < **6** feature redox events at more anodic potentials. These redox trends corroborate the trend reported by Abbotto *et al*. for the π-electron-withdrawing power of the ligands $BBTM^-$ > $BBZM^-$ > $BBIM^-$. Compared to complexes $[Co(HBMIM^{Ph2})_2](BF_4)_2$ and $[Co(HBMIM^{Ph2-})_2]$ we conclude that the relatively weaker donating bisbenzazolyl ligands make complex **1**-**6** less electron-rich, more prone to reduction, up to +650 mV and harder to oxidize, up to +1350 mV. Complexes **1**-**3** are all electrocatalytically active for the HER, in which **2** features the highest activity (TOF) and **3** the lowest overpotential (490 mV). **1** and **2** hold an overpotential comparable to that of $[Co(HBMIM^{Ph2})_2](BF_4)_2$ (~600 mV) indicating that the modulated redox features in **1**-**3** only result in advanced HER features for **3** in terms of the overpotential requirement. Bulk electrolysis with **2**, coupled to in-line GC measurements, confirmed hydrogen formation with moderate activity and FE, which does not appear competitive towards the HER performance of $[Co(HBMIM^{Ph2})_2](BF_4)_2$. The electrolysis experiment with **2** also showed the formation of an electrodeposit on the glassy carbon electrode. Further investigations into electrodeposits formed from molecular cobalt complexes during the HER are reported in **Chapter 4**. Overall, we conclude that the alternation of the heterocycle in bis(benzazolyl)methane ligands coordinated to cobalt is an efficient method to modulate the complexes' redox potentials, while the catalytic HER features can be modulated to a much smaller extent.

3.4 Experimental

3.4.1 General remarks

All air-sensitive reactions, as well as the handling and synthesis of cobalt complexes, were carried out under an inert atmosphere (N_2) using standard Schlenk techniques or an Mbraun labmaster dp glovebox workstation. Dry Et_2O, MeCN, hexane, and toluene were obtained from an Mbraun MB SPS-800 solvent purification system. Anhydrous DMF was extra dried over 4

Å molecular sieves. CH_2Cl_2 was dried over CaH_2 and distilled under N_2. THF and MeOH were dried with sodium and magnesium turnings, respectively, and distilled under N_2 prior to use. All dry solvents were degassed by bubbling N_2 through the liquid for approx. 30 min or by freeze-pump-thaw degassing (3 cycles) prior to use and stored over 3 or 4 Å molecular sieves. CH_3CN was filtered over activated alumina after storage over 4 Å molecular sieves to remove the molecular sieve dust that is formed. All other chemicals were commercially obtained and used as received. ^{1}H-NMR spectra were recorded at 298 K unless stated otherwise on a Varian VNMRS400 or an Oxford NMR AS400 spectrometer at 400 MHz. Chemical shifts (δ) are reported in ppm and referenced against the residual solvent signal. UV-Vis spectra were recorded on a PerkinElmer 950, wavelengths are reported in nm, and extinction coefficients (ε) are given in L mol^{-1} cm^{-1}. ESI-MS spectra were recorded on a Waters LCT Premier XE KE317 Micromass Technologies spectrometer. Unpaired electrons in the complexes were determined by the Evans NMR method in MeCN-d_3 with 1% TMS at 298 K.[60] Infrared spectra were recorded on a Perkin Elmer Spectrum One FT-IR instrument.

Electrochemical sweeping experiments were performed using a hanging mercury drop electrode setup in the fumehood (*vide infra*) or in a nitrogen-filled Mbraun labmaster dp glovebox, on an IVIUM potentiostat/galvanostat using a 3-electrode setup including a Pt-wire counter electrode, a glassy carbon-working electrode (3 mm Ø) and an Ag/Ag(NO_3) reference electrode used directly in solution. The potentiostat was kept external to the glovebox, and the electrode leads were connected with a custom shielded electrode cable feedthrough. All scans were absolutely referenced to the ferrocenium/ferrocene redox couple and taken at a scan rate of 100 mV/s, unless reported differently. The working electrodes were polished with 0.3 μm aluminium oxide powder deionized water slurries and rinsed with water for 30 seconds to remove the residual polishing powder. Before all experiments, background voltammograms were recorded at a scan rate of 100 mV/s. Solutions were mixed by shaking before each measurement and the working electrode surface was cleaned with a tissue after every scan. All measurements were recorded in a 0.1 M nBu$_4$NBF$_4$/nBu$_4$NPF$_6$ solution in dry, degassed DMF.

Appendix B contains the supplementary information for this Chapter.

3.4.2 Synthesis

Ligands bis(*N*-methylbenzimidazol-2-yl)methane (HBBIM), bis(benzoxazol-2-yl)methane (HBBZM) and bis(benzothiazol-2-yl)methane (HBBTM) were synthesized using adapted literature procedures.[67] Compounds **4-6** and **5^{Zn}** have been reported before by Abbotto *et al*.[41-45] Here, we report on additional characterization of these compounds.

[Co(HBBIM)$_2$](BF$_4$)$_2$ (1): Bis(benzimidazol-2-yl)methane (HBBIM) (1.1 g, 0.4 mmol) was dissolved in dry THF (10 mL) and [Co(BF$_4$)$_2$·6H$_2$O] (0.680 g, 0.2 mmol) was added to the solution. Direct precipitation of a pink solid was observed and the mixture was stirred for another 3 h. THF was removed under reduced pressure affording pink solids, which were washed with dry diethyl ether (3 x 10 mL) and dried under reduced pressure. The title compound was obtained as a pink solid in 95% yield (1.5 g, 0.19 mmol). A pink crystal suitable for single crystal X-ray diffraction was grown through slow vapor diffusion of diethyl ether into a concentrated solution of **1** in MeCN at –40 °C. **^{1}H NMR** (400 MHz, MeCN-d_3, 25°C) δ = 160, 98, 75, 47, 39, 36, 35, 33, 30, 21, 3.00, –10, –15, –37, –82 ppm. Solution state magnetic susceptibility (Evans method, 1% TMS in MeCN-d_3): 3.9 μ_B **^{1}H NMR** (400 MHz, DMSO-d_6, 25 °C) δ = 140, 66, 49, 42, 31, 23, 18, 10, 7, 3, –9, –53, –61 ppm. **ESI-MS** (MeCN) m/z = 610.2 {[Co(HBBIM)$_2$–H]$^+$, calc. 610.20}. **ATR-IR** ν = 1511 (m), 1483 (w), 1460 (m), 1403 (m), 1320 (w), 1288 (m), 1156 (w), 1055 (s), 1038 (s), 1008 (s), 943 (m), 931 (w), 899 (m), 791 (w), 762 (m), 748 (s), 742 (s), 566 (w), 554 (w), 520 (w) cm^{-1}. **E.A.** (Formula: C$_{34}$H$_{32}$CoN$_8$B$_2$F$_8$ (+0.5 Et$_2$O), Mw: 785.21 g mol^{-1}): calc. C 52.58, H 4.54, N 13.63; found C 52.66, H 4.85, N 13.30. **UV-vis** (MeCN, pink solution, ε [mol^{-1} dm^3 cm^{-1}]): λ_{max} = 350 (2500) nm. **X-ray Crystal Structure Determination** [C$_{34}$H$_{32}$CoN$_8$](BF$_4$)$_2$ · 0.5(C$_2$H$_3$N), Fw = 805.75, red plate, 0.45 × 0.34 × 0.07 mm^3, monoclinic, P2$_1$ (no. 4), a = 15.7176(4), b = 14.7950(5), c = 15.9012(3) Å, β = 103.236(1) °, V = 3599.48(16) Å^3, Z = 4, D$_x$ = 1.487 g/cm^3, μ = 0.56 mm^{-1}. The diffraction experiment was performed on a Bruker Kappa ApexII diffractometer with sealed tube and Triumph monochromator (λ = 0.71073 Å) at a temperature of 150(2) K up to a resolution of (sin θ/λ)$_{max}$ = 0.65 Å^{-1}. The intensity integration was performed with the Eval15 software.[68] A numerical absorption correction and scaling was performed with SADABS[69] (correction range 0.83-0.97). A total of 73357 reflections was measured, 16546 reflections were unique (R$_{int}$ = 0.040), 12486 reflections were observed [I>2σ(I)]. The structure was solved with Patterson superposition methods using SHELXT.[70] Structure refinement was performed with SHELXL-2018[71] on F^2 of all reflections. Non-

hydrogen atoms were refined freely with anisotropic displacement parameters. One BBIM ligand, three BF_4 anions and the acetonitrile solvent were refined with a disorder model. The disorder could not be fully resolved. Hydrogen atoms were introduced in calculated positions and refined with a riding model. 1311 Parameters were refined with 2442 restraints (distances, angles, displacement parameters and ring flatness in the disordered moieties). R1/wR2 [$I > 2\sigma(I)$]: 0.0482 / 0.1228. R1/wR2 [all refl.]: 0.0696 / 0.1332. S = 1.046. Flack parameter[72] x = 0.003(4). Residual electron density between -0.36 and 0.67 e/Å^3. Geometry calculations and checking for higher symmetry was performed with the PLATON program.[73]

$[Co(HBBZM)_2(solv)_2](BF_4)_2$ (2): Bis(benzoxazol-2-yl)methane (HBBZM) (1.0 g, 4.0 mmol) was dissolved in THF (40 mL) giving a transparent yellow solution. To the stirring solution, $[Co(BF_4)_2 \cdot 6H_2O]$ (0.680 g 2.0 mmol) was added and a dark red solution formed. The reaction mixture was stirred for 3 h, during which the precipitation of a brown/crème solid was observed, while the solution remained red. THF was removed under reduced pressure and the obtained solids were washed with dry diethyl ether (3 x 15 mL) and dried under reduced pressure to obtain the title compound as an off-white solid in 89% yield (1.5 g, 1.96 mmol). A transparent yellowish crystal suitable for single crystal X-ray diffraction was grown through slow vapor diffusion of diethyl ether into a concentrated solution of **5** in MeCN. **^{1}H NMR** (400 MHz, MeCN-d_3, 25 °C) δ = 177, 68, 33, 31, 8, 7, 4, 2, 2, –2, –2, –9, –11, –17, –24, –41, –61 ppm. Solution state magnetic susceptibility (Evans method, 1% TMS in MeCN-d_3): 4.1 μ_B. **ESI-MS** (MeCN)**:** m/z = 558.1 {$[Co(HBBZM)_2–H]^+$, calc. 558.08}. **ATR-IR** ν = 3506 (w), 3399 (w), 2956 (w), 2880 (w), 1658 (w), 1577 (w), 1574 (w), 1456 (w), 1352 (w), 1312 (w), 1242 (w), 1132 (w), 1084 (s), 1016 (m), 991 (m), 851 (w), 751 (s), 634 (w) cm^{-1}. **E.A.** (Formula: $C_{34}H_{32}CoN_4O_4B_2F_8$ (+3 H_2O, 1 THF), Mw: 733.05 g mol^{-1}): calc. C 47.59, H 3.88, N 6.53; found C 47.25, H 4.04, N 6.44. **UV-vis** (MeCN, yellow solution, ε [mol^{-1} dm^3 cm^{-1}]): λ_{max} = 358 (4000), 350 (3000) nm. **X-ray Crystal Structure Determination** $[C_{34}H_{26}CoN_6O_4](BF_4)_2 \cdot 2(C_2H_3N)$, Fw = 897.26, yellow block, 0.25 × 0.19 × 0.08 mm^3, monoclinic, $P2_1/c$ (no. 14), a = 10.6429(5), b = 16.3993(9), c = 12.1954(6) Å, β = 107.827(3) °, V = 2026.34(18) Å^3, Z = 2, D_x = 1.471 g/cm^3, μ = 0.51 mm^{-1}. The diffraction experiment was performed on a Bruker Kappa ApexII diffractometer with sealed tube and Triumph monochromator (λ = 0.71073 Å) at a temperature of 150(2) K up to a resolution of $(\sin\theta/\lambda)_{max}$ = 0.65 Å^{-1}. The intensity integration was performed with the Eval15 software.[68] A multi-scan absorption correction and scaling was performed with SADABS[2] (correction range 0.69-0.75).

A total of 48768 reflections was measured, 4651 reflections were unique (R_{int} = 0.035), 3832 reflections were observed [I>2σ(I)]. The structure was solved with Patterson superposition methods using SHELXT.[70] Structure refinement was performed with SHELXL-2018[71] on F^2 of all reflections. Non-hydrogen atoms were refined freely with anisotropic displacement parameters. The BF_4 anion was refined with a disorder model. The disorder could not be fully resolved. All hydrogen atoms were located in difference Fourier maps and refined with a riding model. 307 Parameters were refined with 123 restraints (distances, angles and displacement parameters in the disordered BF_4). R1/wR2 [I > 2σ(I)]: 0.0394 / 0.0995. R1/wR2 [all refl.]: 0.0511 / 0.1063. S = 1.062. Residual electron density between -0.52 and 0.61 e/Å^3. Geometry calculations and checking for higher symmetry was performed with the PLATON program.[73]

[Co(HBBTM)$_2$](BF$_4$)$_2$ (3): Bis(benzthiozol-2-yl)methane (HBBTM) (0.513 g 1.8 mmol) was partially dissolved under stirring in THF (40 mL) at 50 °C for 1 h. The ligand in THF forms a green suspension. To the green suspension, [$Co(BF_4)_2 \cdot 6H_2O$] (0.321 g 0.9 mmol) was added, upon which the suspension turned brown. The reaction was stirred at 50 °C overnight. Then the stirring was stopped and the solvent was removed by filtration affording a green/brown solid. The solid was dissolved in acetonitrile (20 mL) and transferred to another Schlenk tube under a nitrogen atmosphere. Acetonitrile was removed under reduced pressure and the desired complex was obtained as a greenish/brown solid in 56% yield (0.424 mg, 0.5 mmol). **^{1}H NMR** (400 MHz, MeCN-d_3, 25°C) δ = 144, 64, 45, 32, 28, 27, 14, 11, 8, 3, 1, 0, –2, –4, –8, –29, –37, –61 ppm. Solution state magnetic susceptibility (Evans method, 1% TMS in MeCN-d_3): 3.910 μ_B **ESI-MS (**MeCN**)** m/z = 621.8 {[Co(HBBTM)$_2$–H]$^+$, calc. 621.98}, m/z = 796.5 {[Co(HBBTM)$_2$]$^+$, calc. 797.00}. **ATR-IR** ν = 3480 (w), 3225 (w), 2965 (w), 2867 (w), 1659 (w), 1539 (w), 1464 (w), 1312 (w), 1216 (w), 1037 (m), 888 (w), 761 (m), 731 (w), 656 (w) cm^{-1}. **E.A.** (Formula: $C_{30}H_{20}CoN_4S_4B_2F_8$, Mw: 797.31 g mol^{-1}): calc. C 45.19, H 2.53, N 7.02, S 16.09; found C 43.98, H 3.50, N 6.81, S 14.93. Deviation 3-7 %. The relative ratio of CHNS corresponds to **3**, but the absolute values do not, indicative of an inorganic impurity. **UV-vis** (MeCN, yellow in solution, ε [mol^{-1} dm^3 cm^{-1}]): λ_{max} = 414 (20000), 403 (23390) nm.

[Co(BBIM$^-$)$_2$] (4):[43] Additional characterization (^{1}H-NMR, IR, UV-vis) of the obtained pink solids is provided. In addition, a pinkish crystal suitable for single X-ray diffraction was grown from a saturated solution of **4** in THF at –40 °C over several weeks. **^{1}H NMR** (400 MHz, DMSO-d_6, 25°C) δ (ppm) 36, 23, 12, 10, 8, 7, 5, 4, 3, 2, 2, –1, –26, –93. **ATR-IR** ν = 3059

(w), 3033 (w), 2897 (w), 1670 (w), 1663 (w), 1559 (w), 1552 (m), 1522 (m), 1437 (m), 1403 (m), 1276 (m), 1233 (m), 1006 (m), 929 (m), 894 (m), 737 (s), 669 (w) cm^{-1}. **E.A.** (Formula: $C_{34}H_{30}CoN_8$ (+0.5 H_2O), Mw: 609.60 g mol^{-1}): calc. C 66.11, H 5.05, N 18.11; found C 66.48, H 5.05, N 18.49. **UV-vis** (DMF, orange solution, ε [mol^{-1} dm^3 cm^{-1}]): λ_{max} = 387 (107260), 371 (60050) nm. **X-ray Crystal Structure Determination** $C_{34}H_{30}CoN_8 \cdot 3(C_4H_8O)$, Fw = 825.90, orange block, 0.34 × 0.21 × 0.13 mm^3, triclinic, $P\overline{1}$ (no. 2), a = 11.4532(4), b = 11.7671(4), c = 16.3467(6) Å, α = 75.120(2), β = 79.302(2), γ = 75.514(2) °, V = 2044.07(13) $Å^3$, Z = 2, D_x = 1.342 g/cm^3, μ = 0.47 mm^{-1}. The diffraction experiment was performed on a Bruker Kappa ApexII diffractometer with sealed tube and Triumph monochromator (λ = 0.71073 Å) at a temperature of 150(2) K up to a resolution of $(\sin\theta/\lambda)_{max}$ = 0.65 $Å^{-1}$. The crystal appeared to be twinned with a twofold rotation about *hkl*=(0,1,0) as twin operation. Consequently, two orientation matrices were used for the intensity integration with the Eval15 software[68] resulting in a HKLF5-file.[74] A multi-scan absorption correction and scaling was performed with TWINABS[2] (correction range 0.67-0.75). A total of 75273 reflections was measured, 9424 reflections were unique (R_{int} = 0.034), 8427 reflections were observed [I>2σ(I)]. The structure was solved with Patterson superposition methods using SHELXT.[70] Structure refinement was performed with SHELXL-2018[71] on F^2 of all reflections. Non-hydrogen atoms were refined freely with anisotropic displacement parameters. One THF molecule was refined with a disorder model. All hydrogen atoms were located in difference Fourier maps. Hydrogen atoms H11 and H12 were refined freely with isotropic displacement parameters. All other hydrogen atoms were refined with a riding model. 541 Parameters were refined with 12 restraints (distances and angles in the disordered THF). R1/wR2 [I > 2σ(I)]: 0.0346 / 0.0883. R1/wR2 [all refl.]: 0.0400 / 0.0911. S = 1.031. Twin fraction BASF = 0.2798(8). Residual electron density between -0.45 and 0.57 e/$Å^3$. Geometry calculations and checking for higher symmetry was performed with the PLATON program.[73]

[Co(BBZM$^-$)$_2$] (5):[43] Additional characterization (X-ray, ^{1}H-NMR, IR, UV-vis): An orange crystal suitable for single X-ray diffraction was grown from a saturated solution of **5** in pentane. **^{1}H NMR** (400 MHz, benzene-d_6, 25 °C) δ (ppm) = 40, 2, 0, –16 , –25, –74. **ATR-IR** ν = 3093 (w), 3046 (w), 1625 (m), 1531 (s), 1460 (m), 1368 (m), 1306 (m), 1244 (s), 1132 (m), 1009 (s), 996 (s), 840 (m), 1006 (m), 840 (m), 726 (s), 667 (m), 669 (w) cm^{-1}. **E.A.** (Formula: $C_{30}H_{18}CoN_4O_4$ (+0.5 H_2O), Mw: 557.43g mol^{-1}): calc. C 63.61, H 3.38, N 9.89; found C 63.93, H 3.49, N 9.71. **UV-vis** (DMF, orange solution, ε [mol^{-1} dm^3 cm^{-1}]): λ_{max} = 365 (101970), 349

(80290) nm. **X-ray Crystal Structure Determination** $C_{30}H_{18}CoN_4O_4$, Fw = 557.41, red needle, 0.33 × 0.17 × 0.04 mm^3, monoclinic, $P2_1/n$ (no. 14), a = 20.0029(16), b = 7.7849(7), c = 32.191(2) Å, β = 102.237(4) °, V = 4898.9(7) Å^3, Z = 8, D_x = 1.512 g/cm^3, μ = 0.75 mm^{-1}. The diffraction experiment was performed on a Bruker Kappa ApexII diffractometer with sealed tube and Triumph monochromator (λ = 0.71073 Å) at a temperature of 150(2) K up to a resolution of $(\sin\theta/\lambda)_{max}$ = 0.65 Å^{-1}. The crystal appeared to be twinned with a twofold rotation about *uvw*=[1,0,0] as twin operation. Consequently, two orientation matrices were used for the intensity integration with the Eval15 software[68] resulting in a HKLF5-file.[74] A multi-scan absorption correction and scaling was performed with TWINABS[2] (correction range 0.61-0.75). A total of 108741 reflections was measured, 11563 reflections were unique (R_{int} = 0.081), 9427 reflections were observed [I>2σ(I)]. The structure was solved with Patterson superposition methods using SHELXT.[70] Structure refinement was performed with SHELXL-2018[71] on F^2 of all reflections. Non-hydrogen atoms were refined freely with anisotropic displacement parameters. All hydrogen atoms were introduced in calculated positions and refined with a riding model. 704 Parameters were refined with no restraints. R1/wR2 [I > 2σ(I)]: 0.0613 / 0.1462. R1/wR2 [all refl.]: 0.0790 / 0.1556. S = 1.033. Twin fraction BASF = 0.4981(12). Residual electron density between -1.01 and 1.00 e/Å^3. Geometry calculations and checking for higher symmetry was performed with the PLATON program.[73]

[Co(BBTM$^-$)$_2$] (6):[43] Additional characterization (^{1}H-NMR, UV-vis): **^{1}H NMR** (400 MHz, benzene-d_6, 25°C) δ (ppm) 32, 6, –23, –37, –63. **E.A.** (Formula: $C_{30}H_{18}CoN_4S_4$ (+0.5 Et_2O), Mw: 621.68 g mol^{-1}): calc. C 58.35, H 3.52, N 8.51; found C 58.20, H 3.53, N 8.55. **UV-vis** (DMF, orange solution, ε [mol^{-1} dm^3 cm^{-1}]): λ_{max} = 421 (96450), 402 (65698) nm.

[Zn(HBBZM)$_2$](BF$_4$)$_2$ (2^{Zn}): Bis(benzoxazol-2-yl)methane (HBBZM) (0.305 mg 0.27 mmol) was dissolved in methanol (20 mL) and turns to a light brown solution. To the solution $[Zn(BF_4)_2{\cdot}xH_2O]$ (0.161 g 0.14 mmol) was added. The reaction was stirred overnight to form a beige suspension. Then the stirring was stopped and the solids were filtered, and washed with dry methanol (3 x 5 mL). The compound was dried under reduced pressure and a beige solid was obtained with a 12% yield. **^{1}H NMR** (400 MHz, MeCN-d_3, 25°C) δ (ppm) = 7.39 (d, 2H, -CH$_{arom}$), 7.11 – 6.95 (m, 4H, -CH-CH$_{arom}$), 6.89 (d, 2H, -CH aromatic), 5.54 (s, 2H, -CH$_2$) (the integration of the latter signal is off, see discussion in the main text). **ESI-MS** (MeCN) m/z = 282.0 {$[Zn(HBBZM)_2]^{2+}$, calc. 282.04. **E.A.** (Formula: $C_{34}H_{32}CoN_4O_4B_2F_8$, Mw: 739.50 g mol^{-1}): calc. C 48.73, H 2.73, N 7.58; found C 48.49, H 2.99, N 7.44.

[Zn(BBZM)$_2$] ($\mathbf{5^{Zn}}$):[43] Additional characterization: A white transparent crystal of $\mathbf{5^{Zn}}$, suitable for single X-ray diffraction, was grown by slow vapor diffusion of MeOH into a concentrated solution of $\mathbf{2^{Zn}}$ in diethyl ether. The resolution of the measurement was poor, but we can conclude that the crystal of $\mathbf{5^{Zn}}$ is isostructural to that of **5.** Abbotto *et al.* reported on neutral zinc analog [Zn(BBTM)$_2$], which adopts a similar tetrahedral geometry.[75]

^{1}H NMR: (400 MHz, benzene-d_6, 25°C) δ (ppm) 6.90-6.83 (m, 4H, -CH$_{arom}$), 6.58-6.51 (m, 4H, CH-CH$_{arom}$), 5.67 (s, 1H, CH) (the integration of the latter signal is off, see discussion in the main text) **E.A.** (Formula: $C_{30}H_{18}ZnN_4O_4$, Mw: 563.88 g mol^{-1}): calc. C 63.90, H 3.22, N 9.90; found C 63.92, H 3.34, N 9.90. **X-ray Crystal Structure Determination** $C_{30}H_{18}N_4O_4Zn$, Fw = 563.85, colourless needle, 0.50 × 0.07 × 0.02 mm^3, monoclinic, P2$_1$/n (no. 14), a = 19.996(3), b = 7.8018(10), c = 31.814(4) Å, β = 102.323(7) °, V = 4848.6(11) Å^3, Z = 8, D$_x$ = 1.545 g/cm^3, μ = 1.06 mm^{-1}. The diffraction experiment was performed on a Bruker Kappa ApexII diffractometer with sealed tube and Triumph monochromator (λ = 0.71073 Å) at a temperature of 150(2) K up to a resolution of (sin θ/λ)$_{max}$ = 0.61 Å^{-1}. Reflections were smeared out which indicates a very large anisotropic mosaicity (**Figure 14**). For modeling the anisotropic mosaicity with the Eval15 software,[68] two orientation matrices were used, related by a 2.3° rotation approximately about *hkl*=(1,0,-1). A multi-scan absorption correction and scaling was performed with TWINABS[2] (correction range 0.40-0.75). A total of 49646 reflections was measured, 10714 reflections were unique (R$_{int}$ = 0.127), 6347 reflections were observed [I>2σ(I)]. As starting model, the coordinates of the Co compound **5** were used.

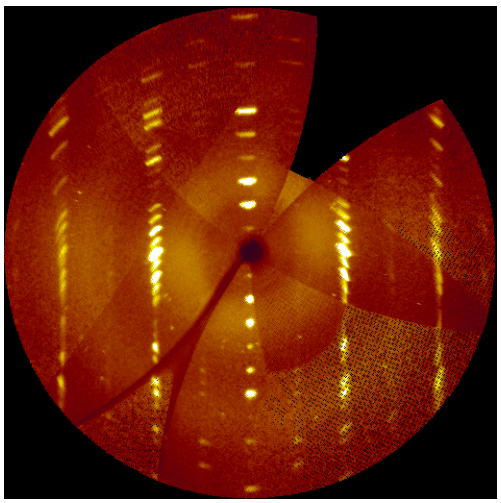

Figure 14. Simulated precession image of crystal $\mathbf{5^{Zn}}$ in the *0kl* plane showing a very large anisotropic mosaicity.

Structure refinement was performed with SHELXL-2018[71] on F^2 of all reflections. Non-hydrogen atoms were refined freely with anisotropic displacement parameters. All hydrogen atoms were introduced in calculated positions and refined with a riding model. 704 Parameters were refined with 720 restraints (displacement parameters of all atoms. R1/wR2 [$I > 2\sigma(I)$]: 0.1299 / 0.3047. R1/wR2 [all refl.]: 0.1950 / 0.3417. S = 1.104. Residual electron density between -1.59 and 2.84 e/Å^3. Geometry calculations and checking for higher symmetry was performed with the PLATON program.[73]

3.5 Author Contributions

S.D. de Vos and R.J.M. Klein Gebbink devised the project, designed experiments, and wrote the manuscript. S.D. de Vos, S. Verboom., and M. Basauri. performed experiments and analyzed the data. M. Lutz performed X-ray crystal structure determinations. Funding acquisition, administration, and oversight were done by R.J.M. Klein Gebbink. The original draft was written by S.D. de Vos and reviewing, and editing was done by D.L.J. Broere and R.J.M. Klein Gebbink with contributions by all authors.

3.6 References

(1) Schlapbach, L.; Züttel, A. In *Materials for sustainable energy: a collection of peer-reviewed research and review articles from nature publishing group*; World Scientific, 2011.

(2) Turner, J. A. Sustainable Hydrogen Production. *Science* **2004,** *305* (5686), 972.

(3) Zhu, J.; Hu, L.; Zhao, P.; Lee, L. Y. S.; Wong, K.-Y. Recent advances in electrocatalytic hydrogen evolution using nanoparticles. *Chem. Rev.* **2019,** *120* (2), 851.

(4) Dong, S.; Li, Y.; Zhao, Z.; Li, R.; He, J.; Yin, J.; Yan, B.; Zhang, X. A Review of the Application of Heterostructure Catalysts in Hydrogen Evolution Reaction. *ChemistrySelect* **2022,** *7* (14), e202104041.

(5) Zhang, W.; Cui, L.; Liu, J. Recent advances in cobalt-based electrocatalysts for hydrogen and oxygen evolution reactions. *J. Alloys Compd.* **2020,** *821*, 153542.

(6) Wang, M.; Chen, L.; Sun, L. Recent progress in electrochemical hydrogen production with earth-abundant metal complexes as catalysts. *Energy Environ. Sci.* **2012,** *5* (5), 6763.

(7) Thoi, V. S.; Sun, Y.; Long, J. R.; Chang, C. J. Complexes of earth-abundant metals for catalytic electrochemical hydrogen generation under aqueous conditions. *Chem. Soc. Rev.* **2013,** *42* (6), 2388.

(8) Agarwal, T.; Kaur-Ghumaan, S. HER catalysed by iron complexes without a Fe_2S_2 core: A review. *Coord. Chem. Rev.* **2019,** *397*, 188.

(9) Beyene, B. B.; Hung, C.-H. Recent progress on metalloporphyrin-based hydrogen evolution catalysis. *Coord. Chem. Rev.* **2020,** *410*, 213234.

(10) Wilken, M.; Siewert, I. Electrocatalytic Hydrogen Production with a Molecular Cobalt Complex in Aqueous Solution. *ChemElectroChem* **2020,** *7* (1), 217.

(11) Drosou, M.; Kamatsos, F.; Mitsopoulou, C. A. Recent advances in the mechanisms of the hydrogen evolution reaction by non-innocent sulfur-coordinating metal complexes. *Inorg. Chem. Front.* **2020,** *7* (1), 37.
(12) Helm, M. L.; Stewart, M. P.; Bullock, R. M.; DuBois, M. R.; DuBois, D. L. A Synthetic Nickel Electrocatalyst with a Turnover Frequency Above 100,000 s^{-1} for H_2 Production. *Science* **2011,** *333* (6044), 863.
(13) Kilgore, U. J.; Roberts, J. A. S.; Pool, D. H.; Appel, A. M.; Stewart, M. P.; DuBois, M. R.; Dougherty, W. G.; Kassel, W. S.; Bullock, R. M.; DuBois, D. L. $[Ni(P^{Ph}_2N^{C6H4X}_2)_2]^{2+}$ Complexes as Electrocatalysts for H_2 Production: Effect of Substituents, Acids, and Water on Catalytic Rates. *J. Am. Chem. Soc.* **2011,** *133* (15), 5861.
(14) Henry, R. M.; Shoemaker, R. K.; DuBois, D. L.; DuBois, M. R. Pendant Bases as Proton Relays in Iron Hydride and Dihydrogen Complexes. *J. Am. Chem. Soc.* **2006,** *128* (9), 3002.
(15) Rakowski Dubois, M.; Dubois, D. L. Development of Molecular Electrocatalysts for CO_2 Reduction and H_2 Production/Oxidation. *Acc. Chem. Res.* **2009,** *42* (12), 1974.
(16) Yeh, C.-Y.; Chang, C. J.; Nocera, D. G. "Hangman" Porphyrins for the Assembly of a Model Heme Water Channel. *J. Am. Chem. Soc.* **2001,** *123* (7), 1513.
(17) Dogutan, D. K.; Bediako, D. K.; Teets, T. S.; Schwalbe, M.; Nocera, D. G. Efficient Synthesis of Hangman Porphyrins. *Org. Lett.* **2010,** *12* (5), 1036.
(18) Roubelakis, M. M.; Bediako, D. K.; Dogutan, D. K.; Nocera, D. G. Proton-coupled electron transfer kinetics for the hydrogen evolution reaction of hangman porphyrins. *Energy Environ. Sci.* **2012,** *5* (7), 7737.
(19) Graham, D. J.; Nocera, D. G. Electrocatalytic H_2 Evolution by Proton-Gated Hangman Iron Porphyrins. *Organometallics* **2014,** *33* (18), 4994.
(20) Ghosh, P.; de Vos, S.; Lutz, M.; Gloaguen, F.; Schollhammer, P.; Moret, M.-E.; Klein Gebbink, R. J. M. Electrocatalytic Proton Reduction by a Cobalt Complex Containing a Proton-Responsive Bis(alkylimdazole)methane Ligand: Involvement of a C−H Bond in H2 Formation. *Chem. Eur. J.* **2020,** *26* (55), 12560.
(21) Dauer, D. R.; Koehne, I.; Herbst-Irmer, R.; Stalke, D. From Bis (imidazol-2-yl) methanes to Asymmetrically Substituted Bis (heterocyclo) methanides in Metal Coordination. *Eur. J. Inorg. Chem.* **2017,** *2017* (13), 1966.
(22) Koehne, I.; Bachmann, S.; Niklas, T.; Herbst-Irmer, R.; Stalke, D. A Novel Bulky Heteroaromatic-Substituted Methanide Mimicking NacNac: Bis (4, 6-tert-butylbenzoxazol-2-yl) methanide in s-Block Metal Coordination. *Chem. Eur. J.* **2017,** *23* (53), 13141.
(23) Koehne, I.; Graw, N.; Teuteberg, T.; Herbst-Irmer, R.; Stalke, D. Introducing NacNac-Like Bis (4, 6-isopropylbenzoxazol-2-yl) methanide in s-Block Metal Coordination. *Inorg. Chem.* **2017,** *56* (24), 14968.
(24) Hong, S.; Tian, S.; Metz, M. V.; Marks, T. J. C2-Symmetric Bis(oxazolinato)lanthanide Catalysts for Enantioselective Intramolecular Hydroamination/Cyclization. *J. Am. Chem. Soc.* **2003,** *125* (48), 14768.
(25) Takacs, J. M.; Reddy, D. S.; Moteki, S. A.; Wu, D.; Palencia, H. Asymmetric catalysis using self-assembled chiral bidentate P, P-ligands. *J. Am. Chem. Soc.* **2004,** *126* (14), 4494.
(26) Dagorne, S.; Bellemin-Laponnaz, S.; Maisse-François, A.; Rager, M. N.; Jugé, L.; Welter, R.; Wiley Online Library, 2005.
(27) Buch, F.; Harder, S. A Study on Chiral Organocalcium Complexes: Attempts in Enantioselective Catalytic Hydrosilylation and Intramolecular Hydroamination of Alkenes. *Zeitschrift für Naturforschung B* **2008,** *63* (2), 169.

(28) Arii, H.; Nakadate, F.; Mochida, K.; Kawashima, T. Lewis Base Complexes of an Enantiomeric Germanium (II) Cation Bearing a Bis (oxazoline) Ligand. *Organometallics* **2011,** *30* (17), 4471.

(29) Le Roux, E.; Merle, N.; Törnroos, K. W. Synthesis and characterisation of trigonal C 2-chiral di-and tetra-substituted bis (oxazoline) alkyl zinc complexes and their reactivity towards protic reagents. *Dalton Trans.* **2011,** *40* (8), 1768.

(30) Arii, H.; Matsuo, M.; Nakadate, F.; Mochida, K.; Kawashima, T. Coordination of a chiral tin (II) cation bearing a bis (oxazoline) ligand with tetrahydrofuran derivatives. *Dalton Trans.* **2012,** *41* (36), 11195.

(31) Marchi, E.; Locritani, M.; Baroncini, M.; Bergamini, G.; Sinisi, R.; Monari, M.; Botta, C.; Mróz, W.; Bandini, M.; Ceroni, P. Blue and highly emitting [Ir (IV)] complexes by an efficient photoreaction of yellow luminescent [Ir (III)] complexes. *J. Mater. Chem. C* **2014,** *2* (22), 4461.

(32) Kögel, J. F.; Kusaka, S.; Sakamoto, R.; Iwashima, T.; Tsuchiya, M.; Toyoda, R.; Matsuoka, R.; Tsukamoto, T.; Yuasa, J.; Kitagawa, Y. Heteroleptic [Bis (oxazoline)](dipyrrinato) zinc (II) complexes: bright and circularly polarized luminescence from an originally achiral dipyrrinato Ligand. *Angew. Chem.* **2016,** *128* (4), 1399.

(33) Walli, A.; Dechert, S.; Bauer, M.; Demeshko, S.; Meyer, F. BOX Ligands in Biomimetic Copper-Mediated Dioxygen Activation: A Hemocyanin Model. *Eur. J. Inorg. Chem.* **2014,** *2014* (27), 4660.

(34) Li, J.; Liao, S. H.; Xiong, H.; Zhou, Y. Y.; Sun, X. L.; Zhang, Y.; Zhou, X. G.; Tang, Y. Highly Diastereo-and Enantioselective Cyclopropanation of 1, 2-Disubstituted Alkenes. *Angew. Chem.* **2012,** *124* (35), 8968.

(35) Li, J.; Liao, S.-H.; Xiong, H.; Zhou, Y.-Y.; Sun, X.-L.; Zhang, Y.; Zhou, X.-G.; Tang, Y. Highly Diastereo- and Enantioselective Cyclopropanation of 1,2-Disubstituted Alkenes. *Angew. Chem. Int. Ed.* **2012,** *51* (35), 8838.

(36) Xiong, H.; Xu, H.; Liao, S.; Xie, Z.; Tang, Y. Copper-catalyzed highly enantioselective cyclopentannulation of indoles with donor–acceptor cyclopropanes. *J. Am. Chem. Soc.* **2013,** *135* (21), 7851.

(37) Rendina, V. L.; Goetz, S. A.; Neitzel, A. E.; Kaplan, H. Z.; Kingsbury, J. S. Scalable synthesis of a new enantiomerically pure π-extended rigid amino indanol. *Tetrahedron Lett.* **2012,** *53* (1), 15.

(38) Dauer, D.-R.; Stalke, D. Heterocyclic substituted methanides as promising alternatives to the ubiquitous nacnac ligand. *Dalton Trans.* **2014,** *43* (38), 14432.

(39) Dauer, D.-R.; Flügge, M.; Herbst-Irmer, R.; Stalke, D. Group 13 metal complexes containing the bis-(4-methylbenzoxazol-2-yl)-methanide ligand. *Dalton Trans.* **2016,** *45* (14), 6149.

(40) Koehne, I.; Herbst-Irmer, R.; Stalke, D. Bis (4-methylbenzoxazol-2-yl) methanide in s-Block Metal Coordination. *Eur. J. Inorg. Chem.* **2017,** *2017* (27), 3322.

(41) Bradamante, S.; Pagani, G. A. Charge-carbon-13 empirical relationships in organic ions: an improvement extending the access to experimental charge maps. *J. Org. Chem.* **1984,** *49* (16), 2863.

(42) Bradamante, S.; Pagani, G. A. α-Substituted toluenes as carbon acids: structural reorganization and free energy changes upon carbanion formation. *Journal of the Chemical Society, Perkin Transactions 2* **1986**, 1035-1046.

(43) Abbotto, A.; Bradamante, S.; Facchetti, A.; Pagani, G. A. Metal Chelation Aptitudes of Bis (o-azaheteroaryl) methanes As Tuned by Heterocycle Charge Demands1. *J. Org. Chem.* **2002,** *67* (16), 5753.

(44) Abbotto, A.; Bradamante, S.; Pagani, G. A. Diheteroarylmethanes. 5.1 E− Z Isomerism of Carbanions Substituted by 1, 3-Azoles: 13C and 15N π-Charge/Shift Relationships as Source for Mapping Charge and Ranking the Electron-Withdrawing Power of Heterocycles. *J. Org. Chem.* **1996,** *61* (5), 1761.

(45) Abbotto, A.; Facchetti, A.; Bradamante, S.; Pagani, G. A. 8-Purinyl versus 2-Benzimidazolyl Carbanions: Charge Demands of the Heterocycles and Ligand Properties of the Bis (heteroaryl) methanes1. *J. Org. Chem.* **1998,** *63* (3), 436.

(46) Ghosh, P.; Naastepad, R.; Riemersma, C. F.; Lutz, M.; Moret, M.-E.; Klein Gebbink, R. J. M. Noninnocent β-Diiminate Ligands: Redox Activity of a Bis(alkylimidazole)methane Ligand in Cobalt and Zinc Complexes. *Chem. Eur. J.* **2017,** *23* (45), 10732.

(47) Abbotto, A.; Bruni, S.; Cariati, F.; Pagani, G. A. A spectroscopic and magnetic study of complexes of bis(2–benzothiazolyl)methanate and bis(2–benzoxazolyl) methanate with Co(II), Ni(II), Cu(II) and Zn(II). *Spectrochimica Acta Part A: Molecular and Biomolecular Spectroscopy* **2000,** *56* (8), 1543.

(48) Piryazev, D.; CSD, 2017

(49) Marshak, M. P.; Chambers, M. B.; Nocera, D. G. Cobalt in a Bis-β-diketiminate Environment. *Inorg. Chem.* **2012,** *51* (20), 11190.

(50) Sakurai, T.; Yamamoto, K.; Seino, N.; Katsuta, M. Chloro-[alpha],[beta],[gamma],[delta]-tetraphenylporphinatopyridinecobalt(III). *Acta Crystallogr. Sect. B* **1975,** *31* (10), 2514.

(51) Weiss, M. C.; Bursten, B.; Peng, S.-M.; Goedken, V. L. Effects of peripheral steric constraints and metal ion size on the structure of three five-coordinate macrocyclic ligand complexes of the type [M($C_{22}H_{22}N_4$)X], M = cobalt(III), iron(III), manganese(II); X = iodine, chlorine, triethylamine. *J. Am. Chem. Soc.* **1976,** *98* (25), 8021.

(52) Scheidt, W. R.; Cunningham, J. A.; Hoard, J. L. Stereochemistry of low-spin cobalt porphyrins. II. Bis(piperidine)-.alpha.,.beta.,.gamma.,.delta.-tetraphenylporphinatocobalt(III) cation in a crystalline solvated salt. *J. Am. Chem. Soc.* **1973,** *95* (25), 8289.

(53) Khaledi, H.; Olmstead, M. M.; Mohd Ali, H.; Thomas, N. F. Indolenine meso-Substituted Dibenzotetraaza[14]annulene and Its Coordination Chemistry toward the Transition Metal Ions MnIII, FeIII, CoII, NiII, CuII, and PdII. *Inorg. Chem.* **2013,** *52* (4), 1926.

(54) Dey, S.; Wayland, B. B.; Zdilla, M. J. Solution and Solid State Properties for Low-Spin Cobalt(II) Dibenzotetramethyltetraaza[14]annulene [(tmtaa)CoII] and the Monopyridine Complex. *Inorganic Chemistry* **2019,** *58* (2), 1224.

(55) Whyte, A. M.; Shuku, Y.; Nichol, G. S.; Matsushita, M. M.; Awaga, K.; Robertson, N. Planar Ni(ii), Cu(ii) and Co(ii) tetraaza[14]annulenes: structural, electronic and magnetic properties and application to field effect transistors. *J. Mater. Chem.* **2012,** *22* (34), 17967.

(56) Ryu, H.; Mulyana, Y.; Park, I.-H.; Kim, J.; Lindoy, L. F.; Lee, S. S. Discrete and polymeric complexes of a macrocyclic pillar ligand in the absence and presence of dicarboxylic acid coligands. *CrystEngComm* **2015,** *17* (30), 5717.

(57) Weiss, M. C.; Gordon, G.; Goedken, V. L. Crystal and molecular structure of the macrocyclic nickel(II) complex [Ni(C18H14N4)]: dibenzo[b,i][1,4,8,11]tetraaza[14]annulenenickel(II). *Inorg. Chem.* **1977,** *16* (2), 305.

(58) de Vos, S. D.; Otten, M.; Wissink, T.; Broere, D. L. J.; Hensen, E. J. M.; Klein Gebbink, R. J. Hydrogen Evolution Electrocatalysis with a Molecular Cobalt

Bis(alkylimidazole)methane Complex in DMF: a critical activity analysis. *ChemSusChem* **2022***, 15, e2022013*.

(59) de Vos, S. D.; Otten, M.; Wissink, T.; Broere, D. L. J.; Hensen, E. J. M.; Klein Gebbink, R. J. M. Hydrogen Evolution Electrocatalysis with a Molecular Cobalt Bis(alkylimidazole)methane Complex in DMF: a Critical Activity Analysis. *ChemSusChem* **2022,** *15*, e202201308.

(60) Evans, D. 400. The determination of the paramagnetic susceptibility of substances in solution by nuclear magnetic resonance. *Journal of the Chemical Society (Resumed)* **1959**, 2003.

(61) Marcus, R. A. Chemical and electrochemical electron-transfer theory. *Annu. Rev. Phys. Chem.* **1964,** *15* (1), 155.

(62) Bard, A. J.; Faulkner, L. R. *Electrochemical Methods: Fundamentals and Applications*, 2001.

(63) Baffert, C.; Artero, V.; Fontecave, M. Cobaloximes as Functional Models for Hydrogenases. 2. Proton Electroreduction Catalyzed by Difluoroborylbis(dimethylglyoximato)cobalt(II) Complexes in Organic Media. *Inorg. Chem.* **2007,** *46* (5), 1817.

(64) Bullock, R. M.; Appel, A. M.; Helm, M. L. Production of hydrogen by electrocatalysis: making the H–H bond by combining protons and hydrides. *Chem. Commun.* **2014,** *50* (24), 3125.

(65) Klug, C. M.; Cardenas, A. J. P.; Bullock, R. M.; O'Hagan, M.; Wiedner, E. S. Reversing the Tradeoff between Rate and Overpotential in Molecular Electrocatalysts for H_2 Production. *ACS Catalysis* **2018,** *8* (4), 3286.

(66) McCarthy, B. D.; Martin, D. J.; Rountree, E. S.; Ullman, A. C.; Dempsey, J. L. Electrochemical Reduction of Brønsted Acids by Glassy Carbon in Acetonitrile—Implications for Electrocatalytic Hydrogen Evolution. *Inorg. Chem.* **2014,** *53* (16), 8350.

(67) Elgafi, S.; D. Field, L.; A. Messerle, B.; W. Hambley, T.; Turner, P. Synthesis of novel ruthenium complexes containing bidentate imidazole-based ligands. *J. Chem. Soc., Dalton Trans.* **1997**, 2341-2346.

(68) Schreurs, A. M.; Xian, X.; Kroon-Batenburg, L. M. EVAL15: a diffraction data integration method based on ab initio predicted profiles. *J. Appl. Crystallogr.* **2010,** *43* (1), 70.

(69) G. M. Sheldrick (2014). SADABS and TWINABS. Universität Göttingen, Germany.

(70) Sheldrick, G. SHELXT - Integrated space-group and crystal-structure determination. *Acta Crystallogr. Sect. A* **2015,** *71* (1), 3.

(71) Sheldrick, G. M. Crystal structure refinement with SHELXL. *Acta Crystallogr. Sect. C: Structural Chemistry* **2015,** *71* (1), 3.

(72) Parsons, S.; Flack, H. D.; Wagner, T. Use of intensity quotients and differences in absolute structure refinement. *Acta Crystallogr. Sect. B: Structural Science, Crystal Engineering and Materials* **2013,** *69* (3), 249.

(73) Spek, A. Structure validation in chemical crystallography. *Acta Crystallogr. Sect. D* **2009,** *65* (2), 148.

(74) Herbst-Irmer, R.; Sheldrick, G. M. Refinement of twinned structures with SHELXL97. *Acta Crystallogr. Sect. B: Struct. Sci.* **1998,** *54* (4), 443.

(75) A. Abbotto, V. A., S. Bradamante, G. A. Pagani, C. Rizzoli and G. Calestani. *Gazz. Chim.ltal.* **1991,** *121*, 365.

Chapter 4

Hydrogen Evolution Electrocatalysis with a Molecular Cobalt Bis(alkylimidazole)methane Complex in DMF: a Critical Activity Analysis

Abstract

$[Co(HBMIM^{Ph2})_2](BF_4)_2$ (**1**), ($HBMIM^{Ph2}$ = bis(1-methyl-4,5-diphenyl-1*H*-imidazol-2-yl)methane), was investigated for its electrocatalytic hydrogen evolution performance in DMF using voltammetry and during controlled potential/current electrolysis (CPE/CCE) in a novel in-line product detection setup. Performances were benchmarked against three reported molecular cobalt HER electrocatalysts: $[Co(dmgBF_2)_2(solv)_2]$ (**2**), ($dmgBF_2$ = difluoroboryldimethylglyoximato), [Co(TPP)] (**3**), (TPP = 5,10,15,20-tetraphenylporphyrinato) and [Co(bapbpy)Cl](Cl) (**4**), (bapbpy = 6,6'-bis-(2-aminopyridyl)-2,2'-bipyridine) showing distinct performances differences with **1** being the runner up in H_2 evolution during CPE and the best catalyst in terms of overpotential and Faradaic Efficiency (FE) during CCE. After bulk electrolysis, with all of the complexes, a deposit on the glassy carbon electrode was observed, and post-electrolysis X-ray photoelectron spectroscopy (XPS) analysis of the deposit formed from **1** demonstrated only a minor cobalt contribution (0.23%), mainly consisting of Co^{2+}. Rinse tests on the deposits derived from **1** and **2** showed that the initially observed distinct activity is (partly) preserved for the deposits. These observations indicate that the molecular design of the complexes dictates the features of the formed deposit and therewith the observed activity.

S.D. de Vos, M. Otten, T. Wissink, D.L.J. Broere, E.J.M. Hensen R.J.M. Klein Gebbink, based on *ChemSusChem* **2022**, 15, e202201308

4.1 Introduction

Hydrogen generation from carbon-neutral sources is an important part of a multifaceted strategy to meet growing global energy demands.[1] A promising approach is the electrocatalytically splitting of water into oxygen and protons and follow-up hydrogen formation.[2] To facilitate the hydrogen evolution reaction (HER), Pt is the catalytic material of choice, because of its high activity and low overpotential.[3] However there remains a strong interest to move to cheaper and more abundant catalyst materials.[4] Approaches include the use of carbon-based electrode materials with deposited first-row transition metals,[5] and the use of coordination complexes of first-row transition metals able to catalyze the HER at a potential close to the standard potential of the H^+/H_2 couple.[6-8] Coordination complexes allow for precise molecular designs, leading to enhanced selectivity and activity as well as mechanistic insights on key-intermediates.[9] In particular, cobalt-based complexes gained significant attention, because of their HER activity at low overpotentials.[10-15] The electrocatalytic performance of molecular complexes are typically assessed using a combination of voltammetry and bulk electrolysis in organic solvents or water using a sacrificial proton donor. One disadvantage is the fragility of molecular complexes under the electro-reductive conditions, sometimes changing the initial molecular complex into a structurally distinct active catalyst.[16,17] Over the last decade, the molecular electrocatalysis field, encouraged by the work of Savéant and co-workers, developed an increased understanding of the voltametric responses and the identification of the true electrocatalytic species.[18] Complementary to voltammetry, bulk electrolysis allows for the generation of sufficient hydrogen to determine catalytic rates and Faradaic efficiencies. However, monitoring the chemical integrity of the catalyst during electrolysis and identifying the chemical structure of the active species in catalysis remains challenging.[17,19,20] A number of studies have focused on transformations of molecular complexes during HER catalysis and reveal that catalyst as well as electrode modifications can take place to form active materials with distinct chemical compositions.[20-27]

Recently, our group has reported on the dicationic cobalt complex $[Co(HBMIM^{Ph2})_2](BF_4)_2$ (**1**), comprising two neutral $HBMIM^{Ph2}$ diimine ligands, and its use as a HER electrocatalyst.[28] Cyclic voltammetry experiments showed an irreversible, peak-shaped reductive response for **1** in MeCN at –1.96 V vs Fc^+/Fc, which was assigned to the fast reduction of Co(II) to Co(I). Combined experimental and DFT studies supported that **1** undergoes H-atom loss upon reduction (either electrochemically or chemically using KC_8) and consecutive H_2 formation, resulting in formal deprotonation and generation of cobalt complex

[Co(HBMIM^{Ph2})(BMIM^{Ph2-})](BF$_4$) (**1a**), containing one deprotonated BMIM^{Ph2-} ligand (**Figure 1**). Under catalytic conditions, protonation restores complex **1** and closes a catalytic cycle. Isolation and characterization of **1a** in combination with mechanistic investigations using DFT suggested that dihydrogen formation proceeds via the intramolecular combination of an intermediate Co^{III}–H moiety with a ligand C–H proton, providing a unique HER mechanism. Robustness tests were carried out by means of bulk electrolysis with acetic acid (as proton source) in MeCN using a mercury electrode and demonstrated that **1** suffered from fast deactivation with a total turnover number of 0.25. Nevertheless, the involvement of the ligand C–H moiety was further demonstrated as a dimethylated analogue of **1**, that is devoid of a proton relay functionality in the ligand backbone, is not catalytically active. Here, we report on a detailed study of the electrochemical behavior of complex **1** and its use in electrocatalytic hydrogen production during electrolysis studies in both MeCN and DMF solution. We particularly sought to optimize the electrocatalytic conditions using analytical electrochemical sweeping voltammetry techniques.[29] Subsequent bulk electrolysis experiments were performed in a newly designed electrocatalytic HER-model cell to allow for precise monitoring of the current density, quantitative H_2 product formation via fast inline GC analysis, and catalyst stability over time. The performance of **1** was then benchmarked to three established molecular catalysts in the field. Overall, this study provides comparative and quantitative insight in the electrocatalytic performance of molecular cobalt complexes in non-aqueous HER, and sheds light on the stability of the complexes in a bulk-electrolysis set-up.

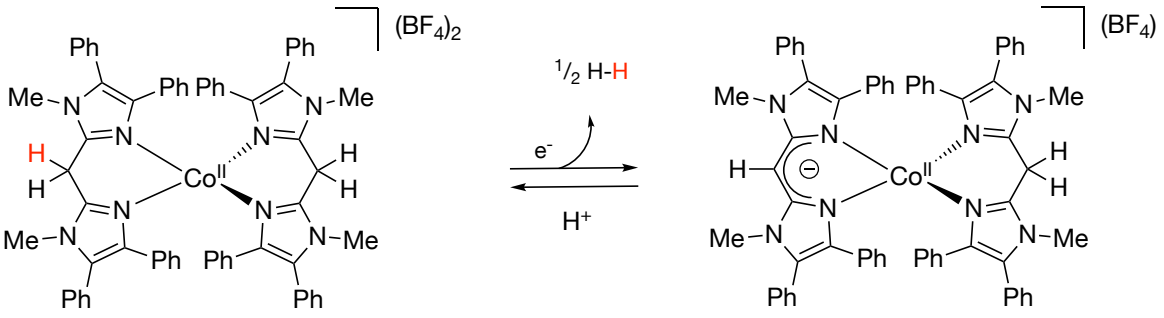

Figure 1. Proposed ligand-mediated HER reactivity for **1**.

4.2 Results and Discussion

4.2.1 Electrochemical properties

Following our initial investigation in MeCN solution,[28] we have investigated the electrochemical properties of **1** in DMF solution. The cyclic voltammogram (CV) and

differential pulse voltammogram (DPV) of **1**, recorded at a glassy carbon (GC) electrode in DMF (0.1M nBu$_4$NBF$_4$) at 100 mV/s, display one irreversible reductive response at $E_{p,c} = -2.00$ V and $E_{p,a} = -1.93$ V versus Fc^+/Fc, respectively (**Figure 2**, left). The reductive response was assigned to the Co(I/II) redox couple coupled with a follow-up chemical reaction, presumably formal loss of a methylene H-atom (overall deprotonation), in line with our earlier studies on **1** in MeCN (*vide supra*).[28] Increasing the scan rate in CV up to 2,000 mV/s, the irreversible nature of the reductive response changes to a well-defined and quasi-reversible redox couple at $E_{1/2} = -1.96$ V versus Fc^+/Fc (ΔE_p = 130 mV) (**Figure 2**, right). This observation indicates that the electrochemical oxidation of reduced **1** becomes feasible at higher scan rates in DMF, suggesting that the chemical reactivity is impaired on this timescale. Surprisingly, this behavior is not consistent between solvents, as parallel experiments in MeCN do not show any quasi-reversible responses up to scan rates of 2,000 mV/s, corroborating the increased stability of reduced **1** in DMF (Appendix C, Figure C1). Next, we sought to obtain further, quantitative data on the electrochemical behavior of **1** in DMF. Using the Randles-Sevcik equation, the diffusion coefficient of **1** was determined through a variable scan rate study (Appendix C, Figure C2), affording a value of $3.5 \cdot 10^{-6}$ cm^2 s^{-1} (see Appendix C and section 4.4.3), which is in the same order of magnitude as related molecular cobalt(II) complexes ranging from 3.4 to 8.2×10^{-6} cm^2 s^{-1}.[15,30-32] When plotting the peak currents i_p vs. the square root of the scan rate, a good linear fit is observed (Appendix C, Figure C3), which indicates that electron transfer between the electrode and **1** takes place in a truly homogeneous fashion.[33] Plots of the anodic and cathodic peak potentials ($E_{p,a}$ and $E_{p,c}$) versus the logarithm of the scan rate ranging

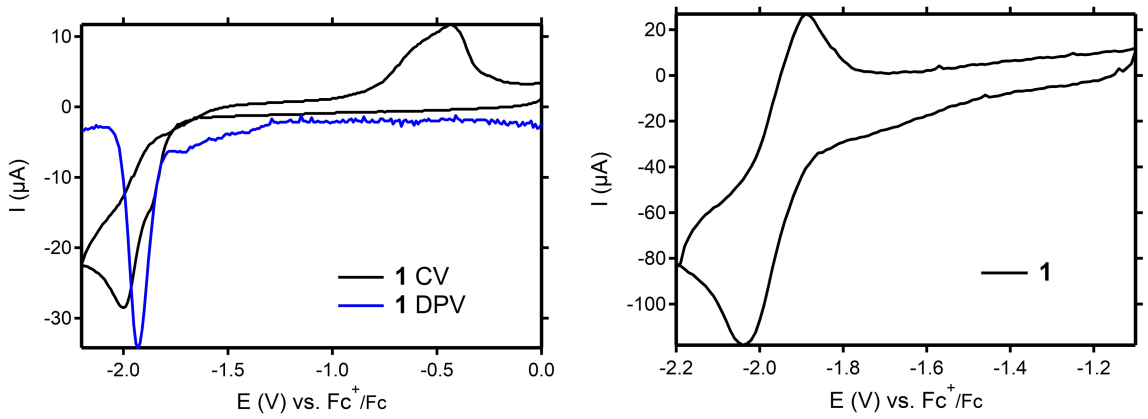

Figure 2. Left: cyclic voltammogram (black) and differential pulse voltammogram (blue) of **1** (2 mM) in DMF (containing 0.1 M nBu$_4$NBF$_4$ as supporting electrolyte) at 100 mV/s. Right: cyclic voltammogram of **1** (2 mM) in DMF (0.1 M nBu$_4$NBF$_4$) at 2,000 mV/s. Potentials in V vs Fc^+/Fc; working electrode: glassy carbon; counter-electrode: Pt wire; reference electrode: Ag/Ag(NO$_3$).

from 2,000 mV.s^{-1} to 20,000 mV.s^{-1} show linear trends to more anodic/cathodic potentials, indicating a slow electron transfer rate (Appendix C, Figure C3).[33] Unbalanced slopes of opposite signs (+40 and −130 mV/dec) were determined for the Co(I/II) couple, highlighting an asymmetry of the energy barrier for electron transfer.[18] These observations lend further credit to the relative ease with which **1** can be reduced and undergo a subsequent chemical transformation, while the reversed oxidation reaction is relatively slow. Since this behavior is well suited for electrocatalysis, we continued our investigations by examining the electrocatalytic HER properties.

4.2.2 Electrocatalytic properties

The electrocatalytic activity of **1** towards hydrogen evolution was initially examined by recording cyclic voltammograms in DMF using *n*Bu$_4$NBF$_4$ as supporting electrolyte and increasing amounts of a sacrificial proton source. Two proton sources with distinct acid dissociation constants and standard potentials for the HA/A$^-$,H$_2$ half reaction in DMF were selected: triethylammonium Et$_3$NHBF$_4$ (pK_a = 9.2, $E°_{HA}$ = −1.31 V) and phenol (pK_a = >18, $E°_{HA}$ = < −1.83 V).[34] First, the stability of **1** in the presence of increasing amounts of the strongest acid (Et$_3$NHBF$_4$) was monitored by ^{1}H-NMR spectroscopy, showing no signs of protonation nor degradation (Appendix C, Figure C4 & C5). Therefore, it is expected that **1** needs to be reduced first before participating in a chemical reaction involving a proton. **Figure 3** shows the cyclic voltammograms of **1** in the presence of increasing amounts of Et$_3$NHBF$_4$. The addition of acid triggers the development of a "peak-shaped" catalytic wave at the Co(I/II)

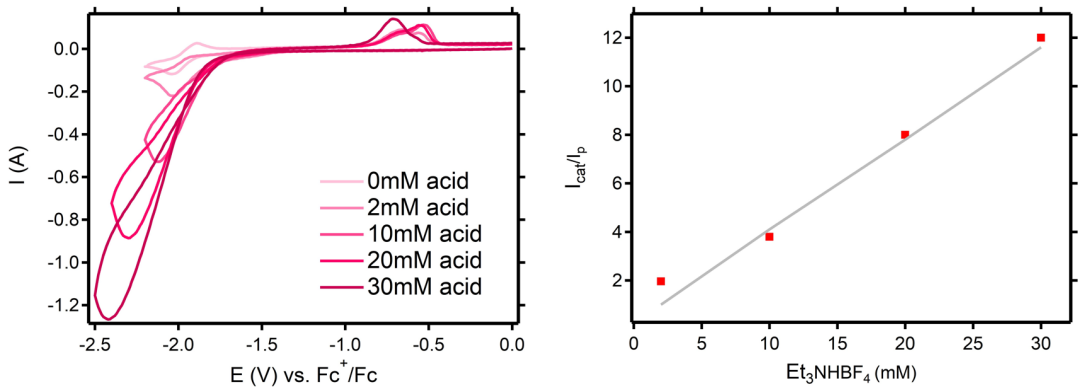

Figure 3. Left: cyclic voltammogram of **1** (2 mM) recorded in the presence of increasing amounts of Et$_3$NHBF$_4$: 2, 5, 10, 20, 30 mM in DMF (0.1 M *n*Bu$_4$NBF$_4$). Potentials in V vs Fc$^+$/Fc. Conditions: scan rate 2000 mV/s; working electrode: glassy carbon; counter-electrode: Pt wire; reference electrode: Ag/Ag(NO$_3$). Right: corresponding plot of i_c/i_p vs. the Et$_3$NHBF$_4$ concentration.

couple, regardless of acid concentration and with complete loss of the coupled oxidative response. The catalytic peak current (i_{cat}) is proportional to the acid concentration (Appendix C, Figure C6) and the catalytic wave keeps increasing over the whole range of acid concentrations (2-30 mM), without reaching an upper limit. The Co(I/II) reductive response ($E_{p,c}$) did not progressively shift towards more anodic potentials, which indicates that the complex needs to be reduced first before participating in a subsequent chemical reaction such as protonation.[35] This observation agrees with the unaltered ^{1}H-NMR spectra of **1** in the presence of excess Et_3NHBF_4. In the presence of Et_3NHBF_4 (5 equiv.) a scan rate study was performed, in which the peak current (i_{cat}) remained proportional to the square root of the scan rate (Appendix C, Figure C7). This observation indicates that the catalytic process is diffusion limited under the applied conditions.[18] Moreover, during bulk electrolysis experiments it became evident that the direct acid reduction by the bare glassy carbon electrode hardly contributes to the overall HER activity (vide infra). A plot of the ratio between the catalytic currents over the initial complex current (i_{cat}/i_p) and the acid concentration yields a linear correlation (**Figure 3**, right), from which the k_{obs} (TOF) was determined using equation 1.[36] In the presence of 2, 10, 20, and 30 mM Et_3NHBF_4 ($E°_{HA}$ = −1.31 V)[34] the catalytic current corresponds to a k_{obs} (TOF) of 15, 57, 269, and 555 s^{-1}, respectively. The catalysis experiment was also carried out with the much weaker proton source phenol ($E°_{HA}$ = < −1.83 V)[34] in DMF (Appendix C, Figure C8), demonstrating a lower catalytic rate at a lower overpotential (k_{obs} (TOF) dropped almost 10-fold), which is consistent with the scaling relationship between rate and overpotential in electrocatalysis and confirms that **1** reacts as a true electrocatalyst.[37,38] The absolute catalytic rate for **1** in the presence of 30 mM Et_3NHBF_4 in DMF on the CV time scale (TOF 555 s^{-1}) is an increase as compared to the previously reported HER performance of **1** in MeCN (160 equiv. AcOH ($E°_{HA}$ = < −1.46 V), TOF 200 s^{-1}).[28] The cyclic voltammogram of the acid alone shows a weak electrocatalytic response at more negative potentials (Appendix C, Figures C9).

4.2.3 Bulk electrolysis

Next, bulk electrolysis experiments were performed in a custom-made two-compartment HER model-cell (Appendix C, Figure C10), using a glassy carbon rotating-disk-electrode (RDE) with a well-defined surface area (0.196 cm^2) as working electrode (cathode) operating at 0 or

$$k_{obs}(TOF) = 1.94 \cdot v \cdot \left(\frac{i_{cat}}{i_p}\right)^2 \qquad \text{(eq.1)}$$

2,000 rpm. In situ H_2 quantification was achieved by in-line measurements using a GC-TCD apparatus (see **Chapter 2**, section 2.4.3, p73). The electrolysis cell design has been reported for solid-state electrocatalysis and we have adopted the design to be able to assess the electrocatalytic HER performance for molecular complexes in solution.[5]

Based on our findings in the CV studies, controlled-potential electrolysis (CPE) was performed at −2.00 V versus Fc^+/Fc. The reported thermodynamic reduction potential $E°_{HA}$ of the Et_3NHBF_4 proton source in DMF is –1.31 V vs Fc^+/Fc, corresponding to an overpotential of 690 mV at the applied potential.[34] During 3 h electrolysis of a 1.0 mM (bright pink) solution of **1** in DMF (10 mL) containing 0.1 M Et_3NHBF_4 and 0.1 M nBu$_4$NBF$_4$ (supporting electrolyte) solution at 0 rpm, a relatively stable current with an average current density of 8.7 mA/cm^2 (total charge of 18.7 C) and >99% FE was achieved (Appendix C, Table C1 and **Figure 4**). A control experiment in the absence of **1** did deliver only 0.3 C after 2 h. These results demonstrate that **1** is catalytically activity for HER during CPE) under these conditions with high selectivity. The catalyst solution did not change color over the course of the

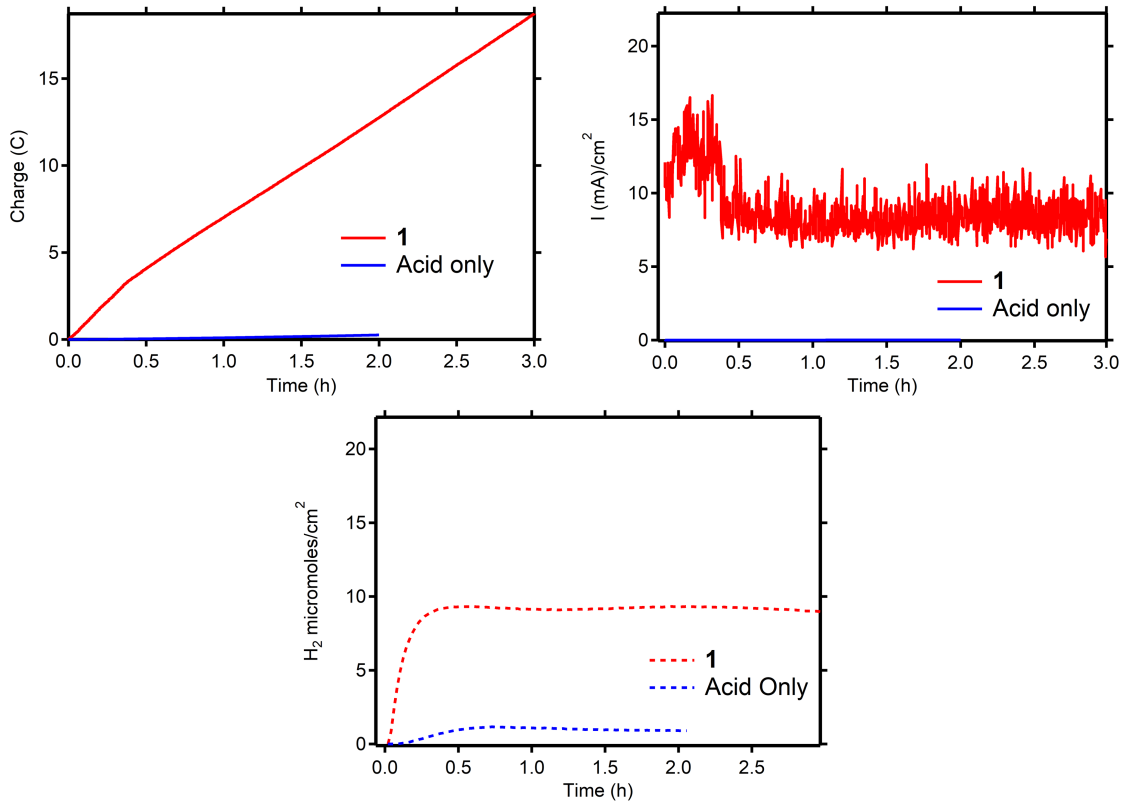

Figure 4. Top left: charge vs. time. Top right: current density vs. time. Bottom: hydrogen production vs. time. During CPE in DMF (0.1 M nBu$_4$NBF$_4$ and 0.1 M Et_3NHBF_4) at −2.00 V versus Fc^+/Fc at 0 rpm. Blue trace: control experiment in the absence of **1**. red trace: 1 mM **1**. Working electrode: glassy carbon RDE; Counter-electrode: Pt wire; Reference electrode: Ag/Ag(NO_3). H_2 quantification was determined by in line GC measurements.

electrolysis experiment and ^{1}H-NMR analysis furthermore confirmed the presence of **1** as the major paramagnetic species in solution after electrolysis. This is in contrast with our previously reported bulk electrolysis experiments in MeCN using a mercury electrode, which showed that **1** is not stable for longer times (2 h) at an applied potential of −1.9 V in MeCN.[28] Next, our novel setup (with the glassy carbon cathode) prompted us to re-evaluate the activity of **1** during CPE in MeCN solution with AcOH as a proton source. The bulk solution did not show any optical changes over the course of the experiment, but interestingly also no catalytic activity was observed for **1** under these conditions (Appendix C, Figure C10). We therefore conclude that the stability and activity of **1** under CPE conditions is sensitive to both the electrode material and the solvent. Accordingly, we have continued our studies using DMF as the reaction solvent in combination with a glassy carbon electrode. Our CV experiments indicated a diffusion-controlled reductive process for **1** near the glassy carbon electrode surface, which encouraged us to enhance the substrate and catalyst delivery (mass transfer) towards the electrode by rotating the working electrode. In addition, the accumulation of H_2 bubbles under the electrode surface was diminished upon rotation. CPE at 2,000 rpm at −2.00 V versus Fc^+/Fc in DMF (1 mM **1**, 0.1M Et_3NHBF_4 and 0.1M $n$$Bu_4NBF_4$) showed a significant enhancement in catalytic performance (**Table 1** and **Figure 6**, pink trace). During 3 h electrolysis, an average current density of 23.8 mA/cm^2 (total charge 50.4 C), with an overall FE of >99% was observed, which is a 2.5-fold increase in activity without any loss of the quantitative FE. Control experiments in the absence of **1** did show significantly lower amounts of H_2 being formed (**Table 1** and **Figure 6**, black trace) and experiments in the absence of acid did not yield any hydrogen gas at all. These results denote the electrocatalytic HER rate of **1** can be increased upon better mass transfer. Next, the HER performance of **1** was benchmarked against three reported molecular cobalt(II) HER catalysts, including $[Co(dmgBF_2)_2(solv)_2]$ (**2**),[39] ($dmgBF_2$ = difluoroboryldimethylglyoximato), [Co(TPP)] (**3**),[40] (TPP = 5,10,15,20-tetraphenylporphyrinato) and [Co(bapbpy)Cl](Cl) (**4**),[41] (bapbpy = 6,6'-bis-(2-aminopyridyl)-2,2'-bipyridine) (**Figure 5**). CVs of **2**-**4** were taken in DMF and all matched those reported in the literature and showed catalytic activity in the presence of Et_3NHBF_4 (Appendix C, Figures C11-C13). Complexes **2**-**4** were then tested under the same rotating disk CPE conditions as described for **1** (**Table 1** and **Figure 6**), and all demonstrated catalytic proton reduction with average current densities (mA/cm^2) increasing from 8.1 for **3**, 19.3 for **2**, and 34,2 for **4**. CPE performances were reproducible over several measurements. A closer look at the performances reveals that the selected conditions yield high Faradaic efficiency (> 92%) for H_2 for all complexes. In addition, a linear charge increase (equivalent to a stable current density) was

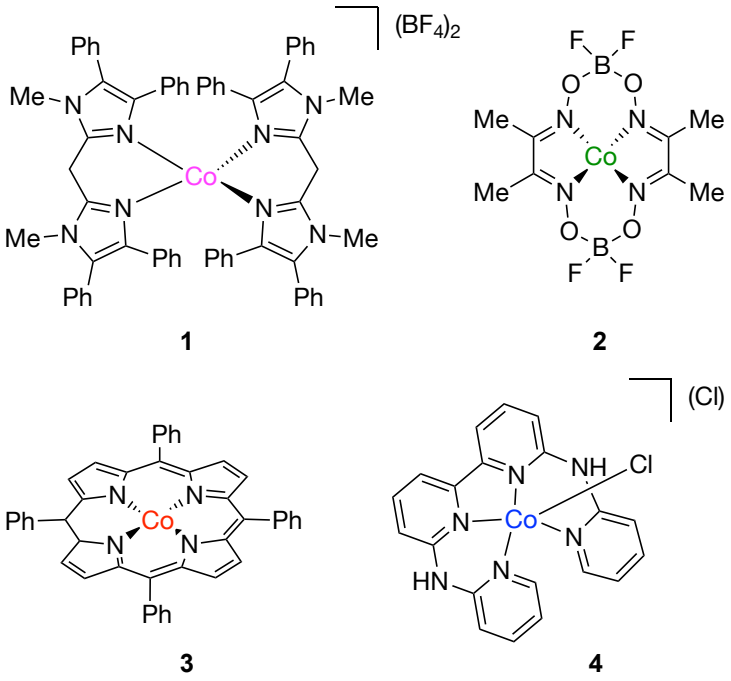

Figure 5. Molecular HER complexes **1**-**4**

Table 1. Bulk Electrolysis Experiments for H_2 Evolution using molecular Co(II) complexes **1**-**4**.[a]

Catalyst (1 mM)	Charge (C)	Current Density (mA/cm^2)	FE (%)
-	3.8 ± 0.5[b]	1.8	98[b]
1	50.4 ± 0.7[c]	23.8	>99[c]
2	40.9 ± 0.2[c]	19.3	95[c]
3	17.1	8.1	92
4	72.4 ± 2.1[c]	34.2	95[c]

[a]10 mL DMF, 0.1 M nBu$_4$NBF$_4$, 0.1 M Et$_3$NHBF$_4$ at –2.00 V vs Fc^+/Fc, glassy carbon RDE, 2000 rpm, 3 h. H_2 quantification by gas chromatography analysis. [b]Average of four measurements. [c]Average of two measurements.

observed for complexes **1**-**3**, which indicates a steady HER performance. Complex **4** is most active under these conditions, but shows an increase in current density as well as hydrogen formation after 45 min. This observation is reproducible over two measurements and seems to indicate a structural change to **4** during catalysis that is not yet understood (Appendix C, Figure C14; vide infra). Complex concentrations near the electrode and diffusion coefficients are assumed to be similar between experiments and therefore the current densities obtained for these 3 h experiments give an insight in the relative rate of the proton reduction for complexes **1**-**4** under the same conditions. The strong variations in performance demonstrate that the

choice of molecular cobalt(II) complex (structure, overall charge, ligand) has a significant influence on the overall proton reduction performance under the applied conditions, with complex **1** showing a stable performance, which is second best in this series.

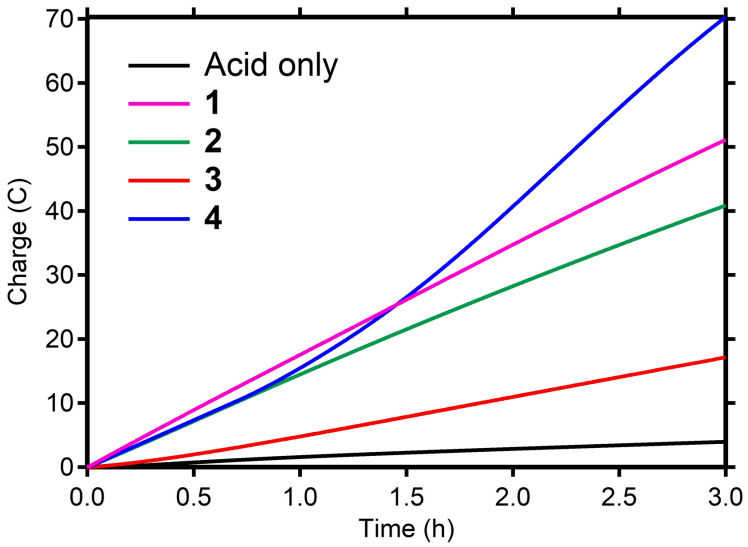

Figure 6. Rotating disk CPE: charge passed over the course of a bulk electrolysis experiment performed in the presence of 1 mM catalyst; Pink: **1**, Green: **2**, Red: **3**, Blue: **4**, Black: no catalyst, 0.1 M Et_3NHBF_4 in DMF (containing 0.1 M nBu$_4$NBF$_4$ as the supporting electrolyte) at –2.00 V vs Fc^+/Fc at 2,000 rpm.

4.2.4 Catalytic overpotential

In a next set of experiments, we investigated the overpotential requirement during a series of controlled current electrolysis (CCE) experiments for a current density of 10 mA/cm^2, an amount relevant for the cathodic side of a solar water splitting device.[5] The three most active complexes under the above CPE conditions, **1**, **2**, and **4** were tested in a series of 2 h CCE experiments under the same conditions as the CPE experiments (1 mM **1**, **2**, or **4**, 0.1 M Et_3NHBF_4 and 0.1 M nBu$_4$NBF$_4$) and product formation was again measured by in-line GC-TCD analysis. To determine the overpotential, the dynamic voltages were recorded and subtracted from the reported thermodynamic reduction potential for Et_3NHBF_4 in DMF.[34] The overpotential requirements at t = 0 and t = 2 h, shown in **Figure 7**, illustrate that the bare glassy carbon electrode (black) requires an overpotential of around 2,000 mV to reach the necessary current density with a poor FE of 8%. In contrast, **1** (pink) has an overpotential of 370 mV at t = 0 which slowly increases over time to 383 mV at t = 2 h, with 96% FE. **2** (green) requires a larger overpotential, starting at 486 mV and moving to 490 mV at t = 2 h, with 90% FE. Complex **4** (blue) shows an overpotential at t = 0 of 470 mV, which surprisingly decreases overtime to 406 mV, meaning that less energy is required at t = 2 h (FE = 90%). This decrease

is in line with the rate increase observed during the CPE. Under the applied conditions, **1** performs best by requiring the lowest overpotential at t = 0 as well as at t = 2 h, combined with the highest FE.

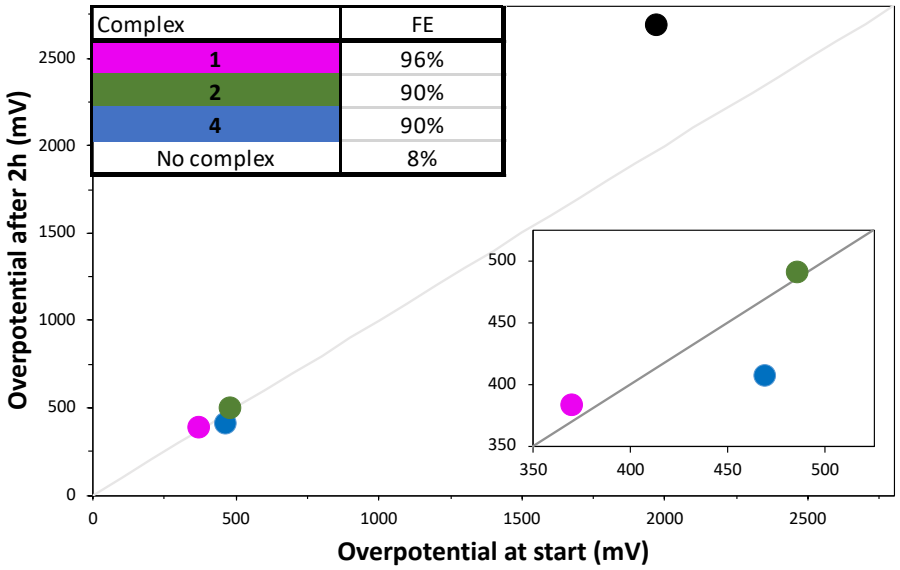

Figure 7. Plot of the overpotential requirement and stability for HER complexes **1** (pink), **2** (green), **4** (blue) and no complex (black) during controlled potential electrolysis in 10 mL DMF, 0.1 M nBu$_4$NBF$_4$, 0.1 M Et$_3$NHBF$_4$ at –2.00 V vs Fc$^+$/Fc, glassy carbon RDE, 2000 rpm, 3 h. H_2 quantification by gas chromatography analysis. The x-axis represents the overpotential required to achieve 10 mA cm^{-2} per geometric area at time t = 0. The y-axis represents the overpotential required to achieve 10 mA cm^{-2} per geometric area at time t = 2 h. The diagonal gray line is the expected response for a stable catalyst that does not change in activity during 2 h constant polarization. The region of interest for benchmarking is expanded in the inset plot.

4.2.5 Post electrolysis analysis

Whereas no color changes were observed for the reaction solutions during CPE and CCE experiments, distinct optical changes to the glassy carbon working electrode surface were observed after electrocatalytic electrolysis experiments with all four complexes **1**-**4**, *i.e.* the electrode surface was covered with a thin layer of black deposit. To obtain insight into the formation and the role in electrocatalysis of these deposits, the deposits formed in the presence of molecular complexes **1** and **2** were further investigated. First, the catalytic HER activity of the deposit derived from **1** was investigated by a rinse test. A pristine glassy carbon RDE was put in a 0.5 mM solution of **1** and a CPE experiment was performed (**Table 2**, entry 1, **Figure 8**, pink trace). After 3 h, the pink reaction solution was removed from the electrocatalytic cell, while the electrode was kept under inert conditions. Next, the working electrode compartment was washed with 10 mL dry DMF, followed by the addition of a fresh reaction solution without

1. Visual inspection did not indicate any physical changes to the working electrode, including its surface modifications, during the washing and replacement of the reaction medium, which suggests that the deposition is not merely an electrostatic interaction of the dicationic cobalt complex with the cathode when a cathodic potential is applied. Finally, another CPE experiment was carried out (**Table 2**, entry 2, **Figure 8**, light pink trace), showing that the deposition on the electrode surface is an active catalytic material for proton reduction. Monitoring the activity of the deposit over time shows that the current density decreases over time (Appendix C, Figure C15). Over 3 h, a current density average of 19.4 mA/cm^2 with a quantitative FE was observed, which is a slight decrease in performance compared to the initial CPE in the presence of **1**. The same rinse test experiment was performed for **2** (**Table 2**, entry

Table 2. Rinse Test HER Electrolysis.[a]

Entry	Catalyst (0.5mM)	Charge (C)	Current Density (mA/cm^2)	FE (%)
1	**1**	42.7	20.2	98
2	Rinse test	41.1	19.4	>99
3	**2**	31.8	15	97
4	Rinse test	20.7	9.8	99

[a]10 mL DMF, 0.1 M nBu$_4$NBF$_4$, 0.1 mM Et$_3$NHBF$_4$ at –2.00 V vs Fc$^+$/Fc, glassy carbon RDE, 2000 rpm, 3 h. H_2 quantification by gas chromatography analysis.

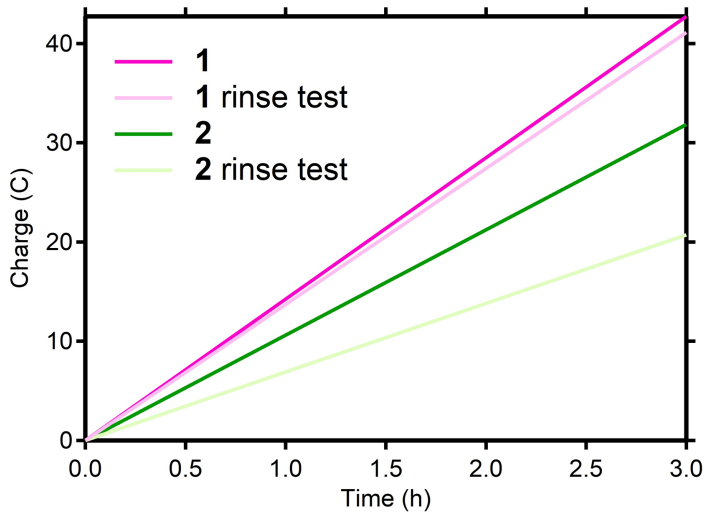

Figure 8. Charge passed over the course of 3 h controlled potential electrolysis performed in 0.1 M Et$_3$NHBF$_4$ in DMF (containing 0.1 M nBu$_4$NBF$_4$ as the supporting electrolyte) at –2.00 V vs Fc$^+$/Fc at 2,000 rpm. Ultra-pink trace 0.5 mM **1** (pristine electrode), rose pink trace subsequent electrolysis with no homogeneous molecular complex **1** (modified electrode). Deep green trace 0.5 mM **2** (pristine electrode), bright-green traces subsequent electrolysis with no homogeneous molecular catalyst **2** (modified electrode).

3-4, **Figure 8**, green traces). The rinse test for **2** also demonstrated catalytic activity for the deposit, albeit with a significantly decreased current density (initial: 15.0 mA/cm^2, rinse test: 9.8 mA/cm^2). Whereas the rinse tests clearly show electrocatalytic HER activity for the deposits formed from **1** and **2**, differences in the overall activity of the deposits were observed. This observation suggests that putative decomposition of the molecular complexes does not lead to the same deposit, i.e. the molecular complex governs the activity of the deposit, either by leading to a different composition or a different structure of the deposit. More importantly, these results indicate that electrocatalytic HER activity during CPE by the complexes used in our investigations is not merely a feature of the molecular complex in solution, but is to a large extent determined by a deposit formed during the CPE experiment.

4.2.6 Analysis of the deposit

To gain information on the structure and composition of the electrode deposits formed during CPE, post-electrolysis XPS analysis of the deposit formed from **1** was performed. The elements Co, B, F, N, O, and C were found to be present in the deposit, in relative atomic amounts of 0.23%, 5.0%, 15.7%, 4.04%, 4.29%, and 68.4%, respectively (Appendix C, Figure C16). Firstly, these atomic percentages indicate that **1** (Co 4.98%, B 1.81%, F 12.73%, N 9.39%, C 66.41%) does not simply absorb on the electrode surface, nor that **1** is completely reduced to metallic cobalt. Instead, the surface is covered with a combination of atoms originating from **1**, the DMF solvent, the electrolyte salt, and/or the sacrificial proton source. Important to note is that the high contribution of carbon is caused by the usage of carbon tape to support the sample. The 4.29% oxygen most likely originates from the DMF solvent and air exposure before XPS analysis as no other oxygen source was added during electrolysis. Nitrogen could originate from all components in the reaction medium. Fluor and boron signals can originate from both the electrolyte salt and the counterions of **1**, although in both cases a relative ratio closer to 4:1 would have been expected. Cobalt is with 0.23% only a minor contributor to the deposition. A closer look at the cobalt signal (Appendix C, Figure C17) revealed a broad signal for the $2p_{3/2}$ core level of Co 2p with several contributions (i.e. at 781.2 and 786.0 eV, and a minor contribution at 777.4 eV). The former values can be assigned to Co^{II} species, while the latter corresponds to metallic cobalt (see the work of Biesinger for the deconvolution of the Co spectrum).[20,42-44] Hence it became clear that most of the absorbed cobalt remains in the 2^+ oxidation state, although some reduced cobalt is present. Due to the low amount of Co in the deposit, the amount of metallic Co could not be resolved reliably. Further studies will have to

provide information on whether **1** maintains its structural integrity and is somehow incorporated in the deposit, or that it decomposes.

Literature analysis shows some precedence for the formation of deposits during non-aqueous HER experiments using molecular cobalt complexes.[23,25,27,42,45] A dicationic tris(glyoximato) cobalt clathrochelate was reported to form a deposit during HER electrolysis in MeCN with $NaClO_4$ as supporting electrolyte salt and $HClO_4$ as a sacrificial proton donor. In this case, EDX analysis showed a relative ratio of atomic amounts adsorbed to the electrode of 63 ± 7% : 32.5 ± 5% cobalt:heteroatoms (F, O, N, B), which significantly deviates from our observations, particularly in terms of the amount of cobalt.[25]

4.3 Conclusion

Voltammetry investigations have shown that cobalt complex **1** has a more reversible Co(I/II) couple in DMF, as compared to the irreversible behavior in MeCN observed in our previous studies. Accordingly, its electrochemical solution state behavior and electrocatalytic performance could be analyzed in more detail in DMF during voltammetry. **1** was found to be an active HER-electrocatalyst in the presence of a proton donor. In bulk electrolysis experiments in the presence of triethylammonium, **1** is a competitive HER catalyst amongst a benchmarking pool of four molecular cobalt HER catalysts**,** including the widely studied cobalt dimethylglyoxime complex. Bulk electrolysis experiments (CPE and CCE) also showed the formation of a deposit on the carbon electrode during electrolysis for all complexes tested, including **1**. Rinse experiments showed that deposits formed from **1** and **2** have only a somewhat decreased HER activity in a next electrolysis experiment. These observations indicate that, under the current circumstances, all molecular complexes tested in this study (including **1**) seem to act as pre-catalysts that form a heterogenous material (electrode deposit) responsible for HER activity. Importantly, the deposit formed from **1** has a significantly different chemical composition than **1**, based on XPS analysis, with a small but significant percentage of Co (0.23%) composed mostly of Co(II) and with a minor contribution of Co(0). This in contrast with several earlier studies that observed mainly metallic cobalt in their deposits.

With this study, we have shown that the observed catalytic performance for **1** during electrocatalytic voltammetry is distinct from its bulk electrolysis performance due to physical changes at the electrode surface by means of a deposit formation during bulk electrolysis. Similar observations were also made for a series of other molecular, Co-based HER electrocatalysts. Interestingly, our studies showed that the molecular design of the catalysts

influences the composition of the deposit and therewith the observed activity in our model electrolysis cell. These findings are of interest for the development of molecular HER catalysts and of immobilized electrocatalytic materials.

4.4 Experimental

4.4.1 General remarks

All air-sensitive reactions were carried out under an inert atmosphere of water- and oxygen-free N_2 gas using standard Schlenk techniques or were performed in an MBraun labmaster dp glovebox workstation. Dry acetonitrile (MeCN), dichloromethane (CH_2Cl_2) and methanol (MeOH) were used from an MBraun SPS-800 solvent purification system, dried over 3 or 4 Å molecular sieves and degassed by bubbling N_2 for at least 30 min. Tetrahydrofuran (THF) was dried over sodium benzophenone after taking it from an MBraun SPS-800 solvent purification system, subsequently distilled and degassed by bubbling N_2 for at least 30 min. Anhydrous *N,N*-Dimethylformamide (DMF) was purchased from Sigma-Aldrich and subsequently dried over 4 Å molecular sieves and degassed by bubbling N_2 for at least 30 min. All other commercially obtained chemicals were used without further purification, unless stated otherwise. ^{1}H-NMR and ^{13}C-NMR spectra were recorded at 400 MHz, 101 MHz and 376 MHz respectively, at 298 K, on a Varian VNMRS400 or an Oxford NMR AS400 spectrometer. Chemical shifts (δ) are reported in ppm and referenced against the residual solvent signal. XPS was performed with a K-Alpha XPS apparatus (Thermo Scientific). An aluminum anode was used as the X-Ray source (Kα monochromatic irradiation, 1486.6 eV) operating at 72 W and a spot size of 400 µm. High-resolution regional spectra were measured with a pass energy of 50 eV and wide-range survey spectra were recorded at 200 eV pass energy. The pressure inside the analysis chamber was kept below a maximum of $3 \cdot 10^{-7}$ mbar during the measurements. Charge neutralization was applied by a low-energy Ar+ ion beam. The spectra were analyzed using the CasaXPS software.

Electrochemical sweeping experiments were performed in a nitrogen-filled MBraun labmaster dp glovebox, on an IVIUM potentiostat/galvanostat using a 3-electrode setup including a Pt-wire counter electrode, a glassy carbon-working electrode (3 mm Ø) and an Ag/Ag(NO_3) reference electrode used directly in solution. The potentiostat was kept external to the glovebox, and the electrode leads were connected with a custom shielded electrode cable feedthrough. All scans were absolutely referenced to the ferrocenium/ferrocene redox couple and taken at a scan rate of 100 mV/s, unless reported differently. The working electrodes were

polished with 0.3 μm aluminum oxide powder deionized water slurries and rinsed with water for 30 seconds to remove residual polishing powder. All experiments were performed on clear and non-turbid solitons. Before all experiments, background voltammograms were recorded at a scan rate of 100 mV/s. Solutions were mixed by shaking before each measurement and the working electrode surface was cleaned with a tissue after every scan. All measurements were recorded in a 0.1 M tetrabutylammonium tetrafluoroborate (nBu$_4$NBF$_4$) solution in dry, degassed DMF or MeCN. Electrolysis solutions were prepared in the glovebox and electrolysis experiments were performed outside the glovebox using a Autolab PGSTAT204 potentiostat/galvanostat, using a 3-electrode setup including a Pt-plate counter electrode, a RDE glassy carbon-working electrode (5 mm Ø) and a double junction Ag/Ag(NO$_3$) reference electrode used directly in solution. All electrodes for electrolysis experiments were purchased from Methrom. For details on the electrochemical cell for electrolysis experiments, see below.

Typical electrocatalytic controlled potential and current experiments were carried out in a two-compartment three-electrode electrochemical cell (Appendix A, Figure A52). First, the electrochemical cell was put in a glovebox where the counter electrode (CE) compartment was filled with 10 mL electrolyte solution, the double junction reference electrode (RE) was filled with a 0.01 M solution of Ag/Ag(NO$_3$), and the working electrode (WE) compartment was filled with a pre-mixed solution of the electrolyte, sacrificial proton donor, and molecular complex. Then the gas inlet and outlet were closed with rubber stoppers, the CE and RE were positioned on the outer shafts, and a glass stopper was put on the WE shaft. Then, the electrochemical cell was transferred out of the glovebox and put under a flow of N_2 (5 mL/min), which was in-line with the GC-apparatus (see **Chapter 2** section 2.4.3, p73). Subsequently, the RDE was replaced for a glass stopper and the cell was purged until the residual oxygen signal (originating from the assembly of the cell outside of the glovebox) completely disappeared on the GC chromatograms (Appendix A, Figure A54), which usually took 5-10 min. Finally, electrolysis was performed as described.

4.4.2 Acid−base properties and stability factors

The stability of **1** in the presence of increasing amounts of a sacrificial proton source was determined with ^{1}H-NMR. We monitored **1** in the presence of increasing amounts of Et$_3$NHBF$_4$in DMF (pK_a = 9.2).[46] Upon the addition of 10 and 100 equiv. Et$_3$NHBF$_4$, as a solid acid, the solution containing the complex remained pink and no significant changes in paramagnetic chemical shifts and peak intensities relative to the residual solvent signal were

observed (Appendix C, Figures C5 & C6). These observations show that **1** does not degrade nor gets protonated in the presence of substantial amounts of the acid used, which adds to our observations on its stability in the presence of the weaker acid AcOH in MeCN solution.[28]

4.4.3 Calculation of diffusion constants from cyclic voltammograms of 1

The peak current i_p is described by the Randles-Sevcik equation 1.

$$i_p = 0.4463(F/RT)^{1/2}\, n_p^{3/2}\, FAD^{1/2}[Co]v^{1/2} \qquad \text{(eq.1)}$$

In equation 1, i_p is peak current, F is Faraday's constant (F = 96500 C mol^{-1}), R is the universal gas constant (R = 8.31 J K^{-1} mol^{-1}), T is temperature (T = 298 K) n_p is the number of electrons transferred (n_p = 1 for Co(I/II)), A is the active surface area of the electrode (A = 0.07 cm^2), D is the diffusion coefficient for the complex, [Co] is the concentration of the catalyst, and v is the scan rate. The diffusion coefficient (D) was calculated from the i_{pc} of the reversible scans between 4000–20000 mV/s giving a value of 3.5 × 10^{-6} cm^2 s^{-1} (± 0.3 × 10^{-6}).

4.4.4 Synthesis

[Co(HBMIM^{Ph2})$_2$](BF$_4$)$_2$ (**1**), (HBMIMPh2 = bis(1-methyl-4,5-diphenyl-1H-imidazol-2-yl)methane) was synthesized according to our previously reported methods.[28] Dissolving **1** in MeCN or DMF (up to 10 mM) leads to clear and non-turbid pink solutions. All electrochemical measurements were performed at lower concentrations (0.5 – 2 mM)

Additional characterization in MeCN and DMF:

UV-Vis d-d transitions: (MeCN ε [L mol^{-1} cm^{-1}]): λ_{max} 555 (440), 510 (410) nm. UV-Vis (DMF ε [L mol^{-1} cm^{-1}]): λ_{max} 555 (430), 505 (400) nm. **^{1}H NMR** (400 MHz, MeCN-d_3, 25 °C): δ (ppm) = 182.82 (1H, CH$_2$), 28.26 (3H, CH$_3$), 11.69 (1H, Ph *p*-CH), 7.04 (2H, Ph *o*-CH), 5.03 (1H, Ph *p*-CH), 3.64 (1H, Ph *m*-CH), 2.85 (1H, Ph *m*-CH), 2.27 (2H, Ph *m*-CH), –13.74 (2H, Ph *o*-CH). Tentative peak assignments are based on relative integration, and broadness of the resonance (methylene and some *o*-Ph CH protons seem to be in close proximity to the metal center, as observed in a solid-state single crystal X-ray structure, and therefore broaden), chemical shift, and similarity to structural analogs. Some integrals deviate from the expected value, presumably due to the broadness of the resonance. **^{1}H NMR** (400 MHz, (DMF-d_7), 25 °C): δ (ppm) = 185.90 (1H, CH$_2$), 28.13 (3H, CH$_3$), 12.07 (1H, Ph *p*-CH), 7.44 (1H, Ph *m*-CH), 7.14 (2H, Ph *o*-CH), 5.05 (1H, Ph *p*-CH), 3.92 (1H, Ph *m*-CH), 3.65 (1H, Ph *m*-CH), 2.96

(1H, Ph *m*-CH), –12.34 (2H, Ph *o*-CH). Tentative peak assignments are based on relative integration, and broadness of the resonance (methylene and some *o*-Ph CH protons seem to be in close proximity to the metal center, as observed in a solid-state single crystal X-ray structure, and therefore broaden), chemical shift, and similarity to structural analogs. Some integrals deviate from the expected value, presumably due to the broadness of the resonance.
All observed resonances in the ^{1}H NMR spectra in MeCN-d_3 and DMF-d_7 were attributed to **1**. The observed resonances for **1** in these solvents closely match in terms of chemical shifts, broadness of the signals, and integration. Therefore, we propose that **1** in MeCN or DMF solution is one and the same species. This observation also excludes the coordination of MeCN or DMF.

$[Co(dmgBF_2)_2(solv])_2]$ **(2),** ($dmgBF_2$ = difluoroboryldimethylglyoximato), was synthesized according to a literature procedure.[48] Cyclic voltammograms in presence and absence of 1 equiv. Et_3NHBF_4 in DMF (0.1M nBu$_4$NBF$_4$) are reported in Appendix C, Figure C11.
[Co(TPP)] (**3**), (TPP = 5,10,15,20-tetraphenylporphyrinato) was purchased from Sigma Aldrich. Cyclic voltammograms in the presence and absence of 1 equiv. Et_3NHBF_4 in DMF (0.1M nBu$_4$NBF$_4$) are reported in Appendix C, Figure C12.
[Co(bapbpy)Cl](Cl) (**4**), (bapbpy = 6,6'-bis-(2-aminopyridyl)-2,2'-bipyridine) was synthesized according to a literature procedure.[41] Cyclic voltammograms in the presence and absence of 1 equiv. Et_3NHBF_4 in DMF (0.1M nBu$_4$NBF$_4$) are reported in Appendix C, Figure C13.

4.5 Author Contributions

Synthesis, characterization and electrochemical measurements were done by S.D. de Vos and M. Otten. XPS analysis was done by T. Wissink and E.J.M. Hensen. Project design was done by S.D. de Vos and R.J.M. Klein Gebbink. Funding acquisition, administration and oversight were done by R.J.M. Klein Gebbink. The original draft was written by S.D. de Vos and reviewing and editing was done by D.L.J. Broere, R.J.M. Klein Gebbink with contributions by all authors.

4.6 References

(1) Lewis, N. S.; Nocera, D. G. Powering the planet: Chemical challenges in solar energy utilization. *Proc. Natl Acad. Sci.* **2006,** *103* (43), 15729.
(2) Roger, I.; Shipman, M. A.; Symes, M. D. Earth-abundant catalysts for electrochemical and photoelectrochemical water splitting. *Nat. Rev. Chem.* **2017,** *1* (1), 0003.

(3) Trasatti, S. Work function, electronegativity, and electrochemical behaviour of metals: III. Electrolytic hydrogen evolution in acid solutions. *J. Electroanal. Chem. Interfacial Electrochem.* **1972,** *39* (1), 163.
(4) Bullock, R. M.; Chen, J. G.; Gagliardi, L.; Chirik, P. J.; Farha, O. K.; Hendon, C. H.; Jones, C. W.; Keith, J. A.; Klosin, J.; Minteer, S. D.et al. Using nature's blueprint to expand catalysis with Earth-abundant metals. *Science* **2020,** *369* (6505), eabc3183.
(5) McCrory, C. C. L.; Jung, S.; Ferrer, I. M.; Chatman, S. M.; Peters, J. C.; Jaramillo, T. F. Benchmarking Hydrogen Evolving Reaction and Oxygen Evolving Reaction Electrocatalysts for Solar Water Splitting Devices. *J. Am. Chem. Soc.* **2015,** *137* (13), 4347.
(6) Chen, L.; Wang, M.; Han, K.; Zhang, P.; Gloaguen, F.; Sun, L. A super-efficient cobalt catalyst for electrochemical hydrogen production from neutral water with 80 mV overpotential. *Energy Environ. Sci.* **2014,** *7* (1), 329.
(7) Helm, M. L.; Stewart, M. P.; Bullock, R. M.; DuBois, M. R.; DuBois, D. L. A Synthetic Nickel Electrocatalyst with a Turnover Frequency Above 100,000 s^{-1} for H_2 Production. *Science* **2011,** *333* (6044), 863.
(8) Koshiba, K.; Yamauchi, K.; Sakai, K. A Nickel Dithiolate Water Reduction Catalyst Providing Ligand-Based Proton-Coupled Electron-Transfer Pathways. *Angew. Chem. Int. Ed.* **2017,** *56* (15), 4247.
(9) McKone, J. R.; Marinescu, S. C.; Brunschwig, B. S.; Winkler, J. R.; Gray, H. B. Earth-abundant hydrogen evolution electrocatalysts. *Chemical Science* **2014,** *5* (3), 865.
(10) Artero, V.; Chavarot-Kerlidou, M.; Fontecave, M. Splitting Water with Cobalt. *Angew. Chem. Int. Ed.* **2011,** *50* (32), 7238.
(11) Queyriaux, N.; Jane, R. T.; Massin, J.; Artero, V.; Chavarot-Kerlidou, M. Recent developments in hydrogen evolving molecular cobalt(II)–polypyridyl catalysts. *Coord. Chem. Rev.* **2015,** *304-305*, 3.
(12) Dempsey, J. L.; Brunschwig, B. S.; Winkler, J. R.; Gray, H. B. Hydrogen Evolution Catalyzed by Cobaloximes. *Acc. Chem. Res.* **2009,** *42* (12), 1995.
(13) Dolui, D.; Ghorai, S.; Dutta, A. Tuning the reactivity of cobalt-based H2 production electrocatalysts via the incorporation of the peripheral basic functionalities. *Coord. Chem. Rev.* **2020,** *416*, 213335.
(14) Tok, G. C.; Freiberg, A. T. S.; Gasteiger, H. A.; Hess, C. R. Electrocatalytic H_2 Evolution by the Co-Mabiq Complex Requires Tempering of the Redox-Active Ligand. *ChemCatChem* **2019,** *11* (16), 3973.
(15) Roubelakis, M. M.; Bediako, D. K.; Dogutan, D. K.; Nocera, D. G. Proton-coupled electron transfer kinetics for the hydrogen evolution reaction of hangman porphyrins. *Energy Environ. Sci* **2012,** *5* (7), 7737.
(16) Lee, K. J.; McCarthy, B. D.; Dempsey, J. L. On decomposition, degradation, and voltammetric deviation: the electrochemist's field guide to identifying precatalyst transformation. *Chem. Soc. Rev.* **2019,** *48* (11), 2927.
(17) Artero, V.; Fontecave, M. Solar fuels generation and molecular systems: is it homogeneous or heterogeneous catalysis? *Chem. Soc. Rev.* **2013,** *42* (6), 2338.
(18) Savéant, J.-M. *Elements of molecular and biomolecular electrochemistry: an electrochemical approach to electron transfer chemistry*; John Wiley & Sons, 2006.
(19) Widegren, J. A.; Finke, R. G. A review of the problem of distinguishing true homogeneous catalysis from soluble or other metal-particle heterogeneous catalysis under reducing conditions. *J. Mol. Cat. A Chem.* **2003,** *198* (1), 317.
(20) Kaeffer, N.; Morozan, A.; Fize, J.; Martinez, E.; Guetaz, L.; Artero, V. The Dark Side of Molecular Catalysis: Diimine–Dioxime Cobalt Complexes Are Not the Actual

Hydrogen Evolution Electrocatalyst in Acidic Aqueous Solutions. *ACS Catalysis* **2016,** *6* (6), 3727.

(21) Anxolabéhère-Mallart, E.; Costentin, C.; Fournier, M.; Robert, M. Cobalt-Bisglyoximato Diphenyl Complex as a Precatalyst for Electrocatalytic H2 Evolution. *J. Phys. Chem. C* **2014,** *118* (25), 13377.

(22) Martin, D. J.; McCarthy, B. D.; Donley, C. L.; Dempsey, J. L. Electrochemical hydrogenation of a homogeneous nickel complex to form a surface adsorbed hydrogen-evolving species. *Chem. Commun.* **2015,** *51* (25), 5290.

(23) Sconyers, D. J.; Blakemore, J. D. Distinguishing between homogeneous and heterogeneous hydrogen-evolution catalysis with molecular cobalt complexes. *Chem. Commun.* **2017,** *53* (53), 7286.

(24) McCarthy, B. D.; Donley, C. L.; Dempsey, J. L. Electrode initiated proton-coupled electron transfer to promote degradation of a nickel(ii) coordination complex. *Chemical Science* **2015,** *6* (5), 2827.

(25) Anxolabéhère-Mallart, E.; Costentin, C.; Fournier, M.; Nowak, S.; Robert, M.; Savéant, J.-M. Boron-Capped Tris(glyoximato) Cobalt Clathrochelate as a Precursor for the Electrodeposition of Nanoparticles Catalyzing H_2 Evolution in Water. *J. Am. Chem. Soc.* **2012,** *134* (14), 6104.

(26) El Ghachtouli, S.; Fournier, M.; Cherdo, S.; Guillot, R.; Charlot, M.-F.; Anxolabéhère-Mallart, E.; Robert, M.; Aukauloo, A. Monometallic Cobalt–Trisglyoximato Complexes as Precatalysts for Catalytic H_2 Evolution in Water. *J. Phys. Chem. C* **2013,** *117* (33), 17073.

(27) Ghachtouli, S. E.; Guillot, R.; Brisset, F.; Aukauloo, A. Cobalt-Based Particles Formed upon Electrocatalytic Hydrogen Production by a Cobalt Pyridine Oxime Complex. *ChemSusChem* **2013,** *6* (12), 2226.

(28) Ghosh, P.; de Vos, S.; Lutz, M.; Gloaguen, F.; Schollhammer, P.; Moret, M.-E.; Klein Gebbink, R. J. M. Electrocatalytic Proton Reduction by a Cobalt Complex Containing a Proton-Responsive Bis(alkylimdazole)methane Ligand: Involvement of a C−H Bond in H2 Formation. *Chem. Eur. J.* **2020,** *26* (55), 12560.

(29) Lee, K. J.; Elgrishi, N.; Kandemir, B.; Dempsey, J. L. Electrochemical and spectroscopic methods for evaluating molecular electrocatalysts. *Nat. Rev. Chem.* **2017,** *1* (5), 0039.

(30) Elgrishi, N.; Kurtz, D. A.; Dempsey, J. L. Reaction Parameters Influencing Cobalt Hydride Formation Kinetics: Implications for Benchmarking H_2-Evolution Catalysts. *J. Am. Chem. Soc.* **2017,** *139* (1), 239.

(31) Wiedner, E. S.; Bullock, R. M. Electrochemical Detection of Transient Cobalt Hydride Intermediates of Electrocatalytic Hydrogen Production. *J. Am. Chem. Soc.* **2016,** *138* (26), 8309.

(32) Elgrishi, N.; Chambers, M. B.; Artero, V.; Fontecave, M. Terpyridine complexes of first row transition metals and electrochemical reduction of CO_2 to CO. *Phys. Chem. Chem. Phys.* **2014,** *16* (27), 13635.

(33) Graham, D. J. *Standard Operating Procedures for Cyclic Voltammetry*; Lulu Press, Incorporated, 2017.

(34) Felton, G. A. N.; Glass, R. S.; Lichtenberger, D. L.; Evans, D. H. Iron-Only Hydrogenase Mimics. Thermodynamic Aspects of the Use of Electrochemistry to Evaluate Catalytic Efficiency for Hydrogen Generation. *Inorg. Chem.* **2006,** *45* (23), 9181.

(35) Fourmond, V.; Jacques, P.-A.; Fontecave, M.; Artero, V. H2 Evolution and Molecular Electrocatalysts: Determination of Overpotentials and Effect of Homoconjugation. *Inorg. Chem.* **2010,** *49* (22), 10338.

(36) Bullock, R. M.; Appel, A. M.; Helm, M. L. Production of hydrogen by electrocatalysis: making the H–H bond by combining protons and hydrides. *Chem. Commun.* **2014,** *50* (24), 3125.
(37) Tafel, J. Über die Polarisation bei kathodischer Wasserstoffentwicklung. *Zeitschrift für Physikalische Chemie* **1905,** *50U* (1), 641.
(38) Savéant, J.-M. Molecular Catalysis of Electrochemical Reactions. Mechanistic Aspects. *Chem. Rev.* **2008,** *108* (7), 2348.
(39) Razavet, M.; Artero, V.; Fontecave, M. Proton Electroreduction Catalyzed by Cobaloximes: Functional Models for Hydrogenases. *Inorg. Chem.* **2005,** *44* (13), 4786.
(40) Beyene, B. B.; Mane, S. B.; Hung, C.-H. Electrochemical Hydrogen Evolution by Cobalt (II) Porphyrins: Effects of Ligand Modification on Catalytic Activity, Efficiency and Overpotential. *J. Electrochem. Soc.* **2018,** *165* (9), H481.
(41) Queyriaux, N.; Sun, D.; Fize, J.; Pécaut, J.; Field, M. J.; Chavarot-Kerlidou, M.; Artero, V. Electrocatalytic Hydrogen Evolution with a Cobalt Complex Bearing Pendant Proton Relays: Acid Strength and Applied Potential Govern Mechanism and Stability. *J. Am. Chem. Soc.* **2020,** *142* (1), 274.
(42) Cobo, S.; Heidkamp, J.; Jacques, P.-A.; Fize, J.; Fourmond, V.; Guetaz, L.; Jousselme, B.; Ivanova, V.; Dau, H.; Palacin, S.et al. A Janus cobalt-based catalytic material for electro-splitting of water. *Nat. Mat.* **2012,** *11* (9), 802.
(43) Hüfner, S. *Photoelectron spectroscopy: principles and applications*; Springer Science & Business Media, 2013.
(44) Biesinger, M. C.; Payne, B. P.; Grosvenor, A. P.; Lau, L. W. M.; Gerson, A. R.; Smart, R. S. C. Resolving surface chemical states in XPS analysis of first row transition metals, oxides and hydroxides: Cr, Mn, Fe, Co and Ni. *Appl. Surf. Sci.* **2011,** *257* (7), 2717.
(45) Ho, X. L.; Das, S. P.; Ng, L. K.-S.; Ng, A. Y. R.; Ganguly, R.; Soo, H. S. Cobalt Complex of a Tetraamido Macrocyclic Ligand as a Precursor for Electrocatalytic Hydrogen Evolution. *Organometallics* **2019,** *38* (6), 1397.
(46) Izutsu, K.; International Union of, P.; Applied, C.; Commission on Electroanalytical, C. *Acid-base dissociation constants in dipolar aprotic solvents*; Blackwell Scientific Publications: Oxford, 1990.
(47) Kilgore, U. J.; Roberts, J. A. S.; Pool, D. H.; Appel, A. M.; Stewart, M. P.; DuBois, M. R.; Dougherty, W. G.; Kassel, W. S.; Bullock, R. M.; DuBois, D. L. $[Ni(P^{Ph}_2N^{C6H4X}_2)_2]^{2+}$ Complexes as Electrocatalysts for H_2 Production: Effect of Substituents, Acids, and Water on Catalytic Rates. *J. Am. Chem. Soc.* **2011,** *133* (15), 5861.
(48) Hu, X.; Cossairt, B. M.; Brunschwig, B. S.; Lewis, N. S.; Peters, J. C. Electrocatalytic hydrogen evolution by cobalt difluoroboryl-diglyoximate complexes. *Chem. Commun.* **2005**, 4723-4725.

Chapter 5

Photocatalytic Hydrogen Evolution with Cobalt Complexes Derived from Bis(methylimidazole) Ligands

Abstract

Photocatalytic hydrogen evolution with molecular complexes remains an ongoing interest in homogeneous catalysis. Herein, we successfully catalyzed and benchmarked the photocatalytic hydrogen evolution reaction (HER) using dicationic bis-ligated bis(methylimidazole)-based cobalt complexes **1**-**6**. The novel complexes **3**-**6** comprise two bis(methylimidazole)methane (BMIM) ligands with different methylene substituents; BMIM in **3** and **4**, bis(methylimidazole)methanone (BMIK) in **5**, bis(methylimidazole)methanol (BMIA) in **6**. Furthermore, **3** holds BF_4^- counterions, while **4**-**6** hold NO_3^- counterions. Spectroscopic studies on **3**-**6** demonstrated that their small steric encumbrance allows for solvent and nitrate coordination. Voltammetry studies on **4** show a suitable electrocatalytic reduction potential for electron transfer from the commonly used photosensitizer $[Ru(bpy)_3]^{2+}$, bpy = bipyridine. A photocatalytic reaction condition screening yielded ascorbic acid as the optimal electron and proton donor, $[Ru(bpy)_3](X)_2$, X = PF_6 or Cl_2 as the best photosensitizer and the addition of water was necessary for efficiency. Under fully aqueous conditions, the HER performance of complexes **4**-**6** further increased. The substitution of the methylene group in the ligand influenced the photocatalytic HER rate and stability: complexes **5** and **6**, bearing less electron-donating ligands, show lower initial rates but longer lifetimes. Benchmarking the HER performance of **4**-**6** to metal precursor $[Co(H_2O)_6(NO_3)_2]$, well-studied $[Co(dmgH)_2PyCl]$, dmgH = dimethylglyoxime, and high-performing photocatalyst [Co(appy)Br](Br), appy = bis-2,2′-bipyridine-6-yl(pyridine-2-yl)methanol, showed a competitive performance of **4**-**6** towards $[Co(dmgH)_2PyCl]$ but not to [Co(appy)Br](Br). These results demonstrate that bis(methylimidazole) cobalt complexes are active HER photocatalyst and that their HER performance is sensitive to (small) ligand perturbations.

S.D. de Vos, V. Ciurca, N. Dramountanis, M. Lutz, D.L.J. Broere, R.J.M. Klein Gebbink, *manuscript in preparation*

5.1 Introduction

Hydrogen (H_2) has the potential to replace carbon-based fuels as the energy carrier of the future, as it is one of the most abundant elements on earth, and its aerobic combustion in a fuel cell yields electricity with water as the only by-product.[1] However, most of the industrially produced H_2 is currently obtained from fossil resources in non-renewable processes, such as steam-methane reforming.[2] Thus, a major challenge is the production of hydrogen using renewable resources in green processes.[2] In this respect, solar energy is a particularly attractive renewable energy source to harness and exploit in the generation of H_2 from H_2O, an overall green process.[3] However, the direct conversion of water into hydrogen is a complex and challenging process. Not only does the process require a catalyst for splitting water into its constituent elements ($H_2O \rightarrow ½O_2 + 2H^+$), but it also requires a catalyst for reducing protons to molecular hydrogen ($2H^+ + 2e^- \rightarrow H_2$), also known as the hydrogen evolution reaction (HER). The development of highly active and efficient hydrogen evolution catalysts (HECs) for the HER is therefore an important challenge in tackling the energy transition. Two types of HECs are currently being investigated; i) electrocatalysts, which use a potential difference as a driving force (**Chapter 2-4**), and ii) photo-catalysts, that use light energy as their driving force, which is investigated in this chapter.

To investigate the performances of HECs under light irradiation, experimental solutions composed of a photosensitizer (PS), an HEC, and an excess of sacrificial proton and electron donor are irradiated with an appropriate light source **(Figure 1**).[4-9] In such systems, the PS is excited upon irritating and subsequently reduced by the sacrificial electron donor, producing a photogenerated reducing agent, which transfers an electron to the HEC.[5,10,11] When the first photochemical cycle is completed and an electron resides at the HEC, a new photochemical cycle takes place to provide the second electron for the HEC to produce hydrogen.[5,12,13] To study the reductive performances of HECs, photochemical experiments are performed in an organic solvent, in water, or in aqueous mixtures. Under non-aqueous conditions, tertiary amines are typically used as electron donors in combination with a strong acid as a proton

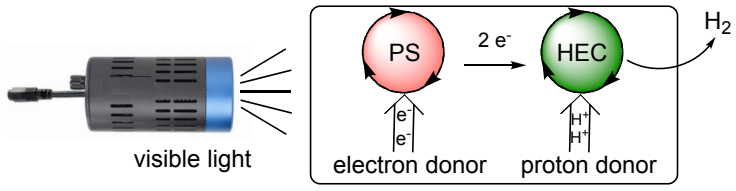

Figure 1. Overview of photocatalytic hydrogen evolution using visible light. PS = photosensitizer, HEC = hydrogen evolution catalyst.

donor, while under aqueous conditions ascorbic acid (AscH) is often used as both the proton as well as the electron donor. For both conditions, noble metal-based PSs, such as $Ru(bpy)_3$, are typically used; these are of particular interest because of their solubility and suitable electron transfer kinetics.[14,15] The use of organic photosensitizers has gained more common ground lately.[16,17] The redox potential energy levels of AscH and $[Ru(bpy)_3]^{2+}$, as well as its excited state $[Ru(bpy)_3]^{2+*}$, in water have been well documented.[10,12,18-21] The favorable thermodynamic redox potential analysis is described in **Chapter 1**, section 1.3.2.1, p31). The overall rate of H_2 formation is determined by the irradiation power, the quantum yield,[18,21] the rate of electron transfer to the HEC, the rate of decomposition of the reduced PS^-,[14,22-24] the rate of re-reduction of the sacrificial donor oxidation products,[25] and the total rate of H_2 formation by the HEC, the latter of which is studied in this chapter.

Early studies of HECs for photocatalytic HER systems have employed photosensitizers in combination with colloidal platinum as a heterogeneous catalyst, which remains one of the most performant catalysts in the field.[26,27] More recently there has been a strong interest in molecular HECs, because of their activity, uniform structure, and their high degree of tunability via synthetic modifications, providing many opportunities for optimization and studying the interactions between PSs and HECs.[28] Early examples of active molecular HECs include platinum and palladium-based complexes (**Figure 2**),[29,30] however, the scarcity of these noble metals do not qualify them as economically viable catalysts for large-scale applications. In this regard, first-row non-noble transition metal complexes based on iron,[31-36] nickel,[11,37-42] copper,[43-45] and especially cobalt (because of its activity) offer a viable alternative and have been shown to catalyze the light-driven reduction of protons in conjunction with suitable

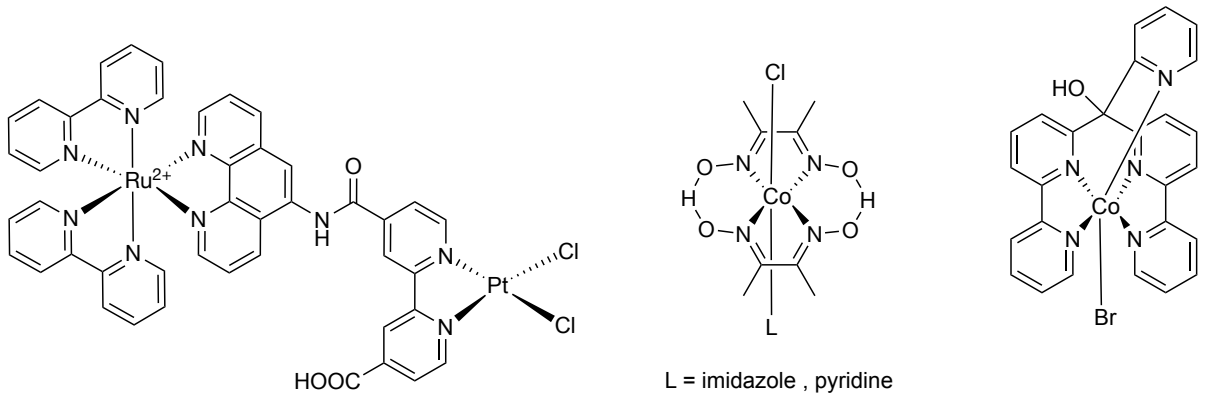

PS **Platinum** **Cobaloxime** **Polypyridyl**

(*Sakai*) (*Panagiotopoulos*) (*Alberto*)

Figure 2. Molecular photocatalytic hydrogen evolution catalysts (HECs). Sakai[29,30], Panagiotopoulos[83], Alberto[25].

photosensitizers.[7,46-64] Considering molecular cobalt-based catalysts, cobaloximes are one of the most well-studied systems in organic solvents and water/organic solvent mixtures.[5,7,55,59,65-83] For example, Panagiotopoulos *et al.* studied photocatalytic H_2 evolution by cobaloximes and reported the influence of the axial *N*-ligand at pH 7 in a MeCN/H_2O mixture (1:1 v/v),[83] finding that a more electron-rich axial ligand such as *N*-methylimidazole gave higher turnovers per hydrogen evolution catalyst (1131 TON(HEC)s), compared to *para*-methylpyridine (443 TON(HEC)s) (**Figure 2**). The more strongly bound imidazole ligand resulted in a longer-lived catalyst with a lower initial turnover rate, while the more weakly coordinated pyridine ligand gave a faster initial rate but resulted in a shorter-lived catalyst. However, cobaloximes tend to suffer from ligand hydrolysis, causing limited rates and poor stability under catalytic conditions, and can therefore show poorer activity under aqueous conditions.[67,78] Other cobalt-based systems have also been studied, including those based on porphyrins,[10,84-89] dithiolenes,[20,42,90-96] *N*-heterocyclic carbenes,[97] diphenylamine macrocycles,[48] pincer ligands,[98] salen-type N,O-ligands,[99-103] peptides,[62] and, in particular, polypyridyl ligands.[25,48,49,104-109] Indeed, polypyridyl cobalt complexes show improved catalytic activities (up to 33,000 TON(HEC)s) and stabilities, as a result of the robustness of the ligand under strongly reducing conditions (**Figure 2**).[25] In addition, polypyridyl complexes can efficiently perform HER catalysis in a purely aqueous environment, which is an important step forward because using water as both the solvent and the substrate (considering the overall water splitting reaction) increases substrate concentration, minimizes organic additives and waste by-products, and represents industrial conditions.[48,110,111]

Recently, our group has reported on the dicationic cobalt complex $[Co(HBMIM^{Ph2})_2](BF_4)_2$ (**1**), comprising two neutral $HBMIM^{Ph2}$ diimine ligands, and its use as an electrocatalytic HEC (**Figure 3**).[13,112] Cyclic voltammetry experiments showed an irreversible, peak-shaped reductive response for **1** in organic solvents (MeCN and DMF) at –1.96 V vs Fc^+/Fc, which was assigned to the fast reduction of Co(II) to Co(I). Combined experimental and DFT studies supported that **1** undergoes H-atom loss upon reduction (either electrochemically or chemically using KC_8) and consecutive H_2 formation, resulting in formal deprotonation and generation of cobalt complex $[Co(HBMIM^{Ph2})(BMIM^{Ph2-})](BF_4)$ (**1a**), containing one deprotonated $BMIM^{Ph2-}$ ligand. Under catalytic conditions, protonation restores complex **1** and closes a catalytic cycle. Isolation and characterization of **1a** in combination with mechanistic investigations using DFT suggested that dihydrogen formation proceeds via the intramolecular combination of an intermediate Co^{III}–H moiety with a ligand C–H proton, demonstrating the bifunctionality of the complex and a unique HER mechanism. In **Chapter 2** the bifunctional

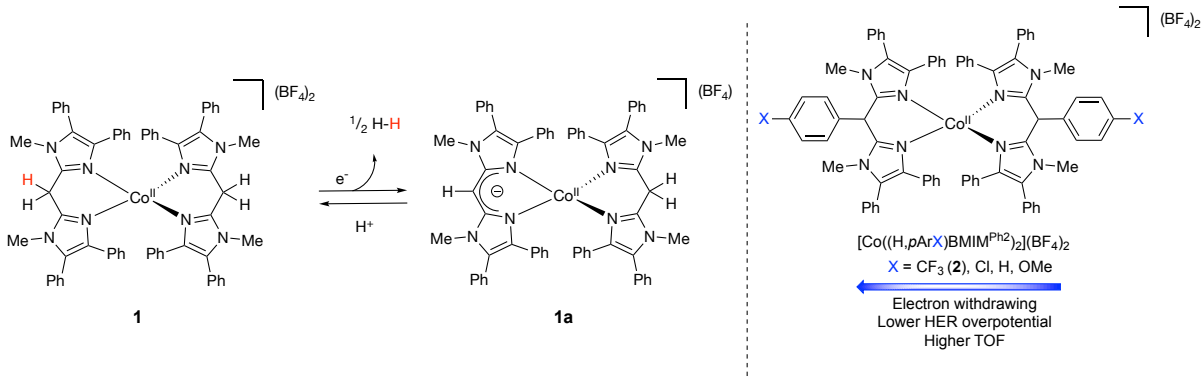

Figure 3. Previous work: left; ligand-mediated HER reactivity for $[Co(HBMIM^{Ph2})_2](BF_4)_2$ (**1**), right; substituent study with enhanced HER performance, including complex $[Co((H,pArCF_3)BMIM^{Ph2})_2(BF_4)_2$ (**2**).

character of complex **1** was further demonstrated by a substituent study in which para-substituted aryl groups with electron-withdrawing functionalities lower the overpotential while increasing the HER activity. In a different follow-up study, HER performance tests were carried out by means of bulk electrolysis with triethylammonium (as a proton source) in DMF using a rotating glassy carbon disk electrode in an electrochemical cell with in-line product detection (**Chapter 4**). This study showed that **1** is a competitive HEC compared to cobalt porphyrin, glyoxime, and polypyridyl complexes in terms of Faradaic efficiency (FE), overpotential, and H_2 production. Furthermore, post-electrolysis analysis revealed that for all molecular complexes tested not merely the pristine complexes, but also a formed electrode deposit significantly contributes to the observed and distinct HER activity. Nevertheless, this study also showed that the molecular design of the catalysts influences the composition of the deposit and therewith the observed activity in the model electrolysis cell.

Inspired by the highly active photocatalytic cobalt polypyridyl complexes, we were interested to test our active electrocatalysts based on complex **1** as homogenous photocatalysts. Furthermore, we wanted to address our desire to develop a water-soluble molecular HEC to meet the overall water-spitting conditions. Next to that, the finding by Panagiotopoulos *et al.,* of increased HER activity using an axial imidazole over a pyridine ligand, made us curious if such an effect could be extrapolated to an imidazole-based ligand. Therefore, we tested a series of cobalt complexes comprising bis(methylimidazole) ligands as photocatalytic HECs. In this study, we included two of our earlier reported cobalt electrocatalysts with bulky imidazole ligands (**1** and **2**) (**Figure 3**),[13,112[Chapter 2]] the well-studied cobaloxime complex $[Co(dmgH)_2PyCl]$, dmgH = dimethylglyoxime, and one of the most active HECs in the field, polypyridyl complex [Co(appy)Br](Br), appy = bis-2,2″-bipyridine-6-yl(pyridine-2-

yl)methanol (**Figure 2**).[5,13,107] To extend the operational conditions of our bis(methylimidazole) complexes to aqueous media, we synthesized four water-soluble cobalt complexes (**3**-**6**) based on the bis(methylimidazole)methane ligand framework **(Figure 4**). These complexes comprise ligands absent of the bulky hydrophobic phenyl groups, as well as sterically and electronically different linker groups between the imidazole groups, in order to get a better understanding of the electronic and steric properties of the complexes with respect to their catalytic properties.[113-115] The ligands include the methylene linker in HBMIM (structurally similar to HBMIM^{Ph2}) and thus holding a C–H proton relay, the carbonyl linker in BMIK, which is absent of such a proton relay, and the alcohol linker in HBMIA retaining one C–H bond on the methylene moiety.

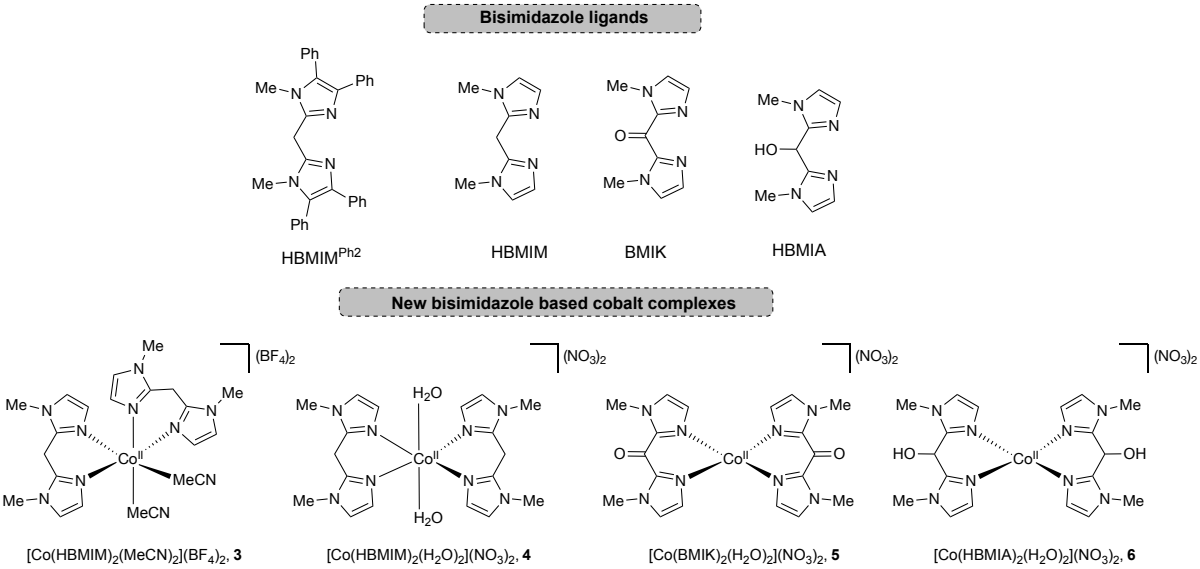

Figure 4. Bis(methylimidazole) ligands and their corresponding cobalt(II) complexes used in this study. Complexes **3** and **4** are depicted as their crystal structures obtained from acetonitrile and water solutions, respectively. Nitrate coordination in complexes **5** and **6** is not explicitly shown.

5.2 Results and Discussion

5.2.1 Synthesis of cobalt complexes

Cobalt complexes **3**-**6** were synthesized by reacting $Co(BF_4)_2 \cdot 6H_2O$ or $Co(NO_3)_2 \cdot 6H_2O$ and the corresponding ligand in a 1:2 molar ratio in THF, from which the complexes precipitate as pinkish powders in good yields (**3** = 86%, **4** = 92%, **5** = 87%, **6** = 84%). In all cases, elemental analysis revealed that the complexes were obtained as pure materials, comprising two ligands (L = HBMIM, BMIK, or HBMIA), one cobalt ion, two counterions (X = BF_4^- or NO_3^-), and no solvent molecules. Mass spectrometry analysis on MeCN solutions demonstrated a strong

signal at *m/z* = 410.0 for $[Co(HBMIM)_2–H]^+$ for **3** and at *m/z* = 409.9 for $[Co(HBMIM)_2–H]^+$ for **4** (Appendix D, Figure D1 and D2, for **3** and **4**, respectively). For **5** and **6** several signals were observed, including signals at *m/z* = 439.1 for singly reduced $[Co(HBMIK)_2]^+$, at *m/z* = 542.0 for the solvated ion $[Co(HBMIK)_2+NO_3+MeCN]^+$, and at *m/z* = 456.0 for $[Co(BMIK)_2+OH]^+$ for **5**, and at *m/z* = 442.1273 for $[Co(HBMIA)_2+NO_3]^+$ and at *m/z* = 505.1228 $[Co(HBMIA)_2+NO_3]^+$ for **6** (Appendix D, Figure D3 and D4 for **5** and **6**, respectively). These MS data indicate that in the gas phase the nitrate ions do not coordinate in **4** and are weakly coordinating in **5** and **6,** while MeCN appears to coordinate to the cobalt center in **5**, but not in **3**, **4**, and **6**. In our initial studies, we also included the HBMIP ligand,[116] comprising a carboxylic acid functional group at the methylene moiety, for which we hypothesized that the carboxylic acid functionalities would increase water solubility and enhance HER activity by acting as an outer sphere proton shuttle, as was observed, *e.g.* in the work of Beyene *et al.*[10,117] Unfortunately, no pure batches of a corresponding cobalt complex could be obtained (see experimental section, compound **7**) and preliminary tests with the obtained batches resulted in poor photocatalytic HER activities (*vide infra*).

5.2.2 X-ray crystal structure analysis

Single crystal X-ray structure determination of $[Co(HBMIM)_2(MeCN)_2](BF_4)_2$ ($\mathbf{3^{2MeCN}}$) was accomplished with a red/brown crystal obtained from slow vapor diffusion of diethyl ether into a concentrated solution of **3** in MeCN at –40 °C. Yellow single crystals suitable for X-ray structure determination of $[Co(HBMIM)_2(H_2O)_2](NO_3)_2$ ($\mathbf{4^{2H_2O}}$) were obtained by cooling down a concentrated solution of **4** in H_2O from 70 to 0 °C. The molecular structures of $\mathbf{3^{2MeCN}}$ and $\mathbf{4^{2H_2O}}$ are depicted in **Figure 5**, with selected bond distances and angles compiled in **Table 1**. The molecular structure of $\mathbf{3^{2MeCN}}$ shows an hexacoordinated cobalt center surrounded by two HBMIM ligands and two mutually *cis*-coordinated MeCN molecules, $[Co(HBMIM)_2(MeCN)_2](BF_4)_2$. The molecular structure of $\mathbf{4^{2H_2O}}$ consists of a centrosymmetric, hexacoordinated cobalt center coordinated by two HBMIM ligands in the equatorial plane and two mutually *trans* water molecules occupying the axial positions, hydrogen bonded to the nitrate anions. In MS analysis, solvent coordination was only observed for **5**. The observation of solvent coordination in crystals grown from **3** and **4** shows that solvent coordination is also possible for these complexes, and indicates the lability of the coordinated solvent molecules. The combined results of the crystal structures and ESI-MS analysis also highlight the coordinative flexibility of the HBMIM ligand and show that its smaller steric bulk

Table 1. Selected bond distances (Å) and angles of $[Co(HBMIM)_2(MeCN)_2](BF_4)_2$ (**3**^{2MeCN}) and $[Co(HBMIM)_2(H_2O)_2](NO_3)_2$ (**4**^{2H_2O}).

$[Co(HBMIM)_2(MeCN)_2](BF_4)_2$ (**3**^{2MeCN})			
Bond	Lengths	Bond Angle	Degrees
Co1–N11	2.1564(7)	N11–Co1–N31	87.45(6)
Co1–N12	2.1160(7)	N12–Co1–N32	87.11(6)
Co1–N13	2.1229(7)	N13–Co1–N14	91.35(6)
Co1–N14	2.1792(15)		
Co1–N31	2.1089(15)		
Co1–N32	2.1161(14)		
N32–C62	1.326(2)		
C62–C12	1.489(3)		
C12–C22	1.496(2)		
C22–N12	1.328(2)		

$[Co(HBMIM)_2(H_2O)_2](NO_3)_2$ (**4**^{2H_2O})			
Bond	Lengths	Bond Angle	Degrees
Co1–O1	2.1564(7)	O1–Co1–N1	90.03(3)
Co1–N1	2.1160(7)	O1–Co1–N3	90.85(3)
Co1–N3	2.1229(7)	N1–Co1–N3	85.05(3)
N1–C3	1.3284(11)		
N3–C5	1.3291(11)		
C4–C5	1.5004(12)		

allows for higher coordination numbers in **3** and **4** compared to the bulkier HBMIM^{Ph2} ligand, which gives rise to a four-coordinate, tetrahedral structure in **1**.[13] A further comparising of the crystal structures of **3**^{2MeCN} and **4**^{2H_2O} shows that the Co–N metal to ligand bond distances and the internal bond distances in the HBMIM ligand are comparable, despite the different orientations of the solvent molecules. The distinct color difference between these crystals, *i.e.* red/brown for **3**^{2MeCN} and yellow for **4**^{2H_2O}, may be indicative of the mutual orientation of the coordinated solvent molecules, *i.e. cis* in **3**^{2MeCN} and *trans* in **4**^{2H_2O}. Attempts to grow single crystals of sufficient quality for X-ray diffraction analysis for **5** and **6** were unsuccessful.

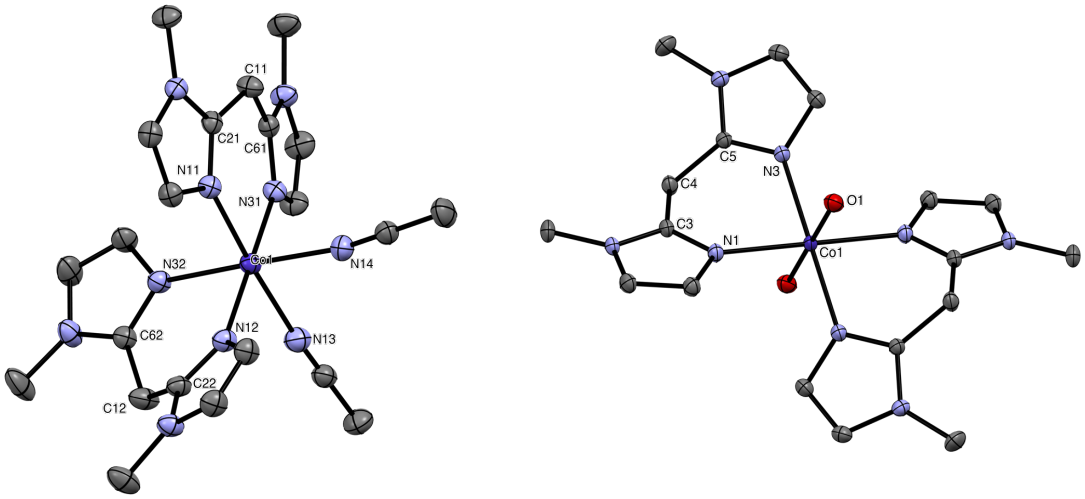

Figure 5. Displacement ellipsoid plots of $[Co(HBMIM)_2(MeCN)_2](BF_4)_2$ (**3**^{2MeCN}, left) and $[Co(HBMIM)_2(H_2O)_2](NO_3)_2$ (**4**^{2H_2O}, right), shown at the 50% probability level. The molecule in **4**^{2H_2O} is presented as an auto-completed metal complex. H-atoms and BF_4 counterions have been omitted for clarity. Symmetry code *i*: 1-x, 1-y, 1-z.

5.2.3 Infrared spectroscopy

Solid-state infrared spectra for complexes **3**-**6** were recorded between 4000 and 800 cm^{-1} (Appendix D, Figure D6-D9) and the imidazole and nitrate vibrations (when applicable) are listed in **Table 2**. These spectra were used to identify the coordination mode of the nitrate ions in complexes **4**-**6**, which could be bound to cobalt in a unidentate, bidentate, or bridging fashion, or be present as free ionic species.[118] In addition, more than one nitrate coordination mode would be possible in **4**-**6** due to the presence of two nitrate ions per cobalt ion.

Hodgson *et al.* described and assigned the vibrations of $[Co(Him)_6](NO_3)_2$ and $[Ni(Him)_6](NO_3)_2$ (Him = imidazole).[119] For the latter, additional structural determination by means of X-ray crystal structure determination revealed the nitrates as free ionic nitrate groups.[120] Of the four normal vibrational modes of a nitrate ion (ν_1-ν_4), ν_1 (which occurs near 1050 cm^{-1}) is IR-inactive but frequently appears in the spectra of complexes in which NO_3^- lies outside the coordination sphere as a result of relaxation of the free ion selection rules under the constraint of the crystal field. The other vibrational modes ν_2 (which occurs near 760, 773, and 825 cm^{-1}), ν_3 (which occurs near 1373 cm^{-1}), and ν_4 (which occurs at 710 cm^{-1}) all appear around the expected wavelength for an ionic nitrate for $[Co(Him)_6](NO_3)_2$ (**Table 2**).[119] In a different study, Curtis and Curtis described that in the combination tone region (1800-1700 cm^{-1}) the ν_1 + ν_4 combination bands of the nitrate (found around 1750 cm^{-1}) are most suited for the

Table 2. NO_3^- and imidazole IR vibrations of complexes $[Co(Him)_6](NO_3)_2$, $[Ln(L)(NO_3)_2]$, $[Co(py)_3(NO_3)_2]$, and **3**–**6**.

IR-vibrations	$[Co(Him)](NO_3)_2$	$[Ln(L)(NO_3)_2]$	$[Co(py)_3(NO_3)_2]$	**3**	**4**	**5**	**6**
NO_3 (coordinated)							
ν_1		1468-1440	1294	-	1289	1290	1288
ν_2		1030-1040	1033	-	1033	1029	1034
ν_3				-			
ν_4			1482	-	1463	1482	1462
ν_5		1320-1283		-	1333		
NO_3 (free ionic)							
ν_1				-	1051	1050	1046
ν_2	825, 773w, 760w			-	811	830	825
ν_3	1373	1380		-	1372	1370	1382
ν_4	710			-			
ν imidazole ring	1536, 1505, 1490, 1436, 1323, 1252, 1067-1136	-	-	1521, 1410, 1293, 1150 1103, 1060, 1033	1542, 1515, 1413, 1243 1134, 1085	1534, 1414, 1341, 1251, 1174, 1090	1510, 1399, 1307, 1189, 1148, 1143, 1085

distinguishment between different coordination modes of the nitrate in coordination complexes.[121,122] When the vibrations appear weak in intensity, the features indicate the exclusive presence of ionic nitrates.[123-126]

For unidentate, bidentate, or bridging nitrates the ν_1-ν_5 are typically found between 1468-1440 and 1320-1300 cm^{-1} (**Table 2**), as described by Gaye *et al.,* Alexander *et al.*, and Guerriero *et al.* for a series of lanthanide(III) nitrate complexes with 2,6-bis-(salicylaldehydehydrazone)-5-chlorophenol, diimine-diamine macrocyclic, and Schiff base ligands, respectively.[127-129] The separation $\Delta\nu$ of ν_1-ν_5 is used to differentiate between mono and bidentate chelating nitrates in which a large $\Delta\nu$ (140-200 cm^{-1}) indicates a strong interaction of the oxygen atoms of the nitrate with the metal center and is typical for bidentate and/or bridging coordinating modes.[130-132] In the combination tone region the $\Delta\nu$ splitting of the ν_2+ν_5 and ν_3+ν_5 for bidentate coordination is smaller (~25-40 cm^{-1}).[132] In addition, Ferarro *et al.* described the mono- and bidentate coordination for Cu and Co pyridine (py) complexes, respectively, of the type $[M(py)_3(NO_3)_2]$.[133] The vibrational modes (ν_1-ν_5) are differently assigned but include the same vibrations (**Table 2**). The separation $\Delta\nu$ of ν_1-ν_4 is 102 cm^{-1} for monodentate nitrate coordination in $[Cu(py)_3(NO_3)_2]$ and 188 cm^{-1} for bidentate nitrate coordination in $[Co(py)_3(NO_3)_2]$. In the combinational tone region, the $\Delta\nu$ (ν_2+ν_3)-(ν_2+ν_5) of $[Cu(py)_3(NO_3)_2]$ is 12 cm^{-1} *vs.* 37 for $[Co(py)_3(NO_3)_2]$. For complex **3** the imidazole vibrations are observed between 1521 and 1033 cm^{-1} and are slightly shifted compared to those reported for $[Co(Him)_6](NO_3)_2$. The absorbance at 1000 was assigned to the BF_4 ion.[134] For **4**, typical

vibrations for free ionic nitrates as well as for coordinated nitrates are observed. The $\Delta\nu$ between the ν_1-ν_4 vibrations is 174 cm^{-1} (1289–1463), indicative of bidentate nitrate coordination. In the combinational tone region, a very weak and broad vibration at 1762 cm^{-1} is observed, which was not further assigned. Upon dissolving **4** in water a strong vibration at 1348 cm^{-1} was observed, which we assigned to the free ionic nitrate (Appendix D, Figure D8). For **5** and **6** free ionic nitrates and coordinated nitrates are also observed, for which the coordinated nitrates $\Delta\nu$ between the ν_1-ν_4 vibrations is 174 (1288–1462) and 192 (1290–1482), respectively, indicative of bidentate nitrate coordination. No signals in the combinational tone region appear strong enough for the assignment.

Based on the above IR-analysis, we conclude that in the solid state of **4-6,** both free nitrate ions, as well as coordinated nitrates, are present. Based on the $\Delta\nu$ between the ν_1-ν_4 vibrations of the coordinated nitrate molecules, we expect a bidentate (or bridging) coordination mode for all complexes. Upon dissolving the complexes in water, we expect all nitrates to be present as free ionic nitrate ions, which agrees with the obtained crystal structure of **4**. Between **4-6**, the most significant spectral differences are found between 1700 and 800 cm^{-1} and are predominantly associated with the imidazole vibrations of the different ligands and changes in the N–O bond vibrations, as was reported before.[135-138] Furthermore, in all spectra, the absence of an intense absorption band around 3600-3500 cm^{-1}, belonging to OH stretching vibrations of interstitial water and hydroxyl groups, indicates no hydroxyl-based cluster formation and the absence of water, which complements the elemental analysis and MS data.[135139] For the free BMIK ligand (present in **5**) a sharp signal for the C=O stretching vibration is reported at 1632 cm^{-1}.[113] The binding of BMIK to the Lewis acidic cobalt center in **5** results in a shift to a higher wavenumber and the C=O stretching vibration is now found at 1650 cm^{-1}. A similar shift was reported before for BMIK binding to an iron(III) metal center.[140] For **6**, a broad band was observed at 3379 cm^{-1}, attributed to the OH stretch vibrations of the HBMIA ligand.

5.2.4 NMR analysis

Upon dissolution of **3-5** in DCM-d_2 the complexes retain their color and pink solutions are formed. The ^{1}H-NMR spectra of these solutions all show one major paramagnetic species with distinct signals between 10 and 47 ppm (**Figure 6**). **6** dissolves very poorly in DCM-d_2 and its resulting ^{1}H-NMR spectrum demonstrates a poor signal-to-noise ratio (Appendix D, Figure D12). For **3**, integration of the signals reveals that the methyl resonance is found around 11 ppm, while the imidazole hydrogen atoms and the methylene hydrogen atoms are more

downfield shifted to 47, 29, and 22 ppm, which all relatively integrate for one hydrogen atom. We attribute the observed resonances to two HBMIM ligands with an internal mirror plane coordinated to cobalt in a highly symmetric manner. Based on the pink color and the non-coordinating BF_4^- anions and solvent, we propose a tetrahedral geometry with a $[Co(HBMIM)_2](BF_4)_2$ composition. For **4**, the methyl resonance is found at 10 ppm, the methylene resonance at 32 ppm, and the imidazole resonances overlap at 43 ppm; all resonances are assigned based on integration and chemical shift. Furthermore, in the spectrum of **4**, a minor paramagnetic species with resonances at the same position as **3** were observed. This minor species is proposed to have a solution structure similar to **3**, in which the counterions are non-coordinating ($[Co(HBMIM)_2](NO_3)_2$). Since nitrate ions are poorly soluble in DCM, the major species, in which the HBMIM ligands seem to have a different coordination environment around cobalt compared to complex **3**, is assigned to a structure in which either one or two nitrate ions are coordinated to cobalt, *i.e.* $[Co(HBMIM)_2(NO_3)](NO_3)$ or $[Co(HBMIM)_2(NO_3)_2]$. The limited number of resonances and the broadness of the resonances observed for this species indicate a high overall symmetry of the HBMIM ligands around the cobalt center. For **5**, very broad signals are observed at 43, 26, and 12 ppm, which are assigned to the imidazole hydrogen atoms and methyl hydrogen atoms, respectively, based on integration and match a $[Co(BMIK)_2(NO_3)_2]$ composition. Also, an additional minor species was observed, which was assigned to either $[Co(BMIK)_2(NO_3)](NO_3)$, or $[Co(BMIK)_2](NO_3)_2$, where one or no nitrates are coordinated. Complexes **4**-**6** were also analyzed by ^{1}H-NMR in

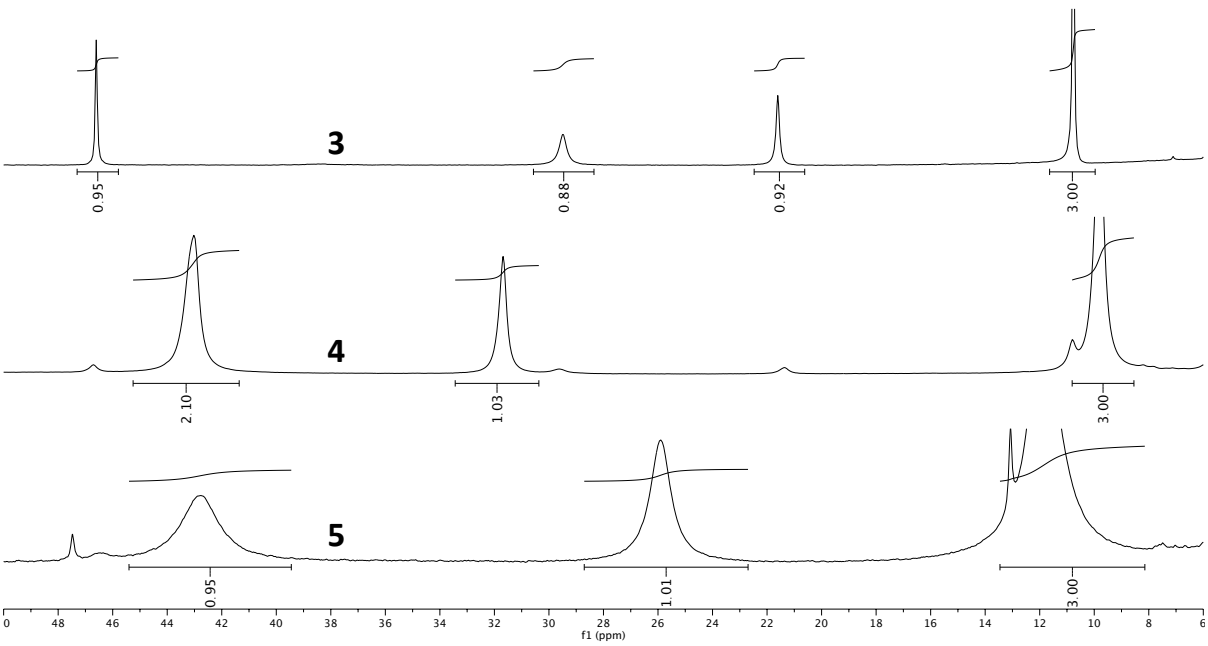

Figure 6. Stacked ^{1}H-NMR (400 Hz) spectra of **3**-**5** (L = HBMIM (**3**,**4**), BMIK (**5**)) in DCM-d_2.

water-d_2, demonstrating clear paramagnetic signals; **3** is not soluble in water-d_2. In water-d_2, **4**-**6** form yellow solutions, and show paramagnetic resonances between 47 and –27 ppm (**Figure 7**). The color change from pink (isolated powders and DCM solution) to yellow (aqueous solution) is attributed to the (*trans*) coordination of water molecules, as indicated by the X-ray crystal structure obtained from a yellow crystal of $\mathbf{4^{2H_2O}}$ (vide supra). The spectrum of **4** shows one major paramagnetic species with signals at 45, 41, 19, and 12 ppm and a minor species with resonances at 34 and 25 ppm. Integration of the major resonances reveals three strongly shifted resonances (45, 41, and 19 ppm) that match the methylene and imidazole hydrogen atoms and shows that the methyl hydrogen atoms and coordinated water hydrogen atoms are found together at 12 ppm. The NMR spectrum is consistent with spectroscopically equivalent HBMIM ligands with an internal mirror plane. The ^{1}H-NMR spectrum of **5** in water-d_2 demonstrates several strongly paramagnetically shifted and broad signals between 47 and –7 ppm, including somewhat shaper signals at 47, 40, and 13 ppm and more broadened signals at 42, 14, 10, –5, and –7 ppm. For **6**, multiple resonances between 43 and 0 ppm were observed, that all appear in pairs and hold different intensities. For **5** and **6**, we suggest that the different resonances originate from the coordination of water-d_2 and the exchange of water-d_2 and nitrate molecules upon dissolving the complexes in water, which is corroborated by the parallel ^{1}H-NMR experiment in DCM-d_2.

Overall, the above analyses demonstrate that in the isolated pink solids, complex **3** is bis-ligated by two bis(methylimidazole) ligands with non-coordination BF_4^- counterions, while complexes

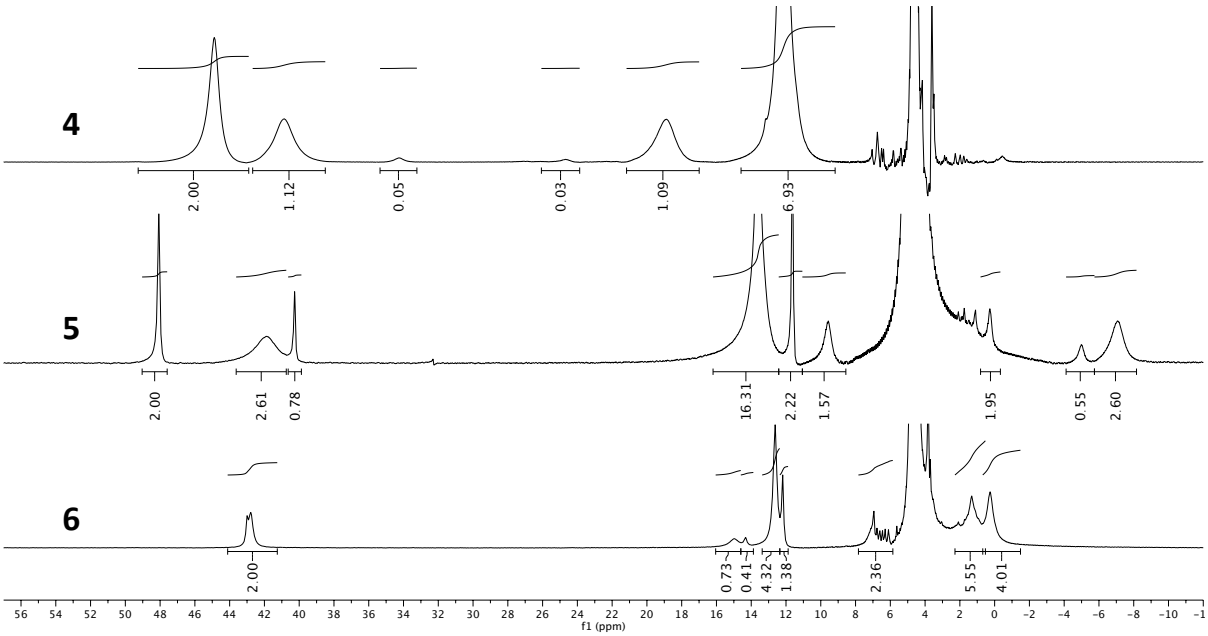

Figure 7. Stacked ^{1}H-NMR (400 Hz) spectra of **4**-**6** (L = HBMIM (**4**), BMIK (**5**), HBMIA (**6**), in water-d_2.

4-**6** are bis-ligated and contain both coordinated and free ionic nitrates as indicated by solid-state IR-analysis. X-ray crystal structure determination on crystals grown from coordinating solvents show that two solvents molecules bind to the 6-coordinated cobalt centers in $\mathbf{3}^{\mathbf{2MeCN}}$ and $\mathbf{4}^{\mathbf{2H_2O}}$, and that the BF_4^- and NO_3^- ions are not coordinated. ESI-MS analysis on MeCN solutions of the complexes indicate nitrate coordination for **5** and **6**. The BMIM ligand is suggested to be more donating compared to the BMIK and BMIA ligands, making the cobalt center in **5** and **6** a better Lewis acid that is more likely to bind a NO_3^- counterion. Solutions of **3**-**5** in DCM remain pink and the ^{1}H-NMR spectra show a single (major) species. Dissolution of **4**-**6** in water demonstrated an immediate color change from pink (powders) to yellow (solutions). The corresponding ^{1}H-NMR spectrum of **4** is consistent with the X-ray crystal structure of $\mathbf{4}^{\mathbf{2H_2O}}$ obtained from a saturated water solution. The aqueous ^{1}H-NMR spectra of **5** and **6** reveal the presence of several paramagnetic species, which is attributed to water coordination and the involvement of nitrate ions in the coordination chemistry of these complexes.

Accordingly, complexes **3**-**6** can be isolated as solvent free complexes from their synthesis in THF, in which the complexes do not dissolve. Both coordinated and non-coordinated nitrate ions are present in complexes **4**-**6**. Upon dissolution in a non-coordinating solvent like DCM, the structure of the complexes does not change significantly. Dissolving complexes **4**-**6** in a coordinating solvent like water or MeCN induces the coordination of solvent molecules to cobalt and leads to a speciation of the complexes that involve labile solvent and possible nitrate coordination. Next, we aimed to investigate the redox chemistry and the acid stability of the imidazole-based cobalt complexes. Complex **4** was selected as the starting point in these investigations as its molecular structure in water is known through single X-ray crystal structure analysis and its ^{1}H-NMR features are more uniform in contrast to those of **5** and **6**.

5.2.5 The interaction of 4 with ascorbic acid (AscH)

We investigated the stability of **4** in the presence of a proton/electron donor (photocatalytic conditions). Under aqueous photocatalytic conditions, ascorbic acid (AscH) is the most applied proton and electron donor, hence, we studied the aqueous photocatalytic HER activity of our complexes using AscH (*vide infra)*. ^{1}H-NMR spectra of **4** in the presence and absence of 1 equiv. ascorbic acid (AscH) were recorded in water-d_2 (**Figure 8**). The presence of free AscH was observed outside the paramagnetic region (at 4.80, 3.91, and 3.6 ppm). Intensified paramagnetic resonances of the minor species present in the spectrum of **4** were observed at

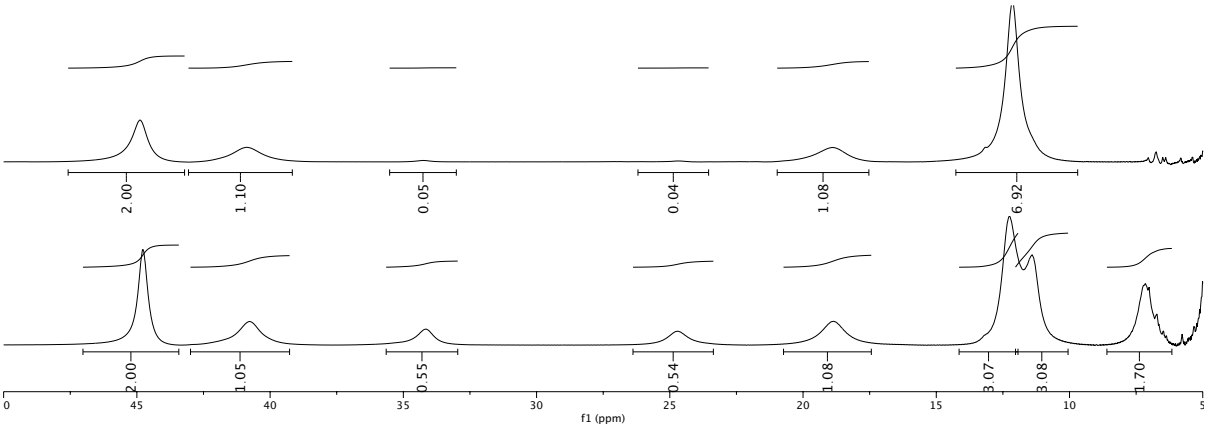

Figure 8. Top: The ^{1}H-NMR (400 Hz) spectrum of $[Co(HBMIM)_2](NO_3)_2$ (**4**) in water-d_2. Bottom: overlay NMR spectra of **4** in water-d_2 + 1 equiv. ascorbic acid. Intensified resonances at 34, 25, 11, and 7 ppm.

34, 25, 11, and 7 ppm. The emerged resonances represent the same number of signals, but show a somewhat different relative integration as the major species. Therefore, we suggest that two structurally related species of **4** are present in the solution (for example, $\mathbf{4}^{\mathbf{2H_2O}}$, $\mathbf{4}^{\mathbf{H_2O}}$, **4**, $\mathbf{4}^{\mathbf{NO_3}}$, and/or $\mathbf{4}^{\mathbf{2NO_3}}$). The effect of AscH on the speciation of **4** is likely related to a change in the pH of the solution, possibly increasing the rate of H_2O exchange at cobalt, causing a decrease in the observed resonance intensity at 12 ppm. The absence of new paramagnetic resonances indicates that neither AscH nor the ascorbate ion coordinates to **4**. These ^{1}H-NMR spectra indicate that in aqueous (photocatalytic) HER experiments using **4** in combination with AscH, a mixture of two structurally related cobalt species is present. The UV-vis absorption spectrum of **4** (0.1 mM) in degassed MiliQ water exhibits a strong band at 331 nm (π– π^*) with a broad shoulder at 480 nm (MLTC), (**Figure 9**, green trace). Upon the addition of 1000 equiv. ascorbic

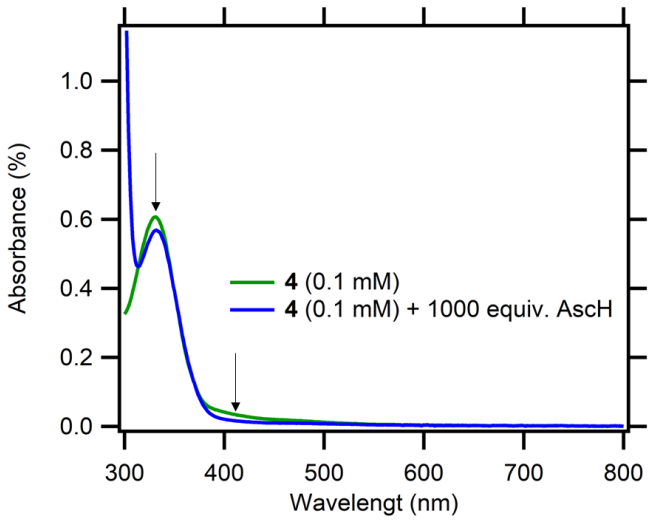

Figure 9. Overlay of the UV-vis spectra of $[Co(HBMIM)_2](NO_3)_2$ (**4**) in H_2O with and without AscH (blue and green traces, respectively).

acid (AscH), as a solid, no visible color change in the yellow solution was observed. The absorption spectrum revealed a small decrease in band intensity at both 331 nm and 480 nm (**Figure 9**, blue trace). We attributed the decrease to the structural changes observed by ^{1}H-NMR**.** UV recordings in the presence of the ([Ru(bpy)$_3$](Cl$_2$) PS and post photocatalytic UV-vis recordings did not provide any useful insight regarding **4**, due to the dominant features of [Ru(bpy)$_3$](Cl$_2$). Overall, we conclude that **4** does not decompose in the presence of large amounts of AscH.

5.2.6 Electrochemical analysis

We analyzed **4** electrochemically in water to determine the reduction potential of the complex, which will allow the selection of a PS for which an electron transfer between the reduced PS and **4** is thermodynamically favorable, and submitted **4** to electrocatalytic HER conditions to confirm that it is able to participate in a catalytic redox reaction involving protons. For these experiments, we used a mercury drop working electrode, known for its cathodic reduction potentials for HER in comparison to other electrode materials (*e.g.* Pt, Au, and glassy carbon).[141] A new mercury electrode drop was used for each experiment to avoid the interference of electrode modifications, such as electrode deposits (see **Chapter 4**).[142-145] We selected KNO$_3$ as an electrolyte to ensure the exclusive presence of nitrate counterions in the solution. The electrochemical response of a solution of **4** in degassed MilliQ H$_2$O (0.1 M KNO$_3$) displayed one major irreversible reduction at $E_{p,c}$ = –1.22 V vs. Ag/AgCl (**Figure 10**, left), assigned to the Co(I/II) reduction with a follow-up chemical reaction, such as the formation of H$_2$.[146] After the major reductive event, a minor reduction event was observed at $E_{p,c}$ = –1.42 V vs. Ag/AgCl, and on the reserve sweep a minor oxidation event was observed at $E_{p,a}$ = –1.35 V vs Ag/AgCl. These responses could originate from a minor impurity and were not further investigated as those were observed at more cathodic potentials. Further anodic, a quasi-reversible redox response was observed at $E_{1/2}$ = –0.3 V, which we tentatively assigned to the Co(II/III) redox couple.

Then, AscH was added to determine the participation of **4** in (electrocatalytic) reduction catalysis with protons from AscH (*vide infra*). The addition of 10 equiv. AscH gave rise to a small reductive response at –0.78 V, which was not further investigated **(Figure 10** right, red trace). At more cathodic potentials a pre-wave and a catalytic current arise at the Co(I/II) reduction potential of **4**. Based on the above NMR analysis, these events are assigned to two structurally related forms of **4**. A pre-wave is also a reliable indication of a (potentially

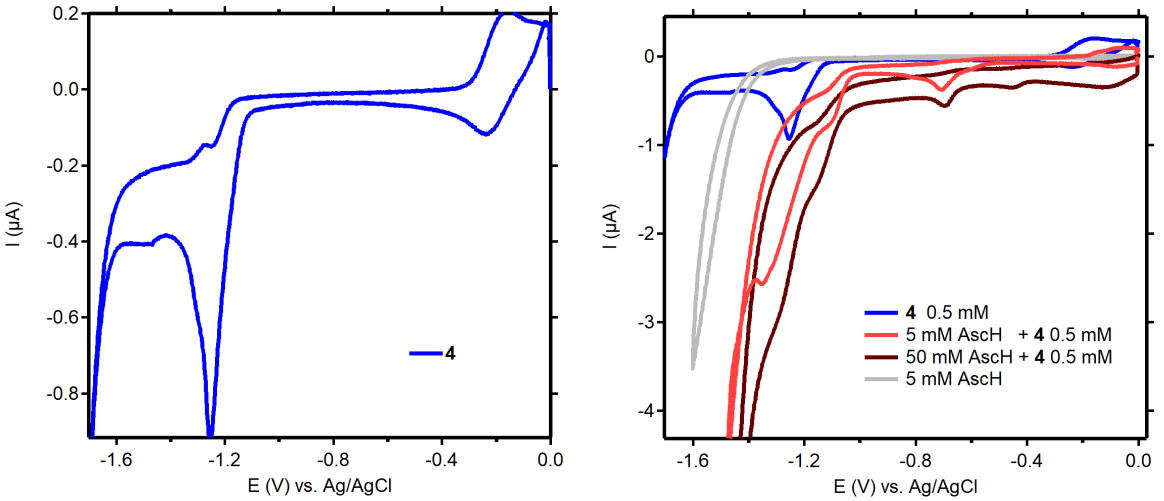

Figure 10. Left: Cyclic voltammogram of $[Co(HBMIM)_2](NO_3)_2$ (**4**) (blue) 0.5 mM in an H_2O (0.1 M KNO_3). Right: red: **4** + 10 equiv. ascorbic acid (AscH), brown: **4** + 100 equiv. AscH, gray blank with 5 mM AscH. Scans are all started at 0 V vs Ag/AgCl and scanned first in the cathodic direction. Scan rate 100 mV/s. Potentials vs Ag/AgCl. Working electrode: Hg drop. Counter-electrode: Carbon rod. Reference electrode: Ag/AgCl.

protonated) species that participates in a catalytic sequence but needs a more negative potential to undergo a necessary second electron transfer, which is plausible as well.[147-152] The catalytic current was assigned to an electrocatalytic HER reaction. The onset potential of the background reaction occurs at a significantly more cathodic potential (**Figure 10** right, gray trace). Upon increasing the AscH concentration to 50 mM (100 equiv.), the baseline intensification and the increased electrocatalytic responses confirm a higher rate of electron transfer (**Figure 10** right, brown trace). This confirms that **4** participates in an electrocatalytic reduction reaction with AscH.

5.2.2 Photocatalysis

We compared the photocatalytic proton-reducing performances of bisimidazole cobalt complexes **1**-**6**, $[Co(dmgH)_2PyCl]$ and [Co(appy)Br](Br) in reaction mixtures containing a sacrificial electron donor, sacrificial proton donor, cobalt complex (as HEC), and photosensitizer (PS) under irradiation using either UV (370 nm) or visible (440-456 nm) light, depending on the PS. Ruthenium polypyridine complexes $[Ru(bpy)_3](PF_6)_2$ or $[Ru(bpy)_3](Cl)_2$ (λ_{max} ~450 nm), organoiridium complex *fac*-$[Ir(ppy)_3]$ (λ_{max} ~375 nm) (bpy = 2,2′-bipyridine; ppy = 2-pyridylphenyl), or organic dye Coumarin 343 (λ_{max} ~445 nm) were used as PS in these studies (**Figure 11**).[17] Photocatalytic conditions were screened in our photocatalytic set-up with in-line product detection (Appendix D, Figure D14) for complexes **1**, **2**, and $[Co(dmgH)_2PyCl]$.

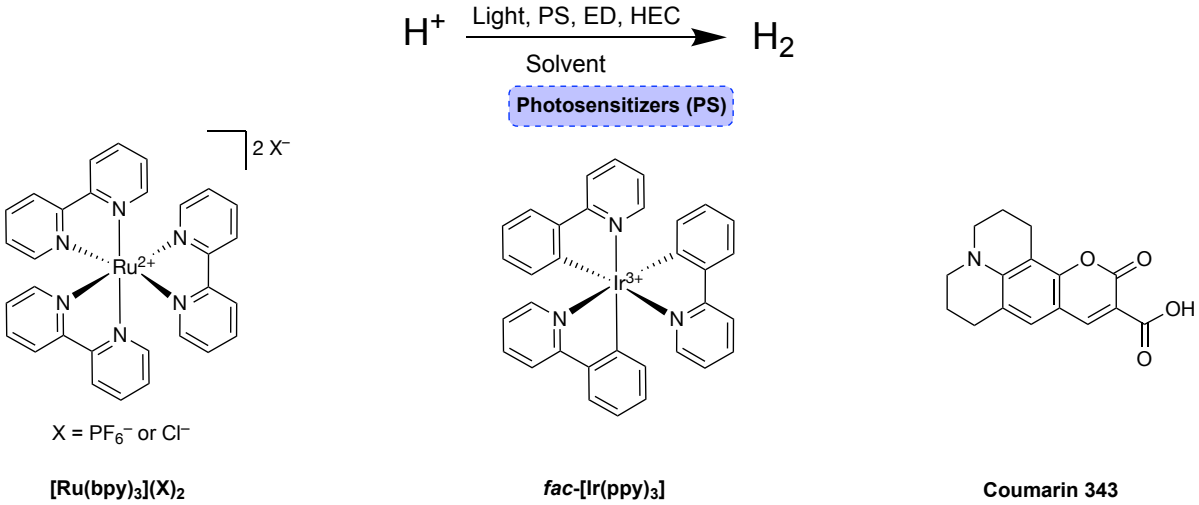

Figure 11. Photosensitizers used in this study.

We started our investigation using the conditions from Hogue *et al.*,[48] using 0.1 mM PS, 1 mM HEC, 1000 mM triethanolamine (TEAO; sacrificial electron donor), and 100 mM HBF_4 (sacrificial proton donor) in DMF (**Table 3**). In the presence of $[Co(dmgH)_2PyCl]$, 65 µmol H_2 was formed over the course of 2 h, whereas in the absence of $[Co(dmgH)_2PyCl]$ no hydrogen was detected at all (**Table 3**, entry 1-2). Complex **1** and **2** produced lower amounts of hydrogen under these conditions, *i.e.* 3.0 and 2.0 µmol H_2, respectively, (**Table 3**, entry 3-4). Optimization of the reaction conditions started by changing the PS to $[Ir(ppy)_3]$, which forms a reduced intermediate with a more cathodic oxidation to its ground-state $[Ir(ppy)_3]^-$ = –2.24 V vs –1.93 V for $[Ru(bpy)_3]^+$ (both measured in MeCN and referenced vs Fc^+/Fc).[10,77,153-155] Therefore, $[Ir(ppy)_3]^-$ holds an increased driving force for electron transfer to the HEC, although its excited triplet state is shorter-lived, making the generation of $[Ir(ppy)_3]^-$ less frequent.[156] Regrettably, $[Ir(ppy)_3]$ in combination with either $[Co(dmgH)_2PyCl]$ or **1** resulted in low to no hydrogen evolution, respectively (**Table 3**, entry 5-6). Accordingly, we continued our studies using $[Ru(bpy)_3](PF_6)_2$ as the PS. Next, we aimed at analyzing and optimizing the electron donor and proton donor. Upon dissolving **1** in DMF and adding electron donor TEAO (*vide supra*), the characteristic pink color of **1** immediately disappeared, indicating a rapid transformation and possible degradation. Presumably, the bis(methylimidazole) ligands are replaced by TEAO ligands. The pink color also disappeared upon dissolving **1** in DMF and adding proton donor HBF_4 (*vide supra*), indicating that **1** is unstable under strongly acidic conditions. These observations prompted us to replace TEAO and HBF_4 by Et_3NHBF_4 as a sacrificial proton and electron donor, in the presence of which **1** is known to be stable.[112] Nevertheless, no hydrogen evolution was observed in a photocatalysis experiment using

Table 3. Reaction condition screening for photocatalytic hydrogen evolution using complexes **1**, **2**, or [Co(dmgH)$_2$PyCl] as HEC, and [Ru(bpy)$_3$](PF$_6$)$_2$ or [Ir(ppy)$_3$] as the PS.[a]

entry	PS (0.1 mM)	HEC (1 mM)	irradiation	Time	µmol H_2	TON(HEC)
1	[Ru(bpy)$_3$](PF$_6$)$_2$	[Co(dmgH)$_2$PyCl]	456 nm	2 h	65.0	13
2	[Ru(bpy)$_3$](PF$_6$)$_2$	-	456 nm	2 h	0	0
3	[Ru(bpy)$_3$](PF$_6$)$_2$	**1**	456 nm	1 h	3.0	0.61
4	[Ru(bpy)$_3$](PF$_6$)$_2$	**2**	456 nm	1 h	2.0	0.39
5	[Ir(ppy)$_3$]	[Co(dmgH)$_2$PyCl]	370 nm	1 h	0.7	0.14
6	[Ir(ppy)$_3$]	**1**	370 nm	1 h	0	0

[a]PS/HEC ratio 1:10, DMF (5 mL), TEAO (1000 mM), HBF$_4$ (100 mM) TON(HEC) = mmol H_2 / mmol HEC

Et_3NHBF_4 in combination with complex **1** and [Ru(bpy)$_3$](PF$_6$)$_2$, nor with [Co(dmgH)$_2$PyCl] (**Table 4**, entries 1-2). Then we tested ascorbic acid (AscH) as a proton and electron donor, as light energy in combination with [Co(dmgH)$_2$PyCl], among other HECs, and AscH is demonstrated to produce H_2, especially under aqueous acidic conditions.[46,157] The overall reaction will provide two electrons and two protons (which can be combined to H_2) upon the oxidation of AscH under the formation of dehydroascorbic acid, causing no accumulation of charged reaction products.[158] Although **1** retains its characteristic pink color in the presence of AscH, no photo-catalytic hydrogen evolution was observed (**Table 4**, entry 3). Then, we changed the solvent from DMF to a 50:50 (v/v) DMF:H_2O mixture, as photocatalytic hydrogen evolution is known to increase under aqueous conditions.[48]. These conditions proved to be suitable for **1**, as small amounts of hydrogen were formed (**Table 4**, entry 4). Using these conditions, we also tested water-soluble organic dye Coumarin 343 as the PS, but this did not yield any hydrogen with either **1** or [Co(dmgH)$_2$PyCl].[159,160] Knowing that **1** is stable and

Table 4. Electron donor (ED) and solvent screening for photocatalytic hydrogen evolution using complexes **1** or [Co(dmgH)$_2$PyCl] as HEC, and [Ru(bpy)$_3$](PF$_6$)$_2$ as the PS.[a]

entry	PS (0.1 mM)	HEC (1 mM)	ED / Acid (mM)	Solvent (5 mL)	µmol H_2	TON (HEC)
1	[Ru(bpy)$_3$](PF$_6$)$_2$	**1**	Et_3NHBF_4 (200)	DMF	0	0
2	[Ru(bpy)$_3$](PF$_6$)$_2$	[Co(dmgH)$_2$PyCl]	Et_3NHBF_4 (200)	DMF	0	0
3	[Ru(bpy)$_3$](PF$_6$)$_2$	**1**	AscH (1000)	DMF	0	0
4	[Ru(bpy)$_3$](PF$_6$)$_2$	**1**	AscH (1000)	DMF/H_2O	0.4	0.08

[a]PS/HEC ratio 1:10, irridiation 456 nm, TON(HEC) = mmol H_2 / mmol HEC

(slightly) active as HEC under aqueous conditions using AscH as the proton/electron donor, we continued by benchmarking the performance of our setup to results from the literature. We applied conditions reported by Deponti and Natali (50:50 (v/v) MeCN:H_2O, 200 equiv. AscH at pH = 5), who reported on an HEC turnover number of ~200 in 2 h, using $[Ru(bpy)_3](PF_6)_2$ and $[Co(dmgH)_2PyCl]$ in a 5:1 ratio.[5] Especially the pH is of importance as the reductive quenching of exited $Ru[bpy]_3^{2+*}$ by the ascorbate ion diminishes under strongly acidic conditions.[4,18,21] Deponti and Natali used a 175 W xenon arc lamp, which we avoided because of the severe heat transmitted by such lamps; instead, we used 45-50 W LEDs and cooled the reaction cell by ventilation (Appendix D, Figure D14). To increase the irradiation as much as possible, we added a second 440 nm LED lamp next to the initial 456 nm LED. Under these conditions, $[Co(dmgH)_2PyCl]$ produced 2.6 µmol H_2 corresponding to a TON(HEC) of 5.2 (**Table 5**, entry 1), which demonstrates that our set-up is overall less efficient compared to the one used during the study of Deponti and Natali.[5] Nevertheless, our set-up allowed us to sufficiently benchmark HECs under these conditions.

Using these conditions, we observed a hydrogen production of 1.3 µmol and a TON(HEC) of 2.6 for **1** (**Table 5**, entry 2), which is a 3-fold increase in H_2 production and a 33-fold increase in TON(HEC), compared to the previous conditions (**Table 3**, entry 4). **2** is less efficient as an HEC under these conditions, with 0.6 µmol H_2 being formed at a TON(HEC) of 0.6 (**Table 5**, entry 3). We then continued to test the photocatalytic activity of complexes **3** and **4**. Complex **3** produced 4.8 µmol H_2 with a TON(HEC) of 9.6. (**Table 5**, entry 4), while **4** produced 3.6 µmol H_2 with a TON(HEC) of 7.3 (**Table 5,** entry 5), making them both competitive HECs with respect to $[Co(dmgH)_2PyCl]$. The difference in activity observed for **3** and **4** demonstrates that changing the counterions in the complexes influences their HER performance. We already saw in the crystal structures of $\mathbf{3^{2MeCN}}$ and $\mathbf{4^{2H_2O}}$ that the complexes can adopt different geometries in MeCN and H_2O. Therefore, it is at this point unclear which geometry is (mainly) responsible for the observed activity. Finally, we performed a control experiment using cobalt salt $[Co(H_2O)_6](NO_3)_2$, which produced 1.4 µmol H_2 with a TON(HEC) of 2.8 per Co atom (**Table 5**, entry 6). An experiment carried out in the absence of any cobalt source produced no hydrogen at all. These results show that complexes **3** and **4** are viable HECs, whose photocatalytic activities compete with that of $[Co(dmgH)_2PyCl]$ under the applied conditions. Furthermore, the control experiments demonstrate that the coordination of bis(methylimidazole) ligands to the cobalt(II) ion increases its photocatalytic activity. Next, we investigated the photocatalytic HER performance of water-soluble complexes **4**-**6** under aqueous conditions (MiliQ), using $[Ru(bpy)_3](Cl)_2$ as the PS. The catalytic activity of **4** under

Table 5. Photocatalytic hydrogen evolution using [Co(dmgH)$_2$PyCl], cobalt complexes **1-4** and [Co(H$_2$O)$_6$](NO$_3$)$_2$ as HEC, and [Ru(bpy)$_3$](PF$_6$)$_2$ as the PS under optimized reaction conditions in aqueous MeCN.[a]

entry	Complex (0.1 mM)	irradiation	µmol H_2	TON (HEC)[b]
1	[Co(dmgH)$_2$PyCl]	440-456 nm	2.6	5.2 ± 0.1
2	**1**	440-456 nm	1.3	2.6 ± 0.4
3	**2**	440-456 nm	0.3	0.6 ± 0.2
4	**3**	440-456 nm	4.8	9.6 ± 0.1
5	**4**	440-456 nm	3.6	7.3 ± 0.03
6	[Co(H$_2$O)$_6$](NO$_3$)$_2$	440-456 nm	1.4	2.8 ± 0.2

[a]PS: 0.5 mM [Ru(bpy)$_3$](PF$_6$)$_2$, PS/HEC ratio 5:1, AscH 100 mM, 50:50 (v/v) MeCN:H$_2$O (total 5 mL) pH adjusted to 5 with 1 M NaOH, reaction time 2 h, TON(HEC) = mmol H_2 / mmol HEC. [b]average of 2 measurements

these conditions increased, producing 5.3 µmol H_2 with a TON(HEC) of 10.6 after 2 h (**Table 6**, entry 1). [Co(dmgH)$_2$PyCl] showed a slight decrease in activity upon moving to fully aqueous conditions, producing 2.3 µmol H_2 with a TON(HEC) of 4.5 after 2 h (**Table 6**, entry 2). This tendency in activity has been reported before for cobalt glyoxime-based HECs in non-aqueous *vs.* aqueous conditions and was attributed to the poor robustness of cobaloximes in water.[59,80] For **4**, photocatalytic hydrogen production also proceeds at a neutral pH, using a phosphate-buffered solution, producing 1.8 µmol H_2 with a TON(HEC) of 3.5 after 2 h (**Table 6**, entry 3), corroborating the importance and influence of the pH of the reaction medium. We tentatively attribute this observation to the decomposition of the PS and the formation of an active cobalt complex with one or more bipyridine ligands (originating from the PS).[18,105,108,161] Complexes **5** and **6** produced 4.3 and 5.4 µmol H_2 with TON(HEC)s of 8.6 and 10.7, respectively, after 2 h (**Table 6**, entry 5-7), making **6** the best HEC in this series. We also tested complex **7**, (see introduction and experimental section), holding a cobalt center with 2 bis(methylimidazole) propanoic acid ligands. **7** produced 2.3 µmol H_2 with a tentative TON(HEC) of 4.5, after 2 h (**Table 6**, entry 7), making it the least efficient HEC in the series of bis(methylimidazole)-based HECs. Finally, one of the current state-of-the-art HECs, [Co(appy)Br](Br), was tested and was found to reach a TON(HEC) of 21.2 (10.6 µmol H_2) after 2 h (**Table 6**, entry 8). The best-reported results for [Co(appy)Br](Br) are 20,000 – 30,000 TON(HEC)s after 11 h, under optimized reaction conditions of low HEC loading (1 µM) and a high PS:HEC ratio (500:1).[25,107,108] The cobalt salt [Co(H$_2$O)$_6$](NO$_3$)$_2$ first appeared to not

Table 6. Photocatalytic hydrogen evolution with **4-7** (L = HBMIM (**4**), BMIK (**5**), HBMIA (**6**), HBMIP (**7**)) under optimized aqueous reaction conditions.[a]

entry	HEC (0.1 mM)	µmol H2	TON (HEC)[b]
1	4	5.3	10.6 ± 0.1
2	$[Co(dmgH)_2PyCl]$	2.3	4.5 ± 0.02
3[c]	4	1.8	3.5 ± 0.1
4	$[Co(H2O)_6](NO_3)_2$	0.8	1.6 ± 0.4
5	5	4.3	8.6 ± 0.04
6	6	5.4	10.7 ± 0.1
7	7	2.3	4.5 ± 0.02
8	[Co(appy)Br](Br)	10.6	21.2 ± 0.05

[a]degassed MiliQ (5 mL), PS $[Ru(bpy)_3](Cl)_2$ (0.5 mM), PS/HEC ratio 5:1, 440-456 nm irraditation, pH adjusted to 5 with 1 M NaOH, reaction time 2 h, 100 mmol AscH, TON(HEC) = mmol H_2 / mmol HEC [b]average of 2 measurements, [c]buffered NaH_2PO_4/Na_2HPO_4 solution at pH = 7

catalyze photocatalytic hydrogen production in detectable amounts under aqueous conditions (**Table 6**, entry 4), however, we did record small amounts of hydrogen after approx. 60 min. These results demonstrate that bis(methylimidazole) cobalt complexes are a competitive class of HECs to the cobalt glyoximes systems, while compared to the benchmark HEC [Co(appy)Br](Br) about 50% of the activity is reached.

The H_2 formation (nmol H_2/min) and the cumulative turnover number in cobalt (TON(HEC); H_2/Co) for **4-6**, $[Co(dmgH)_2PyCl]$, and [Co(appy)Br](Br) are plotted in **Figure 9** (plots correspond to data in **Table 6**). In all experiments, no H_2 was detected during the first 3-5 min, caused by the dimensions of the catalytic cell that contains a 5 mL solution and a headspace of approx. 0.05 dm^3 (50 mL), while the applied flow of the carrier gas was set to 1 mL/min, causing some dilution of the H_2 concentration in the first measurements (an in-line sample was taken every 76 sec). Complex **4** (green traces) showed the highest initial rate, with a peak hydrogen production of 76 nmol H_2/min at t = 31 min, after which the rate decreased. For $[Co(dmgH)_2PyCl]$ (yellow traces) a peak hydrogen production of 25 nmol H_2/min was obtained, which remained relatively stable (20 nmol H_2/min at t = 2 h). Complexes **5** (blue traces) and **6** (black traces) showed an increasing rate during the first 45 min, towards peak rates of 41 and 71 nmol H_2/min, respectively. [Co(appy)Br](Br) (gray traces) demonstrated to be the slowest catalyst during the first 30 minutes, after which hydrogen production quickly increased to a peak rate of 215 nmol H_2/min at t = 110 min, making [Co(appy)Br](Br) the high-performing HEC in this series. The gradual start of [Co(appy)Br](Br) was attributed to a slow

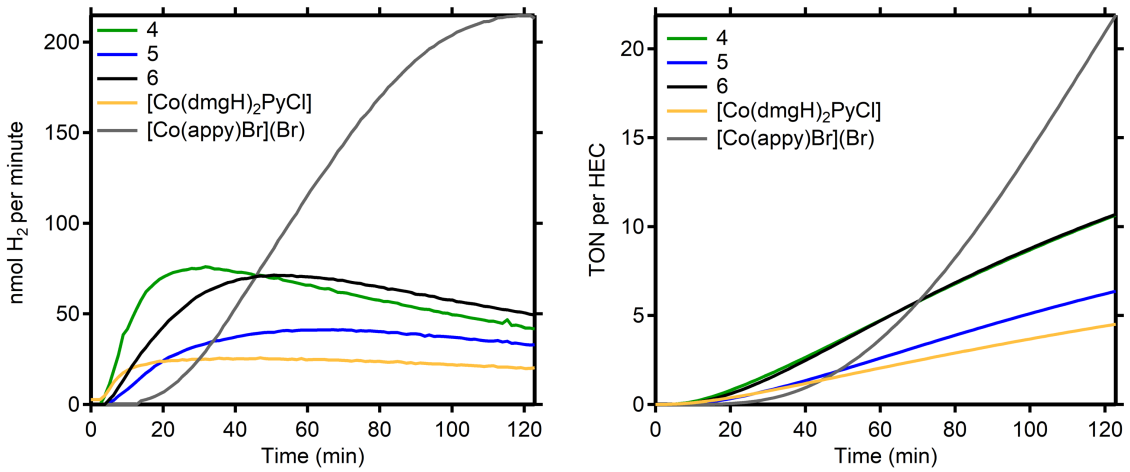

Figure 12. Photocatalytic HER performance over time under optimized aqueous conditions. Left: photocatalytic H_2 production per minute versus the reaction time, Right: cumulative TON(HEC) versus the reaction time: **4** (green); **5** (blue); **6** (black); [Co(dmgH)$_2$PyCl] (yellow); [Co(appy)Br](Br) (gray); [Co(H$_2$O)$_6$](NO$_3$)$_2$. Conditions: MilliQ water (5 mL), 0.5 mM [Ru(bpy)$_3$(Cl)$_2$, 0.1 mM HEC, 100 mM AscH, pH = 5, 2 h irradiation with 440-456 nm.

chemical transformation that forms the active catalyst, as was observed before.[105,162] Comparing the performance of bis(methylimidazole) complexes **4**-**6** shows that **4** displays the highest initial rate and the highest peak production in hydrogen formation. This complex's high (initial) activity could originate from the HBMIM ligands, which are known to function as a proton relay for hydrogen production.[13] During such cooperative hydrogen production the combination of a methylene C–H proton with a metal hydride enables hydrogen formation. The removal of this functionality by introducing a carbonyl group in the BMIK ligand in **5** results in a decrease in activity. The lower activity of **5** could also originate from a decreased electron density at the metal center, resulting in a more positive and less reactive metal center. In electrocatalytic hydrogen evolution, such a trend is rationalized by a lowering of the overpotential, which is linearly correlated to the catalytic rate for hydrogen production.[163-166] Retaining one C–H bond, using HBMIA ligands in **6**, results in a small decrease in hydrogen production rate, while hydrogen production is more stable over time in the presence of **6** compared to **4**. We attribute these results to the anticipated, less donating character of the HBMIA ligand, making the metal center less electron-rich and the HER rate lower. Overall, we conclude that the functionalization of the methylene bridge in bis(methylimidazole) ligands yields cobalt complexes with lower initial turnover rates but an increased stability of hydrogen production over time (lifetimes), best illustrated for **5** and **6**. Over the course of the experiments, other parameters such as the aggregation of species or a temperature increase (although limited by the ventilator) may also contribute to the observed trends, but these parameters were not

individually quantified. For all complexes, no deposition was visually observed after photocatalysis, suggesting only the presence of solvated HECs during catalysis. In addition, no visual color changes were observed during the experiments due to the intense orange color of the solutions, originating from the Ru-based PS.

Overall, we propose the following photocatalytic sequence for hydrogen evolution for complex **4 (Figure 13)**:[5,10,11,167] Excitation of $[Ru(bpy)_3]^{2+}$ produces $[Ru(bpy)_3]^{2+*}$. Efficient reductive quenching of $[Ru(bpy)_3]^{2+*}$ by AscH forms $[Ru(bpy)_3]^{+}$ as a reactive intermediate. Subsequent, electron transfer from $[Ru(bpy)_3]^{+}$ to **4** is thermodynamically favorable by 300 mV (Co(I/II) = –1.22 V for **4** and Ru(I/II) = –1.52 V for $[Ru(bpy)_3]Cl_2$,[10,168] (*vide supra*) and produces reduced **4** with concomitant regeneration of the original photosensitizer, $[Ru(bpy)_3]^{2+}$. Reduced **4** participates in a catalytic redox reaction, with protons from AscH, as confirmed by our electrocatalytic experiments. Based on the photocatalytic performance of **4** the catalytic reaction was assigned to the reduction of protons to hydrogen gas. For **3**, **5,** and **6** an identical sequence is proposed with slightly altered electron transfer kinetics between the PS and HEC. The favorable thermodynamics might also play a part in the increased activity of **4** compared to **1**, as the Co(I/II) reduction of **1** was found around the same potential as the Ru(I/II) redox couple of $[Ru(bpy)_2](PF_6)_2$ (30 mV difference), while the reduction potential of **4** is 300 mV more anodic than the reported Ru(I/II) redox couple of $[Ru(bpy)_2]Cl_2$. To conclude, cobalt complexes **3-6** were shown to catalyze photocatalytic proton reduction under non-aqueous, full aqueous, and mixed conditions. Under aqueous conditions, complexes **4-6** as well as

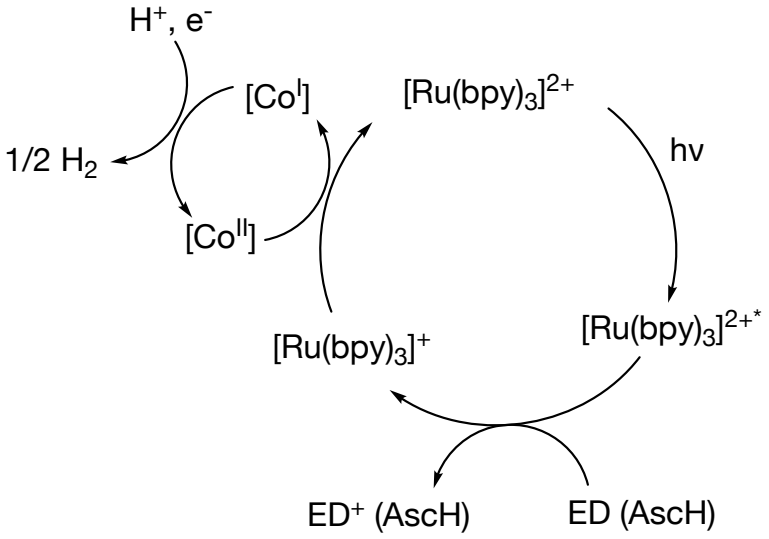

Figure 13. Proposed catalytic cycle for photocatalytic HER using complexes **4-6** as HEC and $[Ru(bpy)_3](Cl)_2$ as PS under aqueous conditions using AscH as proton and electron donor.

[Co(dmgH)$_2$PyCl] immediately produce H_2 upon irradiation. Amongst the cobalt complexes **3**-**6**, complexes **4** and **6** are the most productive and are most competitive with respect to the well-studied photocatalyst [Co(dmgH)$_2$PyCl], but not to polypyridyl complex [Co(appy)Br](Br) which outperforms the other catalysts under the applied conditions in this study.

5.3 Conclusion

Four new (water-soluble) cobalt complexes **3**-**6** derived from a series of structurally related bis(methylimidazole) ligands with (substituted) methylene linkers between the imidazole moieties were synthesized. The X-ray crystal structures of $\mathbf{3}^{\mathbf{2MeCN}}$ and $\mathbf{4}^{\mathbf{2H_2O}}$ show that the small steric encumbrance of these ligands enables coordination flexibility, resulting in complexes with higher coordination numbers in coordinating solvents such as MeCN and water, compared to [Co(HBMIM^{Ph2})$_2$](BF$_4$)$_2$ (**1**). Solid-state IR spectroscopy demonstrated the presence of both coordinated and free ionic nitrates in **4**-**6**. ^{1}H-NMR spectroscopy in non-coordinating solvent DCM, together with the elemental analysis confirmed that the isolated complexes were obtained as bis-ligated cobalt complexes without additional solvent coordination. CV analysis of **4** in the presence of AscH demonstrated a clear electrocatalytic current, confirming **4** as a proton reduction catalyst. For the photocatalytic HER, the PS, solvent, light intensity, proton/electron donor, pH, and catalyst loading were optimized, in which the use of water in the reaction medium turned out to be necessary for efficiency. **1**-**6** all produce hydrogen gas upon irradiation under photocatalytic conditions. Complexes **3**-**6** are more active than complexes **1**-**2**, which we attribute to the coordination flexibility of the complexes and their advantageous redox potentials. **4**-**6** are also active photocatalysts under fully aqueous conditions and their HER performance is competitive to that of the well-studied [Co(dmgH)$_2$PyCl], but is outperformed by high-performing photocatalyst [Co(appy)Br](Br)). Alternation of the methylene linker of the ligand backbone in **4**-**6** resulted in poorer initial activity and peak H_2 production but longer-lived photocatalysts, presumably due to the reduced electron density on the metal center, making the complexes less reactive. Based on our investigations, we conclude that bis(methylimidazole) ligands coordinated to cobalt promote photocatalytic hydrogen evolution and are an interesting class of ligands, in which ligand modifications significantly influence the observed reactivity. These findings may spur the further development of other bis(methylimidazole) ligands and their corresponding metal complexes as novel HECs.

5.4 Experimental

5.4.1 General remarks

All reactions were carried out under an inert atmosphere of water and oxygen-free N_2 gas using standard Schlenk techniques or were performed in an MBraun LabMaster DP glovebox workstation. Dry acetonitrile (MeCN), dichloromethane (DCM), and methanol (MeOH) were used from an MBraun SPS-800 solvent purification system, dried over 3 or 4Å molecular sieves, and degassed by bubbling N_2 for at least 30 minutes. Tetrahydrofuran (THF) was dried over sodium benzophenone after taking it from an MBraun SPS-800 solvent purification system, subsequently distilled and degassed by bubbling N_2 for at least 30 minutes. All other commercially obtained chemicals were used without further purification unless stated otherwise. ^{1}H-NMR and ^{13}C-NMR were recorded at 400 MHz, and 101 MHz, respectively, at 298 K, on a Varian VNMRS400 or an Oxford NMR AS400 spectrometer. Chemical shifts (δ) are reported in ppm and referenced against the residual solvent signal. IR spectroscopy was conducted using a PerkinElmer Spectrum Two FT-IR spectrometer. Peaks are annotated by (w), (m), and (s) to indicate weak, medium and strong signals, respectively. Absorption spectra were recorded using a Varian Cary 50 Scan spectrometer, using Quartz cuvettes with a path length of 1 cm, sealed with a Teflon cap. Unless otherwise stated, UV-vis solutions were prepared in the glovebox using dried and degassed solvents. The absorption spectra were acquired using the PerkinElmer UV Winlab software.

Typical photocatalytic experiments were carried out in a two-neck pear-shaped, angled flask equipped with a stirring bar, stopper, and gas-inlet/outlet glass insert (Appendix D, Figure D14). The flask cell was put under a nitrogen flow (10 mL/min) and the PS was added as a solution (1 mL, typically from a stock solution for consistency), then a solution (1 mL) containing the HEC was added and the volume in the cell was increased to 5 mL. Subsequently, the electron donor, proton donor, and when specified 3 drops of 5 M NaOH solution were added (pH = 5). The cell was purged until the residual oxygen signal completely disappeared on the GC chromatograms (Appendix D, Figure D15), which usually took 2-5 min. The ventilation and stirring were started and the flow was put at 1 mL/min. Finally, 1 or 2 h irradiation by 440(–456) nM LEDs was programmed with the KESSIL light controller, and the H_2 production was monitored by an in-line gas chromatograph.

In the in-line gas chromatography configuration; the photocatalytic cell was continuously flushed by N_2 carrier gas, whose rate is fixed through a Bronkhorst EL FLOW prestige mass

flowmeter/controller at 1 mL/min. The output gas was analyzed with an InterScience CompactGC$^{4.0}$ gas chromatograph (**Chapter 2**, section 2.4.2, p73). The obtained values were then used to relate the area under the H_2 peak given to the experimentally observed production of H_2 in the photocatalytic experiments in time.

Photocatalytic equipment: one or two PR160L LED lights from KESSIL with finely tuned 440 nm (45 W) and 456 nm (50 W) wavelengths were used. The experimental setup was cooled using a KESSIL PR160 ring w/ Fan Kit. The experiment duration was precisely timed using a KESSIL PR Controller.

Electrochemical sweeping experiments were performed in a fume hood, on an Autolab PGSTAT204 potentiostat/galvanostat using a 663 VA stand (Appendix D, Figure D16). This 3-electrode setup includes a carbon counter electrode, a mercury-drop working electrode (±0.01 mm Ø), and an Ag/AgCl reference electrode, used directly in the solution. Before all measurements, the cell was purged with solvent-saturated N_2. All scans were referenced to the Ag/AgCl redox couple (–0.41 V vs Fc^+/Fc)[153] and taken at a scan rate of 100 mV/s unless reported differently. Before all experiments, a new mercury drop was used. background voltammograms were recorded at a scan rate of 100 mV/s. Solutions were mixed by the 663VA stand rotator before each measurement. All measurements were recorded in a 0.1 M potassium nitrate (KNO_3) solution in degassed Milli Q H_2O.

5.4.2 Ligand synthesis

Ligands were synthesized according to adapted literature procedures and their structures were confirmed by NMR spectroscopy, while the purity of the ligand batches was confirmed by elemental analysis.[113-115,169]

5.4.3 Complex synthesis

$[Co(dmgH)_2PyCl]$, and [Co(appy)Br](Br) (dmgH = dimethylglioximate, appy = bis-2,2′-bipyridine-6-yl(pyridine-2-yl)methanol) were synthesized according to reported procedures.[5,107]

$[Co(HBMIM)_2](BF_4)_2$ (3): bis(1-methyl-1*H*-imidazol-2-yl)methane (HBMIM) (176.2 mg, 1.0 mmol) and THF (10 mL) were added to a Schlenk equipped with a stirring bar and immersed in an oil bath under an N_2 flow. The temperature was increased to 45 °C to dissolve all HBMIM.

Subsequently, $Co(BF_4)_2 \cdot 6H_2O$ (145.5 mg, 0.5 mmol) was added under an N_2 flow, and the solution became immediately pink/purple. After 2 h the pink solids were collected, washed with THF (10 mL) at 45 °C, and dried under vacuum yielding off pink solids of **3** in 89% yield (261 mg, 0.4 mmol). Recrystallization by slow evaporation of diethyl ether into a concentrated solution of **3** in MeCN at –40 °C afforded red/brown crystals suitable for X-ray diffraction. **^{1}H NMR** (400 MHz, DCM-d_2, pink, 25°C): δ (ppm) = 47, 29, 22, 11, 5, 1, 0. **ESI-MS** (low-resolution)(MeCN): *m/z* = 410.0 {$[Co(HBMIM)_2–H]^+$, calc. 410.15}.[170] **E.A.** (Formula: $C_{18}H_{24}N_8Co$, Mw: 584,99 g mol^{-1}): Calc. C 36.96, H 4.14, N 19.16; found C 37.01, H 3.68, N 18.87. **ATR-IR** = 3120 (w), 1573 (m), 1521 (w), 1410 (w), 1367 (w), 1293 (w), 1150 (m), 1103 (m), 1060 (s), 1033 (s), 987 (m), 959 (w). **X-ray crystal structure determination** for $[Co(HBMIM)_2(MeCN)_2](BF_4)_2$. $[C_{22}H_{30}CoN_{10}](BF_4)_2 \cdot CH_3CN$, Fw = 708.16, orange block, 0.43 × 0.22 × 0.11 mm^3, triclinic, $P\overline{1}$ (no. 2), a = 11.3749(6), b = 11.6447(5), c = 13.7647(5) Å, α = 69.390(2), β = 87.380(3), γ = 70.982(2) °, V = 1608.48(2) Å^3, Z = 2, D_x = 1.462 g/cm^3, μ = 0.62 mm^{-1}. The diffraction experiment was performed on a Bruker Kappa ApexII diffractometer with sealed a tube and Triumph monochromator (λ = 0.71073 Å) at a temperature of 150(2) K up to a resolution of $(\sin\theta/\lambda)_{max}$ = 0.65 Å^{-1}. The crystal was cracked into two fragments. Consequently, two orientation matrices were used for the integration with the Eval15 software,[171] resulting in an HKLF-5 file.[172] A multi-scan absorption correction and scaling was performed with TWINABS[173] (correction range 0.60-0.75). A total of 46312 reflections were measured, 7407 reflections were unique (R_{int} = 0.032), 6311 reflections were observed [I>2σ(I)]. The structure was solved with Patterson superposition methods using SHELXT.[174] Structure refinement was performed with SHELXL-2018[175] on F^2 of all reflections. Non-hydrogen atoms were refined freely with anisotropic displacement parameters. One BF_4 anion was orientationally disordered. All hydrogen atoms were located in different Fourier maps and refined with a riding model. 460 Parameters were refined with 381 restraints (distances, angles and displacement parameters in the BF_4^- anions). R1/wR2 [I > 2σ(I)]: 0.0341 / 0.0838. R1/wR2 [all refl.]: 0.0419 / 0.0877. S = 1.052. Scale factor for the second crystal fragment BASF = 0.051(5). Residual electron density between -0.39 and 0.66 e/Å^3. Geometry calculations and checking for higher symmetry was performed with the PLATON program.[176]

$[Co(HBMIM)_2](NO_3)_2$ (4): HBMIM (176.2 mg, 1.0 mmol) and THF (10 mL) were added to a Schlenk equipped with a stirring bar and immersed in an oil bath under an N_2 flow. The

temperature was turned on and increased to 45 °C to dissolve all HBMIM. Subsequently, $Co(NO_3)_2{\cdot}6H_2O$ (145.5 mg, 0.5 mmol) was added under an N_2 flow and the solution became immediately pink/purple. After 2 h the pink solids were collected, washed with THF (10 mL) at 45 °C, and dried under vacuum yielding off pink solids of **4** in 92% yield. Recrystallization from hot H_2O (70 °C) afforded $[Co(HBMIM)_2(H_2O)_2](NO_3)_2$ as pure yellow crystals that were suitable for X-ray diffraction. **^{1}H-NMR** (400 MHz, DCM-d_2, pink, 25°C) δ (ppm) 43 (S, 4H, 4x H-imidazole), 32 (S, 2H, CH_2), 10 (S, 6H, CH_3). **^{1}H-NMR** (400 MHz, water-d_2, yellow, 25 °C) δ (ppm) 45, 41, 34, 25, 19, 12, 11, 7. To note, we also analyzed **4** in MeCN-d_3 demonstrating seven paramagnetic resonances between 47 and 9 ppm (Appendix D, Figure D10), indicative of a modular paramagnetic species. This result was not discussed in the main text but included here for future referencing. **^{1}H-NMR** (400 MHz, MeCN-d_2, pink, 25°C) δ (ppm) 47, 43, 41, 26, 22, 11, 9. **ESI-MS** (low-resolution)(MeCN): *m/z* = 409.9 {$[Co(HBMIM)_2–H]^+$, calc. 410.15}. **ATR-IR =** 3676 (w), 3120 (w), 2988 (w), 2901 (w), 1542 (w), 1515 (w), 1463 (w), 1413 (w), 1372 (m), 1333 (m), 1289 (m), 1243 (w), 1134 (w), 1085 (w), 1051 (w), 1033(w), 957 (w), 823 (w) 811 (w). **UV-vis** (MiliQ H_2O), ε [$mol^{-1}dm^3cm^{-1}$]): λ_{max} = 313 (π– π^*), 480 (MLCT) nm. **E.A.** pink powder $[Co(HBMIM)_2](NO_3)_2$ (+ 0.2 THF) (Formula: $C_{18}H_{24}CoN_{10}O_8$, Mw: 535.39 g mol^{-1}): Calc. C 41.09, H 4.66, N 25.49 Found C 41.43, H 4.46, N 25.84. yellow crystals $[Co(HBMIM)_2(H_2O)_2](NO_3)_2$ (Formula: $C_{18}H_{24}CoN_{10}O_8$, Mw: 571.42 g mol^{-1}): Calc. C 37.84, H 4.94, N 24.50 Found C 37.55, H 4.96, N 24.45.

X-ray crystal structure determinations for $[Co(HBMIM)_2(H_2O)_2](NO_3)_2$. $[C_{18}H_{28}CoN_8O_2](NO_3)_2$, Fw = 571.43, yellow block, 0.40 × 0.30 × 0.13 mm^3, monoclinic, $P2_1/n$ (no. 14), a = 8.7006(2), b = 13.2950(4), c = 10.3442(3) Å, β = 100.940(1) °, V = 1174.82(5) $Å^3$, Z = 2, D_x = 1.615 g/cm^3, μ = 0.80 mm^{-1}. The diffraction experiment was performed on a Bruker Kappa ApexII diffractometer with sealed tube and Triumph monochromator (λ = 0.71073 Å) at a temperature of 150(2) K up to a resolution of $(\sin\theta/\lambda)_{max}$ = 0.81 $Å^{-1}$. The intensity integration was done with the Eval15 software.[171] A numerical absorption correction and scaling was performed with SADABS[173] (correction range 0.77-0.92). A total of 34971 reflections was measured, 5170 reflections were unique (R_{int} = 0.033), 4358 reflections were observed [I>2σ(I)]. The structure was solved with Patterson superposition methods using SHELXT.[174] Structure refinement was performed with SHELXL-2018[175] on F^2 of all reflections. Non-hydrogen atoms were refined freely with anisotropic displacement parameters. All hydrogen atoms were located in difference-Fourier maps. O-H hydrogen atoms

were refined freely with isotropic displacement parameters, C-H hydrogen atoms were refined with a riding model. 179 parameters were refined with no restraints. R1/wR2 [$I > 2\sigma(I)$]: 0.0278 / 0.0769. R1/wR2 [all refl.]: 0.0348 / 0.0794. S = 1.039. Residual electron density between -0.34 and 0.49 e/Å^3. Geometry calculations and checking for higher symmetry was performed with the PLATON program.[176]

[Co(BMIK)$_2$(NO$_3$)$_2$] (5): bis(1-methyl-1*H*-imidazol-2-yl)methanone (BMIK) (190.2 mg, 1.0 mmol) and THF (10 mL) were added to a Schlenk equipped with a stirring bar giving an off-white solution. Subsequently, Co(NO$_3$)$_2$·6H$_2$O (145.5 mg, 0.5 mmol) was added under an N_2 flow and immediately light salmon-colored solids were formed. After 2 h the solids were collected, washed with THF (10 mL), and dried under vacuum yielding salmon-colored solids of **5** in 87.4% yield. **^{1}H-NMR** (400 MHz, water-d_2, yellow, 25 °C) δ (ppm) 48, 42, 40, 14, 12, 10, –5, –7. **^{1}H-NMR** (400 MHz, DCM-d_2, pink, 25 °C) δ (ppm) 47, 46, 43, 26, 13, 12, 1, 1, 0, 0. **ESI-MS** (low-resolution)(MeCN): *m/z* = 439.0 {[Co(BMIK)$_2$]$^+$, calc. 439.10}, *m/z* = 456.0 {[Co(BMIK)$_2$+OH]$^+$, calc. 456.11}, 542.0 {[Co(BMIK)$_2$+NO$_3$+MeCN]$^+$, calc. 542.10}. **ATR-IR =** 3107 (w), 2988 (w), 1650 (w), 1534 (w), 1482 (w), 1414 (w), 1370 (s), 1341 (s), 1290 (w), 1251 (w), 1174 (w), 1090 (w), 1029 (w), 957 (w), 899 (s), 830 (w), 802 (m). **E.A.** [Co[BMIK(NO$_3$)$_2$]$_2$ (Formula: $C_{18}H_{20}CoN_{10}O_8$, Mw: 563.36 g mol^{-1}): Calc. C 38.38, H 3.58, N 24.86 Found C 38.64, H 3.65, N 24.39.

[Co(HBMIA)$_2$](NO$_3$)$_2$ (6): bis(1-methyl-1*H*-imidazol-2-yl)methanol (HBMIA) (35 mg, 0.18 mmol) and THF (2 mL) were added to a Schlenk equipped with a stirring bar giving a white suspension. Subsequently, Co(NO$_3$)$_2$·6H$_2$O (26 mg, 0.09 mmol) was added under an N_2 flow and immediately turned the solution purple. Over time the purple solution disappeared, and off-pink solids were formed. After 2 h the pink solids were collected, washed with THF (2 mL), and dried under vacuum yielding off pink solids of **6** in 84% yield. **^{1}H-NMR** (400 MHz, DCM- d_2, pink, 25°C) δ (ppm) 44, 12, 1, 1, 0, 0. **^{1}H-NMR** (400 MHz, water-d_2, yellow, 25 °C) δ (ppm) 43, 43, 15, 14, 13, 12, 7, 4, 1, 0. **HRMS** (FAB$^+$)(MeCN): *m/z* = 442.1273 {[Co(HBMIA)$_2$]–H]$^+$, calc. 442.1276}, *m/z* = 505.1228 {[Co(HBMIA)$_2$]+NO$_3$]$^+$, calc. 505.1232}. **ATR-IR =** 3379 (w), 3127 (w), 1615 (w), 1510 (w), 1462 (m), 1399 (s), 1382 (s), 1307 (s), 1288 (w), 1189 (w), 1148 (w), 1143 (w), 1085 (w), 1046 (w), 1034 (m), 997 (w), 828 (w), 827 (w), 825 (w), 821 (w). **E.A.** [Co(HBMIA)$_2$(NO$_3$)$_2$] (+ 0.5 H$_2$O) (Formula:

$C_{18}H_{24}CoN_{10}O_8$, Mw: 567.39 g mol^{-1}): Calc. C 36.37, H 4.58, N 23.56 Found C 36.59, H 4.36, N 23.21.

$[Co(HBMIP)_2](NO_3)_2$ (7): 3,3-bis(1-methyl-1*H*-imidazol-2-yl)propanoic acid (HBMIP) (234.3 mg, 1.0 mmol) and THF (10 mL) were added to a Schlenk equipped with a stirring bar giving a slightly yellow solution. Subsequently, $Co(NO_3)_2{\cdot}6H_2O$ (145.5 mg, 0.5 mmol) was added under an N_2 flow, and immediately off pink solids were formed. After 2 h pink solids were collected, washed with THF (10 mL), and dried under vacuum yielding off pink solids of **7** in 91% yield. **^{1}H-NMR**: (400 MHz, D_2O, 25 °C) δ (ppm) 79, 60, 49, 42, 35, 23, 18, –11, –28 (Appendix D, Figure D13). **7** does not dissolve in DCM-d_2. **ESI-MS** (low-resolution)(THF): *m/z* = 563.6 {$[M–2NO_3+2H_2O]^+$, calc. 563.18}. **HRMS** (FAB^+)(MeCN): *m/z* = 525.1411 {$[Co(HBMIP)_2–2H]^+$, calc. 525.14092} (Appendix D, Figure D5). **ATR-IR** = 3370 (w) (OH stretch vibration), 3128 (w), 2956 (w), 2732 (w), 2395 (w), 1763 (w) (non-coordinated COOH), 1575 (w), 1369 (w), 823 (w) (Appendix D, Figure D10). For **7**, no good elemental analysis (2-4% carbon deviation) was obtained after several attempts with different batches, however, HRMS confirmed the presence of $[Co(HBMIP)_2](NO_3)_2$.

5.5 Author Contributions and Acknowledgments

Synthesis, characterization, and electrochemical measurements were done by S.D. de Vos and V. Ciurca. X-ray crystal structure determinations were performed by M. Lutz. The project design was done by S.D. de Vos, N. Dramountanis, and R.J.M. Klein Gebbink. Funding acquisition, administration, and oversight were done by R.J.M. Klein Gebbink. The original draft was written by S. D. de Vos, and reviewing and editing was done by D.L.J Broere and R.J.M. Klein Gebbink with contributions by all authors.

[Co(appy)Br](Br) was received from M.B. Brands from the HomKat group at the University of Amsterdam, Van 't Hoff Institute for Molecular Sciences.

5.6 References

(1) Lewis, N. S.; Nocera, D. G. Powering the planet: Chemical challenges in solar energy utilization. *Proc. Natl. Acad. Sci. U.S.A* **2006,** *103* (43), 15729.
(2) Younas, M.; Shafique, S.; Hafeez, A.; Javed, F.; Rehman, F. An Overview of Hydrogen Production: Current Status, Potential, and Challenges. *Fuel* **2022,** *316*, 123317.
(3) Turner, J. A. Sustainable Hydrogen Production. *Science* **2004,** *305* (5686), 972.

(4) Streich, D.; Astuti, Y.; Orlandi, M.; Schwartz, L.; Lomoth, R.; Hammarström, L.; Ott, S. High-Turnover Photochemical Hydrogen Production Catalyzed by a Model Complex of the [FeFe]-Hydrogenase Active Site. *Chem. Eur. J.* **2010,** *16* (1), 60.
(5) Deponti, E.; Natali, M. Photocatalytic hydrogen evolution with ruthenium polypyridine sensitizers: unveiling the key factors to improve efficiencies. *Dalton Trans.* **2016,** *45* (22), 9136.
(6) Teets, T. S.; Nocera, D. G. Photocatalytic hydrogen production. *Chem. Commun.* **2011,** *47* (33), 9268.
(7) Eckenhoff, W. T.; Eisenberg, R. Molecular systems for light driven hydrogen production. *Dalton Trans.* **2012,** *41* (42), 13004.
(8) Zhang, P.; Wang, M.; Na, Y.; Li, X.; Jiang, Y.; Sun, L. Homogeneous photocatalytic production of hydrogen from water by a bioinspired [Fe_2S_2] catalyst with high turnover numbers. *Dalton Trans.* **2010,** *39* (5), 1204.
(9) Mills, I. N.; Porras, J. A.; Bernhard, S. Judicious design of cationic, cyclometalated Ir (III) complexes for photochemical energy conversion and optoelectronics. *Acc. Chem. Res.* **2018,** *51* (2), 352.
(10) Beyene, B. B.; Hung, C.-H. Photocatalytic hydrogen evolution from neutral aqueous solution by a water-soluble cobalt(II) porphyrin. *Sustain. Energy & Fuels* **2018,** *2* (9), 2036.
(11) Martindale, B. C.; Hutton, G. A.; Caputo, C. A.; Reisner, E. Solar hydrogen production using carbon quantum dots and a molecular nickel catalyst. *J. Am. Chem. Soc.* **2015,** *137* (18), 6018.
(12) Tsuji, Y.; Yamamoto, K.; Yamauchi, K.; Sakai, K. Near-Infrared Light-Driven Hydrogen Evolution from Water Using a Polypyridyl Triruthenium Photosensitizer. *Angew. Chem. Int. Ed.* **2018,** *57* (1), 208.
(13) Ghosh, P.; de Vos, S.; Lutz, M.; Gloaguen, F.; Schollhammer, P.; Moret, M.-E.; Klein Gebbink, R. J. M. Electrocatalytic Proton Reduction by a Cobalt Complex Containing a Proton-Responsive Bis(alkylimdazole)methane Ligand: Involvement of a C−H Bond in H2 Formation. *Chem. Eur. J.* **2020,** *26* (55), 12560.
(14) Kalyanasundaram, K. Photophysics, photochemistry and solar energy conversion with tris(bipyridyl)ruthenium(II) and its analogues. *Coord. Chem. Rev.* **1982,** *46*, 159.
(15) Troian-Gautier, L.; Moucheron, C. RutheniumII complexes bearing fused polycyclic ligands: from fundamental aspects to potential applications. *Molecules* **2014,** *19* (4), 5028.
(16) Chen, Y.; Yuan, H.; Lei, Q.; Ming, M.; Du, J.; Tao, Y.; Cheng, B.; Han, Z. Improving Photocatalytic Hydrogen Production through Incorporating Copper to Organic Photosensitizers. *Inorg. Chem.* **2022,** *61* (32), 12545.
(17) Dalle, K. E.; Warnan, J.; Leung, J. J.; Reuillard, B.; Karmel, I. S.; Reisner, E. Electro- and Solar-Driven Fuel Synthesis with First Row Transition Metal Complexes. *Chem. Rev.* **2019,** *119* (4), 2752.
(18) Khnayzer, R. S.; Thoi, V. S.; Nippe, M.; King, A. E.; Jurss, J. W.; El Roz, K. A.; Long, J. R.; Chang, C. J.; Castellano, F. N. Towards a comprehensive understanding of visible-light photogeneration of hydrogen from water using cobalt(II) polypyridyl catalysts. *Energy Environ. Sci.* **2014,** *7* (4), 1477.
(19) Bock, C.; Connor, J.; Gutierrez, A.; Meyer, T. J.; Whitten, D.; Sullivan, B.; Nagle, J. Estimation of excited-state redox potentials by electron-transfer quenching. Application of electron-transfer theory to excited-state redox processes. *J. Am. Chem. Soc.* **1979,** *101* (17), 4815.

(20) McNamara, W. R.; Han, Z.; Yin, C.-J.; Brennessel, W. W.; Holland, P. L.; Eisenberg, R. Cobalt-dithiolene complexes for the photocatalytic and electrocatalytic reduction of protons in aqueous solutions. *Proc. Natl. Acad. Sci. U.S.A* **2012,** *109* (39), 15594.
(21) Krishnan, C.; Sutin, N. Homogeneous catalysis of the photoreduction of water by visible light. 2. Mediation by a tris (2, 2'-bipyridine) ruthenium (II)-cobalt (II) bipyridine system. *J. Am. Chem. Soc.* **1981,** *103* (8), 2141.
(22) Krishnan, C. V.; Creutz, C.; Mahajan, D.; Schwarz, H. A.; Sutin, N. Homogeneous Catalysis of the Photoreduction of Water by Visible Light. 3. Mediation by Polypyridine Complexes of Ruthenium(II) and Cobalt(II). *Isr. J. Chem.* **1982,** *22* (2), 98.
(23) Mulazzani, Q. G.; Emmi, S.; Fuochi, P. G.; Hoffman, M. Z.; Venturi, M. On the nature of tris(2,2'-bipyridine)ruthenium(1+) ion in aqueous solution. *J. Am. Chem. Soc.* **1978,** *100* (3), 981.
(24) Mulazzani, Q. G.; D'Angelantonio, M.; Camaioni, N.; Venturi, M. Reactivity of Ru (bpy)+ 3 towards the radicals originating from the scavenging of hydrogen atoms and hydroxyl radicals by methanol, ethanol, propan-2-ol, tert-butyl alcohol and formate ions in aqueous solution: a pulse radiolytic study. *J. Chem. Soc., Faraday Trans.* **1991,** *87* (14), 2179.
(25) Bachmann, C.; Probst, B.; Guttentag, M.; Alberto, R. Ascorbate as an electron relay between an irreversible electron donor and Ru(II) or Re(I) photosensitizers. *Chem. Commun.* **2014,** *50* (51), 6737.
(26) Amouyal, E. Photochemical production of hydrogen and oxygen from water: A review and state of the art. *Sol. Energy Mater. Sol. Cells* **1995,** *38* (1), 249.
(27) J.M. Lehn, J. P. S. *Nouv. J. Chim.* **1977,** *1*, 499.
(28) McKone, J. R.; Marinescu, S. C.; Brunschwig, B. S.; Winkler, J. R.; Gray, H. B. Earth-abundant hydrogen evolution electrocatalysts. *Chemical Science* **2014,** *5* (3), 865.
(29) Ozawa, H.; Haga, M.-a.; Sakai, K. A photo-hydrogen-evolving molecular device driving visible-light-induced EDTA-reduction of water into molecular hydrogen. *J. Am. Chem. Soc.* **2006,** *128* (15), 4926.
(30) Rau, S.; Schäfer, B.; Gleich, D.; Anders, E.; Rudolph, M.; Friedrich, M.; Görls, H.; Henry, W.; Vos, J. G. A supramolecular photocatalyst for the production of hydrogen and the selective hydrogenation of tolane. *Angew. Chem. Int. Ed.* **2006,** *45* (37), 6215.
(31) Tard, C.; Pickett, C. J. Structural and functional analogues of the active sites of the [Fe]-,[NiFe]-, and [FeFe]-hydrogenases. *Chem. Rev.* **2009,** *109* (6), 2245.
(32) Cavell, A. C.; Hartley, C. L.; Liu, D.; Tribble, C. S.; McNamara, W. R. Sulfinato iron (III) complex for electrocatalytic proton reduction. *Inorg. Chem.* **2015,** *54* (7), 3325.
(33) Hartley, C. L.; DiRisio, R. J.; Screen, M. E.; Mayer, K. J.; McNamara, W. R. Iron Polypyridyl Complexes for Photocatalytic Hydrogen Generation. *Inorg. Chem.* **2016,** *55* (17), 8865.
(34) Schiffman, Z. R.; Margonis, C. M.; Moyer, A.; Ott, M.; McNamara, W. R. Tridentate bis(2-pyridylmethyl)amine iron catalyst for electrocatalytic proton reduction. *Inorg. Chim. Acta* **2020,** *503*, 119394.
(35) Tagliapietra, M.; Squarcina, A.; Hickey, N.; De Zorzi, R.; Geremia, S.; Sartorel, A.; Bonchio, M. Hydrogen Evolution by FeIII Molecular Electrocatalysts Interconverting between Mono and Di-Nuclear Structures in Aqueous Phase. *ChemSusChem* **2017,** *10* (22), 4430.
(36) Lv, H.; Ruberu, T. P. A.; Fleischauer, V. E.; Brennessel, W. W.; Neidig, M. L.; Eisenberg, R. Catalytic light-driven generation of hydrogen from water by iron dithiolene complexes. *J. Am. Chem. Soc.* **2016,** *138* (36), 11654.

(37) Han, Z.; McNamara, W. R.; Eum, M. S.; Holland, P. L.; Eisenberg, R. A nickel thiolate catalyst for the long-lived photocatalytic production of hydrogen in a noble-metal-free system. *Angew. Chem.* **2012,** *124* (7), 1699.
(38) Han, Z.; Shen, L.; Brennessel, W. W.; Holland, P. L.; Eisenberg, R. Nickel pyridinethiolate complexes as catalysts for the light-driven production of hydrogen from aqueous solutions in noble-metal-free systems. *J. Am. Chem. Soc.* **2013,** *135* (39), 14659.
(39) Gross, M. A.; Reynal, A.; Durrant, J. R.; Reisner, E. Versatile photocatalytic systems for H2 generation in water based on an efficient DuBois-type nickel catalyst. *J. Am. Chem. Soc.* **2014,** *136* (1), 356.
(40) Bergamini, G.; Natali, M. Homogeneous vs. heterogeneous catalysis for hydrogen evolution by a nickel (ii) bis (diphosphine) complex. *Dalton Trans.* **2019,** *48* (39), 14653.
(41) Benazzi, E.; Cristino, V.; Boaretto, R.; Caramori, S.; Natali, M. Photoelectrochemical hydrogen evolution using $CdTe_xS_{1-x}$ quantum dots as sensitizers on NiO photocathodes. *Dalton Trans.* **2021,** *50* (2), 696-704.
(42) Rao, H.; Wang, Z.-Y.; Zheng, H.-Q.; Wang, X.-B.; Pan, C.-M.; Fan, Y.-T.; Hou, H.-W. Photocatalytic hydrogen evolution from a cobalt/nickel complex with dithiolene ligands under irradiation with visible light. *Cat. Sci. & Technol.* **2015,** *5* (4), 2332.
(43) Wang, J.; Li, C.; Zhou, Q.; Wang, W.; Hou, Y.; Zhang, B.; Wang, X. Photocatalytic hydrogen evolution by Cu(II) complexes. *Dalton Trans.* **2016,** *45* (13), 5439.
(44) Lv, H.; Gao, Y.; Guo, W.; Lauinger, S. M.; Chi, Y.; Bacsa, J.; Sullivan, K. P.; Wieliczko, M.; Musaev, D. G.; Hill, C. L. Cu-based Polyoxometalate Catalyst for Efficient Catalytic Hydrogen Evolution. *Inorg. Chem.* **2016,** *55* (13), 6750.
(45) Abudayyeh, A. M.; Schott, O.; Feltham, H. L. C.; Hanan, G. S.; Brooker, S. Copper catalysts for photo- and electro-catalytic hydrogen production. *Inorg. Chem. Front.* **2021,** *8* (4), 1015.
(46) Brown, G. M.; Brunschwig, B. S.; Creutz, C.; Endicott, J. F.; Sutin, N. Homogeneous catalysis of the photoreduction of water by visible light. Mediation by a tris (2, 2'-bipyridine) ruthenium(II)-cobalt(II) macrocycle system. *J. Am. Chem. Soc.* **1979,** *101* (5), 1298.
(47) Creutz, C.; Sutin, N.; Brunschwig, B. S. Excited-state photochemistry in the tris (2, 2'-bipyridine) ruthenium(II)-sulfite system. *J. Am. Chem. Soc.* **1979,** *101* (5), 1297.
(48) Hogue, R. W.; Schott, O.; Hanan, G. S.; Brooker, S. A smorgasbord of 17 cobalt complexes active for photocatalytic hydrogen evolution. *Chem. Eur. J.* **2018,** *24* (39), 9820.
(49) Rajak, S.; Vu, N.-N.; Kaur, P.; Duong, A.; Nguyen-Tri, P. Recent progress on the design and development of diaminotriazine based molecular catalysts for light-driven hydrogen production. *Coord. Chem. Rev.* **2022,** *456*, 214375.
(50) Abudayyeh, A. M.; Schott, O.; Feltham, H. L.; Hanan, G. S.; Brooker, S. Copper catalysts for photo-and electro-catalytic hydrogen production. *Inorg. Chem. Front.* **2021,** *8* (4), 1015.
(51) Lucarini, F.; Bongni, D.; Schiel, P.; Bevini, G.; Benazzi, E.; Solari, E.; Fadaei-Tirani, F.; Scopelliti, R.; Marazzi, M.; Natali, M. Rationalizing Photo-Triggered Hydrogen Evolution Using Polypyridine Cobalt Complexes: Substituent Effects on Hexadentate Chelating Ligands. *ChemSusChem* **2021,** *14* (8), 1874.
(52) Mazzeo, A.; Santalla, S.; Gaviglio, C.; Doctorovich, F.; Pellegrino, J. Recent progress in homogeneous light-driven hydrogen evolution using first-row transition metal catalysts. *Inorg. Chim. Acta* **2021,** *517*, 119950.

(53) Rajak, S.; Schott, O.; Kaur, P.; Maris, T.; Hanan, G. S.; Duong, A. Synthesis, crystal structure, characterization of pyrazine diaminotriazine based complexes and their systematic comparative study with pyridyl diaminotriazine based complexes for light-driven hydrogen production. *Polyhedron* **2020,** *180*, 114412.
(54) Rajak, S.; Chair, K.; Rana, L. K.; Kaur, P.; Maris, T.; Duong, A. Amidine/Amidinate Cobalt Complexes: One-Pot Synthesis, Mechanism, and Photocatalytic Application for Hydrogen Production. *Inorg. Chem.* **2020,** *59* (20), 14910.
(55) Celestine, M. J.; Lawrence, M. A. W.; Evaristo, N. K.; Legere, B. W.; Knarr, J. K.; Schott, O.; Picard, V.; Bullock, J. L.; Hanan, G. S.; McMillen, C. D.et al. N-substituted 2-pyridinecarbothioamides and polypyridyl mixed-ligand cobalt(III)-containing complexes for photocatalytic hydrogen generation. *Inorg. Chim. Acta* **2020,** *510*, 119726.
(56) Rajak, S.; Schott, O.; Kaur, P.; Maris, T.; Hanan, G. S.; Duong, A. Mimicking 2,2′:6′,2″:6″,2‴-quaterpyridine complexes for the light-driven hydrogen evolution reaction: synthesis, structural, thermal and physicochemical characterizations. *RSC Adv.* **2019,** *9* (48), 28153.
(57) Gueret, R.; Castillo, C. E.; Rebarz, M.; Thomas, F.; Sliwa, M.; Chauvin, J.; Dautreppe, B.; Pécaut, J.; Fortage, J.; Collomb, M.-N. Cobalt (II) Pentaaza-Macrocyclic Schiff base complex as catalyst for light-driven hydrogen evolution in water: electrochemical generation and theoretical investigation of the one-electron reduced species. *Inorg. Chem.* **2019,** *58* (14), 9043.
(58) Kurtz, D. A.; Dempsey, J. L. Proton-Coupled Electron Transfer Kinetics for the Photoinduced Generation of a Cobalt (III)-Hydride Complex. *Inorg. Chem.* **2019,** *58* (24), 16510.
(59) Eckenhoff, W. T.; McNamara, W. R.; Du, P.; Eisenberg, R. Cobalt complexes as artificial hydrogenases for the reductive side of water splitting. *Biochim. Biophys. Acta (BBA)-Bioenergetics* **2013,** *1827* (8-9), 958.
(60) Ladomenou, K.; Natali, M.; Iengo, E.; Charalampidis, G.; Scandola, F.; Coutsolelos, A. G. Photochemical hydrogen generation with porphyrin-based systems. *Coord. Chem. Rev.* **2015,** *304*, 38.
(61) Li, C.-B.; Gong, P.; Yang, Y.; Wang, H.-Y. Cobalt(II)–salen complexes for photocatalytic hydrogen production in noble metal-free molecular systems. *Catal. Lett.* **2018,** *148* (10), 3158.
(62) Chakraborty, S.; Edwards, E. H.; Kandemir, B.; Bren, K. L. Photochemical Hydrogen Evolution from Neutral Water with a Cobalt Metallopeptide Catalyst. *Inorg. Chem.* **2019,** *58* (24), 16402.
(63) Eckenhoff, W. T. Molecular catalysts of Co, Ni, Fe, and Mo for hydrogen generation in artificial photosynthetic systems. *Coord. Chem. Rev.* **2018,** *373*, 295.
(64) Kwok, C.-L.; Cheng, S.-C.; Ho, P.-Y.; Yiu, S.-M.; Au, V. K.-M.; Ho, W.-K.; Tsang, P.-K.; Xiang, J.; Leung, C.-F.; Ko, C.-C. Ligand Substituent Effects on Light-Driven Hydrogen Evolution by Cobalt(II) Tripodal Iminopyridine Catalysts under Precious-Metal-Free Conditions. *Eur. J. Inorg. Chem.* **2022**, e202200361.
(65) Fihri, A.; Artero, V.; Pereira, A.; Fontecave, M. Efficient H2-producing photocatalytic systems based on cyclometalated iridium- and tricarbonylrhenium-diimine photosensitizers and cobaloxime catalysts. *Dalton Trans.* **2008,** (41), 5567.
(66) Fihri, A.; Artero, V.; Razavet, M.; Baffert, C.; Leibl, W.; Fontecave, M. Cobaloxime-based photocatalytic devices for hydrogen production. *Angew. Chem.* **2008,** *120* (3), 574.

(67) Lazarides, T.; McCormick, T.; Du, P.; Luo, G.; Lindley, B.; Eisenberg, R. Making hydrogen from water using a homogeneous system without noble metals. *J. Am. Chem. Soc.* **2009,** *131* (26), 9192.
(68) Du, P.; Knowles, K.; Eisenberg, R. A homogeneous system for the photogeneration of hydrogen from water based on a platinum(II) terpyridyl acetylide chromophore and a molecular cobalt catalyst. *J. Am. Chem. Soc.* **2008,** *130* (38), 12576.
(69) Gamache, M. T.; Auvray, T.; Kurth, D. G.; Hanan, G. S. Dinuclear 2,4-di(pyridin-2-yl)-pyrimidine based ruthenium photosensitizers for hydrogen photo-evolution under red light. *Dalton Trans.* **2021,** *50* (45), 16528.
(70) Rupp, M. T.; Auvray, T.; Shevchenko, N.; Swoboda, L.; Hanan, G. S.; Kurth, D. G. Substituted 2, 4-Di (pyridin-2-yl) pyrimidine-Based Ruthenium Photosensitizers for Hydrogen Photoevolution under Red Light. *Inorg. Chem.* **2020,** *60* (1), 292.
(71) Hong, Y. H.; Lee, Y.-M.; Nam, W.; Fukuzumi, S. Photocatalytic Hydrogen Evolution from Plastoquinol Analogues as a Potential Functional Model of Photosystem I. *Inorg. Chem.* **2020,** *59* (20), 14838.
(72) Auvray, T.; Sahoo, R.; Deschênes, D.; Hanan, G. S. Heteroleptic ruthenium bis-terpyridine complexes bearing a 4-(dimethylamino) phenyl donor and free coordination sites for hydrogen photo-evolution. *Dalton Trans.* **2019,** *48* (40), 15136.
(73) Rupp, M.; Auvray, T.; Rousset, E.; Mercier, G. M.; Marvaud, V.; Kurth, D. G.; Hanan, G. S. Photocatalytic hydrogen evolution driven by a heteroleptic ruthenium (II) bis (terpyridine) complex. *Inorg. Chem.* **2019,** *58* (14), 9127.
(74) Du, P.; Schneider, J.; Luo, G.; Brennessel, W. W.; Eisenberg, R. Visible Light-Driven Hydrogen Production from Aqueous Protons Catalyzed by Molecular Cobaloxime Catalysts. *Inorg. Chem.* **2009,** *48* (11), 4952.
(75) Probst, B.; Kolano, C.; Hamm, P.; Alberto, R. An efficient homogeneous intermolecular rhenium-based photocatalytic system for the production of H2. *Inorg. Chem.* **2009,** *48* (5), 1836.
(76) Andreiadis, E. S.; Chavarot-Kerlidou, M.; Fontecave, M.; Artero, V. Artificial Photosynthesis: From Molecular Catalysts for Light-driven Water Splitting to Photoelectrochemical Cells. *Photochem. Photobiol.* **2011,** *87* (5), 946.
(77) Zhang, P.; Jacques, P.-A.; Chavarot-Kerlidou, M.; Wang, M.; Sun, L.; Fontecave, M.; Artero, V. Phosphine coordination to a cobalt diimine–dioxime catalyst increases stability during light-driven H_2 production. *Inorg. Chem.* **2012,** *51* (4), 2115.
(78) McCormick, T. M.; Calitree, B. D.; Orchard, A.; Kraut, N. D.; Bright, F. V.; Detty, M. R.; Eisenberg, R. Reductive side of water splitting in artificial photosynthesis: new homogeneous photosystems of great activity and mechanistic insight. *J. Am. Chem. Soc.* **2010,** *132* (44), 15480.
(79) Natali, M.; Luisa, A.; Iengo, E.; Scandola, F. Efficient photocatalytic hydrogen generation from water by a cationic cobalt(II) porphyrin. *Chem. Commun.* **2014,** *50* (15), 1842.
(80) Guttentag, M.; Rodenberg, A.; Kopelent, R.; Probst, B.; Buchwalder, C.; Brandstätter, M.; Hamm, P.; Alberto, R.; Wiley Online Library, 2012.
(81) Mir, A. Q.; Saha, S.; Mitra, S.; Guria, S.; Majumder, P.; Dolui, D.; Dutta, A. The rational inclusion of vitamin B6 boosts artificial cobalt complex catalyzed green H2 production. *Sustain. Energy Fuels* **2022,** *6* (18), 4160.
(82) Ming, M.; Yuan, H.; Yang, S.; Wei, Z.; Lei, Q.; Lei, J.; Han, Z. Efficient Red-Light-Driven Hydrogen Evolution with an Anthraquinone Organic Dye. *J. Am. Chem. Soc.* **2022,** *144* (43), 19680.

(83) Panagiotopoulos, A.; Ladomenou, K.; Sun, D.; Artero, V.; Coutsolelos, A. G. Photochemical hydrogen production and cobaloximes: the influence of the cobalt axial N-ligand on the system stability. *Dalton Trans.* **2016,** *45* (15), 6732.

(84) Natali, M.; Luisa, A.; Iengo, E.; Scandola, F. Efficient photocatalytic hydrogen generation from water by a cationic cobalt(ii) porphyrin. *Chem. Commun.* **2014,** *50* (15), 1842.

(85) Aoi, S.; Mase, K.; Ohkubo, K.; Fukuzumi, S. Mechanism of a one-photon two-electron process in photocatalytic hydrogen evolution from ascorbic acid with a cobalt chlorin complex. *Chem. Commun.* **2015,** *51* (82), 15145.

(86) Yuan, H.-Q.; Wang, H.-H.; Kandhadi, J.; Wang, H.; Zhan, S.-Z.; Liu, H.-Y. Electrochemical and photocatalytic hydrogen evolution by an electron-deficient cobalt tris(ethoxycarbonyl)corrole complex. *Appl. Organomet. Chem.* **2017,** *31* (11), e3773.

(87) Morales Vásquez, M. A.; Hamer, M.; Neuman, N. I.; Tesio, A. Y.; Hunt, A.; Bogo, H.; Calvo, E. J.; Doctorovich, F. Iron and Cobalt Corroles in Solution and on Carbon Nanotubes as Molecular Photocatalysts for Hydrogen Production by Water Reduction. *ChemCatChem* **2017,** *9* (16), 3259.

(88) Xie, A.; Liu, X.-L.; Xiang, Y.-C.; Luo, G.-G. A homogeneous molecular system for the photogeneration of hydrogen from water based on a $[RuII(bpy)_3]^{2+}$ photosensitizer and a phthalycyanine cobalt catalyst. *J. Alloys Compd.* **2017,** *717*, 226.

(89) Luo, G.-G.; Li, X.-C.; Wang, J.-H. Visible Light-Driven Hydrogen Evolution from Aqueous Solution in a Noble-Metal-Free System Catalyzed by a Cobalt Phthalocyanine. *ChemistrySelect* **2016,** *1* (3), 425.

(90) Drosou, M.; Kamatsos, F.; Mitsopoulou, C. A. Recent advances in the mechanisms of the hydrogen evolution reaction by non-innocent sulfur-coordinating metal complexes. *Inorg. Chem. Front.* **2020,** *7* (1), 37.

(91) McNamara, W. R.; Han, Z.; Alperin, P. J.; Brennessel, W. W.; Holland, P. L.; Eisenberg, R. A Cobalt–Dithiolene Complex for the Photocatalytic and Electrocatalytic Reduction of Protons. *J. Am. Chem. Soc.* **2011,** *133* (39), 15368.

(92) Solis, B. H.; Hammes-Schiffer, S. Computational Study of Anomalous Reduction Potentials for Hydrogen Evolution Catalyzed by Cobalt Dithiolene Complexes. *J. Am. Chem. Soc.* **2012,** *134* (37), 15253.

(93) Zhang, C.; Li, G.; Cai, X. Study on deactivation and reaction mechanism of Co thiolate complexes in photocatalytic hydrogen production system. *Int. J. Energy Res.* **2018,** *42* (3), 977.

(94) Zhao, Y.; Wang, Y.; Wu, Q.; Lin, J.; Wu, S.; Hou, W.; Wu, R.; Luo, G. New tricks for an old dog: Visible light-driven hydrogen production from water catalyzed by fac- and mer- geometrical isomers of tris(thiosemicarbazide) cobalt(III). *Chinese J. Catal.* **2018,** *39* (3), 517.

(95) Fogeron, T.; Porcher, J.-P.; Gomez-Mingot, M.; Todorova, T. K.; Chamoreau, L.-M.; Mellot-Draznieks, C.; Li, Y.; Fontecave, M. A cobalt complex with a bioinspired molybdopterin-like ligand: a catalyst for hydrogen evolution. *Dalton Trans.* **2016,** *45* (37), 14754.

(96) Cai, J.; Zhao, L.; Wei, J.; He, C.; Long, S.; Duan, C. Negatively charged metal–organic hosts with cobalt dithiolene species: improving PET processes for light-driven proton reduction through host–guest electrostatic interactions. *Chem. Commun.* **2019,** *55* (59), 8524.

(97) Kawano, K.; Yamauchi, K.; Sakai, K. A cobalt–NHC complex as an improved catalyst for photochemical hydrogen evolution from water. *Chem. Commun.* **2014,** *50* (69), 9872.

(98) Rao, G. K.; Pell, W.; Gabidullin, B.; Korobkov, I.; Richeson, D. Electro- and Photocatalytic Generation of H_2 Using a Distinctive CoII "PN_3P" Pincer Supported Complex with Water or Saturated Saline as a Hydrogen Source. *Chem. Eur. J.* **2017,** *23* (66), 16763.

(99) Li, C.-B.; Gong, P.; Yang, Y.; Wang, H.-Y. Cobalt(II)–Salen Complexes for Photocatalytic Hydrogen Production in Noble Metal-Free Molecular Systems. *Catal. Lett.* **2018,** *148* (10), 3158.

(100) Fu, L.-Z.; Zhou, L.-L.; Tang, L.-Z.; Zhang, Y.-X.; Zhan, S.-Z. Electrochemical and photochemical-driven hydrogen evolution catalyzed by a dinuclear Co^{II}–Co^{II} complex. *J. Power Sources* **2015,** *280*, 453.

(101) Zhou, L.-L.; Fu, L.-Z.; Tang, L.-Z.; Zhang, Y.-X.; Zhan, S.-Z. Electrochemical and photochemical-driven hydrogen evolution catalyzed by a dinuclear cobalt(II)–triazenido complex with high turnover number. *Int. J. Hydrogen Energy* **2015,** *40* (15), 5099.

(102) Fu, L.-Z.; Zhou, L.-L.; Zhan, S.-Z. A molecular cobalt catalyst supported by an amine-bis(phenolate) ligand for both electrolytic and photolytic water reduction. *RSC Adv.* **2015,** *5* (103), 84770.

(103) Tang, L.-Z.; Lin, C.-N.; Zhang, Y.-X.; Zhan, S.-Z. Electrocatalytic and photocatalytic hydrogen generation from water by a water-soluble cobalt complex supported by 2-ethyl-2-(2-hydroxybenzylideneamino)propane-1,3-diol. *Int. J. Hydrogen Energy* **2016,** *41* (33), 14676.

(104) Droghetti, F.; Lucarini, F.; Molinari, A.; Ruggi, A.; Natali, M. Recent findings and future directions in photosynthetic hydrogen evolution using polypyridine cobalt complexes. *Dalton Trans.* **2022,** *51* (28), 10658.

(105) Schnidrig, S.; Bachmann, C.; Müller, P.; Weder, N.; Spingler, B.; Joliat-Wick, E.; Mosberger, M.; Windisch, J.; Alberto, R.; Probst, B. Structure–Activity and Stability Relationships for Cobalt Polypyridyl-Based Hydrogen-Evolving Catalysts in Water. *ChemSusChem* **2017,** *10* (22), 4570.

(106) Sun, Y.; Sun, J.; Long, J. R.; Yang, P.; Chang, C. J. Photocatalytic generation of hydrogen from water using a cobalt pentapyridine complex in combination with molecular and semiconductor nanowire photosensitizers. *Chemical Science* **2013,** *4* (1), 118.

(107) Bachmann, C.; Guttentag, M.; Spingler, B.; Alberto, R. 3d Element complexes of pentadentate bipyridine-pyridine-based ligand scaffolds: structures and photocatalytic activities. *Inorg. Chem.* **2013,** *52* (10), 6055.

(108) Joliat, E.; Schnidrig, S.; Probst, B.; Bachmann, C.; Spingler, B.; Baldridge, K. K.; von Rohr, F.; Schilling, A.; Alberto, R. Cobalt complexes of tetradentate, bipyridine-based macrocycles: their structures, properties and photocatalytic proton reduction. *Dalton Trans.* **2016,** *45* (4), 1737.

(109) Weder, N.; Grundmann, N. S.; Probst, B.; Blacque, O.; Ketkaew, R.; Creazzo, F.; Luber, S.; Alberto, R. Two Novel Dinuclear Cobalt Polypyridyl Complexes in Electro- and Photocatalysis for Hydrogen Production: Cooperativity Increases Performance. *ChemSusChem* **2022**, e202201049.

(110) Bigi, J. P.; Hanna, T. E.; Harman, W. H.; Chang, A.; Chang, C. J. Electrocatalytic reduction of protons to hydrogen by a water-compatible cobalt polypyridyl platform. *Chem. Commun.* **2010,** *46* (6), 958.

(111) Queyriaux, N.; Jane, R. T.; Massin, J.; Artero, V.; Chavarot-Kerlidou, M. Recent developments in hydrogen evolving molecular cobalt(II)–polypyridyl catalysts. *Coord. Chem. Rev.* **2015,** *304-305*, 3.

(112) de Vos, S. D.; Otten, M.; Wissink, T.; Broere, D. L. J.; Hensen, E. J. M.; Klein Gebbink, R. J. Hydrogen Evolution Electrocatalysis with a Molecular Cobalt Bis(alkylimidazole)methane Complex in DMF: a critical activity analysis. *ChemSusChem* **2022***, 15, e2022013*

(113) Braussaud, N.; Rüther, T.; Cavell, K. J.; Skelton, B. W.; White, A. H. Bridged 1-Methylbisimidazoles as Building Blocks for Mixed Donor Bi- and Tridentate Chelating Ligands. *Synthesis* **2001,** *2001* (04), 0626.

(114) Bruijnincx, P. C.; Lutz, M.; Spek, A. L.; van Faassen, E. E.; Weckhuysen, B. M.; van Koten, G.; Klein Gebbink, R. J. Bis(1-methylimidazol-2-yl)propionates and Bis(1-methylbenzimidazol-2-yl)-propionates: A New Family of Biomimetic *N*,*N*,*O* Ligands – Synthesis, Structures and Cu^{II} Coordination Complexes *Eur. J. Inorg.Chem.* **2005**, 4, 779–787

(115) Elgafi, S.; D. Field, L.; A. Messerle, B.; W. Hambley, T.; Turner, P. Synthesis of novel ruthenium complexes containing bidentate imidazole-based ligands. *J. Chem. Soc., Dalton Trans.* **1997**, 2341-2346.

(116) Bruijnincx, P. C. A.; Lutz, M.; Spek, Anthony L.; van Faassen, E. E.; Weckhuysen, B. M.; van Koten, G.; Klein Gebbink, R. J. M. Bis(1-methylimidazol-2-yl)propionates and Bis(1-methylbenzimidazol-2-yl)-propionates: A New Family of Biomimetic *N,N,O* Ligands – Synthesis, Structures and Cu^{II} Coordination Complexes. *Eur. J. Inorg. Chem.* **2005,** *2005* (4), 779-787.

(117) Beyene, B. B.; Mane, S. B.; Hung, C.-H. Electrochemical Hydrogen Evolution by Cobalt (II) Porphyrins: Effects of Ligand Modification on Catalytic Activity, Efficiency and Overpotential. *J. Electrochem. Soc.* **2018,** *165* (9), H481.

(118) James, David W., Nolan, M. J. Vibrational Spectra of Transition Metal Complexes and the Nature of the Metal-Ligand Bond Progress in *Inorg. Chem.* 1967 195-275

(119) Hodgson, J. B.; Percy, G. C.; Thornton, D. A. The infrared spectra of imidazole complexes of first transition series metal(II) nitrates and perchlorates. *J. Mol. Struct.* **1980,** *66*, 81.

(120) Santoro, A.; Mighell, A. D.; Zocchi, M.; Reimann, C. W. The crystal and molecular structure of hexakis(imidazole)nickel(II) nitrate, $(C_3H_4N_2)_6Ni(NO_3)_2$. *Acta Crystallogr. Sect. B* **1969,** *25* (5), 842.

(121) Curtis, N.; Curtis, Y. M. Some nitrato-amine nickel (II) compounds with monodentate and bidentate nitrate ions. *Inorg. Chem.* **1965,** *4* (6), 804.

(122) Lever, A. B. P.; Mantovani, E.; Ramaswamy, B. S. Infrared Combination Frequencies in Coordination Complexes containing Nitrate Groups in various Coordination Environments. A Probe for the Metal–Nitrate Interaction. *Can. J. Chem.* **1971,** *49* (11), 1957.

(123) Karayannis, N. M.; Mikulski, C. M.; Pytlewski, L. L.; Labes, M. M. Metal nitrate and thiocyanate complexes with 2,6-lutidine n-oxide. *J. Inorg. Nucl. Chem.* **1972,** *34* (10), 3139.

(124) Karayannis, N.; Mikulski, C.; Pytlewski, L.; Labes, M. 2-, 3-and 4-Picoline N-oxide complexes with cobalt(II), nickel(II) and copper(II) nitrates. *Inorg. Chem.* **1974,** *13* (5), 1146.

(125) Ahuja, I. S.; Singh, R.; Rai, C. P. Structural information on silver(I), zinc(II) and cadmium(II) nitrate complexes with 1,10-phenanthroline, 2,2'-bipyridine and 2,2'-bipyridine N, N'-dioxide from their infrared spectra. *J. Mol. Struct.* **1978,** *49* (1), 201.

(126) Ahuja, I. S.; Singh, R.; Yadava, C. L. Structural information on cobalt(II), nickel(II), copper(II), zinc(II), silver(I) and cadmium(II) nitrate complexes with hexamethylenetetramine from their magnetic moments, electronic and infrared spectra. *J. Mol. Struct.* **1980,** *68*, 333.

(127) Gaye, M.; Tamboura, F.; Sall, A. Spectroscopic studies of some lanthanide(III) nitrate complexes synthesized from a new ligand 2, 6-bis-(salicylaldehyde hydrazone)-4-chlorophenol. *Bull. Chem. Soc. Ethiop.* **2003,** *17* (1).
(128) Kumar, D. S.; Alexander, V. Macrocyclic complexes of lanthanides in identical ligand frameworks part 1. Synthesis of lanthanide(III) and yttrium(III) complexes of an 18-membered dioxatetraaza macrocycle. *Inorg. Chim. Acta* **1995,** *238* (1), 63.
(129) Guerriero, P.; Casellato, U.; Tamburini, S.; Vigato, P. A.; Graziani, R. Lanthanide complexes with compartmental schiff bases. *Inorg. Chim. Acta* **1987,** *129* (1), 127.
(130) Nakamoto, K. *Infrared and Raman spectra of inorganic and coordination compounds, part B: applications in coordination, organometallic, and bioinorganic chemistry*; John Wiley & Sons, 2009.
(131) Radecka-Paryzek, W. The template synthesis and characterization of hexaaza 18-membered macrocyclic complexes of cerium(III), praseodymium(III) and neodymium(III) nitrates. *Inorg. Chim. Acta* **1985,** *109* (3), L21.
(132) Carnall, W. T.; Siegel, S.; Ferraro, J. R.; Tani, B.; Gebert, E. New series of anhydrous double nitrate salts of the lanthanides. Structural and spectral characterization. *Inorg. Chem.* **1973,** *12* (3), 560.
(133) Choca, M.; Ferraro, J. R.; Nakamoto, K. Vibrational spectra of anhydrous metal pyridine nitrates. *J. Chem. Soc., Dalton Trans.* **1972**, 2297-2301.
(134) A similar vibration was observed for cobalt(II) tetrafluroroborate hexahydrate
(135) Ramesh, T.; Taj, A. Luminescent Studies of Brucite based Layered Materials. *Inernational Journal of Science Research* **2013,** *01* (04), 487.
(136) Shaffer, C. J.; Schröder, D. Microhydrated cobalt-nitrate cations [Co(NO3)(H2O)n]+ (n=2, 3) studied by infrared spectroscopy in the gas phase. *Int. J. Mass spectrom.* **2012,** *311*, 17.
(137) Tanaka, N.; Sugi, H.; Fujita, J. Infrared Spectroscopic Studies of Acido-pentammine Cobalt(III) Complexes, Sulfato, Nitrito, Nitrato and Carbonato Complexes. *Bull. Chem. Soc. Jpn.* **1964,** *37* (5), 640.
(138) Talebi, S.; Abedi, A.; Amani, V. Cobalt(II) complexes with small variations in the heterocycle ligand, crystal structure and DFT calculations. *J. Mol. Struct.* **2021,** *1230*, 129911.
(139) A control experiment with $[Co(H_2O)_6](NO_3)_2$ did reveal a strong absorption at 3300 cm^{-1} (Appendix D, Figure D7).
(140) Bruijnincx, P. C. A.; Buurmans, I. L. C.; Huang, Y.; Juhász, G.; Viciano-Chumillas, M.; Quesada, M.; Reedijk, J.; Lutz, M.; Spek, A. L.; Münck, E.et al. Mono- and Dinuclear Iron Complexes of Bis(1-methylimidazol-2-yl)ketone (bik): Structure, Magnetic Properties, and Catalytic Oxidation Studies. *Inorg. Chem.* **2011,** *50* (19), 9243-9255.
(141) Felton, G. A. N.; Glass, R. S.; Lichtenberger, D. L.; Evans, D. H. Iron-Only Hydrogenase Mimics. Thermodynamic Aspects of the Use of Electrochemistry to Evaluate Catalytic Efficiency for Hydrogen Generation. *Inorg. Chem.* **2006,** *45* (23), 9181-9184.
(142) Bernhardt, P. V.; Jones, L. A. Electrochemistry of macrocyclic cobalt(III/II) hexaamines: electrocatalytic hydrogen evolution in aqueous solution. *Inorg. Chem.* **1999,** *38* (22), 5086.
(143) Tong, L.; Zong, R.; Thummel, R. P. Visible light-driven hydrogen evolution from water catalyzed by a molecular cobalt complex. *J. Am. Chem. Soc.* **2014,** *136* (13), 4881.
(144) Tong, L.; Kopecky, A.; Zong, R.; Gagnon, K. J.; Ahlquist, M. S.; Thummel, R. P. Light-driven proton reduction in aqueous medium catalyzed by a family of cobalt complexes with tetradentate polypyridine-type ligands. *Inorg. Chem.* **2015,** *54* (16), 7873.

(145) Kaeffer, N.; Morozan, A.; Fize, J.; Martinez, E.; Guetaz, L.; Artero, V. The Dark Side of Molecular Catalysis: Diimine–Dioxime Cobalt Complexes Are Not the Actual Hydrogen Evolution Electrocatalyst in Acidic Aqueous Solutions. *ACS Catalysis* **2016,** *6* (6), 3727.
(146) Bard, A. J.; Faulkner, L. R. *Electrochemical Methods: Fundamentals and Applications*, 2001.
(147) Lee, K. J.; McCarthy, B. D.; Dempsey, J. L. On decomposition, degradation, and voltammetric deviation: the electrochemist's field guide to identifying precatalyst transformation. *Chem. Soc. Rev.* **2019,** *48* (11), 2927.
(148) Martin, D. J.; McCarthy, B. D.; Donley, C. L.; Dempsey, J. L. Electrochemical hydrogenation of a homogeneous nickel complex to form a surface adsorbed hydrogen-evolving species. *Chem. Commun.* **2015,** *51* (25), 5290.
(149) McCarthy, B. D.; Donley, C. L.; Dempsey, J. L. Electrode initiated proton-coupled electron transfer to promote degradation of a nickel(ii) coordination complex. *Chemical Science* **2015,** *6* (5), 2827.
(150) Anxolabéhère-Mallart, E.; Costentin, C.; Fournier, M.; Robert, M. Cobalt-Bisglyoximato Diphenyl Complex as a Precatalyst for Electrocatalytic H_2 Evolution. *J. Phys. Chem. C* **2014,** *118* (25), 13377.
(151) Anxolabéhère-Mallart, E.; Costentin, C.; Fournier, M.; Nowak, S.; Robert, M.; Savéant, J.-M. Boron-Capped Tris(glyoximato) Cobalt Clathrochelate as a Precursor for the Electrodeposition of Nanoparticles Catalyzing H2 Evolution in Water. *J. Am. Chem. Soc.* **2012,** *134* (14), 6104.
(152) El Ghachtouli, S.; Fournier, M.; Cherdo, S.; Guillot, R.; Charlot, M.-F.; Anxolabéhère-Mallart, E.; Robert, M.; Aukauloo, A. Monometallic Cobalt–Trisglyoximato Complexes as Precatalysts for Catalytic H_2 Evolution in Water. *J. Phys. Chem. C* **2013,** *117* (33), 17073.
(153) Pavlishchuk, V. V.; Addison, A. W. Conversion constants for redox potentials measured versus different reference electrodes in acetonitrile solutions at 25°C. *Inorg. Chim. Acta* **2000,** *298* (1), 97.
(154) Prier, C. K.; Rankic, D. A.; MacMillan, D. W. Visible light photoredox catalysis with transition metal complexes: applications in organic synthesis. *Chem. Rev.* **2013,** *113* (7), 5322.
(155) Koike, T.; Akita, M. Fine design of photoredox systems for catalytic fluoromethylation of carbon–carbon multiple bonds. *Acc. Chem. Res.* **2016,** *49* (9), 1937.
(156) Hofbeck, T.; Yersin, H. The Triplet State of fac-Ir(ppy)$_3$. *Inorg. Chem.* **2010,** *49* (20), 9290.
(157) Pellegrin, Y.; Odobel, F. Sacrificial electron donor reagents for solar fuel production. *Comptes Rendus Chimie* **2017,** *20* (3), 283.
(158) Shen, J.; Griffiths, P. T.; Campbell, S. J.; Utinger, B.; Kalberer, M.; Paulson, S. E. Ascorbate oxidation by iron, copper and reactive oxygen species: review, model development, and derivation of key rate constants. *Sci. Rep.* **2021,** *11* (1), 7417.
(159) Drexhage, K.; Erikson, G.; Hawks, G.; Reynolds, G. Water-soluble coumarin dyes for flashlamp-pumped dye lasers. *Opt. Commun.* **1975,** *15* (3), 399.
(160) Dalle, K. E.; Warnan, J.; Leung, J. J.; Reuillard, B.; Karmel, I. S.; Reisner, E. Electro- and solar-driven fuel synthesis with first row transition metal complexes. *Chem. Rev.* **2019,** *119* (4), 2752.
(161) Lo, W. K.; Castillo, C. E.; Gueret, R.; Fortage, J.; Rebarz, M.; Sliwa, M.; Thomas, F.; McAdam, C. J.; Jameson, G. B.; McMorran, D. A. Synthesis, characterization, and photocatalytic H_2-evolving activity of a family of $[Co(N_4Py)(X)]_n^+$ complexes in aqueous solution. *Inorg. Chem.* **2016,** *55* (9), 4564.

(162) Xie, J.; Zhou, Q.; Li, C.; Wang, W.; Hou, Y.; Zhang, B.; Wang, X. An unexpected role of the monodentate ligand in photocatalytic hydrogen production of the pentadentate ligand-based cobalt complexes. *Chem. Commun.* **2014,** *50* (49), 6520.
(163) Hu, X.; Brunschwig, B. S.; Peters, J. C. Electrocatalytic Hydrogen Evolution at Low Overpotentials by Cobalt Macrocyclic Glyoxime and Tetraimine Complexes. *J. Am. Chem. Soc.* **2007,** *129* (29), 8988.
(164) Wakerley, D. W.; Reisner, E. Development and understanding of cobaloxime activity through electrochemical molecular catalyst screening. *Phys. Chem. Chem. Phys.* **2014,** *16* (12), 5739.
(165) Kilgore, U. J.; Stewart, M. P.; Helm, M. L.; Dougherty, W. G.; Kassel, W. S.; DuBois, M. R.; DuBois, D. L.; Bullock, R. M. Studies of a Series of $[Ni(PR_2N^{Ph2})2(CH_3CN)]^{2+}$ Complexes as Electrocatalysts for H_2 Production: Substituent Variation at the Phosphorus Atom of the P_2N_2 Ligand. *Inorg. Chem.* **2011,** *50* (21), 10908.
(166) Huo, P.; Uyeda, C.; Goodpaster, J. D.; Peters, J. C.; Miller, T. F., III. Breaking the Correlation between Energy Costs and Kinetic Barriers in Hydrogen Evolution via a Cobalt Pyridine-Diimine-Dioxime Catalyst. *ACS Catalysis* **2016,** *6* (9), 6114.
(167) Natali, M. Elucidating the key role of PH on light-driven hydrogen evolution by a molecular cobalt catalyst. *ACS Catalysis* **2017,** *7* (2), 1330.
(168) Ellgen, P. C.; Gerlach, J. N. Kinetics and mechanism of the substitution reactions of bis(mercaptotricarbonyliron) complexes. *Inorg. Chem.* **1973,** *12* (11), 2526.
(169) Ghosh, P.; Naastepad, R.; Riemersma, C. F.; Lutz, M.; Moret, M.-E.; Klein Gebbink, R. J. M. Noninnocent β-Diiminate Ligands: Redox Activity of a Bis(alkylimidazole)methane Ligand in Cobalt and Zinc Complexes. *Chem. Eur. J.* **2017,** *23* (45), 10732.
(170) James, D. W.; Nolan, M. J. In *Prog. Inorg. Chem.*, **1967**, 9, 195-275.
(171) Schreurs, A. M.; Xian, X.; Kroon-Batenburg, L. M. EVAL15: a diffraction data integration method based on ab initio predicted profiles. *J. Appl. Crystallogr.* **2010,** *43* (1), 70.
(172) Herbst-Irmer, R.; Sheldrick, G. M. Refinement of twinned structures with SHELXL97. *Acta Crystallogr. Sect. B: Struct. Sci.* **1998,** *54* (4), 443.
(173) Sheldrick, G. SADABS-2012/1. *Bruker/Siemens Area Detector Absorption Correction Program* **2012**.
(174) Sheldrick, G. SHELXT - Integrated space-group and crystal-structure determination. *Acta Crystallogr. Sect. A* **2015,** *71* (1), 3.
(175) Sheldrick, G. M. Crystal structure refinement with SHELXL. *Acta Crystallogr. Sect. C: Struct. Chem.* **2015,** *71* (1), 3.
(176) Spek, A. Structure validation in chemical crystallography. *Acta Crystallogr. Sect. D* **2009,** *65* (2), 148.

Chapter 6

A Perspective on Molecular Hydrogen Evolution Catalysis

6.1 Introduction

Hydrogen's importance as a chemical reagent and green energy carrier has become widely acknowledged over the last decade and provides great motivation for developing sustainable processes for its production. Electro- and photoelectrochemical water splitting offers a promising strategy for renewable H_2 generation from water using the energy from sunlight, but this technology is currently not viable for widespread implementation. Especially the use of scarce and expensive noble-metal catalysts must be circumvented. From this perspective, earth-abundant metals hold economic advantages such as cost and abundant supply, making them promising catalyst candidates. However, their catalytic activity is not yet suitable for practical applications and requires further research efforts. As extensively described in this Doctoral Thesis, a particularly interesting class of earth-abundant metal-based catalysts are molecular complexes, because of their activity and uniform structure. The former is a result of the intricate interplay between structural and electronic aspects of the active site, while the latter allows for in-depth structure-reactivity analysis through optimization studies, which are some of the main advantages of molecular complexes compared to other materials. Recent advances in combining advanced knowledge in synthesis techniques, spectroscopy, voltammetry, computational modeling, and application techniques allow us to enter a new era of rational catalyst design. In order to push the boundaries of molecular catalyst design, new integrated research strategies are required that combine the lessons learned during catalyst optimization, implementation, and application.

In this chapter, we will discuss how the unraveling of the structures of hydrogenase enzymes, which can produce hydrogen with high efficiency and went through millions of years of structural evolution, has led to one of today's most inspiring molecular hydrogen evolution catalysts. Furthermore, we discuss how one may be able to measure and benchmark new

molecular catalysts, that include the most recent design principles, with current state-of-the-art equipment and methods in common laboratories. This combination leads us to establish a total overview of catalytic hydrogen evolution with molecular complexes. The chapter ends with a brief outlook on the near future developments within the field of molecular hydrogen evolution catalysis.

6.2 Unraveling the Design Principles from Nature for Efficient Hydrogen Evolution

All hydrogen evolution processes rely on the selective input of multiple protons (H^+) and electrons (e^-) to accomplish the chemical cascade reaction that yields hydrogen. The challenges in the organization of proton and electron inventories, a fundamental requirement for achieving product selectivity and catalytic stability, remain in artificial hydrogen evolution systems and emphasize the complexity of the apparently simple combination of two electrons and two protons to form hydrogen. Yet, nature is capable of achieving the above in a highly efficient way using abundant elements only. Therefore, design principles for new molecular complex functionalities are typically derived from nature, from the hydrogenases specifically, which was extensively referred to in this Doctoral Thesis.

The most important and understood principles and effects of the hydrogenases can be divided per coordination sphere (, FeFe-hydrogenase in this example).[1] The outer coordination sphere (purple) effects include; (i) electron transfer from a redox site or redox partner (*i.e.* iron-sulfur clusters), (ii) a proton transfer channel with polar amino acids and functional water molecules, and (iii) a hydrophobic gas channel for product release to the surface of the enzyme. The second coordination sphere (white) contains groups that facilitate proton transfers (a pendant amine base proton relay) and electron delivery (another iron-sulfur cluster, specifically [4Fe–4S]). Furthermore, the second coordination sphere comprises hydrophobic contacts (iv) and hydrogen-bonding contacts (v) that contribute to the interaction with the protein structure and the reactivity of the active site. The first coordination sphere (light magenta) is defined by the ligands (two cyanides, three COs, a cysteine, and an azadithiolate) that are directly bound to the iron ions on one end and on the other end interact with amino acids (i.e. serine, proline, alanine, lysine, and glutamic acid) and the iron-sulfur cluster.[2] These ligands are the major contributors to establishing the electronic environment of the active site and its reactivity. Lastly, the protonation state and polarity of the active site are influenced by the charge distribution across all coordination spheres through electric field effects, such that the active

site can be tuned for H_2 production or oxidation (vi). Then, H_2 production or oxidation is achieved through concerted electron-proton transfer steps at significant rates.[3]

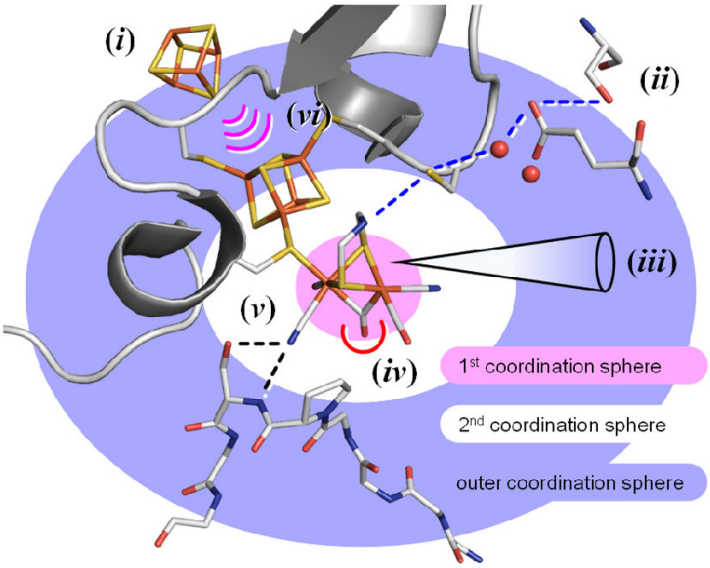

Figure 1. Conceptual partitioning of FeFe-hydrogenases into first, second, and outer coordination spheres. The first coordination sphere contains the ligands directly attached to the active metal center (light magenta). The second coordination sphere (white) includes proton and electron transfer groups, hydrogen-bonding contacts (v), and hydrophobic interactions (i*v*). The outer coordination sphere (purple) effects include electron transfer (i), proton transfer (ii), hydrophobic gas channels (iii), and electric field effects (vi). Reproduced from Ribbe *et al.* with permission.[1] Copyright 2022 American Chemical Society.

6.3 Artificial Molecular HER Complexes

In reported molecular hydrogen evolution reaction (HER) catalysts the reactivity of the hydrogenase active site is aimed to be replicated using a transition metal, coordinated with appropriate ligands. In such complexes, earth-abundant metal centers (e.g. Mn, Fe, Co, Ni, Cu, Zn), with ligands featuring different coordinating atoms (e.g. phosphorus, oxygen, nitrogen, and sulfur) have been used (**Chapter 1**).[4-6] Many different metal complexes have been reported with high catalytic rates or low overpotentials (additional lost energy) under optimized conditions.[7] Yet, it remains challenging to achieve both, *i.e.* high catalytic rates at a low overpotential, as there is a general trade-off between the catalytic rate of HER catalysis at the metal center and the overpotential required for electron transfer (in general a significant overpotential is applied to accelerate the HER).[8-11] Thus, lowering the overpotential is often not promoting overall catalysis at a practical rate. In this Doctoral Thesis, a main question to address was whether we could modulate the molecular complex and understand the resulting changes in its catalytic HER reactivity. Furthermore, it often proves ambitious to predict the

reactivity of a molecular complex based on its structure, as the HER involves multiple chemical and redox transformations, and the overall performance needs to be experimentally determined, as documented in **Chapters 2**-**5**. Upon modulating the complexes, we were able to provide a further understanding of the interplay between the ligand and metal center. For example, we and others demonstrated that boosting the proton transfer processes taking place in the second and outer coordination spheres can increase catalytic rates, while bypassing the general increase in overpotential (**Chapter 2**).

Specific functionalization of the second coordination sphere has been shown to lead to increased catalytic activities.[12-15] Some successfully applied design principles include the installation of proton and electron relays (**Figure 2** & **Figure 3**). Dubois reported on an amine functionality in organophosphorus ligands, that have been used (by them and others) in manganese, iron, cobalt, and nickel complexes to promote hydrogen production, in which the pendant amine can effectively shuttle protons to the active site, but also enhances the product release step, making the redistribution of protons and the H_2 evolution a very facile process.[16-27] Nocera used a carboxylic acid group in modified iron and cobalt porphyrin complexes to increase the electron and proton transfer rates.[28-30] Our group reported on the use of C–H bonds in cobalt bisimidazole complexes to facilitate hydrogen formation, which was investigated as part of this Doctoral Thesis.[31] In these above studies, the catalytic rate (turnover frequency) is increased upon the use of the proton relay. This emphasizes that the design principles from nature can successfully be installed in synthetic molecular complexes. Next to proton relays, also electron relays are successfully applied to promote hydrogen evolution catalysis. For example, cobalt, nickel, and copper complexes with thiosemicarbazone ligands have been demonstrated by Orio *et al*. and others to promote hydrogen evolution by storing an electron in the ligand framework (**Figure 3**).[32-35] The same ligand was even demonstrated to produce

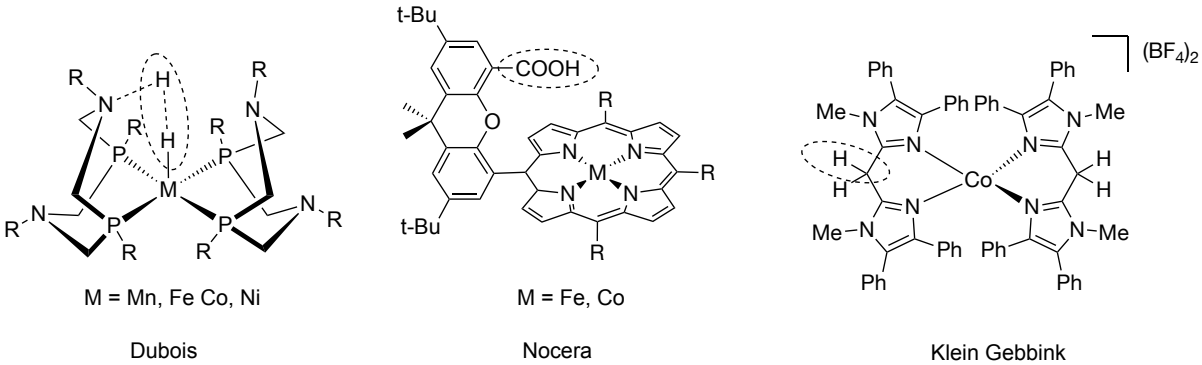

Figure 2. Selected molecular complexes with proton relay functionalities in the second coordination sphere.

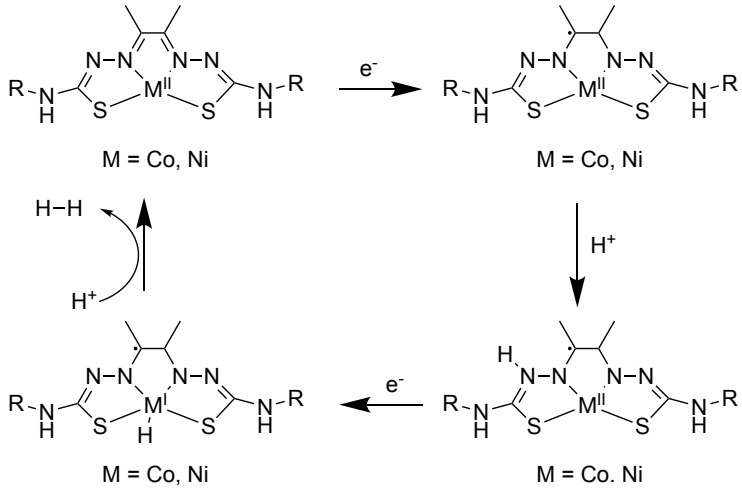

Figure 3. Molecular complexes with electron relay functionalities in the second coordination sphere.[33]

hydrogen upon its combination with a redox-innocent zinc ion.[36] We expect that such electron relays will be much more often investigated in the near future, as research towards redox non-innocent ligands receives significant attention recently and their chemistry is increasingly understood.[37,38]

Lately, also the outer coordination sphere is utilized to promote the HER. For example, the work of Beyene *et al*. demonstrates that acidic functionalities in the outer sphere of cobalt porphyrin complexes enable higher catalytic rates.[39] In **Chapter 2**, we have demonstrated that a functionalized phenyl substituent on the outer sphere of cobalt bisimidazole complexes can effectively modulate the metal-based redox potentials and electrocatalytic hydrogen evolution potentials, in which higher rates are observed at lower overpotentials. The nickel system of Dubois is most investigated and has been functionalized on the outer coordination sphere with substituted phenyl groups, as well as amino acids including acidic and basic side chains (**Figure 4**), both promoting the hydrogen evolution performance.[40-43] The amino acids promote H_2 production by concentrating protons and electrons around the nickel catalyst, which results in increased catalytic rates up to 5-fold enhancements compared to their bare counter parts.[44]

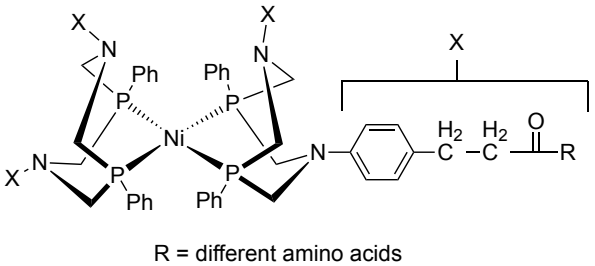

Figure 4. Amino acid functionalization of the outer sphere of Dubois' nickel organophosphorus HER catalyst.[40]

Furthermore, enhanced stability to oxygen and to strongly acidic or basic conditions was achieved, and in some cases, this also resulted in water solubility.

These results indicate that merely optimizing the first and second coordination spheres of a molecular hydrogen evolution catalyst and therewith neglecting an effective catalysis promoter (the outer coordination sphere) will likely prove insufficient to replicate the high performance of hydrogenase enzymes.[45] Indeed, the outer coordination sphere in an enzyme has structural and functional features that are crucial for efficient catalysis, as these functionalities collaborate with catalysis-promoting groups in the second coordination sphere, such as proton and electron relays, and can also lead to transition state stabilization or increased stability and solubility. For molecular complexes, the precise influence of outer coordination sphere effects on catalysis is far from fully understood, making this research area important to investigate.

Optimization of the second and outer coordination spheres can facilitate substrate transfer and can also help in stabilizing substrate-bound intermediates. Furthermore, properties such as H-bonding, the acidity of the catalytic site, and through-space electrostatic effects may all play part in the later-stage immobilization of molecular complexes and may contribute to approaching the Sabatier principle, in which an ideal catalyst has an optimal substrate binding, neither too strong nor too weak. Stabilization of intermediates may lower the energy barrier for product formation (Hammond postulate), thereby lowering the overpotential for electrocatalysis. Incorporating multiple second and outer sphere effects in molecular electrocatalysts is promising for boosting kinetic factors with minimal compromise of the overpotential and therefore circumventing the general trade-off between lower overpotentials and the catalytic rate. Thus, a holistic approach to catalyst design that extends beyond the first coordination sphere and focuses as well on higher coordination sphere effects will push the field of (electro)catalytic hydrogen production closer to understanding the complicated chemical cascade reaction involved in hydrogen evolution catalysis and will increase the overall activity of synthetic HER catalysts. Furthermore, the above design principles should be applicable to other small molecule conversions, including those of N_2, CO_2, and O_2.[46-50] Thus, in the next few years, we expect a considerable advancement in understanding of the role of the outer coordination sphere in HER catalysis and in our ability to use an overall ligand scaffold design to control catalytic HER performance by including all coordination spheres.

6.4 Mechanistic and HER Performance studies

Studying the mechanisms of synthetic HER catalysts enables the uncovering of reactive intermediates, which can provide important information for the design of new catalysts.[51] A

molecular complex can undergo many transformations during catalysis, including alteration of oxidation states and substrate binding. However, these redox processes and substrate interactions frequently involve intermediates with short lifetimes, making their study challenging. For example, metal hydrides are considered ubiquitous active species, not only for the enzymatic processes with hydrogenases[52] but also in material sciences[53] and for synthetic molecular systems,[15,54-56] but detection and isolation of metal hydrides proved to be rather difficult because of their intrinsic reactivity,[57] transiency,[58] and existence in tautomeric forms.[59,60] Next to elucidating the mechanistic, adequate performance studies to quantify efficiencies during HER catalysis are of utmost importance and a prerequisite for the immobilization of active complexes (catalysts) onto electrode materials, which may be further implemented in technological devices such as electrolyzers or photo-electrocatalytic cells. To elucidate key transformations in the overall HER performance, different electroanalytical tools as well as in situ spectro-electrochemistry and scanning electrochemical microscopy techniques, and computational approaches are applied.[61-63] Here, we provide a short overview of the most important and frequently applied methods and tools to study molecular HER catalysis.

6.4.1 Voltammetry

The most widely applied technique is voltammetry,[64] in which a potential is scanned linearly over time, resulting in a molecular complex undergoing reduction and oxidation at the electrode surface when the potential reaches a sufficiently negative/positive value, yielding an electrical current (**Figure 5a** and **b**, and *E* mechanism).[65] The occurrence of HER catalysis is an important mechanistic feature, which can be easily observed by voltammetry (**Chapter 2-5**). Namely, under catalytic conditions, the current of the CV response in the forward direction increases and the onset potential becomes smaller in magnitude, since the catalytical species are regenerated near the electrode interface (**Figure 5c**, an *EC* mechanism), while the peak on the reverse scan is being diminished to an extent determined by the kinetics of the chemical steps. Under these non-limiting conditions (a peak-shaped catalytic response), the catalytic rate for the two-electron HER-reduction process is calculated using the equation reported by Bullock, Appel, and Helm (eq. 1).[19] Here, the measured current in the presence and absence of substrate (an acid as a sacrificial proton donor) are recorded and provide a good estimate of the catalytic

$$k_{obs}(TOF) = 1.94 \cdot v \cdot \left(\frac{i_{cat}}{i_p}\right)^2 \qquad \text{(eq. 1)}$$

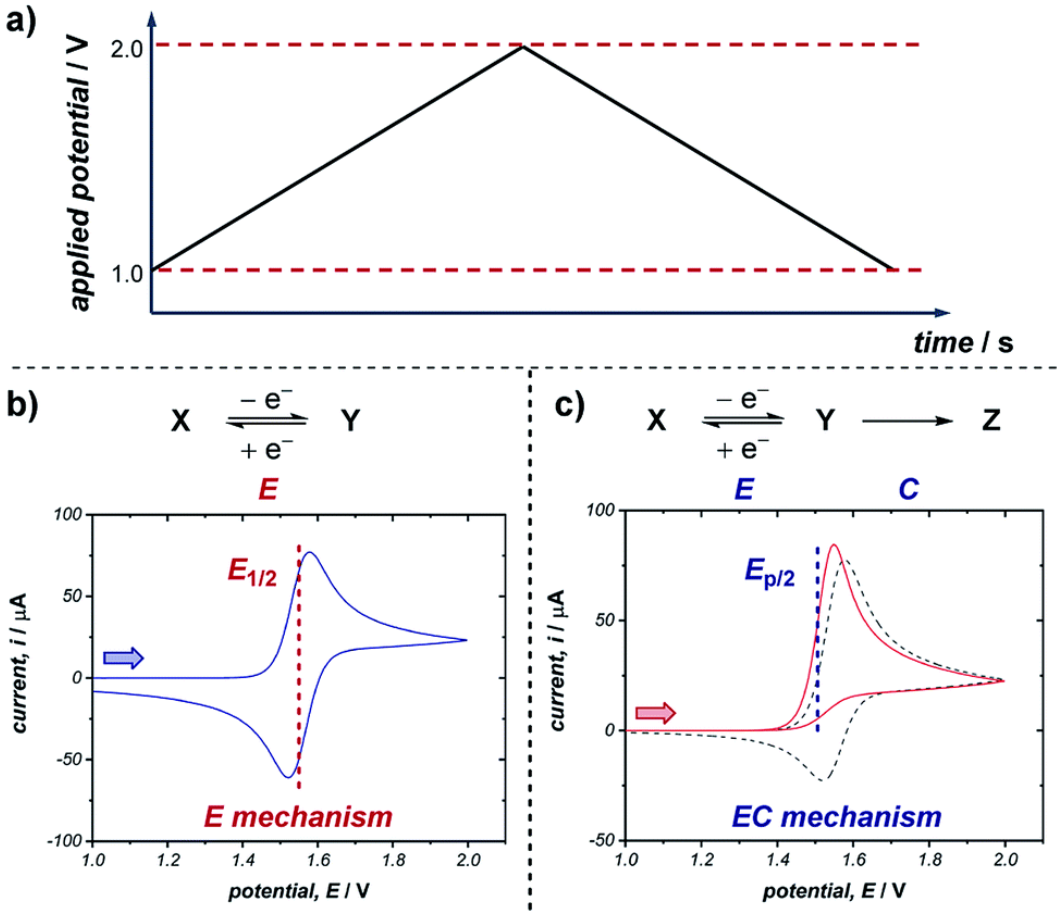

Figure 5. (a) Example of a triangular potential waveform applied in the generation of a cyclic voltammogram. Representative CV responses for (b) a chemically reversible electron transfer (*E* mechanism), and (c) a chemically irreversible electron transfer in which the redox event is followed by a chemical reaction (*EC* mechanism). Two lines in (c) represent different rates of the same chemical reaction, where the dashed grey line has a lower rate constant, and the solid red line has a higher rate constant (with $E_{p/2\ \text{labeled}}$ for the latter). Arrows in the figures demonstrate the direction of the scan. Reproduced from Minteer *et al*. with permission (creative commons).[65]

rate, which can easily be compared between different complexes. As the concentration of the substrate increases, catalytic turnover becomes more rapid, leading to a sequential increase in the current of the CV response in the forward direction. At sufficiently high concentrations of substrate, the CV response in the presence of catalysis appears as a plateau, instead of a peak followed by a diffusional tail. The plateau height (i_{cat}) depends on the concentrations of the catalyst and substrate, and this waveshape occurs when the current is limited by the rate of the chemical (catalytic) step (**Figure 6**).[66] Under these limiting conditions (plateau currents), plateau current analysis is applied,[19,55,62,64,67-75]. The measured current plateau in presence of substrate and the current in absence of substrate are used to calculate the catalytic rate using an adapted Randles–Sevcik equation. This technique was applied by DuBois and Bullock to

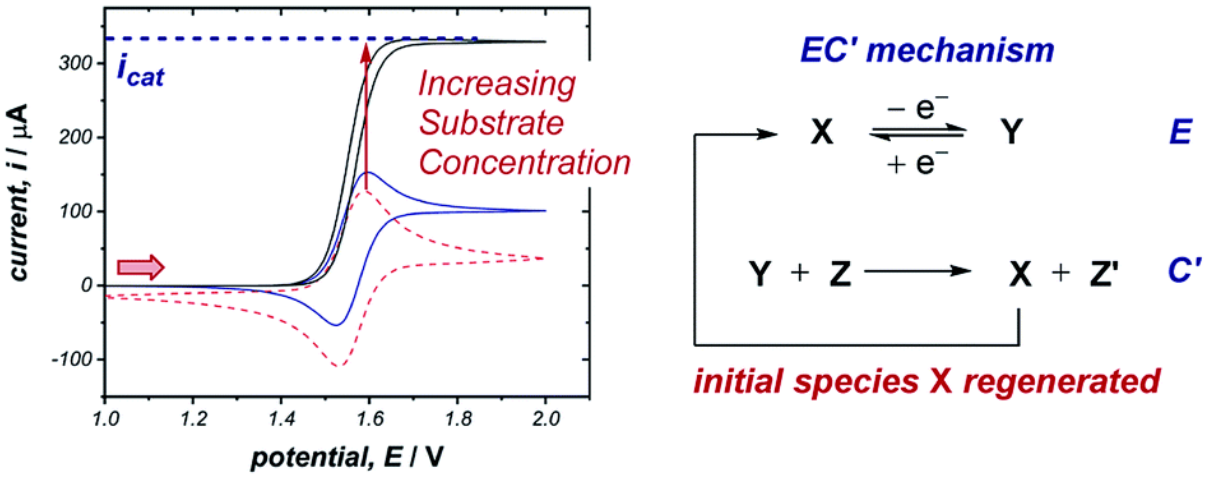

Figure 6. Representative CV responses for a catalytic (EC') mechanism, demonstrating the change between peak-shaped response and plateau response as the substrate concentration increases. Simulations run with 0 equivalents (dashed red line), 10 equivalents (solid blue line) and 100 equivalents (solid black line) of substrate respectively. The arrow in the figure demonstrates the direction of the scan. Reproduced from Minteer *et al*. with permission (creative commons).[65]

demonstrate the significant catalytic rate of 100.000 s^{-1} for their nickel phosphine complex (**Figure 2**),[19] where hydrogenase enzymes are reported to have rates between 6000-9000 s^{-1}.[76] Alternative to peak and plateau current analysis, the Foot-of-the-wave analysis (FOWA) is used,[15,55,64,68,77-79] mainly in case of fast substrate depletion, product inhibition, or unwanted side phenomena. With this technique, a recorded CV in which no characteristic catalytic peak or plateau is observed is analyzed. To do so, the observed non-ideal catalytic current is idealized to obtain a catalytic plateau current that is used to calculate the catalytic rate. For example, Artero *et al*. reported on a cobalt polypyridyl complex (used in **Chapter 4**), in which the hydrogen evolution mechanism was kinetically controlled by the second protonation step and FOWA allowed to determine the rate constant.[15] It should however be noted that the values for catalytic rate obtained from FOWA are often much larger than the actual rate constants that can be determined by follow-up electrolysis experiments, because FOWA assumes a scenario in which no side phenomena are operative. However, when new functionalities are built into a molecular scaffold, a FOWA can be quite informative. Thus, CV is an adequate method to demonstrate HER catalysis but is often limited to showing the first electron transfer and coupled chemical reaction only. Additionally, pulsed voltammetric techniques[80] can be used, as these are more sensitive and therefore sometimes enable the detection of different electroactive species at very low concentrations (as low as 10^{-7} M) and facilitate the resolution of overlapping redox features of multiple electroactive species.[81] In this Doctoral Thesis

(**Chapter 2** and **4**), differential pulse voltammetry was used to demonstrate that electrogenerated species with a more negative reduction potential were not formed during catalysis. Lately, more advanced electrochemical equipment is also used to study the HER performance of molecular complexes. For example, rotating disk electrodes (RDE), see **Chapter 4**, and rotating ring disk electrodes (RRDE) are used to gain information about the kinetic parameters of a catalytic system. With the RDE electrode, rotation speed studies can be performed which are widely adopted to quantitatively evaluate the intrinsic kinetics of HER, owing to its well-defined mass transport behaviors that can be rigorously derived from the hydrodynamics.[82,83] These studies yield information about the number of electrons transferred.[84] Next to the RDE also the RRDE is used to obtain kinetic information. In an RRDE, a second working ring electrode is outside of an inner working disk electrode. When products are formed at the inner disk electrode, they are immediately sent to the second ring working electrode at which a different potential is applied. By varying the rotation speed of the electrode, kinetic information on the catalytic reaction can be obtained.[85,86] Although this technique is not yet directly used to develop better HER processes, the technique was recently reported to monitor undesired HER during vanadium redox-flow battery studies.[87]

6.4.2 Spectroelectrochemical and Theoretical Methods

To further uncover the electrogenerated species observed during voltammetry, coupled spectroscopy (spectroelectrochemistry (SEC)) can be applied, in which information on reaction intermediates and product formation in the complicated HER cascade reaction can be obtained.[88] Since spectroscopic techniques can be applied in situ within the electrochemical cell, SEC allows the simultaneous acquisition of both spectroscopic and electrochemical information. In our group, we were able to assign a reaction intermediate generated during the HER using in situ UV-vis (**Figure 7**).[31] Using an optically transparent thin layer electrochemical (OTTLE) cell, optical changes associated with the primary reduction of $[Co(HBMIM^{Ph_2})_2](BF_4)_2$ were observed. $[Co(HBMIM^{Ph_2})_2](BF_4)_2$ itself shows weak d–d transitions at 555 and 510 nm, while the electro-generated, reduced complex absorbs strongly at 370 nm. A parallel UV-vis experiment using an independently prepared sample of $[Co(HBMIM^{Ph_2})(BMIM^{Ph_2})](BF_4)_2$ revealed a strong absorbance at 370 nm as well. Subsequently, theoretical studies by means of DFT were used to propose a catalytic sequence for hydrogen evolution. Nocera *et al*. gained new insight into the mechanisms by which hydrogen evolution proceeds for the nickel (hangman)porphyrin electrocatalysts using

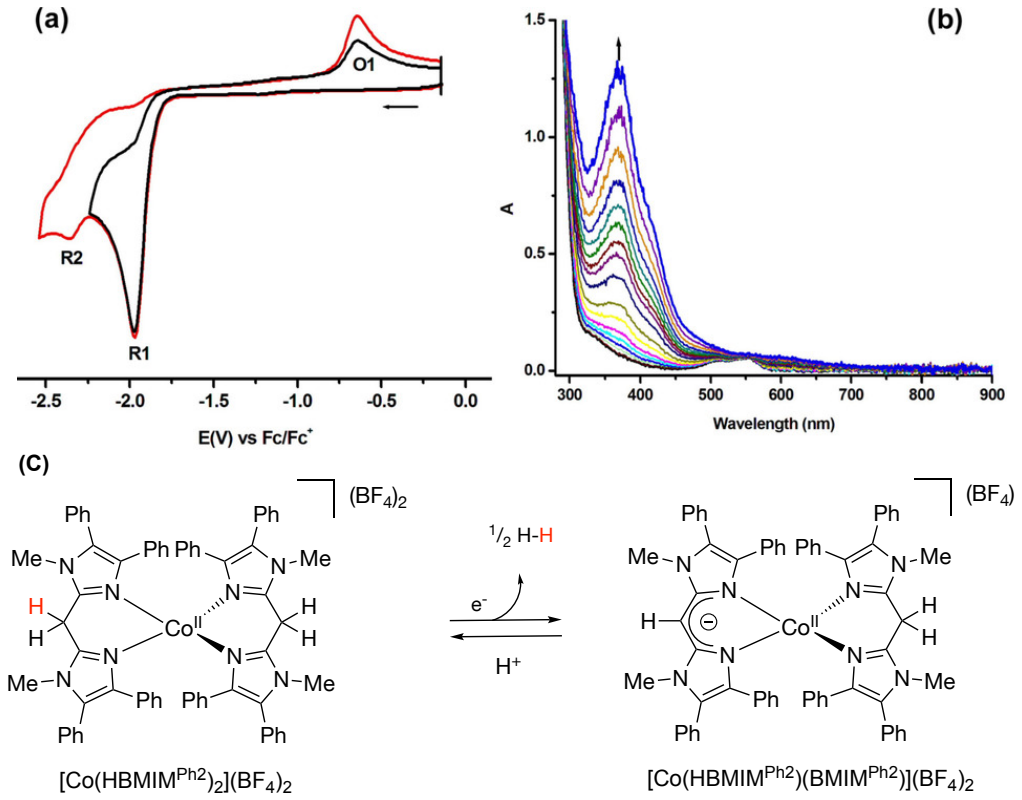

Figure 7. (a) CV of complex $[Co(HBMIM^{Ph_2})_2](BF_4)_2$ in $CH_3CN/[Bu_4N]PF_6$ (scan rate 100 mV/s) (b) UV-vis spectral change upon reduction of $[Co(HBMIM^{Ph_2})_2](BF_4)_2$ in $CH_3CN/[Bu_4N]PF_6$ (c) proposed ligand-mediated HER reactivity for $[Co(HBMIM^{Ph_2})_2](BF_4)_2$ Reproduced from Klein Gebbink *et al*. with permission (creative commons).[31]

combined thin-layer UV-SEC on a nickel porphyrin structure and theoretical studies on the nickel hangman porphyrin electrocatalyst.[89,90] When no potential is applied, the absorption spectrum of the neutral nickel porphyrin shows absorption bands at 520 and 555 nm (**Figure 8**, black trace). Upon electrochemical reduction, the spectrum features a lowering in the intensity of these bands and the appearance of new bands at 608 and 841 nm (**Figure 8**, black trace). A subsequent electrochemical reduction induces the formation of a broader and slightly more intense absorption band at 613 nm (**Figure 8**, green trace), assigned to the doubly reduced Ni porphyrin. Then, upon holding the potential and adding phenol, an acid strong enough to singly protonate the doubly reduced porphyrin but too weak to generate H_2, results in the appearance of a broad band at 769 nm (**Figure 8**, blue trace). This peak is similar to spectral features observed for related phlorin metal complexes, providing strong evidence for the formation of a phlorin intermediate. In the above HER studies, UV-vis SEC was employed as a useful tool to enable the identification of intermediates for the electrocatalytic HER. Also, differentiation between ligand- and metal-based protonation was demonstrated. Therefore, these kinds of SEC experiments can be useful in identifying catalytic intermediates for

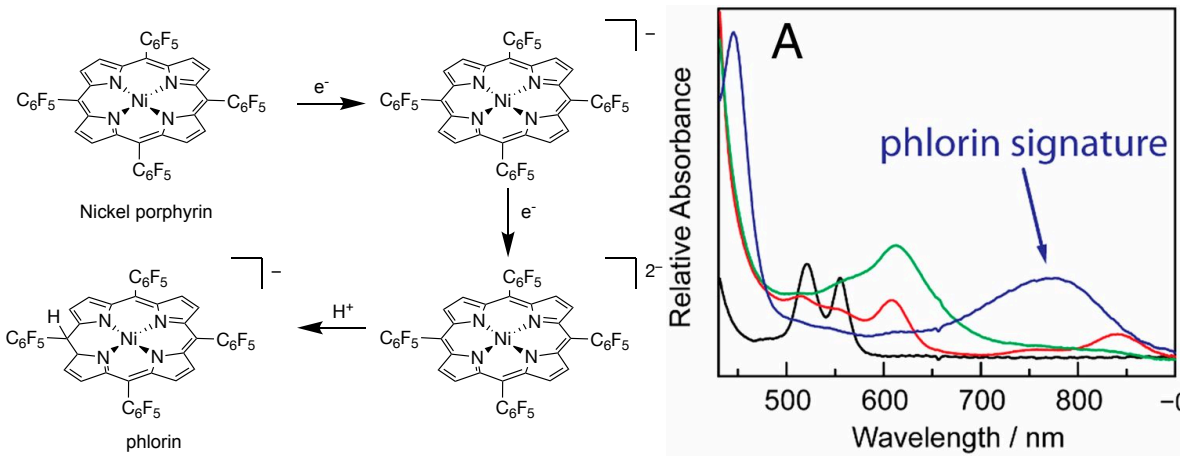

Figure 8. Left: proposed (redox) reactivity for nickel porphyrin electrocatalysts Right: absorption spectra of nickel porphyrin acquired using thin-layer spectroelectrochemistry. Spectra taken before reduction (black), single electron reduction (red), double electron (green), and after double reduction of the complex with 10 mM phenol (blue). Reproduced from Hammes-Schiffer *et al*. with permission.[89,90] Copyright 2016 National Academy of Sciences.

situations in which assignment based on electrochemistry alone is not possible. In addition, theoretical studies can also provide valuable information on HER mechanisms, when the interpretation of (spectro)electrochemical data is not straightforward.[91-94] For example, Nocera *et al*. studied the mechanism of their nickel porphyrin hangman complex and proposed a new catalytic intermediate on the basis of density functional theory calculations (**Figure 9**). Upon reducing complex [**1**–**H**]^{0} twice to [**1**–**H**]$^{2-}$ the pathway for hydrogen evolution involves an energetically favorable protonation of the *meso*-carbon of the porphyrin ring in [**1**–**H**$_c$]$^{2-}$ rather than the nickel center. Subsequently, protonation of the carboxylate forms [**1-HHC**]$^{-}$, which is reduced to [**1-HHC**]$^{2-}$ and H_2 is evolved from either self-elimination to the deprotonated [**1**]$^{2-}$ or a reaction with an external proton, forming [**1-H**]$^{-}$. This result is particularly striking in that it highlighted the non-innocence of porphyrin ligands, which can thus relay both substrates (electrons and protons) to enable HER electrocatalysis. Furthermore, this result is particular interesting, since metalloporphyrins are well-studied and by no means a new motif. Therefore, this study highlights that our knowledge of the HER is continually expanding.

Also, more sophisticated techniques have been developed, such as scanning electrochemical microscopy (SECM), in which a microelectrode is positioned very close to the surface of the active electrode to probe the reaction intermediates or image electrocatalytic sites.[95] Currently this technique is mainly applied to analyze the HER of solid-state catalysts in aqueous environments.[96]

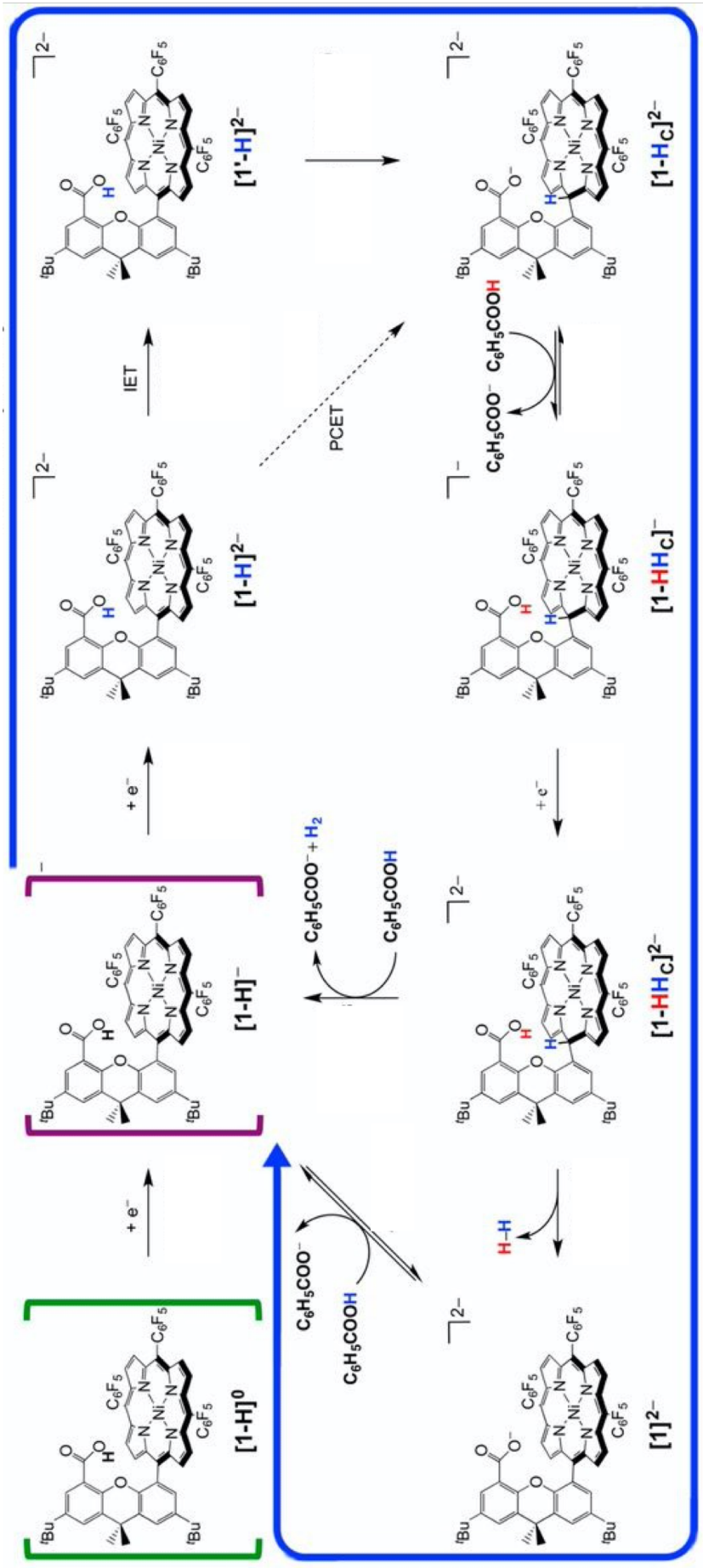

Figure 9. Proposed mechanistic sequence for nickel hangman porphyrin [**1-H**]^0 (green brackets). Starting from [**1-H**]^0, reduction proceeds at –1.37 V (vs. Fc^+/Fc) to yield to [**1-H**]$^-$ (purple brackets). Additional reduction is required to form [**1-H**]$^{2-}$ that undergoes a subsequent intramolecular PCET step, which is thermodynamically favorable and can occur either concertedly (dotted line) or sequentially via intramolecular ET from nickel to the porphyrin to form the bent structure [**1'-H**]$^{2-}$ followed by intramolecular PT to produce [**1-H$_C$**]$^{2-}$. Protonation of the carboxylate by benzoic acid forms [**1-HHC**]$^-$, which is subsequently reduced. H_2 is evolved from [**1-HHC**]$^{2-}$, either via self-elimination to the deprotonated [**1**]$^{2-}$ or by reaction with benzoic acid, forming [**1-H**]$^-$. Reproduced from Hammes-Schiffer *et al*. with permission.[89,90] Copyright 2016 National Academy of Sciences.

6.4.3 Electrolysis Studies

The voltammetry, advanced (spectro)electrochemical, and theoretical methods discussed above can provide insights into the activity of various molecular systems. The experimental efficiencies that are found by means of these electrochemical (scanning) techniques are however not always transferable to (endured) performances during bulk electrolysis experiments. Moreover, the stability of the molecular catalysts under electrolysis conditions can be quite different as well. From this thesis alone, we learned that the stability of molecular complexes under electrolysis conditions is sometimes poor (**Chapters 2** & **3**). This, in some cases, leads to inactive catalytic materials, but sometimes also to active materials with high activity and low overpotentials. For example, in **Chapter 4** we report on a catalytic overpotential of 690 mV in DMF for the HER catalyzed by $[Co(HBMIM^{Ph_2})_2](BF_4)_2$ (measured by CV). During controlled potential electrolysis, in the presence of $[Co(HBMIM^{Ph_2})_2](BF_4)_2$, at the same overpotential, high current densities and near quantitative Faradaic efficiencies were observed. However, rinse test analysis demonstrated that not only the pristine complex but also an electrode deposit significantly contributed to the observed catalytic performance. Not only $[Co(HBMIM^{Ph_2})_2](BF_4)_2$, but also well-studied cobaloxime $[Co(dmgBF_2)]$ demonstrated this behavior. Subsequently, we reported on controlled current studies in which we applied the electricity produced by a 10% efficient solar panel (10 mA/cm^2) and varied the potential. This resulted in an overpotential requirement of only ~375 mV, which was much lower than the intrinsic difference between the reduction potential of our complex measured by CV and the thermodynamic reduction potential, indicating that the initial reduction potential of the molecular complex was not the leading factor for the overpotential. These results requested a further analysis of the catalyst transformation during electrolysis and revealed that a benchmark pool of four reported molecular hydrogen evolution catalysts all formed active electrode deposits, which were mainly responsible for the observed activity. The interference of electrode deposits during HER is also reported by others for different types of complexes.[97] Therefore, we need to develop more adequate methods to measure the long-term performance of molecular catalysts, to measure their structural changes over time, and to study their robustness overall under operating conditions. An applicable method for verifying catalyst robustness was reported by Jaramillo *et al.*[98] in an elaborated review article, where they tested various heterogenous catalysts for 2 h under the electricity produced by a 10% efficient solar-to-fuels conversion device under 1 sun illumination (10 mA/cm). Plots of the overpotential requirement at t = 0 and t = 2 h gave an informative representation of the robustness of catalysts. Much

insight can also be obtained by testing new molecular complexes under photocatalytic conditions as was demonstrated in **Chapter 5**. During such photocatalytic experiments, the phase transition between solid-state electrodes and homogeneous molecular complexes is (possibly) circumvented, and therefore the benchmarking of different molecular complexes is sometimes made easier.

6.5 Immobilization of Molecular Complexes

Although a library of effective homogeneous electrocatalysts bearing optimized coordination spheres for multi-proton and -electron transfer catalysis has been documented, practical energy devices to address global energy challenges demand heterogeneous electrocatalysts for efficient charge transfer between the electrode and catalyst. Therefore, the immobilization of molecular electrocatalysts on solid electrodes is an interesting practice in the electrocatalysis field. From a heterogenous perspective, the use of immobilized molecular catalysts results in a decreased metal requirement, as every molecular complex is a single metal atom catalyst. While from a homogeneous perspective, a reduced catalyst loading, the avoidance of binuclear or multinuclear decomposition pathways, and easier determining of the catalyst lifetime is achieved. Furthermore, surface immobilization may greatly facilitate performance benchmarking (also to heterogeneous materials), since catalysts are tested under identical conditions without limitations on their solubility in, *e.g.*, water. In several studies, molecular electrocatalysts have been immobilized onto surfaces by means of covalent bonds or through non-covalent interactions, and their current densities and overpotentials have been benchmarked. In an illustrative example, Fontecave *et al.* reported the immobilization of Dubois' nickel bis(diphosphine) complex to multi-walled carbon nanotubes (MWCNTs) and the deposition of the resulting material on an indium tin oxide (ITO) electrode (**Figure 10**).[72,99] The modified electrode turned out to be both air- and water-stable. Hydrogen evolution from aqueous sulfuric acid (0.5 M, pH 0 to 1) with this modified electrode showed an exceptionally high stability (100.000 turnovers, +/- 30%), and a current density of about 4 mA/cm^2 at an overpotential of 300 mV. In a follow-up study, Artero *et al.* used the same functionalized MWCNTs and reported on the identity of the surface-immobilized species.[100] Using X-ray photoelectron spectroscopy (XPS) analysis the presence of nickel(II)-phosphine complexes was confirmed, although they were unable to assign a definitive structure.[100] In the same study, the functionalized MWCNTs were deposited onto a less compact gas diffusion electrode, using a drop-casting method, which resulted in higher surface areas and an increased current density

of 16 mA/cm^2 at an overpotential of 300 mV in aqueous sulfuric acid (0.5 M, pH 0 to 1). This performance is competitive with that of Pt-based catalysts (that are used in fuel-cells).

Besides these studies, immobilization studies have been reported for other molecular hydrogen evolution catalysts, such as those based on nickel bis(diphosphine) complexes,[101-109] cobaloxime complexes,[14,110-116] a rhodium bipyridine complex,[117-119] and molecular cobalt

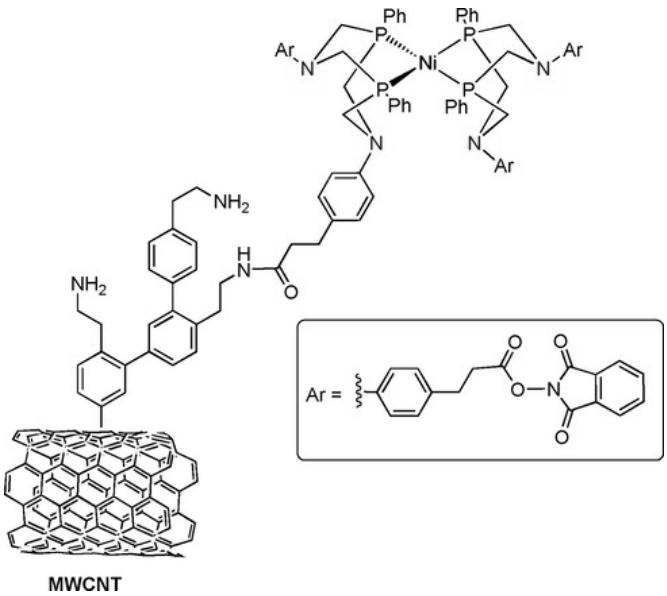

Figure 10. Immobilization of the nickel bis(diphosphine) complex of Dubois onto multi-walled carbon nanotubes, which was subsequently deposited on an indium tin oxide(ITO) electrode.[72,99] Reproduced from Apple *et al*. with permission. Copyright 2017 Wiley-VCH.

dithiolene complexes.[120-123] Immobilization strategies for the electrocatalytic catalysis of other fuel-forming processes are recently summarized in a mini-review by Bullock *et al*.[99] and a more tutorial feature article by Artero *et al*.[124] To conclude, the immobilization of molecular complexes provides further insight into the HER performances of these complexes and sometimes demonstrates industrially suitable activities. However, immobilization also results in several different challenges, including the characterization of the resulting heterogeneous catalysts and reaction intermediates, the variability of catalytic sites, and the determination of the number of active sites. This last challenge complicates a discussion of these immobilized catalysts in terms of catalytic performance, such as turnover number (TON) and turnover frequency (TOF), as ambiguity about the number of active sites often occurs.

6.6 Concluding Remarks and Outlook

The key to designing catalytically active molecular complexes for HER from first principles is by understanding the different parameters that determine catalytic activity. Over the last

decades the large number of new molecular HER catalysts that resulted from different optimization strategies, *i.e.*, installation of functionalities in the first, second, and outer coordination spheres, have contributed to this understanding. In this Thesis Chapter, we have explored a selection of the most important strategies for developing active molecular HER catalysts and discussed the reactivity and HER performance of these catalysts. We started by reviewing nature's design principles, then discussed the implementation of these principles into novel molecular catalysts, and finished with the immobilization of these catalysts on solid materials that are becoming competitive to the solid-state platinum catalyst used in current fuel cells. This account has allowed us to draw some general conclusions on how to improve molecular catalysts for hydrogen evolution and to provide an outlook as to what are some promising current leads.

First, while the contributions of molecular complexes to a fundamental understanding of the highly active HER enzymatic processes are undeniable, in this Doctoral Thesis we have shown that the insights that are thus provided bring us only the slightest step forward in understanding the efficiency of nature's processes. When incorporating a specific (isolated) functionality of the enzyme scaffold into a molecular complex, enormous sacrifices are made in simplifying the incredibly complex enzymatic process where much is interrelated. Thus, the measurable effects can only marginally enhance our fundamental understanding of enzymatic HER catalysis. At the same time, we should be aware that relying on activity measures, such as overpotential and catalytic rates, will hide much of the details necessary to fully understand all coordination spheres of molecular complexes. Second, considering the complexity of the enzymes, represented by their huge scaffolds, there is no desire to implement all functionalities, but only a selection of the most promoting features, into the new catalytic materials we require for our global energy challenges. This way our catalytic materials will not become highly complicated structures, require shorter development periods and allow for faster activity and stability analyses. When analyzing the HER reactivity, we should consider the key processes of the enzymes, such as the electron and proton transfer rates towards the active site, as predominantly those are enhanced by the enzymes, and report on such parameters in relation to the HER activity. Third and most importantly, the full complexity of molecular complexes should be explored in a way that relates to applied HER processes, which currently rely exclusively on solid-state electrode materials. We are facing a world energy transition and optimized catalytic electrode materials will play part in the pace of this transition. The electrochemical conversion of small molecules (*e.g.* H_2, CO_2, CO, N_2) into energy carriers is

one of the most promising fields for storing our green (electric) energy, but current catalytic processes are based on scarce elements that are too expensive for economic viability. Some molecular catalysts based on affordable and abundant elements pose competitive performances on a laboratory scale but need to be further developed as their complicated synthetic routes are undesirable. However, these molecular catalysts demonstrate that taking advantage of concepts that are fully developed in nature, such as the electron and proton transfers toward the active site of the catalyst, may allow overcoming the challenges that we are currently facing.

Herein, the tradeoff between overpotential and the catalytic rate is one of the biggest challenges in HER catalysis research. For many molecular HER catalysts, including the cobalt complexes discussed in this Doctoral Thesis, there is a fierce loss in energy (overpotential) when HER rates speed up to practical use. In designing new catalysts, it is important to define best practices as enzymatic, molecular, and solid-state catalysis will continue to merge. Using second and outer sphere modifications, nature has proven that earth-abundant metals can be great catalysts. These practices have also been applied to molecular complexes and have indeed led to enhanced catalysis. The further utilization of molecular complexes into or onto solid state materials has started recently as well and is expected to take acceleration in the near future. However, a long road is still ahead before practical applications are reached, especially because of the long (costly) synthetic routes and upscaling challenges that need to be addressed. To overcome these, new molecular structures should be developed based on straightforward synthesis methods yielding catalytically active complexes that can firmly bind to electrode materials, are stable, and feature fast electron and proton transfer kinetics, as this will eventually provide the materials and solutions necessary.By taking a multifaceted approach, in which all coordination spheres of a molecular catalyst are addressed, we may approach efficient catalysis with earth-abundant metals for the electrochemical conversion of small molecules into energy carriers in the future. These catalysts can help society's transition to use renewable energy sources in order to become less dependent on large-scale hydrocarbon chemistry that is mainly fossil-based.

Let's move together towards a renewable energy society!

6.7 Authors Contributions

S.D. de Vos devised the aim, scope, and structure of this perspective and wrote the manuscript. R. J. M. Klein Gebbink and D. L. J. Broere provided input on the manuscript during its creation.

6.8 References

(1) Stripp, S. T.; Duffus, B. R.; Fourmond, V.; Léger, C.; Leimkühler, S.; Hirota, S.; Hu, Y.; Jasniewski, A.; Ogata, H.; Ribbe, M. W. Second and Outer Coordination Sphere Effects in Nitrogenase, Hydrogenase, Formate Dehydrogenase, and CO Dehydrogenase. *Chem. Rev.* **2022**, *122* (14), 11900.

(2) Lampret, O.; Adamska-Venkatesh, A.; Konegger, H.; Wittkamp, F.; Apfel, U.-P.; Reijerse, E. J.; Lubitz, W.; Rüdiger, O.; Happe, T.; Winkler, M. Interplay between CN– Ligands and the Secondary Coordination Sphere of the H-Cluster in [FeFe]-Hydrogenases. *J. Am. Chem. Soc.* **2017**, *139* (50), 18222.

(3) Lampret, O.; Duan, J.; Hofmann, E.; Winkler, M.; Armstrong, F. A.; Happe, T. The roles of long-range proton-coupled electron transfer in the directionality and efficiency of [FeFe]-hydrogenases. *Proc. Natl. Acad. Sci. U.S.A* **2020**, *117* (34), 20520.

(4) Losse, S.; Vos, J. G.; Rau, S. Catalytic hydrogen production at cobalt centres. *Coord. Chem. Rev.* **2010**, *254* (21), 2492.

(5) Mazzeo, A.; Santalla, S.; Gaviglio, C.; Doctorovich, F.; Pellegrino, J. Recent progress in homogeneous light-driven hydrogen evolution using first-row transition metal catalysts. *Inorg. Chim. Acta* **2021**, *517*, 119950.

(6) Artero, V.; Chavarot-Kerlidou, M.; Fontecave, M. Splitting Water with Cobalt. *Angew. Chem. Int. Ed.* **2011**, *50* (32), 7238.

(7) Zaccaria, F.; Menendez Rodriguez, G.; Rocchigiani, L.; Macchioni, A. Molecular Catalysis in "Green" Hydrogen Production. *Frontiers in Catalysis* **2022**, *2,* 1-14.

(8) Hu, X.; Brunschwig, B. S.; Peters, J. C. Electrocatalytic Hydrogen Evolution at Low Overpotentials by Cobalt Macrocyclic Glyoxime and Tetraimine Complexes. *J. Am. Chem. Soc.* **2007**, *129* (29), 8988.

(9) Wakerley, D. W.; Reisner, E. Development and understanding of cobaloxime activity through electrochemical molecular catalyst screening. *Phys. Chem. Chem. Phys.* **2014**, *16* (12), 5739.

(10) Kilgore, U. J.; Stewart, M. P.; Helm, M. L.; Dougherty, W. G.; Kassel, W. S.; DuBois, M. R.; DuBois, D. L.; Bullock, R. M. Studies of a Series of $[Ni(P^{R}_2N^{Ph}_2)_2(CH_3CN)]^{2+}$ Complexes as Electrocatalysts for H_2 Production: Substituent Variation at the Phosphorus Atom of the P_2N_2 Ligand. *Inorg. Chem.* **2011**, *50* (21), 10908.

(11) Huo, P.; Uyeda, C.; Goodpaster, J. D.; Peters, J. C.; Miller, T. F., III. Breaking the Correlation between Energy Costs and Kinetic Barriers in Hydrogen Evolution via a Cobalt Pyridine-Diimine-Dioxime Catalyst. *ACS Catalysis* **2016**, *6* (9), 6114.

(12) Barton, B. E.; Olsen, M. T.; Rauchfuss, T. B. Aza- and Oxadithiolates Are Probable Proton Relays in Functional Models for the [FeFe]-Hydrogenases. *J. Am. Chem. Soc.* **2008**, *130*, (50), 16834.

(13) Bhunia, S.; Rana, A.; Hematian, S.; Karlin, K. D.; Dey, A. Proton Relay in Iron Porphyrins for Hydrogen Evolution Reaction. *Inorg. Chem.* **2021**, *60* (18), 13876.

(14) Kaeffer, N.; Chavarot-Kerlidou, M.; Artero, V. Hydrogen Evolution Catalyzed by Cobalt Diimine–Dioxime Complexes. *Acc. Chem. Res.* **2015**, *48* (5), 1286.

(15) Queyriaux, N.; Sun, D.; Fize, J.; Pécaut, J.; Field, M. J.; Chavarot-Kerlidou, M.; Artero, V. Electrocatalytic Hydrogen Evolution with a Cobalt Complex Bearing Pendant Proton Relays: Acid Strength and Applied Potential Govern Mechanism and Stability. *J. Am. Chem. Soc.* **2020**, *142* (1), 274.

(16) Rakowski DuBois, M.; DuBois, D. L. The roles of the first and second coordination spheres in the design of molecular catalysts for H_2 production and oxidation. *Chem. Soc. Rev.* **2009**, *38* (1), 62.

(17) Wilson, A. D.; Newell, R. H.; McNevin, M. J.; Muckerman, J. T.; Rakowski DuBois, M.; DuBois, D. L. Hydrogen Oxidation and Production Using Nickel-Based Molecular Catalysts with Positioned Proton Relays. *J. Am. Chem. Soc.* **2006**, *128* (1), 358.

(18) Wiedner, E. S.; Roberts, J. A. S.; Dougherty, W. G.; Kassel, W. S.; DuBois, D. L.; Bullock, R. M. Synthesis and Electrochemical Studies of Cobalt(III) Monohydride Complexes Containing Pendant Amines. *Inorg. Chem.* **2013**, *52* (17), 9975.

(19) Helm, M. L.; Stewart, M. P.; Bullock, R. M.; DuBois, M. R.; DuBois, D. L. A Synthetic Nickel Electrocatalyst with a Turnover Frequency Above 100,000 s^{-1} for H_2 Production. *Science* **2011,** *333* (6044), 863.

(20) Jacobsen, G. M.; Yang, J. Y.; Twamley, B.; Wilson, A. D.; Bullock, R. M.; Rakowski DuBois, M.; DuBois, D. L. Hydrogen production using cobalt-based molecular catalysts containing a proton relay in the second coordination sphere. *Energy Environ. Sci.* **2008**, *1* (1), 167.

(21) Wiedner, E. S.; Yang, J. Y.; Dougherty, W. G.; Kassel, W. S.; Bullock, R. M.; DuBois, M. R.; DuBois, D. L. Comparison of Cobalt and Nickel Complexes with Sterically Demanding Cyclic Diphosphine Ligands: Electrocatalytic H_2 Production by $[Co(P^{tBu}_2N^{Ph}_2)(CH_3CN)_3](BF_4)_2$. *Organometallics* **2010**, *29* (21), 5390.

(22) Curtis, C. J.; Miedaner, A.; Ciancanelli, R.; Ellis, W. W.; Noll, B. C.; Rakowski DuBois, M.; DuBois, D. L. $[Ni(Et_2PCH_2NMeCH_2PEt_2)_2]^{2+}$ as a Functional Model for Hydrogenases. *Inorg. Chem.* **2003**, *42* (1), 216.

(23) Henry, R. M.; Shoemaker, R. K.; DuBois, D. L.; DuBois, M. R. Pendant Bases as Proton Relays in Iron Hydride and Dihydrogen Complexes. *J. Am. Chem. Soc.* **2006**, *128* (9), 3002.

(24) Wiedner, E. S.; Appel, A. M.; DuBois, D. L.; Bullock, R. M. Thermochemical and Mechanistic Studies of Electrocatalytic Hydrogen Production by Cobalt Complexes Containing Pendant Amines. *Inorg. Chem.* **2013**, *52* (24), 14391.

(25) Hulley, E. B.; Welch, K. D.; Appel, A. M.; DuBois, D. L.; Bullock, R. M. Rapid, Reversible Heterolytic Cleavage of Bound H2. *J. Am. Chem. Soc.* **2013**, *135* (32), 11736.

(26) Welch, K. D.; Dougherty, W. G.; Kassel, W. S.; DuBois, D. L.; Bullock, R. M. Synthesis, Structures, and Reactions of Manganese Complexes Containing Diphosphine Ligands with Pendant Amines. *Organometallics* **2010**, *29* (20), 4532.

(27) Raugei, S.; Chen, S.; Ho, M.-H.; Ginovska-Pangovska, B.; Rousseau, R. J.; Dupuis, M.; DuBois, D. L.; Bullock, R. M. The Role of Pendant Amines in the Breaking and Forming of Molecular Hydrogen Catalyzed by Nickel Complexes. *Chem. Eur. J.* **2012**, *18* (21), 6493.

(28) Roubelakis, M. M.; Bediako, D. K.; Dogutan, D. K.; Nocera, D. G. Proton-coupled electron transfer kinetics for the hydrogen evolution reaction of hangman porphyrins. *Energy Environ. Sci.* **2012**, *5* (7), 7737.

(29) Fu, L.-Z.; Zhou, L.-L.; Tang, L.-Z.; Zhang, Y.-X.; Zhan, S.-Z. Electrochemical and photochemical-driven hydrogen evolution catalyzed by a dinuclear Co^{II}–Co^{II} complex. *J. Power Sources* **2015**, *280*, 453.

(30) Graham, D. J.; Nocera, D. G. Electrocatalytic H2 Evolution by Proton-Gated Hangman Iron Porphyrins. *Organometallics* **2014**, *33* (18), 4994.

(31) Ghosh, P.; de Vos, S.; Lutz, M.; Gloaguen, F.; Schollhammer, P.; Moret, M.-E.; Klein Gebbink, R. J. M. Electrocatalytic Proton Reduction by a Cobalt Complex Containing a Proton-Responsive Bis(alkylimdazole)methane Ligand: Involvement of a C–H Bond in H2 Formation. *Chem. Eur. J.* **2020**, *26* (55), 12560.

(32) Straistari, T.; Hardré, R.; Fize, J.; Shova, S.; Giorgi, M.; Réglier, M.; Artero, V.; Orio, M. Hydrogen Evolution Reactions Catalyzed by a Bis(thiosemicarbazone) Cobalt Complex: An Experimental and Theoretical Study. *Chem. Eur. J.* **2018**, *24* (35), 8779.
(33) Straistari, T.; Fize, J.; Shova, S.; Réglier, M.; Artero, V.; Orio, M. A Thiosemicarbazone–Nickel(II) Complex as Efficient Electrocatalyst for Hydrogen Evolution. *ChemCatChem* **2017**, *9* (12), 2262.
(34) Barrozo, A.; Orio, M. From Ligand- to Metal-centered Reactivity: Metal Substitution Effect in Thiosemicarbazone-based Complexes for H_2 Production. *Chemphyschem* **2022**, *23* (9), e202200056.
(35) Haddad, A. Z.; Cronin, S. P.; Mashuta, M. S.; Buchanan, R. M.; Grapperhaus, C. A. Metal-Assisted Ligand-Centered Electrocatalytic Hydrogen Evolution upon Reduction of a Bis(thiosemicarbazonato)Cu(II) Complex. *Inorg. Chem.* **2017**, *56* (18), 11254.
(36) Haddad, A. Z.; Garabato, B. D.; Kozlowski, P. M.; Buchanan, R. M.; Grapperhaus, C. A. Beyond Metal-Hydrides: Non-Transition-Metal and Metal-Free Ligand-Centered Electrocatalytic Hydrogen Evolution and Hydrogen Oxidation. *J. Am. Chem. Soc.* **2016**, *138* (25), 7844.
(37) Barrozo, A.; Orio, M. Molecular Electrocatalysts for the Hydrogen Evolution Reaction: Input from Quantum Chemistry. *ChemSusChem* **2019**, *12* (22), 4905.
(38) Lyaskovskyy, V.; de Bruin, B. Redox Non-Innocent Ligands: Versatile New Tools to Control Catalytic Reactions. *ACS Catalysis* **2012**, *2* (2), 270.
(39) Beyene, B. B.; Mane, S. B.; Hung, C.-H. Electrochemical Hydrogen Evolution by Cobalt(II) Porphyrins: Effects of Ligand Modification on Catalytic Activity, Efficiency and Overpotential. *J. Electrochem. Soc.* **2018**, *165* (9), H481.
(40) Jain, A.; Lense, S.; Linehan, J. C.; Raugei, S.; Cho, H.; DuBois, D. L.; Shaw, W. J. Incorporating Peptides in the Outer-Coordination Sphere of Bioinspired Electrocatalysts for Hydrogen Production. *Inorg. Chem.* **2011**, *50* (9), 4073.
(41) Jain, A.; Reback, M. L.; Lindstrom, M. L.; Thogerson, C. E.; Helm, M. L.; Appel, A. M.; Shaw, W. J. Investigating the Role of the Outer-Coordination Sphere in $[Ni(P^{Ph}_2N^{Ph-R}_2)_2]^{2+}$ Hydrogenase Mimics. *Inorg. Chem.* **2012**, *51* (12), 6592.
(42) Reback, M. L.; Ginovska-Pangovska, B.; Ho, M.-H.; Jain, A.; Squier, T. C.; Raugei, S.; Roberts, J. A. S.; Shaw, W. J. The Role of a Dipeptide Outer-Coordination Sphere on H_2-Production Catalysts: Influence on Catalytic Rates and Electron Transfer. *Chem. Eur. J.* **2013**, *19* (6), 1928.
(43) Kilgore, U. J.; Roberts, J. A. S.; Pool, D. H.; Appel, A. M.; Stewart, M. P.; DuBois, M. R.; Dougherty, W. G.; Kassel, W. S.; Bullock, R. M.; DuBois, D. L. $[Ni(P^{Ph}_2N^{C6H4X}_2)_2]^{2+}$ Complexes as Electrocatalysts for H_2 Production: Effect of Substituents, Acids, and Water on Catalytic Rates. *J. Am. Chem. Soc.* **2011**, *133* (15), 5861.
(44) Ginovska-Pangovska, B.; Dutta, A.; Reback, M. L.; Linehan, J. C.; Shaw, W. J. Beyond the Active Site: The Impact of the Outer Coordination Sphere on Electrocatalysts for Hydrogen Production and Oxidation. *Acc. Chem. Res.* **2014**, *47* (8), 2621.
(45) Dutta, A.; Appel, A. M.; Shaw, W. J. Designing electrochemically reversible H_2 oxidation and production catalysts. *Nat. Rev. Chem.* **2018**, *2* (9), 244.
(46) Nichols, A. W.; Machan, C. W. Secondary-sphere effects in molecular electrocatalytic CO_2 reduction. *Frontiers in Chemistry* **2019**, 397.
(47) Zee, D. Z.; Nippe, M.; King, A. E.; Chang, C. J.; Long, J. R. Tuning Second Coordination Sphere Interactions in Polypyridyl–Iron Complexes to Achieve Selective Electrocatalytic Reduction of Carbon Dioxide to Carbon Monoxide. *Inorg. Chem.* **2020**, *59* (7), 5206.
(48) Vereshchuk, N.; Matheu, R.; Benet-Buchholz, J.; Pipelier, M.; Lebreton, J.; Dubreuil, D.; Tessier, A.; Gimbert-Suriñach, C.; Ertem, M. Z.; Llobet, A. Second Coordination

Sphere Effects in an Evolved Ru Complex Based on Highly Adaptable Ligand Results in Rapid Water Oxidation Catalysis. *J. Am. Chem. Soc.* **2020**, *142* (11), 5068.

(49) Talukdar, K.; Sinha Roy, S.; Amatya, E.; Sleeper, E. A.; Le Magueres, P.; Jurss, J. W. Enhanced Electrochemical CO_2 Reduction by a Series of Molecular Rhenium Catalysts Decorated with Second-Sphere Hydrogen-Bond Donors. *Inorg. Chem.* **2020**, *59* (9), 6087.

(50) Loipersberger, M.; Zee, D. Z.; Panetier, J. A.; Chang, C. J.; Long, J. R.; Head-Gordon, M. Computational Study of an Iron(II) Polypyridine Electrocatalyst for CO_2 Reduction: Key Roles for Intramolecular Interactions in CO_2 Binding and Proton Transfer. *Inorg. Chem.* **2020**, *59* (12), 8146.

(51) Dempsey, J. L.; Esswein, A. J.; Manke, D. R.; Rosenthal, J.; Soper, J. D.; Nocera, D. G. Molecular Chemistry of Consequence to Renewable Energy. *Inorg. Chem.* **2005**, *44* (20), 6879.

(52) Reijerse, E. J.; Pham, C. C.; Pelmenschikov, V.; Gilbert-Wilson, R.; Adamska-Venkatesh, A.; Siebel, J. F.; Gee, L. B.; Yoda, Y.; Tamasaku, K.; Lubitz, W.et al. Direct Observation of an Iron-Bound Terminal Hydride in [FeFe]-Hydrogenase by Nuclear Resonance Vibrational Spectroscopy. *J. Am. Chem. Soc.* **2017**, *139* (12), 4306.

(53) Copéret, C.; Estes, D. P.; Larmier, K.; Searles, K. Isolated Surface Hydrides: Formation, Structure, and Reactivity. *Chem. Rev.* **2016**, *116* (15), 8463.

(54) Jiang, B.; Gil-Sepulcre, M.; Garrido-Barros, P.; Gimbert-Suriñach, C.; Wang, J. W.; Garcia-Anton, J.; Nolis, P.; Benet-Buchholz, J.; Romero, N.; Sala, X. Unravelling the Mechanistic Pathway of the Hydrogen Evolution Reaction Driven by a Cobalt Catalyst. *Angew. Chem. Int. Ed.* **2022**, *134* (40), e202209075.

(55) Elgrishi, N.; McCarthy, B. D.; Rountree, E. S.; Dempsey, J. L. Reaction Pathways of Hydrogen-Evolving Electrocatalysts: Electrochemical and Spectroscopic Studies of Proton-Coupled Electron Transfer Processes. *ACS Catalysis* **2016**, *6* (6), 3644.

(56) Dempsey, J. L.; Winkler, J. R.; Gray, H. B. *J. Am. Chem. Soc.* **2011**, *132*, 16774.

(57) Lacy, D. C.; Roberts, G. M.; Peters, J. C. The Cobalt Hydride that Never Was: Revisiting Schrauzer's "Hydridocobaloxime". *J. Am. Chem. Soc.* **2015**, *137* (14), 4860.

(58) Wiedner, E. S.; Bullock, R. M. Electrochemical Detection of Transient Cobalt Hydride Intermediates of Electrocatalytic Hydrogen Production. *J. Am. Chem. Soc.* **2016**, *138* (26), 8309.

(59) Estes, D. P.; Grills, D. C.; Norton, J. R. The Reaction of Cobaloximes with Hydrogen: Products and Thermodynamics. *J. Am. Chem. Soc.* **2014**, *136* (50), 17362.

(60) Bhattacharjee, A.; Chavarot-Kerlidou, M.; Andreiadis, E. S.; Fontecave, M.; Field, M. J.; Artero, V. Combined Experimental–Theoretical Characterization of the Hydrido-Cobaloxime [$HCo(dmgH)_2(P\mathit{n}Bu_3)$]. *Inorg. Chem.* **2012**, *51* (13), 7087.

(61) Skubi, K. L.; Blum, T. R.; Yoon, T. P. Dual Catalysis Strategies in Photochemical Synthesis. *Chem. Rev.* **2016**, *116* (17), 10035.

(62) Lee, K. J.; Elgrishi, N.; Kandemir, B.; Dempsey, J. L. Electrochemical and spectroscopic methods for evaluating molecular electrocatalysts. *Nat. Rev. Chem.* **2017**, *1* (5), 0039.

(63) Bard, A. J.; Faulkner, L. R. *Electrochemical Methods: Fundamentals and Applications*, 2001.

(64) Rountree, E. S.; McCarthy, B. D.; Eisenhart, T. T.; Dempsey, J. L. Evaluation of Homogeneous Electrocatalysts by Cyclic Voltammetry. *Inorg. Chem.* **2014**, *53* (19), 9983.

(65) Sandford, C.; Edwards, M. A.; Klunder, K. J.; Hickey, D. P.; Li, M.; Barman, K.; Sigman, M. S.; White, H. S.; Minteer, S. D. A synthetic chemist's guide to

electroanalytical tools for studying reaction mechanisms. *Chem. Sci.* **2019**, *10* (26), 6404.

(66) Savéant J-M.; Costentin C. Elements of Molecular and Biomolecular Electrochemistry: An Electrochemical Approach to Electron Transfer Chemistry, 2019.

(67) Saveant, J. M.; Vianello, E. Potential-sweep chronoamperometry: Kinetic currents for first-order chemical reaction parallel to electron-transfer process (catalytic currents). *Electrochimica Acta* **1965**, *10* (9), 905.

(68) Costentin, C.; Savéant, J.-M. Multielectron, Multistep Molecular Catalysis of Electrochemical Reactions: Benchmarking of Homogeneous Catalysts. *ChemElectroChem* **2014**, *1* (7), 1226.

(69) Delahay, P.; Stiehl, G. L. Theory of catalytic polarographic currents. *J. Am. Chem. Soc.* **1952**, *74* (14), 3500.

(70) Thoi, V. S.; Karunadasa, H. I.; Surendranath, Y.; Long, J. R.; Chang, C. J. Electrochemical generation of hydrogen from acetic acid using a molecular molybdenum–oxo catalyst. *Energy Environ. Sci.* **2012**, *5* (7), 7762.

(71) Hartley, C. L.; DiRisio, R. J.; Screen, M. E.; Mayer, K. J.; McNamara, W. R. Iron Polypyridyl Complexes for Photocatalytic Hydrogen Generation. *Inorg. Chem.* **2016**, *55* (17), 8865.

(72) Le Goff, A.; Artero, V.; Jousselme, B.; Tran, P. D.; Guillet, N.; Métayé, R.; Fihri, A.; Palacin, S.; Fontecave, M. From Hydrogenases to Noble Metal-Free Catalytic Nanomaterials for H_2 Production and Uptake. *Science* **2009**, *326* (5958), 1384.

(73) Kal, S.; Filatov, A. S.; Dinolfo, P. H. Electrocatalytic Proton Reduction by a Dicobalt Tetrakis-Schiff Base Macrocycle in Nonaqueous Electrolyte. *Inorg. Chem.* **2014**, *53* (14), 7137.

(74) Connor, G.; Mayer, K.; Tribble, C.; McNamara, W. Hydrogen evolution catalyzed by an iron polypyridyl complex in aqueous solutions. *Inorg. Chem.* **2014**, *53* (11), 5408.

(75) Bigi, J. P.; Hanna, T. E.; Harman, W. H.; Chang, A.; Chang, C. J. Electrocatalytic reduction of protons to hydrogen by a water-compatible cobalt polypyridyl platform. *Chem. Commun.* **2010**, *46* (6), 958.

(76) Frey, M. Hydrogenases: Hydrogen-Activating Enzymes. *ChemBioChem* **2002**, *3* (2-3), 153.

(77) Costentin, C.; Drouet, S.; Robert, M.; Savéant, J.-M. Turnover Numbers, Turnover Frequencies, and Overpotential in Molecular Catalysis of Electrochemical Reactions. Cyclic Voltammetry and Preparative-Scale Electrolysis. *J. Am. Chem. Soc.* **2012**, *134* (27), 11235.

(78) Wiedner, E. S.; Brown, H. J.; Helm, M. L. Kinetic analysis of competitive electrocatalytic pathways: New insights into hydrogen production with nickel electrocatalysts. *J. Am. Chem. Soc.* **2016**, *138* (2), 604.

(79) Gomez-Mingot, M.; Porcher, J.-P.; Todorova, T. K.; Fogeron, T.; Mellot-Draznieks, C.; Li, Y.; Fontecave, M. Bioinspired Tungsten Dithiolene Catalysts for Hydrogen Evolution: A Combined Electrochemical, Photochemical, and Computational Study. *J. Phys. Chem. B* **2015**, *119* (43), 13524.

(80) Nadjo, L.; Savéant, J. Linear sweep voltammetry: Kinetic control by charge transfer and/or secondary chemical reactions: I. Formal kinetics. *J. Electroanalyt. Chem. Interfacial Electrochem.* **1973**, *48* (1), 113.

(81) Mirceski, V.; Gulaboski, R.; Lovric, M.; Bogeski, I.; Kappl, R.; Hoth, M. Square-wave voltammetry: a review on the recent progress. *Electroanalysis* **2013**, *25* (11), 2411.

(82) Sheng, W.; Gasteiger, H. A.; Shao-Horn, Y. Hydrogen Oxidation and Evolution Reaction Kinetics on Platinum: Acid vs Alkaline Electrolytes. *J. Electrochem. Soc.* **2010**, *157* (11), B1529.

(83) Zheng, J.; Yan, Y.; Xu, B. Correcting the Hydrogen Diffusion Limitation in Rotating Disk Electrode Measurements of Hydrogen Evolution Reaction Kinetics. *J. Electrochem. Soc.* **2015**, *162* (14), F1470.
(84) Treimer, S.; Tang, A.; Johnson, D. C. A Consideration of the application of Koutecký-Levich plots in the diagnoses of charge-transfer mechanisms at rotated disk electrodes. *Electroanalysis* **2002**, *14* (3), 165.
(85) Yin, G.; Zhang, J. *Rotating electrode methods and oxygen reduction electrocatalysts*; Elsevier, 2014.
(86) Prater, K. B.; Bard, A. J. Rotating Ring-Disk Electrodes: III. Catalytic and ECE Reactions. *J. Electrochem. Soc.* **1970**, *117* (12), 1517.
(87) Tichter, T.; Schneider, J.; Nguyen Viet, D.; Diaz Duque, A.; Roth, C. Rotating ring-disc electrode measurements for the quantitative electrokinetic investigation of the V3+-reduction at modified carbon electrodes. *J. Electroanal. Chem.* **2020**, *859*, 113843.
(88) Kaim, W.; Fiedler, J. Spectroelectrochemistry: the best of two worlds. *Chem. Soc. Rev.* **2009**, *38* (12), 3373.
(89) Bediako, D. K.; Solis, B. H.; Dogutan, D. K.; Roubelakis, M. M.; Maher, A. G.; Lee, C. H.; Chambers, M. B.; Hammes-Schiffer, S.; Nocera, D. G. Role of pendant proton relays and proton-coupled electron transfer on the hydrogen evolution reaction by nickel hangman porphyrins. *Proc. Natl. Acad. Sci. U.S.A* **2014**, *111* (42), 15001.
(90) Solis, B. H.; Maher, A. G.; Dogutan, D. K.; Nocera, D. G.; Hammes-Schiffer, S. Nickel phlorin intermediate formed by proton-coupled electron transfer in hydrogen evolution mechanism. *Proc. Natl. Acad. Sci. U.S.A* **2016**, *113* (3), 485.
(91) Britz, D.; Strutwolf, J. In *Digital Simulation in Electrochemistry*; Springer, 2017.
(92) Messersmith, S. J. Cyclic voltammetry simulations with DigiSim software: An upper-level undergraduate experiment. *J. Chem. Educ.* **2014**, *91* (9), 1498.
(93) Brown, J. H. Development and use of a cyclic voltammetry simulator to introduce undergraduate students to electrochemical simulations. *J. Chem. Educ.* **2015**, *92* (9), 1490.
(94) Wang, S.; Wang, J.; Gao, Y. Exfoliation of Covalent Organic Frameworks into Few-Layer Redox-Active Nanosheets as Cathode Materials for Lithium-Ion Batteries *J. Am. Chem. Soc.* **2017**, 139, 12, 4258–4261.
(95) Amemiya, S.; Bard, A. J.; Fan, F.-R. F.; Mirkin, M. V.; Unwin, P. R. Scanning electrochemical microscopy. *Annu. Rev. Anal. Chem.* **2008**, *1*, 95.
(96) Liang, Z.; Ahn, H. S.; Bard, A. J. A Study of the Mechanism of the Hydrogen Evolution Reaction on Nickel by Surface Interrogation Scanning Electrochemical Microscopy. *J. Am. Chem. Soc.* **2017**, *139* (13), 4854.
(97) Kaeffer, N.; Morozan, A.; Fize, J.; Martinez, E.; Guetaz, L.; Artero, V. The Dark Side of Molecular Catalysis: Diimine–Dioxime Cobalt Complexes Are Not the Actual Hydrogen Evolution Electrocatalyst in Acidic Aqueous Solutions. *ACS Catalysis* **2016**, *6* (6), 3727.
(98) McCrory, C. C. L.; Jung, S.; Ferrer, I. M.; Chatman, S. M.; Peters, J. C.; Jaramillo, T. F. Benchmarking Hydrogen Evolving Reaction and Oxygen Evolving Reaction Electrocatalysts for Solar Water Splitting Devices. *J. Am. Chem. Soc.* **2015**, *137* (13), 4347.
(99) Bullock, R. M.; Das, A. K.; Appel, A. M. Surface Immobilization of Molecular Electrocatalysts for Energy Conversion. *Chem. Eur. J.* **2017**, *23* (32), 7626.
(100) Huan, T. N.; Jane, R. T.; Benayad, A.; Guetaz, L.; Tran, P. D.; Artero, V. Bio-inspired noble metal-free nanomaterials approaching platinum performances for H_2 evolution and uptake. *Energy Environ. Sci.* **2016**, *9* (3), 940.

(101) Tran, P. D.; Le Goff, A.; Heidkamp, J.; Jousselme, B.; Guillet, N.; Palacin, S.; Dau, H.; Fontecave, M.; Artero, V. Noncovalent Modification of Carbon Nanotubes with Pyrene-Functionalized Nickel Complexes: Carbon Monoxide Tolerant Catalysts for Hydrogen Evolution and Uptake. *Angew. Chem. Int. Ed.* **2011**, *50* (6), 1371.
(102) Dutta, A.; Lense, S.; Hou, J.; Engelhard, M. H.; Roberts, J. A. S.; Shaw, W. J. Minimal Proton Channel Enables H2 Oxidation and Production with a Water-Soluble Nickel-Based Catalyst. *J. Am. Chem. Soc.* **2013**, *135* (49), 18490.
(103) Rodriguez-Maciá, P.; Dutta, A.; Lubitz, W.; Shaw, W. J.; Rüdiger, O. Direct Comparison of the Performance of a Bio-inspired Synthetic Nickel Catalyst and a [NiFe]-Hydrogenase, Both Covalently Attached to Electrodes. *Angew. Chem. Int. Ed.* **2015**, *54* (42), 12303.
(104) Das, A. K.; Engelhard, M. H.; Bullock, R. M.; Roberts, J. A. S. A Hydrogen-Evolving $Ni(P_2N_2)_2$ Electrocatalyst Covalently Attached to a Glassy Carbon Electrode: Preparation, Characterization, and Catalysis. Comparisons with the Homogeneous Analogue. *Inorg. Chem.* **2014**, *53* (13), 6875.
(105) Seo, J.; Pekarek, R. T.; Rose, M. J. Photoelectrochemical operation of a surface-bound, nickel-phosphine H_2 evolution catalyst on p-Si(111): a molecular semiconductor|catalyst construct. *Chem. Commun.* **2015**, *51* (68), 13264.
(106) Kim, H. J.; Seo, J.; Rose, M. J. H_2 Photogeneration Using a Phosphonate-Anchored Ni-PNP Catalyst on a Band-Edge-Modified p-Si(111)|AZO Construct. *ACS Appl. Mat. Interfaces* **2016**, *8* (2), 1061.
(107) Gross, M. A.; Reynal, A.; Durrant, J. R.; Reisner, E. Versatile Photocatalytic Systems for H2 Generation in Water Based on an Efficient DuBois-Type Nickel Catalyst. *J. Am. Chem. Soc.* **2014**, *136* (1), 356.
(108) Shan, B.; Das, A. K.; Marquard, S.; Farnum, B. H.; Wang, D.; Bullock, R. M.; Meyer, T. J. Photogeneration of hydrogen from water by a robust dye-sensitized photocathode. *Energy Environ. Sci.* **2016**, *9* (12), 3693.
(109) Brunner, F. M.; Neville, M. L.; Kubiak, C. P. Investigation of Immobilization Effects on Ni $(P_2N_2)_2$ Electrocatalysts. *Inorg. Chem.* **2020**, *59* (23), 16872.
(110) Berben, L. A.; Peters, J. C. Hydrogen evolution by cobalt tetraimine catalysts adsorbed on electrode surfaces. *Chem. Commun.* **2010**, *46* (3), 398.
(111) Andreiadis, E. S.; Jacques, P.-A.; Tran, P. D.; Leyris, A.; Chavarot-Kerlidou, M.; Jousselme, B.; Matheron, M.; Pécaut, J.; Palacin, S.; Fontecave, M. Molecular engineering of a cobalt-based electrocatalytic nanomaterial for H_2 evolution under fully aqueous conditions. *Nat. Chem.* **2013**, *5* (1), 48.
(112) Reuillard, B.; Warnan, J.; Leung, J. J.; Wakerley, D. W.; Reisner, E. A Poly (cobaloxime)/Carbon Nanotube Electrode: Freestanding Buckypaper with Polymer-Enhanced H_2-Evolution Performance. *Angew. Chem.* **2016**, *128* (12), 4020.
(113) Willkomm, J.; Muresan, N. M.; Reisner, E. Enhancing H_2 evolution performance of an immobilised cobalt catalyst by rational ligand design. *Chem. Sci.* **2015**, *6* (5), 2727.
(114) Muresan, N. M.; Willkomm, J.; Mersch, D.; Vaynzof, Y.; Reisner, E. Immobilization of a Molecular Cobaloxime Catalyst for Hydrogen Evolution on a Mesoporous Metal Oxide Electrode. *Angew. Chem. Int. Ed.* **2012**, *51* (51), 12749.
(115) Reuillard, B.; Warnan, J.; Leung, J. J.; Wakerley, D. W.; Reisner, E. A Poly(cobaloxime)/Carbon Nanotube Electrode: Freestanding Buckypaper with Polymer-Enhanced H_2-Evolution Performance. *Angew. Chem. Int. Ed.* **2016**, *55* (12), 3952.
(116) Kaeffer, N.; Massin, J.; Lebrun, C.; Renault, O.; Chavarot-Kerlidou, M.; Artero, V. Covalent Design for Dye-Sensitized H2-Evolving Photocathodes Based on a Cobalt Diimine–Dioxime Catalyst. *J. Am. Chem. Soc.* **2016**, *138* (38), 12308.

(117) Blakemore, J. D.; Gupta, A.; Warren, J. J.; Brunschwig, B. S.; Gray, H. B. Noncovalent Immobilization of Electrocatalysts on Carbon Electrodes for Fuel Production. *J. Am. Chem. Soc.* **2013**, *135* (49), 18288.
(118) Jackson, M. N.; Kaminsky, C. J.; Oh, S.; Melville, J. F.; Surendranath, Y. Graphite Conjugation Eliminates Redox Intermediates in Molecular Electrocatalysis. *J. Am. Chem. Soc.* **2019**, *141* (36), 14160.
(119) Jackson, M. N.; Oh, S.; Kaminsky, C. J.; Chu, S. B.; Zhang, G.; Miller, J. T.; Surendranath, Y. Strong Electronic Coupling of Molecular Sites to Graphitic Electrodes via Pyrazine Conjugation. *J. Am. Chem. Soc.* **2018**, *140* (3), 1004.
(120) Clough, A. J.; Yoo, J. W.; Mecklenburg, M. H.; Marinescu, S. C. Two-Dimensional Metal–Organic Surfaces for Efficient Hydrogen Evolution from Water. *J. Am. Chem. Soc.* **2015**, *137* (1), 118.
(121) Downes, C. A.; Marinescu, S. C. Efficient Electrochemical and Photoelectrochemical H2 Production from Water by a Cobalt Dithiolene One-Dimensional Metal–Organic Surface. *J. Am. Chem. Soc.* **2015**, *137* (43), 13740.
(122) Eady, S. C.; Peczonczyk, S. L.; Maldonado, S.; Lehnert, N. Facile heterogenization of a cobalt catalyst via graphene adsorption: robust and versatile dihydrogen production systems. *Chem. Commun.* **2014**, *50* (59), 8065.
(123) Eady, S. C.; MacInnes, M. M.; Lehnert, N. A Smorgasbord of Carbon: Electrochemical Analysis of Cobalt–Bis(benzenedithiolate) Complex Adsorption and Electrocatalytic Activity on Diverse Graphitic Supports. *ACS Applied Materials & Interfaces* **2016**, *8* (36), 23624.
(124) Coutard, N.; Kaeffer, N.; Artero, V. Molecular engineered nanomaterials for catalytic hydrogen evolution and oxidation. *Chem. Commun.* **2016**, *52* (95), 13728.

Appendix A

Supporting Information to Chapter 2

A. 1 Spectra of compounds 1-12

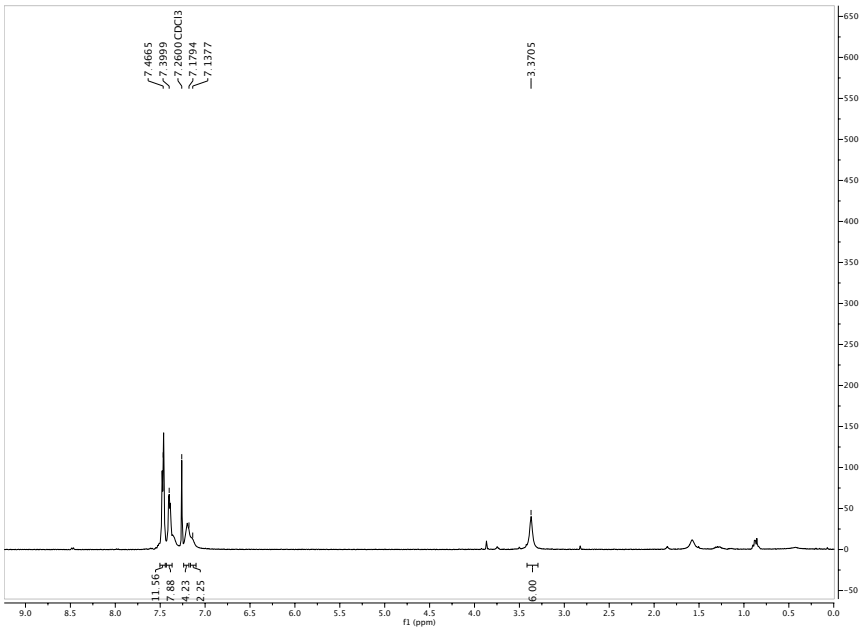

Figure A1. ^{1}H-NMR (400 MHz, $CDCl_3$, 25 ˚C): Bis(1-methyl-4,5-diphenyl-1H-imidazol-2-yl)(phenyl)methanol (OH,*p*ArH)BMIM^{Ph_2}) (**1**).

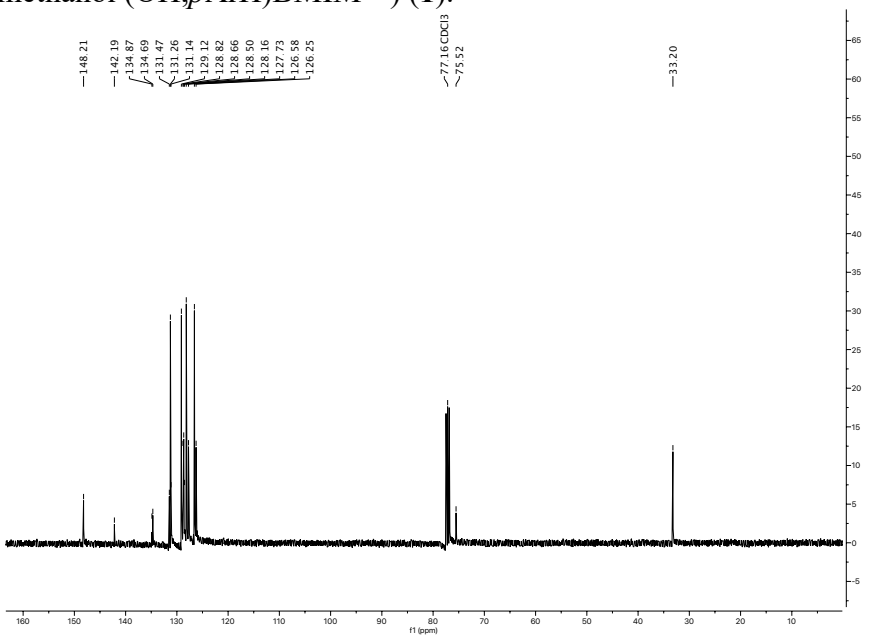

Figure A2. ^{13}C-NMR (101 MHz, $CDCl_3$, 25 ˚C): Bis(1-methyl-4,5-diphenyl-1H-imidazol-2-yl)(phenyl)methanol (OH,*p*ArH)BMIM^{Ph_2}) (**1**).

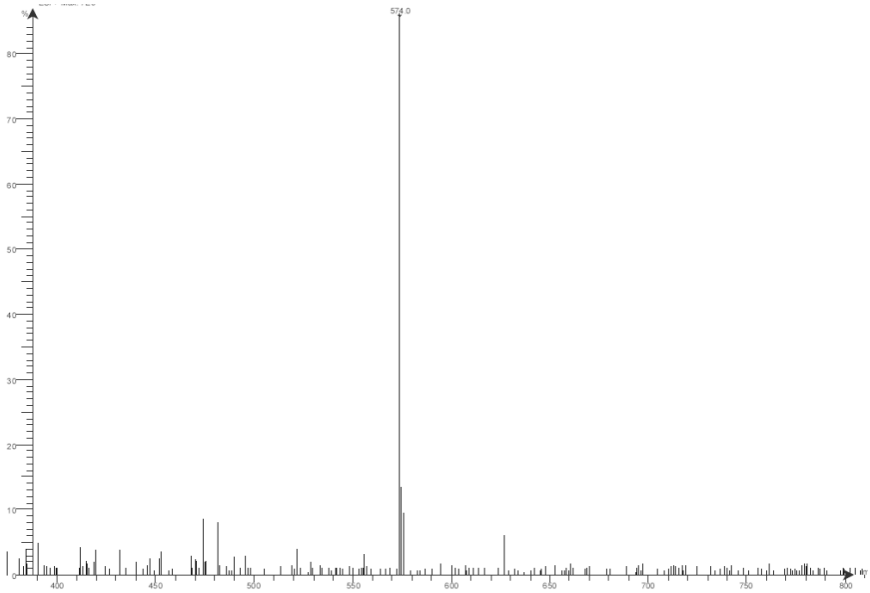

Figure A3. Low resolution ESI-MS spectra of complex Bis(1-methyl-4,5-diphenyl-1H-imidazol-2-yl)(phenyl)methanol (OH,*p*ArH)BMIM^{Ph_2}) (**1**) in MeCN.

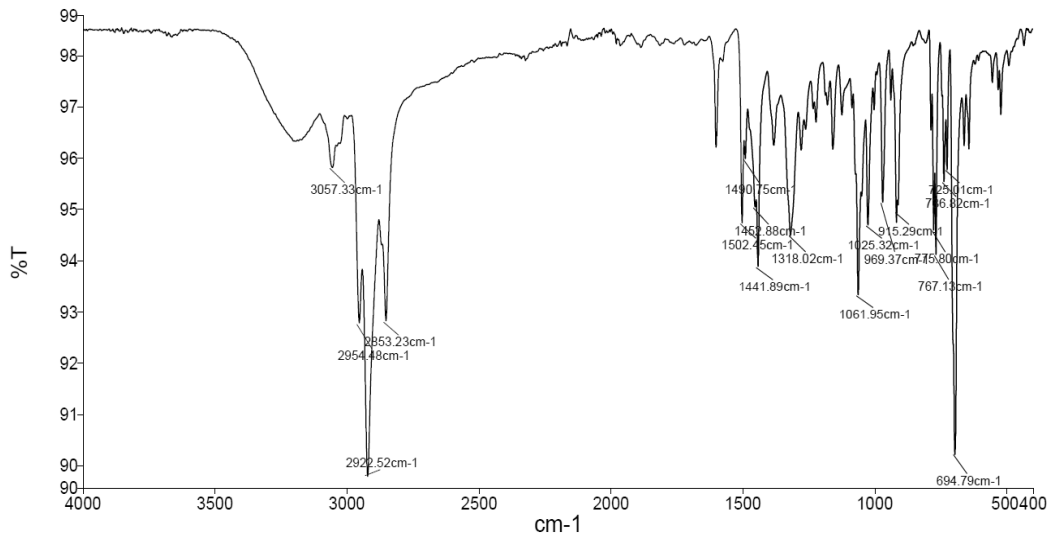

Figure A4. Infrared spectrum of Bis(1-methyl-4,5-diphenyl-1H-imidazol-2-yl)(phenyl)methanol (OH,*p*ArH)BMIM^{Ph_2}) (**1**).

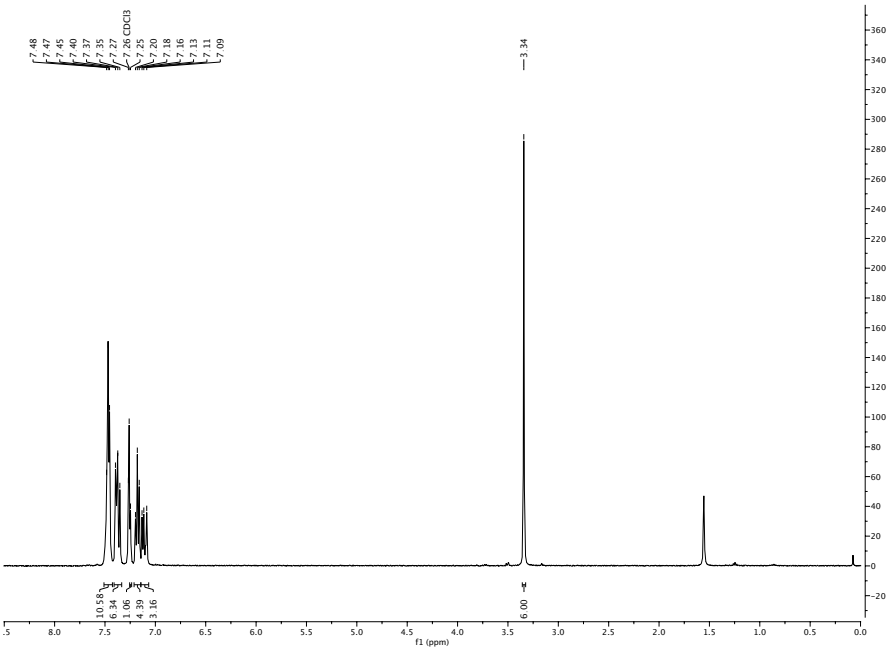

Figure A5. ^{1}H-NMR (400 MHz, $CDCl_3$, 25 °C): Bis(1-methyl-4,5-diphenyl-1H-imidazol-2-yl)4-chloroarylmethanol (OH,*p*ArCl)BMIM^{Ph_2}) (**2**).

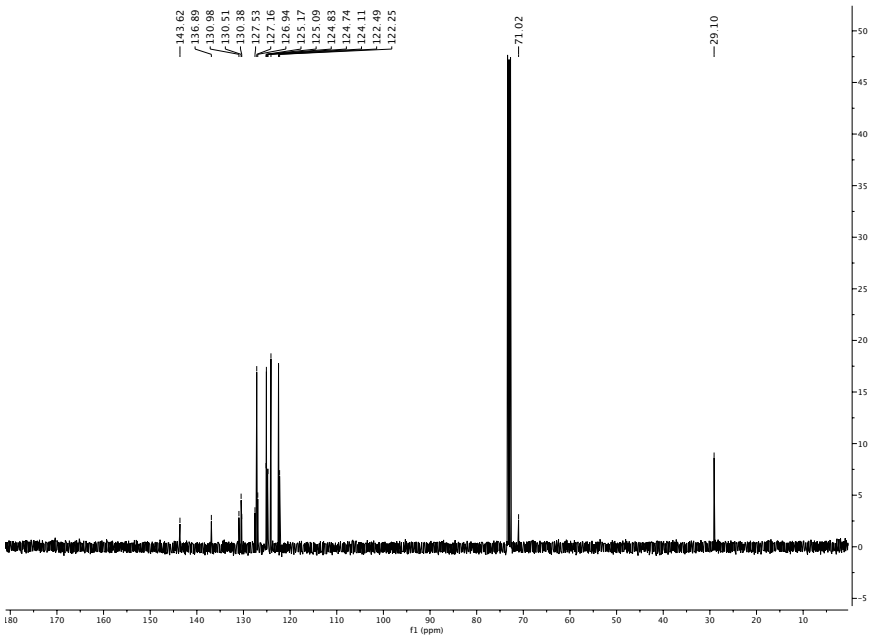

Figure A6. ^{13}C-NMR (100 MHz, $CDCl_3$, 25 °C): Bis(1-methyl-4,5-diphenyl-1H-imidazol-2-yl)4-chloroarylmethanol (OH,*p*ArCl)BMIM^{Ph_2}) (**2**).

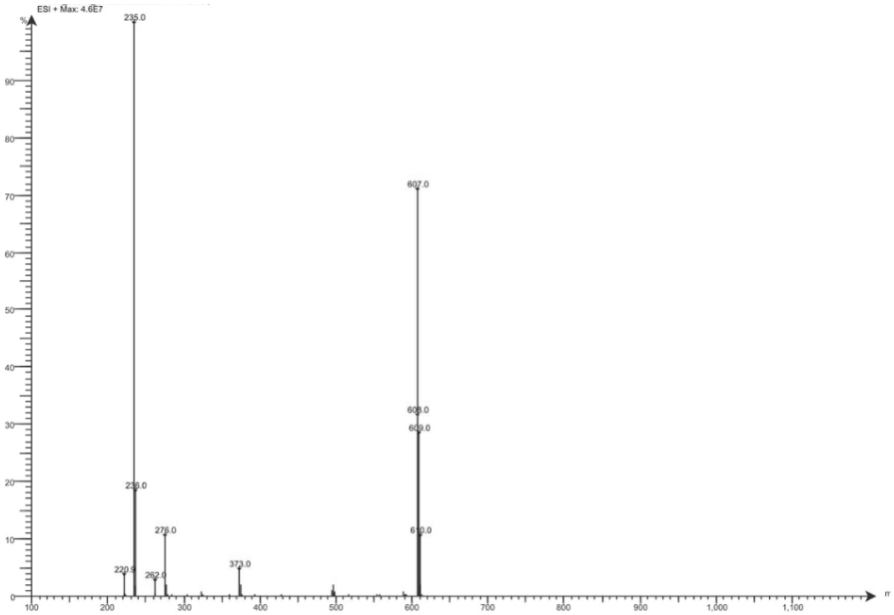

Figure A7. Low resolution ESI-MS spectra of complex Bis(1-methyl-4,5-diaryl-1H-imidazol-2-yl)4-chloroarylmethanol (OH,*p*ArCl)BMIM^{Ph_2}) (**2**) in MeCN.

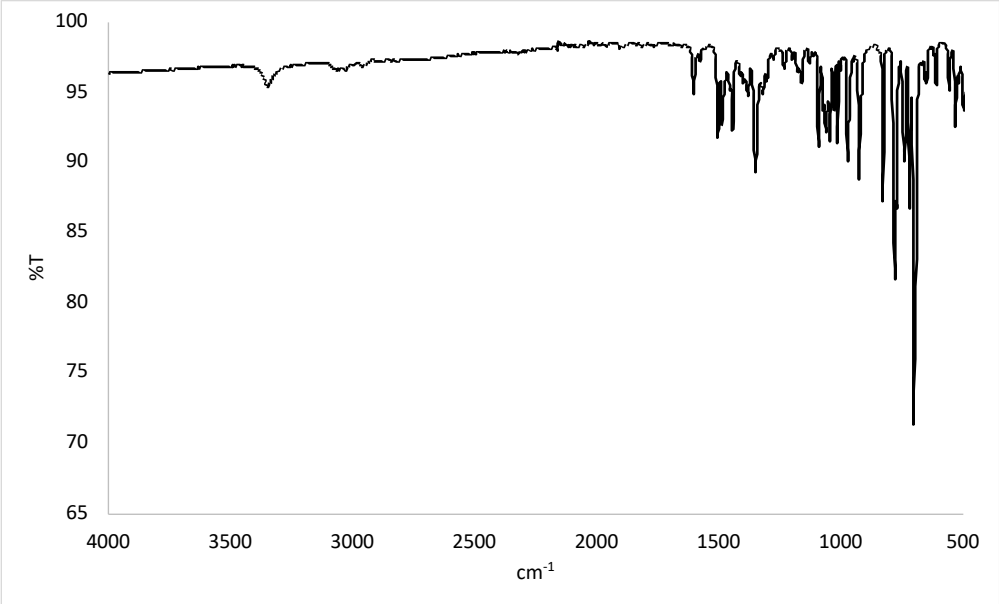

Figure A8. Infrared spectrum of Bis(1-methyl-4,5-diphenyl-1H-imidazol-2-yl)4-chloroarylmethanol (OH,*p*ArCl)BMIM^{Ph_2}) (**2**).

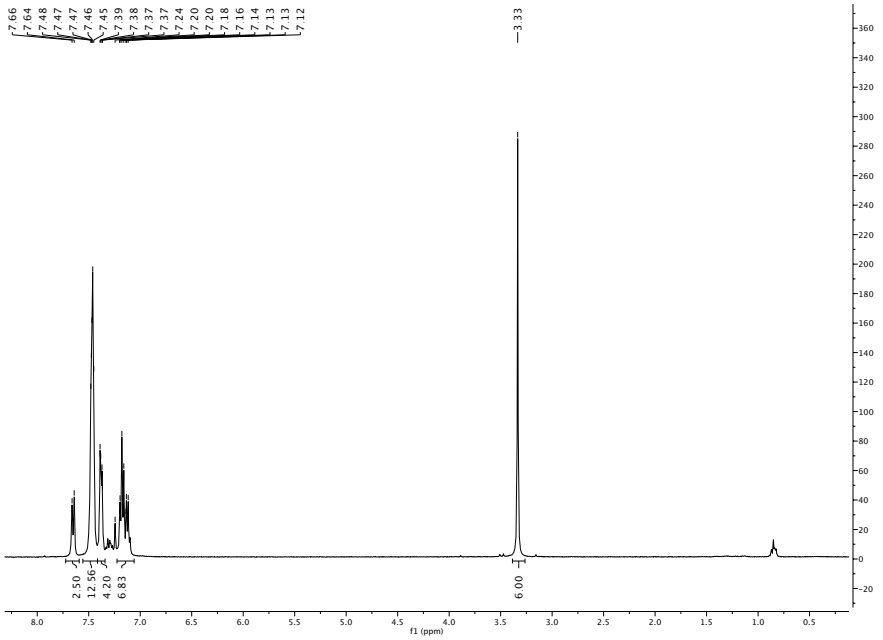

Figure A9. ^{1}H-NMR (400 MHz, $CDCl_3$, 25 ˚C): bis(1-methyl-4,5-diphenyl-1H-imidazol-2-yl)(4-(trifluoromethyl)-aryl)methanol (OH,*p*ArCF_3)BMIM^{Ph_2}) (**3**).

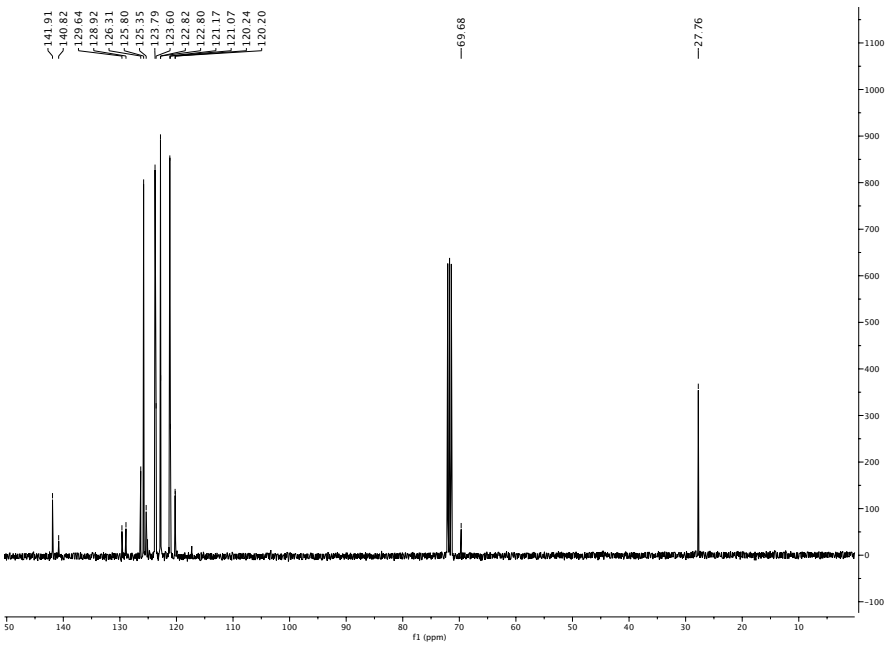

Figure A10. ^{13}C-NMR (101 MHz, $CDCl_3$, 25 ˚C) bis(1-methyl-4,5-diphenyl-1H-imidazol-2-yl)(4-(trifluoromethyl)-aryl)methanol (OH,*p*ArCF_3)BMIM^{Ph_2}) (**3**).

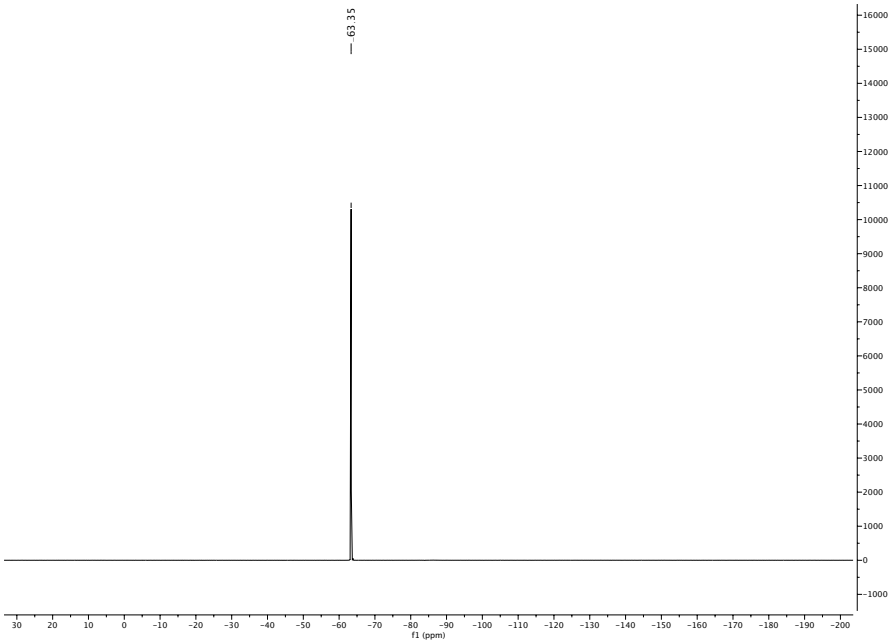

Figure A11. ^{19}F-NMR (376 MHz, $CDCl_3$, 25 ˚C): bis(1-methyl-4,5-diphenyl-1H-imidazol-2-yl)(4-(trifluoromethyl)-aryl)methanol (OH,*p*ArCF_3)BMIM^{Ph_2}) (**3**).

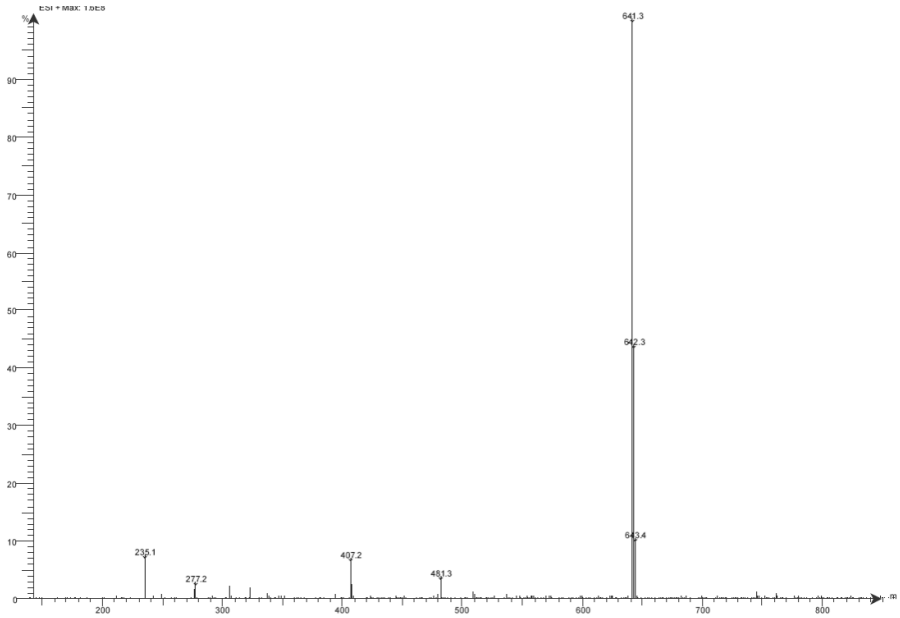

Figure A12. Low resolution ESI-MS spectra of complex bis(1-methyl-4,5-diphenyl-1H-imidazol-2-yl)(4-(trifluoromethyl)-aryl)methanol (OH,*p*ArCF_3)BMIM^{Ph_2}) (**3**) in MeCN.

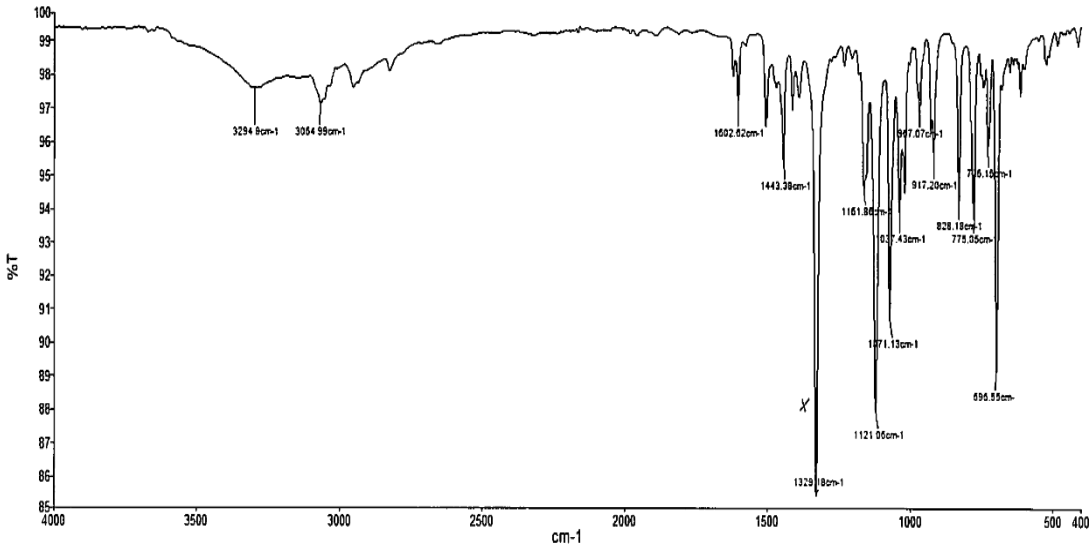

Figure A13. Infrared spectrum of bis(1-methyl-4,5-diphenyl-1H-imidazol-2-yl)(4-(trifluoromethyl)-aryl)methanol (OH,*p*ArCF$_3$)BMIM^{Ph_2}) (**3**).

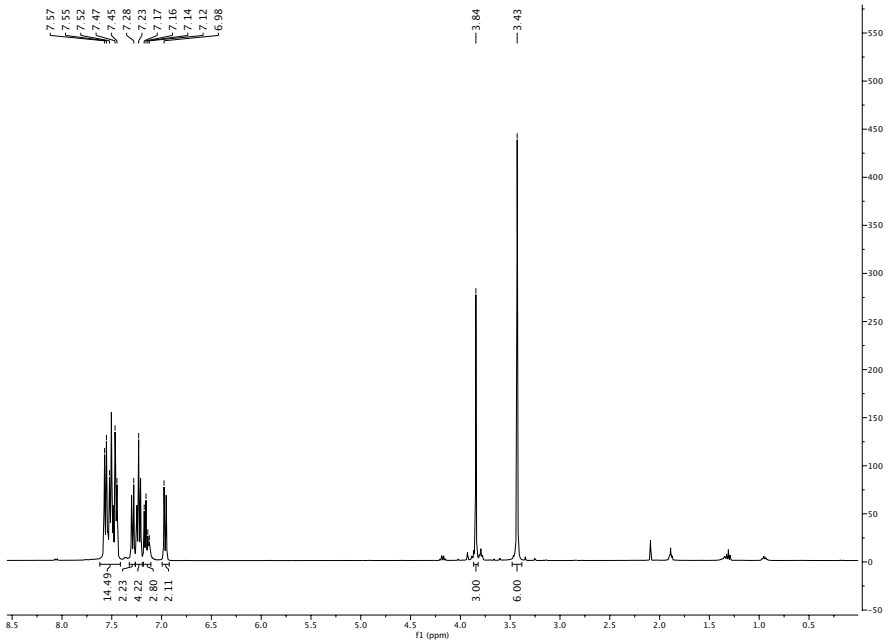

Figure A14. ^{1}H-NMR (400 MHz, CD$_3$CN, 25 ˚C) bis(1-methyl-4,5-diphenyl-1H-imidazol-2-yl)(4-(trifluoromethyl)-aryl)methanol (OH,*p*ArOMe)BMIM^{Ph_2}) (**4**).

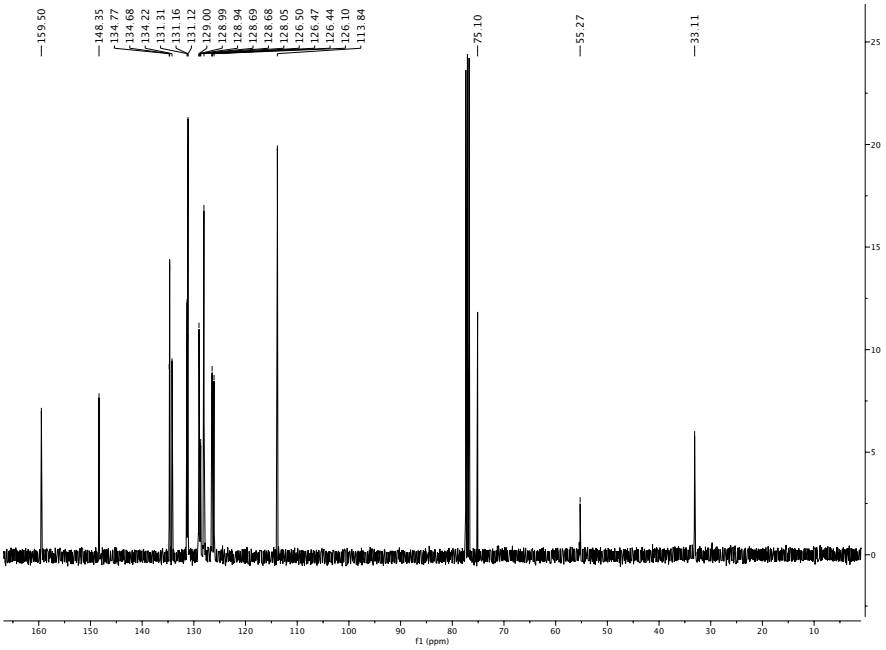

Figure A15. ^{13}C-NMR (101 MHz, $CDCl_3$, 25 ˚C): bis(1-methyl-4,5-diphenyl-1H-imidazol-2-yl)(4-(trifluoromethyl)-aryl)methanol (OH,*p*ArOMe)BMIM^{Ph_2}) (**4**).

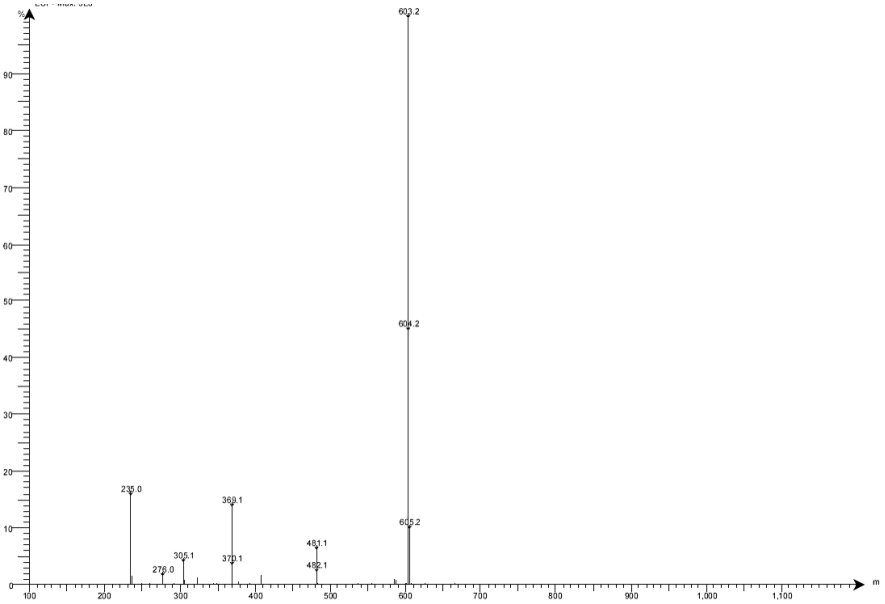

Figure A16. Low resolution ESI-MS spectra of complex bis(1-methyl-4,5-diphenyl-1H-imidazol-2-yl)(4-(trifluoromethyl)-aryl)methanol (OH,*p*ArOMe)BMIM^{Ph_2}) (**4**) in MeCN.

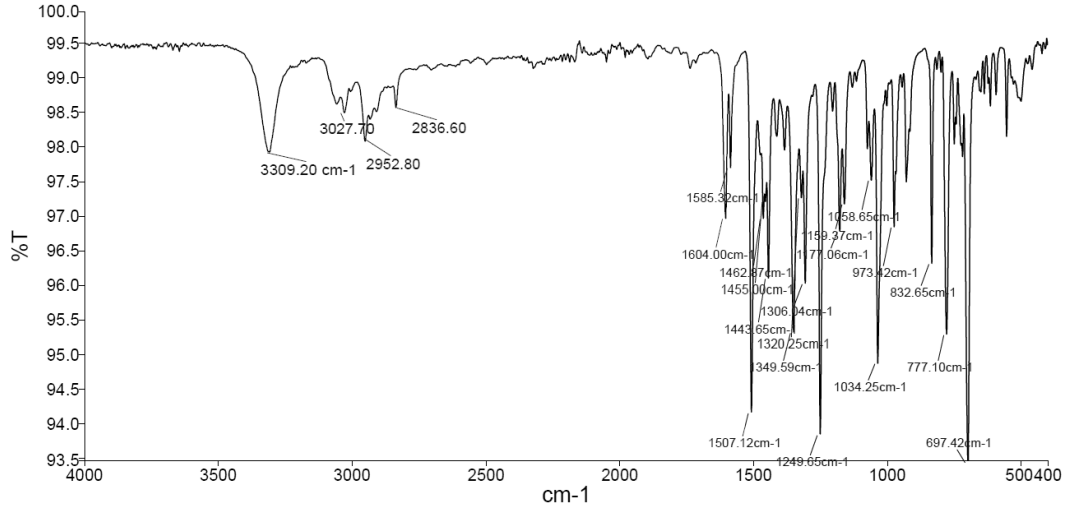

Figure A17. Infrared spectrum of bis(1-methyl-4,5-diphenyl-1H-imidazol-2-yl)(4-(trifluoromethyl)-aryl)methanol (OH,*p*ArOMe)BMIM^{Ph_2}) (**4**).

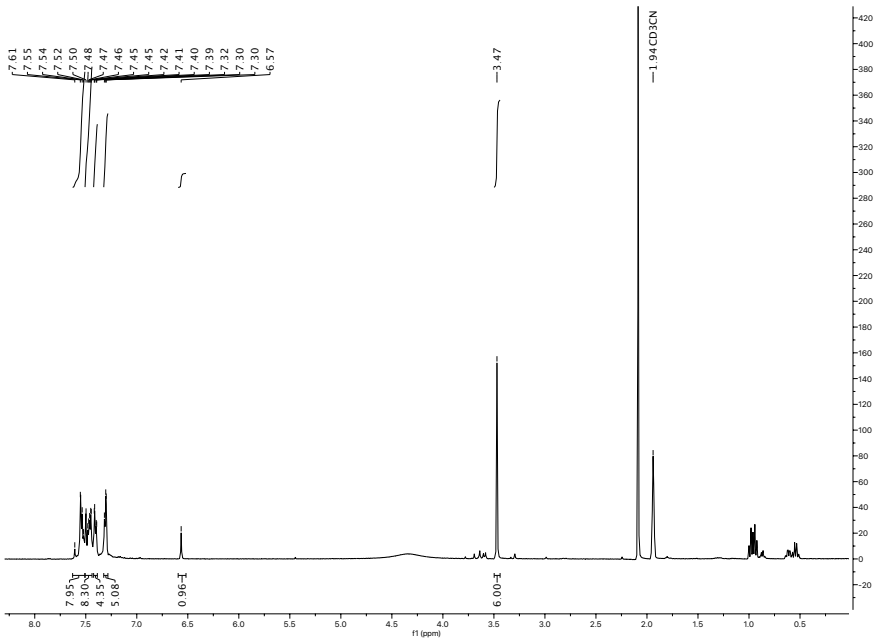

Figure A18. ^{1}H-NMR (400 MHz, CD_3CN, 25 ˚C): 2,2'-(phenylmethylene)bis(1-methyl-4,5-diphenyl-1H-imidazole), (H,*p*ArH)BMIM^{Ph_2}) (**5**).

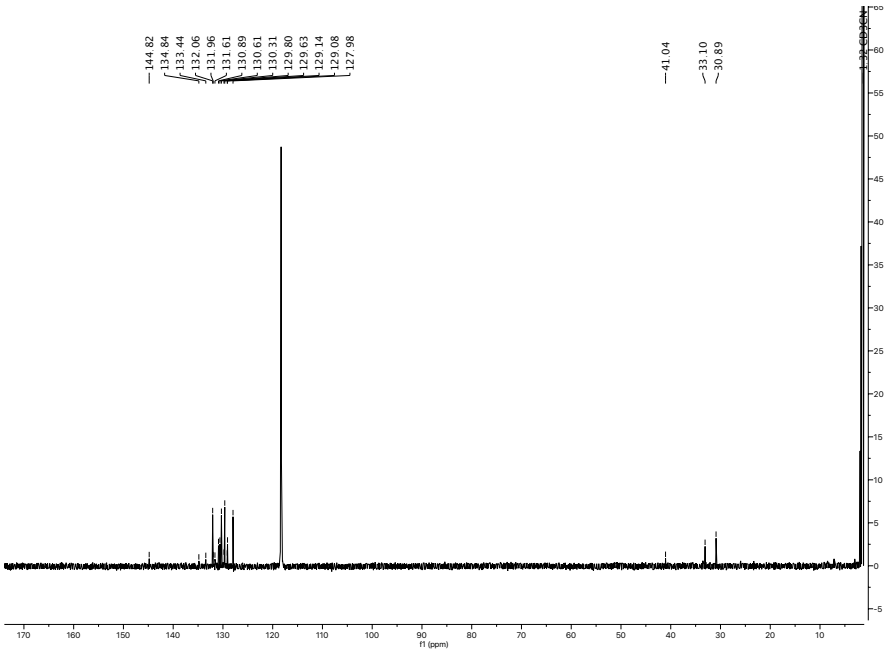

Figure A19. ^{13}C-NMR (101 MHz, CD_3CN, 25 ˚C): 2,2'-(phenylmethylene)bis(1-methyl-4,5-diphenyl-1H-imidazole), (H,*p*ArH)BMIM^{Ph_2}), (**5**).

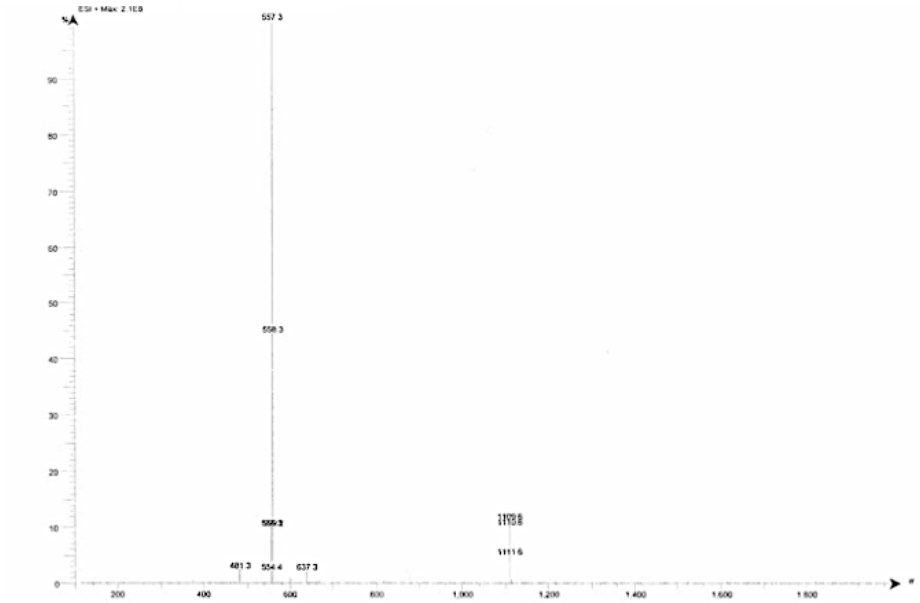

Figure A20. Low resolution ESI-MS spectra of complex 2,2'-(phenylmethylene)bis(1-methyl-4,5-diphenyl-1H-imidazole), (H,*p*ArH)BMIM^{Ph_2}) (**5**) in MeCN.

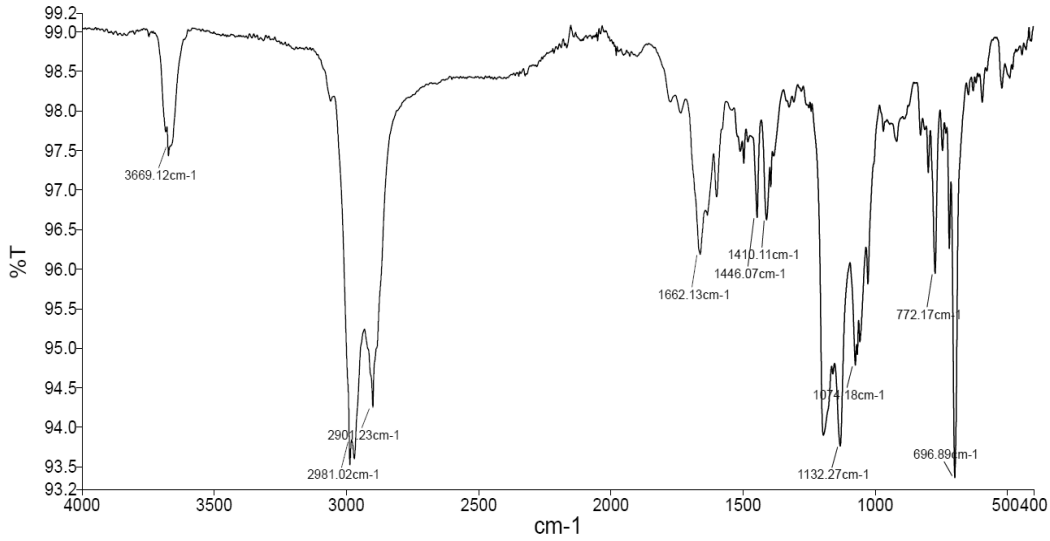

Figure A21. Infrared spectrum of 2,2'-(phenylmethylene)bis(1-methyl-4,5-diphenyl-1H-imidazole), (H,*p*ArH)BMIM^{Ph_2}) (**5**).

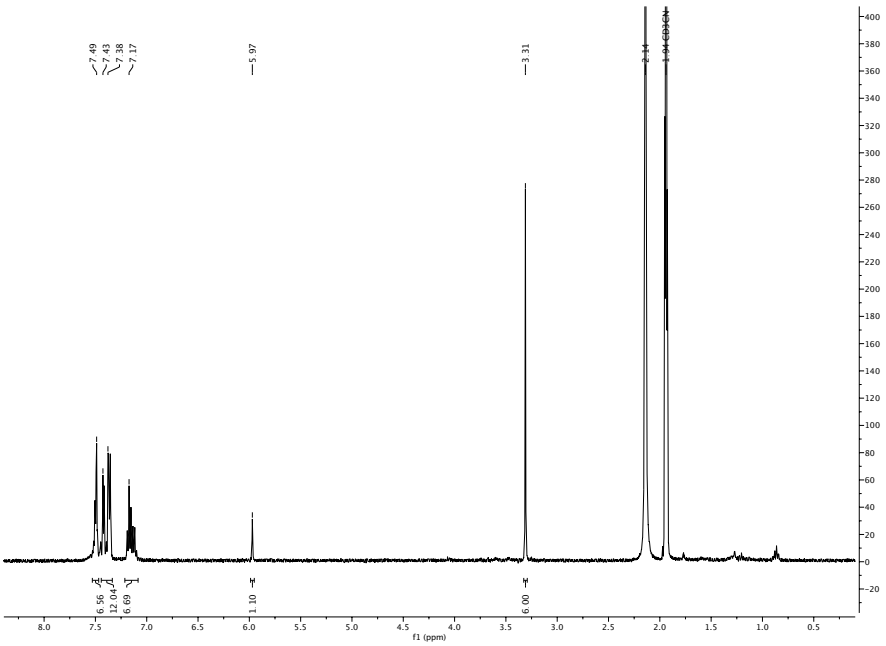

Figure A22. ^{1}H-NMR (400 MHz, CD_3CN, 25 °C): Bis(1-methyl-4,5-diphenyl-1H-imidazol-2-yl)4-chloroarylmethane, (H,*p*ArCl)BMIM^{Ph_2}) (**6**).

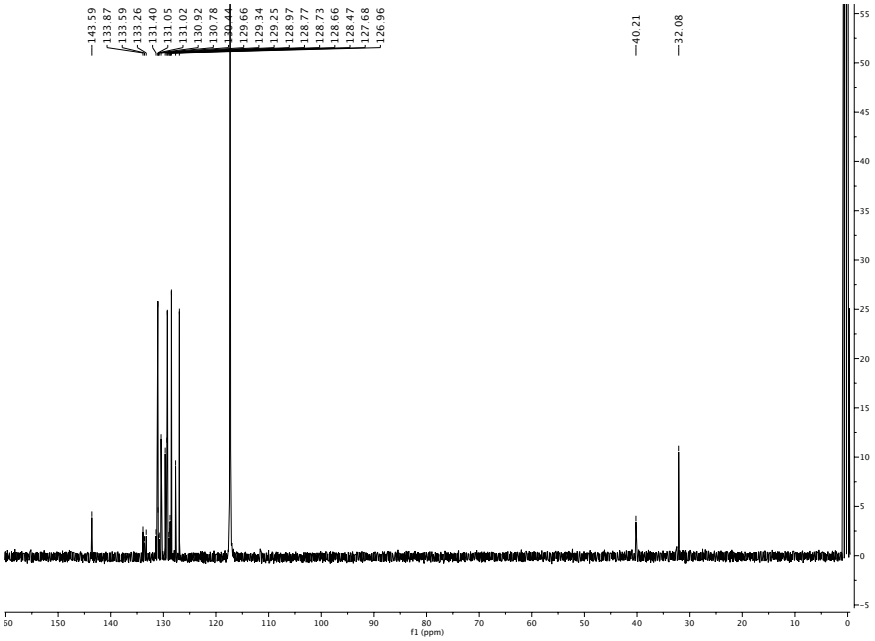

Figure A23. ^{13}C-NMR(100 MHz, CD_3CN, 25 °C) Bis(1-methyl-4,5-diphenyl-1H-imidazol-2-yl)4-chloroarylmethane, (H,*p*ArCl)BMIM^{Ph_2}) (**6**).

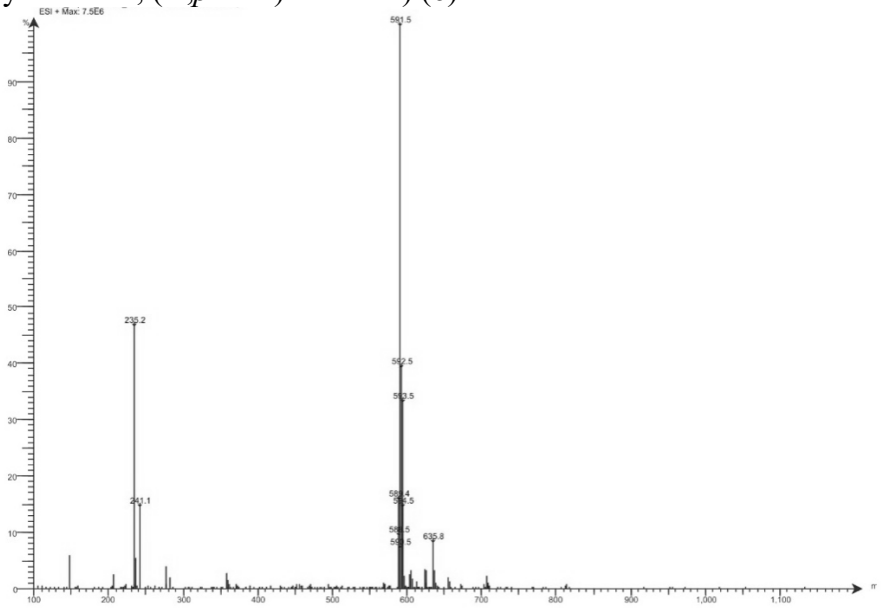

Figure A24. Low resolution ESI-MS spectra of complex Bis(1-methyl-4,5-diphenyl-1H-imidazol-2-yl)4-chloroarylmethane, (H,*p*ArCl)BMIM^{Ph_2}) (**6**) in MeCN.

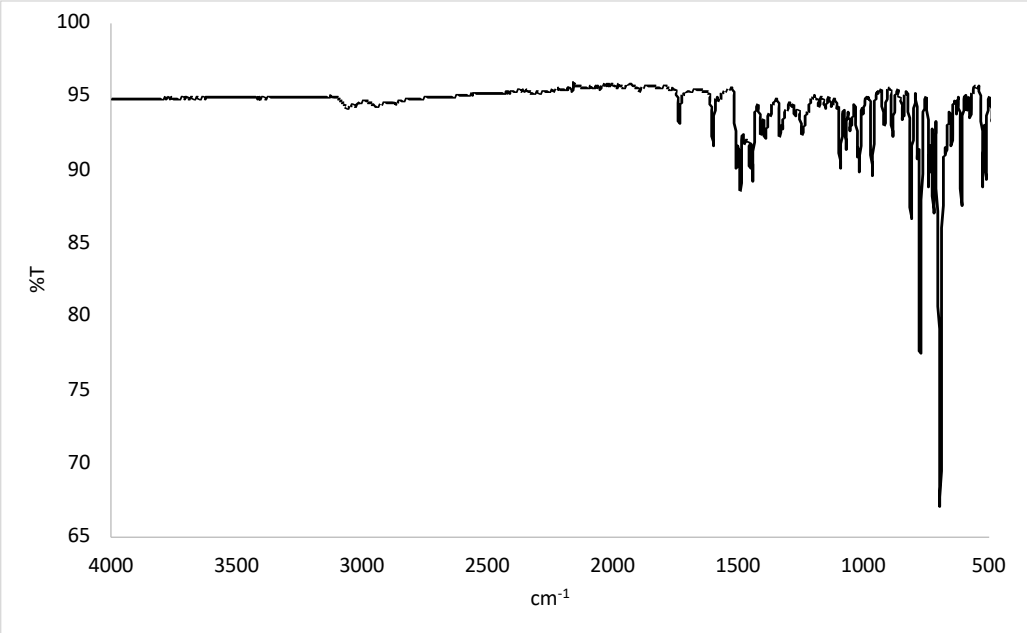

Figure A25. Infrared spectrum of spectra of complex Bis(1-methyl-4,5-diphenyl-1H-imidazol-2-yl)4-chloroarylmethane, (H,*p*ArCl)BMIM^{Ph_2}) (**6**).

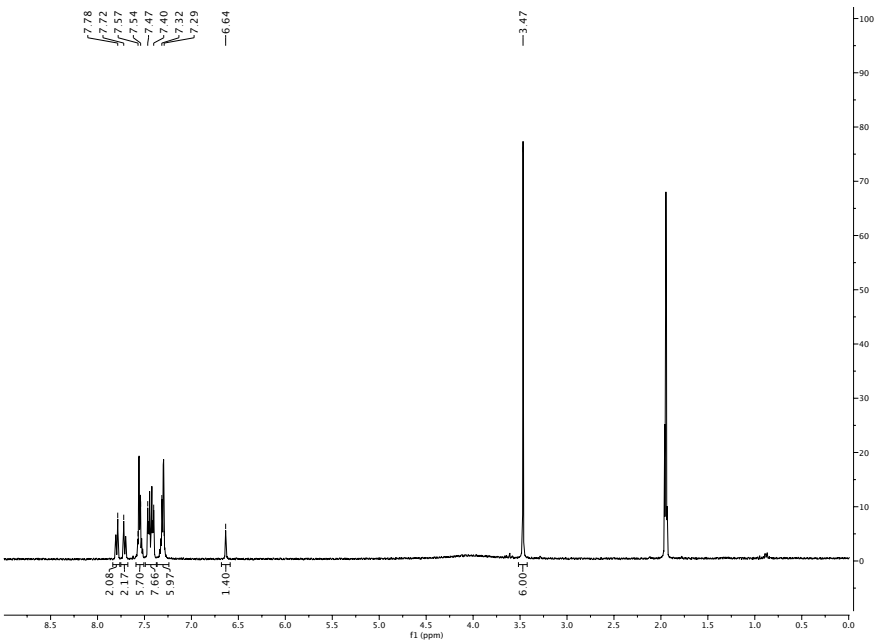

Figure A26. ^{1}H-NMR (400 MHz, CD_3CN, 25 ˚C): 2,2'-((4-(trifluoromethyl)aryl)methylene)bis(1-methyl-4,5-diphenyl-1H-imidazole), (H,*p*ArCF$_3$)BMIM^{Ph_2}) (**7**).

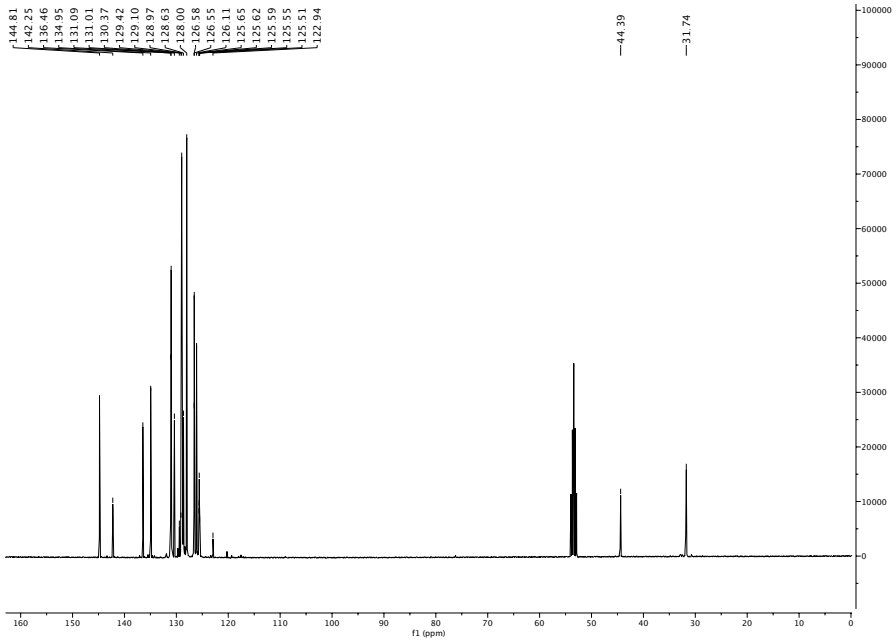

Figure A27. ^{13}C-NMR (101 MHz, CD_3CN, 25 ˚C): 2,2'-((4-(trifluoromethyl)aryl)methylene)bis(1-methyl-4,5-diphenyl-1H-imidazole), (H,*p*ArCF_3)BMIM^{Ph_2}) (**7**).

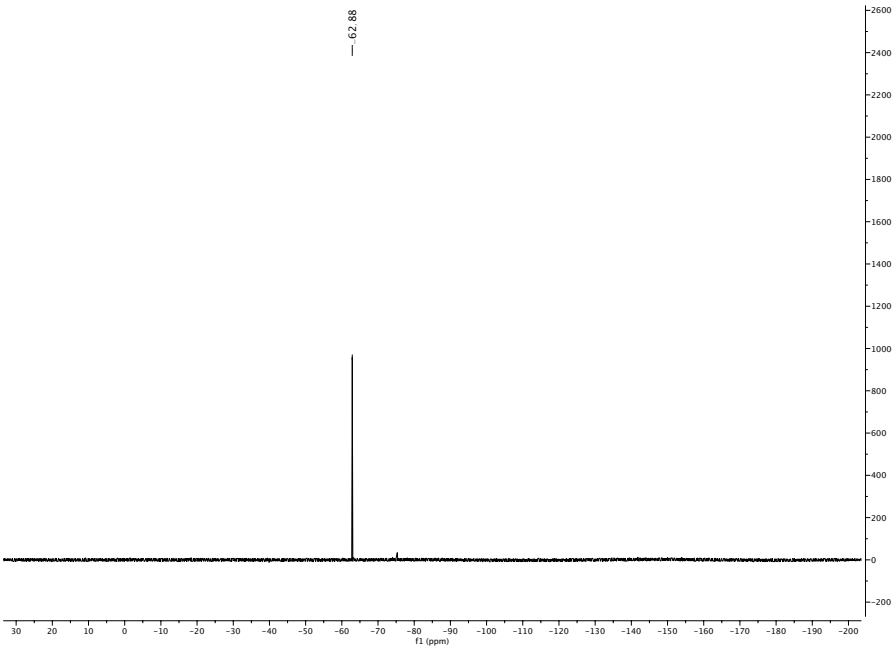

Figure A28. ^{19}F-NMR (376 MHz, $CDCl_3$, 25 ˚C): 2,2'-((4-(trifluoromethyl)aryl)methylene)bis(1-methyl-4,5-diphenyl-1H-imidazole), (H,*p*ArCF_3)BMIM^{Ph_2}) (**7**), the minor second signal at –74 was assigned to a small impurity of residual trifluoroacetic acid.

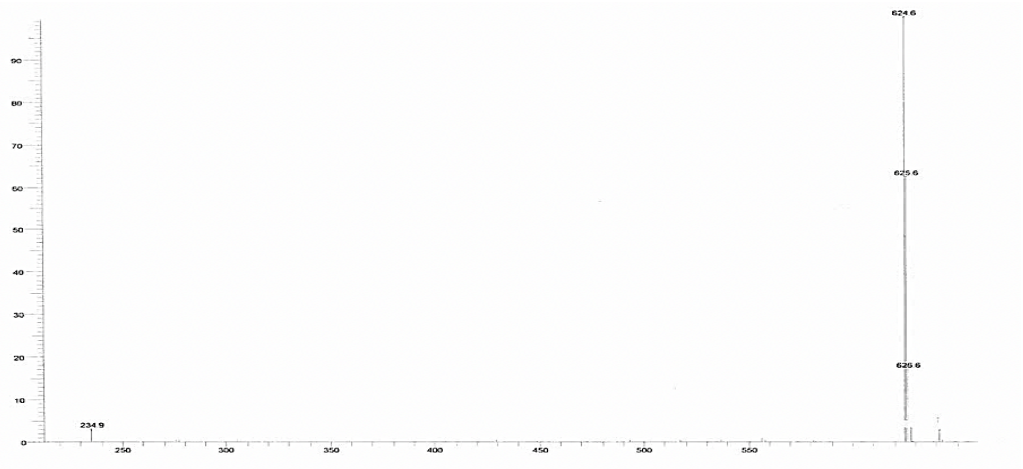

Figure A29. Low resolution ESI-MS spectra of complex 2,2'-((4-(trifluoromethyl)aryl)methylene)bis(1-methyl-4,5-diphenyl-1H-imidazole), (H,*p*ArCF$_3$)BMIM^{Ph_2}) (**7**) in MeCN.

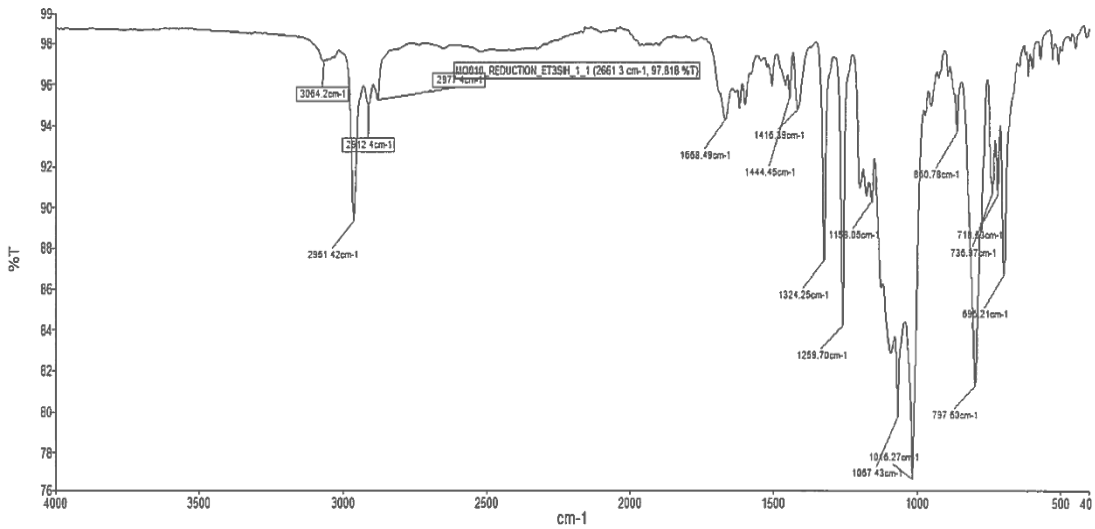

Figure A30. Infrared spectrum of 2,2'-((4-(trifluoromethyl)aryl)methylene)bis(1-methyl-4,5-diphenyl-1H-imidazole), (H,*p*ArCF$_3$)BMIM^{Ph_2}) (**7**).

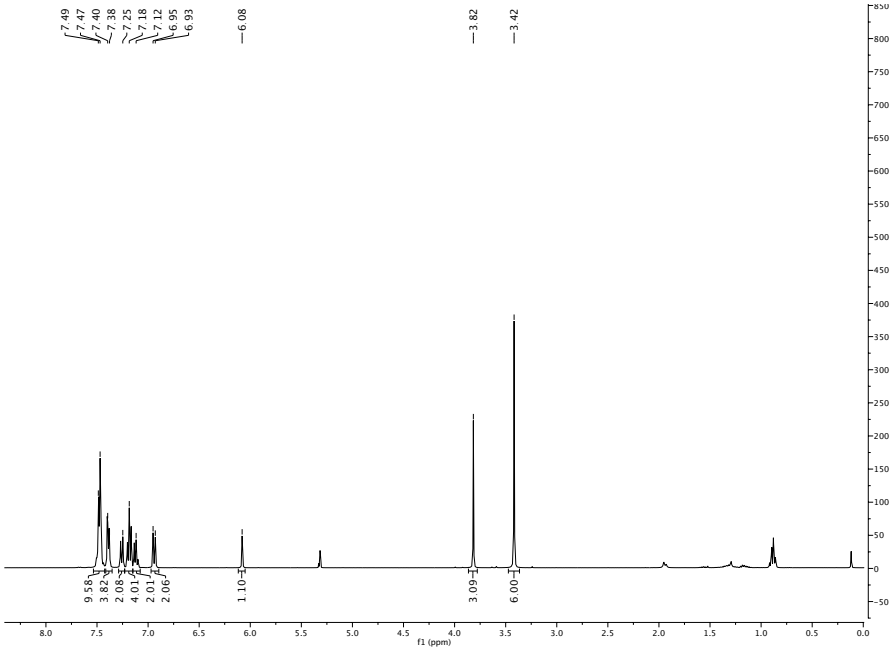

Figure A31. ^{1}H-NMR (400 MHz, DCM-d_2, 25 ˚C): 2,2'-((4-methoxyaryl)methylene)bis(1-methyl-4,5-diphenyl-1H-imidazole), (H,*p*ArOMe)BMIM^{Ph_2}) (**8**).

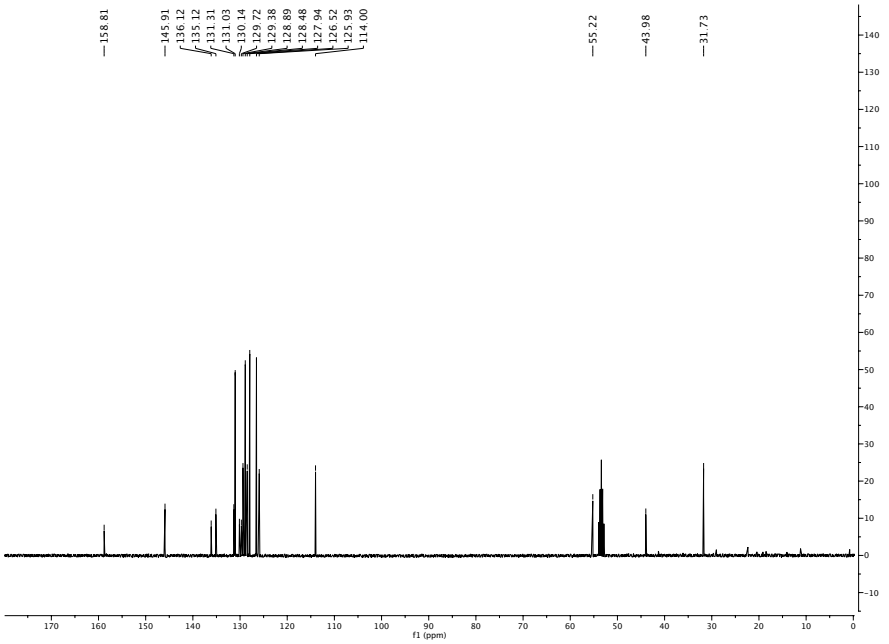

Figure A32. ^{13}C-NMR (101 MHz, DCM-d_2, 25 ˚C): 2,2'-((4-methoxyaryl)methylene)bis(1-methyl-4,5-diphenyl-1H-imidazole), (H,*p*ArOMe)BMIM^{Ph_2}) (**8**).

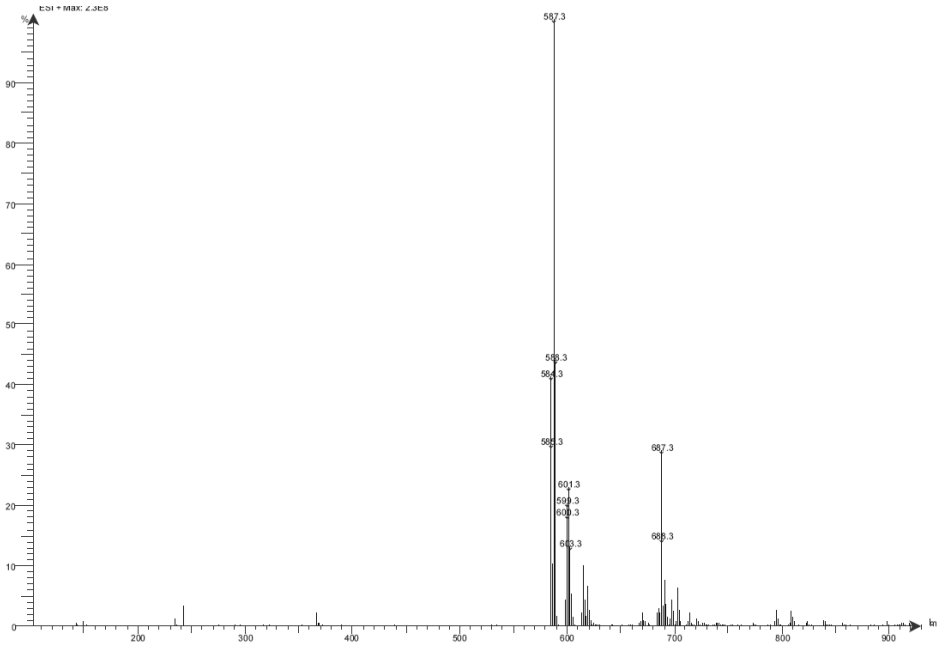

Figure A33. Low resolution ESI-MS spectra of complex2,2'-((4-methoxyaryl)methylene)bis(1-methyl-4,5-diphenyl-1H-imidazole), (H,*p*ArOMe)BMIM^{Ph_2}) (**8**) in MeCN.

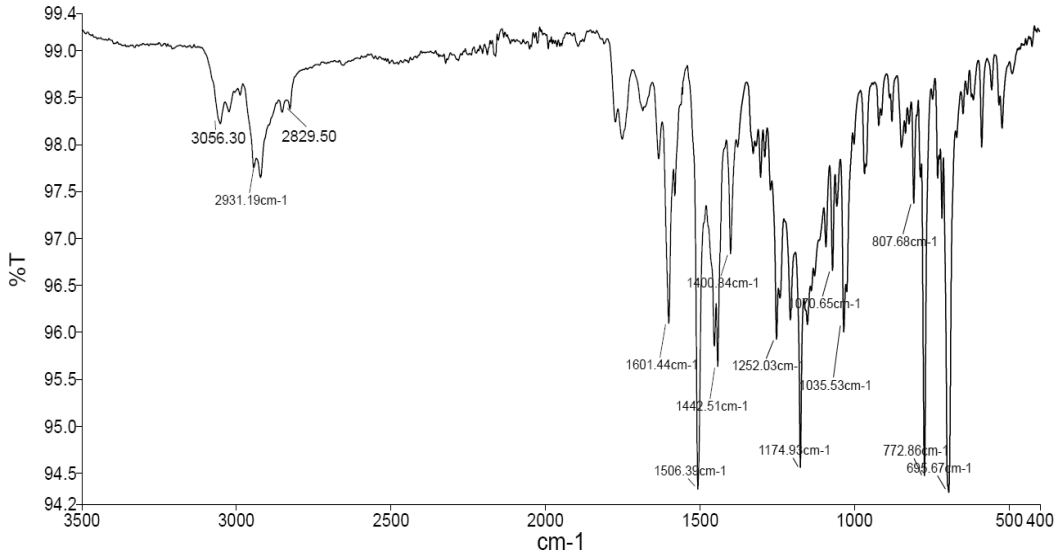

Figure A34. Infrared spectrum of 2,2'-((4-methoxyaryl)methylene)bis(1-methyl-4,5-diphenyl-1H-imidazole), (H,*p*ArOMe)BMIM^{Ph_2}) (**8**).

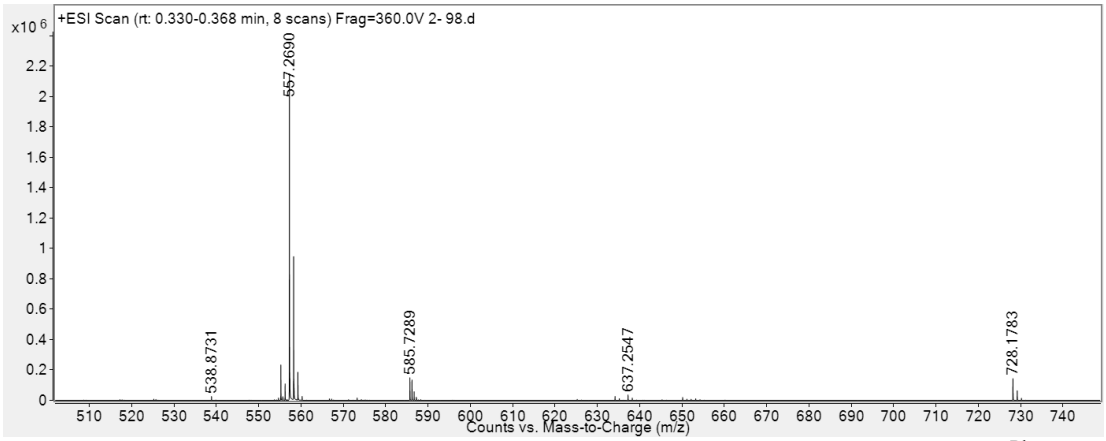

Figure A35. High resolution ESI-MS spectrum of complex $[Co((H,pArH)BMIM^{Ph_2})_2](BF_4)_2$ (**9**) in MeCN.

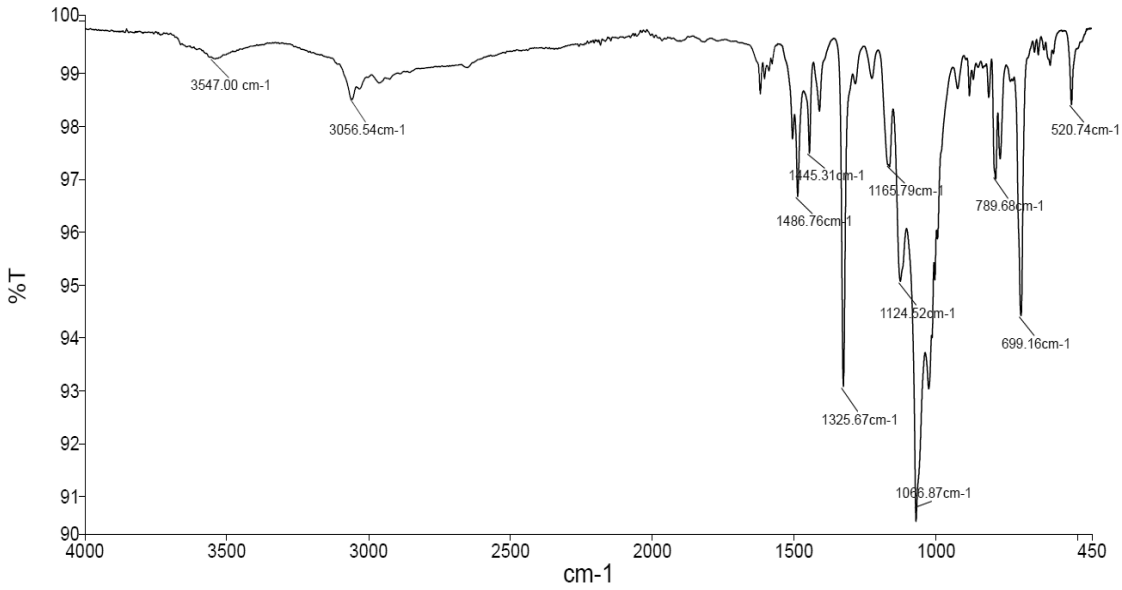

Figure A36. Infrared spectrum of $[Co((H,pArH)BMIM^{Ph_2})_2](BF_4)_2$ (**9**).

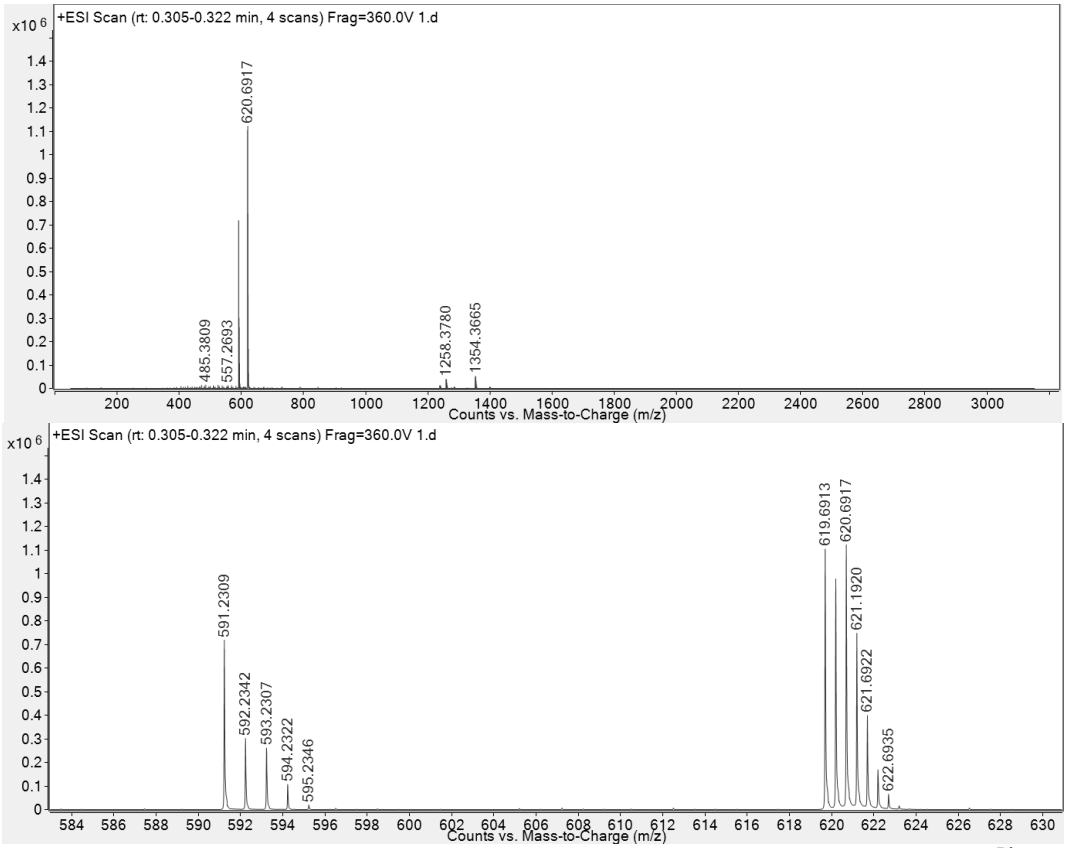

Figure A37. High resolution ESI-MS spectra of complex $[Co((H,pArCl)BMIM^{Ph_2})_2](BF_4)_2$ (**10**) in MeCN. Top: full spectrum. Bottom: zoom in on ligand [L+H] and complex $[M]^{2+}$ signals.

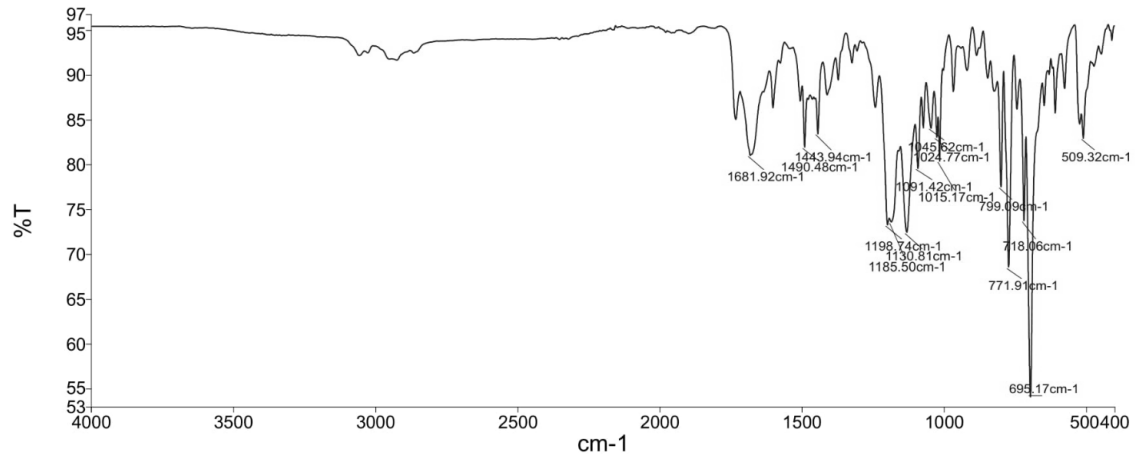

Figure A38. Infrared spectrum of $[Co((H,pArCl)BMIM^{Ph_2})_2](BF_4)_2$ (**10**).

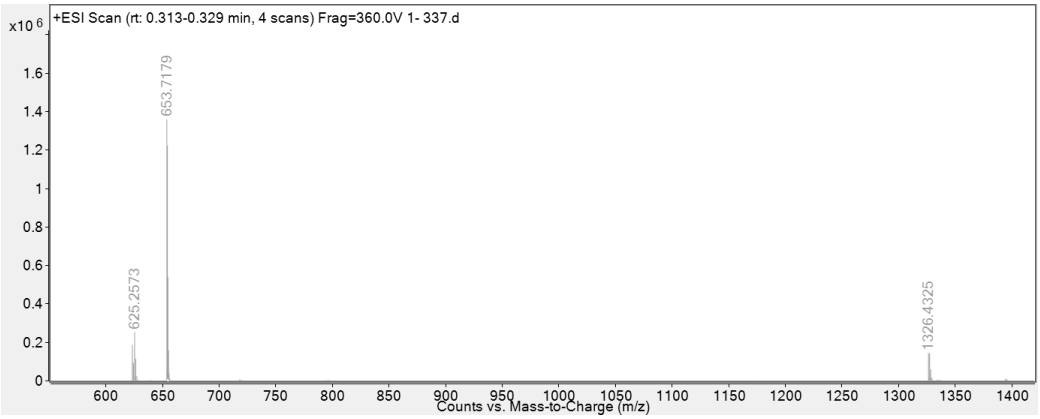

Figure A39. High resolution ESI-MS spectrum of complex $[Co((H,pArCF_3)BMIM^{Ph_2})_2](BF_4)_2$ (**11**) in MeCN.

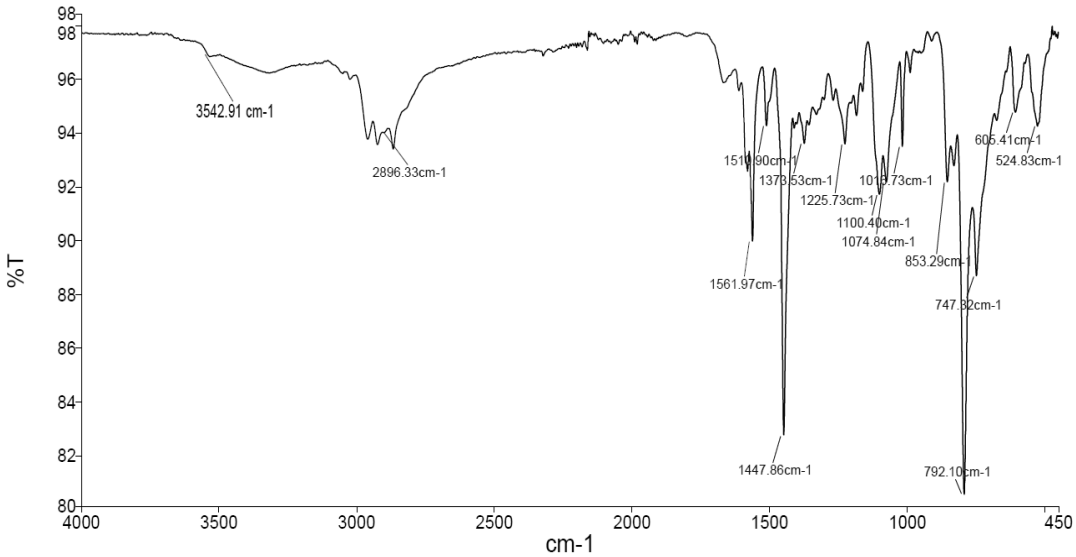

Figure A40. Infrared spectrum of $[Co((H,pArCF_3)BMIM^{Ph_2})_2](BF_4)_2$ (**11**).

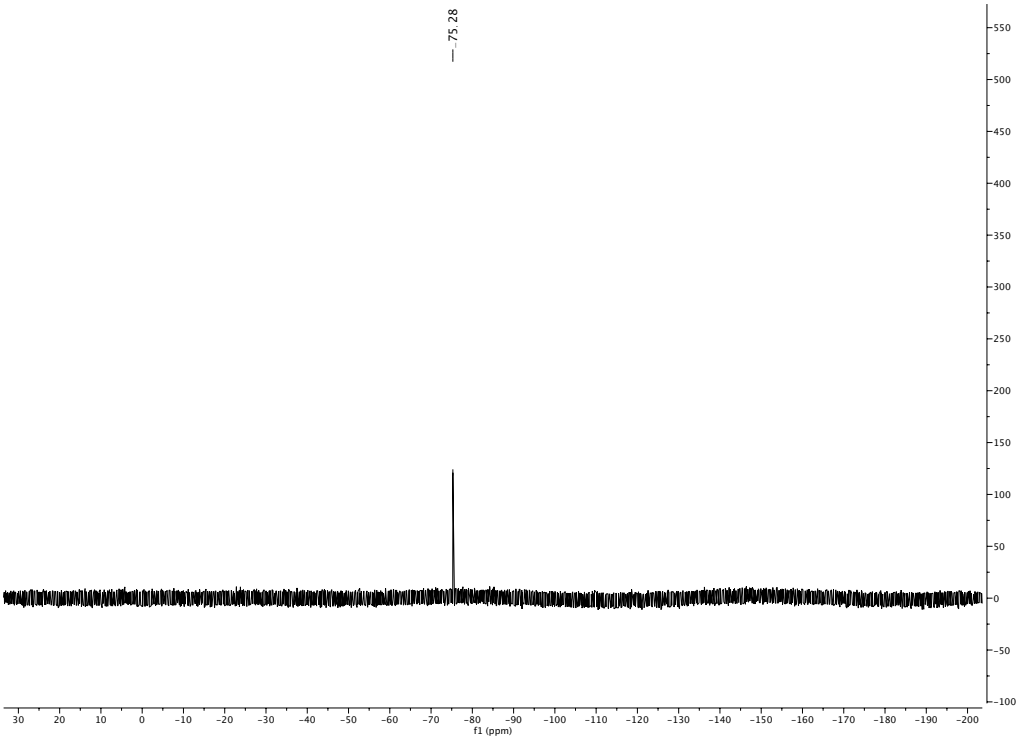

Figure A41. ^{19}F-NMR (376 MHz, MeCN-d_3, 25 °C): [Co((H,*p*ArCF$_3$)BMIM^{Ph_2})$_2$](BF$_4$)$_2$ (**11**).

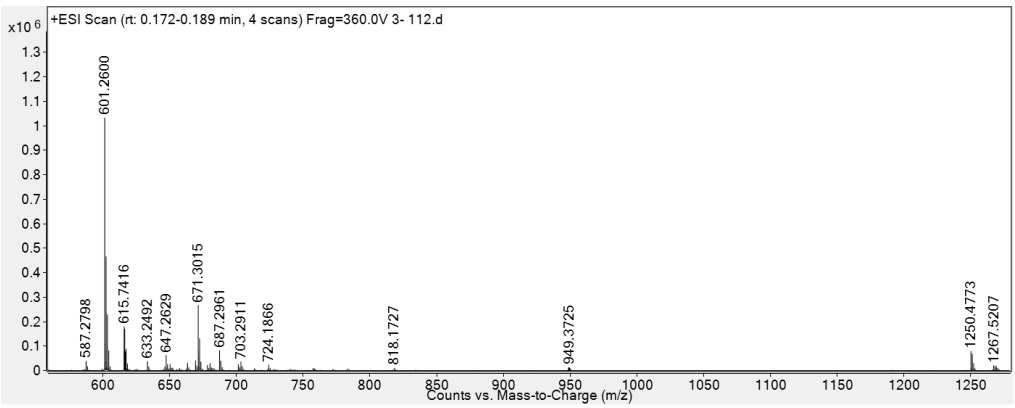

Figure A42. High resolution ESI-MS spectrum of complex [Co((H,*p*ArOMe)BMIM^{Ph_2})$_2$](BF$_4$)$_2$ (**12**) in MeCN.

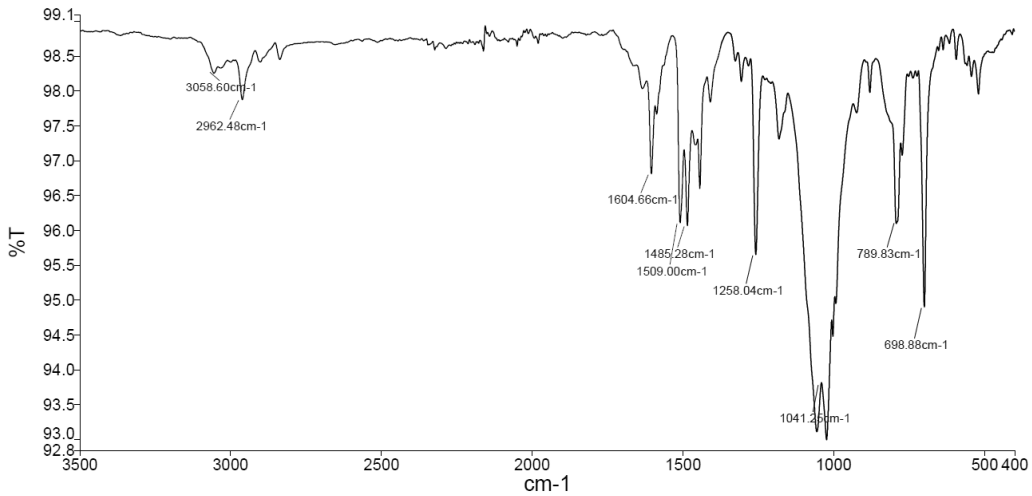

Figure A43. Infrared spectrum of [Co((H,*p*ArOMe)BMIM^{Ph_2})$_2$](BF$_4$)$_2$ (**12**).

A. 2 Additional characterization of literature compounds

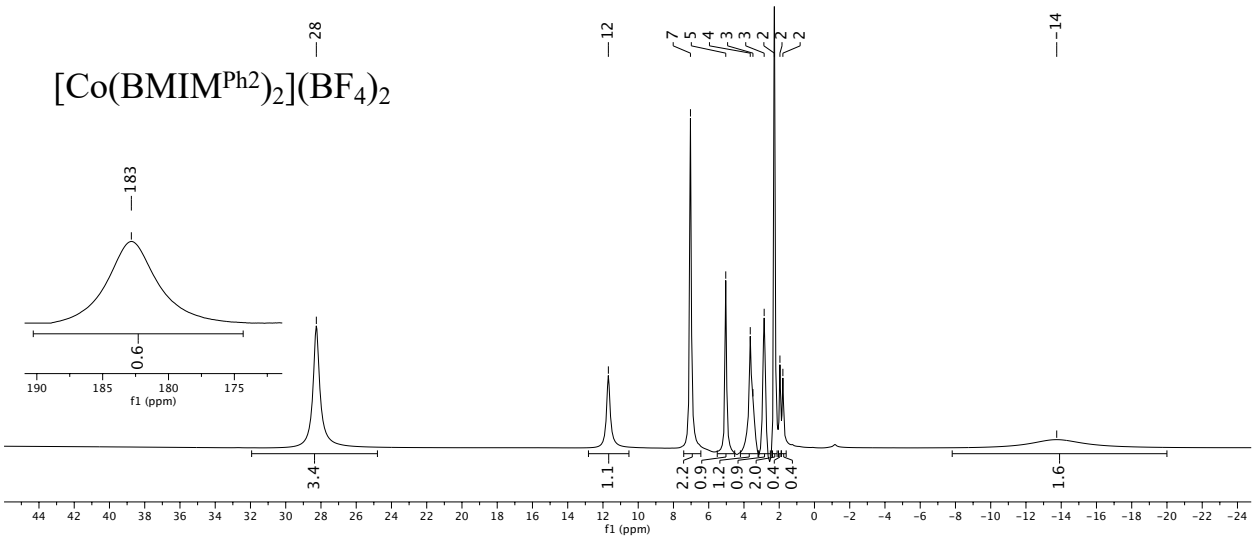

Figure A44. ^{1}H-NMR spectrum of [Co(BMIM^{Ph2})$_2$](BF$_4$)$_2$ in MeCN-d_3.

^{1}H NMR (400 MHz, MeCN-d_3, 25 °C): δ (ppm) = 183 (1H, ½CH$_2$), 28 (3H, CH$_3$), 12 (1H, Ph *p*-CH), 7 (2H, Ph *o*-CH), 5 (1H, Ph *p*-CH), 4 (1H, Ph *m*-CH), 3 (1H, Ph *m*-CH), 2 (2H, Ph *m*-CH), –14 (2H, Ph *o*-CH).Tentative peak assignments were based on relative integration, and broadness of the resonance (methylene and some *o*-Ph CH protons seemed to be in close proximity to the metal center (observed in a solid-state single crystal X-ray structure), and therefore broaden), chemical shift, and similarity to structural analogs.

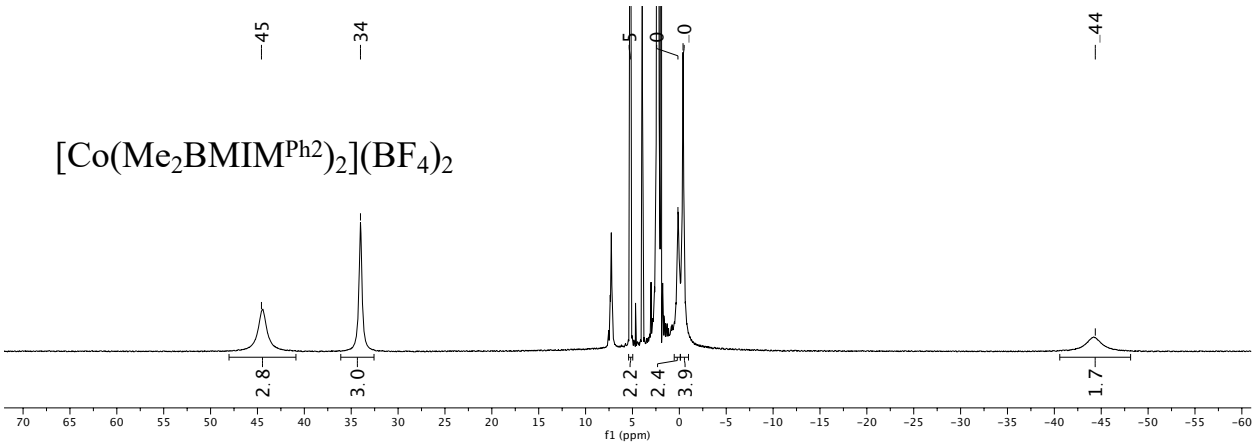

Figure A45. ^{1}H-NMR spectrum of $[Co(Me_2BMIM^{Ph2})_2](BF_4)_2$ in MeCN-d_3.

^{1}H NMR (400 MHz, MeCN-d_3, 25 °C): δ (ppm) = 45 (3H, methylene-CH_3), 34 (3H, imidazole-CH_3), 5 (2H, Ph *p*-CH), 0 (2H, Ph *o*-CH), 0 (4H, Ph *m*-CH), –44 (2H, Ph *o*-CH).Tentative peak assignments were based on relative integration, and broadness of the resonance (methylene and some *o*-Ph CH protons seemed to be in close proximity to the metal center (observed in a solid-state single crystal X-ray structure), and therefore broaden), chemical shift, and similarity to structural analogs.

A. 3 UV-vis spectra of 9-12

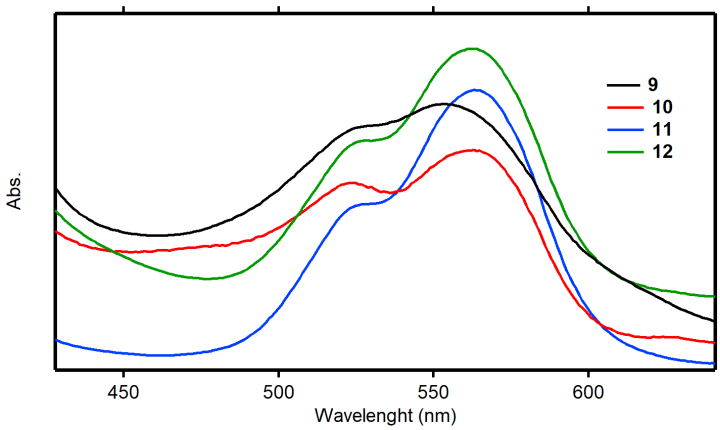

Figure A46. UV-Vis spectra of **9** (H) (black), **10** (Cl) (red), **11** (CF_3) (blue) and **12** (OMe) (green) in CH_3CN (1 mM).

Table A1. Absorption maxima of the d-d transition of **9-12** in MeCN (1 mM)

Complex	Formula	λ_{max} (nm)	λ_{max} (nm)
9	[Co((H,*p* ArH)BMIM^{Ph2})$_2$](BF$_4$)$_2$	522	558
10	[Co((H,*p* ArCl)BMIM^{Ph2})$_2$](BF$_4$)$_2$	523	563
11	[Co((H,*p* ArCF$_3$)BMIM^{Ph2})$_2$](BF$_4$)$_2$	525	563
12	[Co((H,*p* ArOMe)BMIM^{Ph2})$_2$](BF$_4$)$_2$	523	561

A. 4 X-ray crystal structural data [Co((H,*p*ArCF$_3$)BMIM^{Ph_2})$_2$](BF$_4$)$_2$ (11)

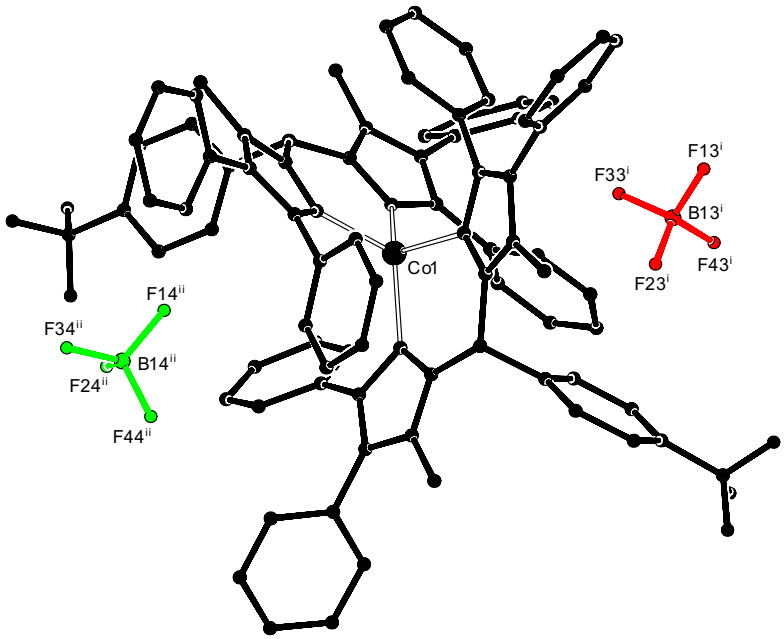

Figure A47. Closest BF$_4$ neighbors of the Co-complex in [Co((H,*p*ArCF$_3$)BMIM^{Ph_2})$_2$](BF$_4$)$_2$ **(11)** Shortest distances: Co1…F33^{i} 4.8923(18) Å and Co1…F14^{ii} 5.181(2) Å. Symmetry codes *i*: x, y-1, z; *ii*: 1.5-x, y+0.5, 1.5-z.

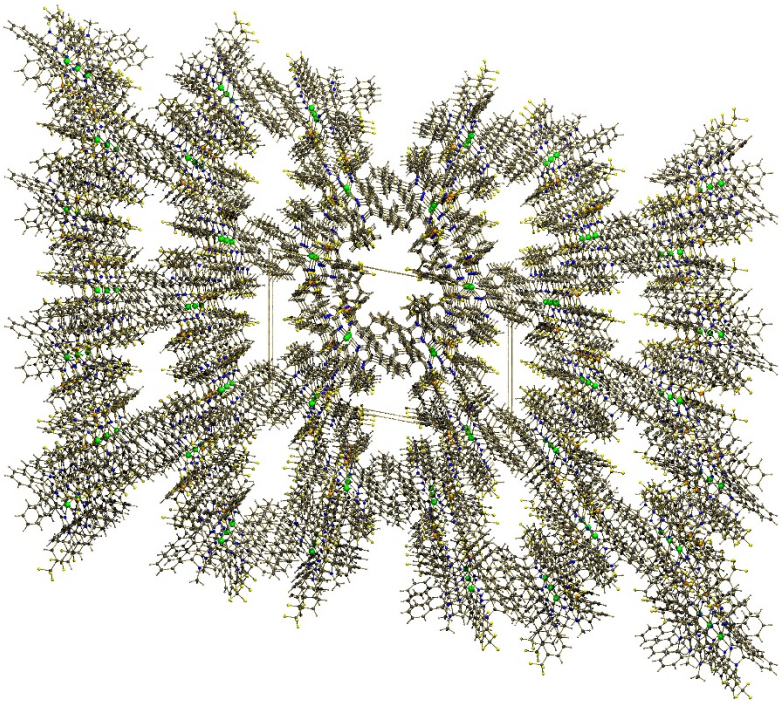

Figure A48. Solvent channels in the crystal structure of [Co((H,*p*ArCF$_3$)BMIM^{Ph_2})$_2$](BF$_4$)$_2$ **(11)**. View along the b-axis. The solvent channels occupy ~19% of the unit cell volume. They are filled with ordered and disordered acetonitrile and diethyl ether molecules which are omitted in the drawing.

Table A2. Angular variance[1] for the cobalt environment in the crystal structures of [Co((H,*p*ArCF$_3$)BMIM^{Ph_2})$_2$](BF$_4$)$_2$ **(11)** and [Co(BMIM^{Ph2})$_2$](BF$_4$)$_2$.

[Co((H,*p*ArCF$_3$)BMIM^{Ph_2})$_2$](BF$_4$)$_2$ **(11)**	[Co(BMIM^{Ph2})$_2$](BF$_4$)$_2$	
	molecule 1	molecule 2
198.03 deg^2	195.61 deg^2	176.98 deg^2

Table A3. Continuous shape measure[2] of the cobalt environment in the crystal structures of [Co((H,*p*ArCF$_3$)BMIM^{Ph_2})$_2$](BF$_4$)$_2$ **(11)** and [Co(BMIM^{Ph2})$_2$](BF$_4$)$_2$. Deviation from ideal tetrahedral symmetry (T$_d$).

[Co((H,*p*ArCF$_3$)BMIM^{Ph_2})$_2$](BF$_4$)$_2$ **(11)**	[Co(BMIM^{Ph2})$_2$](BF$_4$)$_2$	
	molecule 1	molecule 2
2.154	2.511	2.218

A. 5 Electrochemical and electrocatalytic definitions

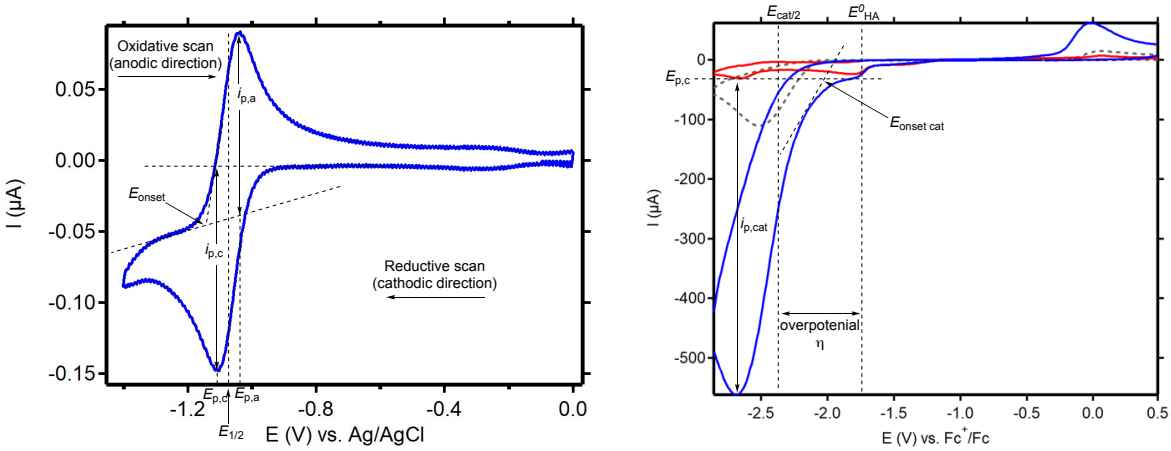

Figure A49. Cyclic voltammogram definitions
Left: The E_{onset} of oxidation/reduction is the crossing point between the redox event's tangent and the baseline's tangent. E_p is the peak potential, in which a = anodic and c = cathodic. $E_{1/2}$ is the halfwave potential and is defined as the $(E_{p,a} + E_{p,c})/2$. i_p, in which a = anodic and c = cathodic, is defined as the current difference between the peak current and the tangent of the baseline at E_p.[3]
Right: The $E_{onset\ cat}$ is the crossing point between the catalytic current tangent and the $E_{p,c}$ in the absence of a catalytic current. $i_{p,\ cat}$ is defined as the current enhancement from $i_{p,c}$. $E_{cat/2}$ is the potential at half of the $i_{p,\ cat}$ current. E^0_{HA} is the thermodynamic reduction potential of the sacrificial proton donor (see also **Table A4**).[4] The overpotential η is defined as the potential difference between the $E_{cat/2}$ and the E^0_{HA}.[3]

A. 6 Additional electrochemical data of 9, 10, and 12

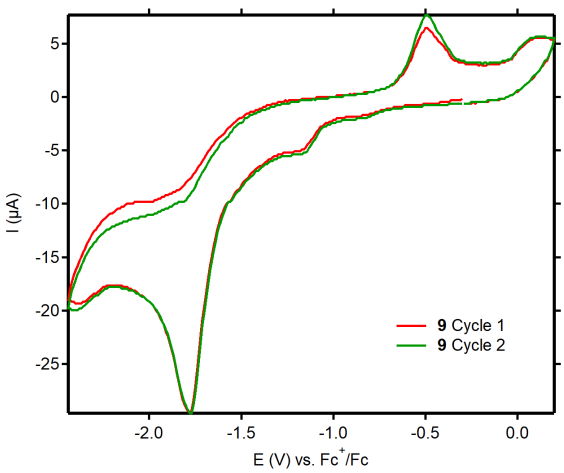

Figure A50. CVs of 2 mM **9** (H) in 0.1 M nBu$_4$NPF$_6$ in MeCN, referenced *vs.* the ferrocenium/ferrocene redox couple at a scan rate of 100 mV/s. Measurements are first scanned in the cathodic direction. The irreversible redox couple at $E_{p,c}$ = –1.79 V was assigned to the Co(I/II) redox couple, and the oxidative event at $E_{p,a}$ = –0.55 V was assigned to the oxidation of a new chemical species that is structurally related to **9** and forms after the irreversible reduction.

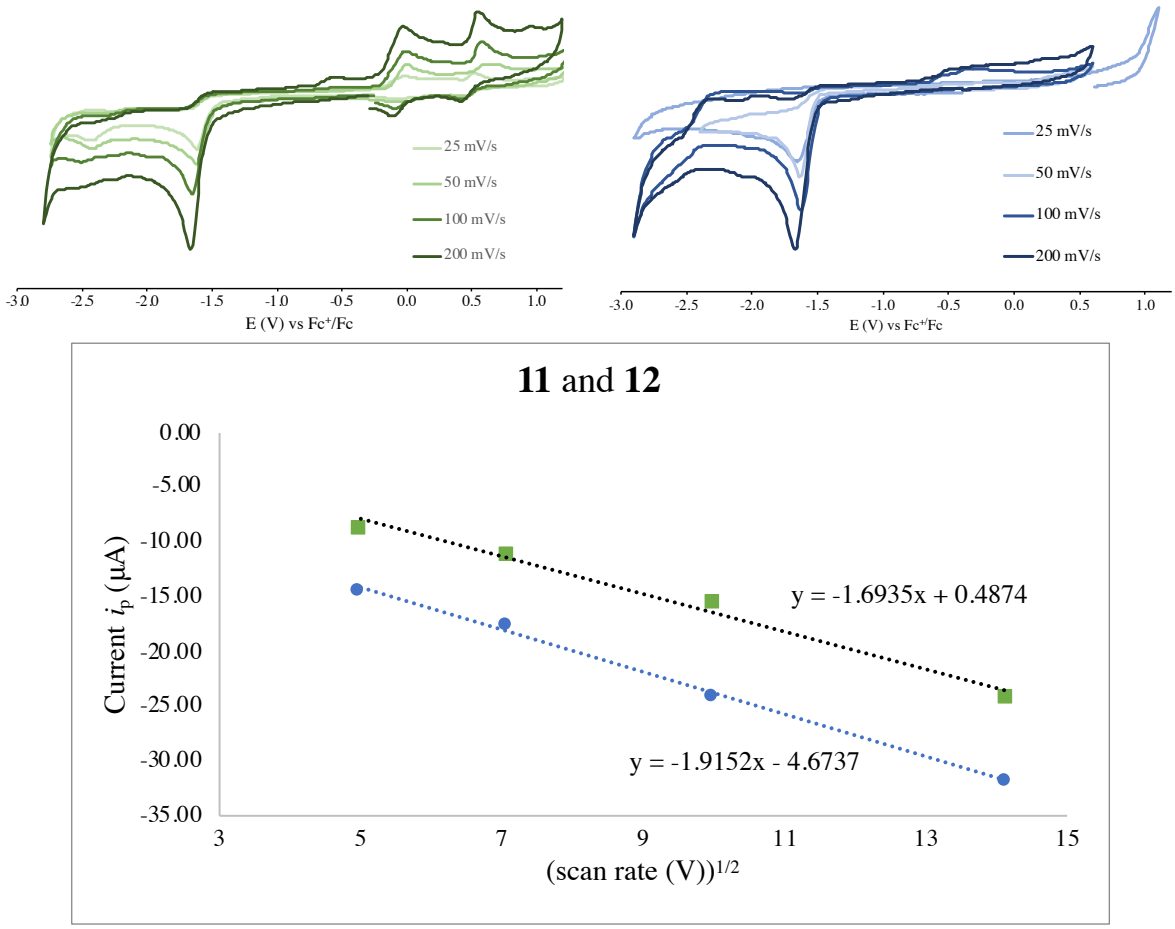

Figure A51. Scan rate CV analysis. Top: CVs of 2 mM **11** (CF_3) (left) and **12** (OMe) (right) in 0.1 M nBu$_4$NPF$_6$ in MeCN, referenced *vs.* the ferrocenium/ferrocene redox couple at different scan rates of 25-200 mV/s. Bottom: Plots of the peak currents ($i_{p,c}$) versus the square root of the scan rate.

Table A4. Brønsted acids for electrocatalytic HER studies in MeCN.[4] E^0_{HA} = thermodynamic reduction potential, E_{inf} = the direct reduction potential of the acid by a glassy carbon electrode vs Fc^+/Fc.[4]

	Acetonitrile		
Acid	pK_a	E^0_{HA}	E_{inf} vs Fc^+/Fc (V)
Triethylammonium	18.7	–1.25	–2.29 ± 0.02
Benzoic acid	20.7	–1.36	–2.25 ± 0.02
Acetic acid	22.3	–1.46	–2.36 ± 0.05
Phenol	27.2	–1.75	–2.60 ± 0.06

A. 7 The electrolysis Cell

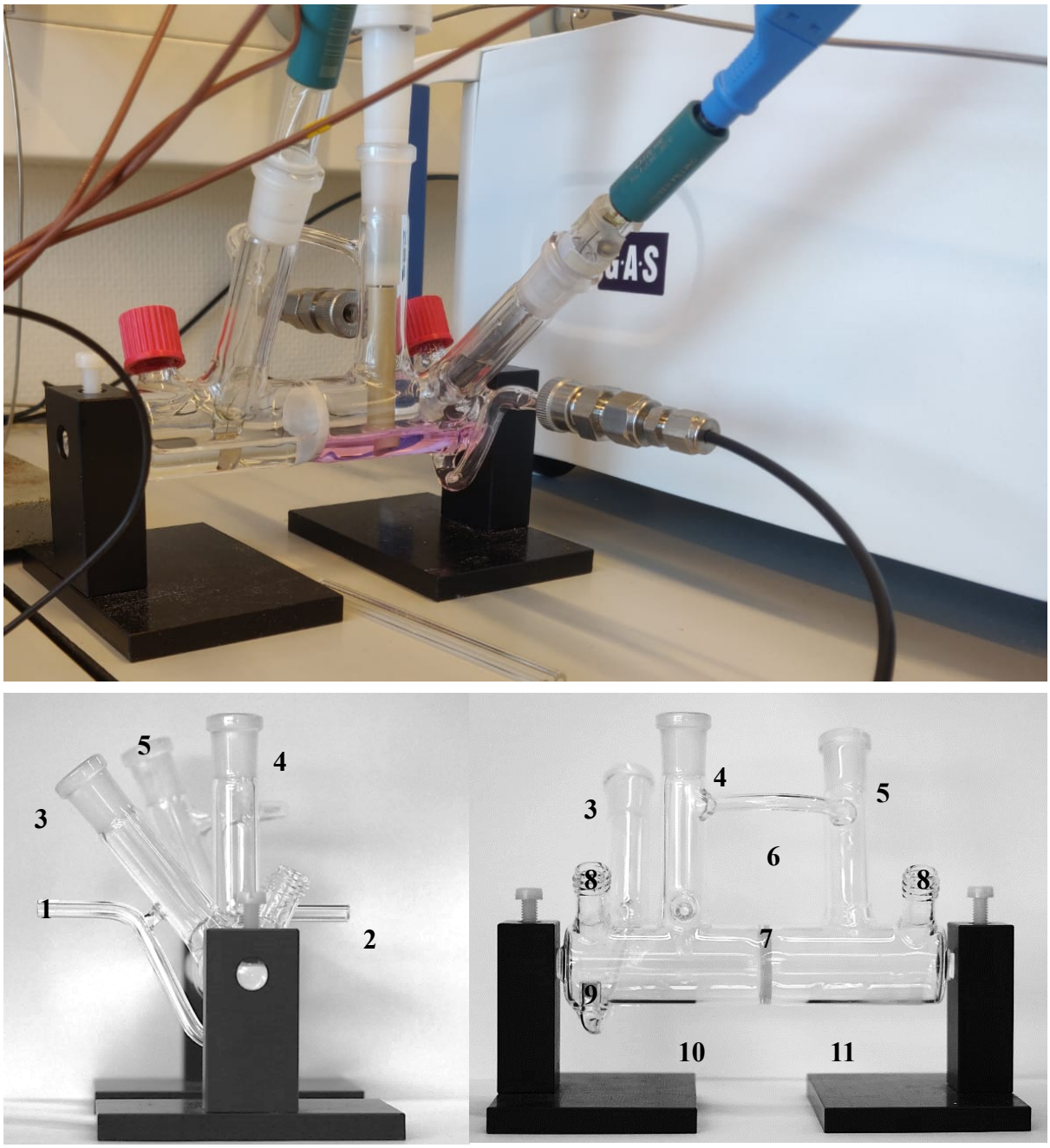

Figure A52. Pictures of the two-compartment three-electrode HER model-cell used for bulk electrolysis. 1. Gas inlet, 2. Gas outlet, 3. Reference electrode shaft, 4. Rotating Disk Electrode shaft, 5. Counter electrode shaft, 6. Pressure equalizer tube, 7. Porous P5 glass filter, 8. Opening with screw thread for possible addition or removal of materials, 9. Porous P1 glass filter on gas inlet 10. WE and RE compartment, 11. CE compartment.

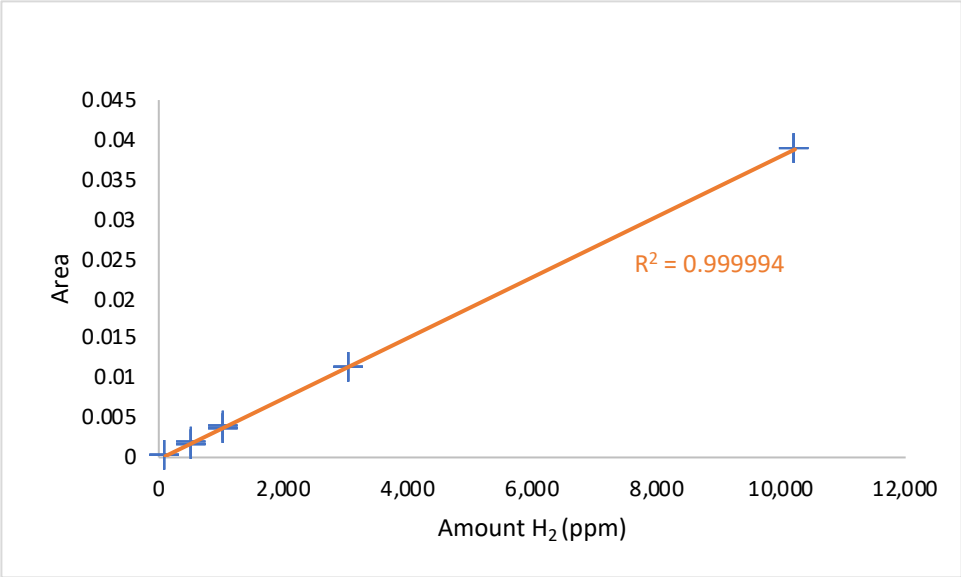

Figure A53. GC-TCD calibration with five H_2/N_2 mixtures of known composition containing 97.5, 508, 1036, 3046, 10210 ppm H_2 gas. Number of calibration points: 45.

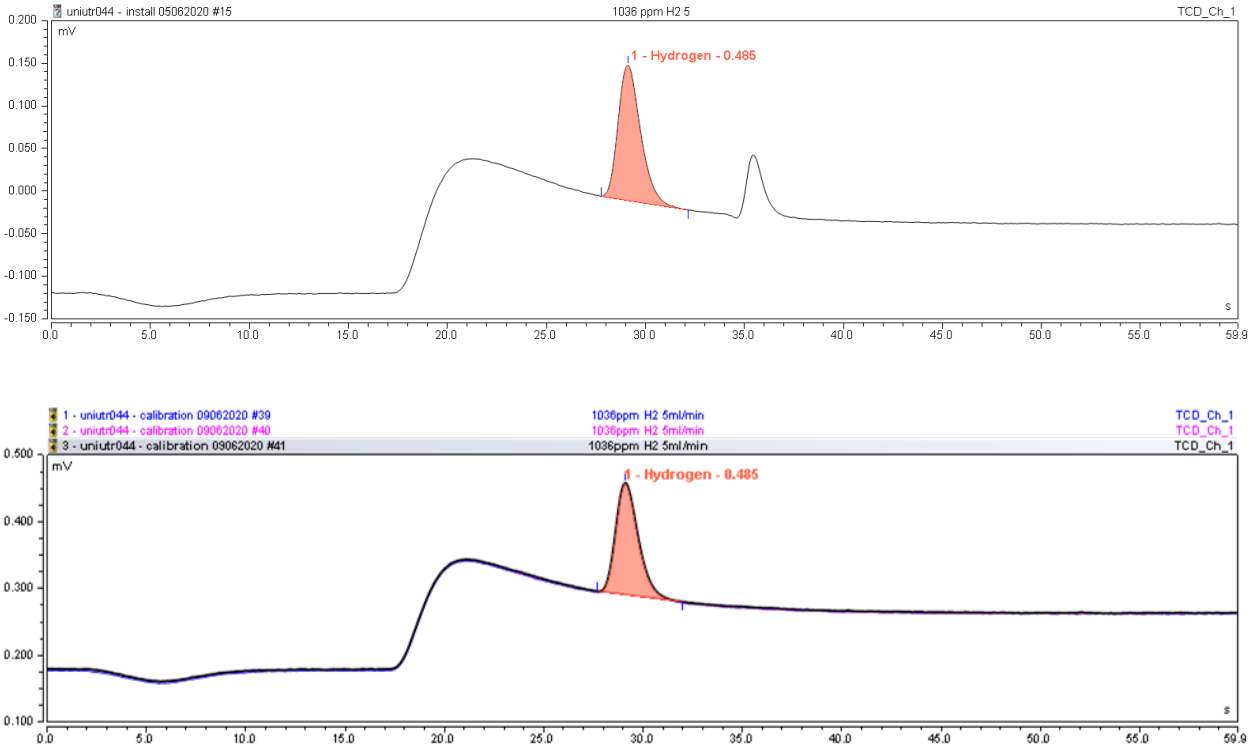

Figure A54. GC-TCD chromatograms of a 1036 ppm H_2 in N_2 mix gas overtime. Top: t = 60 s hydrogen at 29.0 retention time and residual oxygen at 35.4 retention time. Bottom: t = 600 s no oxygen is observed.

A. 8 References

(1) Robinson, K.; Gibbs, G.; Ribbe, P. Quadratic elongation: a quantitative measure of distortion in coordination polyhedra. *Science* **1971,** *172* (3983), 567.

(2) Pinsky, M.; Avnir, D. Continuous symmetry measures. 5. The classical polyhedra. *Inorganic chemistry* **1998,** *37* (21), 5575.

(3) Bard, A. J.; Faulkner, L. R. *Electrochemical Methods: Fundamentals and Applications*, 2001.

(4) McCarthy, B. D.; Martin, D. J.; Rountree, E. S.; Ullman, A. C.; Dempsey, J. L. Electrochemical Reduction of Brønsted Acids by Glassy Carbon in Acetonitrile—Implications for Electrocatalytic Hydrogen Evolution. *Inorganic Chemistry* **2014,** *53* (16), 8350.

Appendix B

Supporting Information to Chapter 3

B. 1 Spectra of complexes 1-6

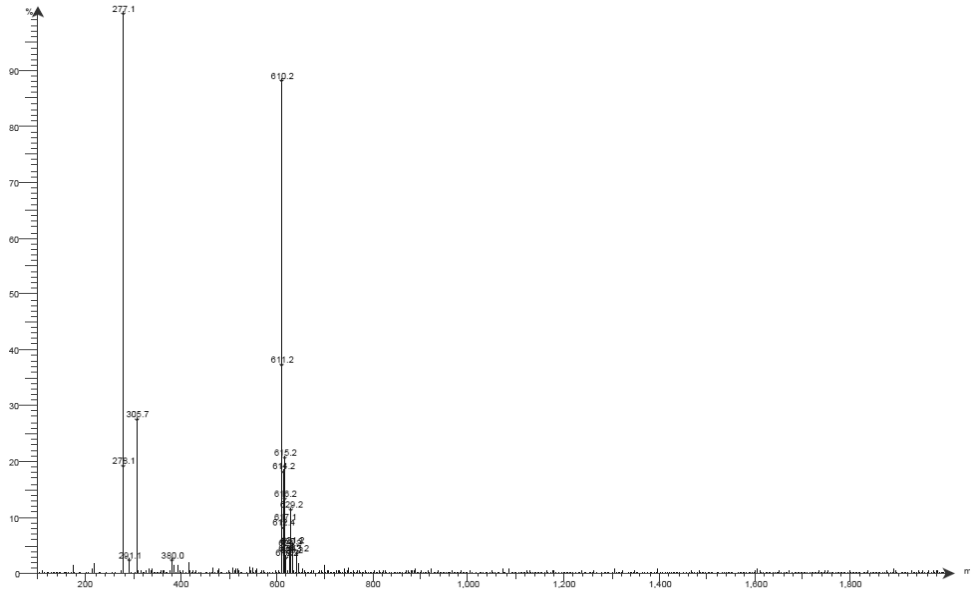

Figure B1. ESI-Mass spectroscopy of $[Co(HBBIM)_2](BF_4)_2$ **1** (MeCN)

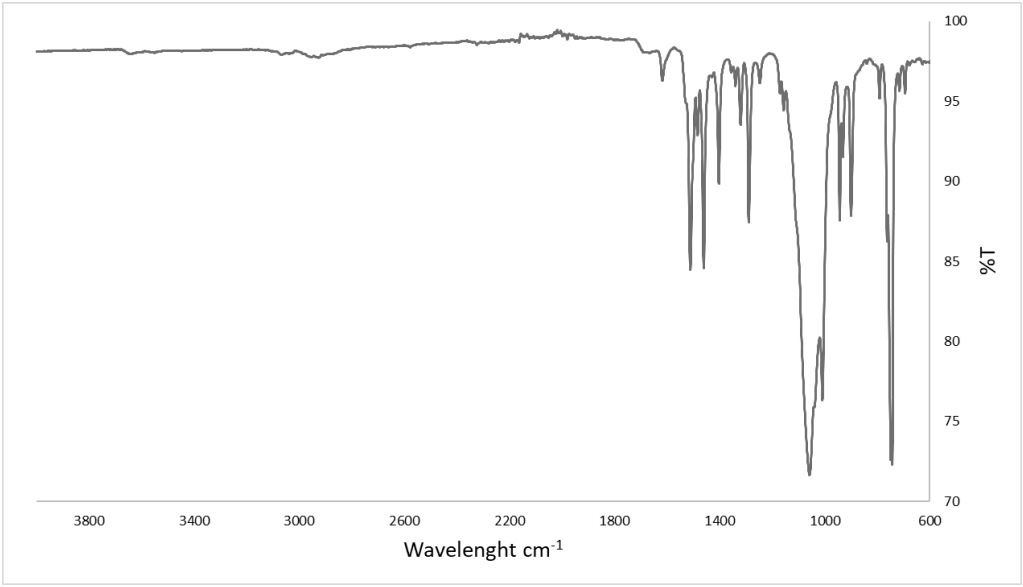

Figure B2. IR spectrum of $[Co(HBBIM)_2](BF_4)_2$ **1**

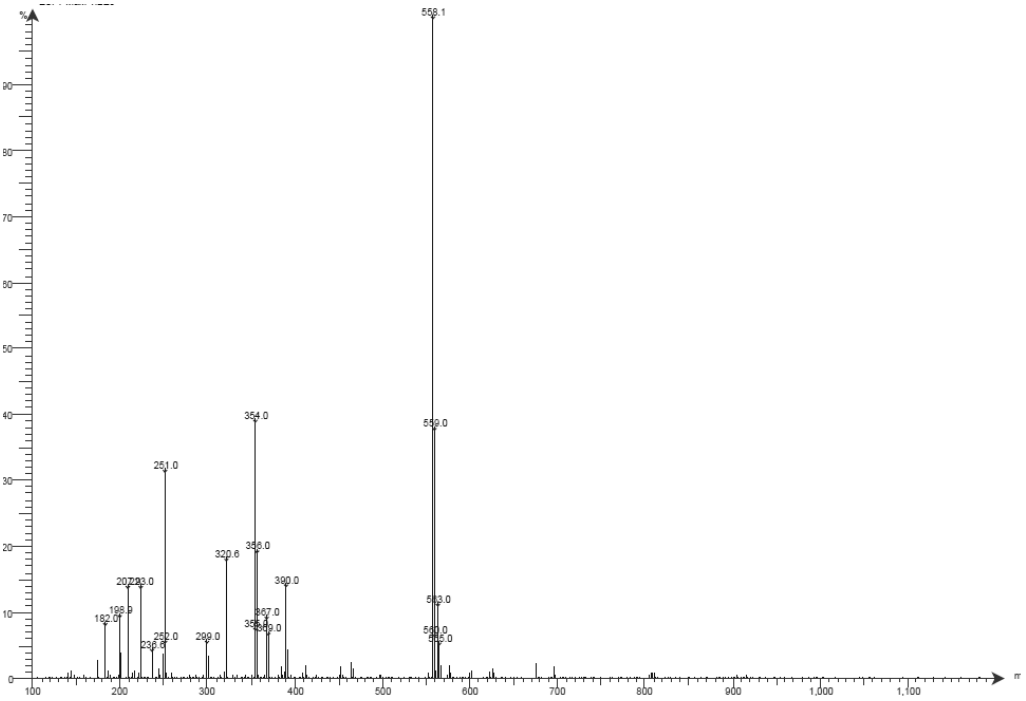

Figure B3. ESI-Mass spectroscopy of $[Co(HBBZM)_2](BF_4)_2$ **2** (MeCN)

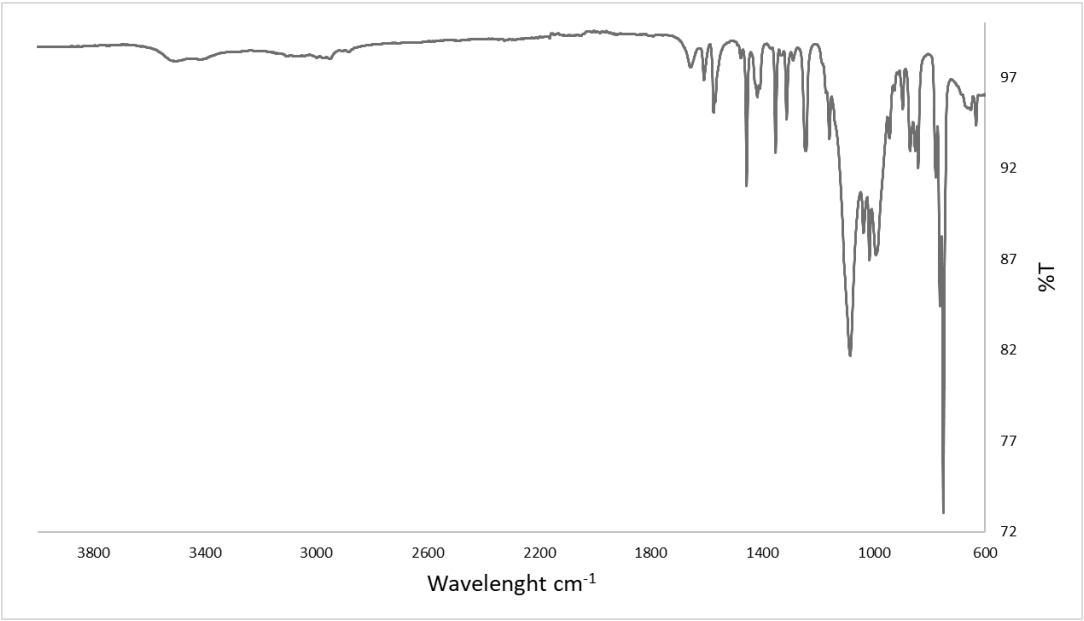

Figure B4. IR spectrum of $[Co(HBBZM)_2](BF_4)_2$ (**2**)

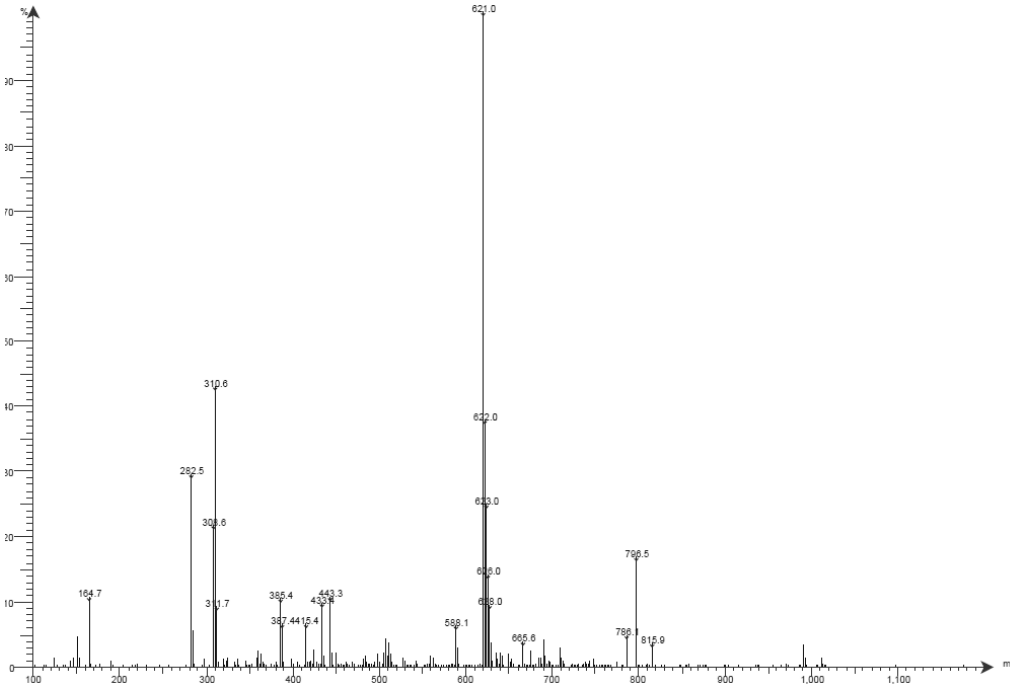

Figure B5. ESI-Mass spectroscopy of $[Co(HBBTM)_2](BF_4)_2$ **3** (MeCN)

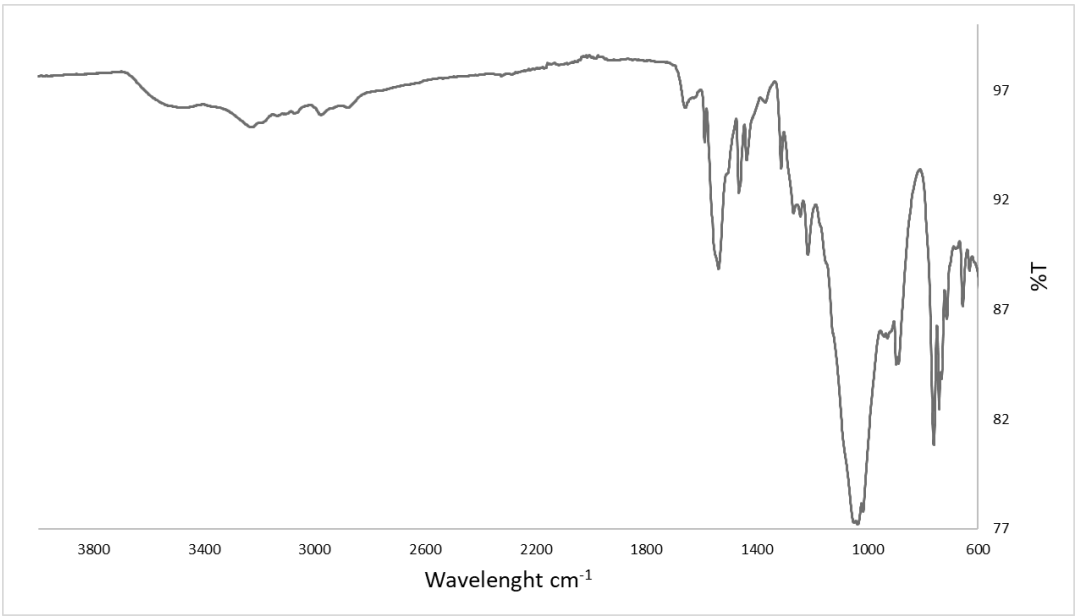

Figure B6. IR spectrum of $[Co(HBBTM)_2](BF_4)_2$ **3**

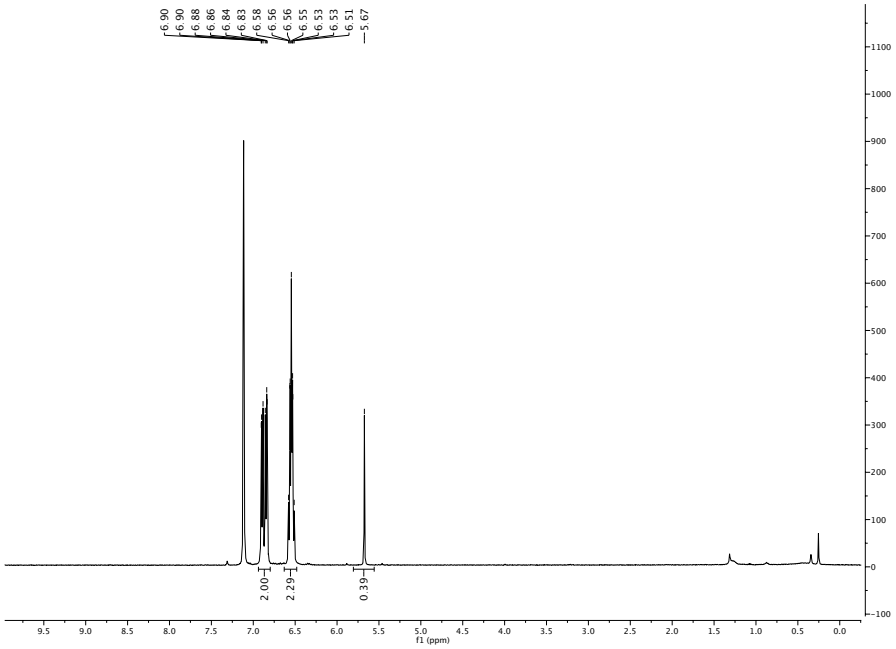

Figure B7. ^{1}H-NMR spectrum of [Zn(BBZM)$_2$] $\mathbf{5^{Zn}}$ in benzene-d_6

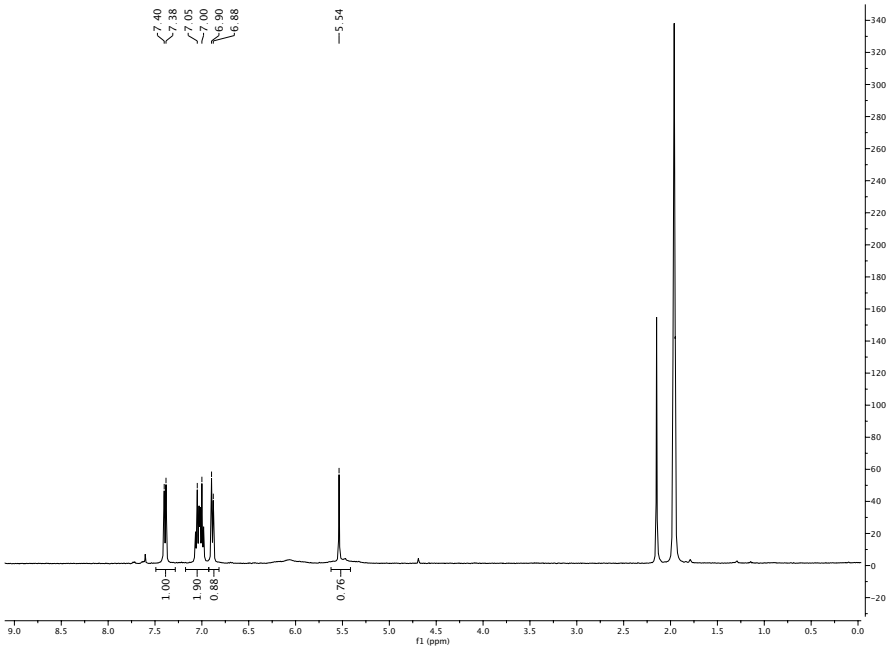

Figure B8. ^{1}H-NMR spectrum of [Zn(HBBZM)$_2$](BF$_4$)$_2$ $\mathbf{2^{Zn}}$ in MeCN-d_3

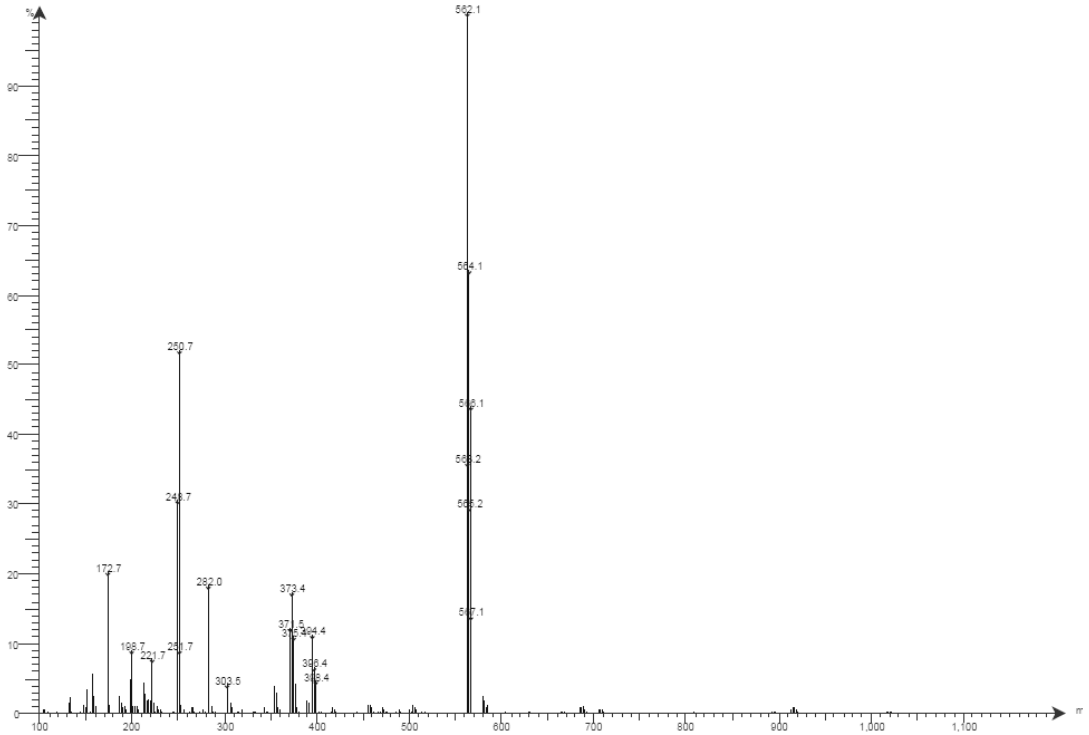

Figure B9. ESI-Mass spectroscopy of $[Zn(HBBZM)_2](BF_4)_2$ $\mathbf{5^{Zn}}$ (MeCN)

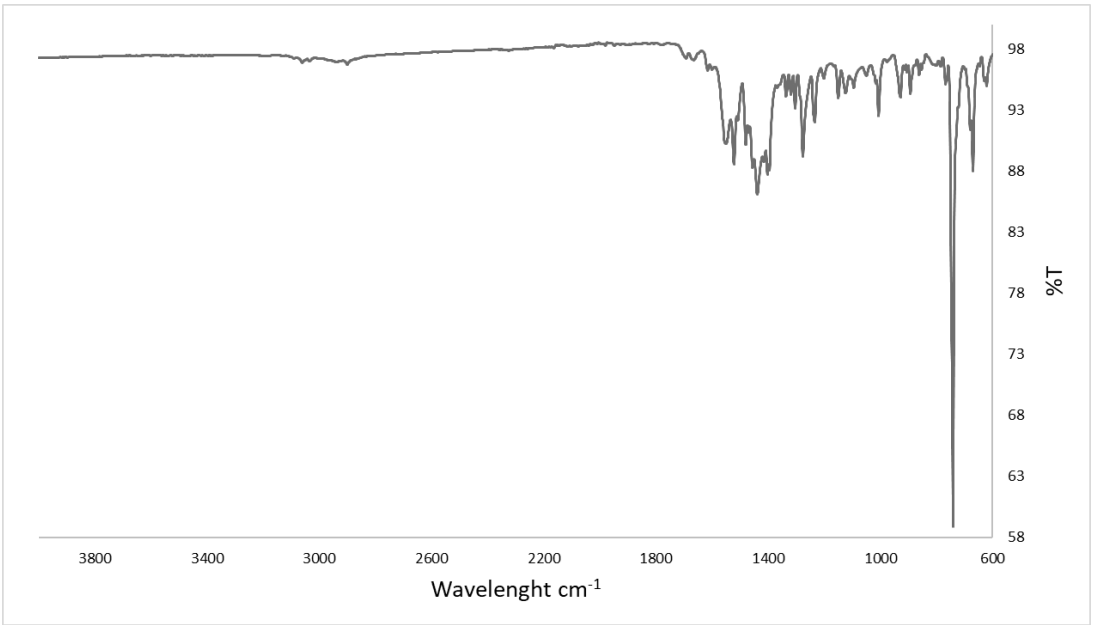

Figure B10. IR spectrum of $[Co(BBIM)_2]$ **4**

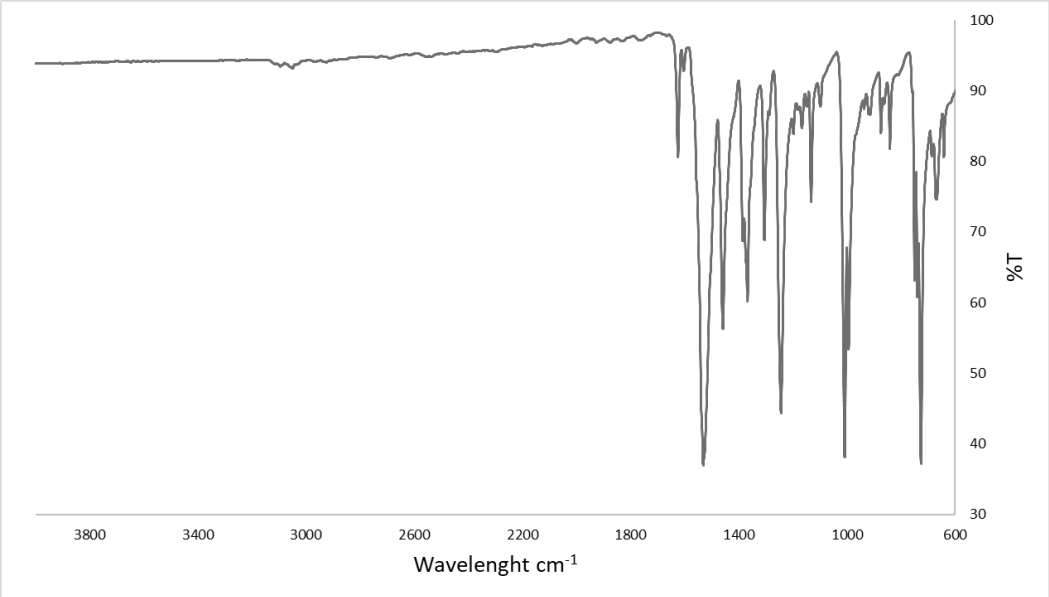

Figure B11. IR spectrum of $[Co(BBZM)_2]$ (**5**)

B. 2 Electrochemistry

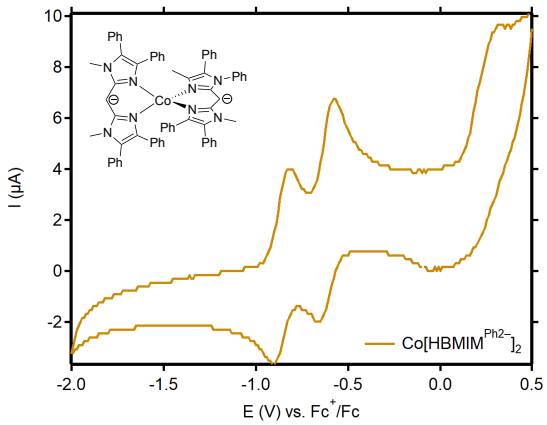

Figure B12. Cyclic voltammogram of $[Co(BMIM^{Ph2})_2]$ recorded in DMF (0.1 mM nBu$_4$NBF$_4$) at 100 mV/s at a glassy carbon electrode.

Appendix C

Supporting Information to Chapter 4

C. 1 Electrochemical and spectroscopic characterization of 1

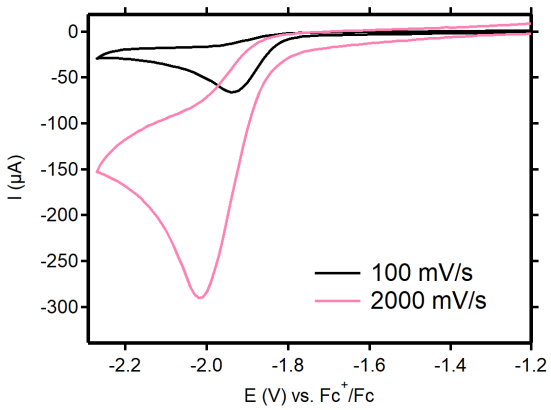

Figure C1. CV of **1** (2 mM) in MeCN (containing 0.1 M nBu_4NBF_4 as supporting electrolyte) at different scan rates; 100 and 2000 mV/s. Potentials in V vs Fc^+/Fc. Working electrode: Glassy carbon. Counter-electrode: Pt wire. Reference electrode: $Ag/Ag(NO_3)$.

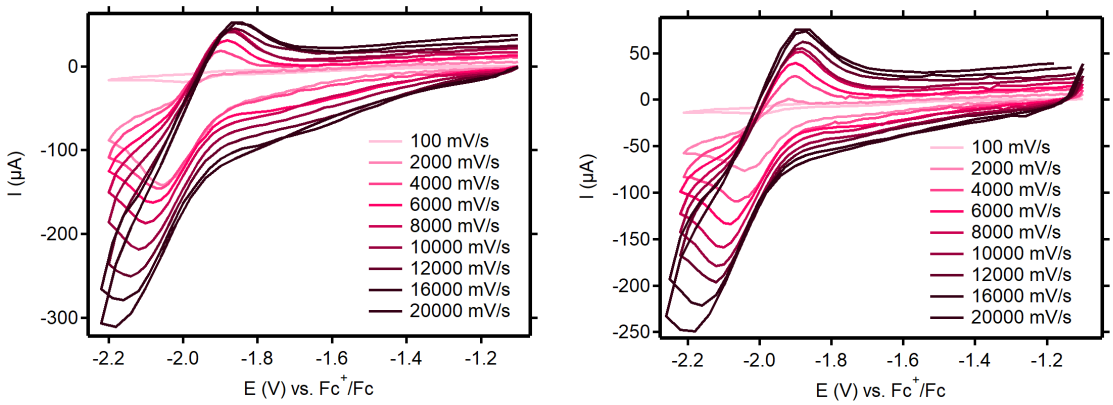

Figure C2. CV of **1** (2 mM) in DMF (containing 0.1 M nBu_4NBF_4 as supporting electrolyte) at different scan rates (9); 100-2000 mV/s. Potentials in V vs Fc^+/Fc. Left: 1st cycle, Right: 2nd consecutive cycle. Working electrode: Glassy carbon. Counter-electrode: Pt wire. Reference electrode: $Ag/Ag(NO_3)$.

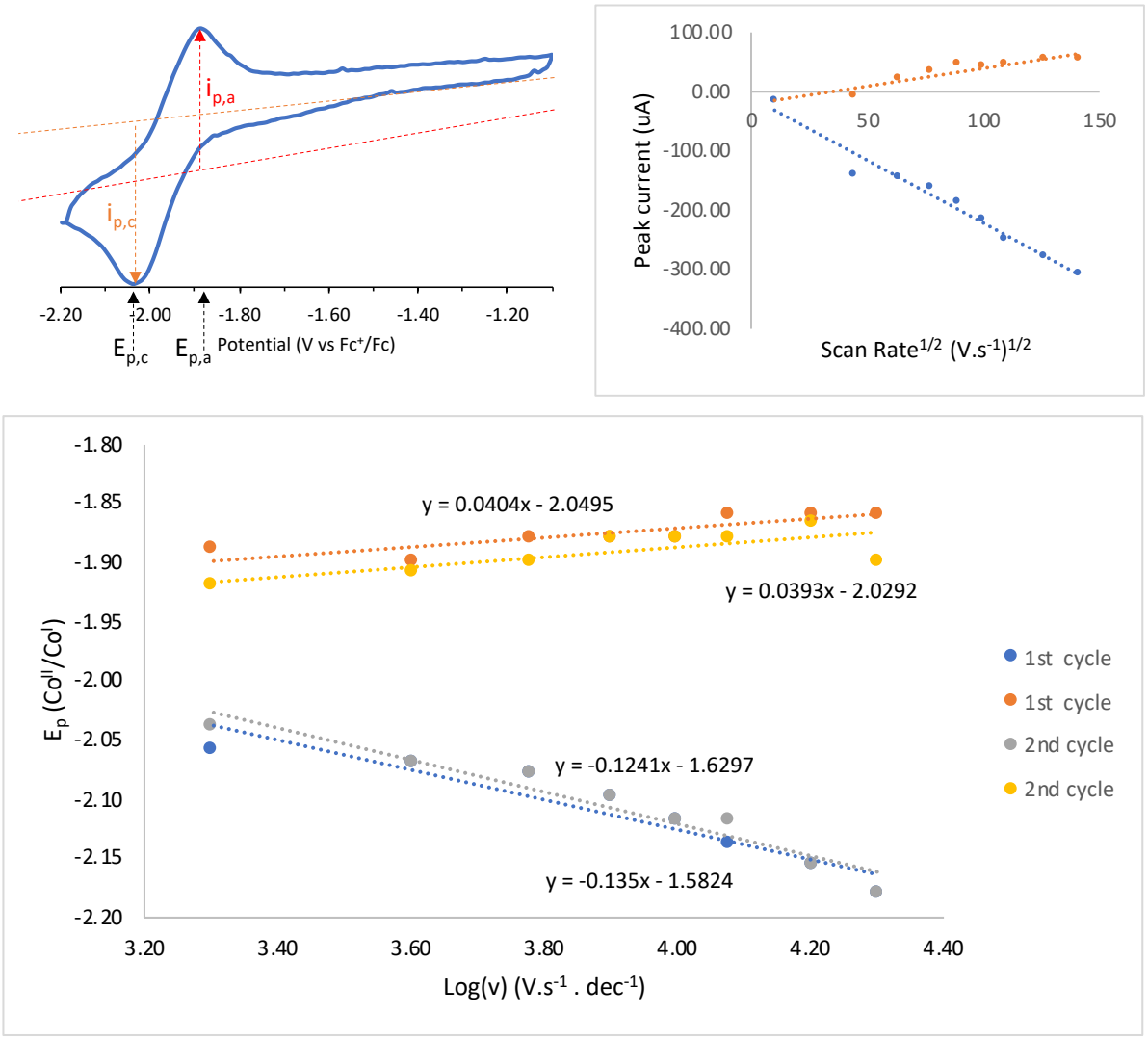

Figure C3. Top Left: Analysis of $i_{p,a}$, $i_{p,c}$, $E_{p,a}$, $E_{p,c}$ of **1** at 4000 mV/s. Top right: Plot of the anodic ($i_{p,a}$) and cathodic ($i_{p,c}$) peak currents for the Co(II)/Co(I) process of **1** versus the square-root of scan rate. Measurements performed in DMF (containing 0.1 M nBu$_4$NBF$_4$ as supporting electrolyte). Bottom: Plot of the anodic ($E_{p,a}$) and cathodic ($E_{p,c}$) peak potentials for the Co(II)/Co(I) processes of **1** *versus* the square-root of scan rate. Measurements performed in DMF (containing 0.1 M nBu$_4$NBF$_4$ as supporting electrolyte). Scan rate: 2000-20000 mV.s^{-1}. Potentials in V vs Fc$^+$/Fc. Working electrode: glassy carbon. Counter-electrode: Pt wire. Reference electrode: Ag/Ag(NO$_3$).

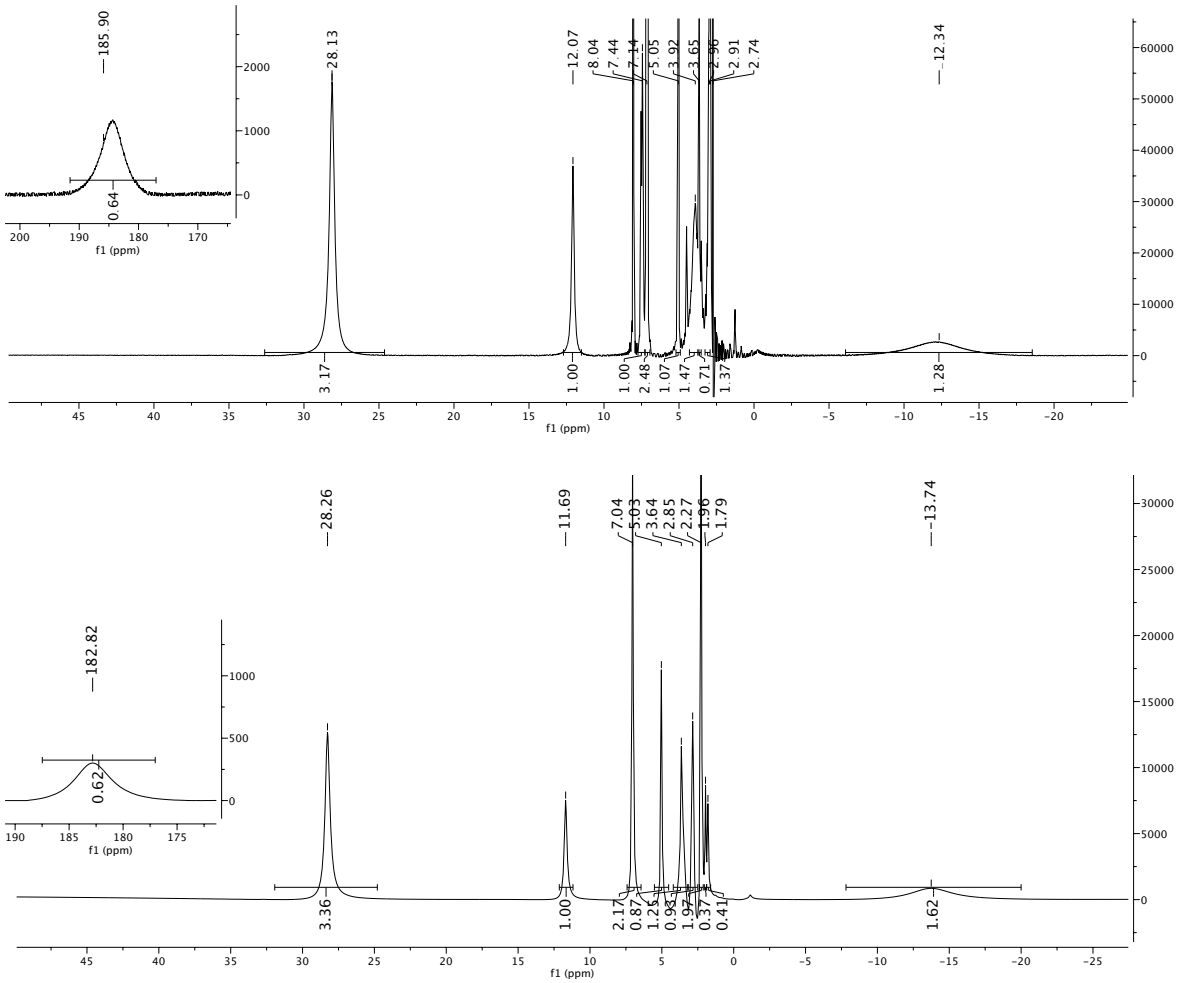

Figure C4. Top: ^{1}H NMR of **1** (400 MHz, DMF-d_7, 25 °C): Inset: paramagnetic signal at 185 ppm. The diamagnetic region includes solvent signals at δ (ppm): 8.03, 2.92, 2.75. Bottom: ^{1}H NMR of **1** (400 MHz, MeCN-d_3, 25 °C): Inset: paramagnetic signal at 182 ppm. The diamagnetic region includes the solvent signal at δ (ppm): 1.94.

C. 2 Spectroscopic and electrocatalytic characterization of 1

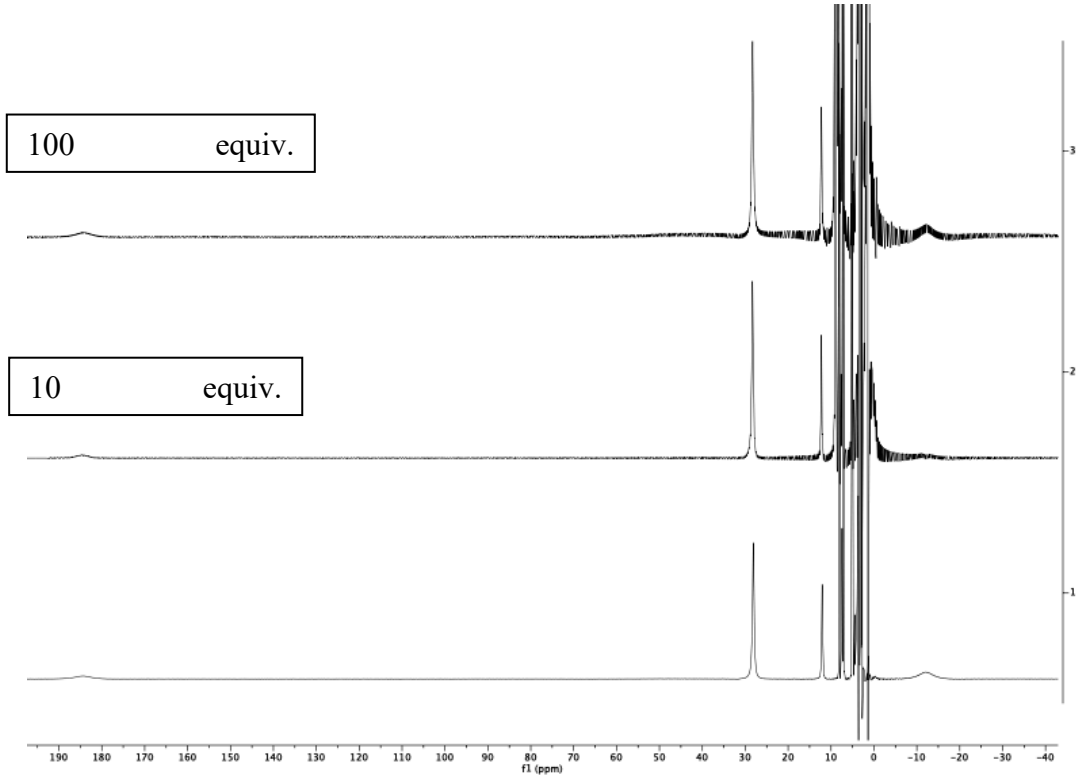

Figure C5. ^{1}H-NMR of **1** (400 MHz, DMF-d_7) in the presence of 0, 10 or 100 equiv. Et_3NHBF_4.

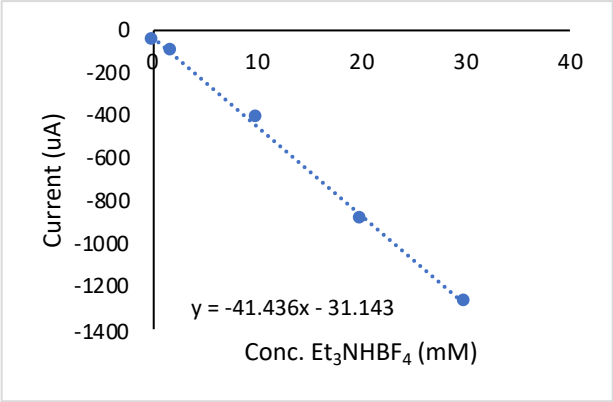

Figure C6. Proportional catalytic peak currents ($i_{p,c}$) as a function of the acid concentration for **1** (2 mM) in DMF (containing 0.1 M nBu$_4$NBF$_4$ as supporting electrolyte)with Et_3NHBF_4 (2, 10, 20, 30 mM).

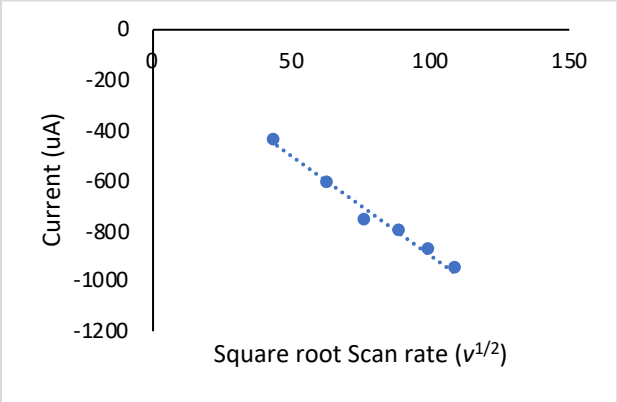

Figure C7. Proportional catalytic peak currents ($i_{p,c}$) as a function of the square root of the scan rate (v), indicating a diffusion limited catalytic process for **1** (2 mM) in the presence of 10 mM Et_3NHBF_4 in DMF (containing 0.1 M nBu_4NBF_4 as supporting electrolyte); Scan rates: 1000, 2000, 4000, 6000, 8000, 10000 and 12000 mV/s. Working electrode: glassy carbon. Counter electrode: Pt wire. Reference electrode: $Ag/Ag(NO_3)$.

Electrocatalysis phenol:

Phenol is a weak proton source with a more negative thermodynamic reduction potential ($E°_{HA}$ = <–1.83 V) compared to Et_3NHBF_4 ($E°_{HA}$ = −1.31 V) in DMF.[1] When phenol was added to an electrolyte solution with **1**, a smaller decrease of the oxidative response and a smaller increase in current at the Co(I/II) couple was observed, resulting in a lower electrocatalytic rate at a lower overpotential (Figure S8). Using equation 1 (**Chapter 4**, 4.2.4, p133), a k_{obs}(*TOF*) of 8 s^{-1} in presence of 10 mM phenol was determined. The required overpotential is only 130 mV, which is among the lowest overpotentials found for non-aqueous electrocatalytic molecular HER catalysis.

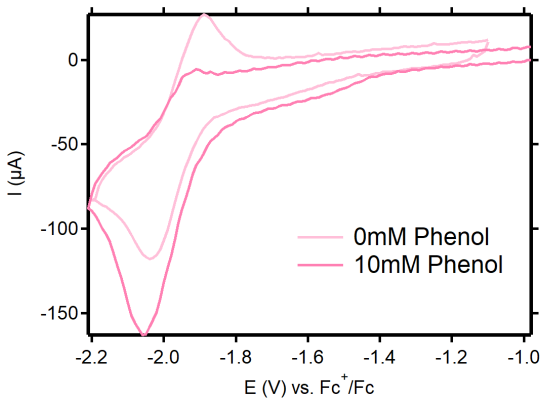

Figure C8. Cyclic voltammogram of **1** (2 mM) recorded in the absence or presence of 10 mM phenol in DMF (0.1 M nBu_4NBF_4). Potentials in V vs Fc^+/Fc. Scan rate 2000 mV/s. Working electrode: glassy carbon. Counter-electrode: Pt wire. Reference electrode: $Ag/Ag(NO_3)$.

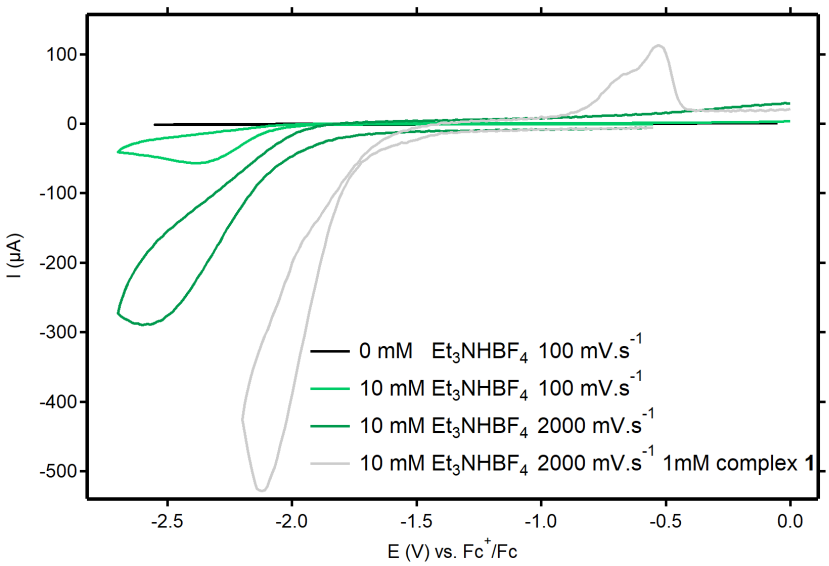

Figure C9. Cyclic voltammograms in the absence (black trace) or in the presence of 10 mM of Et_3NHBF_4 (green traces: scan rate 100 and 2000 mV/s) recorded in DMF (containing 0.1 M nBu$_4$NBF$_4$ as supporting electrolyte). For reference: **1** in the presence of 10 mM Et_3NHBF_4 (gray trace). Working electrode: glassy carbon. Counter-electrode: Pt wire. Reference electrode: Ag/Ag(NO_3). Potentials in V vs Fc^+/Fc.

C. 3 Bulk electrolysis

Table C1. Stationary (RDE at 0 rpm) bulk electrolysis experiments for H_2 evolution in DMF (0.1 M nBu$_4$NBF$_4$) in the presence of 0.1 M Et_3NHBF_4 at –2.00 V vs Fc^+/Fc (690 mV overpotential, coupled to gas chromatography analysis

Catalyst (1mM)	Time (h)	Charge Consumption (C)	Current denisty mA/cm^2	TON[a]	Faradaic efficiency
-	2	0.3	0.18	-	>98%
1	3	18.7	8.7	9.7	>99%

[a]Working electrode: Glassy Carbon (0.196 cm^2). Counter-electrode: Pt plate. Reference electrode: Ag/Ag(NO_3).

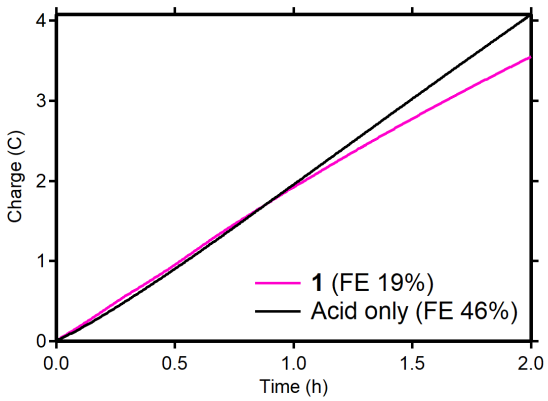

Figure C10. Charge consumed during CPE at –2.00 V versus Fc^+/Fc in the absence (black) and presence (pink) of 1 mM **1**, 0.1 M AcOH in MeCN (containing 0.1 M nBu$_4$NBF$_4$ as the supporting electrolyte). Working electrode: glassy carbon; Counter-electrode: Pt wire; Reference electrode: Ag/Ag(NO_3).

C. 4 Electrochemical and electrocatalytic characterization of 2-4

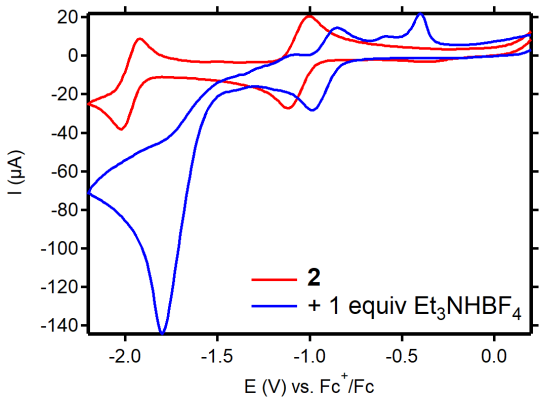

Figure C11.[2] Cyclic voltammograms of [Co(dmgBF$_2$)$_2$(solv)$_2$] (**2**) recorded in DMF (0.1 M nBu$_4$NBF$_4$) in the absence (red trace) or in the presence of 1 equiv. Et$_3$NHBF$_4$ (blue trace). Scan rate 100 mV/s. Potentials in V vs Fc^+/Fc. Working electrode: glassy carbon. Counter-electrode: Pt wire. Reference electrode: Ag/Ag(NO_3).

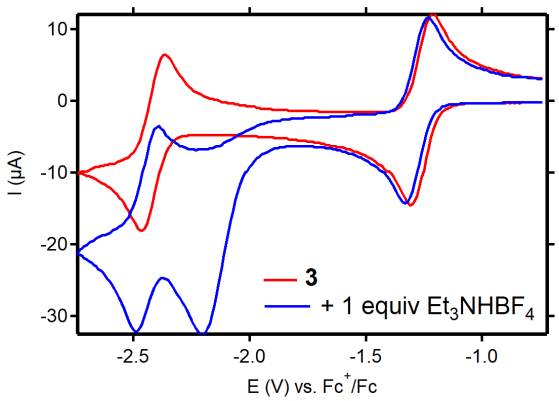

Figure C12.[3] Cyclic voltammograms of [Co(TPP)] (3) recorded in DMF (0.1 M nBu$_4$NBF$_4$) in the absence (red trace) or in the presence of 1 equiv. Et$_3$NHBF$_4$ (blue trace). Scan rate 100 mV/s. Potentials in V vs Fc$^+$/Fc. Working electrode: glassy carbon. Counter-electrode: Pt wire. Reference electrode: Ag/Ag(NO$_3$).

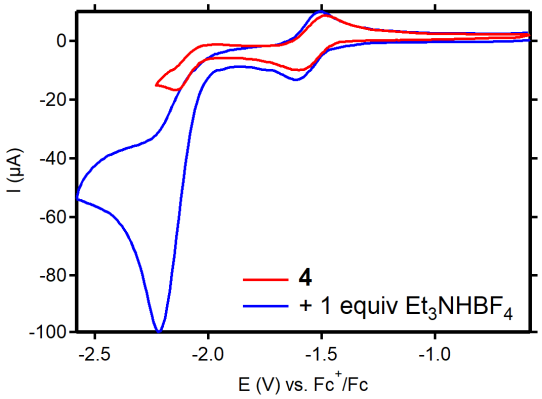

Figure C13.[4] Cyclic voltammograms of [Co(bapbpy)Cl](Cl) (**4**) recorded in DMF (0.1 M nBu$_4$NBF$_4$) in the absence (red trace) or in the presence of 1 equiv. Et$_3$NHBF$_4$ (blue trace). Scan rate 100 mV/s. Potentials in V vs Fc$^+$/Fc. Working electrode: glassy carbon. Counter-electrode: Pt wire. Reference electrode: Ag/Ag(NO$_3$).

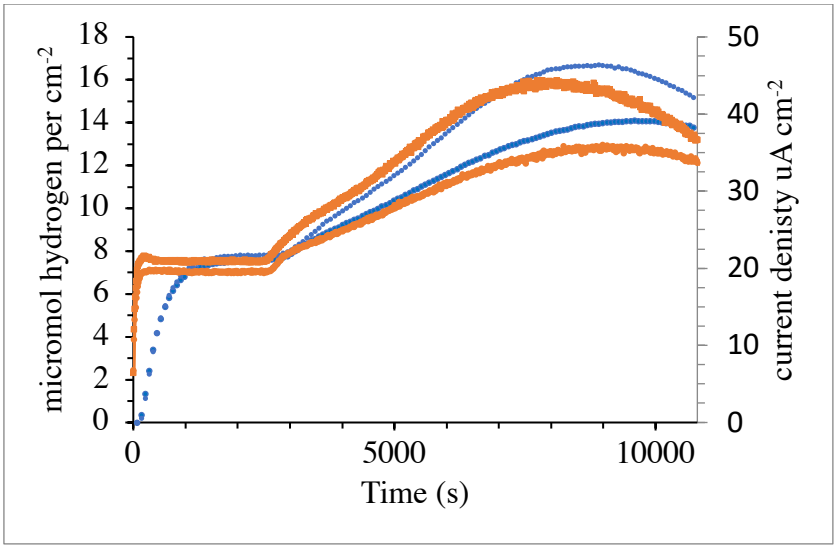

Figure C14. Controlled potential electrolysis (duplo measurement) in the presence of 1 mM **4**, 0.1 M Et_3NHBF_4 in DMF (containing 0.1 M nBu$_4$NBF$_4$ as the supporting electrolyte) at –2.00 V vs Fc^+/Fc at 2000 rpm. Blue dotted traces (left vertical axis): Hydrogen production. Orange (right vertical axis): current density. Indicating the reproducibility of the suggested structural changes after 45 minutes (2700 second).

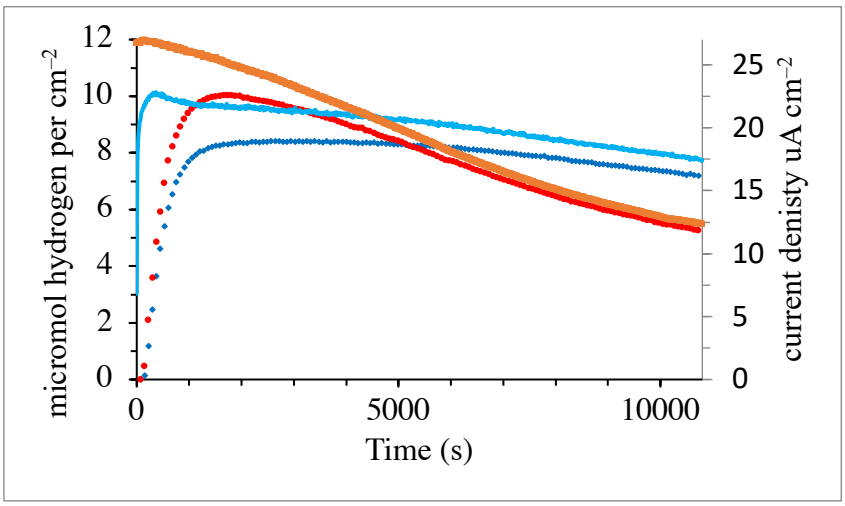

Figure C15. Data corresponding to **Chapter 4**, Figure 8, pink traces: raw data showing that the deposition on the electrode surface is an active catalytic material for HER. Left axis (hydrogen production) blue dots: initial CPE (pristine electrode), red dots: rinse test CPE (modified electrode). Right axis (current density) Light cyan trace: initial CPE (pristine electrode), Orange trace: rinse test (modified electrode) Solution: 0.1 mM Et_3NHBF_4 (containing 0.1 M nBu$_4$NBF$_4$ as the supporting electrolyte) at –2.00 V vs Fc^+/Fc, 2000 rpm. Initial: + 0.5 mM **1**, rinse test: fresh solution with no complex added. Note: The higher initial current for the rinse test is caused by the direct presence of the active deposition in the vicinity of a fresh acid solution.

C. 5 XPS analysis of 1

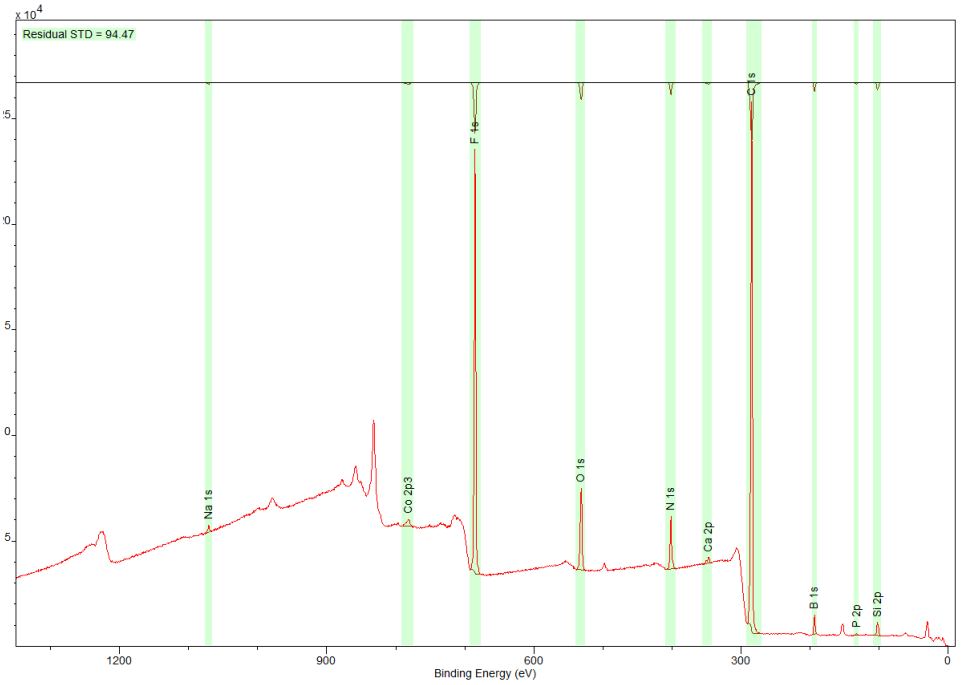

The relative percentage of selected atoms

C	68.5%
N	4.04%
O	4.29%
B	5.0%
F	15.7%
Co	0.23%

Figure C16. XPS spectrum of the electrode deposit after 3 h electrolysis in DMF 0.1 M Et_3NHBF_4,0.1 M nBu_4NBF_4, 1 mM **1** at –2.00 V vs. Fc^+/Fc and its relative atomic ratios. High percentages of carbon are caused using carbon tape during the analysis.

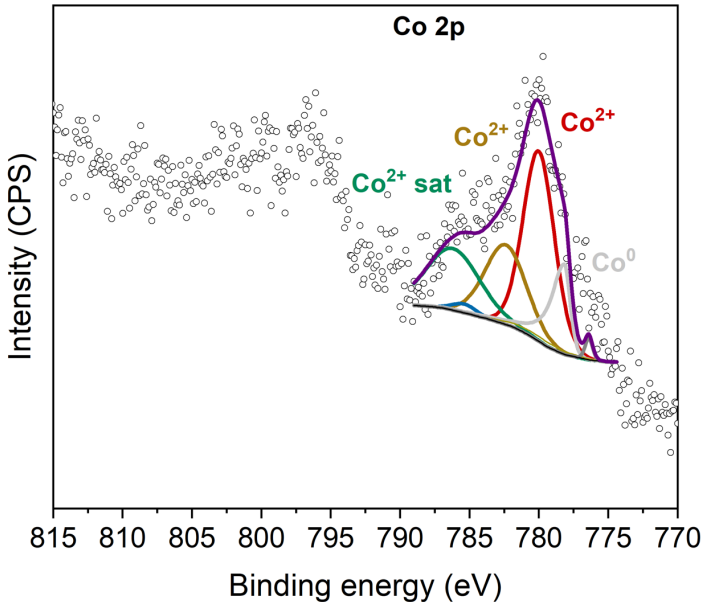

Figure C17. XPS spectrum of the Co region from the electrode deposit after 3 h electrolysis in DMF 0.1 M Et_3NHBF_4,0.1 M nBu_4NBF_4, 1 mM **1** at –2.00 V vs. Fc^+/Fc and its relative atomic ratios. The satellite peaks indicate a large contribution of the 2^+ oxidation state. The spectrum was fitted according to the work of Biesinger et. al.[5]

C. 7 References

(1) Felton, G. A. N.; Glass, R. S.; Lichtenberger, D. L.; Evans, D. H. Iron-Only Hydrogenase Mimics. Thermodynamic Aspects of the Use of Electrochemistry to Evaluate Catalytic Efficiency for Hydrogen Generation. *Inorg. Chem.* **2006,** *45* (23), 9181.

(2) Hu, X.; Cossairt, B. M.; Brunschwig, B. S.; Lewis, N. S.; Peters, J. C. Electrocatalytic hydrogen evolution by cobalt difluoroboryl-diglyoximate complexes. *Chem. Commun.* **2005**, 4723-4725.

(3) Beyene, B. B.; Mane, S. B.; Hung, C.-H. Electrochemical Hydrogen Evolution by Cobalt(II) Porphyrins: Effects of Ligand Modification on Catalytic Activity, Efficiency and Overpotential. *J. Electrochem. Soc.* **2018,** *165* (9), H481.

(4) Queyriaux, N.; Sun, D.; Fize, J.; Pécaut, J.; Field, M. J.; Chavarot-Kerlidou, M.; Artero, V. Electrocatalytic Hydrogen Evolution with a Cobalt Complex Bearing Pendant Proton Relays: Acid Strength and Applied Potential Govern Mechanism and Stability. *J. Am. Chem. Soc.* **2020,** *142* (1), 274.

(5) Biesinger, M. C.; Payne, B. P.; Grosvenor, A. P.; Lau, L. W. M.; Gerson, A. R.; Smart, R. S. C. Resolving surface chemical states in XPS analysis of first row transition metals, oxides and hydroxides: Cr, Mn, Fe, Co and Ni. *Appl. Surf. Sci.* **2011,** *257* (7), 2717.

Appendix D

Supporting Information to Chapter 5

D. 1 Spectra

D. 1.1 ESI-MS spectra

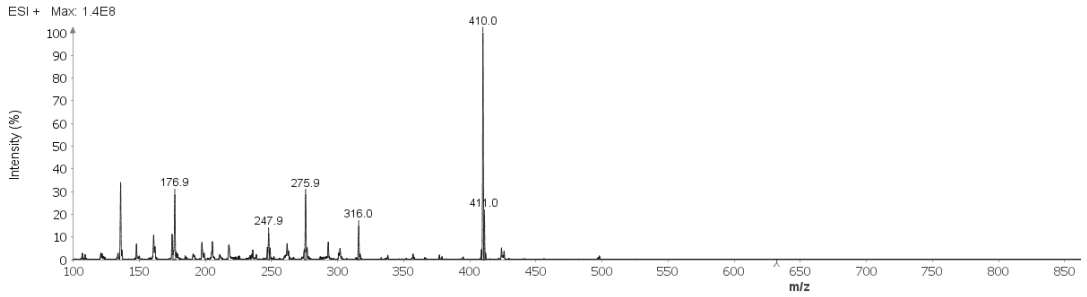

Figure D1. ESI-MS spectra of complex $[Co(HBMIM)_2](BF_4)_2$ (**3**) in MeCN.

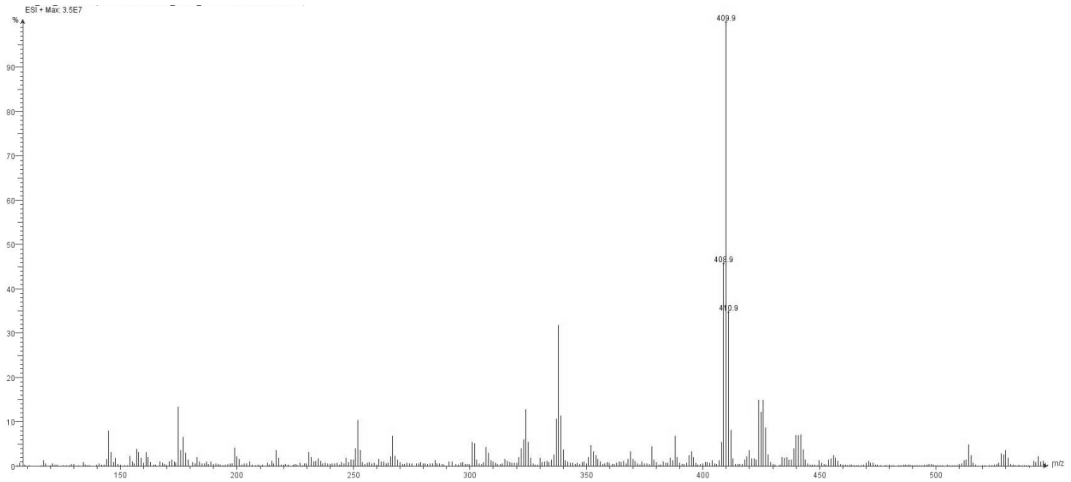

Figure D2. ESI-MS spectra of complex $[Co(HBMIM)_2](NO_3)_2$ (**4**) in MeCN.

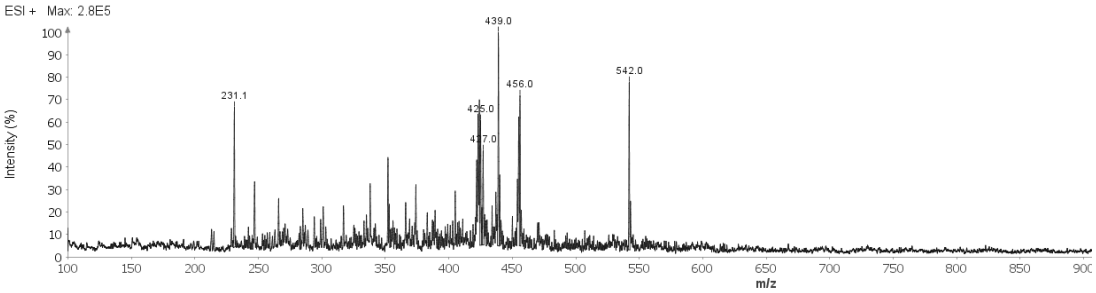

Figure D3. ESI-MS spectra of complex $[Co(BMIK)_2(NO_3)_2]$ (**5**) (MeCN)

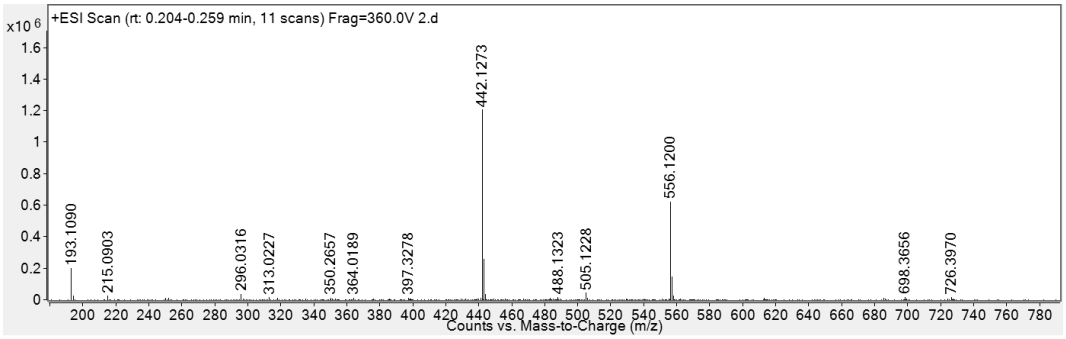

Figure D4. High-resolution ESI-MS spectra of complex $[Co(HBMIA)_2](NO_3)_2$ (**6**) in MeCN.

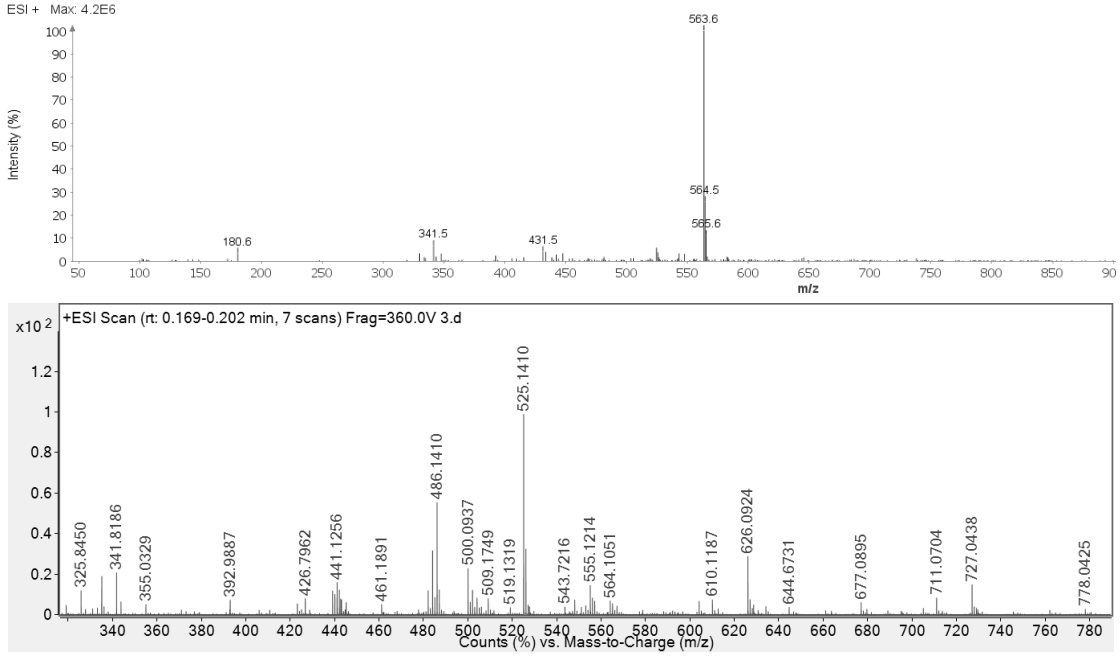

Figure D5. Low-resolution ESI-MS spectra of complex $[Co(HBMIP)_2](NO_3)_2$ (**7**) in THF (top) High-resolution ESI-MS spectra of complex $[Co(HBMIP)_2](NO_3)_2$ (**7**) in MeCN (bottom).D.

D. 1.2 FT-IR spectra

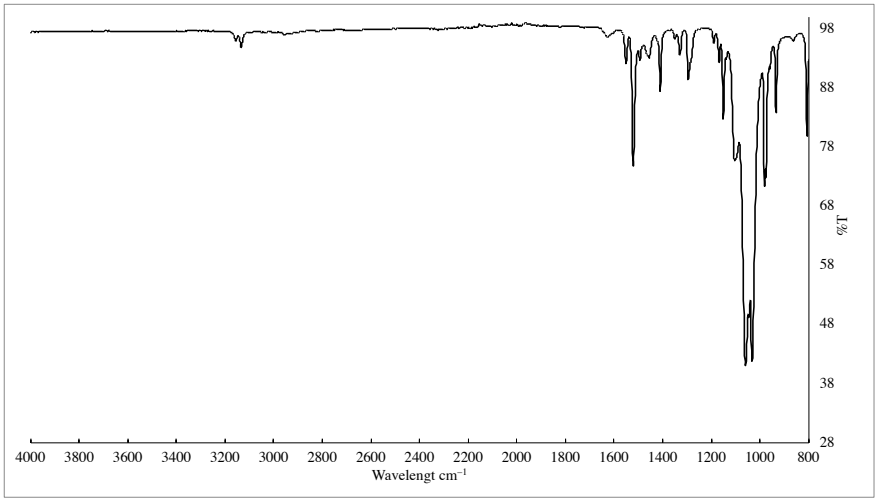

Figure D6. IR spectrum of $[Co(HBMIM)_2](BF_4)_2$ (**3**)

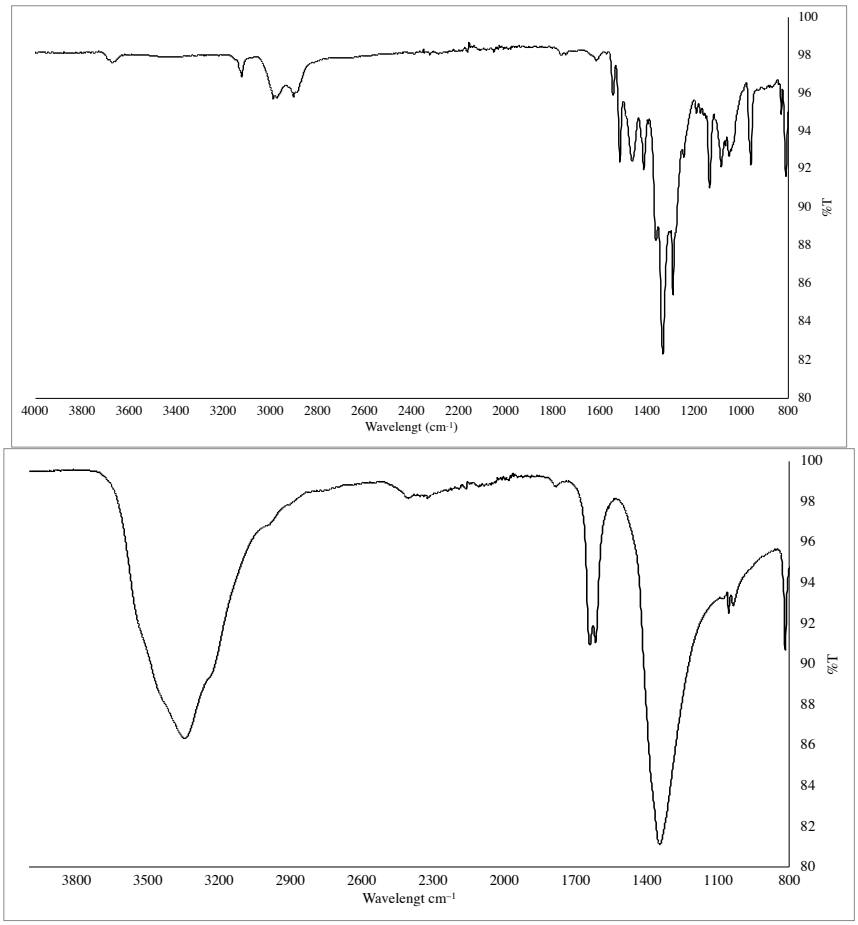

Figure D7. IR spectrum of $[Co(HBMIM)_2](NO_3)_2$ (**4**) as solid (top) and solid $[Co{\cdot}6H_2O](NO_3)_2$ (bottom).

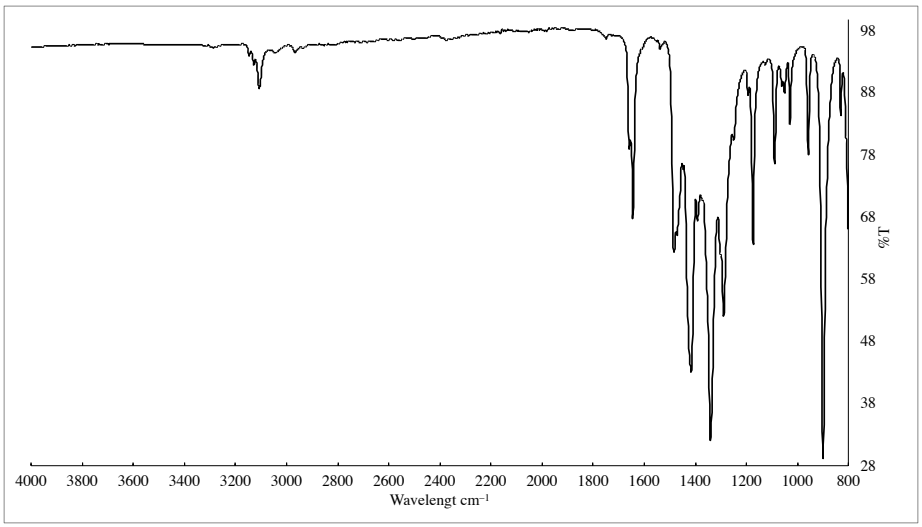

Figure D8. IR spectrum of $[Co(BMIK)_2(NO_3)_2]$ (**5**) as solid.

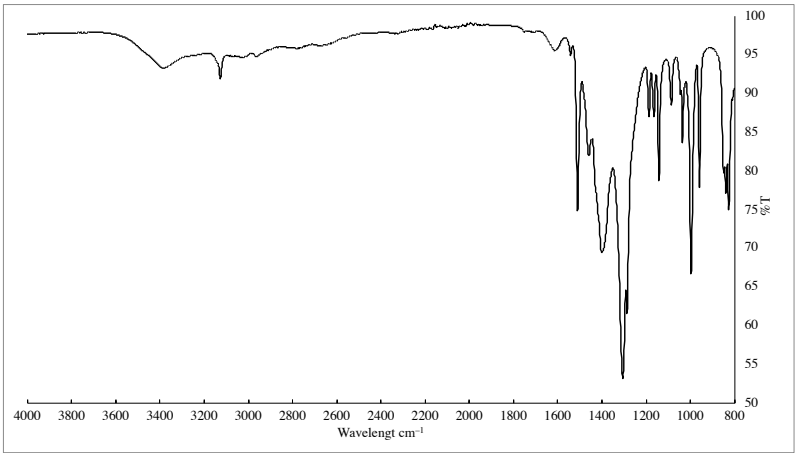

Figure D9. IR spectrum of $[Co(HBMIA)_2](NO_3)_2$ (**6**)

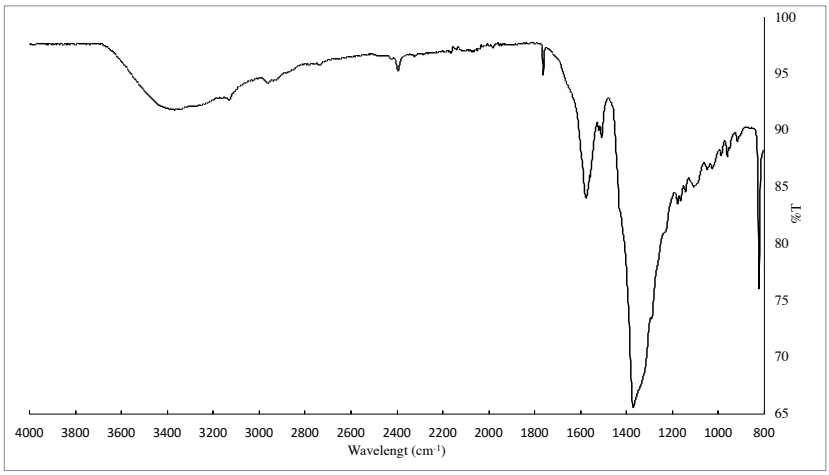

Figure D10. IR spectrum of $[Co(HBMIP)_2](NO_3)_2$ (**7**)

D. 1.3 ^{1}H-NMR spectra

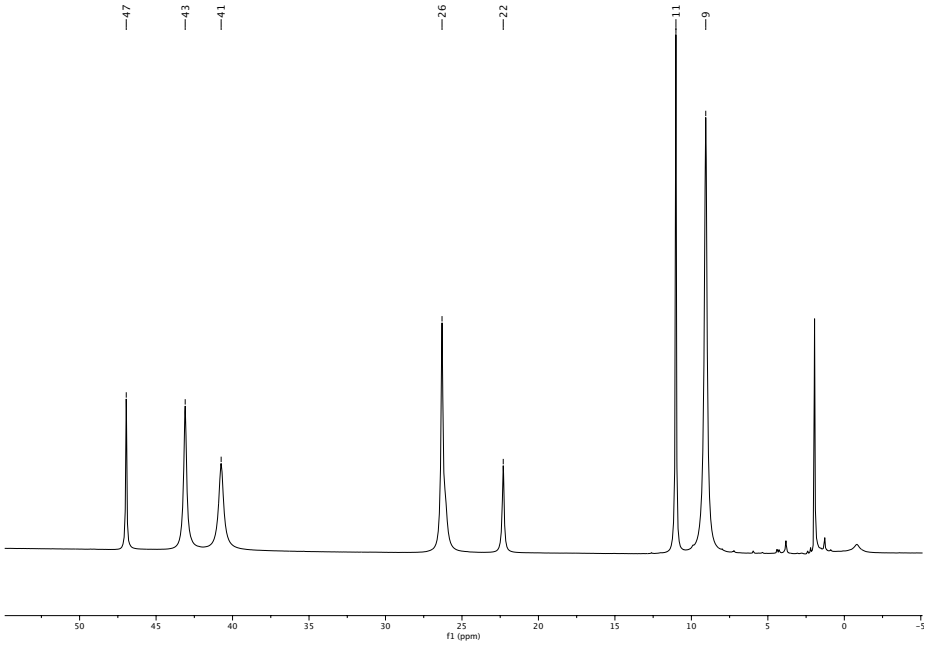

Figure D11. ^{1}H-NMR of $[Co(HBMIM)_2](NO_3)_2$ (**4**) in MeCN-d_3.

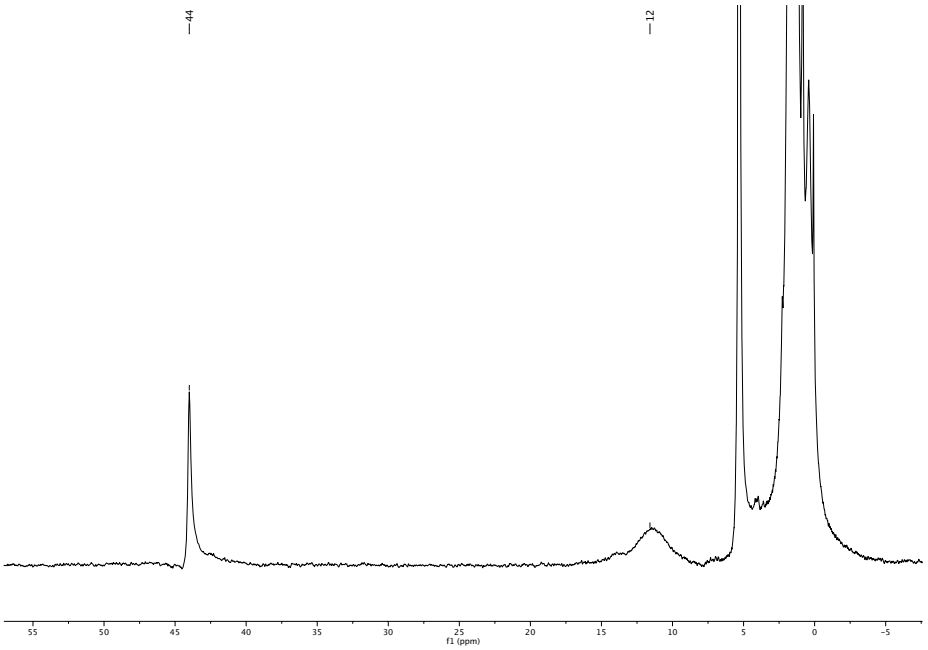

Figure D12. ^{1}H-NMR of $[Co(HBMIA)_2](NO_3)_2$ (**6**) in DCM-d_2 (bottom).

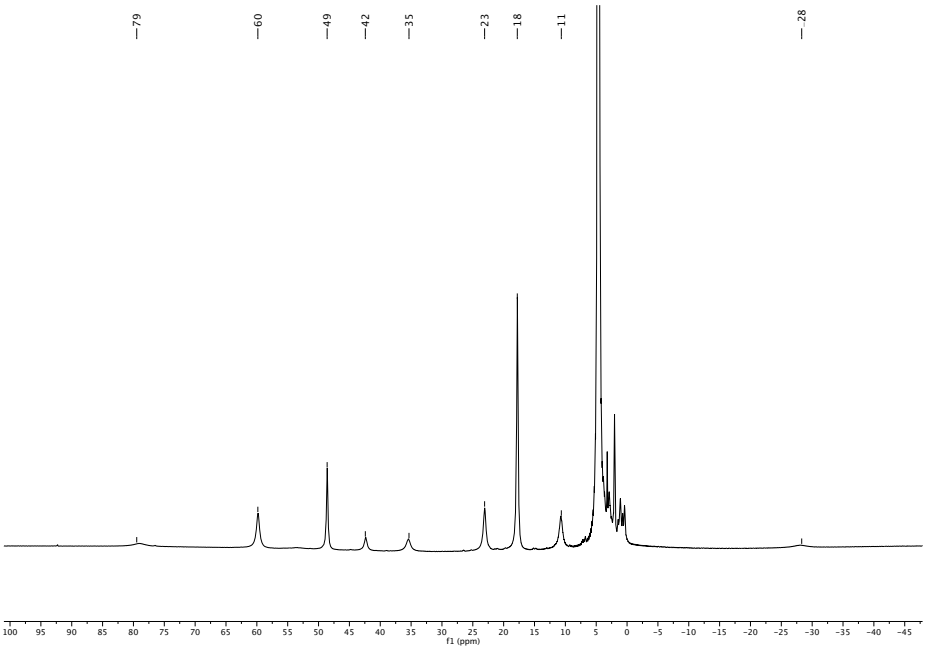

Figure D13. ^{1}H-NMR of $[Co(HBMIP)_2](NO_3)_2$ (**7**) in water-d_2 (bottom).

D. 2 Photocatalytic experiments

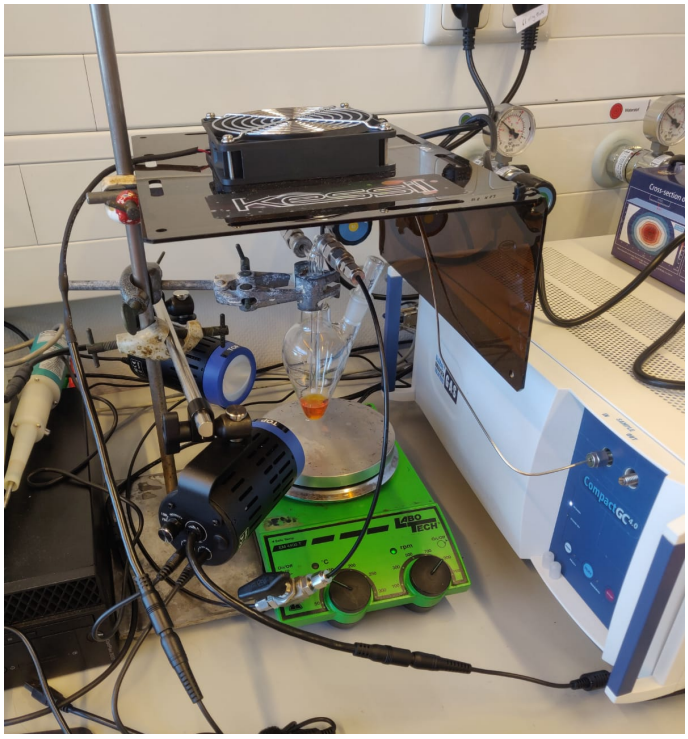

Figure D14. photocatalytic setup containing: 2 Kessil LEDs (440 + 456nm), a top-centered ventilator, stirring plate, in-line GC-apparatus (Leak test **Figure D15**), and a two-neck pear-shaped, angled flask equipped with stirring bar, stopper and a gas-inlet/outlet glass insert.

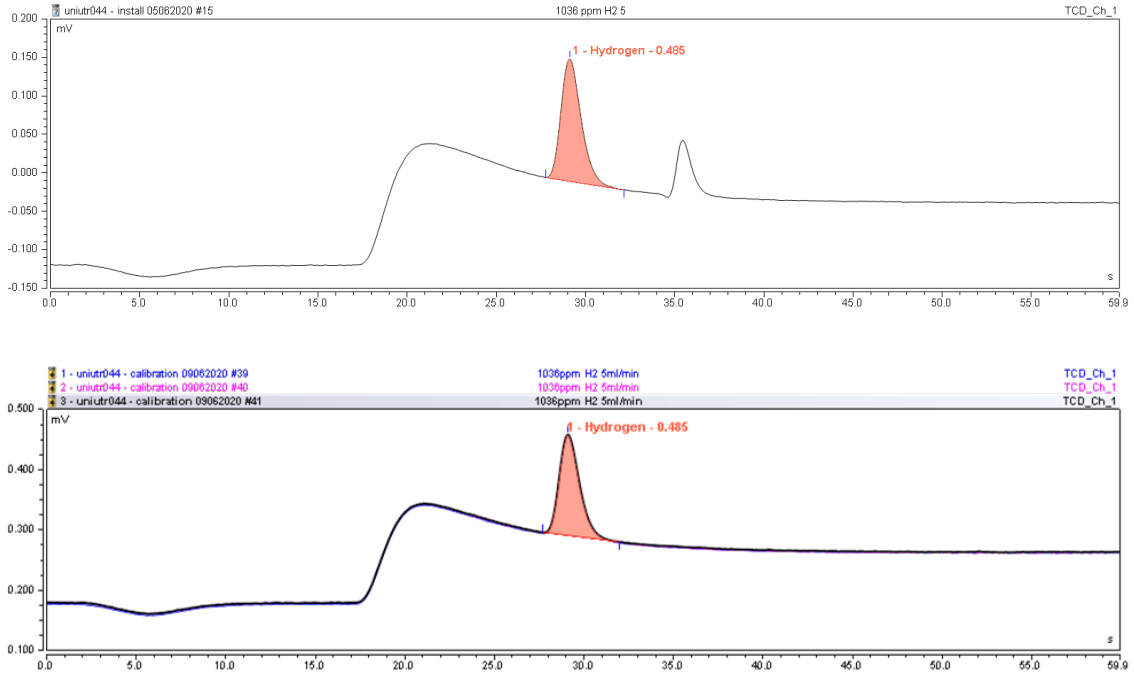

Figure D15. GC-TCD chromatograms of a 1036 ppm H_2 in N_2 mix gas over time. Top: t = 60 s hydrogen at 29.0 retention time and residual oxygen at 35.4 retention time. Bottom: t = 600 s no oxygen is observed.

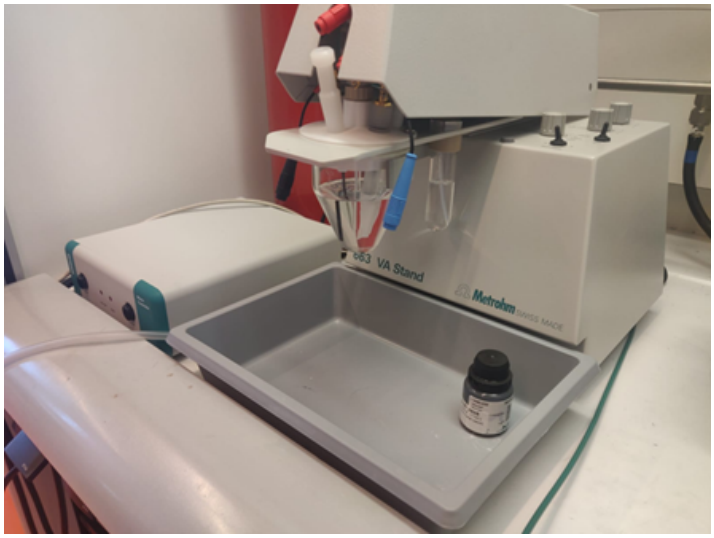

Figure D16. 663 VA stand Methrom (electrochemical mercury setup).

Appendix E

E. 1 A Bis-diimidazolylidine cobalt complex

In a pursuit to make our bisimidazole-based cobalt complexes more stable, we have set out to alter the coordination mode of the ligands from the typical amine donor atoms to N-heterocyclic carbene (NHC) donors (**Figure E1**), which are generally considered stronger donors and, therefore, expected to generate more stable complexes.[1,2] The first cobalt-NHC complex was reported in 1977,[3] whereas the first use of cobalt-NHC complexes in catalysis was reported about fifteen years ago.[4-16] Only a few cobalt-NHC complexes have been electrochemically analyzed[13-16] and even fewer have been used for the photo- or electrocatalytically hydrogen evolution reaction (HER).[13,16-18]

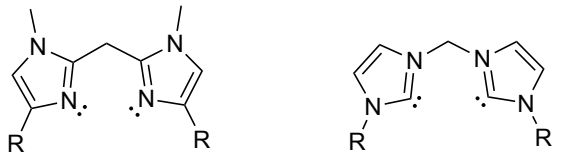

Figure E1. Amine vs. carbene donor ligands considered in this study.

We aimed to use a methylene-bridged bis-imidazole carbene ligand, to minimize the structural changes in the ligands used in **Chapter 2-5**. We considered the work of Jenkins *et al*., who reported on a square pyramidal macrocyclic tetra imidazole carbene cobalt complex comprising two diphenyl bisimidazole methane moieties in the ligand (*cf*. the coordinating motifs used in **Chapter 4**) (**Figure E2**, left).[19,20] However, the cobalt atom in this complex sits slightly above the plane created by the carbene carbons and the complex contains an extra coordination site (a triflate in the crystal structure), which would not allow for a direct comparison of the

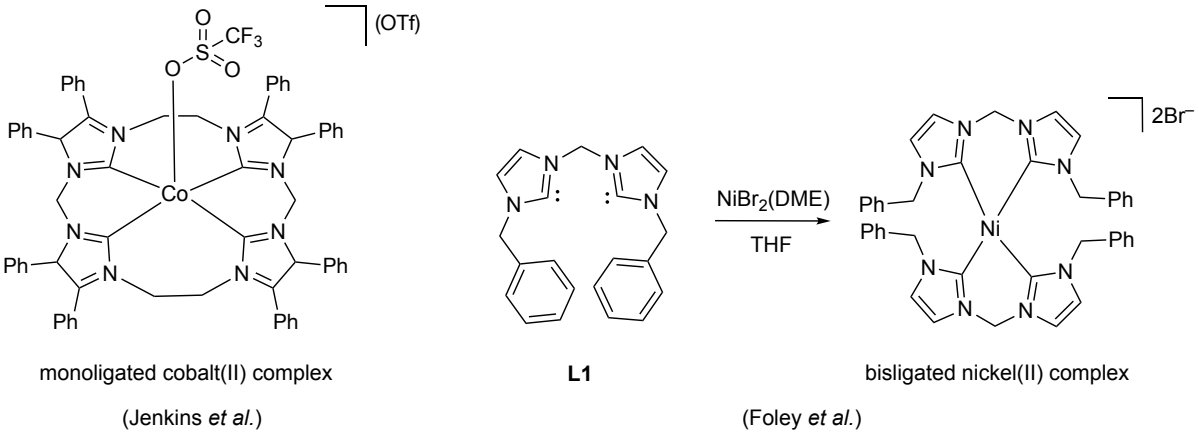

Figure E2. Reported tetra carbene complexes by Jenkins *et al*. and Foley *et al*.[19,21]

electrochemical HER properties of our bisimidazole-based cobalt complexes. Foley *et al*. reported on the synthesis of the bis-diimidazolylidine ligand **L1,** which forms an air and moisture-stable bis-ligated nickel(II) complex with a distorted square planar geometry (**Figure E2**, right).[21] We aimed to use ligand **L1** to form a bis-ligated dicationic cobalt complex. The dibromo diimidazolium salt of **L1** was synthesized according to the literature and obtained as a pure sample as confirmed by elemental analysis (**Scheme E1**).[21] Subsequently, biscarbene **L1** was synthesized upon deprotonating the dibromo diimidazolium salt with a base (KHMDS) and was isolated as a red powder, whose spectroscopic characterization matched those reported in the literature. **L1** is soluble in THF and benzene, but not in hexane. Then we aimed to synthesize a bis-ligated dicationic cobalt complex by treating **L1** with a cobalt(II) precursor. **L1** was dissolved in THF forming a red solution, which was slowly added to a blue solution of $CoBr_2$ (0.5 equiv.) in THF. A direct solution color change to brown was observed and within the first 5 min dark green/brown solids precipitated. Elemental analysis of the solids showed the right CHN distribution but also indicated a significant inorganic impurity (see experimental section), excluding the possibility of a pure mono or bis-ligated cobalt complex. ESI-MS analysis (in MeCN solution) showed different ionized species, including $[Co(\mathbf{L1})_2Br_2]^+$ (*m/z* 875.2), $[Co(\mathbf{L1})_2BrCl]^+$ (*m/z* 831.2), $[Co(\mathbf{L1})_2Br]^+$, (*m/z* 794.2), $[Co(\mathbf{L1})]^+$ (*m/z* 386.9), and $[Co(\mathbf{L1})_2]^{2+}$ (*m/z* 357.8) (**Figure E3**). Based on the ESI-MS analysis, we expect the major species to be a bis-ligated cobalt complex. ^{1}H-NMR analysis of the solids in MeCN-d_3 showed several strongly shifted and broad signals between –27.97 and 49.79 ppm, typical for a high-spin Co(II) complex, for which no further assignment was possible (**Figure E4**). Then, the reaction was repeated on a bigger scale, which afforded a sufficient batch of brown solids for further analysis. Transparent green crystals suitable for X-ray crystal structure determination were obtained by slow vapor diffusion of hexane into a concentrated solution of the brown solid in DMF after two weeks. X-ray crystal structure determination revealed two independent

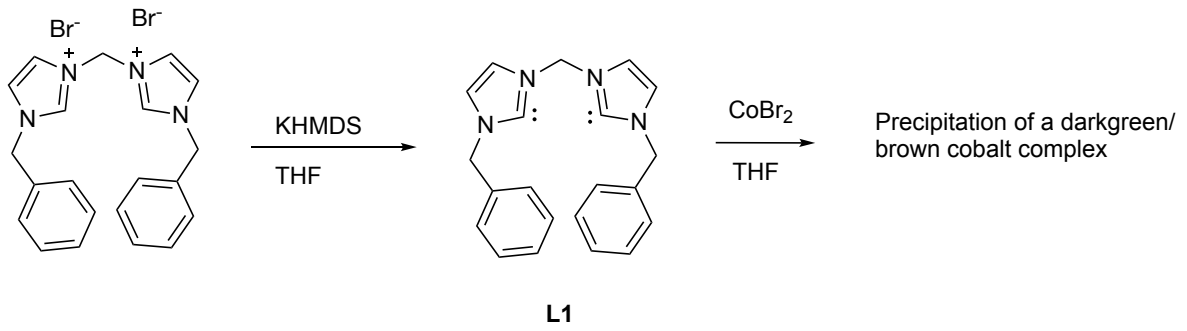

Scheme E1. Synthesis route towards a bis-diimidazolylidine cobalt complex.

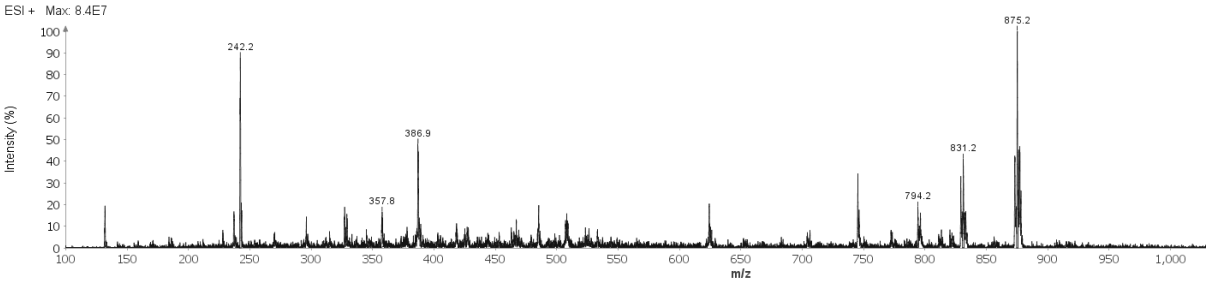

Figure E3. ESI-MS analysis (MeCN) of **1**.

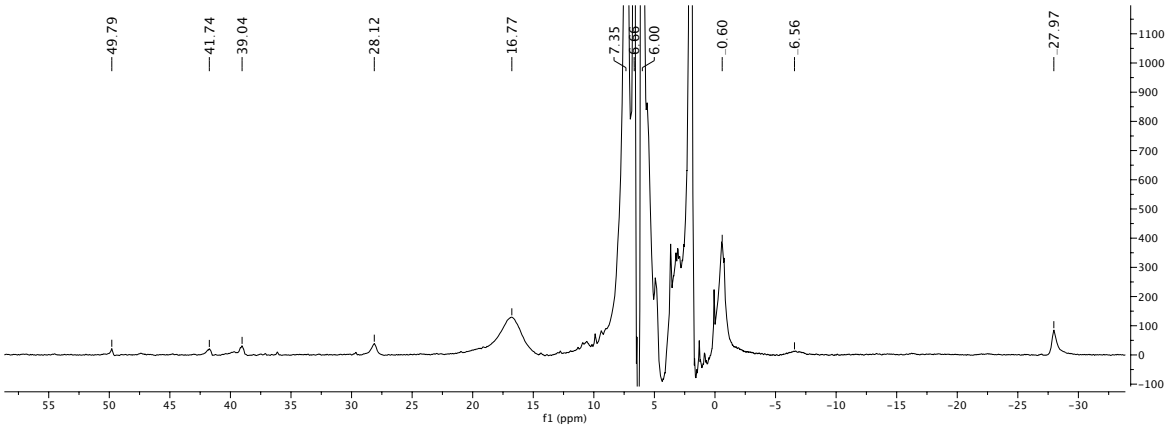

Figure E4. ^{1}H-NMR spectrum of **1** in MeCN-d_3.

cobalt complexes in the unit cell which both have inversion symmetry. Additionally, a co-crystallized DMF molecule is present. The geometry of both complexes is octahedral comprising two biscarbene ligands **L1** in the equatorial plane, two axially coordinated halogen ions (substitutional disorder between bromine and chlorine), and one non-coordinated bromide counterion, [Co(**L1**)$_2$X$_2$](Br) [X=Br,Cl] (**1**) (**Figure E5**). The unexpected presence of three

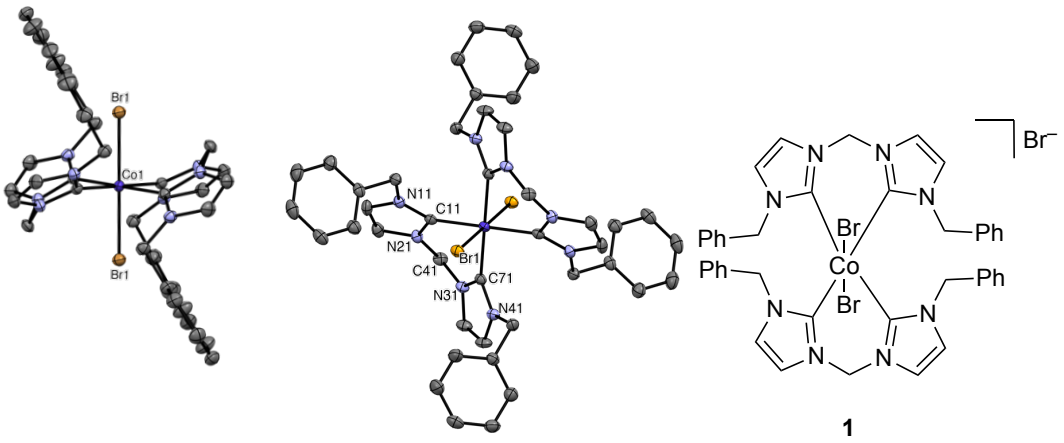

Figure E5. Displacement ellipsoid plot of [Co(**L1**)$_2$X$_2$](Br) **1** (50% probability). Only one of two independent molecules is shown. H-atoms and Br counterion have been omitted for clarity. Left, side-view; middle, front view; right, ChemDraw representation.

halogenide ions in the structure suggests the cobalt center within the complex is in a Co(III) oxidation state. To the best of our knowledge, this is only the second Co(III) tetra-carbene complex reported to date. However, this is in contrast to our aim and hypothesis for the formation of a bis-ligated Co(II) complex and this is presumably caused by a disproportionation reaction or air oxidation reaction. The observed substitutional disorder between bromine and chlorine in the X-ray crystal structure is consistent with the observation of the $[Co(\mathbf{L1})_2BrCl]^+$ ion by ESI-MS (on a different batch). The origin of the chloride ions remains unclear since no chloride was used during the synthesis and the ligand precursor was deemed pure based on E.A. Therefore, we believe the origin of the chlorides is due to an impurity in either the THF solvent, $CoBr_2$, or the KHMDS base. Further analysis of the obtained crystal structure revealed that the phenyl groups of one bis-carbene ligand are orientated in the same direction, pointing away from the cobalt center. Selected bond lengths and angles in **1** are compiled in **Table E1**. The only other octahedral tetra NHC cobalt(III) complex was reported by Chen *et al*., but the crystal's poor quality prevented them from reporting on the metrics of the crystal.[22] The Co^{III}–C(NHC) ligand to metal coordination bonds in **1** are comparable to those reported for tetra-NHC cobalt(II) complexes by Deng *et al*. (square planar), Jenkins *et al*. (square pyramidal), and Xue (square planar),[14,19,23] and slightly shorter to those reported by Murphy *et al*. (Co^{II}, tetrahedral).[15]

Cyclic voltammetry analysis of the obtained brown solids (~1 mM) in MeCN (0.1 M nBuNBF$_4$) was performed by starting at 0 V and sweeping first in the cathodic direction (**Figure E6**, gray trace). On the cathodic sweep reduction events at $E_{p,c} = -0.97$ and $E_{p,c} = -1.65$ V vs Fc^+/Fc were observed. We assigned the former event to an impurity and the latter event to the Co(I/II) reduction, based on the redox potentials of related cobalt carbene complexes measured in DMF and THF.[13-15] In the reversed anodic scan a small oxidation event at $E_{p,a} = -1.52$ V vs Fc^+/Fc

Table E1. Selected bond lengths (Å) and bond angles (º) for $[Co(\mathbf{L1})_2X_2]](Br)$ [X=Br,Cl] **1**. Only one of two molecules is given.

$[Co(\mathbf{L1})_2X_2](Br)$ (**1**)			
Bond	Lenghts (Å)	Bond Angle	Degrees
Co1–X1	2.4369(2)	C11–Co1–C71	86.53(8)
Co1–C11	1.982(2)	X1–Co1–C11	93.17(6)
Co1–C71	1.975(2)	X1–Co1–C71	91.97(6)
C11–N11	1.360(3)		
C11–N21	1.360(3)		
C71–N31	1.364(3)		
C71–N41	1.357(3)		

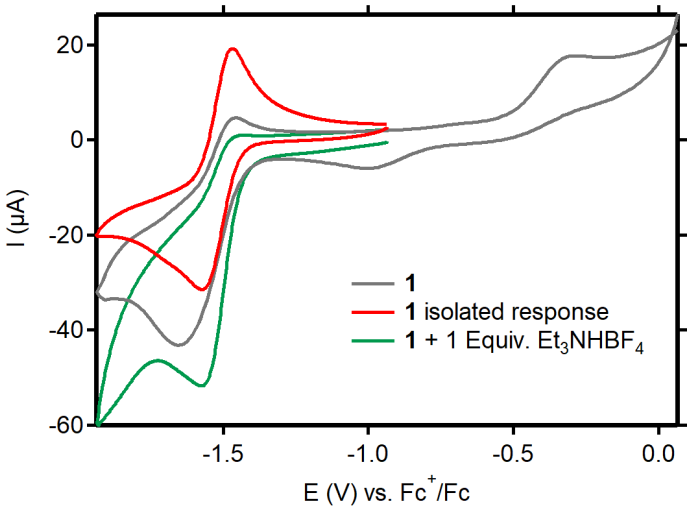

Figure E6. Cyclic voltammogram of the obtained brown solids (~1 mM) in MeCN (0.1 M *n*BuNBF$_4$). Full voltammogram gray, isolated reductive response red, the addition of 1 equiv. Et_3NHBF_4 (green).

was observed, assigned to the Co(I/II) reoxidation, and an oxidation event at $E_{p,a} = -0.32$ V vs Fc^+/Fc which we assigned to oxidation of a reaction product of the irreversible reduction or an impurity. When isolating the Co(I/II) reductive feature, the redox event becomes chemically reversible with an $E_{1/2} = -1.55$ V vs Fc^+/Fc (**Figure E6**, red trace). Upon addition of 1 equiv. of Et_3NHBF_4, as a sacrificial proton donor, the current intensity of the Co(I/II) reduction increased, which could point to an electrocatalytic current (**Figure E6**, green trace). These initial electrochemical results indicate that the formed complex is likely a dicationic cobalt complex. Furthermore, the complex might be able to catalyze the HER reaction at a relatively low overpotential (~300 mV),[24] as compared to those observed for $[Co(HBMIM^{Ph2})_2](BF_4)_2$ in DMF (690 mV, **Chapter 4**) or MeCN (590 mV).[25] Nevertheless, further electrocatalytic investigations on the obtained batches were omitted because of purity concerns, the presence of Cl^-, and the unpredicted result of a Co(III) crystal. However, these initial results indicate that cobalt carbene complexes might be worth investigating as HER catalysts.

E. 2 Conclusion

An isolated free bisimidazole carbene ligand (**L1**) was used to synthesize a bis-ligated Co(II) complex. However, an impure dark green/brown solid material was obtained. The ^{1}H-NMR spectrum of the solids is consistent with a paramagnetic Co(II) species and ESI-MS demonstrates several bis-ligated complexes. In contrast, an unexpected Co(III) crystal structure of $[Co(\mathbf{L1})_2X_2](Br)$ (**1**) was obtained [X=Br,Cl]. **1** represents an example of an octahedral

Co(III) complex in which four NHC moieties and two bromide ions ligate the trivalent cobalt ion accompanied by one additional bromide counterion. To the best of our knowledge, this is only the second Co(III) tetra-carbene complex reported. The synthesis route to **1** was not expected as a neutral ligand reacts with a Co(II) precursor. Therefore we suggest that Co(III) complex **1** is formed upon disproportionation or oxidation during the recrystallization experiment. Initial voltammetry experiments on the impure brown solids demonstrated a Co(I/II) redox couple at relative anodic potentials, that increased in current intensity in the presence of a weak acid. This wave development could possibly point to HER catalysis at an overpotential of ~300 mV. We, therefore, consider it worthwhile to further study the development of NHC cobalt complexes in pursuit of new molecular HER catalysts. Fine-tuning of the biscarbene ligand could render complexes that can be isolated in sufficient purity to allow for their detailed study.

E. 3 Experimental

General experimental information is similar to the one in **Chapter 2**.

L1 was synthesized according to literature procedures.[21]

E. 3.1 Synthesis of a dicationic cobalt complex and crystallization of [Co(**L1**)$_2$Br$_2$](Br) (**1**)

The dibromo diimidazolium salt of **L1** (200 mg, 0.4 mmol) was added to THF (5 mL), forming a white suspension. KHMDS (180 mg, 0.9 mmol) was added to the suspension, forming a red solution with a white precipitate. The mixture was stirred for 5 min and filtered, using a paper filter. The red filtrate was added dropwise to a blue solution of $CoBr_2$ (65.6 mg, 0.3 mmol) in THF (5 mL) and the resulting mixture was stirred for 1 h while dark green/brown solids formed. The dark green/brown solids were collected on a glass filter, washed with THF (2 x 10 mL), and dried under vacuum, yielding 32 mg of dark green/brown solids. **^{1}H NMR** (400 MHz, MeCN-d_3, 25 °C): δ (ppm) = 49.79, 41.74, 39.04, 28.12, 16.17, 7.35, 6.66, 6.00, -0.60, –6.56, –27.97. **ESI-MS** (MeCN): [Co(**L1**)$_2$Br$_2$]$^+$, (*m/z* 875.1), [Co(**L1**)$_2$BrCl]$^+$ (*m/z* 831.2), [Co(**L1**)$_2$Br]$^+$, (*m/z* 794.2), [Co(**L1**)]$^+$ (*m/z* 386.9), and [Co(**L1**)$_2$]$^{2+}$ (*m/z* 357.8) **E.A.** (Formula: $C_{42}H_{40}CoN_8Br_2$, Mw: 875.58 g mol^{-1}): Calc. C 57.61, H 4.60, N 12.80; found C 23.16, H 1.92, N 5.20. (Please note: the right CHN distribution was found with a major inorganic impurity, presumably caused by scraping some glass from the glass filter or some residual KBr)

From a different synthesis experiment, following the same procedure but on a twofold scale, 160 mg of brown solids were obtained. Recrystallization of the brown solids by slow

evaporation of hexane into a concentrated solution of the brown solids in DMF over 2 weeks afforded transparent green crystals suitable for single crystal X-ray crystal structure determination. **X-ray crystal structure determination** $[C_{42}H_{40}Br_{1.62}Cl_{0.38}CoN_8](Br) \cdot C_3H_7NO$, Fw = 1011.68, green plate, 0.34 × 0.19 × 0.05 mm^3, triclinic, $P\overline{1}$ (no. 2), a = 9.4168(2), b = 13.4979(4), c = 16.9624(4) Å, α = 90.042(1), β = 94.394(1), γ = 92.912(1) °, V = 2146.91(9) Å^3, Z = 2, D_x = 1.565 g/cm^3, μ = 2.91 mm^{-1}. The diffraction experiment was performed on a Bruker Kappa ApexII diffractometer with sealed tube and Triumph monochromator (λ = 0.71073 Å) at a temperature of 150(2) K up to a resolution of $(\sin\theta/\lambda)_{max}$ = 0.65 Å^{-1}. The crystal was broken into two fragments. Consequently, two orientation matrices were used for the intensity integration with the Eval15 software,[26] resulting in a HKLF-5 file.[27] A multi-scan absorption correction and scaling was performed with TWINABS[28] (correction range 0.30-0.43). A total of 59397 reflections was measured, 9887 reflections were unique (R_{int} = 0.040), 8324 reflections were observed [I>2σ(I)]. The structure was solved with Patterson superposition methods using SHELXT.[29] Structure refinement was performed with SHELXL-2018[30] on F^2 of all reflections. Non-hydrogen atoms were refined freely with anisotropic displacement parameters. The structure contains two independent Co atoms, both located on inversion centers. The positions of the coordinated halogen atoms showed substitutional disorder between bromine and chlorine. Constraints were used for the positions and displacement parameters of the disordered halogens, and the occupancy refinement resulted in a ratio Br:Cl = 0.8086(17):0.1914(17). The non-coordinated halogen was refined with a 100% occupancy for bromine. All hydrogen atoms were introduced in calculated position and refined with a riding model. 539 Parameters were refined with no restraints. R1/wR2 [I > 2σ(I)]: 0.0299 / 0.0685. R1/wR2 [all refl.]: 0.0396 / 0.0721. S = 1.036. Batch scale factor for the second crystal fragment BASF = 0.0417(6). Residual electron density between -0.51 and 1.01 e/Å^3. Geometry calculations and checking for higher symmetry was performed with the PLATON program.[31]

E. 4 Author contributions

Initial scientific efforts were done by E. Kirtosun. Synthesis, characterization, and electrochemical measurements were done by S. D. de Vos, and X-ray crystal structure determinations were performed by M. Lutz. The project design was done by S.D. de Vos and R.J.M. Klein Gebbink. Funding acquisition, administration, and oversight were done by R.J.M.

Klein Gebbink. The original draft was written by S. D. de Vos, and reviewing/editing was done by, M. Lutz, D.L.J Broere, and R.J.M. Klein Gebbink.

E. 5 References

(1) Teng, Q.; Ng, P. S.; Leung, J. N.; Huynh, H. V. Donor Strengths Determination of Pnictogen and Chalcogen Ligands by the Huynh Electronic Parameter and Its Correlation to Sigma Hammett Constants. *Chem. Eur. J.* **2019,** *25* (61), 13956.

(2) Bera, S. S.; Szostak, M. Cobalt–N-Heterocyclic Carbene Complexes in Catalysis. *ACS Catalysis* **2022,** *12* (5), 3111.

(3) Lappert, M. F.; Pye, P. L. Carbene complexes. Part 12. Electron-rich olefin-derived neutral mono- and bis-(carbene) complexes of low-oxidation-state manganese, iron, cobalt, nickel, and ruthenium. *J. Chem. Soc., Dalton Trans.* **1977**, 2172-2180.

(4) Andjaba, J. M.; Tye, J. W.; Yu, P.; Pappas, I.; Bradley, C. A. Cp*Co(IPr): synthesis and reactivity of an unsaturated Co(i) complex. *Chem. Commun.* **2016,** *52* (12), 2469.

(5) Danopoulos, A. A.; Braunstein, P. Mono-N-heterocyclic carbene amido and alkyl complexes. Cobalt-mediated C–H activation and C–C coupling reactions involving benzyl ligands on a putative 3-coordinate intermediate. *Dalton Trans.* **2013,** *42* (20), 7276.

(6) Danopoulos, A. A.; Simler, T.; Braunstein, P. N-Heterocyclic Carbene Complexes of Copper, Nickel, and Cobalt. *Chem. Rev.* **2019,** *119* (6), 3730.

(7) Day, B. M.; Pal, K.; Pugh, T.; Tuck, J.; Layfield, R. A. Carbene Rearrangements in Three-Coordinate N-Heterocyclic Carbene Complexes of Cobalt(II) Bis(trimethylsilyl)amide. *Inorg. Chem.* **2014,** *53* (19), 10578.

(8) Du, J.; Wang, L.; Xie, M.; Deng, L. A Two-Coordinate Cobalt(II) Imido Complex with NHC Ligation: Synthesis, Structure, and Reactivity. *Angew. Chem. Int. Ed.* **2015,** *54* (43), 12640.

(9) Hansen, C. B.; Jordan, R. F.; Hillhouse, G. L. Protonolysis and Amide Exchange Reactions of a Three-Coordinate Cobalt Amide Complex Supported by an N-Heterocyclic Carbene Ligand. *Inorg. Chem.* **2015,** *54* (10), 4603.

(10) Hering, F.; Berthel, J. H. J.; Lubitz, K.; Paul, U. S. D.; Schneider, H.; Härterich, M.; Radius, U. Synthesis and Thermal Properties of Novel NHC-Stabilized Cobalt Carbonyl Nitrosyl Complexes. *Organometallics* **2016,** *35* (17), 2806.

(11) Simler, T.; Braunstein, P.; Danopoulos, A. A. Cobalt PNCNHC 'pincers': ligand dearomatisation, formation of dinuclear and N2 complexes and promotion of C–H activation. *Chem. Commun.* **2016,** *52* (13), 2717.

(12) Simler, T.; Choua, S.; Danopoulos, A. A.; Braunstein, P. Reactivity of a dearomatised pincer CoIIBr complex with PNCNHC donors: alkylation and Si–H bond activation via metal–ligand cooperation. *Dalton Trans.* **2018,** *47* (24), 7888.

(13) Kawano, K.; Yamauchi, K.; Sakai, K. A cobalt–NHC complex as an improved catalyst for photochemical hydrogen evolution from water. *Chem. Commun.* **2014,** *50* (69), 9872.

(14) Mo, Z.; Li, Y.; Lee, H. K.; Deng, L. Square-Planar Cobalt Complexes with Monodentate N-Heterocyclic Carbene Ligation: Synthesis, Structure, and Catalytic Application. *Organometallics* **2011,** *30* (17), 4687.

(15) Park, S. R.; Findlay, N. J.; Garnier, J.; Zhou, S.; Spicer, M. D.; Murphy, J. A. Electron transfer activity of a cobalt crown carbene complex. *Tetrahedron* **2009,** *65* (52), 10756.

(16) Luo, S.; Siegler, M. A.; Bouwman, E. Transition Metal Compounds of Pyridine-Amide-Functionalized Carbene Ligands: Synthesis, Structure, and Electrocatalytic Properties in Proton Reduction. *Eur. J. Inorg. Chem.* **2019,** *2019* (5), 617.

(17) Yatsuzuka, K.; Yamauchi, K.; Kawano, K.; Ozawa, H.; Sakai, K. Improving the overall performance of photochemical H2 evolution catalyzed by the Co-NHC complex via the redox tuning of electron relays. *Sustainable Energy & Fuels* **2021,** *5* (3), 740.

(18) Hogue, R. W.; Schott, O.; Hanan, G. S.; Brooker, S. A smorgasbord of 17 cobalt complexes active for photocatalytic hydrogen evolution. *Chem. Eur. J.* **2018,** *24* (39), 9820.

(19) Lu, Z.; Cramer, S. A.; Jenkins, D. M. Exploiting a dimeric silver transmetallating reagent to synthesize macrocyclic tetracarbene complexes. *Chemical Science* **2012,** *3* (10), 3081.

(20) de Vos, S. D.; Otten, M.; Wissink, T.; Broere, D. L. J.; Hensen, E. J. M.; Klein Gebbink, R. J. Hydrogen Evolution Electrocatalysis with a Molecular Cobalt Bis(alkylimidazole)methane Complex in DMF: a critical activity analysis. *ChemSusChem* **2022**, 15, e2022013

(21) Paulose, T. A. P.; Wu, S.-C.; Olson, J. A.; Chau, T.; Theaker, N.; Hassler, M.; Quail, J. W.; Foley, S. R. Bis-diimidazolylidine complexes of nickel: Investigations into nickel catalyzed coupling reactions. *Dalton Trans.* **2012,** *41* (1), 251.

(22) Xi, Z.; Liu, B.; Lu, C.; Chen, W. Cobalt(iii) complexes bearing bidentate, tridentate, and tetradentate N-heterocyclic carbenes: synthesis, X-ray structures and catalytic activities. *Dalton Trans.* **2009**, 7008-7014.

(23) Liu, Y.-Z.; Wang, J.; Zhao, Y.; Chen, L.; Chen, X.-T.; Xue, Z.-L. Four-coordinate Co(ii) and Fe(ii) complexes with bis(N-heterocyclic carbene)borate and their magnetic properties. *Dalton Trans.* **2015,** *44* (3), 908.

(24) Felton, G. A. N.; Glass, R. S.; Lichtenberger, D. L.; Evans, D. H. Iron-Only Hydrogenase Mimics. Thermodynamic Aspects of the Use of Electrochemistry to Evaluate Catalytic Efficiency for Hydrogen Generation. *Inorg. Chem.* **2006,** *45* (23), 9181.

(25) Ghosh, P.; de Vos, S.; Lutz, M.; Gloaguen, F.; Schollhammer, P.; Moret, M.-E.; Klein Gebbink, R. J. M. Electrocatalytic Proton Reduction by a Cobalt Complex Containing a Proton-Responsive Bis(alkylimdazole)methane Ligand: Involvement of a C–H Bond in H2 Formation. *Chem. Eur. J.* **2020,** *26* (55), 12560.

(26) Schreurs, A. M.; Xian, X.; Kroon-Batenburg, L. M. EVAL15: a diffraction data integration method based on ab initio predicted profiles. *J. Appl. Crystallogr.* **2010,** *43* (1), 70.

(27) Herbst-Irmer, R.; Sheldrick, G. M. Refinement of twinned structures with SHELXL97. *Acta Crystallogr. Sect. B: Struct. Sci.* **1998,** *54* (4), 443.

(28) Sevvana, M.; Ruf, M.; Usón, I.; Sheldrick, G. M.; Herbst-Irmer, R. Non-merohedral twinning: from minerals to proteins. *Acta Crystallogr. Sect. D: Structural Biology* **2019,** *75* (12), 1040.

(29) Sheldrick, G. SHELXT - Integrated space-group and crystal-structure determination. *Acta Crystallogr. Sect. A* **2015,** *71* (1), 3.

(30) Sheldrick, G. M. Crystal structure refinement with SHELXL. *Acta Crystallogr. Sect. C: Structural Chemistry* **2015,** *71* (1), 3.

(31) Spek, A. Structure validation in chemical crystallography. *Acta Crystallogr. Sect. D* **2009,** *65* (2), 148.

Summary

The central theme of this PhD thesis is the development of molecular cobalt catalysts for the hydrogen evolution reaction (HER), i.e., the reduction of protons to form molecular hydrogen. As explained in **Chapter 1**, hydrogen plays a pivotal role in strategies to prevent further global warming and in society's dependence on fossil fuels. A transition from fossil fuels to renewable energy will be necessary, for which we need to make more use of the largest renewable energy sources, wind and solar. Since these sources are intermittent, part of the energy needs to be stored. One promising option to store this energy is in the form of chemical bonds. This can lead to high energy-density fuels, which can be easily warehoused and transported. A green process for the storage of energy is the conversion of water into oxygen and protons and the subsequent reductions of protons to hydrogen. Both reactions proceed thermodynamically uphill and have severe activation energies (lost energy) to speed up the process to practical use. Therefore, catalysts will have to be employed to produce these renewable fuels to minimize energy losses. This thesis has focused on research towards catalysts for the HER half-reaction. For this reaction, platinum is the best catalytic material, but widespread usage is prevented due to its low abundance and high price. As a result, research on alternative catalytic materials is ongoing. Currently, some promising materials include cobalt-based catalysts, of which specifically cobalt-based molecular complexes have gained a lot of attention.

Chapter 1 also provides a tutorial on strategies for the development of molecular (cobalt-based) hydrogen evolution catalysts (HECs). First, photosynthesis strategies applied in nature are discussed, in which hydrogenase enzymes can produce hydrogen at a fast rate with almost no lost energy. Then, the available artificial photosynthesis methods are introduced, and guidelines are provided for the evaluation of molecular complexes as HER catalysts. In the last part of **Chapter 1**, the progress in the field of molecular cobalt catalysts for hydrogen evolution is highlighted. Important contributions to the field of electrocatalytic and photocatalytic hydrogen evolution are discussed in which design principles, molecular trends, and mechanistic insight are highlighted. In **Chapter 2**, the recently developed molecular cobalt electrocatalyst ($[Co(HBMIM^{Ph2})_2](BF_4)_2$, HBMIM = bis(methylimidazole)methane) is further studied. $[Co(HBMIM^{Ph2})_2](BF_4)_2$ operates through a unique mechanism, in which the formation of dihydrogen is accomplished through the combination of a metal hydride and a ligand-based acidic C–H methylene proton (a proton relay). New cobalt complexes with (H,*p*ArX)BMIM^{Ph2}-

type ligands were developed in which para-substituted aryl groups, holding different EWG/EDG (X = H, Cl, CF_3, and OMe), are installed on the methylene bridge, next to the C–H proton relay (**Figure 1**, left). Structural and spectroscopic analysis confirmed that these complexes have a structurally related, tetrahedral geometry. The alternation of the para-substituent on the aryl group results in the effective modulation of the electrochemical properties of the complexes. The observed cobalt-based reduction potentials correlate with the Hammett σ-parameters of the *para*-aryl substituent. Electrocatalytic studies pointed at a similar trend in the electrocatalytic reduction potential, corresponding to an overpotential requirement modulation for hydrogen evolution based on the aryl substituent. Most interestingly, complexes with a lower overpotential show higher activity for hydrogen evolution (**Figure 1**, right), which opposes the usual trend in which overpotential speeds up a chemical transformation. This observation is attributed to the bifunctional role of the complexes as HECs, lending credit to the earlier proposed intramolecular proton relay during hydrogen formation. In **Chapter 3**, dicationic and neutral molecular cobalt complexes of the type $[Co(LH)_2](BF_4)_2$ and $[Co(L^-)_2]$ were investigated, in which L and L^- represent the neutral and the deprotonated versions of a series of bisheterocyclic benzazolyl ligands (see **Figure 2**). The smaller steric encumbrance of the benzazolyl ligands, as compared to the diphenylmethylimidazole ligands used in Chapter 2, results in coordination flexibility and the formation of complexes with tetrahedral or octahedral geometries. The dicationic complexes demonstrate an irreversible Co(I/II) reduction event at different potentials (spread of 600 mV), showing an effective modulation of the metal-based electronic properties upon variation of the hetero-atom in the benzazole rings of the ligands. A similar modulation is found for the redox events in the analogous neutral

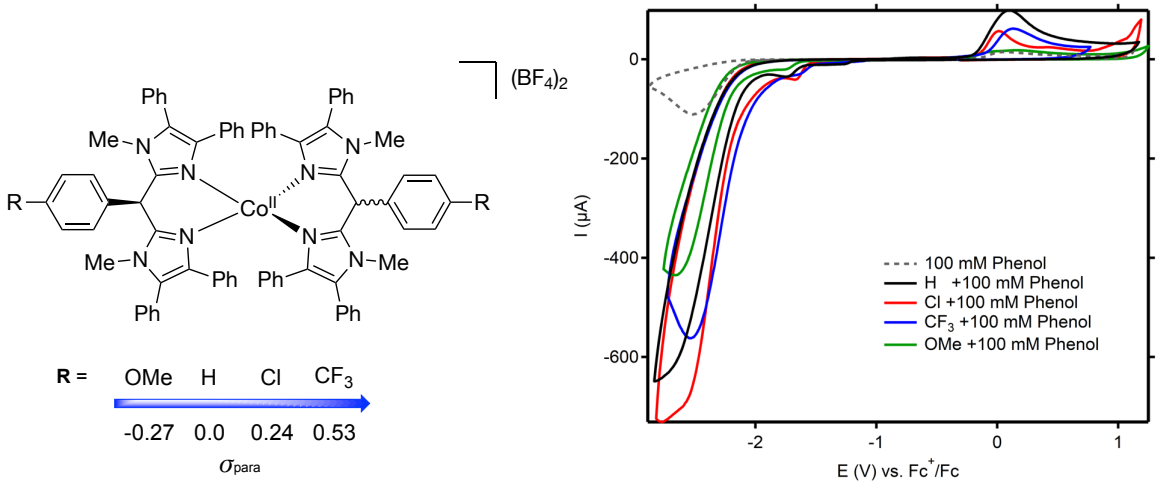

Figure 1. Left: structure of complexes $[Co((H,pArX)BMIM^{Ph_2})_2](BF_4)_2$ (X = H, Cl, CF_3 and, OMe) studied in **Chapter 2**. Right: cyclic voltammograms of the complexes (1 mM) in the presence of 100 mM phenol (colored traces) and the acid-only trace (dotted).

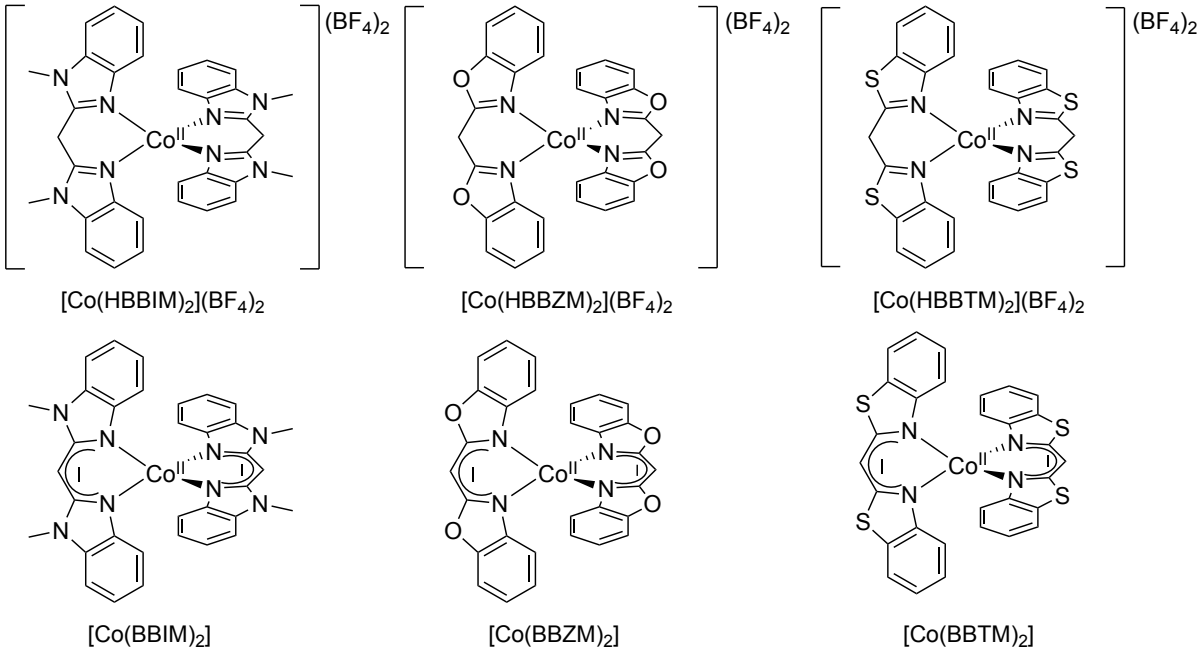

Figure 2. Overview of cobalt complexes studied in **Chapter 3**, bearing bis(2-benzazolyl)methanane and bis(2-benzazoyl)methanide ligands.

complexes. Both trends corroborate the electronic trend reported by Abbotto *et al*. for the π-electron-withdrawing power of the ligands: $BBTM^-$ > $BBZM^-$ > $BBIM^-$. Electrocatalytic studies showed that the dicationic complexes $[Co(HBBIM)_2](BF_4)_2$, $[Co(HBBZM)_2](BF_4)_2$, and $[Co(HBBTM)_2](BF_4)_2$ are all electrocatalysts for the hydrogen evolution reaction (HER) at overpotentials of 610, 580, and 490 mV, respectively. Electrolysis studies on $[Co(HBBZM)_2](BF_4)_2$ showed electrocatalytic H_2 formation at a moderate Faradaic Efficiency (FE) of 72% and a current density of 2.00 mA/cm^2. This study demonstrates that the redox features of bis(benzazolyl)methane-derived cobalt complexes can effectively be modulated by changing the nature of their heterocycles and that the complexes are active as HER catalysts.

The electrocatalytic hydrogen evolution performance of molecular complex $[Co(HBMIM^{Ph2})_2](BF_4)_2$ in DMF was studied in detail in **Chapter 4** and its activity benchmarked towards three well-studied electrocatalysts (**Figure 3**, left). Electrochemical analyses were performed using voltammetry and during controlled potential/current electrolysis (CPE/CCE) in a novel in-line product detection setup. Electrolysis experiments demonstrated a competitive performance of $[Co(HBMIM^{Ph2})_2](BF_4)_2$ towards the reported electrocatalysts in terms of charge consumption (**Figure 3**, right), H_2 production, Faradaic efficiency, and overpotential. After bulk electrolysis a deposit on the glassy carbon electrode was observed for all of the complexes and post-electrolysis X-ray photoelectron spectroscopy (XPS) analysis of the deposit formed from $[Co(HBMIM^{Ph2})_2](BF_4)_2$ demonstrated only a minor

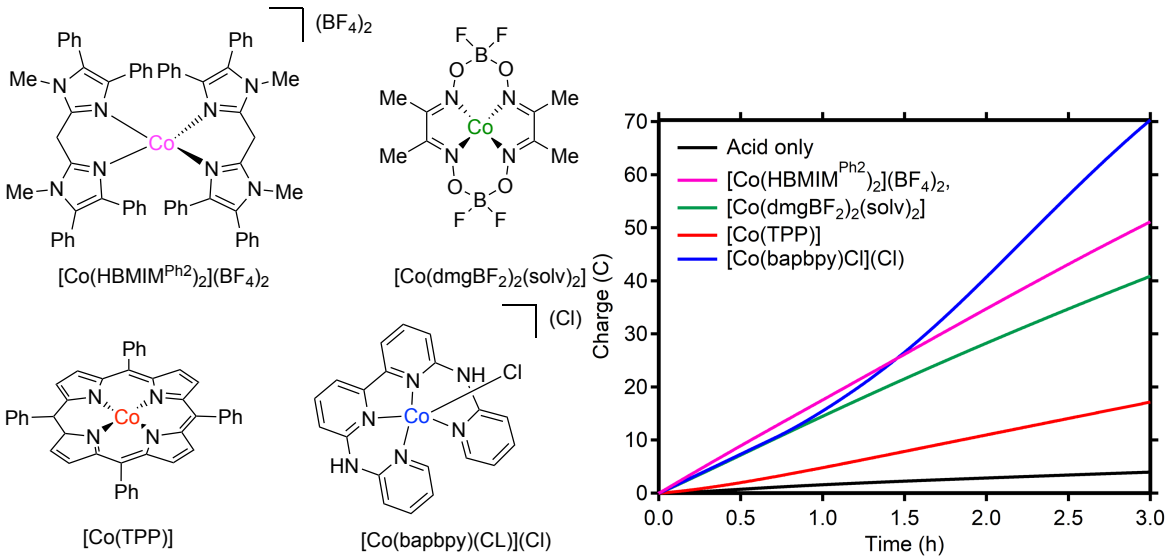

Figure 3. Left: molecular cobalt complexes studied in **Chapter 4**. Right: Comparison of the HER activity of the complexes by means of rotating disk CPE, as the charge passed over the course of time.

cobalt contribution (0.23%), mainly consisting of Co^{2+}. Rinse tests on the deposits derived from $[Co(HBMIM^{Ph2})_2](BF_4)_2$ and $[Co(dmgBF_2)_2(solv)_2]$ showed that the initially observed distinct activity is (partly) preserved for the deposits. Overall, further insight was obtained into HER catalysis with molecular cobalt complexes by demonstrating an important transformation pathway toward a different catalytically active material, in which the molecular design of the complexes dictates the features of the formed deposit and therewith the observed activity. **Chapter 5** describes efforts to modulate complex ($[Co(HBMIM^{Ph2})_2](BF_4)_2$) such that it becomes water-soluble in order to apply it in aqueous photocatalytic HER catalysis. To this end, a number of (water-soluble) cobalt complexes were developed based on bis(imidazole)methane-type ligands (**Figure 4**, left). In coordinating solvents, these complexes adopt octahedral structures in which two molecules coordinate to cobalt in either a *cis* or a *trans* fashion. The photocatalytic HER performance of the complexes was optimized using ascorbic acid as the electron and proton donor and $[Ru(bpy)_3](PF_6)_2$, bpy = bipyridine, as a photosensitizer. Water-soluble complexes $[Co(HBMIM)_2](NO_3)_2$ and $[Co(HBMIA)_2](NO_3)_2$ demonstrate the highest photo-catalytically activity, followed by $[Co(BMIK)_2](NO_3)_2$ (**Figure 4**, right). These observations show that alternation of the methylene group influenced the photocatalytic HER rate and stability, in which less electron-donating ligands provide complexes with lower initial rates but longer lifetimes. Benchmarking the photocatalytic activity of these complexes showed a competitive performance with respect to metal precursor $[Co(H_2O)_6(NO_3)_2]$ and well-studied complex $[Co(dmgH)_2PyCl]$, while the complexes are

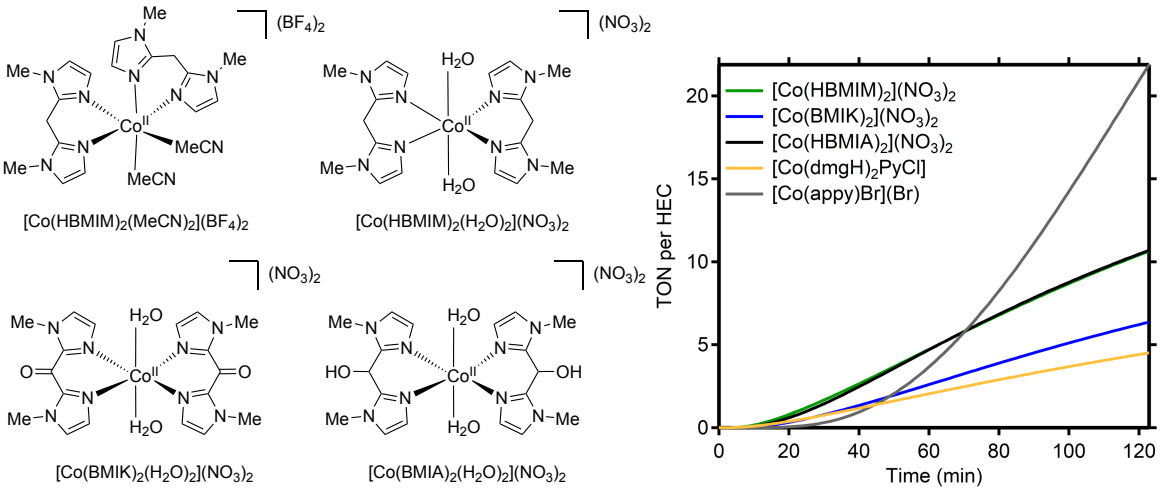

Figure 4. **L**eft: Cobalt(II) complexes reported in **Chapter 5**. Right: comparison of the aqueous photocatalytic HER performance of new and reported Co-complexes on the basis of cumulative TON versus the reaction time, using $[Ru(bpy)_3(Cl)_2$, as photosensitizer and AscH as electron and proton source.

outperformed by the best catalyst in the field, [Co(appy)Br](Br). Finally, **Chapter 6** provides a perspective on how recent advances in molecular cobalt hydrogen evolution catalyst design and characterization may help to unify appropriate descriptors to be applied in the overall water-splitting process. In doing so, the chapter provides a framework of thinking to design and assess improved catalytic frameworks for the hydrogen evolution half-reaction.

Concluding remarks

Huge gains in the activity of earth-abundant catalysts have been achieved over the last several years, and cobalt-based complexes remain a promising class of catalysts. With the increased understanding of imidazole-based molecular cobalt complexes as HER catalysts and the optimized HER catalysis reported in this Doctoral Thesis, alongside recent examples in the literature, a next step in sufficiently controlling the hydrogen evolution kinetics was made, but further advancements are necessary.

From a fundamental point of view, we only just started to understand the complex hydrogenase enzyme system that includes multiple adjustable proton- and electron relays. In this Doctoral Thesis, we have shown how ligand modifications in the second and outer coordination sphere of molecular complexes contribute to the understanding of electron and proton transfer processes for H_2 production. A particular focus in this work was the involvement of a C–H proton relay during the H_2 bond-making process, which allowed for new insights into catalytic

parameters such as overpotential and catalytic rate. Many molecular complexes are inspired by the active centers of natural enzymes and meet their performances outside the cell membranes. Yet in this Doctoral thesis, we have shown that the activity is not easy to mimic and sometimes even difficult to measure. In **Chapters 2** and **3** we have shown that effective modulation of the reactivity of our molecular complexes can be achieved in a controlled manner. Nevertheless, the modifications also made the complexes fragile, and electrolysis studies demonstrated poor stability.

From an applied chemistry viewpoint, the level of understanding and the design control achievable with molecular complexes is an outstanding tool to uncover functionalities that can promote hydrogen evolution in later-stage, solid-state structures that are more difficult to characterize. Improving the stability and turnover numbers during electrolysis could provide even further advancements. As new, effective strategies for molecular complexes are developed, it is also increasingly important to test the limits of these approaches. Eventually, lessons learned must be applied in devices that have long-time stability under aqueous conditions to make water splitting economically viable. So far, only a few studies have reported on incorporating the distinct design principles, that led to improved HER performances in molecular catalysts, into solid-state electrodes for aqueous electrochemical cells.

Finally, not only the HER but many small molecule activation reactions are redox reactions and, therefore, the design principles that stimulate electron transfer in HER catalysis can likely be applied to study mechanisms and enhance performances in other redox processes. Therefore, our current research aim should not limit the use of cobalt-based imidazole complexes to the HER. In fact, in the future, reactants such as CO_2 and N_2 could also be exposed to bisimidazole-type cobalt complexes to study both the involvement of the proton relay and the overall reduction performance of the complexes. Such experiments could allow the further elucidation of the elementary steps in catalytic cycles, most notably the coordination of the substrate and activation pathways involving the C–H proton relay.

Samenvatting

Dit proefschrift richt zich op de ontwikkeling van moleculaire kobaltkatalysatoren voor de waterstofevolutiereactie, oftewel de reductie van protonen tot moleculaire waterstof. **Hoofdstuk 1** benadrukt hoe waterstof een belangrijke rol speelt in strategieën om verdere opwarming van de aarde te voorkomen en om de samenleving gedeeltelijk onafhankelijk te maken van fossiele brandstoffen. Aangezien de grootste hernieuwbare bronnen zoals wind en zon intermitterend zijn, moet een deel van de energie worden opgeslagen. Een veelbelovende manier om deze energie op te slaan is in de vorm van chemische bindingen. Dit kan leiden tot brandstoffen met een hoge energiedichtheid, die gemakkelijk kunnen worden opgeslagen en vervoerd. Een groen proces voor de opslag van energie is de omzetting van water in zuurstof en protonen en de daaropvolgende reductie van protonen tot waterstof. Beide reacties verlopen thermodynamisch bergopwaarts en hebben hoge activeringsenergieën (verloren energie) om het proces te versnellen tot praktisch gebruik. Daarom zullen katalysatoren moeten worden gebruikt om het energieverlies te minimaliseren tijdens het produceren van deze hernieuwbare brandstoffen. Dit proefschrift heeft zich gericht op onderzoek naar katalysatoren voor laatste genoemde reactie, de reductie van proton tot waterstof. Voor deze reactie is platina het beste katalytische materiaal, maar mondiaal gebruik wordt verhinderd door schaarste en een hoge element prijs. Als gevolg daarvan is het onderzoek naar alternatieve katalytische materialen gaande. Enkele veelbelovende materialen zijn kobalt gebaseerde katalysatoren, waarvan specifiek kobalt gebaseerde moleculaire complexen veel aandacht hebben gekregen.

Hoofdstuk 1 geeft vervolgens een overzicht van strategieën voor de ontwikkeling van moleculaire (op kobalt gebaseerde) waterstof evolutie katalysatoren. Eerst worden de in de natuur toegepaste fotosynthese strategieën besproken, waarin hydrogenase enzymen waterstof kunnen produceren op hoge snelheid met bijna geen energieverlies. Vervolgens worden de beschikbare kunstmatige fotosynthesemethoden besproken en worden belangrijke aspecten voor de evaluatie van moleculaire complexen als waterstof evolutie katalysatoren besproken. In het laatste deel van **hoofdstuk 1** wordt de vooruitgang op het gebied van moleculaire kobaltkatalysatoren voor waterstofevolutie belicht. Belangrijke bijdragen op het gebied van elektro katalytische en foto katalytische waterstof productie worden besproken, waarbij ontwerpprincipes, moleculaire trends en mechanistisch inzicht worden besproken. In **hoofdstuk 2** wordt de recent ontwikkelde moleculaire kobalt-elektrokatalysator

($[Co(HBMIM^{Ph2})_2](BF_4)_2$, HBMIM = bis(methylimidazool)methaan) verder bestudeerd. $[Co(HBMIM^{Ph2})_2](BF_4)_2$ werkt via een uniek mechanisme, waarbij de vorming van waterstof tot stand komt door de combinatie van een metaalhydride en een ligand gebaseerd zuur C–H methyleen proton (een protonrelais). Nieuwe kobaltcomplexen met (H,*p*ArX)$BMIM^{Ph2}$-type liganden werden ontwikkeld waarin para-gesubstitueerde aryl groepen, met verschillende elektronzuigende en elektrondonerende groepen (X = H, Cl, CF_3, en OMe), geïnstalleerd zijn op de methyleenbrug, naast de C–H protonrelais (**Figuur 1**, links). Structurele en spectroscopische analyse bevestigde dat deze complexen een structureel verwante, tetrahedrale geometrie hebben. De afwisseling van het para-substituent op de aryl groep resulteert in een effectieve modulatie van de elektrochemische eigenschappen van de complexen. De waargenomen kobalt gebaseerde reductiepotentialen correleren met de Hammett σ -parameters van het para-arylsubstituent. Elektrokatalytische studies wezen op een soortgelijke trend in het elektrokatalytisch reductiepotentialen, overeenkomend met een overpotentiaal modulatie voor waterstofevolutie op basis van het arylsubstituent. Het interessantste is dat complexen met een lager overpotentiaal een hogere activiteit voor waterstofevolutie vertonen (**Figuur 1**, rechts), wat ingaat tegen de gebruikelijke trend waarbij overpotentiaal een chemische transformatie versnelt. Deze waarneming wordt toegeschreven aan de bifunctionele rol van de complexen als waterstof productie katalysator wat het gebruik van de eerder voorgestelde intramoleculaire protonrelais tijdens waterstofvorming ten goede komt. In **hoofdstuk 3** werden dikationische en neutrale moleculaire kobaltcomplexen van het type $[Co(LH)_2](BF_4)_2$ en $[Co(L^-)_2]$ onderzocht, waarbij L en L^- de neutrale en de gedeprotoneerde versies van een reeks

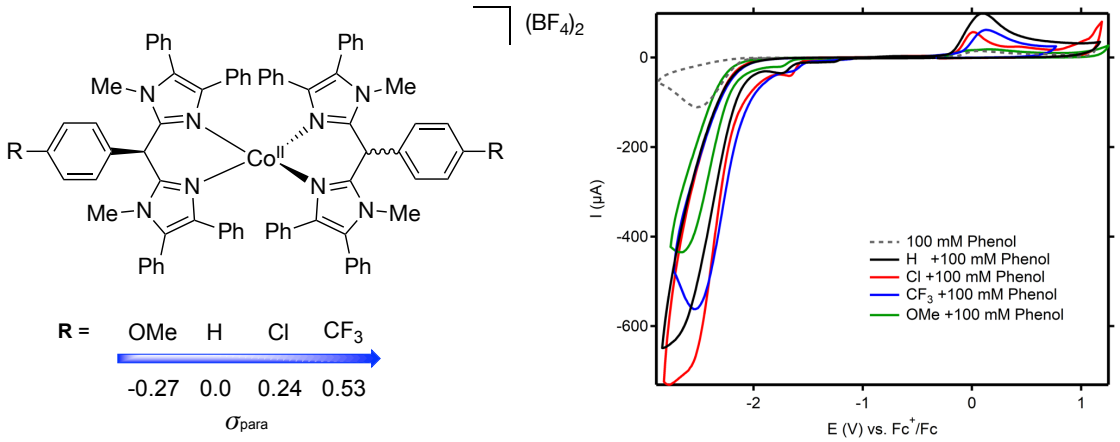

Figuur 1. Links: structuur van de complexen $[Co((H,pArX)BMIM^{Ph_2})_2](BF_4)_2$ (X = H, Cl, CF_3 and, OMe) bestudeerd in **hoofdstuk 2**. Rechts: cyclische voltammogrammen van de complexen (1 mM) in aanwezigheid van 100 mM fenol (gekleurde lijnen) en de lijn met alleen zuur (gestippeld).

bisheterocyclische benzazolylliganden vertegenwoordigen (zie **Figuur 2**). De kleinere sterische belasting van de benzazolylliganden, in vergelijking met de in **hoofdstuk 2** gebruikte difenylmethylimidazolliganden, resulteert in coördinatieflexibiliteit en de vorming van complexen met tetra- of octaëderale geometrieën. De dikationische complexen vertonen een onomkeerbare Co(I/II)-reductie bij verschillende potentialen (spreiding van 600 mV), waaruit een effectieve modulatie van de elektronische eigenschappen van het metaal bij variatie van het hetero-atoom in de benzazoolringen van de liganden blijkt. Een soortgelijke modulatie wordt gevonden voor de redoxreacties in de analoge neutrale complexen. Beide trends bevestigen de door Abbotto *et al*. gerapporteerde elektronische trend voor het π-elektron-zuigend vermogen van de liganden: $BBTM^- > BBZM^- > BBIM^-$. Elektrokatalytische studies toonden aan dat de dicationische complexen $[Co(HBBIM)_2](BF_4)_2$, $[Co(HBBZM)_2](BF_4)_2$, en $[Co(HBBTM)_2](BF_4)_2$ allen elektrokatalysatoren zijn voor de waterstofevolutiereactie bij overpotentialen van respectievelijk 610, 580 en 490 mV. Elektrolysestudies met $[Co(HBBZM)_2](BF_4)_2$ toonden elektrokatalytische H_2-vorming bij een matige Faradaic Efficiency (FE) van 72% en een stroomdichtheid van 2,00 mA/cm^2. Deze studie toont aan dat de redoxeigenschappen van bis(benzazolyl)methaan-afgeleide kobaltcomplexen effectief kunnen worden gemoduleerd door de aard van hun heterocyclen te veranderen en dat de complexen actief zijn als waterstofevolutie-katalysatoren. Het katalytische vermogen van het moleculaire complex $[Co(HBMIM^{Ph2})_2](BF_4)_2$ in DMF op het gebied van waterstofevolutie

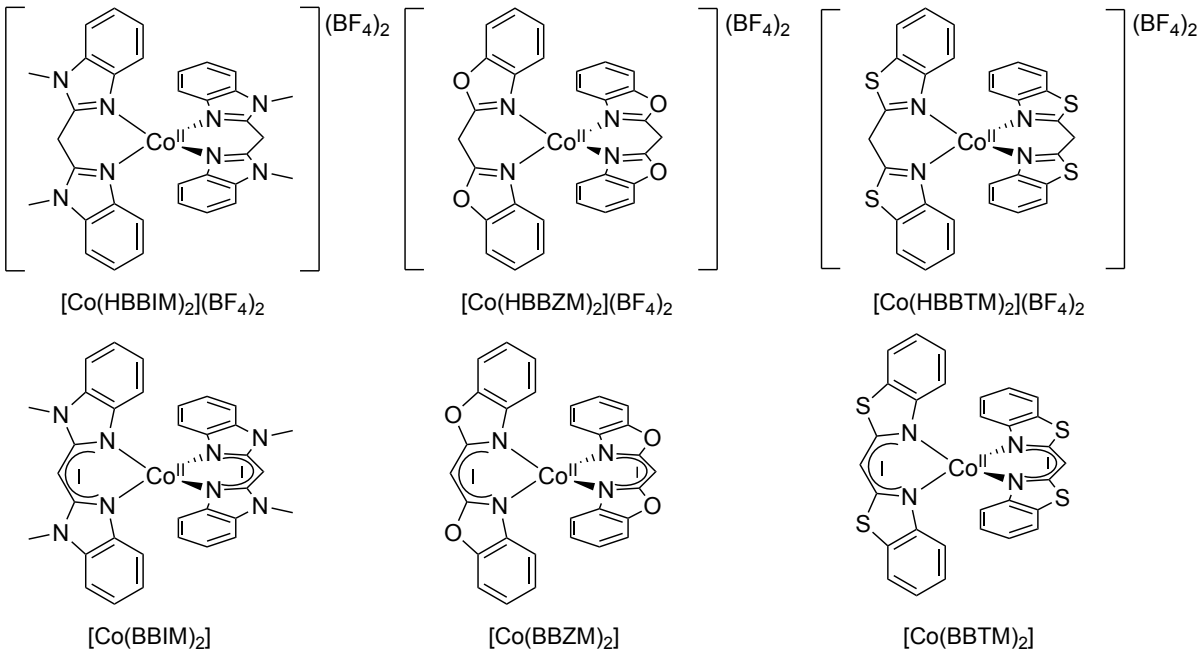

Figuur 2. Overzicht van de in **hoofdstuk 3** bestudeerde kobaltcomplexen met bis(2-benzazolyl)methanaan en bis(2-benzazoyl)methanide liganden.

werd in **hoofdstuk 4** in detail bestudeerd en de activiteit ervan werd vergeleken met die van drie goed bestudeerde elektrokatalysatoren (**Figuur 3**, links). Elektrochemische analyses werden uitgevoerd met voltammetrie en tijdens gecontroleerde potentiaal-/stroomelektrolyse in een nieuwe elektrochemische cel met in lijn product detectie. Elektrolyse-experimenten toonden een competitief katalytische vermogen van $[Co(HBMIM^{Ph2})_2](BF_4)_2$ ten opzichte van de gerapporteerde elektrokatalysatoren in termen van overgedragen lading (**Figuur 3**, rechts), H_2-productie, FE en overpotentiaal. Na bulk elektrolyse werd voor alle complexen een afzetting op de glasachtige koolstofelektrode waargenomen en post-elektrolyse X-ray photoelectron spectroscopy (XPS) analyse van de afzetting gevormd uit $[Co(HBMIM^{Ph2})_2](BF_4)_2$ toonde slechts een kleine kobaltbijdrage (0,23%), voornamelijk bestaande uit Co^{2+}. Een twede experiment met alleen de afzettingen afkomstig van $[Co(HBMIM^{Ph2})_2](BF_4)_2$ of $[Co(dmgBF_2)_2(solv)_2]$ toonden aan dat de aanvankelijk waargenomen activiteit (gedeeltelijk) behouden blijft voor de afzettingen. In het algemeen werd verder inzicht verkregen in waterstofevolutie-katalyse met moleculaire kobaltcomplexen door het aantonen van een belangrijke transformatieweg naar een ander katalytisch actief materiaal, waarbij het moleculaire ontwerp van de complexen de kenmerken van het gevormde neerslag en daarmee de waargenomen activiteit dicteert. **Hoofdstuk 5** beschrijft pogingen om complex ($[Co(HBMIM^{Ph2})_2](BF_4)_2$) zodanig te moduleren dat het in water oplosbaar wordt, om het complex te testen in waterige fotokatalytische waterstofevolutie-katalyse. Daartoe werd een aantal (in water oplosbare) kobaltcomplexen ontwikkeld op basis van bis(imidazool)methaan-type liganden (**Figuur 4**, boven). In coördinerende oplosmiddelen nemen deze complexen octahedrale structuren aan, waarin twee oplosmoleculen *cis*- of *trans*-coördineren met kobalt.

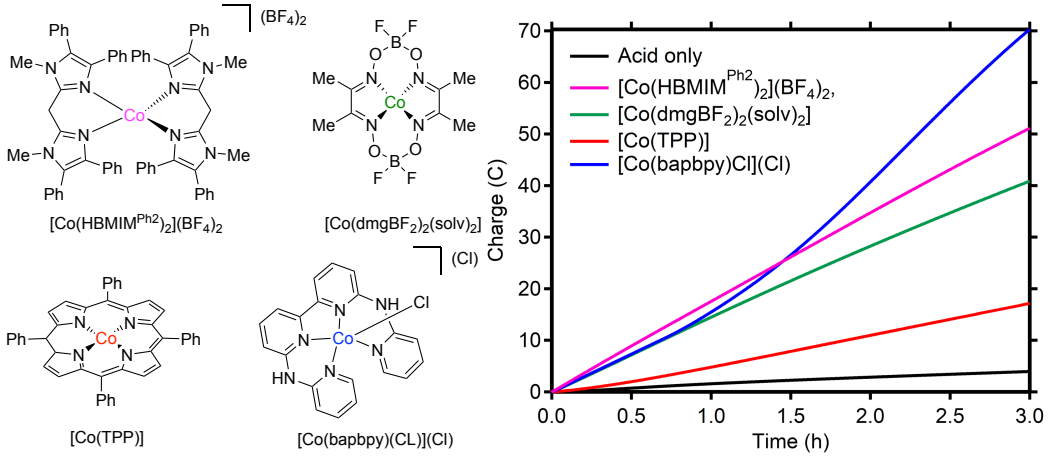

Figuur 3. Links: moleculaire kobaltcomplexen bestudeerd in **hoofdstuk 4**. Rechts: plot van de waterstofevolutie-activiteit van de complexen met behulp van roterende schijf gecontroleerde potentiaal elektrolyse, waarin de stroom is uitgezet tegen de tijd.

De fotokatalytische waterstofevolutie-prestaties van de complexen werden geoptimaliseerd met ascorbinezuur als elektronen- en protonendonor en $[Ru(bpy)_3](PF_6)_2$, bpy = bipyridine, als fotosensitizer. De in water oplosbare complexen $[Co(HBMIM)_2](NO_3)_2$ en $[Co(HBMIA)_2](NO_3)_2$ vertonen de hoogste fotokatalytische activiteit, gevolgd door $[Co(BMIK)_2](NO_3)_2$ (**Figuur 4**, onder). Uit deze waarnemingen blijkt dat de afwisseling van de methyleengroep de fotokatalytische waterstof evolutie snelheid en -stabiliteit beïnvloedt, waarbij minder elektrondonerende liganden complexen opleveren met een lagere beginsnelheid maar een langere levensduur. Benchmarking van de fotokatalytische activiteit van deze complexen toonde een concurrerende prestatie ten opzichte van de metaalprecursor $[Co(H_2O)_6(NO_3)_2]$ en het goed bestudeerde complex $[Co(dmgH)_2PyCl]$, terwijl de complexen worden overtroffen door de beste katalysator in het veld, [Co(appy)Br](Br). Ten slotte biedt hoofdstuk 6 een perspectief op hoe recente vooruitgang in het ontwerp en de karakterisering van moleculaire kobalt waterstofevolutiekatalysatoren kan helpen bij het verenigen van geschikte descriptoren die kunnen worden toegepast in het totale watersplitsingsproces. Daarbij biedt het hoofdstuk een denkkader voor het ontwerpen en beoordelen van verbeterde katalytische kaders voor de waterstofevolutiereactie.

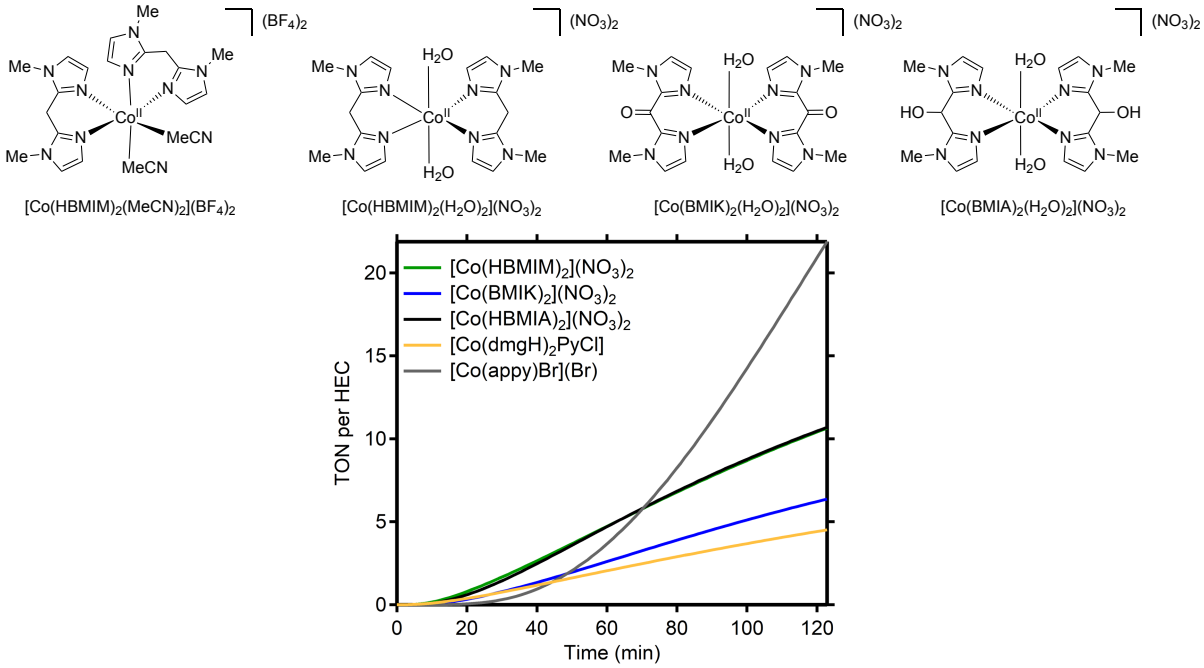

Figuur 4. Boven: kobalt(II)-complexen uit **hoofdstuk 5**. Onder: plot van de waterige fotokatalytische waterstofevolutie-prestaties van nieuwe en gerapporteerde Co-complexen op basis van het cumulatieve TON versus de reactietijd, met $[Ru(bpy)_3(Cl)_2$, als fotosensitizer en AscH als elektronen- en protonenbron.

Tot slot

In de afgelopen jaren is de activiteit van kobaltrijke katalysatoren enorm toegenomen, en kobaltcomplexen blijven een veelbelovende klasse van katalysatoren. Met het toegenomen begrip van op imidazolen gebaseerde moleculaire kobaltcomplexen als waterstofevolutie-katalysatoren en de geoptimaliseerde waterstofevolutie-katalyse waarvan in dit proefschrift verslag wordt gedaan, naast recente voorbeelden in de literatuur, is een volgende stap gezet in het voldoende beheersen van de waterstofevolutiekinetiek, maar verdere vooruitgang is noodzakelijk.

Vanuit een fundamenteel oogpunt zijn we nog maar net begonnen met het begrijpen van het complexe hydrogenase enzymsysteem dat meerdere instelbare proton- en elektronrelais omvat. In dit proefschrift hebben we laten zien hoe ligandmodificaties in de tweede en buitenste coördinatiesfeer van moleculaire complexen bijdragen tot het begrip van elektronen- en protonen overdrachtsprocessen voor H_2-productie. Een bijzondere focus in dit werk was de betrokkenheid van een C–H proton relais tijdens het H_2 bindingsvormingsproces, wat nieuwe inzichten gaf in katalytische parameters zoals overpotentiaal en katalytische snelheid. Veel moleculaire complexen zijn geïnspireerd op de actieve centra van natuurlijke enzymen en leveren hun prestaties buiten de celmembranen. Toch hebben we in dit proefschrift aangetoond dat de activiteit niet gemakkelijk na te bootsen en soms zelfs moeilijk te meten is. In de **hoofdstukken 2** en **3** hebben wij aangetoond dat een effectieve modulatie van de reactiviteit van onze moleculaire complexen op een gecontroleerde manier kan worden bereikt. De modificaties maakten de complexen echter ook kwetsbaar, en elektrolyse studies toonden een geringe stabiliteit aan.

Vanuit het oogpunt van de toegepaste chemie is het begripsniveau en de ontwerpcontrole die haalbaar zijn met moleculaire complexen een uitstekend hulpmiddel om functionaliteiten bloot te leggen die waterstofevolutie kunnen bevorderen in latere, moeilijker te karakteriseren structuren in vaste toestand. Verbetering van de stabiliteit en het omzetgetal tijdens elektrolyse zou voor nog meer vooruitgang kunnen zorgen. Naarmate nieuwe, effectieve strategieën voor moleculaire complexen worden ontwikkeld, wordt het ook steeds belangrijker om de grenzen van deze benaderingen te testen. Uiteindelijk moeten de geleerde lessen worden toegepast in apparaten die langdurig stabiel zijn onder waterige omstandigheden om watersplitsing economisch haalbaar te maken. Tot dusver hebben slechts enkele studies verslag gedaan van de integratie van de verschillende ontwerpbeginselen die hebben geleid tot betere

waterstofevolutie prestaties in moleculaire katalysatoren, in elektroden in vaste vorm voor waterige elektrochemische cellen.

Ten slotte zijn niet alleen de waterstof evolutie reactie maar ook veel kleine molecuul activeringsreacties redoxreacties en daarom kunnen de ontwerpprincipes die elektronenoverdracht in waterstofevolutie-katalyse stimuleren waarschijnlijk ook worden toegepast om mechanismen te bestuderen en de prestaties in andere redoxprocessen te verbeteren. Daarom moet ons huidige onderzoeksdoel het gebruik van kobalt-gebaseerde imidazoolcomplexen niet beperken tot waterstofevolutie. In de toekomst zouden reactanten zoals CO_2 en N_2 ook kunnen worden blootgesteld aan kobaltcomplexen van het bisimidazooltype om zowel de betrokkenheid van het protonrelais als de algemene reductieprestaties van de complexen te bestuderen. Dergelijke experimenten zouden de elementaire stap in katalytische cycli, met name de coördinatie van het substraat en activeringswegen waarbij de C–H protonrelais betrokken is, verder kunnen ophelderen.

Acknowledgments

De afgelopen jaren waren een bijzondere periode voor mij en ik wil graag de mensen bedanken die belangrijk voor mij zijn geweest en hebben bijgedragen aan mijn PhD. Mededankzij jullie kijk ik terug op een mooi avontuur waarin ik enorm veel heb geleerd.

Ten eerste wil ik graag diegene bedanken die het project heeft bedacht, de financiering heeft verkregen en voor deze PhD positie in mij de juiste kandidaat zag om dit onderzoek uit te voeren. **Bert**, bedankt voor het vertrouwen in mij en de prachtige uitdaging die goed bij mij paste; een PhD in een (voor mij) nieuw veld: “de moleculaire elektrochemie/katalyse”. Dit veld was niet alleen nieuw voor mij, maar ook voor onze onderzoeksgroep. De instrumentatie binnen onze vakgroep was aan vernieuwing en uitbreiding toe en ik kreeg van jou de vrijheid, tijd en het vertrouwen om de EChem kamer opnieuw in te richten, een soms spannende maar ook enthousiasmerende uitdaging. Voor het voltooien van mij PhD was het ook belangrijk om goed het onderzoeksveld te definiëren en te leren kennen. Ik heb ontzettend veel interessant en inspirerend werk in de literatuur gelezen, maar een meeting waarin wij de volgende stappen in het project bespraken en concrete doelen formuleerden inspireerde mij het meest en zorgde ervoor dat ik mij weer opgeladen voelde om een project de volgende push te geven. Tijdens mijn projecten hielp jij mij om trouw te blijven aan mijn onderzoeksvragen en mij de juiste richting te wijzen. Ik heb heel veel van je geleerd over systematisch onderzoek doen en het positieve zien in resultaten. Ik wil je bedanken dat voor alle meetings, tijd en discussies. Co-promoter **Danny Broere**, bedankt voor alle input die jij hebt gegeven. Vooral in de eindfase van mijn PhD kon ik rekenen op jouw snelle en constructieve feedback.

De vakgroep organisch chemie en katalyse (**OCC**) heeft mijn een groep fantastische collega’s en vrienden opgeleverd. Vanaf het eerste moment heb ik mij bevoorrecht gevoeld omringt te zijn met een groep intelligente en gemotiveerde pioniers die opzoek waren/zijn naar nieuwe ontdekkingen in de onvoorspelbare, uitdagende en mooie wereld van de chemische wetenschap. En vandaag is dat gevoel niet anders. Ik ben geïnspireerd door jullie toewijding en kennis en wil graag een aantal personen specifiek benoemen.

Master studenten; **Maartje**, bedankt voor al het werk dat je hebt gedaan voor Hoofdstuk 2. Je was/bent een hardwerkende student/PhD, een fijne collega en gezellige vriendin. Tijdens onze wetenschappelijke samenwerking waardeerde ik jouw openheid over de onderzoekresultaten, jouw zorgvuldigheid van werken en de volledigheid van je documentatie. Het lijkt mij nu al ontzettend leuk om straks ook jouw PhD verhalen te lezen. **Sjoerd**, bedankt voor al het werk dat jij hebt verricht voor Hoofdstuk 3, jij hebt grote hobbels gekend tijdens je master thesis maar uiteindelijk keihard gewerkt om je master thesis af te ronden omdat je dit zelf graag wilde en dat waardeer ik enorm. Dit doorzettingsvermogen gaat je zeker in de toekomst ook nog van pas komen. Bachelor studenten; **Lars**, je was altijd leergierig en enthousiast over jouw project en de onderzoeksgroep. Ik vond onze tijd erg leuk en leerzaam en ik wens je heel veel succes met de rest van je PhD. **Koen**, je ben een vrolijke, eerlijke en oprechte student. Je verliest je zelf niet snel in de theorie maar blijft vasthouden aan de concepten die je kent, een nuttig een succesvolle eigenschap. Bedankt voor je tijd en inzet. **Janneke**, wij hebben erg prettig samengewerkt en jij hebt mooie resultaten kunnen verzamelen, maar vooral onze wetenschappelijke discussies gingen altijd erg gemakkelijk omdat jij zo geordend en gestructureerd te werk ging. Bedankt voor een leuke tijd! **Vito**, mister HBMIM, BMIK, of HBMIMP, jij hebt de grondslag gelegd voor de verbindingen in Hoofdstuk 5 en daar ben ik je erg dankbaar voor. Je vliegt in gedachten af en toe van mars naar de maan, maar over onze samenwerking kan ik mij vooral herinneren dat jij erg hard wilde werken op het lab! Succes met je volgende baan! **Lada** & **Nikos** thanks for your extensive literature reports, it was a pleasure to work with you and I learnt a lot about the topic you were investigating. **Erkay**, je hebt een zeer brede interesse en de kwaliteit om mensen aan het lachen te maken. Helaas werkte ons project en samenwerking niet uit op de manier die wij dit voor ogen hadden. Ik wil je graag bedanken voor de tijd en energie die jij in jouw project hebt gestoken. **Brecht**, mijn eerste student. We zijn een leuk avontuur gestart waarin we beide veel moesten leren. Helaas was de wetenschappelijke wereld niet iets waar jij je energie in kwijt kon. Ik wil je graag bedanken voor leuke tijd.

Emily, waar moet ik beginnen met jou! Enorm bedankt voor alles wat je hebt gedaan tijdens mijn PhD. Wij hadden elkaar al snel gevonden op de vakgroep. Onze 1-methyl-4,5-diphenyl-1*H*-imidazole business (€40.000 K/kg) is nog steeds mijn back-up plan. Daarnaast heb ik met jou vele successen, mislukkingen, mentale ups-and-downs en work/PhD life issues kunnen delen. We hebben ook veel gepraat over onderzoeksstrategieën, synthese benaderingen en complex karakteriseringen, dit waardeerde ik altijd! Verder heb je verschillende van mijn thesis

hoofdstukken gelezen, van input voorzien en verbeterd! Door jou is mijn PhD ongetwijfeld een stuk succesvoller geworden. Ook buiten de UU zijn wij goede vrienden geworden, ik ben erg blij dat ik jou zo goed heb leren kennen en ik vind het fantastisch dat juist jij mijn paranimf wil zijn!

Het OCC-personeel: **Marc-Etienne**, **Arnaud**, and **Pieter**, thank you for your scientific input during work discussions and oral presentations. It was a pleasure to work in the same group as you. **Thomas**, **Léon**, **Johann**, en **Stijn** bedankt voor jullie borrels, NMR-kennis, ondersteuning en humor. **Silvia**, een stille kracht in de OCC-groep die altijd klaar staat om te helpen, heel erg bedankt voor je hulp, vooral aan het einde van mijn PhD.
Martin Lutz, jij bent de medewerker buiten de OCC-groep waarmee ik het meest heb samengewerkt. In drie van de vier experimentele hoofdstukken heb ik prachtige kristalstructuren opgenomen. Heel erg bedankt voor deze en andere wetenschappelijke input.

Thanks to former and present OCC members for a wonderful environment: **Eduard**, thank you for the warm welcome in the BKG-group. You were always friendly to me, and I admire your work attitude. **María** thank you for being a nice colleague to me. You are a very dedicated, smart, and successful researcher. **Pamela**, the dancing queen! Thank you for a lot of laughs, funny moments, and dedication to the glovebox. **Pablo**, you are a colleague everyone should wish for. You are always willing to help, give your advice on any topic, and are honest about the things you are less familiar with. It really was a pleasure to work with you. **Fanshi**, what a man you are! I really appreciate you as a friend/colleague. You are so open, warm, and friendly. I have deep respect for the journey you take to secure a healthy life for your family. In the future, I will hopefully have the time to visit you! Papa **Cody**, wat fantastisch dat jij mijn collega bent geweest. Ik heb zo veel met jou gelachen en aan jou gehad gedurende mijn PhD. Bedankt voor al je tijd en aandacht. **Jochem**, de alles kunner! Ik kan me letterlijk geen topic indenken waar jij niet over kan meepraten (oke, misschien alleen elektrochemie), jij bent heel erg breed georiënteerd en wij hebben altijd interessante gesprekken gehad over van alles en nog wat. Ik hoop voor je dat Steinhof nu echt een keer een klapper gaat maken en wens je ook veel succes met het afronden van je PhD. **Roel**, jij bent met afstand één van de meeste geordende en doelgerichte collega's die ik heb gehad. Of je doet heel goed alsof! Je bent een zeer geïnteresseerde all-round onderzoeker en het was ontzettend leuk en leerzaam om jou als college te hebben. **Razvan**, I truly admire your knowledge and working attitude. You are always so professional and dedicated. It was a pleasure to work with you on the lab chief team

and have you as a colleague. **Luke**, you have a serious job, gathering an enormous amount of results but you are still as cheerful as a lad, and that's what makes it so nice to work with you. Thank you for bringing more joy to the group, I am going to miss that! **Joel**, you are a great example of a dedicated scientist who isn't captured by the academic bubble. You can put our work and position easily in a broader societal perspective. But one thing, if you boycott the FIFA World Cup, you cannot know all the final scores by heart! **Stanislav**, my comrade, I really appreciate you as a person. Sometimes it must be challenging for you to find your way in our society, but I barely notice that. Your kindness, humor and sarcasm are outstanding. I remember your answer when I asked for your favorite element. Without a blink of an eye, you pointed to plutonium, haha! **Martine**, in de eerste maanden van mijn PhD was ik wat zoekende, maar toen ik naast jou kwam zitten in de open office ging alles een stuk beter. Jij bent een hardwerkende enthousiaste collega die het belang van de groep en anderen op de eerste plaats zet, een prachtige eigenschap! Ik wens je heel veel succes met het afronden van je PhD! **Jacco**, ouwe rups, wat was het eerlijk om binnen de OCC-groep een lekkere nuchtere vent tegen te komen die mij af en toe kon vertellen dat een PhD ook gewoon een baan is en je hard moet werken maar niet hoeft te proberen bergen te gaan verzetten. We zijn goede vrienden geworden en ik hoop dat we in de toekomst nog vaak koffietjes, biertjes, en spareribs kunnen delen. **Errikos**, mijn Griekse god! Wat een heerlijk mentaliteit heb jij. Jij weet wat je wilt, laat je niet gek maken en helpt iedereen om je heen. Je hebt een voorliefde voor alles wat een mens gelukkig maakt. **Serhii**, in the beginning, I was sitting next to you but didn't understand you at all. You had a very particular working schedule and interests. Later on, we got along very well and these days we always had fruitful conversations about everything we discussed. **Eva**, je bent een vrolijke, hardwerkende PhD met een groot hart voor duurzaamheid. Ik wens je heel veel succes met je PhD, geniet ervan! **Angshuk**, the last member of the BKG group. I certainly have respect for your perseverance as a foreign researcher! Good luck with your PhD! **Sanchari**, you are a cheerful and friendly colleague, it was a pleasure to have you as my office back neighbor! I would also like to thank former/current colleagues **Manuel**, **Jianming**, **Pradip**, **Alessio**, **Jing**, **Charl**, **Tharun**, **Agneev**, **Mou, Fuqiang**, **Bjorn**, **Weizhe**, and numerous former/current students who have come and gone from the OCC over the years: **Sam**, **Sam**, **Raoul**, **Laurens**, **Annemiek**, **Daniël**, **Yuri**, **Elena**, **Yoni**, **Bram**, **Arthur**, **Jelle**, **Jesse**, **Max**, **Tom**, **Alex**, **Thomas**, **Bauke**, **Jasmijn**, **Andrea**, **Kasper**, **Abdullah**, **Luuk**, **Marieke** (erg bedankt voor de proofread van Hoofdstuk 5), **Dylan**, **Floris**, **Lisanne**, **Matthijs, Timo**, **Joshua**, **Rik**, **Rutger** and the gossip girls **Puck**, **Marije**, **Minka**, **Marie**, **Annemijn**, **Eline** and **Anne**.

Bedankt **Matthijs** en **Henk-Jan** (UU-werkplaats) voor het maken van de elektrochemische cellen. Thanks to the wonderful DAC crew, **Silvia**, **Sophie**, **Thomas**, **Pegah,** and **Faranaaz**.

Vrienden uit Deventer: **Florian**, **Jeroen**, **Joost**, **Remi**, **Robert** en **Jop** bedankt voor jullie vriendschap! De meesten van jullie ken ik al meer dan 15 jaar en we maken nog steeds mooie herinneringen! Laten we dit nog heel lang zo volhouden. **Philippe**, sinds jij in Utrecht bent komen wonen is onze vriendschap alleen maar versterkt en dit waardeer ik enorm. Vanaf de eerste rang heb jij de meeste van mijn PhD hobbels meegemaakt en ik wil je graag bedanken voor je tijd en geduld. Ik waardeer het enorm dat jij mijn paranimf wilt zijn. Laten we dit avontuur goed afsluiten en met enthousiasme kijken wat de toekomst brengt!

Exstudiantes 6: **Coen**, **Maarten**, **Zdenko**, **Mike**, **Tom**, **Nathan**, **Jindra**, **Pim**, **Marco** en **Vin** elke week lekker ballen, lachen, en af en toe biertjes drinken. Dit was de afgelopen jaren een heerlijke afleiding van mijn PhD. Het werkstuk is af!

Utrecht (Uranymus/studie) vrienden: **Lars**, **Maarten**, **Paul**, **Atze**, **Tim**, **Tim**, **Marc**, **Tom**, **Shaun**, **Feike**, **Fabio**, **Bastijn**, **Kim** en **Malou** bedankt voor alle studie sessies, warm eten op dinsdag, PhD adviezen, BBQs, 3^{e} Kerstdagen, Nieuwjaars Le clochard diners, koningsdagen, wintersport, dakterrassen, verhuizingen, klusmiddagen en vele borrels.

Lieve **Fenne**, halverwege mijn PhD heb wij elkaar leren kennen en jij bent uiteindelijk een belangrijke sleutel geweest voor het afronden van mijn PhD. Vanaf het eerste moment ben jij zorgzaam, betrokken en geïnteresseerd geweest. Jij hebt mijn lastige PhD periodes meegemaakt en vond altijd manieren om mij te ondersteunen! Ik ben blij dat ik al mijn uitdagingen met jou mocht delen. Laten we samen genieten van een prachtige dag!

Familie: **Arjen**, **Danielle**, **Noah** en **Nanne**, jullie zijn een prachtig gezin en zien er altijd gelukkig uit, bedankt voor jullie interesse, medeleven en support! **Annelien**, je bent een fantastische zus die erg geïnteresseerd is in alles wat er in mijn (PhD)leven gebeurt, bedankt daarvoor. **Sietse**, onze meest recente aanwinst in de familie, leuk dat je erbij bent! **Mama**, je bent een sterke, moedige en enorm zorgzame moeder. Bedankt voor al het vertrouwen dat jij en papa hadden in mijn studiekeuzes en mijn eigenwijze, zelfstandige benadering van mijn leerproces. Hierdoor ben ik geworden wie ik nu ben en daar blijf ik jullie altijd dankbaar voor. Helaas kan papa er niet meer bij zijn, maar ik weet dat hij enorm trots zou zijn geweest!

Popular Science Description

99% of our energy originates from the sun. For millions of years, plants have captured and stored this energy in chemical bonds, converting CO_2 into sugar, that later resulted in fossil fuels. Today, we use these fossil fuels much more rapidly than they were produced causing abrupt changes in our climate that lead to severe weather events and the loss of ecosystems and biodiversity. To reduce climate change (a little bit late!), we aim to replace fossil fuels with sustainable energy carriers that are produced with renewable energy. A promising energy carrier is hydrogen gas, a clean burning fuel that produces water and no greenhouse gas upon combustion. Hydrogen gas can be produced from water with renewable energy, but the chemical bonds in water molecules are extremely strong and the breaking of these bonds causes the loss of an enormous amount of energy (to heat) making it a very inefficient use of our (renewable) energy. Not surprisingly, nature has found a way to bypass the loss of energy by using very complex molecular structures (enzymes) that are efficient in hydrogen production by pushing and pulling on molecules in the right position and with the right amount of power. Most inspiring is that these enzymes are built from earth-abundant elements only. As scientists, we are of course thrilled by this achievement and wish to reproduce the efficiency in the laboratory. In this thesis, we built molecular complexes, “artificial enzymes”, based on abundant elements, with which we aimed to facilitate the production of hydrogen gas. We were able to produce hydrogen gas with a cobalt-based molecular complex in which we incorporated a molecular functionality, a proton (substrate) relay, that facilitates the hydrogen gas-making process. With this achievement, we are a small step closer to understanding the fascinating processes in nature and a small step closer to (but still far from) energy-efficient hydrogen production using earth-abundant elements.

About the Author

Sander Dinand de Vos was born on 6th November 1992 in Deventer, The Netherlands. He completed his school education at the Etty Hillesum Lyceum, Deventer, in 2010 and began his bachelor's in chemistry at the Hogeschool Utrecht - University of Applied Science – that same year. In 2012, he spent 6 months in the industry at PFW Aroma Chemicals (currently named Keva), Barneveld, optimizing a synthesis route for Methoxy Melonal, a melon fragrance. In 2014 he spent 6 months at Stockholm University, preparing homogenous iron catalysts for the C–H oxidation of unactivated hydrocarbons. In 2015, he started the master's program Molecular Design, Synthesis, and Catalysis at the University of Amsterdam. His final master's project, conducted at the University of New South Wales, Sydney Australia, was focused on the utilization of the tropylium cation as an organocatalyst in organic synthesis. After finishing his master's program, he worked at Yokogawa European Solutions, as a life cycle sales engineer for 1 year.

In 2018, he began his Ph.D. under the supervision of Prof. dr. Klein Gebbink in the group of Organic Chemistry and Catalysis (OCC), at Utrecht University. The most important results of this research are presented in this doctoral thesis. The project was financially supported by the Netherlands Organization for Scientific Research within its joint NWO-NSFC program on *Supramolecular Chemistry and Catalysis*. Parts of this thesis have been presented at national and international conferences, including the Conference of Chemistry and Catalysis (NCCC 2020 and 2022, Noordwijkerhout, The Netherlands), Electrochemical Conversion & Materials Conference (ECCM 2020, Apeldoorn), and the Conference of Chemistry As Innovating Science (CHAINS 2021, online).

In 2023, he moved back to the industry to start as Product Manager Bio-based Chemicals at Will&Co in Amsterdam.

List of Publications

Modulation of the Co(I/II) Redox Couple and Electrocatalytic HER Activity of a Molecular Cobalt Complex by the Introduction of para-Aryl Substituents on the Outer Sphere. Sander D. de Vos, Maartje Otten, Lars Killian, Janneke. de Vries, Koen. Pons, Dr. Martin Lutz, Dr. Daniël. L. J. Broere, Prof. Dr. R. J. M. Klein Gebbink, manuscript in preparation (**Chapter 2**).

Hydrogen Evolution Electrocatalysis with a Molecular Cobalt Bis(alkylimidazole)methane Complex in DMF: a Critical Activity Analysis. Sander D. de Vos, Maartje Otten, Tim Wissink, Dr. Ing. Daniël L. J. Broere, Prof. Dr. Emiel J. M. Hensen, Prof. Dr. Robertus J. M. Klein Gebbink, *ChemSusChem* **2022**, 15, e202201308 (**Chapter 4**).

Facile Electrochemical Affinity Measurements of Small and Large Molecules. Pouya Zareea, Ilhan Tomrisa, Sander D. de VosO, Roosmarijn van der Woude, Frits M. Flesch, Robertus J. M. Klein Gebbink, Robert P. de Vries and Roland J. Pieter, *RSC Adv*., **2023**, 13, 9756-9760.

Combining Metal-Metal Cooperativity, Metal-Ligand Cooperativity and Chemical Non-Innocence in Diiron Carbonyl Complexes. Cody B. van Beek, Nicolaas P. van Leest, Martin Lutz, Sander D. de Vos, Prof. Dr. Robertus J. M. Klein Gebbink, Prof. Dr. Bas de Bruin and Dr. Daniel L. J. Broere *Chem. Sci.,* **2022**, 13, 2094–2104.

Electrocatalytic Proton Reduction by a Cobalt Complex Containing a Proton-Responsive Bis(alkylimdazole)methane Ligand: Involvement of a C−H Bond in H_2 Formation. Dr. Pradip Ghosh, Sander de Vos, Dr. Martin Lutz, Dr. Frederic Gloaguen, Prof. Dr. Philippe Schollhammer, Dr. Marc-Etienne Moret, Prof. Dr. Robertus J. M. Klein Gebbink, *Chem. Eur. J.* **2020**, 26, 12560 – 12569.

Tropylium-Promoted Oxidative Functionalization of Tetrahydroisoquinolines. Giulia Oss, Sander D. de Vos, Kevin N. H. Luc, Dr. Jason B. Harper, and Dr. Thanh V. Nguyen, *J. Org. Chem.* **2018**, 83, 1000−1010.

OMSLAG
NTHNRS